A study on the microstructure and high temperature oxidation of Nb-silicide based alloys with Hf and Ge or Al additions and the $NbCr_2$ Laves phase

By Gary E Bywater

Supervisor: Professor Panos Tsakiropoulos

Thesis submitted for the Degree of Doctor of Phillosophy (PhD)

The Department of Materials Science & Engineering,

University of Sheffield

January 2017

This page is intentionally left blank.

This Thesis is lovingly dedicated to my Mum and late Father, thank you both for helping mould me into who I am today. Dad, I miss you ever so much. Mum, I promise to visit you more now that this is finished!

Acknowledgements

Without shadow of doubt I wish to thank the University of Sheffield, Engineering and Physical Sciences Research Council (EPSRC) and Rolls-Royce plc for their hugely appreciated financial support and upmost patience with me. I deeply thank my supervisor Prof Panos Tsakiropoulos for his patience also and for his invaluable assistance and guidance to me throughout my PhD life.

Numerous other academic and technical staff deserve notice for a variety of things that helped facilitate my research; Ms Beverly Lane for the use of thermal analysis equipment (before we finally got our own and thanks for letting us use the room too), Mr Andrew Mould for using his TGA on occasion, Mr Kyle Arnold for alloy heat treatments, Mr Michael Bell for running a tight ship of the sample prep lab, Dr Adrian Leyland for attempts with EB-PVD coatings, Dr Nik Reeves-McLaren for an excellently run XRD lab, Dr Geoff West at the University of Loughborough for stylistic dual beam FIB-SEM training, Dr Christopher Hayward at the University of Edinburgh for calibration and tutelage of EPMA equipment and of course excellent conversation, a shared love of coffee, Korean food and Italian restaurants, Dr Howard Stone of the University of Cambridge for electric arc melting and Dr Mark Ward of the University of Birmingham for plasma arc melting as without your services I'd have had no alloys to work with and been rather scuppered to say the least!

From the the University of Cranfield I thank Dr Christine Chalk, Dr Jeff Rao, Dr Tony Gray and Prof J R Nicholls for the preparation and completion of diffusion coatings on alloy GB2. I must also give them my sincerest apologies due to my inability to dedicate quality time in investigating such coated specimens.

Special mention must be given to Dr Peter Korgul, Dr Cheryl Shaw, Dr Peng Zeng and Dr Le Ma of the University of Sheffield Sorby Centre of microscopy for putting up with my tardiness, cancellations, cheeky SEM session scalping, SEM & TEM training, and out-of-hours sessions (that aren't really allowed and I'll totally deny if in court) that are hugely appreciated.

Much deserved thanks go to Dr Claire Hinchliffe for running a seamlessly organised and well oil machine that is the Advanced Metallics Systems CDT with additional thanks for being so generous to print, bind and hand in my thesis for me!

Related to my PhD life but with stronger connection outside of academics I have numerous others to thank. My dear friends from school-boy-days who are still the most excellent bunch to date; Dr (to be!) Phillip Moxley, Dr Richard Bourne and Mr Patrick Histon for their unrivalled comradery and comedy. My best-men-to-be and PhD colleagues Dr Andre Tweedle (the Golden Child) and Dr Jack Nelson for sharing this PhD journey and bestowing me with their much entertaining personalities.

I thank the infinitely beautiful love of my life, my darling fiancée Samantha Whistler who was incredibly supportive and tolerant throughout my PhD. I vow to repay the attention my PhD had deprived you of me.

Finally I leave the reader with a picture of my beloved cat, Lila, who in my many times of stress and frustration while writing this thesis was on hand to relax and calm me with her much more important and urgent need for tuna.

This page is intentionally left blank.

Abstract

Aspirations for improved gas turbine engine efficiency opens the door for Nb-silicide based alloys to potentially be used as turbine blades in the hottest section of the engines. Such alloys are, however, susceptible to high temperature oxidation and their balance of chemistry and mechanical properties is yet to be optimised for structural application. As oxidation is a particularly big hurdle, this thesis investigates the gap in research on the microstructure and oxidation behaviour at 800, 1000 and 1200°C of high $NbCr_2$ phase fraction Nb-silicide based alloys with Hf and Ge or Al additions.

The alloy compositions investigated in at.% were the Nb-17Si-22Ti-20Cr-2.5Al-9Hf alloy denoted GB1 and the Nb-17.5Si-20Ti-18Cr-5Ge-4Hf alloy denoted GB2. By electric arc casting in an argon atmosphere, both alloys formed as cast microstructures consisting of Nb_5Si_3, $NbCr_2$ and a Ti and Cr rich body centred cubic (bcc) Nb solid solution denoted $(Nb,Ti,Cr)_{ss}$. For both alloys the 5-3 silicide was the primary phase formed with crystal structure strongly influenced by the Hf content of the alloy and synergistic effects with either Ti, Cr, or Ge.

In the case of alloy GB1 with no Ge additions the Hf and Ti synergy strongly stabilised the hexagonal hP16 γNb_5Si_3 structure as the primary silicide, this has been well documented in literature. In alloy GB2, with Ge but less Hf and Ti than GB1, the tetragonal tI32 βNb_5Si_3 structure was stabilised as the primary phase due to Ge and Cr additions. Alloy GB2 also possessed some γNb_5Si_3 which predominantly resided at the bottom of the as cast ingot, minimally present at the centre and top positions. Higher cooling rates at the bottom of the ingot were considered to have induced Ti and Hf partitioning to the melt, resulting in subsequent γNb_5Si_3 formation at interdendritic regions.

After heat treatment at 1300°C for 100h in an argon atmosphere the microstructures were essentially the same with subtle differences. In alloy GB1-HT the small amount of metastable Nb_3Si in the as cast condition had decomposed via eutectoid reaction to $(Nb,Ti,Cr)_{ss}$ and γNb_5Si_3. In alloy GB2-HT the γNb_5Si_3 had become incredibly scarce indicating decomposition had not completed, but most significantly the $\beta Nb_5Si_3 \rightarrow \alpha Nb_5Si_3$ isomorphous structure transformation had occurred that also did not fully complete as βNb_5Si_3 was detected in minor proportion.

Isothermal oxidation testing at 800, 1000 and 1200°C by thermogravimetric method up to 100h was performed on cubed specimens cut from ingots of each alloy. At 800°C for 100h neither alloy degraded by pest and the oxidation behaviours were linear for GB1 and parabolic for GB2 with little surface oxide scale formed, which was identified on both alloys to consist of Ti/Cr niobates and TiO_2. Alloy GB1 suffered weight gain of 0.8 mg/cm^2 whilst GB2 suffered 0.6

mg/cm^2. There was precipitation of micron sized internal phases, likely oxides and/or nitrides, but these were not decisively identified at this temperature.

At 1000°C the specimens were fully covered with oxide scale again identified to be Ti/Cr niobate and TiO_2. The rates of mass gain were linear for GB1 and parabolic for GB2 and gained 5mg/cm^2 and 10mg/cm^2 respectively. Internal precipitation again occurred and were likely similar oxides and/or nitrides as seen at 800°C, but were not conclusively identified at this temperature. As with the 800°C specimens the internal phases had been contaminated by oxygen.

Oxidation testing and analysis at 1200°C for up to 100h covers the majority of oxidation work of this thesis. At this temperature both the as cast and heat treated conditions were tested but for the purpose of brevity the alloys will be referred to generically as the resulting test differences by condition were not remarkable. The behaviours of both alloys and all conditions at 1200°C were parabolic with rate constant of magnitude 10^{-10} $g^2cm^{-4}s^{-1}$, the GB2 specimens, however, showed less overall weight gain and a better adhered slightly thinner oxide scale. Both alloys displayed a layered oxide structure formation, from outer to inner layers they were;

For GB1: TiO_2 || Cr-Niobate || (Ti,Cr)-Niobate$_{coarse}$ + (Niobate + HfO_2 + SiO_2 + $HfSiO_4$)$_{fine}$

For GB2: (Cr,Ti)-Niobate || Niobate$_{coarse}$ + (Niobate + SiO_2 + HfO_2 + $HfSiO_4$)$_{fine}$ ||

(Cr,Ti)-Niobate || Niobate$_{coarse}$ + (Niobate + SiO_2 + HfO_2 + $HfSiO_4$)$_{fine}$ ||

(SiO_2 + $(Nb,Hf)_5Ge_3$)$_{substrate\text{-}oxide}$

The addition of Ge in GB2 was responsible for the formation of a SiO_2 + $(Nb,Hf)_5Ge_3$ layer during oxidation at the substrate-oxide interface and enabled better oxide scale adhesion in comparison to GB1, which possessed a fragile scale that easily spalled when handling the sample.

Internal oxidation of both alloy microstructures was apparent. Precipitates were identified to be HfO_2 and O/N-rich Ti_{ss}, the latter was considered to be a coarser version of the micron sized precipitates found in 800 and 1000°C tests. Although internal Ti oxides and nitrides were not conclusively identified, they are deemed highly probable. Alloys GB1 and GB2 both had significantly better oxidation behaviour at 1200°C than numerous other Nb-silicide alloys reported throughout literature. It was concluded that Cr addition is only beneficial to Nb-silicide alloy oxidation behaviour when a $NbCr_2$ Laves phase volume fraction is formed that is significant enough to result in a disconnected Nb_{ss} architecture. The Laves phase can thereby act as an internal diffusion barrier for the oxygen susceptible Nb_{ss}.

Table of Contents

Introduction

The economic drive for gas turbine engines to run more efficiently and environmentally friendly requires their turbine inlet temperature (TIT) to be pushed even hotter. Alternatively, operation at the same temperatures but without cooling air channels of the turbine blades will eliminate their inherent efficiency loss (Perepezko, 2009).

Currently used Ni-based superalloys set an incredible standard as the most reliable and proven turbine blade material for high temperature engine sections. This is due to their excellent strength, courtesy of the coherent cube-cube orientation between the face centred cubic (FCC) γ-Ni matrix and ordered primitive cubic ($L1_2$) γ'-Ni_3Al phase of their microstructures. Their strength originates from the hindering of dislocation movement, dislocations in γ on the (111) plane with <110> vector must travel in pairs to form and close an anti-phase boundary (APB) in order to penetrate γ'. This is in part due to γ' possessing twice the lattice vector as γ, and the APB formation requiring a substantial energy penalty. Upon yielding, as the APB energy is anisotropic, dislocations in γ' will be encouraged to cross-slip from the (111) to the (001) where the APB is lower. The cross-slipped segements of the dislocation will become stuck in microstrucual locks known as Kear-Wilsdorf locks due to the dislocation residing partly on the (111) and (001) planes. As cross-slipping is also thermally activated, Ni-based superalloys show an anomalous but impressive increase in strength up to 800°C.

For aero engine materials, time at temperature and load is a pertinent topic, arising the issue of creep. Even before failure, in the form of component rupture, the close tolerances required of aero engine turbine blades can result in blades being deemed "failed" on dimensional grounds due to excess in-service creeping. This is yet another categorgy that Ni-based superalloys set an impressive standard for, especially with the advent of single crystal superalloys since the 1980s where grain boundaries are eliminated to afford the best creep properties. Ni-based superalloys do however, require ceramic thermal barrier coatings (TBCs) in conjuction with cooling air channels to create a temperature gradient. Additionally, due to the harsh conditions they require environmental protection, which is satiated by a wide menu of bond coats that are either diffusive or overlay in application. Overall, these substrate-coating systems allow Ni-based superalloys to operate at TITs of ~1450˚C while the alloy substrate surface temperatures are ~1100°C (Reed, 2006).

Yet, even with their impressive liquidus temperatures of up to ~1425°C, Ni-based superalloys can still suffer from incipient melting at ~1270˚C, while their environmental resistant bond coat-substrate interface can melt at temperatures less than ~1250˚C (Bewlay et al., 2003). It is

fair to say they are being pushed to their limits, making the prospect of a new substrate material capable of operation without cooling air channels, or, at temperatures beyond Ni-based superalloys, an incredibly attractive field of research.

Numerous rivalling alloy systems are being investigated to date. Co-based superalloys are a good starting point for discussion since they possess the accompanying "superalloy" label which was generally prescribed to the Ni, Fe-Ni and Co based alloys used above ~540°C. Such commercially used Co-based superalloys are strengthed by carbide precipitates and solid solution alloying additions as opposed to benefitting from a stable coherent precipitation of an ordered γ' phase alike Ni-based superalloys. Unfortunately, these Co-based superalloys are inferior to Ni-superalloys based on stress-rupture strength (Donachie, 2002).

Upon the relatively recent discovery by Sato et al., (2006) of a stable γ'-Co_3(Al,W) phase, coherent within a fcc γ-Co matrix, Co-based superalloys have suddenly jumped in potential as a next generation high temperature material, igniting motivation for further research. Of particular importance, they have been found to display an anomalous strength-temperature behaviour alike Ni-based superalloys, possess solidus and liquidus temperatures up to 1490°C, and show promising strength properties (Suzuki et al., 2007; Suzuki and Pollock, 2008; Pollock et al., 2010). Minimum creep rates have been found comparable to Ni-based superalloy René N4 by Titus et al., (2012), but in general creep data is quite rare and further research is needed on this topic for commercial viability.

Environmentally, Co-based superalloys perform well in hot corrosion conditions courtesy of their Cr content but it is well known that Cr_2O_3 scales cannot be relied upon for oxidation resistance above ~1000°C due to volatilisation issues. Oxidation wise, Co-based superalloys are inferior to Ni-based superalloys making this an area for improving substrate chemistry and developing suitable coatings (Pollock et al., 2010; Yan et al., 2012). A huge issue in this day and age of costly manufacturing, Co is ~6 times more expensive than Ni, and that the world Co reserves are disproportionately located in the Democratic Republic of Congo (Geddes et al., 2010). This does raise economic concerns of using Co.

The class of refractory metal intermetallic composite (RMICs) alloys, however, provides multiple contenders aiming to surpass Ni-based superalloys. Specifically, those based on the Mo-Si, Cr-Ta, Nb-Al and Nb-Si systems, with the latter being the subject of this thesis. The use of such elements are rather obvious choices for high temperature applications based on their rather high melting points of 2623°C for Mo, 1907°C for Cr, 3020°C for Ta, and 2469°C for Nb. These alloys have parallels with Ni-based superalloys; the ductile fcc γ matrix is mimicked by a body centre cubic (bcc) metal solid solution (ss) with intermetallic phases either silicide and/or

Laves acting as a strengthening constituent alike the γ' but lacking the coherent cube-cube orientation of Ni-based superalloys (Perkins and Meier, 1990a; Brady et al., 2000; Perepezko, 2009).

The Cr-Ta alloy microstructures that consist of $TaCr_2$ Laves phase and Cr_{ss}, have been particularly researched by the Oak Ridge National Laboratory. Near eutectic Cr-Fe-Ta alloys with Mo, Ti, Si and La additions have shown remarkable 1000°C tensile yield strengths ranging from 240 – 593 MPa and room temperature fracture toughness up to 21 MPa $m^{1/2}$. Environmentally, oxidation resistance from Cr_2O_3 formation is also remarkable, reporting a maximum weight gain of only 5mg/cm^2 at 1100°C for 11x100h (1100h total) cycles (Brady et al., 2005). As mentioned Cr_2O_3 formation cannot be relied upon above ~1000°C so such Cr-Ta alloys will require environmental coatings. Also, the density of near eutectic Cr-Cr_2Ta alloys is 8.5 – 8.9 g/cm^3. This is similar to that of commercial single crystal Ni-based superalloys, which typically contain very high concentrations of W, Ta, and Re – all very dense elements. In the above example data, Ta was used up to only 8 at.% but it is integral for $TaCr_2$ Laves phase fraction and alloy strength. Optimising alloy density is of paramount importance for this system to be successfully commercialised.

For the Mo-Si alloys, a historic amount of research has been centred around the $MoSi_2$ silicide as a high temperature coating material (Vasudévan and Petrovic, 1992). $MoSi_2$ is particularly attractive due to its formidable melting point of 2030°C and low density of 6.24 g/cm^3 making future engines significantly lighter when compared with 3rd generation Ni-based superalloy CMSX-10 of density 9.05 g/cm^3 (Shah, 1992; Reed, 2006). Research has progressed to more complex Mo-Si alloys with varying additions of Nb, Al, B, Ge, Zr, C and W for use as potential structural substrates as well as to improve environmental behaviour for coating purposes. Despite the general good oxidation behaviour of $MoSi_2$, and still being improved thanks to developments with B additions, pest degredation, high temperature strength, low temperature ductility, creep rate, and fracture toughness are still particular hurdles for Mo-silicide based alloys to over come (Shah, 1992; Mueller et al., 1992a, 1992b; Petrovic, 1995; Majumdar et al., 2008; Heilmaier et al., 2009; Majumdar and Sharma, 2011; Perepezko et al., 2014; Perepezko, 2015).

Nb-Si, or Nb-silicide based alloys, the system of focus in this thesis, are particularly attractive next generation gas turbine materials also due to their low densities of 6.8 - 7.8 g/cm^3 (Li and Tsakiropoulos, 2013) in comparison to 3rd generation Ni-based superalloys, and their high liquidus temperatures up to ~1750°C (Bewlay et al., 2003). This alloy system is currently being researched using a wide variety of alloying additions such as Ti, Cr, Al, Hf, Ge, Mo, Ta, B, Zr, W,

Y, and Sn to name a few (Bewlay and Jackson, 2000; Li and Tsakiropoulos, 2013; Knittel et al., 2014b; Su et al., 2014a; Thomas and Varma, 2015a).

Their strong case for application is from comparable mechanical properties such as the 370MPa 1200°C tensile yield stress of a directionally solidified Nb-silicide based alloy of composition Nb-24.7Ti-16Si-8.2Hf-2Cr-1.9Al (at.%), dubbed "MASC" by researchers at General Electric (GE) (Bewlay and Jackson, 2000). This compares relatively well to CMSX-10 with reported tensile yield strength of ~500MPa at 1100°C (Erickson, 1996). Tensile stress-rupture creep life of the MASC alloy is found similar to 2nd generation single crystal Ni-based superalloys, at 1100°C and 105MPa MASC performed slightly better by 500h, but worse at loads above 105MPa.

Fracture toughness, amongst the other mechanical properties, is where particular improvements are needed for Nb-silicide based alloys to be commercially viable. This is not an issue for Ni-based superalloys as they are inherently tough with K_{1c} ~ 100 MPa $m^{1/2}$. Achieving $K_{1c} \geq 20$ MPa $m^{1/2}$ for Nb-silicide based alloys is proving quite difficult due to their strong but brittle silicide and Laves phase fractions (Mendiratta et al., 1991; Bewlay et al., 1996; Davidson et al., 1996; Chan and Davidson, 2003).

The focal topic of this thesis, the high temperature oxidation resistance of Nb-silicide based alloys, is arguably the biggest barrier to their commercial application (Pint et al., 2006). Their oxidation behaviour is different to Ni-based superalloys due to a relatively high solid solubility of O in the matrix Nb phase. Problems resulting from the dissolved O are embrittlement and internal oxidation. The situation is further complicated by Nb's multiple oxides; NbO, NbO_2 and Nb_2O_5 each having metastable polymorphs and are all porous and non-protective to O diffusion. To make matters worse, Nb-silicide based alloys (similar to Mo-Si) can be susceptible to catastrophic pest degradation, reducing an intermetallic alloy to powder (Westbrook and Wood, 1964). Developing oxidation resistance is of paramount importance for Nb-silicide based alloys to be feasible as a high temperature material.

According to an Ellingham diagram, one could attempt to improve oxidation resistance by utilising an alloying element with a more thermodynamically stable and protective oxide, such as Al, the element with arguably the most dense, stable and protective oxide of Al_2O_3. The work and review by Perkins et al., (1990) sadly voids such idea. Such work outlines the inability of $NbAl_3$ to sustain an exclusive Al_2O_3 scale, resulting in a semi-protective Al_2O_3 + $NbAlO_4$ scale. Binary Nb-Al alloys on the other hand cannot form protective Al_2O_3 in air at 1200°C unless Al content exceeds 75 at.%. Such alloys are Al-based and offer no worthiness as a high temperature material.

More complex Nb-Ti-Al alloys were found to provide the best oxidation results, they included additions of V, Hf, Zr, Cr, Mn, Si intended to reduce the diffusivity and solubility of O in the Nb_{ss} matrix. This was also to no avail, Al content needed to be at least 35 at.% to form Al_2O_3 at 1200°C, where yet again, alloying with so much Al diminishes the high temperature properties of the alloy. This explains why an alloying approach away from Al is deemed necessary for Nb-silicide based alloys.

Numerous additions have been investigated to improve the oxidation resistance of Nb-silicide based alloys, Ti being the most useful as it not only improves oxidation behaviour but enhances fracture toughness of the solid solution by lowering the Peierls-Nabarro barrier energy (Chan and Davidson, 2003). Frustratingly, when alloying is used to improve oxidation resistance it is always to the detriment of another property. For example Al, although 5 at.% addition is found to improve oxidation behaviour, beyond this content there is a significant increase to the ductile to brittle transition temperature (DBTT), and is responsible for promoting the nucleation and propagation of cleavage cracks in Nb-Cr-Ti-Al solid solution alloys for two phase alloys (Davidson and Chan, 1999). Clearly, a tight balancing act is required to improve oxidation resistance while maintaining mechanical properties.

Considering the reliance of Ni-based superalloys on environmental coatings, it is envisaged that Nb-silicide based alloys will also need environmental bond/diffusion coats and ceramic top coats. For coatings, the requirements are focused predominantly on oxidation resistance but there are other issues to resolve. Such as the selection of an appropriate deposition method and its effect on the evolved microstructure, the adhesion between the bond coat and substrate material, the coefficient of thermal expansion (CTE) that should closely match the substrate to avoid spallation during thermal cycling, the type of surface oxide formed, the interface melting point, and the likelihood of inter-diffusion problems.

Clearly there are many issues to consider when coating a new alloy system. First and foremost, a composition providing good oxidation resistance needs to be found and the oxidation behaviour understood. The aim of this PhD research was to study the high temperature oxidation of Nb-silicide alloys with a high Cr content and expectedly with a high phase fraction of the $NbCr_2$ Laves phase in the microstructure. The objective was to study the effect of Laves phase containing microstructures with different metalloid/metal alloying additions Ge, Al, and Hf on microstructure, phase stability, and the oxidation performance and products at 800, 1000, and 1200°C with the latter temperature being of most interest.

This thesis will begin with a literature review firstly considering the phase equilibria of alloying elements and chemistry relevant to the alloys investigated. Secondly the oxidation review will outline the individual oxidation behaviour of key alloying elements Nb, Ti, Si, Cr, and will discuss the reported oxidation behaviours of Nb-silicide based alloys of varying alloy chemistry. The experimental procedure, results and discussion will follow. The thesis will penultimately finish with the reiteration of conclusions, ending with an outlook on the research topic and suggestions for future work.

1 Literature Review: Phase Equilibria

1.1 The Nb-Si system

Seven phases are stable within the Nb-Si system, as reported through the work of Schlesinger et al., (1993) and Okamoto (2005), namely:

1. Liquid (L),
2. Terminal bcc solid solution Nb_{ss},
3. Tetragonal Ti_3P prototype Nb_3Si,
4. Tetragonal W_5Si_3 prototype βNb_5Si_3,
5. Tetragonal Cr_5B_3 prototype αNb_5Si_3,
6. Hexagonal $NbSi_2$,
7. Diamond cubic Si_{ss}.

The Nb-Si binary phase diagram is presented in Figure 1. Table 1 and Table 2 give the crystal structure data and various phase transformations in the system. Differences between the temperature of transformation in Figure 1 and Table 2 are indicative of the minor disagreement about the Nb-Si binary phase equilibria. In this system Si is soluble in Nb up to 3.5 at.% at the eutectic temperature of 1915°C, while Nb is insoluble in Si. Considering the silicides, Nb_5Si_3 is of particular interest as it exists in the forms α, β, and γ (Figure 2). The former two are both tetragonal and isomorphous with tI32 crystal structure but they possess different lattice parameters (Table 1). The γ form is the metastable hexagonal γNb_5Si_3 with hP16 crystal structure (Schachner et al., 1954) that is stabilised by interstitial impurities and by alloying with Ti and Hf (Alyamovskii et al., 1962). The γNb_5Si_3 silicide is detrimental to creep performance due to basal slip in hexagonal crystal systems (Bewlay et al., 2003; Bewlay and Jackson, 2000). The αNb_5Si_3 silicide forms after the decomposition of Nb_3Si via the eutectoid reaction $Nb_3Si \rightarrow Nb_{ss} + \alpha Nb_5Si_3$ at 1765°C or via peritectoid reaction in a hypereutectic alloy at 1935°C; $Nb_3Si + \beta Nb_5Si_3 \rightarrow \alpha Nb_5Si_3$.

Whether Nb-silicide based alloys will operate at the same temperature as current Ni-based superalloys without cooling air channels to offset inefficiency or they will operate at higher temperatures with cooling air, in either case the alloys are envisaged to operate below temperatures where the Nb_3Si phase field is stable, making them Nb_{ss} + Nb_5Si_3 alloys. Commonly, Nb-silicide based alloys solidify with Nb_3Si and βNb_5Si_3 (Balsone et al., 2001), which are not the equilibrium phases at room temperature. Operation of alloys at potential use TITs

will effectively be a heat treatment, inducing decomposition reactions such as $Nb_3Si \rightarrow Nb_{ss} + \alpha Nb_5Si_3$ and $\beta Nb_5Si_3 \rightarrow \alpha Nb_5Si_3 + NbSi_2$ (Mendiratta and Dimiduk, 1991). Such in-service changes are undesireable as they will have a knock on effect to mechanical and probably oxidation behaviour of the alloys. Therefore, thermally stable alloys are needed for potential use.

In Nb-silicide based alloys, the ductility is provided by the Nb_{ss} whilst the high temperature strength and creep resistance are provided by the silicide phases. However, the hexagonal γNb_5Si_3 is undesirable. Additions of Ti and Hf to Nb-silicide based alloys have been found to improve oxidation behaviour, but their excess addition can stabilise γNb_5Si_3 (Bewlay and Jackson, 2000). The Ti and Hf effects will be discussed in the Nb-Si-Ti and Nb-Si-Hf systems and when considering oxidation behaviour.

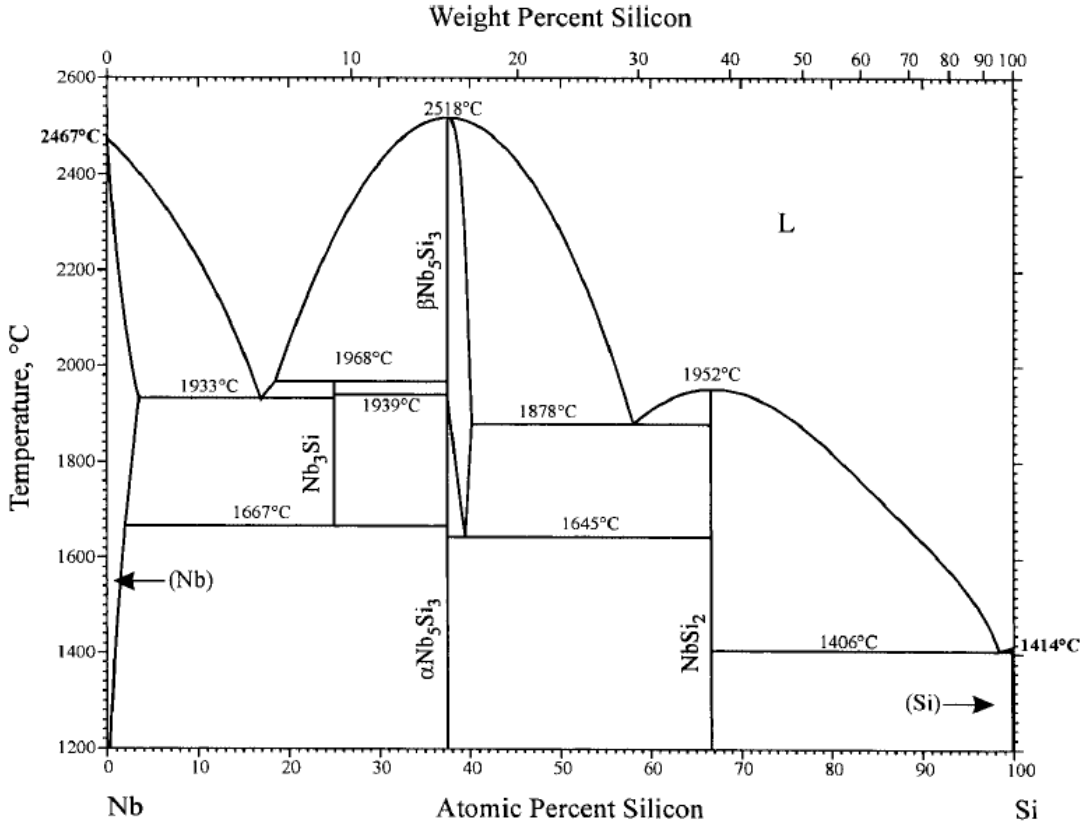

Figure 1. The Nb-Si phase diagram reported by Okamoto (2005).

Table 1. Crystal structure data of the Nb-Si system (Villars and Calvert, 1991; Schlesinger et al., 1993).

Phase	Temp. Range (°C)	Pearson symbol, Space group	Structure Type, Prototype	Lattice parameter (Å)			
				a	b	c	γ
Nb	< 2467	cI2, $Im\bar{3}m$	A2, W	3.307	-	-	-
Si	<1414	cF8, $Fd\bar{3}m$	A4, C	5.431	-	-	-
Nb_3Si	1765- 1975	tP32, $P4_2/n$	Ti_3P	10.22	-	5.189	-
βNb_5Si_3	> 1935	tI32, I4/mcm	$D8_m$, W_5Si_3	10.04	-	5.081	-
αNb_5Si_3	< 1935	tI32, I4/mcm	$D8_1$, Cr_5Si_3	6.571	-	11.89	-
γNb_5Si_3		hP16, $P6_3/mcm$	$D8_8$, Mn_5Si_3	7.52	-	5.23	-
$NbSi_2$	< 1935	hP9, $P6_222$	C40, $CrSi_2$	4.81	-	6.61	120°

Table 2. Reactions of the Nb-Si phase diagram (Schlesinger et al., 1993).

Reaction	Si Composition of the respective phases (at.%)			T (°C)	Reaction type
L ←→ Nb_{ss}		0		2467	Melting
L ←→ Nb_{ss} + Nb_3Si	17.5	3.5	25	1915	Eutectic
L + βNb_5Si_3 ←→ Nb_3Si	19.5	37.5	25	1975	Peritectic
Nb_3Si ←→ Nb_{ss} + αNb_5Si_3	25	1.6	35.5	1765	Eutectoid
L ←→ βNb_5Si_3		37.5		2515	Melting
Nb_3Si + βNb_5Si_3 ←→ αNb_5Si_3	25	37.5	37.5	1935	Peritectoid
βNb_5Si_3 ←→ αNb_5Si_3+ $NbSi_2$	39.5	38.5	66.7	1645	Eutectoid
L ←→ βNb_5Si_3 + $NbSi_2$	57	40.5	66.7	1895	Eutectic
L ←→ $NbSi_2$		66.7		1935	Melting
L←→ $NbSi_2$ + Si_{ss}	98	68.8	100	1395	Eutectic
L ←→ Si_{ss}		100		1414	Melting

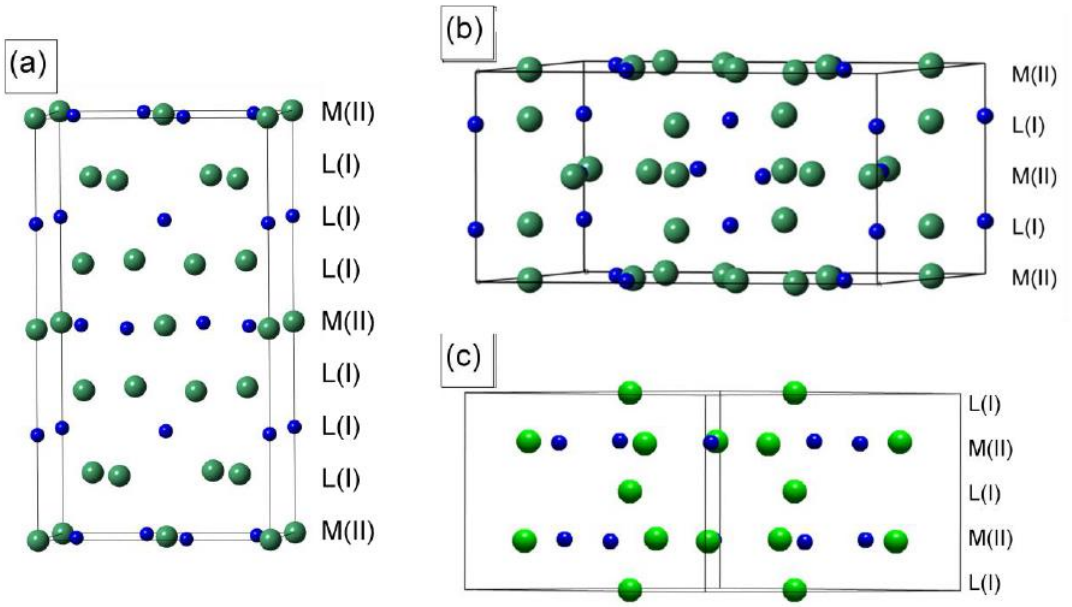

Figure 2. Crystal structures of (a) α, (b) β, and (c) γ Nb_5Si_3. The large green spheres represent Nb atoms while the smaller blue spheres represent Si atoms (Chen et al., 2007).

1.2 The Nb-Ti system

Ti is a major alloying element in Nb-silicide based alloys, improving oxidation resistance and room temperature fracture toughness (Bewlay and Jackson, 2000; Chan, 2002). The Nb-Ti binary phase diagram is shown in Figure 3. No compounds form in the Nb-Ti system. The stable phases are the bcc $\beta(Ti,Nb)_{ss}$, with Pearson symbol cI2 and space group $Im\bar{3}m$, where Nb and Ti are completely miscible above 882°C. Below 882°C the hcp $\alpha(Ti,Nb)_{ss}$ is the other stable solid solution, with Pearson symbol hP2 and space group $P6_3/mmc$, where Nb is soluble up to ~2.5 at.%, beyond this a two phase field of $\alpha(Ti,Nb)_{ss}$ + $\beta(Ti, Nb)_{ss}$ exists.

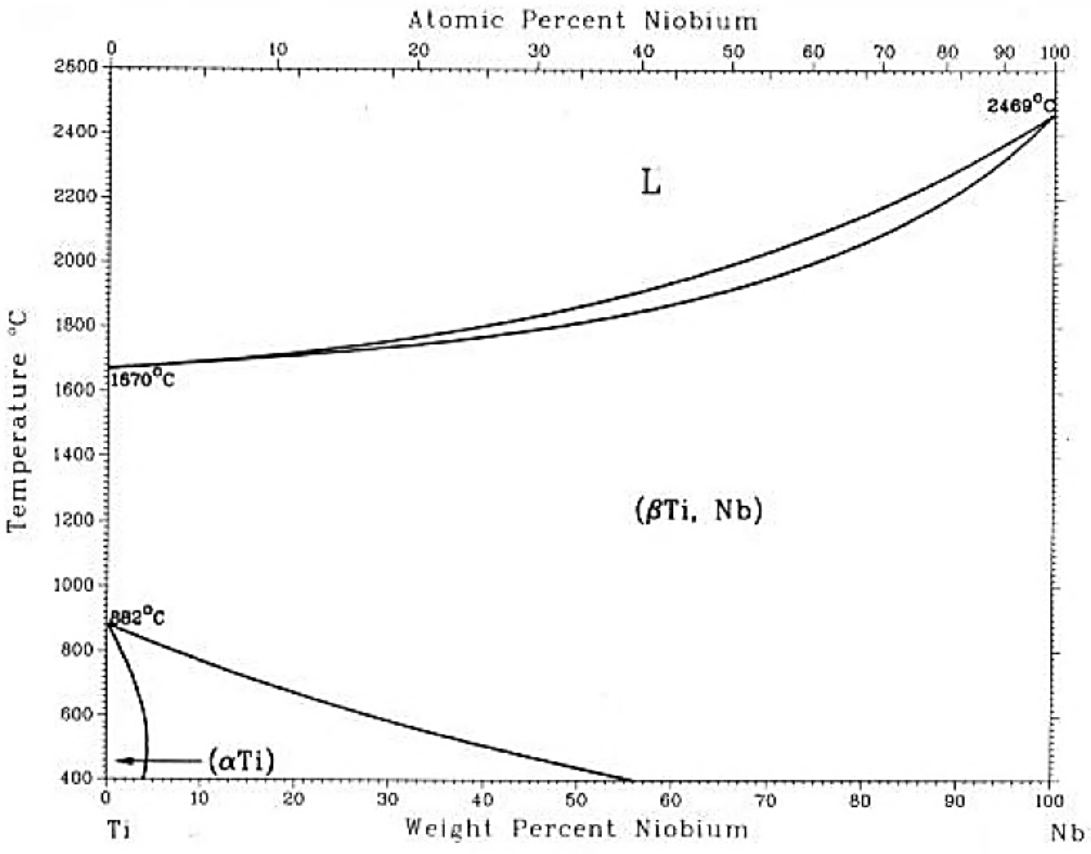

Figure 3. The Nb-Ti binary phase diagram (Murray, 1987a).

1.3 The Ti-Si system

The Ti-Si system is shown in Figure 4 is very similar to the Nb-Si system. The phases of this system are:

1. Liquid (L),
2. Terminal bcc solid solution (βTi),
3. Terminal hcp solid solution (αTi),
4. Tetragonal Ti_3Si,
5. Hexagonal Ti_5Si_3,
6. Tetragonal Ti_5Si_4,
7. Stoichiometric TiSi,
8. Stoichiometric $TiSi_2$,
9. Diamond cubic Si_{ss}.

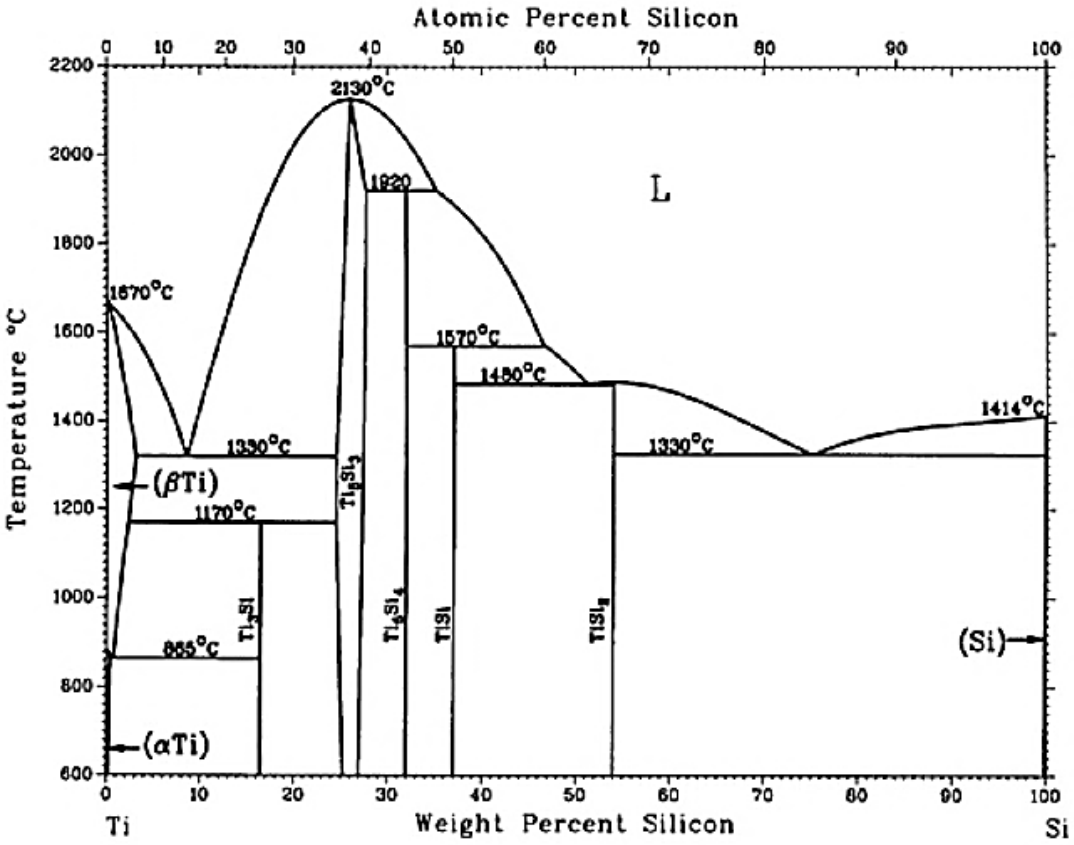

Figure 4. The TI-Si binary phase diagram (Murray, 1987b).

The crystal structure data of the Ti-Si system are given in Table 3 and the phase reactions in Table 4. It is important to note that Ti_3Si and Nb_3Si are isomorphous with tP32 crystal structures. Ti_3Si is stable to temperatures < 1170°C, which is much lower in comparison to Nb_3Si, which is stable between 1770 – 1880°C. Hence, Ti addition in the Nb-Si system stabilises Nb_3Si to lower temperatures (Bewlay et al., 1997, 1998; Subramanian et al., 1994; Zelenitsas and Tsakiropoulos, 2005, 2006a). The Ti_5Si_3 is only isomorphous with γNb_5Si_3 as they both possess hP16 crystal structures.

Table 3. Crystal structure data of the Ti-Si system (Murray, 1987b).

Phase	Si Comp. (at.%)	Pearson symbol, Space Group	Structure Type, Prototype	Lattice Parameter (Å)			
				a	b	c	γ°
αTi	0 - 0.5	hP2, $P6_3/mmc$	A3, Mg	2.9486	-	4.67	120
βTi	0 – 3.5	cI2, $Im\bar{3}m$	A2, W	3.33	-	-	90
Si	100	cF8, $Fd\bar{3}m$	A4, C	5.4309	-	-	90
Ti_3Si	25	tP32, $P4_2/n$	-, Ti_3P	10.206	-	5.069	90
Ti_5Si_3	35.5 – 39.5	hP16, $P6_3/mmc$	$D8_8$, Mn_5Si_3	7.461	-	5.1508	120
Ti_5Si_4	44.4	tP36, $P4_12_12$	-, Zr_5Si_4	6.702	-	12.174	90
TiSi	50	oP8, Pnma	B24, BFe	6.5383	3.6413	0.5002	90
$TiSi_2$	66.7	oF24, Fddd	C54, $TiSi_2$	4.8	8.2671	8.5505	90

Table 4. Phase reactions of the Ti-Si binary system (Murray, 1987b).

Reaction	Composition of the phases in at% Si			Temp. (°C)	Reaction Type
$\beta Ti_{ss} \rightarrow \alpha Ti_{ss} + Ti_3Si$	1.1	0.5	25	865	Eutectoid
$\beta Ti_{ss} + Ti_5Si_3 \rightarrow Ti_3Si$	3.5	37.5	25	1170	Peritectoid
$L \rightarrow \beta Ti_{ss} + Ti_5Si_3$	13.5	4.7	37.5	1330	Eutectic
$L \rightarrow Ti_5Si_3$		37.5		2130	Congruent
$L + Ti_5Si_3 \rightarrow Ti_5Si_4$	48.1	37.5	44.4	1920	Peritectic
$L + Ti_5Si_4 \rightarrow TiSi$	60	44.4	50	1570	Peritectic
$L \rightarrow TiSi + TiSi_2$	64.2	50	66.7	1480	Eutectic
$L \rightarrow TiSi_2$		66.7		1500	Congruent
$L \rightarrow TiSi_2 + Si_{ss}$	83.8	66.7	100	1330	Eutectic
$L \rightarrow \beta Ti_{ss}$		0		1670	Melting
$\beta Ti_{ss} \rightarrow \alpha Ti_{ss}$		0		882	Allotropic
$L \rightarrow Si_{ss}$		100		1414	Melting

1.4 The Nb-Si-Ti system

This system has been investigated by numerous authors (Bewlay et al., 1998, 1997, 1994; Subramanian et al., 1994; Zhao et al., 2001b, 2004a). Ti, although a key element for increasing room temperature fracture toughness and oxidation resistance (Bewlay and Jackson, 2000; Bewlay et al., 2001, 2002a, 2002b; Chan, 2005; Zelenitsas and Tsakiropoulos, 2005), reduces alloy melting point and stabilises hexagonal γNb_5Si_3 and/or Ti_5Si_3, which are detrimental to creep performance (Bewlay et al., 1996).

The works of Zhao et al. (2004), Bewlay et al. (1997, 1998), and Subramanian et al. (1994) all observed the same $Nb_5Si_3 + Ti_5Si_3 + Ti_3Si$ and $Nb_5Si_3 + Ti_3Si + (Nb,Ti)_{ss}$ three phase equilibria. The isothermal section at 1200°C by Zhao et al., (2004) is shown in Figure 5 and a 3-D Nb-Si-Ti schematic phase diagram in Figure 6. The figures show Nb_3Si and Ti_3Si are isomorphous and that Ti stabilises the Nb_3Si to lower temperatures as a eutectic groove extends from the Nb-Si eutectic to the Ti-Si eutectic (Figure 6).

In Figure 5 and Figure 6 is a pseudo binary system between βNb_5Si_3 and Ti_5Si_3 where Ti is soluble within βNb_5Si_3 up to ~ 28 at.%, beyond this a two phase field exists and beyond ~ 41 at.% Ti the single Ti_5Si_3 phase field is reached, where Nb will be retained in solution. The authors Bewlay et al., (1997) and Zhao et al., (2004a), however, do not mention stabilisation of hexagonal γNb_5Si_3 nor do they discuss the stabilisation of such allotrope with Ti addition, which should be expected as γNb_5Si_3 and Ti_5Si_3 both have the same hP16 crystal structure with very similar lattice parameters. It can only be inferred that the above researchers have used the Ti_5Si_3 phase to encompass the hexagonal $\gamma(Nb,Ti)_5Si_3$ allotrope. In order to avoid the hexagonal silicide and to retain a eutectic temperature above 1700°C, Ti additions in Nb-silicide based alloys should not exceed 25 at.% (Chan, 2002). However, for alloys including Hf the Ti addition should be kept below 21 at.% (Bewlay et al., 1999) as Hf also stabilises the γNb_5Si_3.

There are two key solidification reactions at the metal rich end of the Nb-Si-Ti system (Bewlay et al., 1997, 1998) that are worth mentioning. As outlined in Figure 7, the peritectic ridges of the reactions p1 ($L + (Nb,Ti)_5Si_3 \rightarrow (Ti,Nb)_5Si_3$) and p2 ($L + Nb_5Si_3 \rightarrow Nb_3Si$) intersect one another, as displayed in the partial liquidus projection of Figure 8, to result in reaction U1 at approximately 1600 – 1650°C;

$$U1: \quad L + (Nb,Ti)_5Si_3 \rightarrow (Nb,Ti)_3Si + (Ti,Nb)_5Si_3$$

Note that U1 occurs at high Si concentration of alloy composition Nb-66Ti-19Si. At lower Si content of alloy composition Nb-76Ti-13.5Si the peritectic ridge that descends from transition

reaction U1 now intersects the eutectic groove between the e1 (L → Nb + Nb_3Si) and e2 (L → Ti + Ti_5Si_3) binary eutectics to result in a second transformation reaction U2 at ~ 1350°C;

$$U2: \quad L + (Nb,Ti)_3Si \rightarrow (Nb,Ti,Si)_{ss} + (Ti,Nb)_5Si_3$$

To reiterate, the core findings of the Nb-Si-Ti system are:

1. Ti addition reduces the melting point of Nb-Si alloys,
2. Ti_3Si and Nb_3Si are isomorphous,
3. Ti addition extends the Nb_3Si phase field to lower temperatures,
4. Only γNb_5Si_3 and Ti_5Si_3 are isomorphous with hP16 crystal structures,
5. There is high solubility of Ti in the Nb_5Si_3,
6. Titanium promotes the formation of γNb_5Si_3.

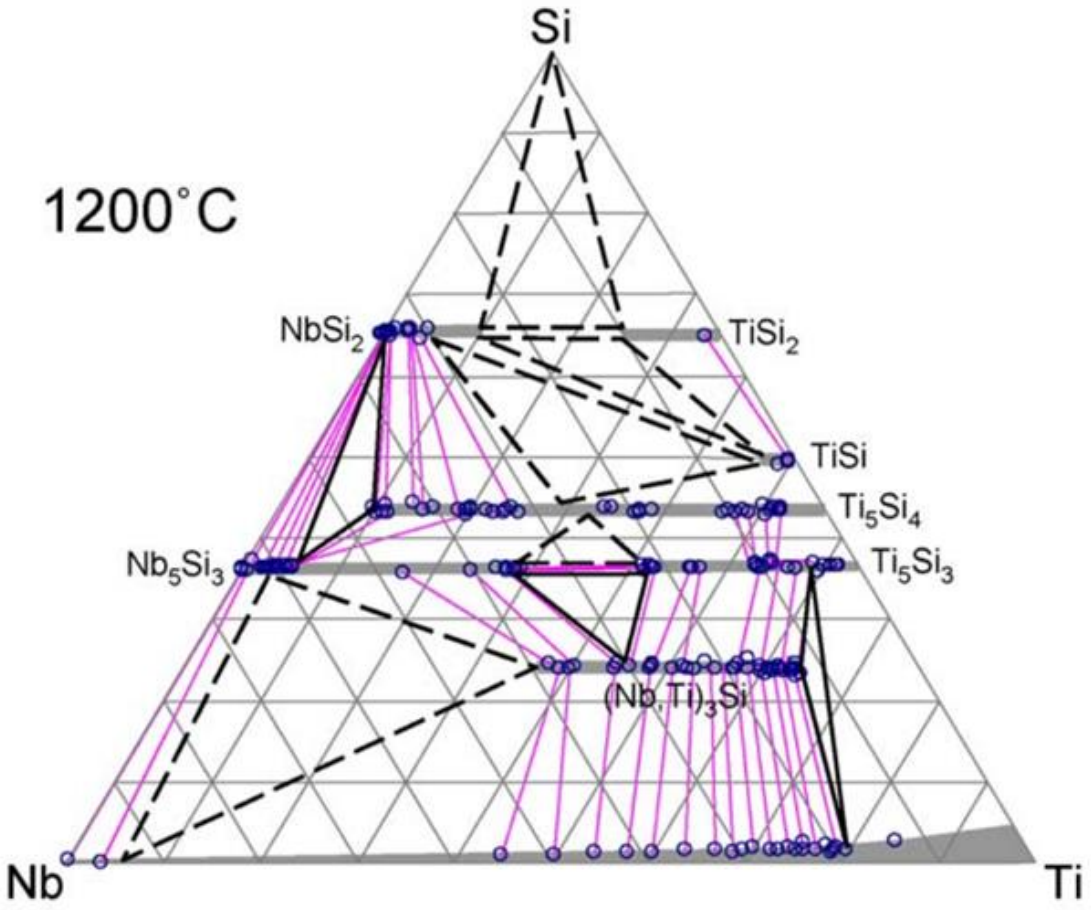

Figure 5. Isothermal section at 1200°C of the Nb-Si-Ti system. The axes are plotted in at.% and were removed for simplicity. The solid triangles indicate well-defined three-phase fields and the open circles show the tie-line compositions. The tie-lines are shown with light lines. The heavy dashed tie-triangles were estimated three-phase equilibria (Zhao et al., 2004a).

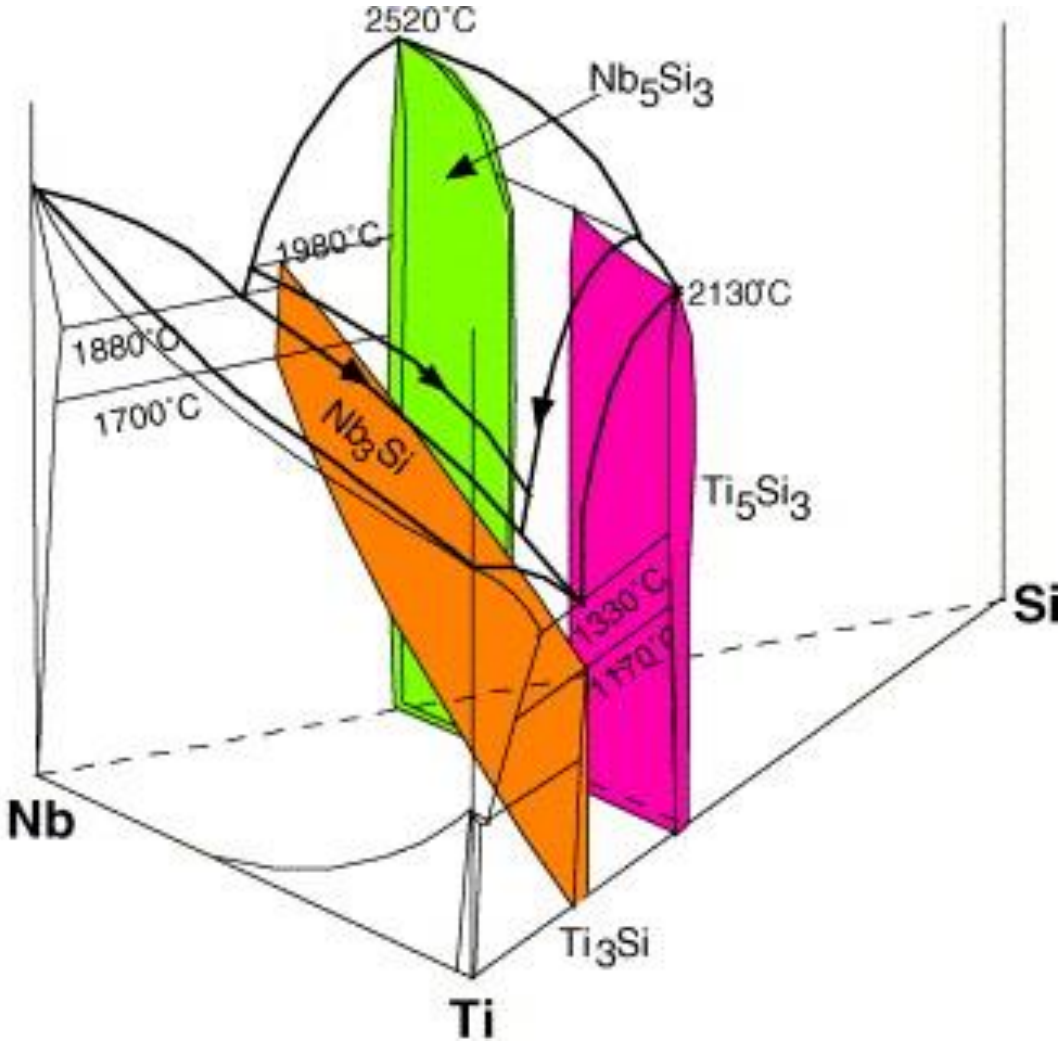

Figure 6. Schematic 3D phase diagram of the Nb-Si-Ti ternary system with Si up to 37.5 at.% (Zhao et al., 2004a).

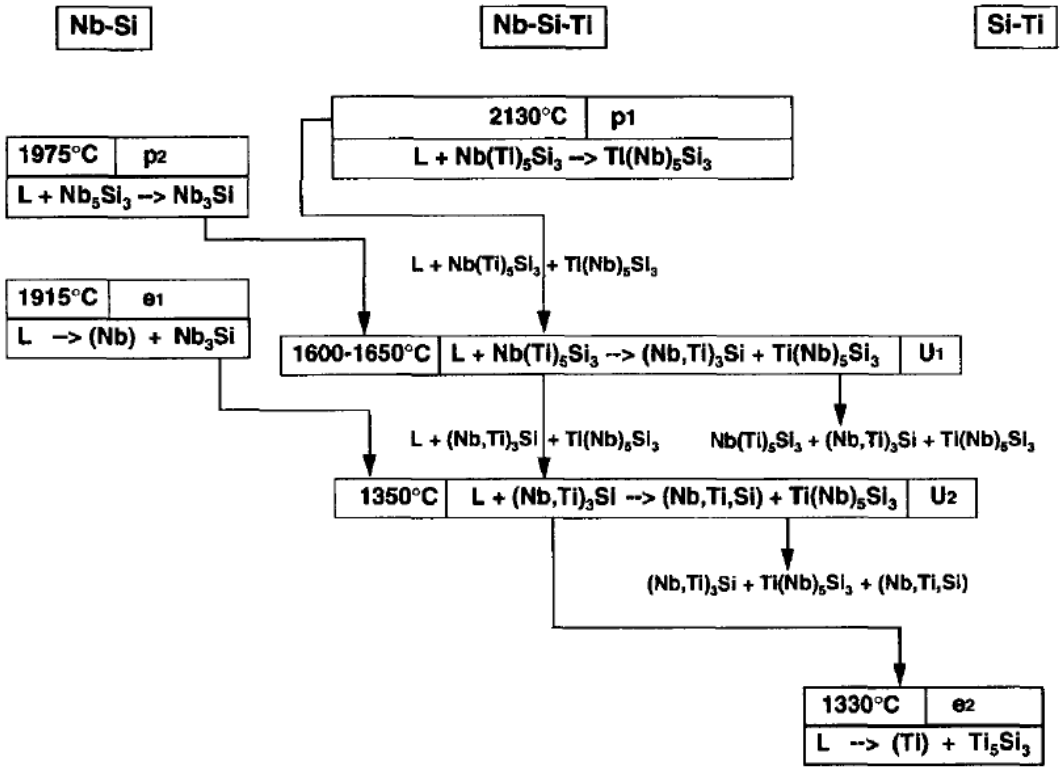

Figure 7. Partial Scheil reaction scheme for the proposed transformation reactions of the Nb-Si-Ti system (Bewlay et al., 1997).

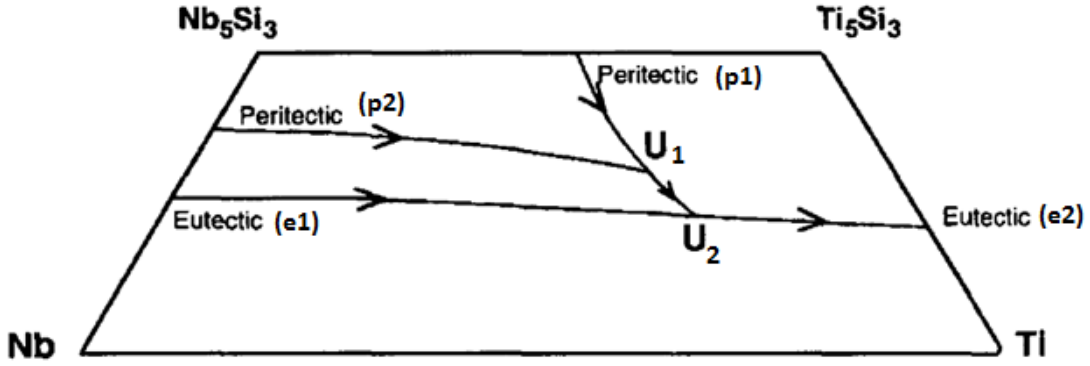

Figure 8. Partial liquidus projection of the Nb-Si-Ti system outlining the intersection of peritectic reactions between Nb_5Si_3 and Ti_5Si_3.

1.5 The Nb-Cr system

The phases which exist in the Nb-Cr system (Figure 9) are;

1. Liquid (L),
2. bcc Nb_{ss},
3. bcc Cr_{ss},
4. High temperature (HT) hexagonal C14 $NbCr_2$ Laves phase,
5. Low temperature (LT) cubic C15 $NbCr_2$ Laves phase,

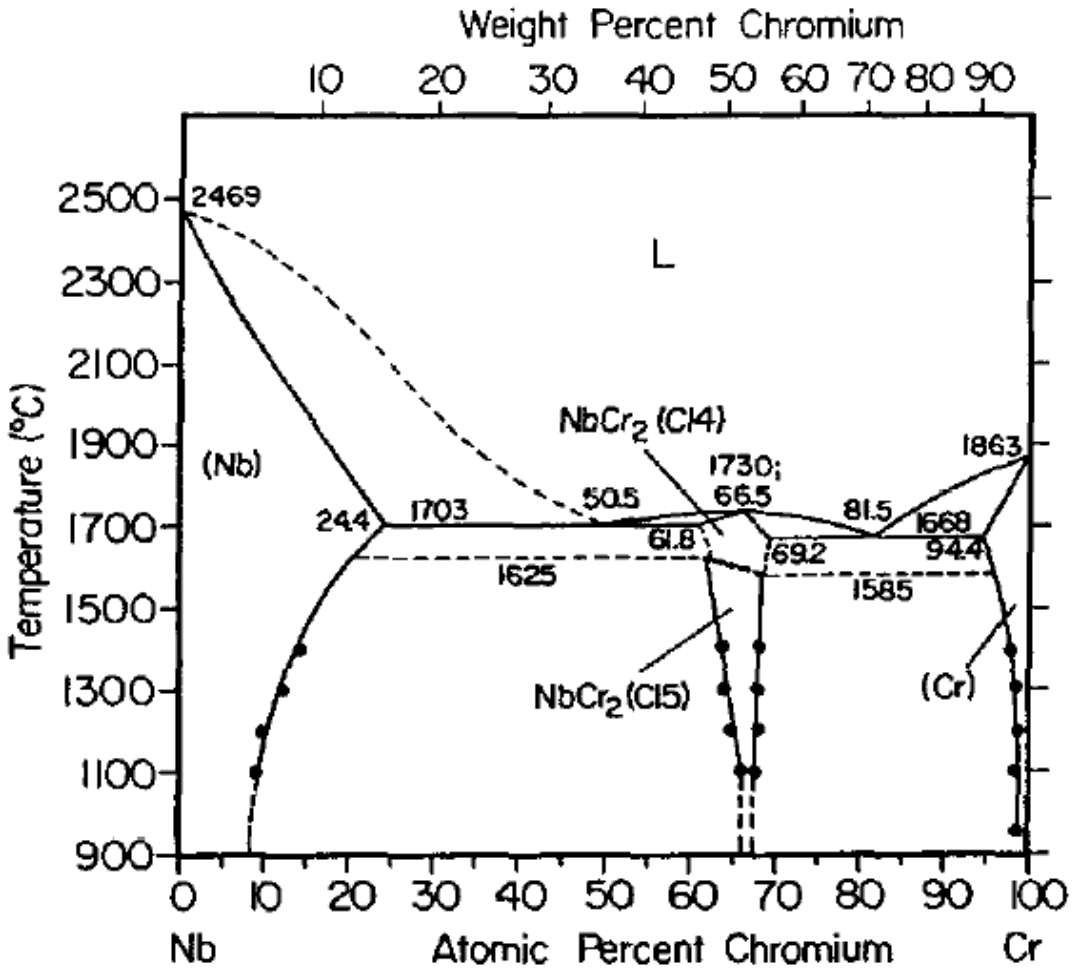

Figure 9. The Nb-Cr binary phase diagram by Thoma and Perepezko (1992).

There are two eutectics in this system involving the HT C14 $NbCr_2$ Laves phase and the terminal solid solutions:

- The L → C14 $NbCr_2$ + Cr_{ss} eutectic occurs at ~ 1668°C with ~12.5 at.% Nb.
- The L → C14 $NbCr_2$ + Nb_{ss} eutectic occurs at ~ 1703°C with ~49.5 at.% Nb.

The main features of this system are well agreed upon by researchers and are primarily based on the work by Goldschmidt and Brand (1961a, 1961b). There are, however, considerable differences as to the locations of the exact phase boundaries compared with the work of Thoma and Perepezko (1992) who published the phase diagram in Figure 9. These authors also presented XRD data of heat treated arc-cast specimens as evidence for the existence of a metastable di-hexagonal C36 $NbCr_2$ crystal structure, formed during the transformation of C14 → C15. The C36 Laves structure is well known amongst Laves phases but due to the limited data in such works a phase field for C36 $NbCr_2$ could not be included in their Nb-Cr diagram. Their phase diagram is a modification of the phase diagram proposed by Venkatraman and Neumann (1986). Crystal structure information of the phases in this system are given in Table 5 and Table 6.

Table 5. Crystal structure types of the phases within the Nb-Cr system (Venkatraman and Neumann, 1986).

Phase	at.% Nb	Pearson Symbol	Space group	Structure designation	Prototype
Cr_{ss}	0 – 6	cI2	Im3m	A2	W
$NbCr_2$ (HT)	30 – 39	hP12	$P6_3/mmc$	C14	$MgZn_2$
$NbCr_2$ (LT)	30 – 39	cF24	Fd3m	C15	$MgCu_2$
Nb_{ss}	85 – 100	cI2	Im3m	A2	W

Table 6. Temperature range and lattice parameters of phases in the Nb-Cr system (Villars and Calvert, 1991).

Phase	Temperature range°C	Lattice parameters (Å)			
		a	b	c	Γ
Cr_{ss}	< 1863	2.891	-	-	-
C14-$NbCr_2$ (HT)	1585 – 1770	4.931	-	8.123	120°
C15-$NbCr_2$ (LT)	< 1625	6.95	-	-	-
Nb_{ss}	< 2469	3.3067	-	-	-

The $NbCr_2$ Laves phase is of particular interest as its presence in Nb-silicide based alloys has been reported to improve oxidation resistance especially when its grain size is small and the volume fraction is high (Bewlay and Jackson, 2000; K. S. Chan, 2004; K. S. Chan, 2004).

The Laves phases were first proposed by Laves and Witte (1935) and are topologically close packed (tcp) structures with binary composition AB_2. The Laves phases cover a vast class of binary intermetallic compounds, which can also exist as ternary phases depending on the alloying addition. Laves phases have one of three crystal structures:

- hexagonal (hP12) C14 $MgZn_2$ (Figure 10a)
- cubic (cF24) C15 $MgCu_2$ (Figure 10b)
- di-hexagonal (hP12) C36 $MgNi_2$ (Figure 10c)

The three crystal structures are different to one another only by the repeat stacking sequence of a four atom layer group. Their tcp structure is due to the best packing arrangement of unlike spheres A and B where atom B is smaller than A. The ideal ratio of atomic radii is r_A/r_B= 1.225 (where r is the radius of the respective atom). However, in reality the radii ratio of known Laves phases varies between 1.05 -1.68 according to Nevitt and Beck (1963) and 1.05-1.67 according to Pearson (1968). For the $NbCr_2$ Takasugi et al. (1996) report the radii ratio to be 1.15.

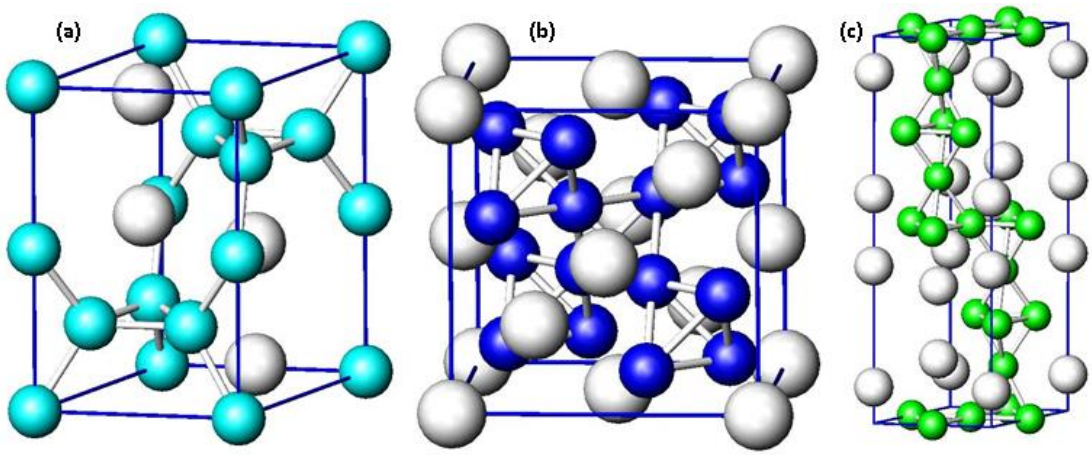

Figure 10. Polymorphic crystal structures of the Laves phase (a) C14 $MgZn_2$, (b) C15 $MgCu_2$, and (c) C36 $MgNi_2$.

1.6 The Cr-Si system

The equilibrium phases of the Cr-Si binary system, shown in Figure 11 according the work of Gokhale and Abbaschian (1987) are:

1. Liquid (L),
2. Terminal (bcc) solid solution Cr_{ss},
3. Terminal (diamond cubic) Si_{ss},
4. Cubic cP8 Cr_3Si,
5. Cubic cP8 CrSi,
6. Hexagonal $CrSi_2$,
7. Tetragonal αCr_5Si_3,
8. Hexagonal βCr_5Si_3.

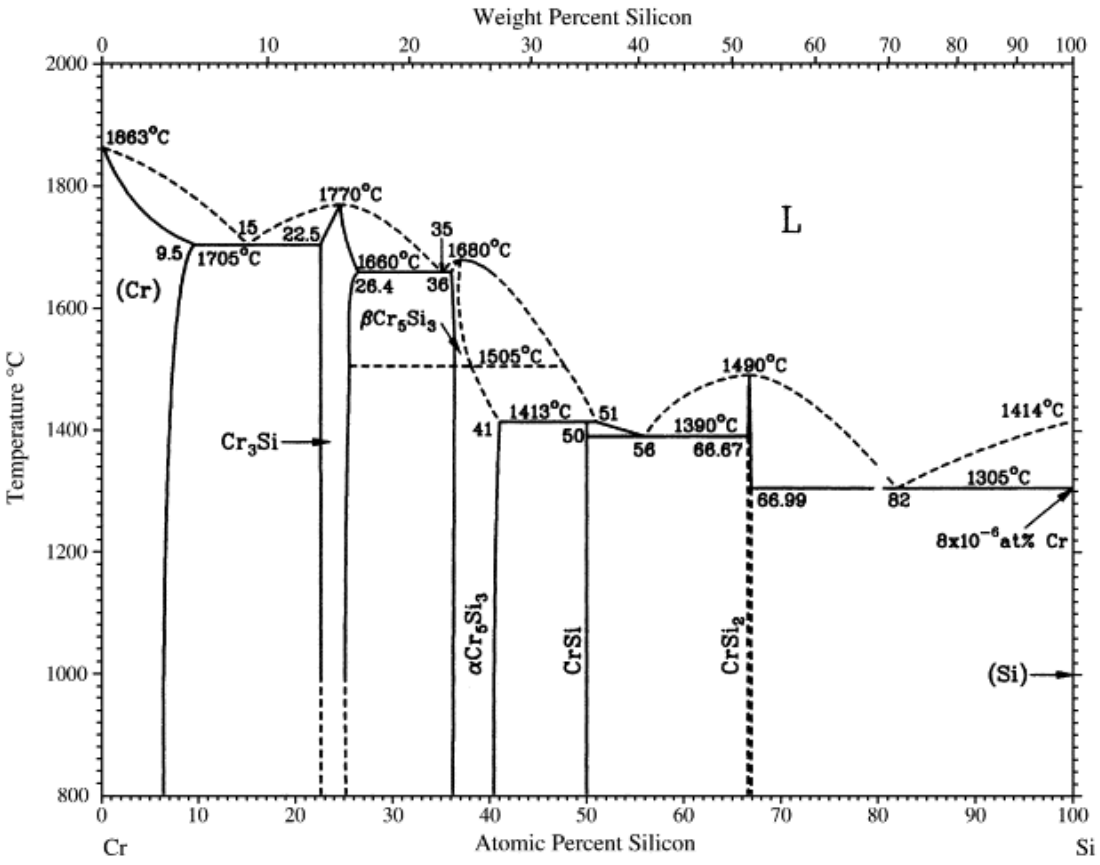

Figure 11. The Cr-Si System (Gokhale and Abbaschian, 1987).

Crystal structure data is given in Table 7. There is some conjecture over the existence of the high temperature hP16 βCr_5Si_3, which was omitted by Okamoto (1997) in the authors first version of the binary system but later included in Okamoto (2001a). The prototype of αCr_5Si_3 is the W_5Si_3 structure and thus the αCr_5Si_3 is isomorphous with the βNb_5Si_3 with the phases having incredibly close lattice parameters, therefore Cr addition to the Nb-Si system is expected to stabilise βNb_5Si_3 to lower temperatures. The Cr_3Si and Nb_3Si are not isomorphous, thus Cr addition to the Nb-Si system is expected to destabilise Nb_3Si (Zelenitsas and Tsakiropoulos, 2005).

Table 7. Phase data of the Cr-Si binary system (Villars and Calvert, 1991).

Phase	at.% Si	Pearson Symbol	Space group	Temp. Range (°C)	Lattice Parameter (Å)			
					a	b	c	γ
Cr_{ss}	0 – 9.5	cI2	$Im\bar{3}m$	< 1863	2.88	-	-	-
Cr_3Si	22.5 - 25	cP8	$Pm\bar{3}n$	< 1770	4.56	-	-	-
αCr_5Si_3	36 – 41	tI32	I4/mcm	<1505	9.15	-	4.64	120°
βCr_5Si_3	36 - 38	hP16	$P6_3/mcm$	1505 – 1680	-	-	-	-
CrSi	50	cP8	$P2_13$	< 1413	4.62	-	-	-
$CrSi_2$	66.5 - 67	hP9	$P6_222$	< 1490	4.43	-	6.37	120°
Si_{ss}	100	cF8	$Fd\bar{3}m$	< 1410	5.43	-	-	-

1.7 The Nb-Si-Cr system

Goldschmidt and Brand (1961a) performed early work on the Nb-Si-Cr system using arc melted alloys that were heat treated at 1000°C. Their isothermal section at 1000°C is shown in Figure 12. In addition to the binary phases, their findings support the existence of 5 ternary compounds;

1. The ρ phase, a hexagonal C14 Laves $Nb(Cr,Si)_2$,
2. A 5-3 silicide with prototype βW_5Si_3 isomorphous with βNb_5Si_3,
3. A θ phase, with ~ 50 at.% Si and 6 – 28 at.% Nb with empirical formula $Cr_7Nb_3Si_{10}$,
4. A τ phase of composition 37Cr, 27Nb, 36Si (at.%) possessing a bcc lattice,
5. A ν phase of composition 45Cr, 15Nb, 40Si (at.%) that was thought to be metastable in a haphazard fashion over a certain composition range.

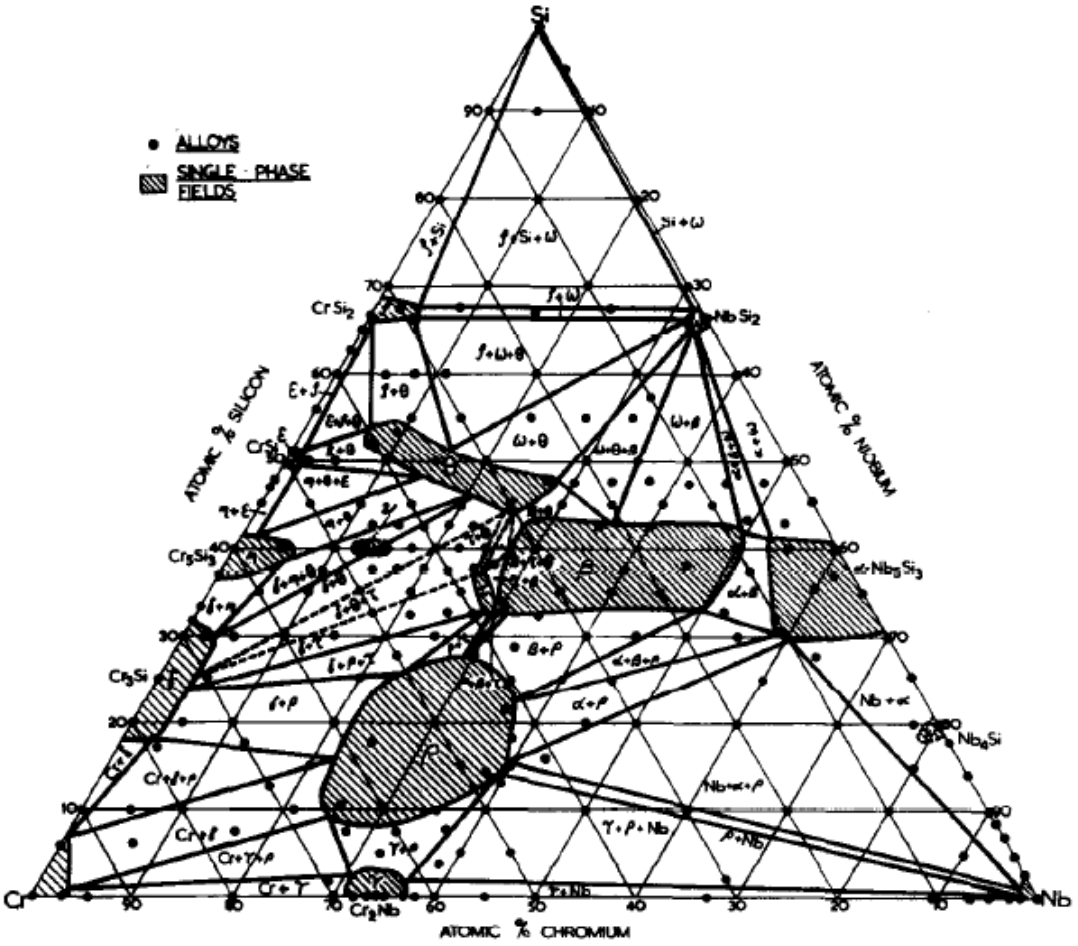

Figure 12. Isothermal section of the Nb-Si-Cr phase diagram at 1000°C (Villars and Calvert, 1991).

It should be noted that the Nb_4Si is included in Figure 12 instead of the Nb_3Si as it was applied in the early version of the Nb-Si binary phase diagram and, therefore, applied in the work. In the Nb-Cr binary system the C14 $NbCr_2$ Laves is stable between 1585 – 1770°C, but with as little as 2.5 at.% Si addition the C14 structure was stabilised down to 1000°C, as illustrated by the ternary ρ phase field in Figure 12, effectively replacing the C15 Laves structure. The ternary ρ Laves phase exhibits considerably high solubility for the primary elements. The Nb-Si-Cr 1000°C isotherm possesses two pseudo-binary sections; (1) one between $CrSi_2$ – $NbSi_2$ that are isomorphous with hP9 structures (Table 1 and Table 7), and (2) between Cr_5Si_3 – Nb_5Si_3, which are isomorphous but complicated by the two α,βNb_5Si_3. At 1000°C the αNb_5Si_3 allotrope is stable with considerable Cr, Nb, and Si solubility but above ~20% Cr_5Si_3 the βNb_5Si_3 allotrope is stabilised, thus Cr has the effect of stabilising the βNb_5Si_3 silicide down to 1000°C and, hence, a wide phase field of ternary βNb_5Si_3 exists (Goldschmidt and Brand, 1961a).

Zhao et al., (2003a) observed the ternary compounds CrNbSi, $(Cr,Nb)_6Si_5$, and $(Cr,Nb)_{11}Si_8$ in their 1000 and 1150°C Nb-Cr-Si isothermal phase diagrams shown in Figure 13 and Figure 14 respectively. The authors also confirmed the stabilisation of the C14 $NbCr_2$ Laves phase to lower temperatures with 6 at.% Si and was soluble up to ~ 26 at.%. Little variation in Si solubility in the C14 Laves phase was found at the two temperatures investigated.

Relating the two works, the θ, ν, τ, and ρ phases are the $(Cr,Nb)_6Si_5$, $(Cr,Nb)_{11}Si_8$, CrNbSi, and $NbCr_2$, respectively. Zhao et al., (2003a) gives a smaller phase region for the Nb_5Si_3 than Goldschmidt and Brand (1961a) and suggested that this was due to untransformed primary βNb_5Si_3 after the heat treatment, indicating that Goldschmidt and Brand (1961a) had not sufficiently heat treated their alloys to equilibrium conditions.

There is some disagreement with the three-phase field that includes the Nb_{ss} and Laves phase. Goldschmidt and Brand (1961a) found that Nb_{ss} cannot be in direct equilibrium with the ternary CrNbSi (γ), thereby giving a Nb_{ss} + Nb_5Si_3 + C14$NbCr_2$ region while Zhao et al., (2003a) propose the Nb_{ss} + Nb_5Si_3 + CrNbSi phase equilibria. The study of a Nb-18Si-15Cr alloy by Geng et al., (2006a) concluded agreement with Goldschmidt and Brand (1961a) on the three phase field, as did the work by Shao (2005). Due to a greater consensus of work the Nb_{ss} + Nb_5Si_3 + C14$NbCr_2$ three phase field is accepted as was initially proposed by Goldschmidt and Brand (1961a). It was agreed by all authors that Cr stabilises the βNb_5Si_3 and Si stabilises C14 $NbCr_2$ down to 1000°C.

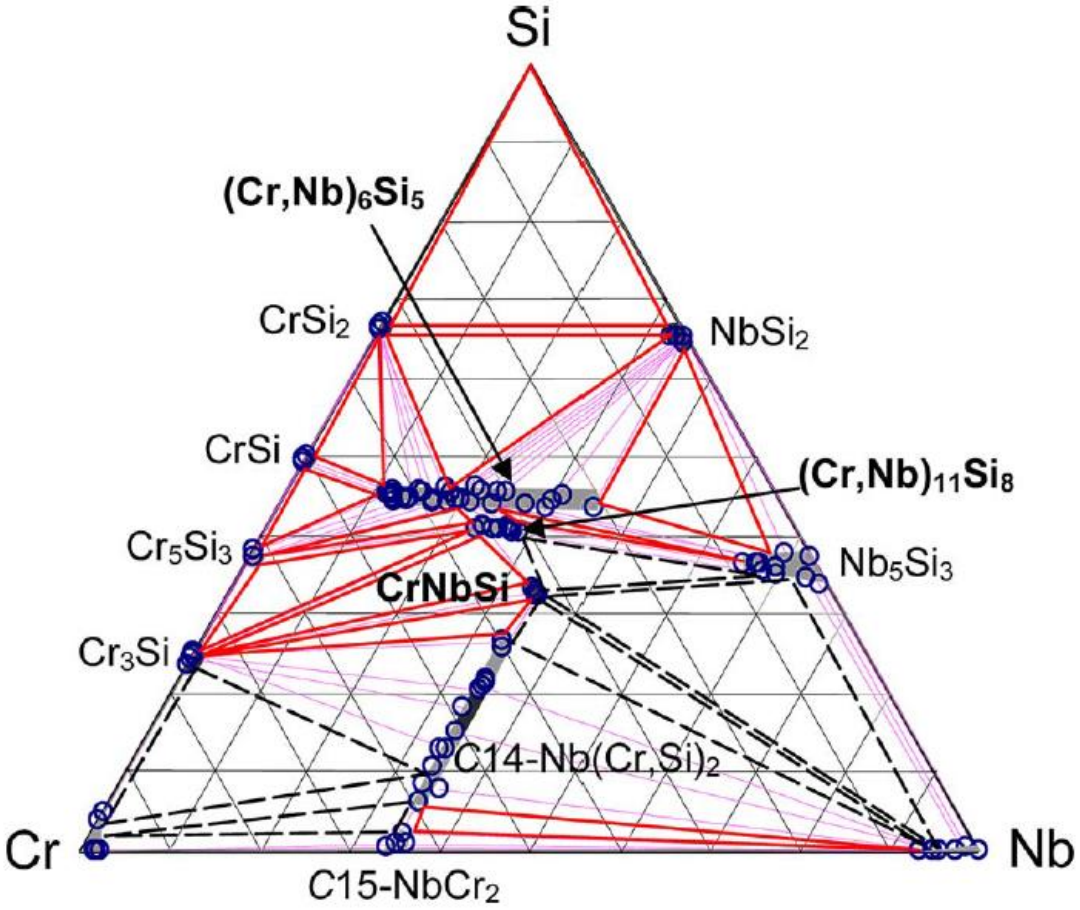

Figure 13. The 1000°C isothermal section by Zhao et al., (2003a) of the Nb-Cr-Si system obtained from the tri-junction area of the diffusion multiple annealed at 1000°C for 4000 h. The axes are in at.% but were removed for simplicity. The solid triangles indicate well-defined three-phase equilibria and the open circles show the tie-line compositions. The tie-lines are shown with dotted lines. The dashed triangles are hypothesized three-phase equilibria.

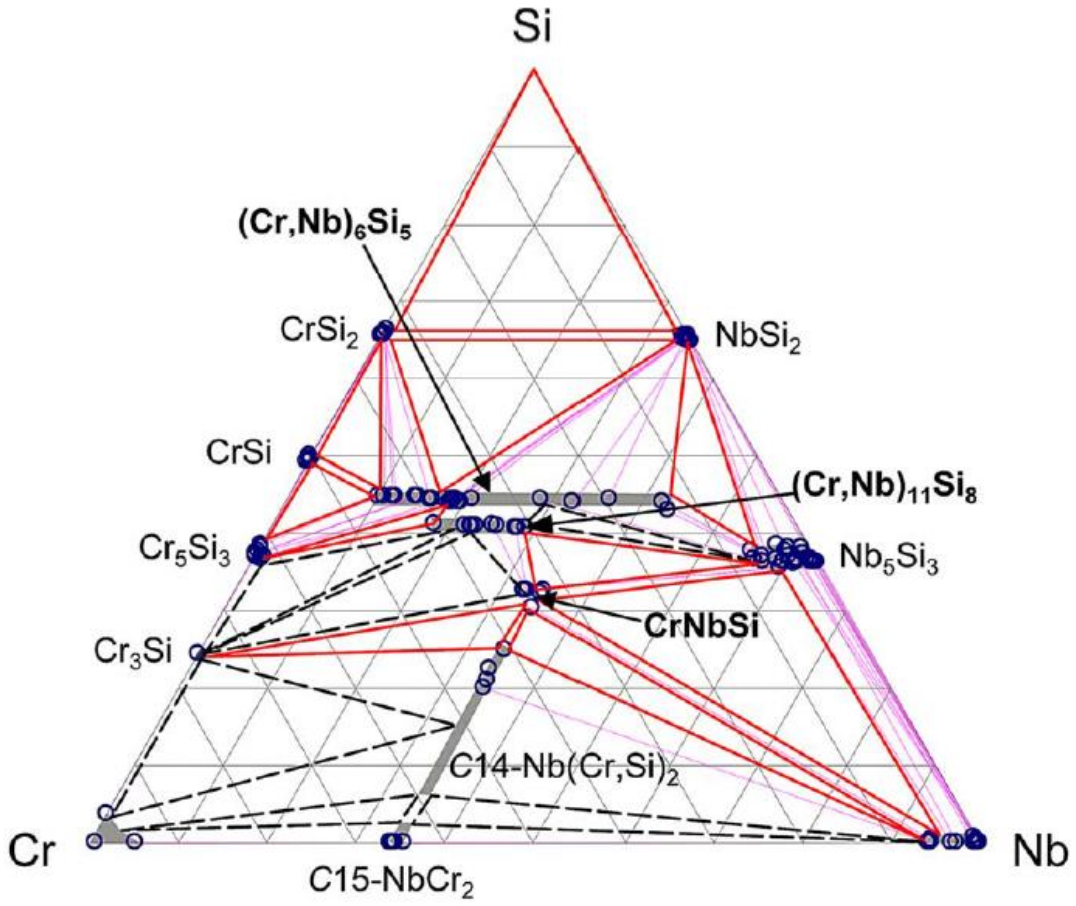

Figure 14. The 1150°C isothermal section by Zhao et al., (2003a) of the Nb-Cr-Si system obtained from the tri-junction area of the diffusion multiple anneal at 1150 C for 2000h. The axes are in at.% but were removed for simplicity. The solid triangles indicate well-defined three-phase equilibria and the open circles show the tie-line compositions. The tie-lines are shown with dotted lines. The dashed triangles are hypothesized three-phase equilibria.

The liquidus projection at the metal rich end of the Nb-Si-Cr system (Figure 15) was studied by Bewlay et al., (2009) using data from Deal et al., (2007). The main features of their proposed partial liquidus projection shown are similar to the liquidus projection proposed by Shao (2005) (Figure 16). When compared there are differences, notably the much larger HT βNb_5Si_3 phase region, no CrNbSi phase region, and the small $Nb_9(Cr,Si)_5$ phase region reported by Bewlay et al., (2009). The discovery of the $Nb_9(Cr,Si)_5$ phase which is isostructural to $Nb_9Co_3Ge_2$, is the key finding of Bewlay et al., (2009). This phase was found in Nb-Si-Cr alloys containing 12, 18, 25 and 30 at.% Si but has not been reported elsewhere and Deal et al., (2007) did not give its chemical composition. The c/a ratio measured by EBSD was used to match the crystal structure of Nb_9GeCo_4 as opposed to $Nb_9Co_3Ge_2$ in Bewlay et al., (2009). Further work is required to corroborate the existence of the $Nb_9(Cr,Si)_5$ phase.

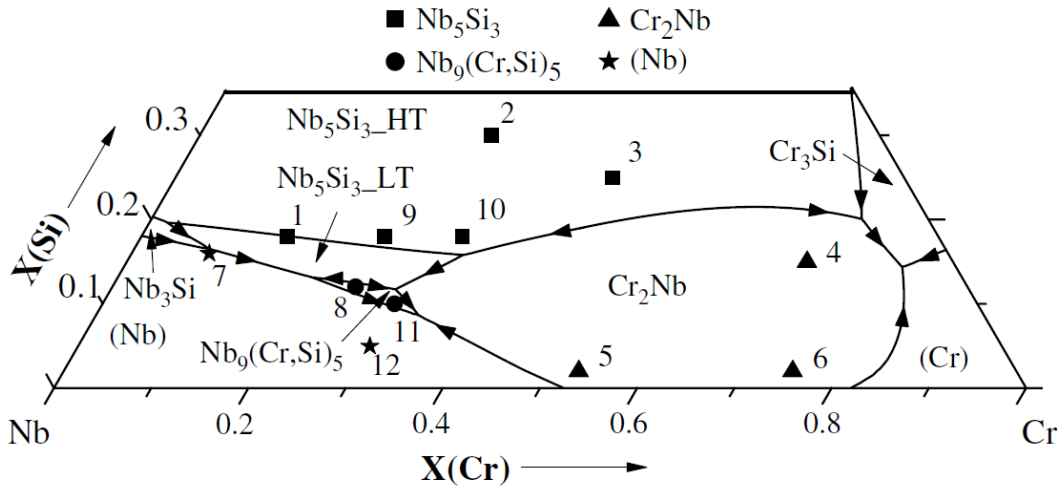

Figure 15. Partial liquidus projection of the Nb-Si-Cr (0< Si < 35 at.%) proposed by Bewlay et al. (2009). The numbered symbols denote the bulk alloy compositions of samples.

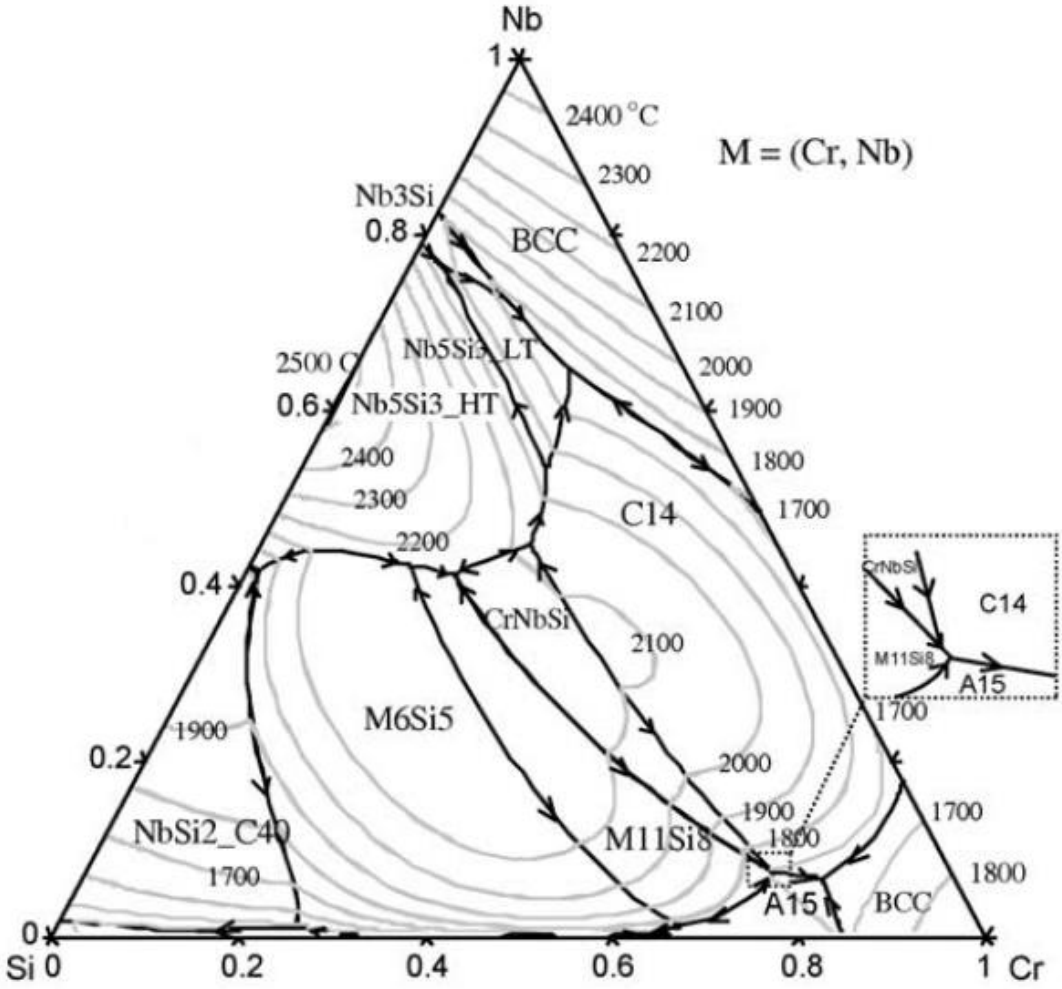

Figure 16. Liquid surface projection with isothermal contours in°C, calculated by Shao (2005).

1.8 The Cr-Ti system

The phases present in this system, shown in Figure 17, by the work of Okamoto (2002) are;

1. The hcp αTi solid solution with a very small solid solubility of Cr ~ 0.2 at.%,
2. The bcc $(Cr,\beta Ti)_{ss}$ where Ti and Cr are completely miscible,
3. The α, β, and γ $TiCr_2$ Laves phases.

This system is similar to the Nb-Cr system with the addition of a wide miscibility gap of bcc $(Cr,\beta Ti)_{ss}$ that narrows around the $TiCr_2$ composition. A detailed section of the $TiCr_2$ polymorphic phase region is presented in Figure 18. Comparing the Laves phases to the Nb-Cr system the α, β, and γ $TiCr_2$ are isomorphous to C15, C14, and C36 $NbCr_2$, respectively (Table 8).

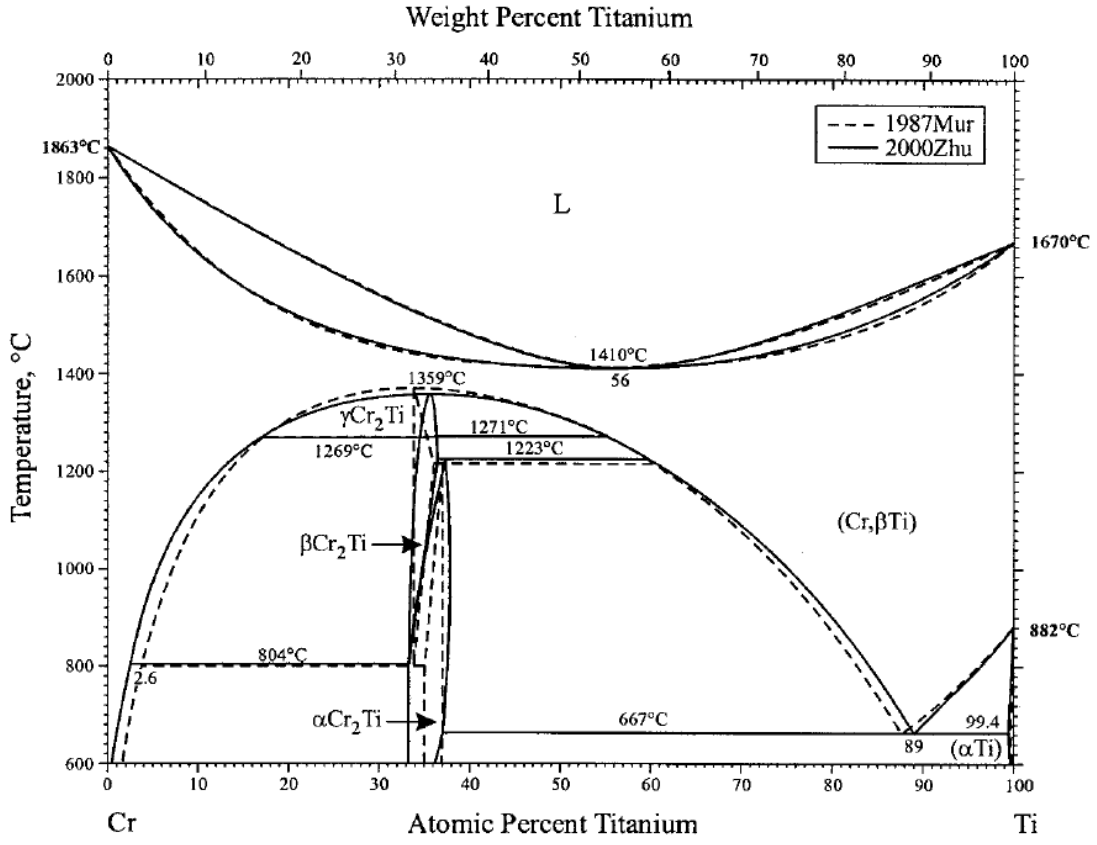

Figure 17. The binary Cr-Ti system (Okamoto, 2002).

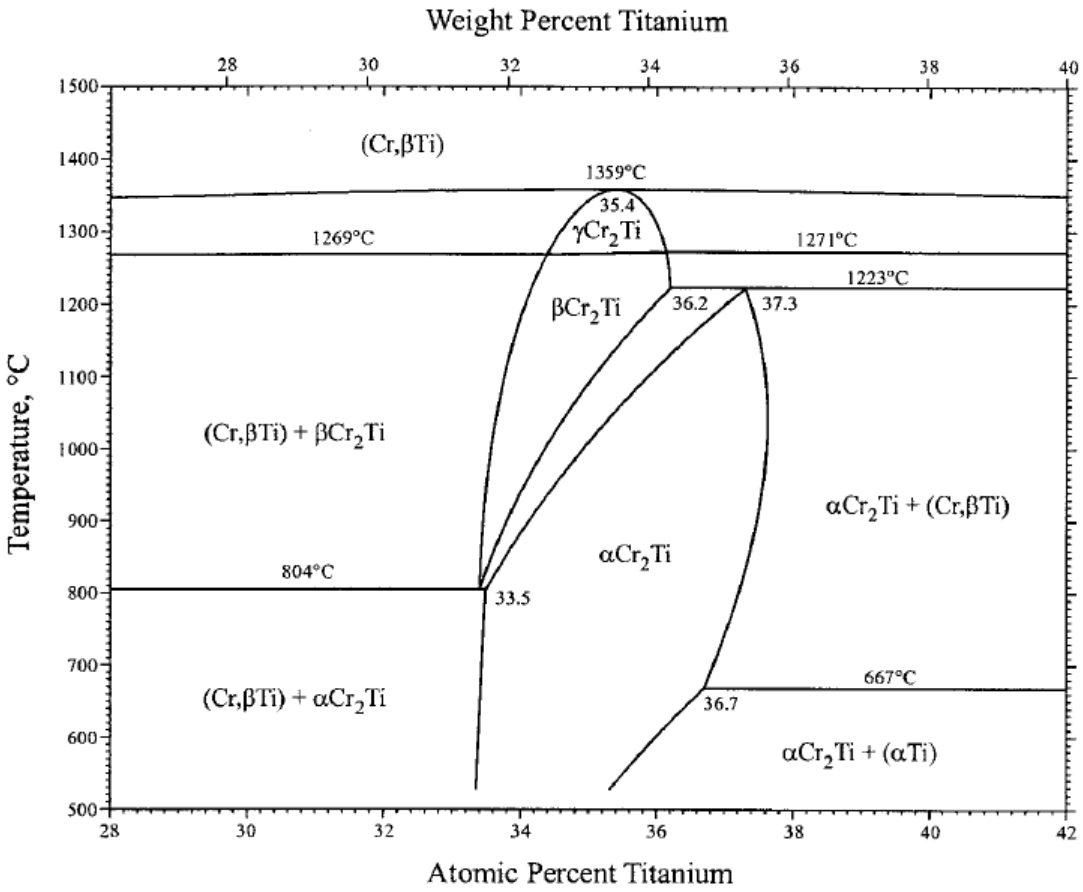

Figure 18. Detailed polymorphic region of the $TiCr_2$ Laves phase from the Cr-Ti system (Okamoto, 2002).

Table 8. Phase cyrstal structure data for the Ti-Cr system (Villars and Calvert, 1991).

Phase	Composition at.% Cr	Pearson Symbol	Space Group	Structure designation	Prototype
(βTi,Cr)	0 – 9	cI2	Im3m	A2	W
αTi	0 – 0.2	hP2	$P6_3/mmc$	A3	Mg
$\alpha TiCr_2$	63 – 65	cF24	Fd3m	C15	$MgCu_2$
$\beta TiCr_2$	64 - 66	hP12	$P6_3/mmc$	C14	$MgZn_2$
$\gamma TiCr_2$	64 - 66	hP24	$P6_3/mmc$	C36	$MgNi_2$
ω (metastable)	…	hP3	$P\bar{3}m1$	…	…

1.9 The Ti-Cr-Si System

Early work on this system was by Lysenko et al., (1971) whose isothermal section is shown in Figure 19. The phases present are equivalent to the respective binary systems with the addition of a $(Ti,Cr)_6Si_5$ ternary phase isomorphous to V_6Si_5 with Pearson symbol oI44 (Steinmetz and Roques, 1977; Smith, 1981; Du and Schuster, 2002). It is noteworthy that there is no CrTiSi ternary phase in this system. In Figure 20, the calculated isothermal section at 1000°C by Du and Schuster (2002) is presented and annotated with their own experimental data and with the work of Lysenko et al., (1971).

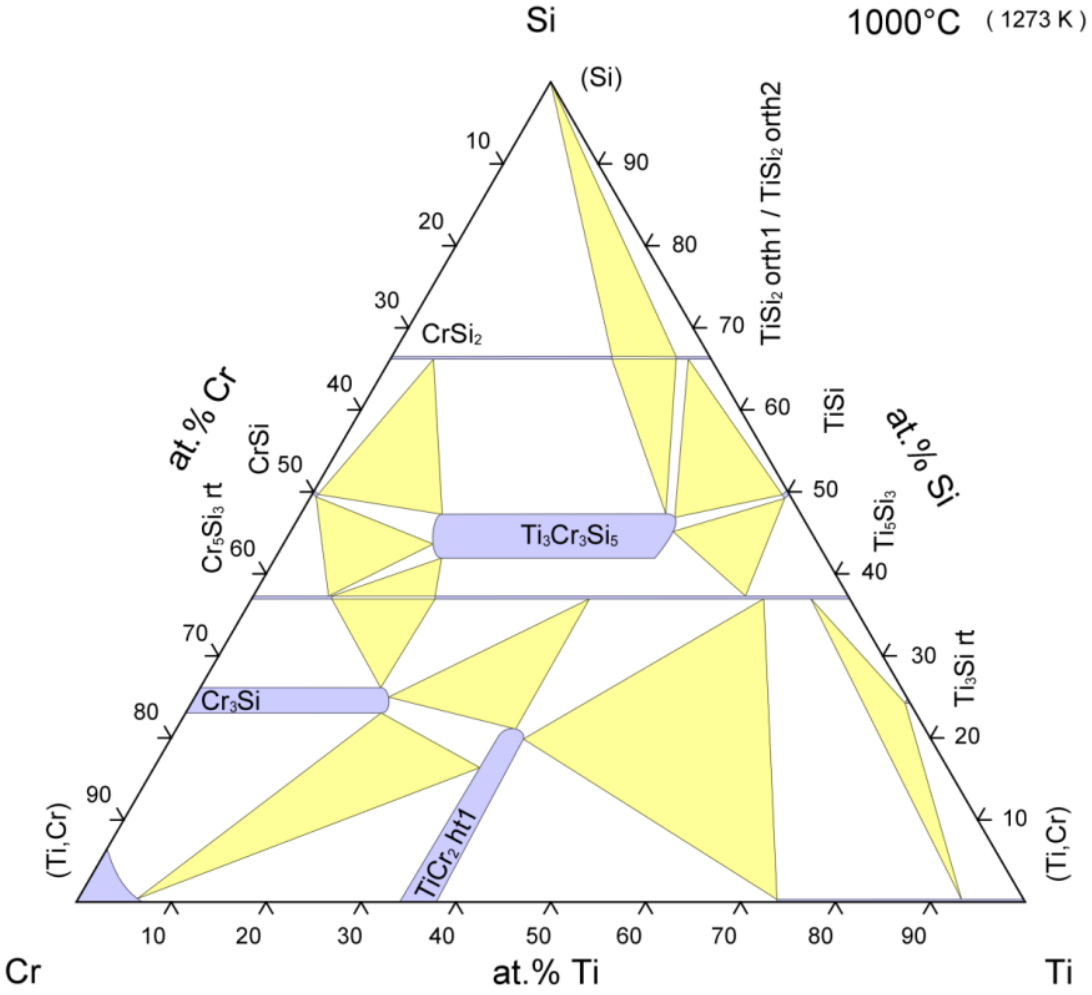

Figure 19. The 1000°C isotherm of the Ti-Cr-Si system by Lysenko et al., (1971).

In general the diagrams are quite similar however, Du and Schuster (2002) include the Ti_5Si_4 phase and two different three phase regions at the Cr_5Si_3 rich side above and below the pseudo binary Cr_5Si_3 - Ti_5Si_3 tie line (forming a rhomboid). The alloys studied by Du and Schuster (2002) and Lysenko et al., (1971) are labelled in Figure 20.

The most relevant features of this system to this thesis are: (1) the $TiSi_2$, Ti_5Si_3, $CrSi_2$, αCr_5Si_3, Cr_3Si and $\beta TiCr_2$ phases, which have high solubilities for the 3rd element, (2) the Ti_3Si phase shows low Cr solubility ~1 at.%, hence Cr stabilises the Ti_5Si_3 while destabilising Ti_3Si formation (Zelenitsas and Tsakiropoulos, 2005).

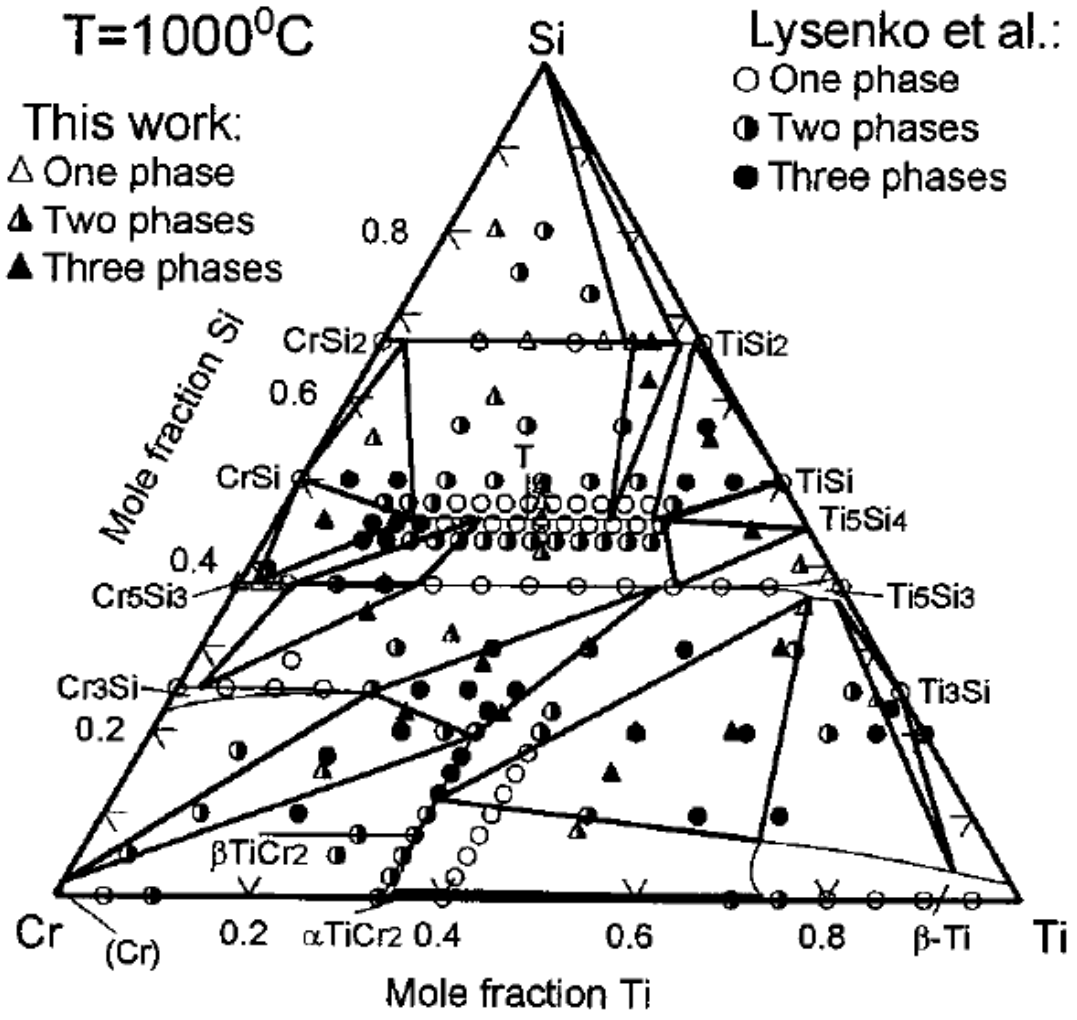

Figure 20. Caluclated 1000°C isothermal section by Du and Schuster (2002) annotated with their own experimental data and data by Lysenko et al., (1971).

1.10 The Nb-Ti-Cr system

Zhao et al., (2004b) studied the Nb-Ti-Cr system (Figure 21) using the diffusion multiple approach and electron microprobe to characterise alloys. The phases of the Nb-Ti-Cr system are the same as the respective binary systems. The solid solution has a wide range in miscibility of the three elements and there is miscibility between the Laves phases, as shown in Figure 21.

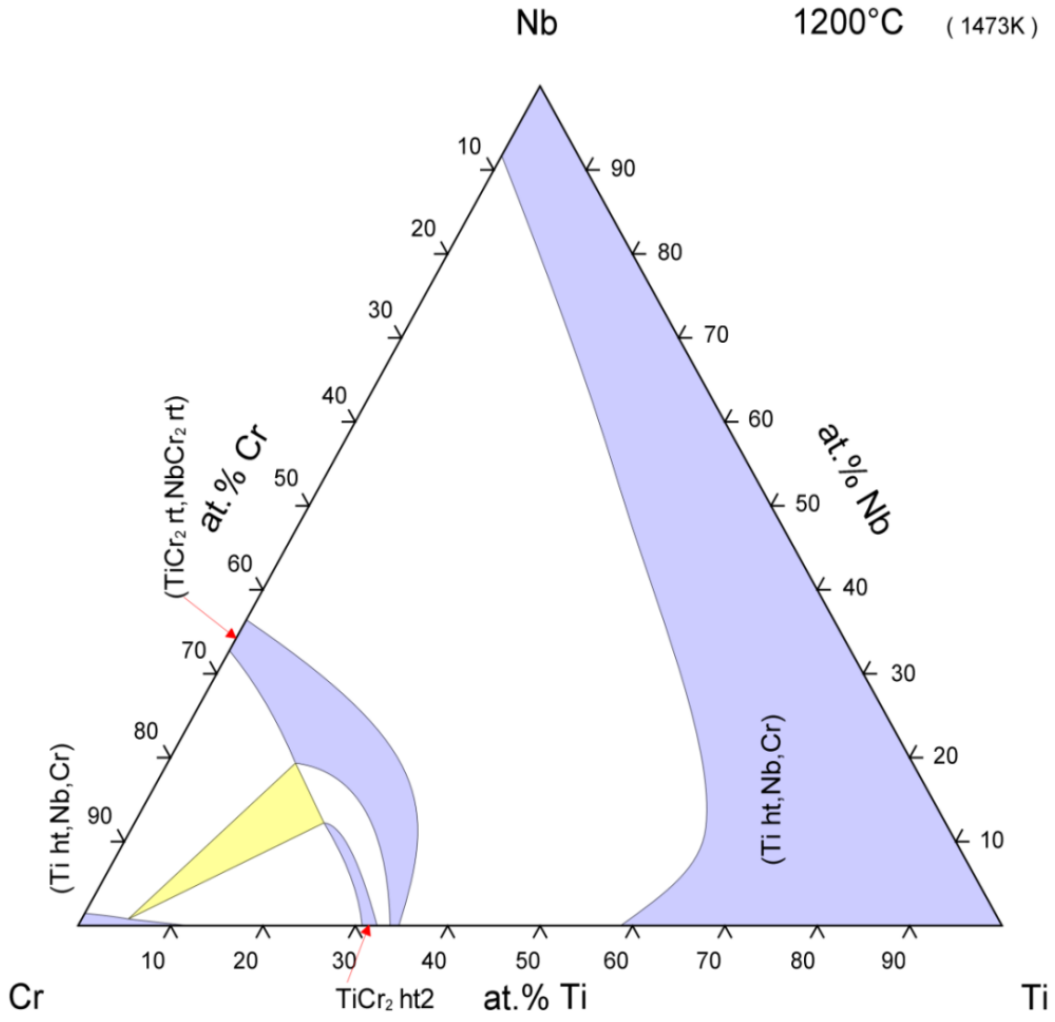

Figure 21. The 1200°C isothermal Nb-Ti-Cr binary phase diagram by Zhao et al., (2004b).

1.11 The Nb-Hf system

The phases in the Nb-Hf system shown in Figure 22 are:

1. Liquid (L),
2. Low temperature hcp αHf,
3. High temperature bcc β(Hf,Nb).

There is low solubility of Nb in the hcp αHf solid solution up to ~ 4.5 at.%. The key relevance of this system is that Hf and Nb are fully miscible in a substitutional bcc solid solution. Crystal structure data of the phases are presented in Table 9.

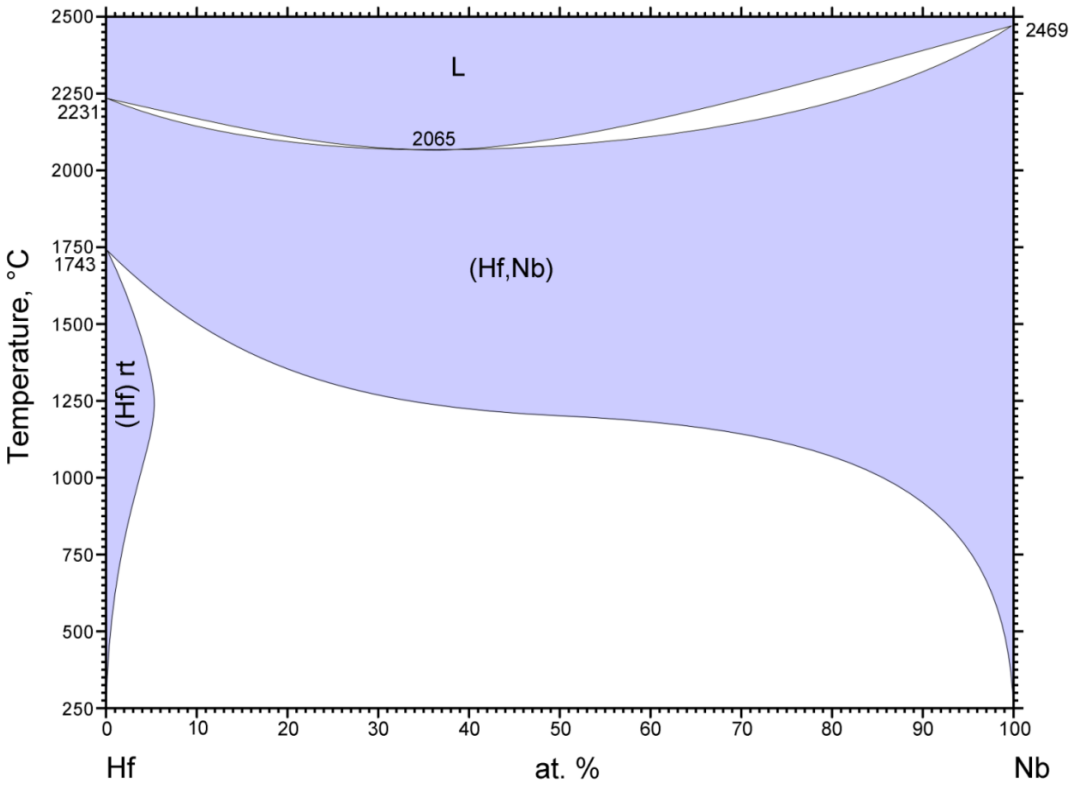

Figure 22. The binary Nb-Hf system (Okamoto, 1991).

Table 9. Phase data of the Hf-Nb binary system by Okamoto (1991).

Phase	Composition at.% Nb	Pearson Symbol	Space Group	Structure designation	Prototype
β(Hf,Nb)	0 – 100	cI2	$Im\bar{3}m$	A2	W
αHf	0 – 4.5	hP2	$P6_3/mmc$	A3	Mg

1.12 The Hf-Si System

The phases in the Hf-Si system based on the collated works of Brukl (1968), Gokhale and Abbaschian (1989), Bewlay et al. (1999), and Zhao et al. (2000) are;

1. Liquid (L),
2. Low temperature hcp α Hf solid solution,
3. High temperature bcc β Hf solid solution,
4. Tetragonal Hf_2Si,
5. Tetragonal Hf_3Si_2,
6. Hexagonal Hf_5Si_3,
7. Tetragonal Hf_5Si_4,
8. Orthorhombic HfSi,
9. Orthorhombic $HfSi_2$,
10. Diamond cubic Si solid solution.

The diagram by Gokhale and Abbaschian (1989), shown in Figure 23, was largely based on the experimental work by Brukl (1968) and does not include the hP16 Hf_5Si_3 as it was considered to be metastable, stabilised by C, O, and N interstitial impurities. Bewlay et al. (1999) found Hf_5Si_3 formation does not require high levels of interstitial impurities as they formed the phase with < 100 ppm of interstitials and that Hf_5Si_3 can exist in a binary or higher alloyed form where Nb or Ti substitute with Hf.

The liquidus and phase boundaries in Figure 23 and Figure 24 are in good agreement and the existence of stable hP16 Hf_5Si_3 is accepted as an appropriate amendment. Unique to this system are the Hf_2Si and Hf_3Si_2 silicides of stoichiometries that do not occur in the Nb-Si, Ti-Si, or Cr-Si systems. Due to their high Hf content they are not particularly relevant to this thesis. The Hf_5Si_3 is isomorphous with Ti_5Si_3 and γNb_5Si_3 and thus, like Ti, Hf is expected to stabilise the γNb_5Si_3. Crystal structure data is shown in Table 10 and invariant reactions of the system are shown in Table 11.

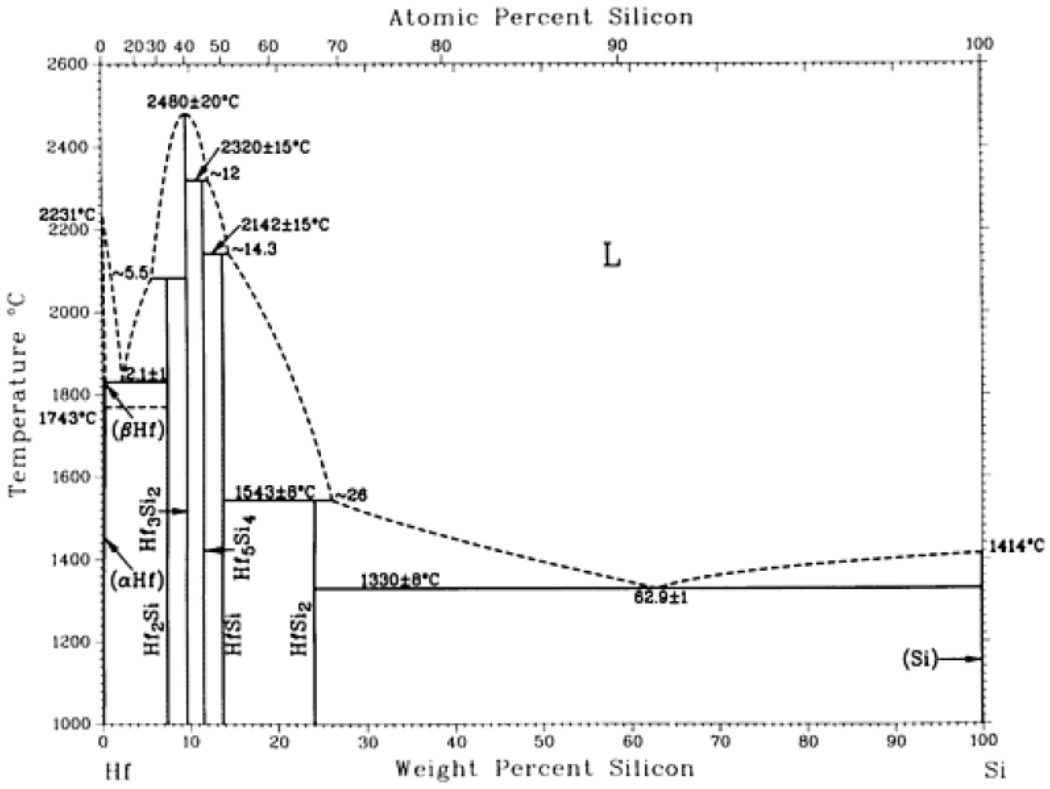

Figure 23. The binary Hf-Si phase diagram by Gokhale and Abbaschian (1989).

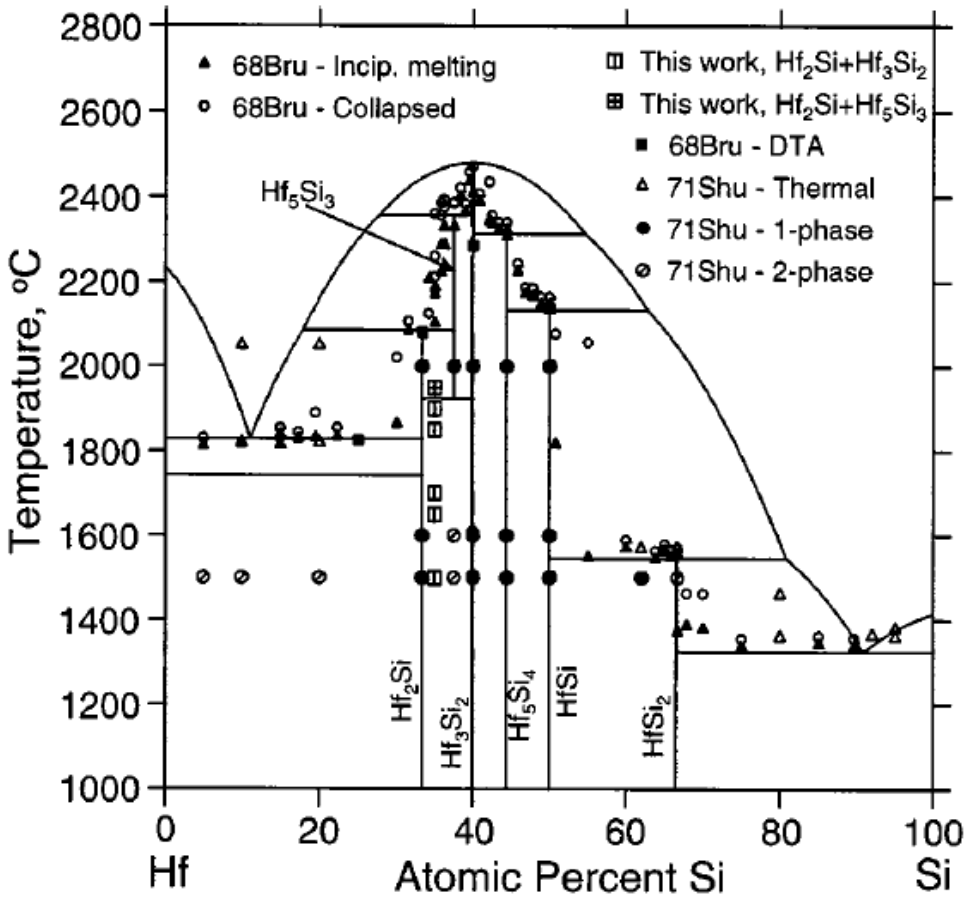

Figure 24. The binary Hf-Si phase diagram by Zhao et al. (2000).

Table 10. Phase crystal structure data for the Hf-Si binary system (Villars and Calvert, 1991; Zhao et al., 2000).

Phase	Si at.% Comp.	Temp Range°C	Pearson Symbol, Space group	Prototype	Lattice Parameters Å		
					a	b	c
αHf	0	< 1743	hP2, $P6_3/mmc$	Mg	3.196	-	5.058
βHf	0	1743-2231	cI2, $Im\bar{3}m$	W	3.44	-	-
Hf_2Si	33.3	<2083 ±12	tI12, I4/mcm	Al_2Cu	6.553	-	5.186
Hf_3Si_2	40	2480 ± 20	tP10, P4/mbm	U_3Si_2	6.988	-	3.675
Hf_5Si_3	37.5	2360 ± 30	hP16, $P6_3/mcm$	Mn_5Si_3	7.844	-	5.492
Hf_5Si_4	44.44	2320 ± 15	tP36, $P4_12_12$	Zr_5Si_4	7.039	-	12.83
HfSi	50	2142 ± 15	oP8, Pnma	FeB	6.889	3.772	5.223
$HfSi_2$	66.6	1543 ± 8	oC12, Cmcm	$ZrSi_2$	3.672	14.57	3.641
Si	100	1330 ± 8	cF8, $Fd\bar{3}m$	C	5.4309	-	-

Table 11. Invariant reactions of the Hf-Si system (Zhao et al., 2000).

Reaction	Liquid Si at.% composition		T (°C)		Reaction type
	Calc.	Exp.*	Calc.	Exp.*	
$L \leftrightarrow \beta Hf_{ss} + Hf_2Si$	11.1	11.5 ± 1	1828	1831 ± 5	Eutectic
$\beta Hf_{ss} + Hf_2Si \leftrightarrow \alpha Hf_{ss}$	…	…	1743	1743	Peritectoid
L + Hf5Si3 $\leftrightarrow$ H_2Si	17.9	21[T]	2086	2083 ± 12	Peritectic
$L + Hf_3Si_2 \leftrightarrow Hf_5Si_3$	27.7	…	2357	2360 ± 30	Peritectic
$Hf_5Si_3 \leftrightarrow H_2Si + Hf_3Si_2$	…	…	1924	1925 ± 25	Eutectoid
$L \leftrightarrow Hf_3Si_2$	40	40	2480	2480 ± 20	Congruent
$Hf_3Si_2 + L \leftrightarrow Hf_5Si_4$	54.6	…	2313	2320 ± 15	Peritectic
$Hf_5Si_4 + L \leftrightarrow HfSi$	62.8	…	2133	2142 ± 15	Peritectic
$HfSi + L \leftrightarrow HfSi_2$	80.8	…	1546	1543 ± 8	Peritectic
$L \leftrightarrow HfSi_2 + Si_{ss}$	90.8	91 ± 2	1325	1330 ± 8	Eutectic

*Experimental data is reported from Brukl (1968).

[T] Experimental data from Bewlay et al. (1999).

1.13 The Nb-Si-Hf system

This system is very important for the development of Nb-silicide based alloys because Hf is considered a key element for improving oxidation and the low and high temperature mechanical properties.

There are no ternary phases in this system, however, the binary phases possess a wide range of solubility for the third element, mainly due to the site substitutional behaviour between Hf and Nb. Zhao et al. (2001a) studied Nb-Si-Hf alloys that were heat treated at 1500°C for 100h to deduce the 1500°C isothermal section shown in Figure 25. Using data from the binary systems Zhao et al. (2001a) also constructed a schematic 3-D projection of the ternary phase diagram, as illustrated in Figure 26.

Similarly to the Nb-Si-Ti system which possess the hexagonal Ti_5Si_3, the Nb-Si-Hf system contains a pseudo binary αNb_5Si_3 – Hf_5Si_3 where according to the 1500°C isothermal section (Figure 25) Hf is soluble within αNb_5Si_3 up to ~ 15 at.% where the two phase field begins. At ~ 25 at.% Hf the single Hf_5Si_3 phase field occurs with Nb in solution, soluble up to ~ 36 at.%.

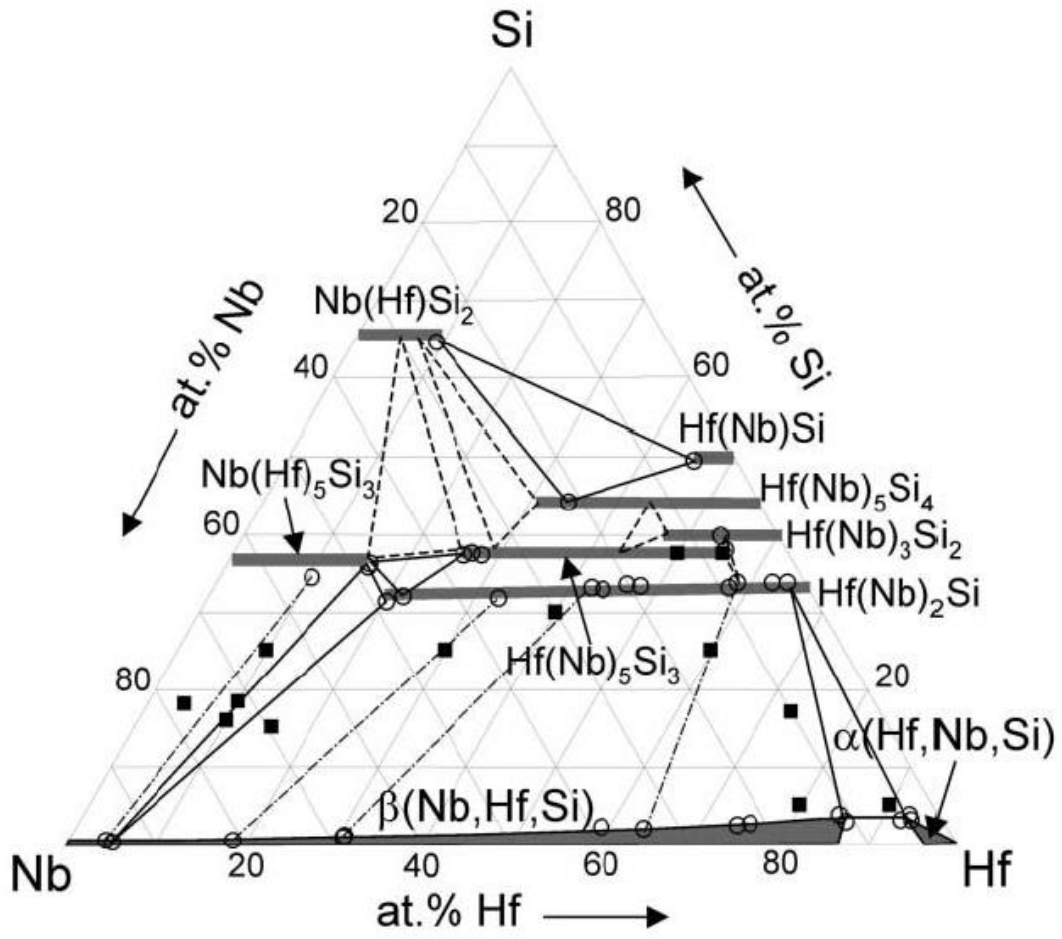

Figure 25. The 1500°C isothermal section of the Nb-Si-Hf ternary system (Zhao et al., 2001a).

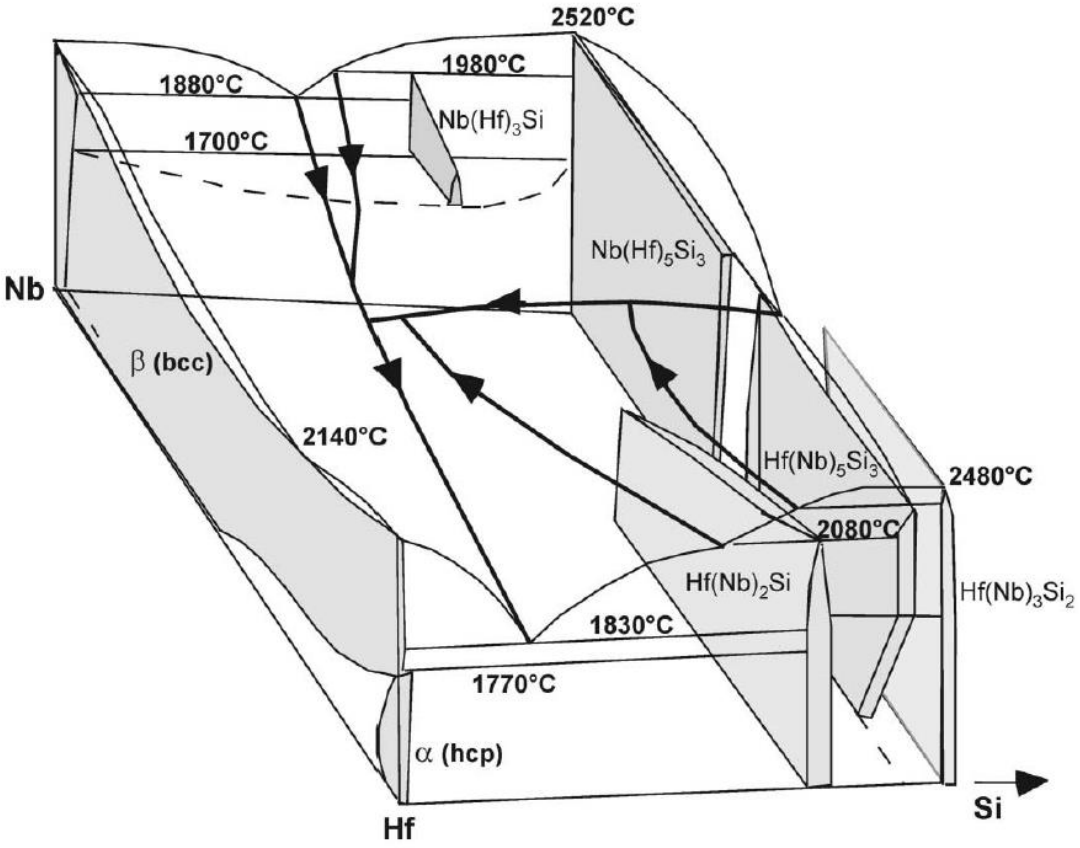

Figure 26. A schematic 3-D projection of the metal rich region of the Nb-Hf-Si phase diagram in at.% (Zhao et al., 2001a).

Yang et al. (2003) calculated a 1500°C isothermal section of the Nb-Si-Hf system using CALPHAD. Their isothermal section (Figure 27) is in agreement with Zhao et al. (2001a). Their key findings were;

- The lack of a two phase equilibrium between $(Nb,Hf)Si_2$ and $(Hf,Nb)_5Si_3$,
- That $\alpha(Nb,Hf)_5Si_3$ and $(Hf,Nb)_5Si_4$ should be in equilibrium with each other.
- The calculated solubilities of Hf in $\alpha(Nb,Hf)_5Si_3$ and Nb in $(Hf,Nb)_5Si_3$ and $(Hf,Nb)_2Si$ were up to 17.6, 43.1 and 37.6 at.% respectively.

A calculated liquidus projection by Yang et al. (2003) with experimental data is presented in Figure 28. The reaction II_1 in Figure 28 is: $L + (Nb,Hf)_3Si \rightarrow (Nb,Hf)_5Si_3 + \beta(Nb,Hf,Si)$, which is different from the reaction proposed by Bewlay et al., (1998), namely: $L + (Nb,Hf)_5Si_3 \rightarrow (Nb,Hf)_3Si + \beta(Nb,Hf,Si)$. Yang et al. (2003) states the shallow nature in this region of the liquidus surface makes it difficult to be certain about the precise nature of the reaction, making both reactions possible given the uncertainty of the experimental measurements and the thermodynamic calculations. It is noteworthy that Yang et al., (2003) treated βNb_5Si_3 as a pure binary compound due to the lack of available solubility data.

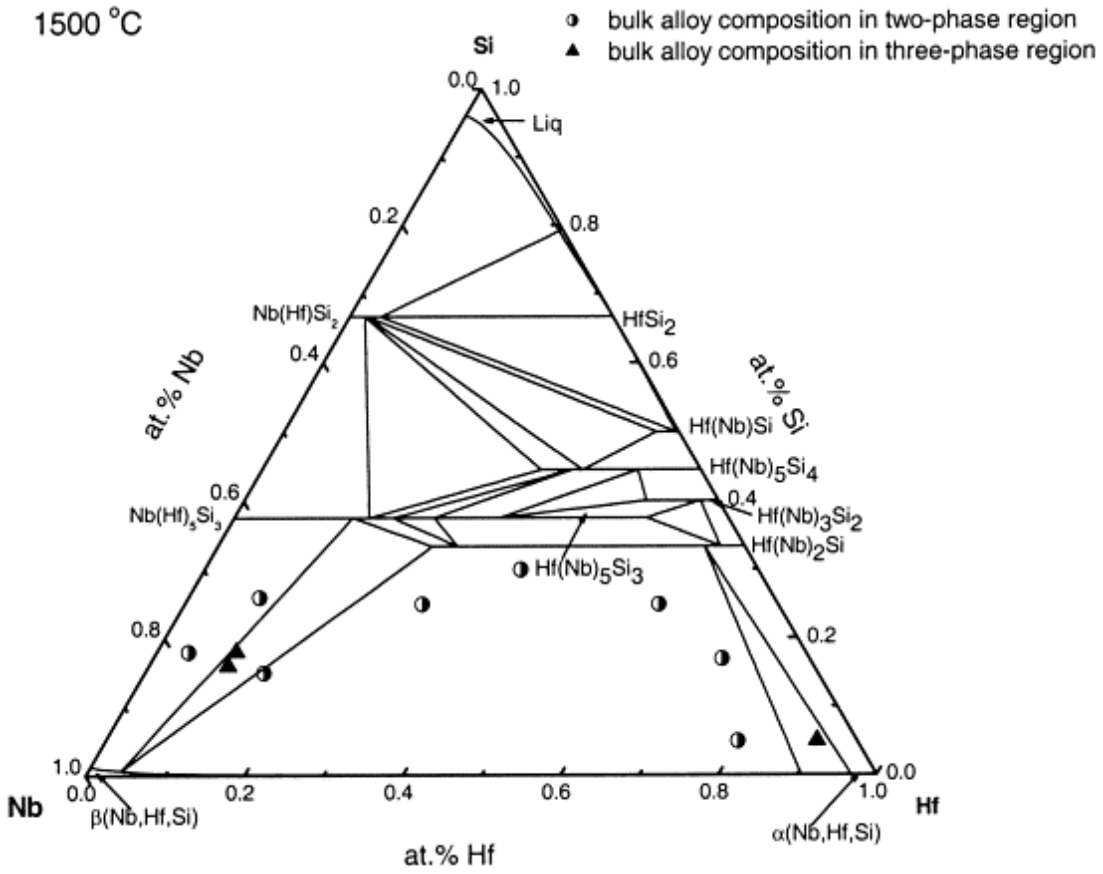

Figure 27. The calculated 1500°C isotherm of the Nb-Si-Hf system, compared with experimental data (Yang et al., 2003).

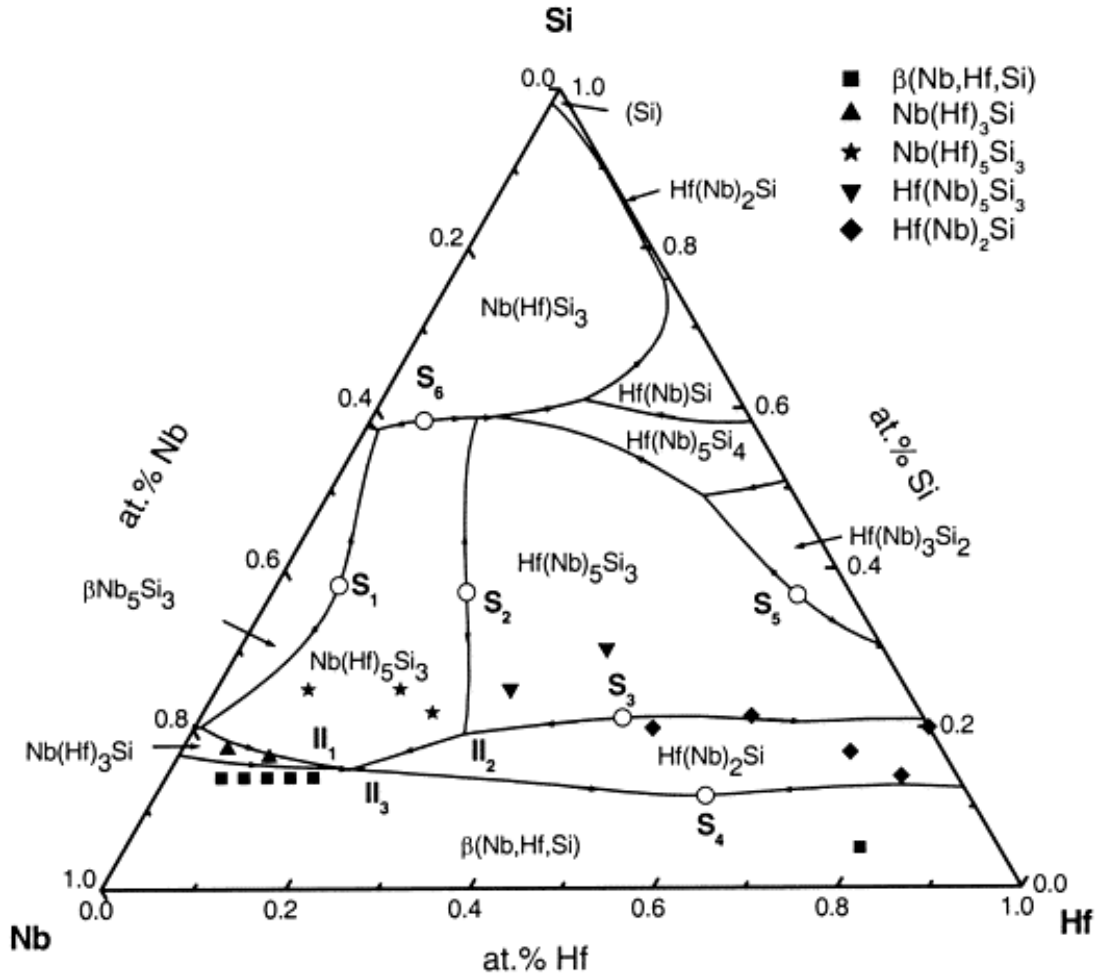

Figure 28. Calculated liquidus projection compared with experimental data (Yang et al., 2003).

1.14 The Nb-Ge system

After revisions of previous work on the Nb-Ge system, Okamoto (2012) prepared a more encompassing Ge-Nb phase diagram largely based on the work of Geng et al., (2011). Their assessment is presented in Figure 29, with crystal structure data in Table 12, which includes the hexagonal Nb_3Ge_2 phase that has also been reported as hexagonal Nb_5Ge_3, βNb_5Ge_3, $Nb_{10}Ge_7$, $NbGe_{0.67}$, $Nb_5Ge_{3.5}$ and is regarded as metastable but stabilised by interstitial elements such as B, C, N, and O (Kloska and Haase, 1984; Pan et al., 1995, 1970; Richter et al., 2001). Key reactions in the Nb-Ge system are the peritectic $L + Nb_{ss} \rightarrow Nb_3Ge$ at 1903°C and eutectic $L \rightarrow Nb_3Ge + Nb_5Ge_3$ at 1865°C. In comparison with the Nb-Si system, there is no $L \rightarrow Nb_{ss} + Nb_3Ge$.

In contrast to Okamoto (2012), Papadimitriou et al., (2015) confirmed the Nb_5Ge_3 as protype W_5Si_3 (isomorphous with βNb_5Si_3) and is the stable silicide in the Nb-Ge system. As an hP16 structure exists in the Ge-Nb system according to Geng et al., (2011), the addition of Ge to the Nb-Si system may also stabilise the hexagonal γNb_5Si_3.

Table 12. Crystal structure data for the Nb-Ge system from Okamoto (2012).

Phase	Pearson symbol	Space group	Structure Type	Prototype	Lattice Parameters (Å)		
					a	b	C
Ge	cF8	$Fd\bar{3}m$	A4	C (diamond)	5.6579	-	-
$NbGe_2$	hP9	$P6_222$	C40	$CrSi_2$	4.967	-	6.783
αNb_5Ge_3	tI32	I4/mcm	$D8_1$	Cr_5B_3*	10.146	-	5.136
Nb_3Ge_2 (βNb_5Ge_3)	hP16	$P6_3/mcm$	$D8_8$	Mn_5Si_3	7.783	-	5.39
Nb_3Ge	cP8	$Pm\bar{3}n$	A15	Cr_3Si	5.1692	-	-
Nb	CI2	$Im\bar{3}m$	A2	W	3.2942	-	-

* Assessed as W_5Si_3 by Papadimitriou et al. (2015) in agreement with Geng et al. (2011).

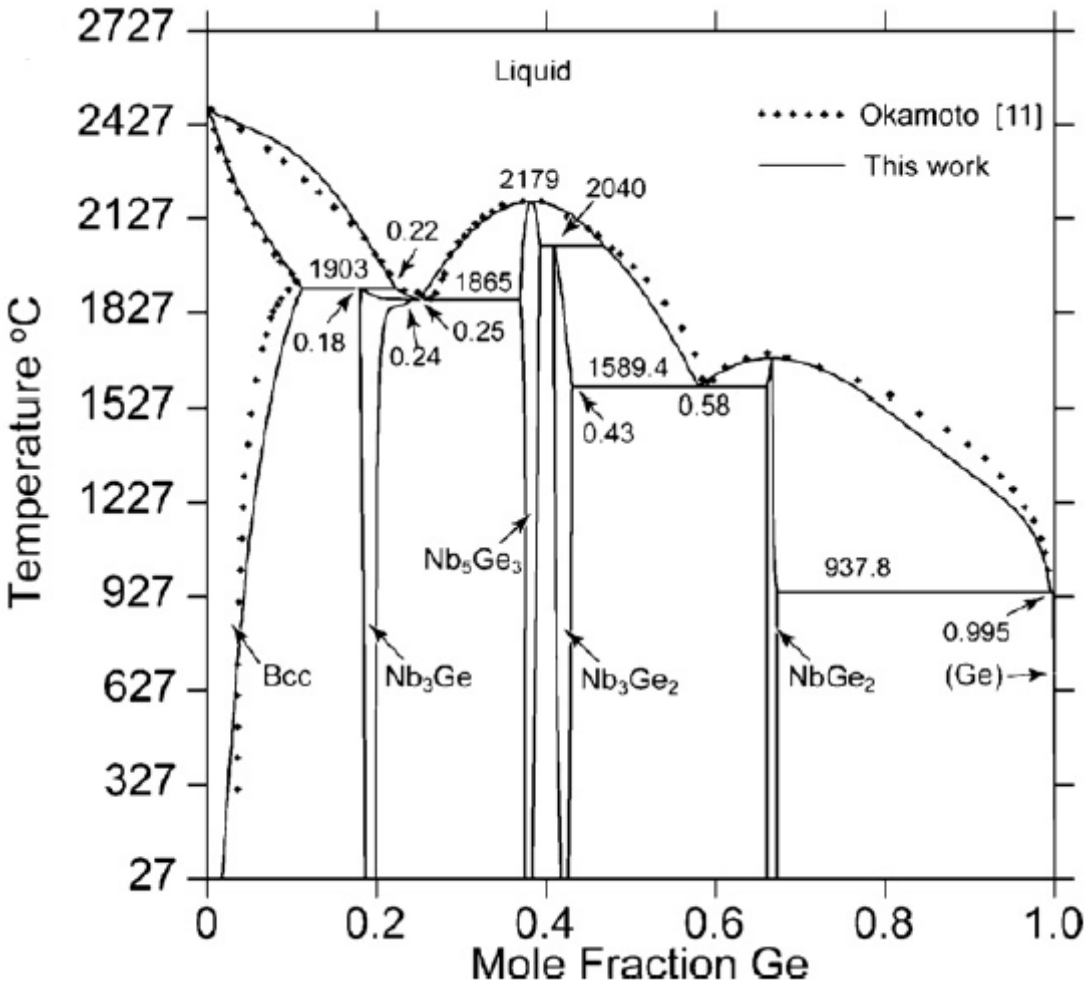

Figure 29. The Nb-Ge phase diagram proposed by Geng et al., (2011).

1.15 The Ge-Si system

The Ge-Si binary is a simple system, as shown in Figure 30. Of most relevance to Nb-silicide based alloys is the substitutional diamond cubic solid solution $(Ge,Si)_{ss}$. Ge and Si have lattice parameter 5.679 and 5.4286 Å, respectively.

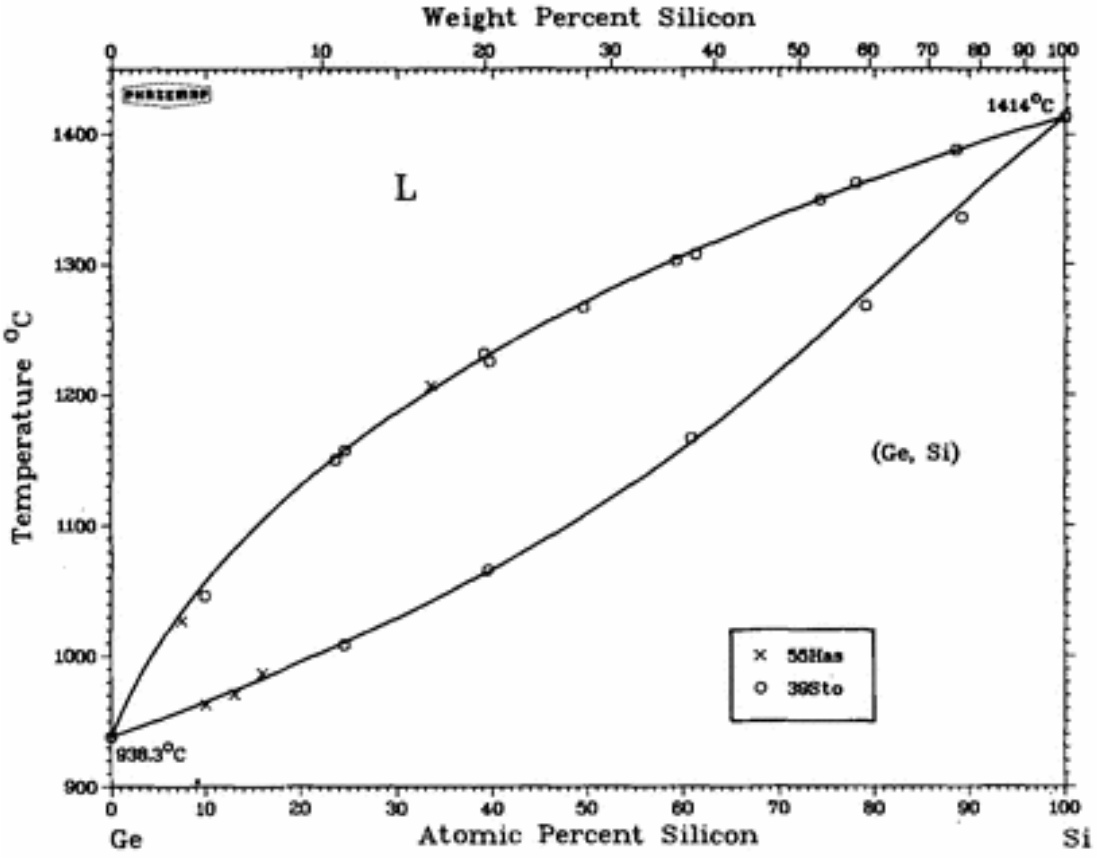

Figure 30. The Ge-Si system (Olesinski and Abbaschian, 1984).

1.16 The Nb-Si-Ge system

Pan et al., (1982) prepared isothermal sections at 1820, 1800, and 1780°C, shown in Figure 31, Figure 32, and Figure 33 respectively. The Nb_3Si has low Ge solubility up to ~ 2 at.% and can be in a two phase equilibrium with Nb_{ss} at 1820 and 1800°C. As the temperature decreases the two phase Nb_{ss} + Nb_3Si region narrows at 1800°C, with Nb_3Si disappearing at 1780°C. At 1800 and 1780°C three phase fields exist, namely; Nb_{ss} + Nb_5Ge_3 + αNb_5Si_3 and Nb_{ss} + Nb_3Ge + Nb_5Ge_3. As Nb_3Si does not exist below 1780°C it is suggested that alloying with Ge has no practical influence on the stability, structure, and temperature range of the Nb_3Si.

The phases $NbGe_2$, αNb_5Ge_3, and Nb_3Ge_2 are isomorphous respectively with $NbSi_2$, $\alpha,\beta Nb_5Si_3$, and γNb_5Si_3 while the Nb_3Ge and Nb_3Si are not isomorphous. Relevant to the Nb-Si system is the tI32 αNb_5Ge_3 phase, which is isomorphous with the $\alpha,\beta Nb_5Si_3$ but with near identical lattice parameter to the βNb_5Si_3 allotrope.

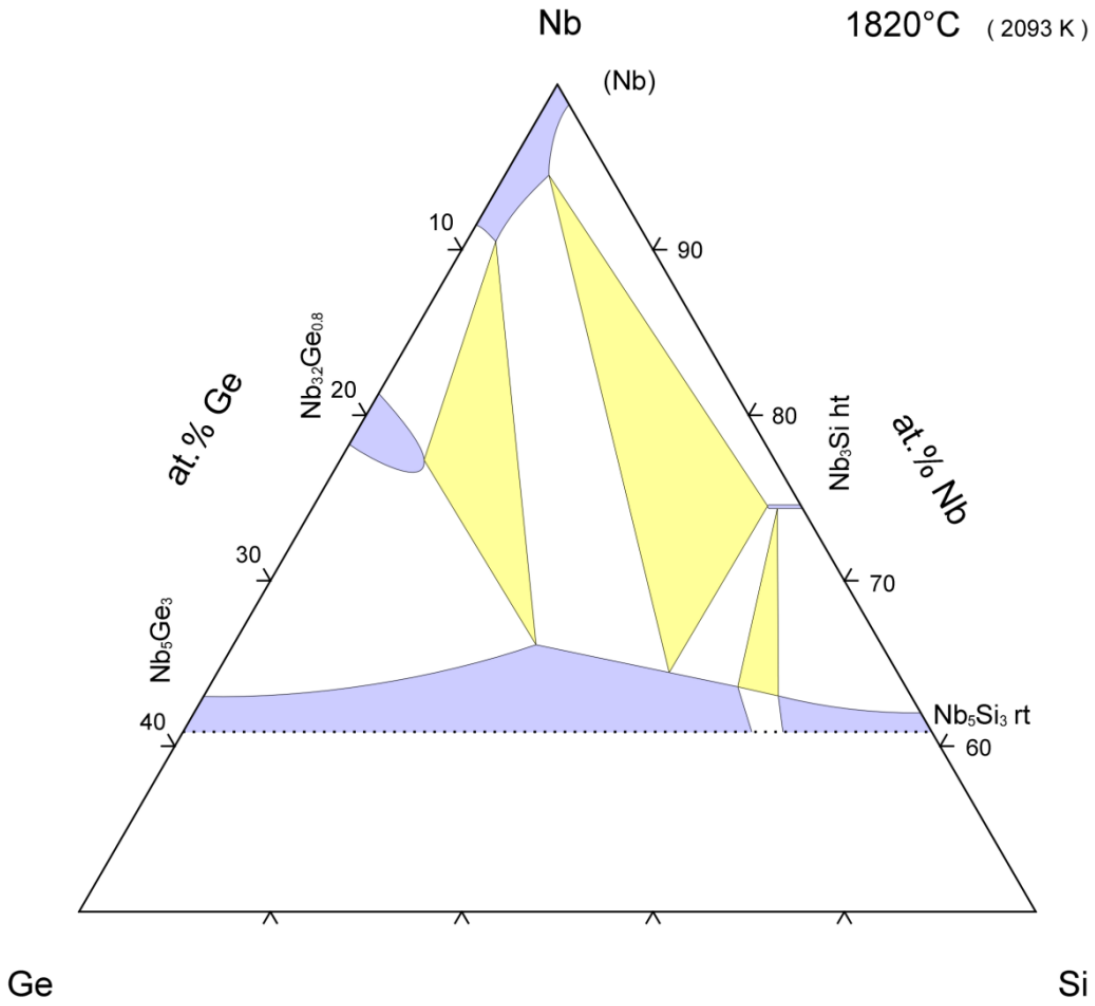

Figure 31. The 1820°C isothermal section of the Ge-Nb-Si system (Pan et al., 1982).

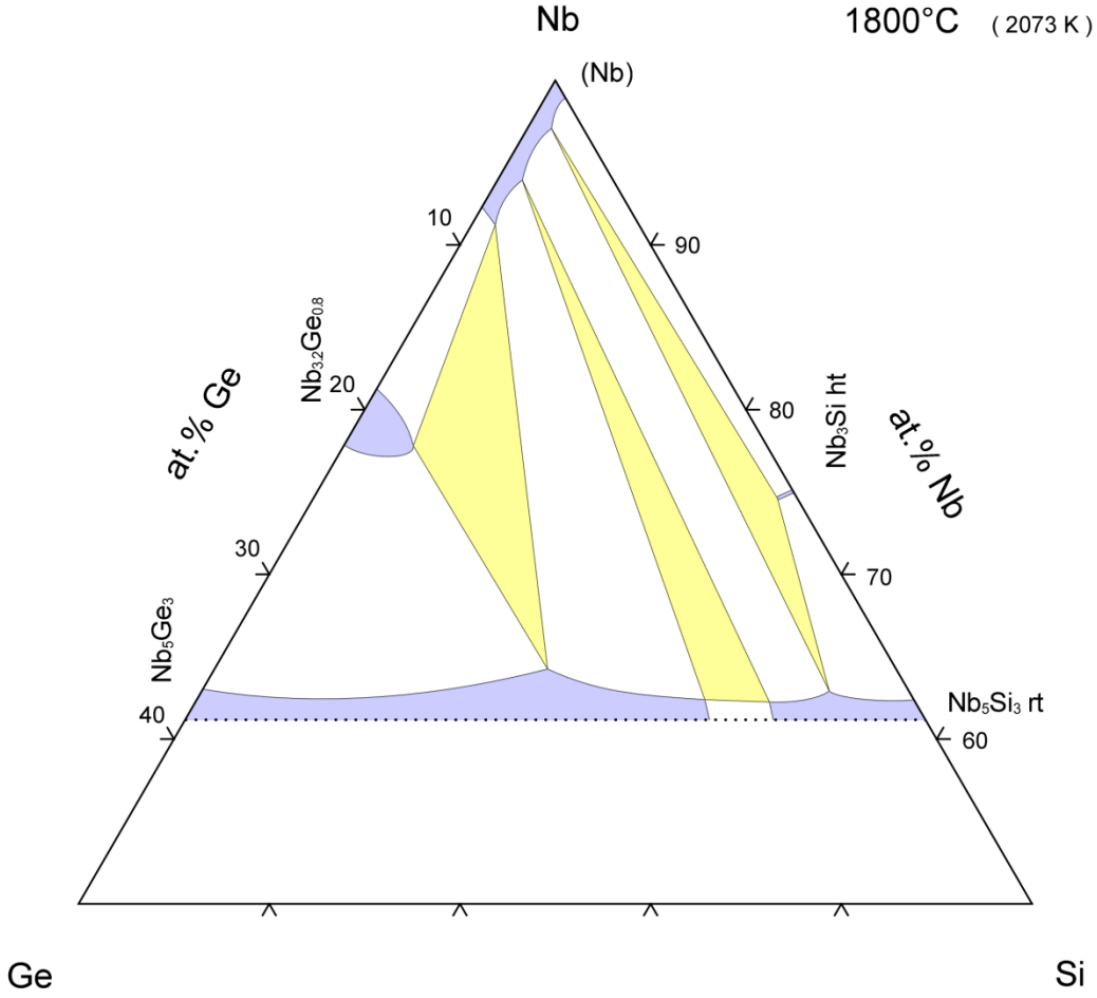

Figure 32. The 1800°C isothermal section of the Ge-Nb-Si system (Pan et al., 1982).

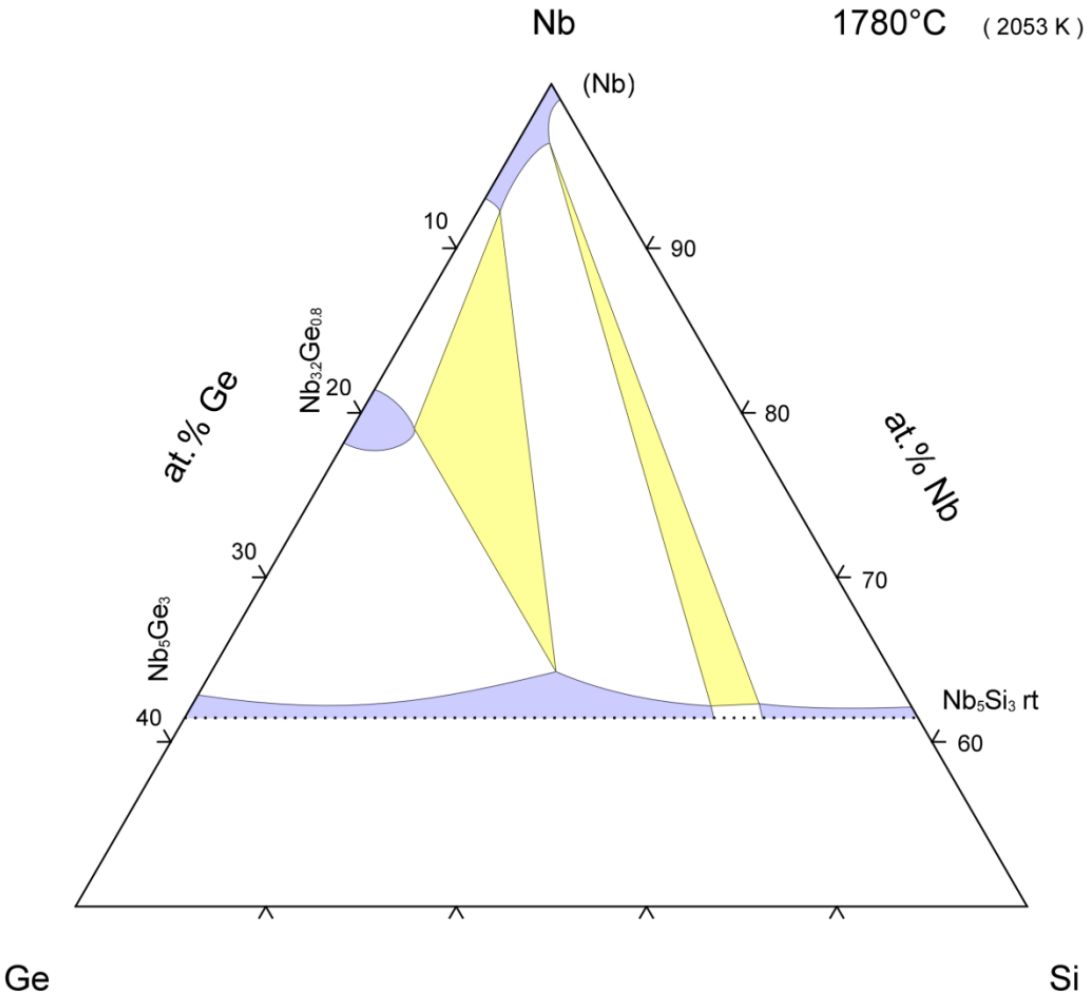

Figure 33. The 1780°C isothermal section of the Ge-Nb-Si system (Pan et al., 1982).

2 Literature Review: Oxidation

2.1 The Nb-O system

The Nb-O phase diagram by Elliot (1960) (Figure 34) is essentially identical with that by Okamoto (1990). The phase diagram indicates that Nb can exist in numerous valence states forming the oxides NbO (Nb^{+2}), NbO_2 (Nb^{+4}), and Nb_2O_5 (Nb^{+5}), with the latter being the most stable (Table 13). The Nb-O system is further complicated by the existence of numerous metastable suboxide phases for NbO and there is conjecture over the polymorphic modifications of Nb_2O_5. These phases are not shown in the phase diagram by Elliot (1960).

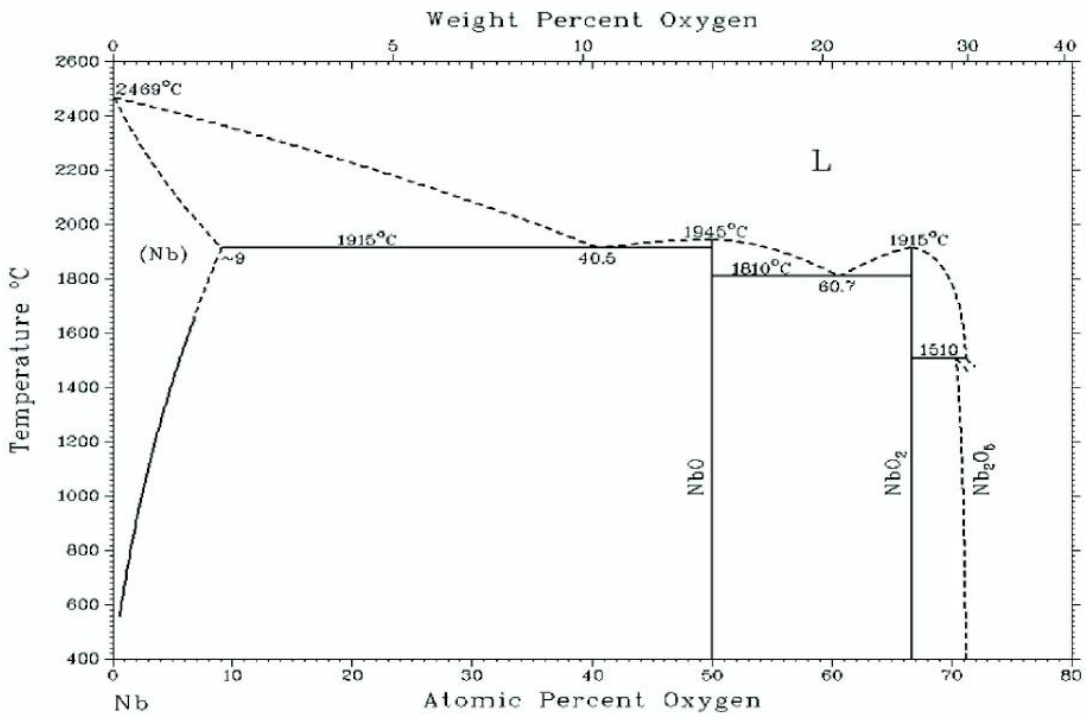

Figure 34. Nb-O phase diagram by Elliot (1960).

Table 13. Heat of formation for the different niobium oxides (Lindau and Spicer, 1974; Samsonov, 1973).

Oxide	ΔH°_{298} (kJ/mol)
NbO	-418.261
NbO_2	-792.147
Nb_2O_5	-1905.831

Noticeable is the high solubility of O in Nb, up to ~ 9 at.% at 1915°C. Elliot (1960) determined the O solubility range of 1 to 4.04 at.% from 500 to 1915°C, whilst Seybolt (1954) reported of

1.38 to 5.52 at.% solubility from 775 to 1100°C. In the bcc Nb lattice O is reported to occupy octahedral rather than tetrahedral interstitial sites (Figure 35), subsequently inducing a strain and expansion of the Nb lattice (Stringer and Rosenfield, 1963; Kofstad, 1966, 1988; Kobyakov and Ponomarev, 2002; Dosch et al., 1986).

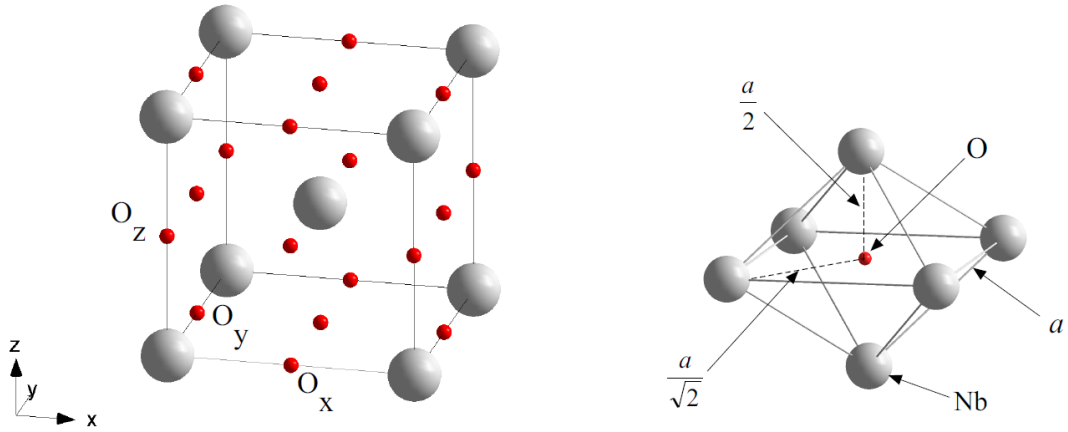

Figure 35. Octahedral interstitial sites within the niobium bcc lattice of lattice parameter a (Delheusy, 2008).

O is reported to display a preferred segregation toward the Nb metal surface before further diffusing into the bulk material where the solubility limit has not been reached (Farrell et al., 1973; Joshi and Strongin, 1974). Dissolution of O into Nb is a very important part of Nb oxidation as it is a prerequisite before suboxide and oxide formation (Norman, 1962; Lindau and Spicer, 1974). The diffusion coefficient D of O in Nb as a function of temperature T is (Powers and Doyle, 1959);

$$D(T) = 0.0212exp\left(-\frac{Q}{RT}\right)\ (cm^2s^{-1})$$

Where R is the molar gas constant (1.987 $calK^{-1}mol^{-1}$) and the activation energy Q is 26910 cal/mol. The solubility limit of O in a metal is reached when the partial free energy of O in the oxide phase formed in equilibrium with the solid solution is equal to the partial free energy of O in the solution. Thus, the measured solubility may be altered by a change in either of these variables Bryant (1962).

Under specific conditions Nb is capable of dissolving more O than given by the Nb-O phase diagram and thus forms a supersaturated solution. This allows the formation of three suboxide phases that can form in 15-20 minutes of oxidation at 320°C (Norman, 1962; Norman et al., 1962). These sub oxides are referred to as NbO_X, NbO_Y, and NbO_Z. Their precipitation out of a super saturated solid solution is to relax lattice strain due to soluble O (Halbritter, 1987).

These sub oxides are metastable and present superlattice structures related to the original Nb metal lattice (Brauer et al., 1962; Norman, 1962; Norman et al., 1962).

The NbO_X has a tetragonal unit cell and forms in the range 270-500°C with O concentration between 2.5 – 3.5 wt.%, equating to an ideal formula of Nb_6O or Nb_5O (Norman, 1962; Brauer et al., 1962). The NbO_Y forms in the range 330-500°C with an ideal formula of Nb_4O. The NbO_Z is also tetragonal and has a unit cell 6 times that of Nb and forms at 400-700°C but its exact composition is unconfirmed (Niebuhr, 1966).

2.1.1 NbO

NbO is the first stable oxide formed. During oxidation, O covalently binds to conduction electrons, depleting the conduction band (Brauer, 1941; Halbritter, 1987). NbO exhibits a defective face centred cubic (fcc) rock-salt (NaCl) structure (a= 4.21 Å, Pearson symbol cP6, Space group $Pm\bar{3}m$) with 25% ordered vacancies in each sublattice. In the NbO structure (Figure 36) Nb atoms are coordinated in a 3D octahedra network with O atoms located between them (Pialoux et al., 1982; Schulz and Wentzcovitch, 1993).

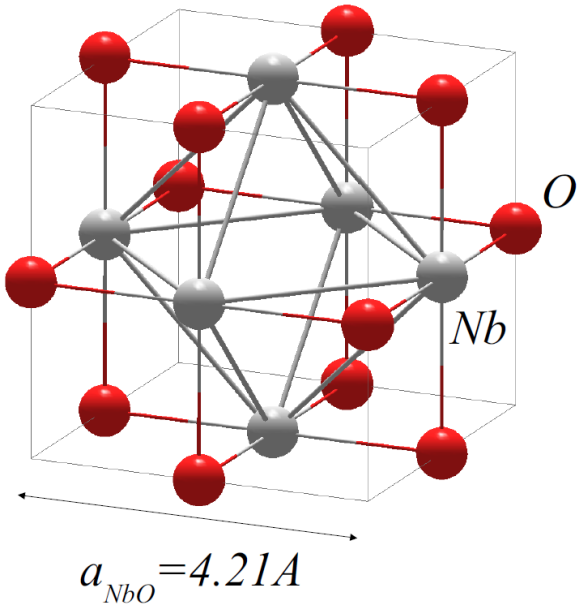

Figure 36. Defective ordered fcc rock-salt crystal structure of NbO (Delheusy, 2008).

2.1.2 NbO_2

With O concentration exceeding the stoichiometry range of NbO and Nb remaining in the Nb^{+2} oxidation state, NbO_2 can form. NbO_2 is reported to possess two forms, at temperatures below 800°C (Figure 37) is an n-type semiconductor consisting of a tetragonal distorted rutile crystal structure (Pearson symbol tI96, space group $I4a_1/a$). Such structure is described as chains of edge-sharing NbO_6 octahedrons alike the ideal rutile structure (Elliott, 1960; Cheetham and Rao, 1976).

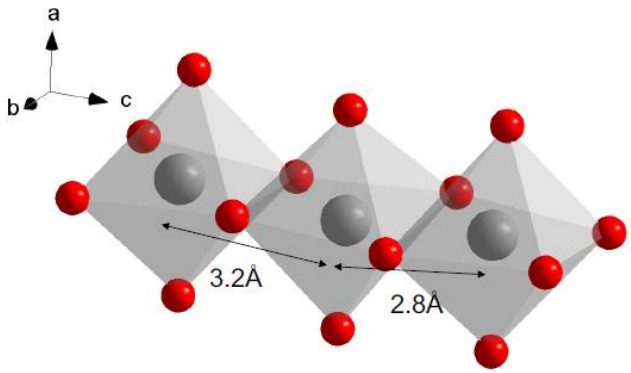

Figure 37. NbO_6 octahedra chains in the low temperature distorted rutile structure of NbO_2 (Delheusy, 2008).

The high temperature NbO_2 structure (Figure 38) is a metallic conductor existing above ~ 800-810°C with a regular rutile structure (Pearson symbol tI48, space group $I4_1$) forming via a reversible second-order phase transition (Brauer, 1941; Elliott, 1960; Pialoux et al., 1982; Jiang and Spence, 2004).

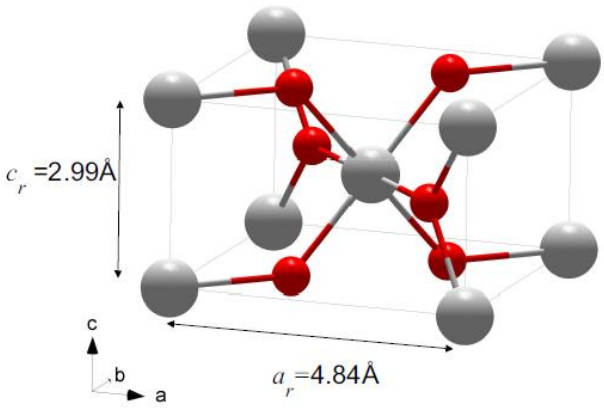

Figure 38. High temperature undistorted rutile NbO_2 (Delheusy, 2008).

2.1.3 Nb_2O_5

The Nb_2O_5 is the the most stable Nb oxide (Table 13) when sufficient O is available to react (Samsonov, 1973; Lindau and Spicer, 1974). Although the initially formed Nb_2O_5 is amorphous, there are several crystalline polymorphic forms that are the subject of conjecture as polymorph formation is found to be highly dependent upon the preparation method and annealing conditions used (Brauer, 1941; Elliott, 1960; Terao, 1963, 1965; Schäfer et al., 1966a; Taylor and Doyle, 1967; Spyridelis et al., 1967; Nowak and Ziolek, 1999; Nikishina et al., 2012). The Nb_2O_5 pentoxide stoichiometry for all polymorphs is maintained by NbO_6 octahedra, where O^- surrounds a central Nb ion. The key polymorphs are:

1. High temperature (HT) monoclinic α-Nb_2O_5
2. Medium temperature (MT) monoclinic β-Nb_2O_5
3. Low temperature (LT) orthorhombic γ-Nb_2O_5

Each polymorph form is irreversible. The most stable polymorph is the high temperature α-Nb_2O_5 monoclinic form with Pearson symbol mP99, space group P12/m1, and lattice parameters of approximately a = 21.34, b = 2.816, c = 19.47Å, β= 120.2° (Holtzberg et al., 1957; Reisman and Holtzberg, 1959; Schäfer et al., 1966a). The existence of monoclinic α-Nb_2O_5 is agreed upon by numerous authors (Elliot, 1960; Kubaschewski and Hopkins, 1960; Terao, 1963; Schäfer et al., 1966b; Balachandran and Eror, 1982; Nowak and Ziolek, 1999; Franke and Neuschütz, 2006). The formation temperature of monoclinic α-Nb_2O_5 has been reported as low as 830°C (Holtzberg et al., 1957) and as high as ~ 1100°C (Schäfer et al., 1966b). The latter and even higher temperatures are, however, more commonly reported.

The HT monoclinic α-Nb_2O_5 unit cell is relatively large, consisting of 28 Nb and 70 O atoms (Figure 39). Such unit cell is built up by arrays of 3 x 5 (Figure 40) and 3 x 4 (Figure 41) ReO_3 type blocks of corner-shared NbO_6 octahedrons (Figure 42) where each block is joined by octahedral edge sharing that constructs octahedral planes. Notably, the 3 x 5 and 3 x 4 blocks of octahedra only equate to a formula of $Nb_{27}O_{70}$. In Figure 40, the locations r and s are noted, while in Figure 41 there are locations p and q. These locations indicate tetrahedral positions where one Nb atom out of 28 per unit cell occupies it, linking the blocks together. Figure 43 illustrates the built up arrays and their block stacking which makes up the pentoxide structure.

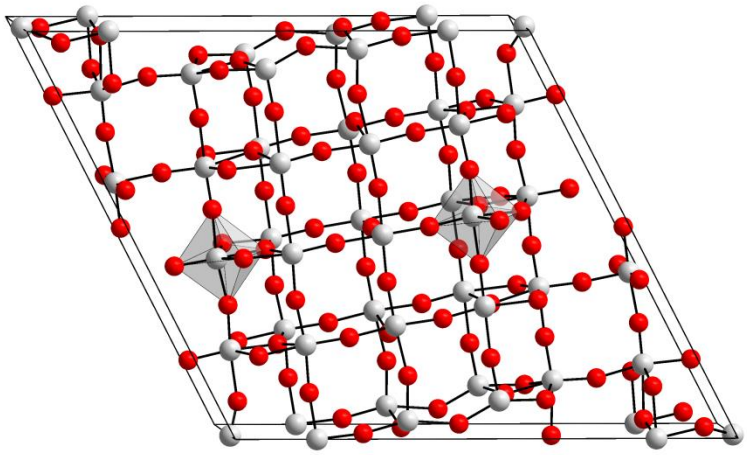

Figure 39. The HT monoclinic α-Nb_2O_5 crystal structure consisting of 28 Nb and 70 O atoms. The white spheres represent Nb atoms whilst the red represent O (Gatehouse and Wadsley, 1964).

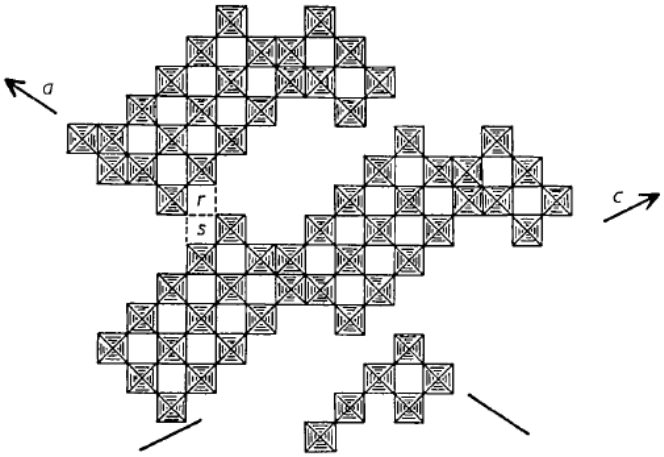

Figure 40. 3 x 5 array of NbO_6 octahedra (Gatehouse and Wadsley, 1964).

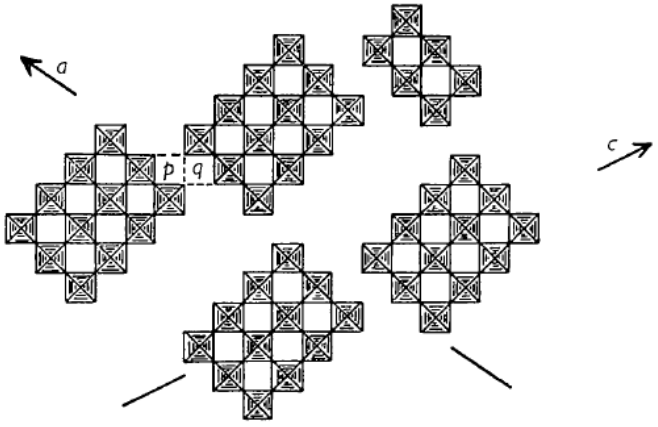

Figure 41. 3 x 4 array of NbO_6 octahedra linked via corner O sharing whilst blocks are linked through edge O sharing (Gatehouse and Wadsley, 1964).

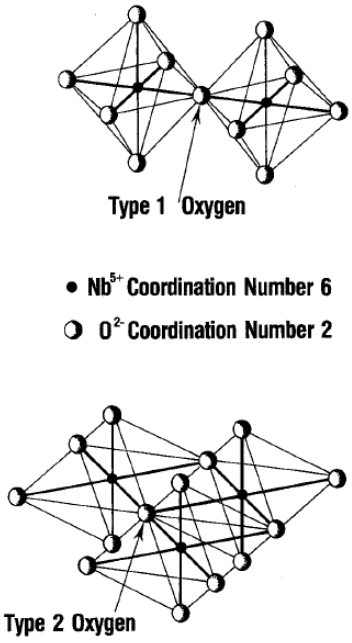

Figure 42. NbO_6 octahedra blocks corner sharing (Type 1) and edge sharing (Type 2) of (Halbritter, 1987).

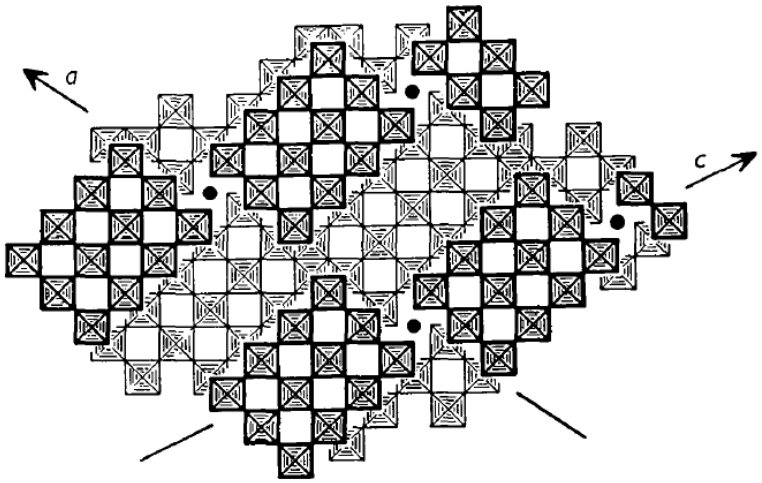

Figure 43. Niobium pentoxide drawn as idealised octahedra. The lighter shade forms the 3 x 5 blocks of Figure 40 while the darker shaded blocks are the 3 x 4 from Figure 41. The black circles are the Nb atoms in tetrahedral positions which outline the monoclinic unit cell in projection (Gatehouse and Wadsley, 1964).

The MT β-Nb_2O_5 is also monoclinic (Nowak and Ziolek, 1999) forming at 830°C, a temperature at which the α-Nb_2O_5 is also reported but not widely accepted. It is more than plausible the two polymorphs have been mistaken for one another over their temperature ranges studied due to their highly similar structures. An important point is that the monoclinic crystal structure dominates beyond the LT orthorhombic γ-Nb_2O_5 polymorph.

The LT γ-Nb_2O_5 is found to form at approximately 500°C (Brauer, 1941; Kato and Tamura, 1975; Okamoto, 1990). Its unit cell consists of 16 Nb and 42 O atoms (Figure 44). The 16 Nb atoms lie in a sheet parallel to (001) and are surrounded by seven or six O atoms forming pentagonal bi-pyramidal or distorted octahedral coordination polyhedral, respectively. The polyhedra are joined by edge or corning sharing within the (001) sheet and exclusively by corner-sharing along [001] (Kato and Tamura, 1975). A summary of the various works studying Nb_2O_5 polymorphism is shown in Table 14 and was adapted here from the work of Nikishina et al., (2012), compounding the elusiveness of the polymorphs.

It is very important to note there is almost a doubling of the unit cell size from the γ → β/α transformation that induces significant stresses in the surface oxide and, hence, the high temperature oxidation of pure Nb studied by Kubaschewski and Hopkins (1960) and Kofstad (1988) report linear growth, poor adhesion, and easy spallation of α-Nb_2O_5 at temperatures above 1000°C, while at 500°C the γ-Nb_2O_5 growth kinetics are parabolic and the oxide appears pore free. The reader should refer to these works for a thorough outline of the Nb oxidation process, but the important fact to be aware of is at the Nb-silicide based alloy potential use temperatures monoclinic α-Nb_2O_5 formation would dominate and is non-protective (Pilling-Bedworth ratio of 2.7).

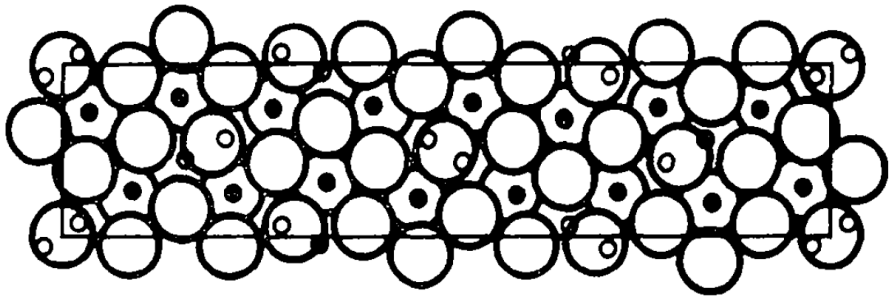

Figure 44. Projection of the low temperature orthorhombic γ-Nb_2O_5 structure along the [001] direction, the large open circles represent O atoms whilst the smaller filled and small unfilled circles are Nb atoms (Kato and Tamura, 1975).

Table 14. Polymorphous transformations of Nb_2O_5 as reported by numerous authors. In this table T, M, and H are abbreviations to *Tief*, *Mittel*, and *Hoc* translated from German to English are; low, medium, and high in reference to temperature. Adapted from (Nikishina et al., 2012).

References	Polymorphous transformations of niobium pentoxide
Brauer (1941)	Amorphous → γ(T) orthorhombic→ β(M) monoclinic→ α(H) monoclinic
Lapitskii et al. (1952)	Amorphous → T + M
Schäfer et al. (1966)	Amorphous $\xrightarrow{400-550°C}$ δ(TT) Hexagonal $\xrightarrow{700°C}$ (T) monoclinic $\xrightarrow{800\,°C}$ β(M) monoclinic $\xrightarrow{1050\,°C}$ α(H) monoclinic Note: TT refers to *tief-tief* which translates to low-low, indicating an additional temperature range of a niobium pentoxide polymorph.
Frevel and Rinn (1995)	Amorphous → Orthorhombic (TT) $\xrightarrow{700°C}$ T Pseudo-hexagonal lattice: a= 3.606 Å, c= 3.925 Å. Monoclinic: a= 7.31 Å, b=15.72 Å, c= 10.75 Å, β= 120°42’
Holtzberg et al., (1957)	Amorph. $\xrightarrow{>440°C}$ δ(γ’) $\xrightarrow{830°C}$ γ → β $\xrightarrow{>1000°C}$ α γ’= Orthorhombic disordered α form. Monoclinic: a = 21.34 Å, b = 3.816 Å, c = 19.47 Å, β = 120° 20’
Resiman and Holtzberg (1957)	Amorph. → III $\xrightarrow{380°C}$ II(β) $\xrightarrow{1060°C}$ I(α) $\xrightarrow{128\,°C}$ I-high(ϵ)
Goldschmidt (1959)	Amorph. $\xrightarrow{<700°C}$ β(M) → α(H)
Nowotny (1960)	Amorph. $\xrightarrow{<1000°C}$ M $\xrightarrow{>1000°C}$ β’(H)
Hicks (1961)	Amorph. $\xrightarrow{400°C}$ δ(TT) hexagonal $\xrightarrow{400-700°C}$ γ(T) → γ’(B) → β(M) $\xrightarrow{700-800°C}$ α(H) δ(TT) Hexagonal: a = 3.621 Å, b = 3.932 Å γ(T) Monoclinic: a = 7.317 Å, b = 15.73 Å, c = 10.75 Å, β = 120° 30’ γ’(B) Monoclinic: a = 7.348 Å, b = 5.962 Å, c = 13.65 Å, β = 115° 30’ β(M) Monoclinic: a = 22.10 Å, b = 7.638 Å, c = 19.52 Å, β = 118° 15’ α(H) Monoclinic: a = 21.20 Å, b = 3.824 Å, c = 19.39 Å, β = 120° 10’
Gatehouse and Wadsley (1964)	Existence of monoclinic α modification; a= 21.16 Å, b= 3.822 Å, c= 19.35 Å, b = 119° 50’
Laves et al., (1964)	Existence of ζ and η modifications
Gruehn et al., (1966)	Existence of high-temperature R-modification; a = 3.98 Å, b = 3.82 Å, C = 12.7 Å, β = 90° 7’
Hibst and Gruehn (1978)	Amorph. $\xrightarrow{400°C}$ TT $\xrightarrow{1000°C}$ M
Chen and Swalin (1966)	Existence at 1350°C of α(H) modification.
Mertin et al., (1970)	Existence of tetragonal M(β) modification; a = 20.44 Å, b = 3.832 Å
Rozhenko et al., (1972)	Amorph. $\xrightarrow{600-840°C}$ β(M) $\xrightarrow{850°C}$ α(H)
Kato and Tamura (1975)	Existence of orthorhombic T(γ) modification; a = 6.175 Å, b = 29.17 Å, C = 3.93 Å
Izumi and Kodama (1978)	Amorph. $\xrightarrow{250°C}$ TT(δ) $\xrightarrow{700°C}$ T(γ) $\xrightarrow{900°C}$ M(β) $\xrightarrow{1000°C}$ H(α)
Kikuchi et al., (1985)	Existence of orthorhombic T(γ) modification; a = 6.179 Å, b = 29.21 Å, c = 3.939 Å
Zibrov et al., (1998) Filonenko et al., (2001)	Existence of high pressure phase (P = 8 GPa, T = 800-1100°C) Z- Nb_2O_5; a = 5.213 Å, b =4.699 Å, c = 5.928 Å, β = 108.56°

2.2 The Ti-O System

The Ti-O system shown in Figure 45 is from Okamoto (2011) and was based on the work of Cancarevic et al., (2007) who used CALPHAD to refine the work of Waldner & Eriksson (1999). Figure 46 is the Ti-O phase diagram from the same works, where O ranges from 58 – 68 at.%. Okamoto (2011) stressed that more experimental work is required to resolve the discrepancies between numerous authors, especially to clarify the stability of the various Ti_nO2_{n-1} (n= 2, 3, 4…) oxides shown in Figure 46 and Table 15. Similarly to Nb, Ti has a high solubility for O in both the hcp α and bcc β forms, dissolving up to 33.3 and 8 at.% O, respectively.

Early work on the oxidation of pure Ti in the 800 – 1200°C temperature range was performed by Kofstad et al., (1961) who agreed with Wallwork & Jenkins (1959) that initial Ti oxidation kinetics were parabolic due to O dissolution into the metal until a composition of $TiO_{0.35}$ was reached. At the $TiO_{0.35}$ composition structural changes are found to occur (Andersson et al., 1957) and heavy oxide growth begins. During this heavy oxidation stage the kinetics change to a linear oxidation rate, as suggested by Kofstad et al. (1961) the linear kinetics are governed by oxide nucleation and growth of oxide nuclei and may be considered to be a result of steady-state nucleation process, which assumes a porous outer oxide-scale permitting rapid O penetration to react at the metal/oxide interface.

The $TiO_{0.35}$ composition falls in the αTi + γTiO above 935°C and αTi + Ti_3O_2 below 935°C two phase regions (Figure 45) and, hence, Kofstad et al. (1961) proposed the oxide nucleation involves TiO formation followed by rapid oxidation to TiO_2. TiO_2 is the most stable and dominant oxide formed on Ti with a tetragonal rutile crystal structure that is non-protective during prolonged oxidation because it is an n-type anion-deficient oxide which O anions can diffuse through and thus oxidation proceeds at the metal/oxide interface growing into the Ti base metal. Above 950°C the recrystallization and sintering of the outer TiO_2 scale is reported to reduce the oxidation rate, however the oxide is still deemed non-protective.

The oxides on Ti will result in varying layers into the base metal. Under the TiO_2 outer layer will be a TiO layer, followed by a O-rich hcp αTi_{ss} layer, aka α-case. The diagram (Figure 45) quite clearly indicates β,αTi_{ss} are stabilised by interstitial O.

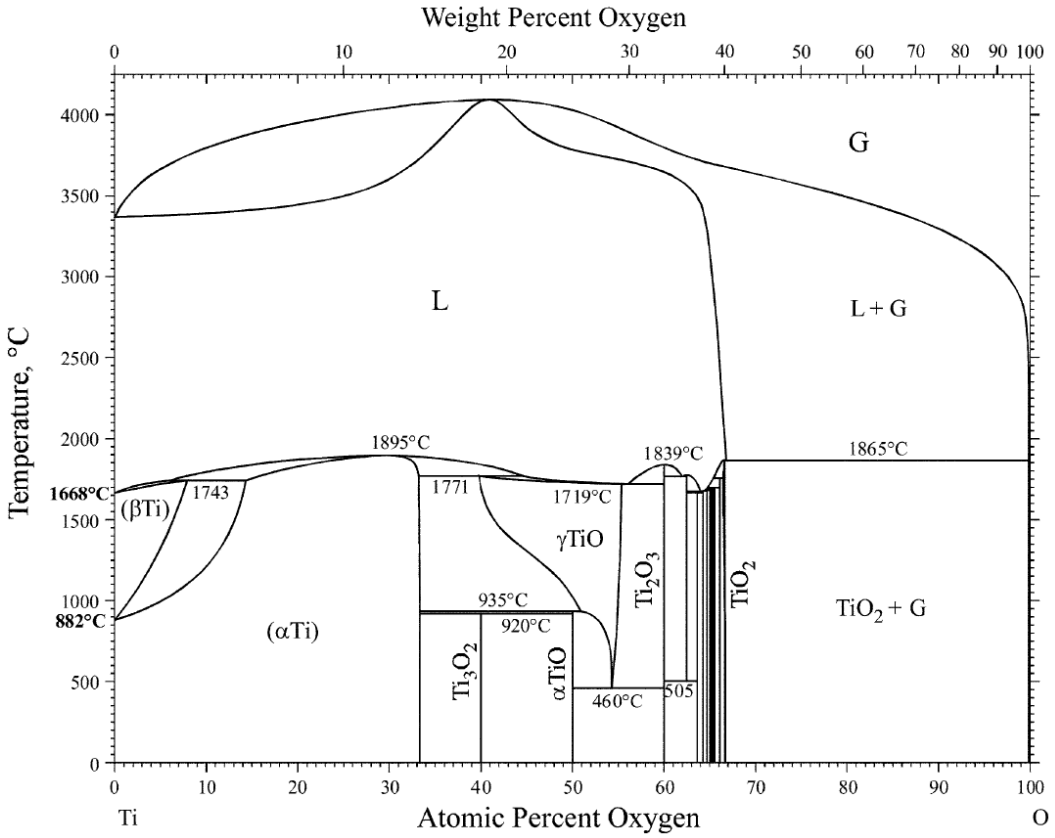

Figure 45. The Ti-O system by Okamoto (2011).

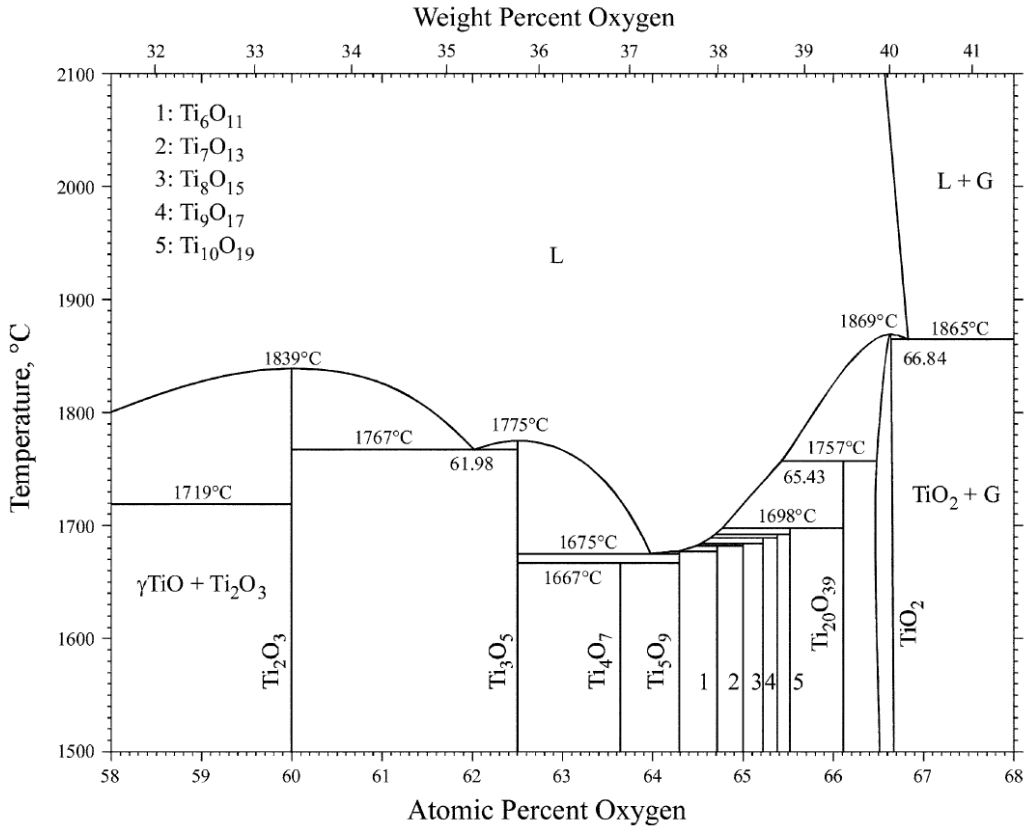

Figure 46. The Ti-O system from Okamoto (2011) with O content ranging from 58 – 68 at.%.

Table 15. Crystal structure and composition data for the Ti-O system from Okamoto (2011) with additions from Murray and Wriedt (1987).

Phase	Composition at.% O	Pearson Symbol	Space Group	Structure designation	Prototype
βTi	0 – 8	cI2	$Im\bar{3}m$	A2	W
αTi	0 – 33.3	hP2	$P6_3/mmc$	A3	Mg
Ti_3O*	20 – 30	hP16	$P\bar{3}1c$	…	…
Ti_2O*	25 – 33.4	hP16	$P\bar{3}m1$	…	…
Ti_3O_2	40	hP5	P63/mmm	…	…
γTiO	40 – 55.3	cF8	$Fm\bar{3}m$	B1	NaCl
βTiO*	…	c**	…	…	…
αTiO	50	mC16	…	…	…
$\beta Ti_{1-x}O$*	55.5	oI12	I222	…	…
$\alpha Ti_{1-x}O$*	55.5	tI18	tI18	I4/m	…
Ti_2O_3	60	hR10	$R\bar{3}c$	$D5_1$	αAl_2O_3
Ti_3O_5	62.5	mC32	C12/m1	…	…
Ti_4O_7	63.64	aP22	$P\bar{1}$	…	…
Ti_5O_9	64.39	aP28	$P\bar{1}$	…	…
Ti_6O_{11}	64.71	aP34	$P\bar{1}$	…	…
Ti_7O_{13}	65	aP40	$P\bar{1}$	…	…
Ti_8O_{15}	65.22	aP46	$P\bar{1}$	…	…
Ti_9O_{17}	65.38	aP52	$P\bar{1}$	…	…
$Ti_{10}O_{19}$	65.52	…	…	…	…
$Ti_{20}O_{39}$	66.11	aP*	$P\bar{1}$	…	…
TiO_2	66.5 – 66.7	tP6	$P4_2/mnm$	C4	

*(Murray and Wriedt, 1987)

2.3 The Nb_2O_5-TiO_2 System

Due to the high content of Nb and Ti in Nb-silicide based alloys the oxides formed are typically mixed. Since the most stable oxides of Nb and Ti are Nb_2O_5 and TiO_2 the Nb_2O_5 – TiO_2 binary system shown in Figure 47 is important and reactions of such oxides are worth consideration. In this system, Nb_2O_5 and TiO_2 can form several intermediate oxides, namely the $TiNb_{24}O_{62}$, $TiNb_{14}O_{37}$, $Ti_2Nb_{10}O_{29}$, and $TiNb_2O_7$. The latter two oxides are most commonly identified in the oxide scales formed on Nb-silicide based alloys. The $TiNb_2O_7$ is reported to possess a monoclinic I2/m crystal structure (similar to α-Nb_2O_5) with lattice parameters a = 11.9, b = 3.77, c = 10.1 Å, β = 120.2°. The cell can also be indexed with a doubled 'a' parameter transforming to a C2/m space group (Dyson, 1957; Gasperin, 1984; Babich et al., 1988; Reich et al., 2001). Comparison with the Nb-O phase diagram (Figure 34) shows that in the presence of TiO_2 the stability of Nb_2O_5 is reduced from ~ 1510 to 1400°C.

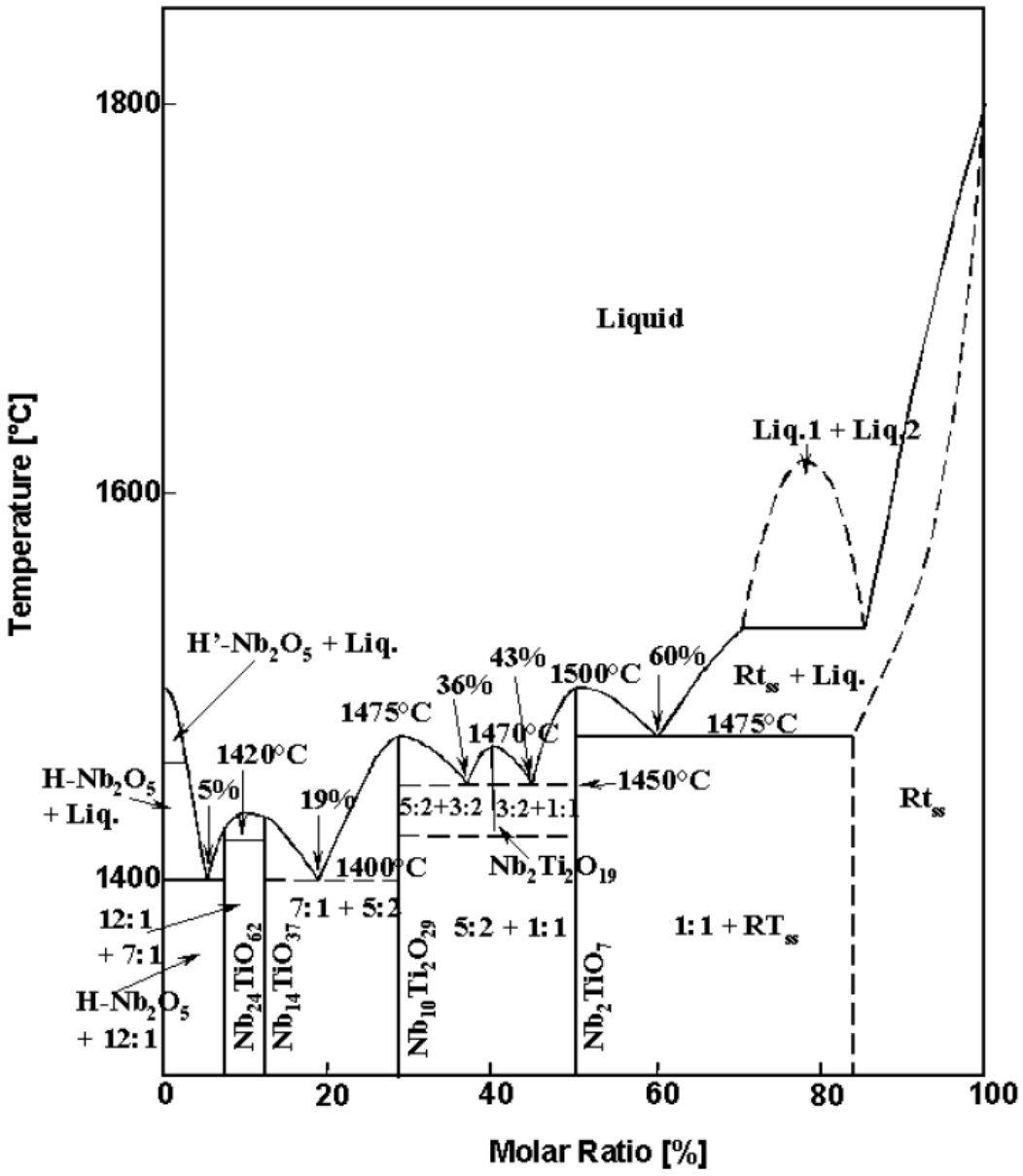

Figure 47. The Nb_2O_5 – TiO_2 phase diagram (Reich et al., 2001).

2.4 The Si-O System

The Si-O phase diagram by Wrledt (1990) is shown in Figure 48 and by Okamoto (2007) in Figure 49. SiO_2 has been found to exist in the polymorphic forms summarised in Table 16, note that the phase diagram by Wrledt (1990) includes tridymite and considers it to be metastable, but it is omitted by Okamoto (2007). In the temperature range of the phase diagram by Okamoto (2007) (Figure 49), only the cristobalite γSiO_2 is stable. The α and β forms are stable from below 575°C and between 575-872°C, respectively.

Unlike Nb_2O_5 and TiO_2, SiO_2 formation is protective with a Pilling-Bedworth Ratio of 2.15 and has relatively slow growth kinetics that are comparable to Al_2O_3, which is arguably the slowest growing and most protective high temperature oxide (Figure 50). However, SiO_2 is not stable under low gas pressures where it decomposes to SiO, although this is unlikely to occur in a gas turbine environment. A more pertinent problem is the susceptibility of SiO_2 to water vapour induced volatility forming $Si(OH)_4$ gas. However, such is not a concern of this thesis for the time being (Birks et al., 2006; Bose, 2007a).

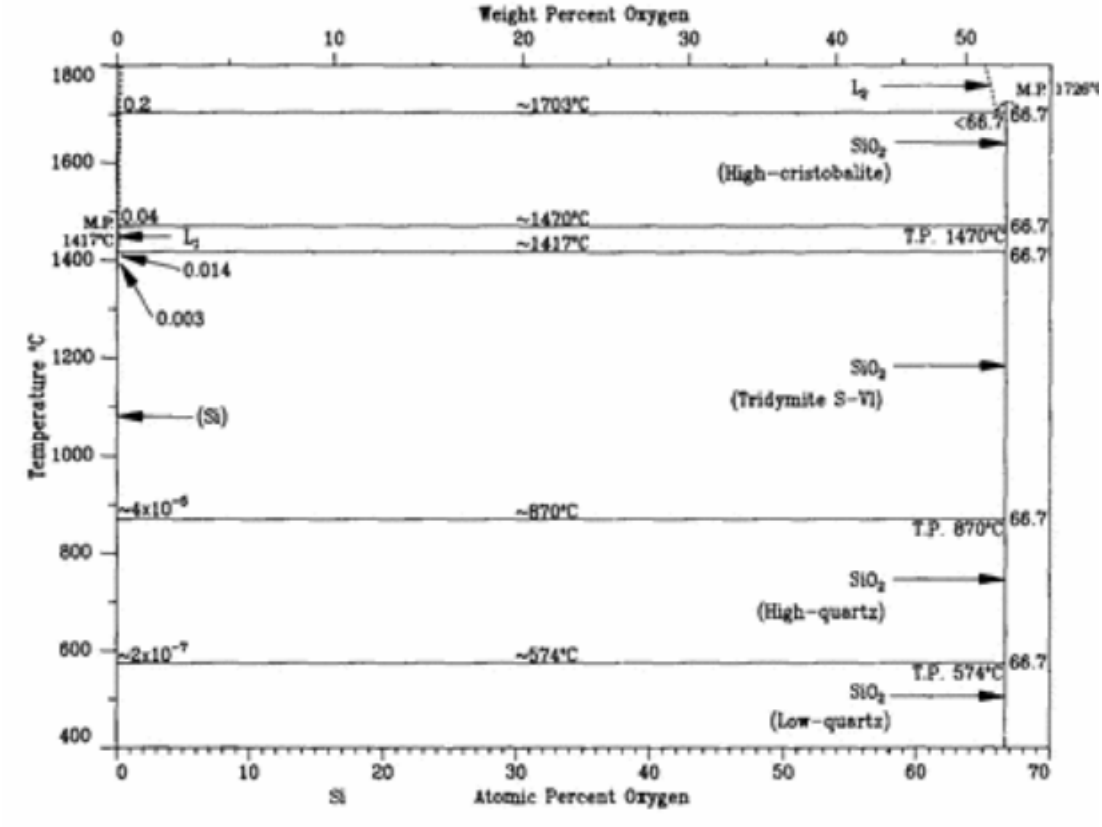

Figure 48. The O-Si system as reported by (Wrledt, 1990).

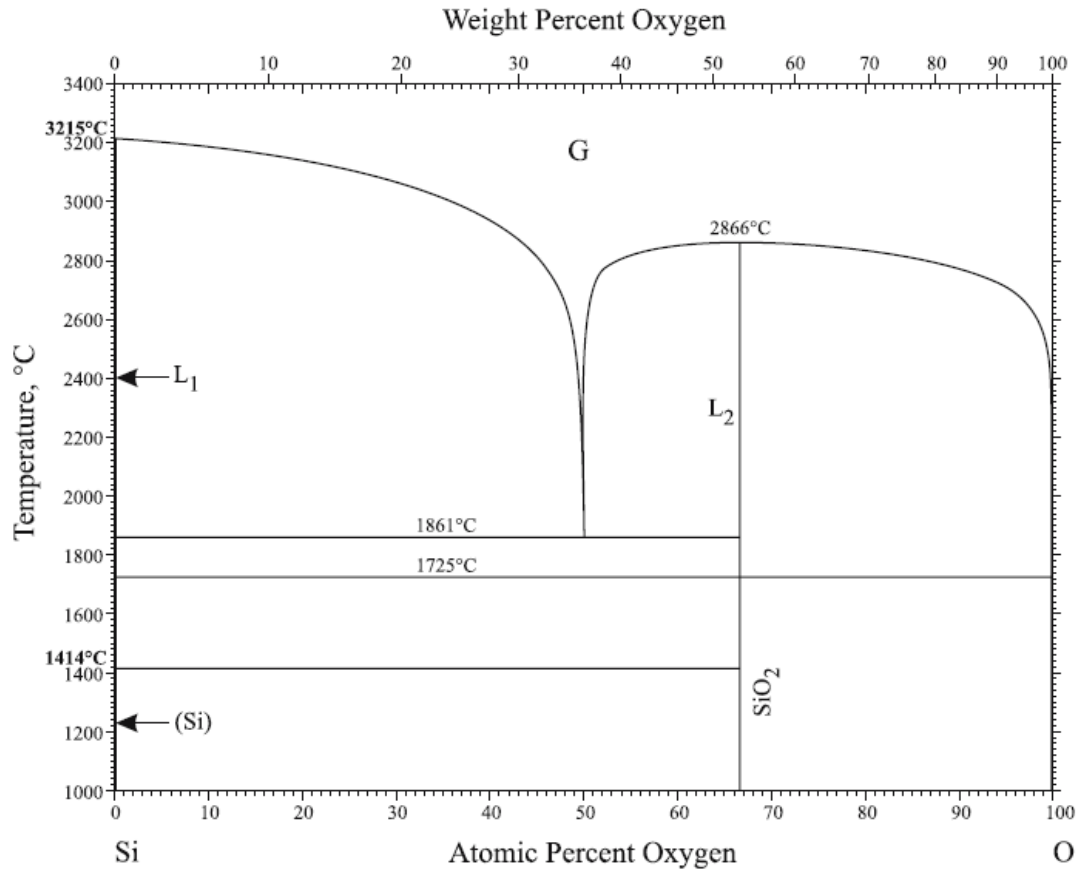

Figure 49. The Si-O system by (Okamoto, 2007).

Table 16. Crystal structures of phases in the Si-O system (Okamoto, 2007; Wrledt, 1990).

Phase	Composition at.% O	Pearson Symbol	Space Group	Structure designation	Prototype
Si	O	cF8	$Fd\bar{3}m$	A4	C (diamond)
S-VI, SiO_2	66.7	hP9	?	…	Tridymite
γSiO_2	66.7	cF104	$Fd\bar{3}m$	…	Cristobalite
βSiO_2	66.7	hP9	$P6_266$	…	High quartz
αSiO_2	66.7	hP9	$P3_221$	…	Low quartz

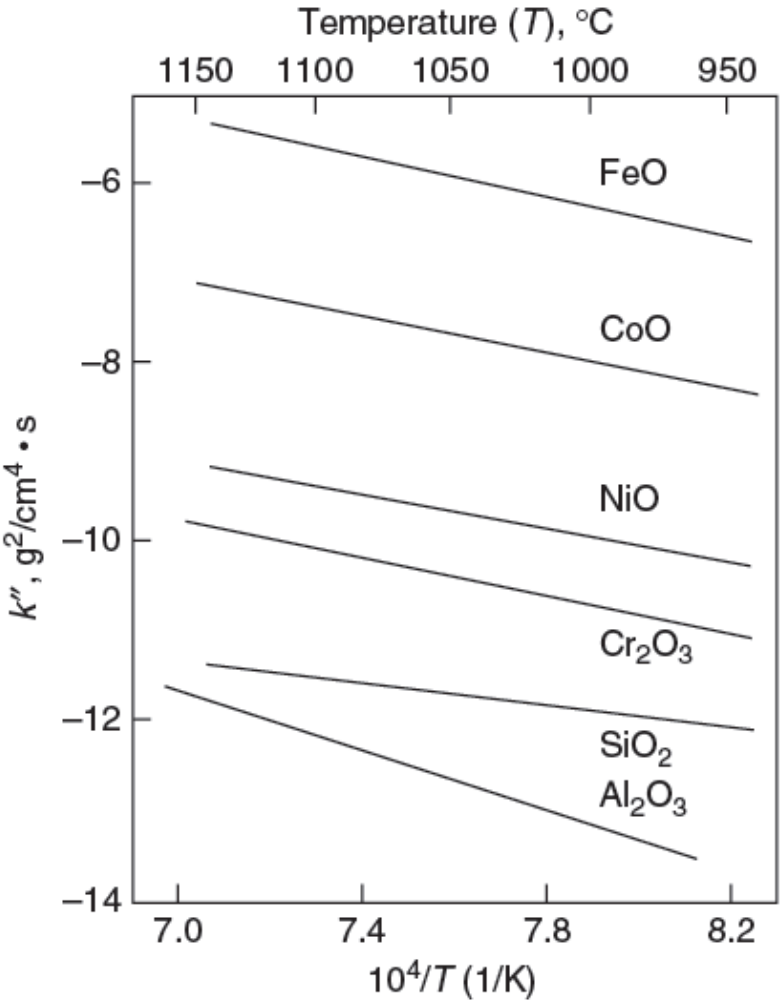

Figure 50. Order-of-magnitude parabolic rate constants for the growth of several oxides (Bose, 2007a).

2.5 The Cr-O System

The Cr-O phase diagram is shown in Figure 51 and crystal structure data in Table 17. This is a relatively simple system where the Cr_{ss} has minimal solubility for O and is seemingly dominated by chromia, Cr_2O_3, formation. However, various works report the intermediate phases CrO_2, CrO_3, Cr_5O_{12}, Cr_6O_{15}, Cr_2O_5, Cr_8O_{21} and CrO_3 but they were deemed unconfirmed by Okamoto (1997b). The calculated Cr_3O_4 phase boundaries in Figure 51 are in close agreement with Toker et al., (1991), although no crystal structure data was reported. Cr_2O_3 is protective with a PBR of 1.99. However, it will volitalise above 1000°C by reacting with O to form gaseous CrO_3 (Bose, 2007b).

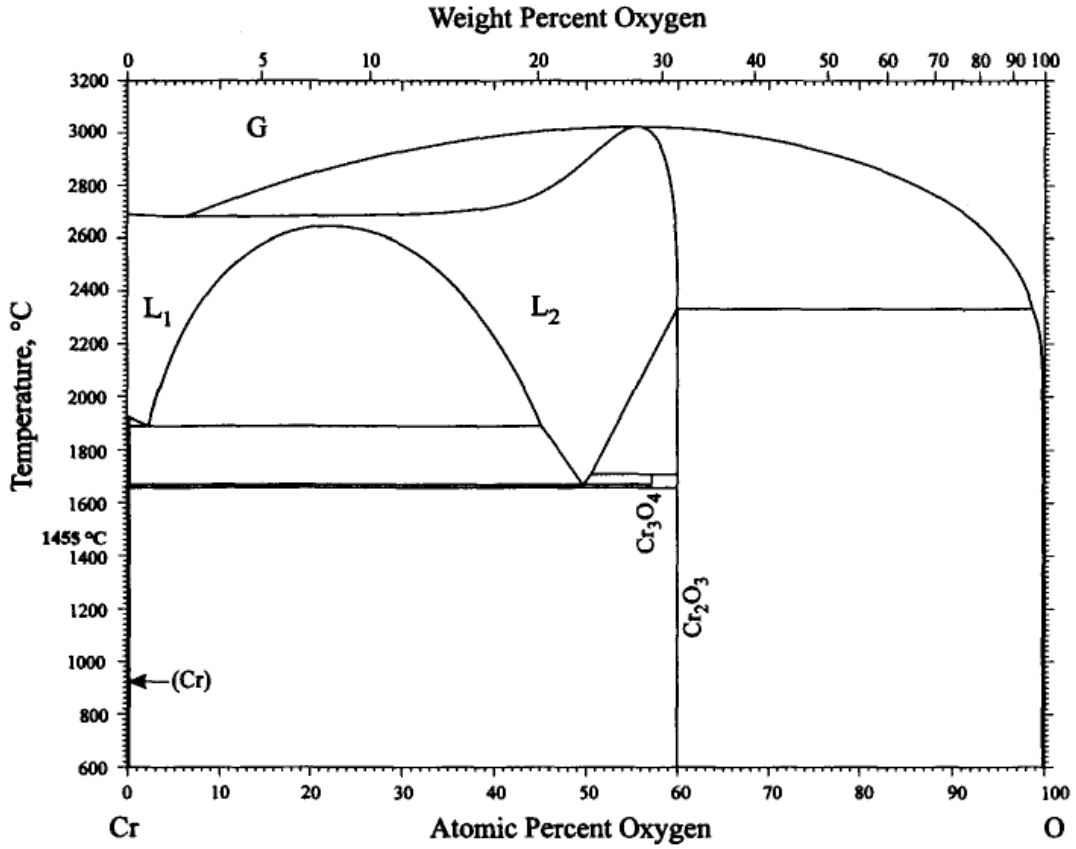

Figure 51. The Cr-O system (Okamoto, 1997b).

Table 17. Crystal structures from the Cr-O system (Okamoto, 1997b).

Phase	Composition at.% O	Pearson Symbol	Space Group	Structure designation	Prototype
Cr_{ss}	~1	cI2	Im3m	A2	W
Cr_3O_4	57	--	--	--	--
Cr_2O_3	60	hR30	$R\bar{3}c$	--	Al_2O_3

2.6 Oxidation of Nb-Silicide based alloys

It quite clear from Figure 52 that simple Nb alloys and binary Nb-Si alloys have poor oxidation behaviour, hence the clear need for alloying. As numerous compositions of Nb-silicide based alloys have been reported throughout literature, and oxidation has been studied under various conditions, a good start for discussing the oxidation of Nb-silicide based alloys is with the MASC alloy. The MASC composition of Nb-24.7Ti-16Si-8.2Hf-2Cr-1.9Al (at.%) that also had small additions of Ge and Sn was developed by General Electric (Bewlay et al., 1996). The MASC alloy was reported to possess a good balance of mechanical properties and oxidation resistance, making it a good baseline reference for oxidation performance against other Nb-silicide based alloys. Its oxidation performance in various forms is depicted in Figure 53.

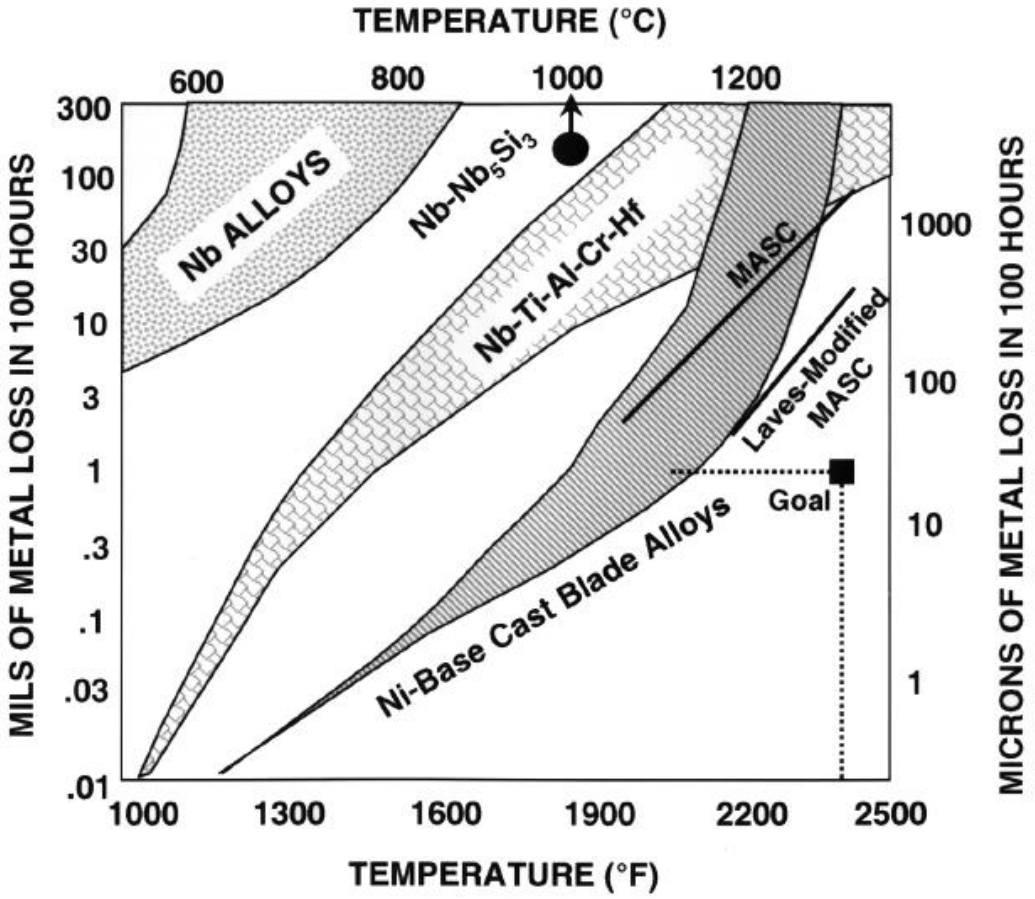

Figure 52. The oxidation behaviour of Nb-silicide based alloys shown as a function of temperature and compared with both Ni-based superalloys and monolithic Nb alloys (Bewlay and Jackson, 2000).

Figure 53 shows deteriorating oxidation performance with increasing fraction of Nb_{ss} in the microstructure, conveying that the Nb_{ss} is (ironically) the Achilles heel of Nb-silicide based alloys in regards to oxidation. This is owed to the aforementioned high solubility of O in Nb and the growth of non-protective Nb_2O_5 oxide. The MASC microstructure after oxidation was not published by the original researchers. However, Mathieu et al., (2012) studied the MASC composition, though it was not clear if their alloy included Ge and Sn. Their oxidised microsctructure is shown in Figure 54 and highlights the susceptibility of the MASC alloys Nb_{ss} to internal O penetration. Thermogravimetric (TGA) isothermal oxidation data are plotted in Figure 55 and follow a para-linear behaviour where no complete passivation was observed after 100h of oxidation. Preferential internal saturation and attack of the Nb_{ss} by inward O^- anions (similar to pure Nb oxidation) was accepted as the mechanism of MASC alloy oxidation.

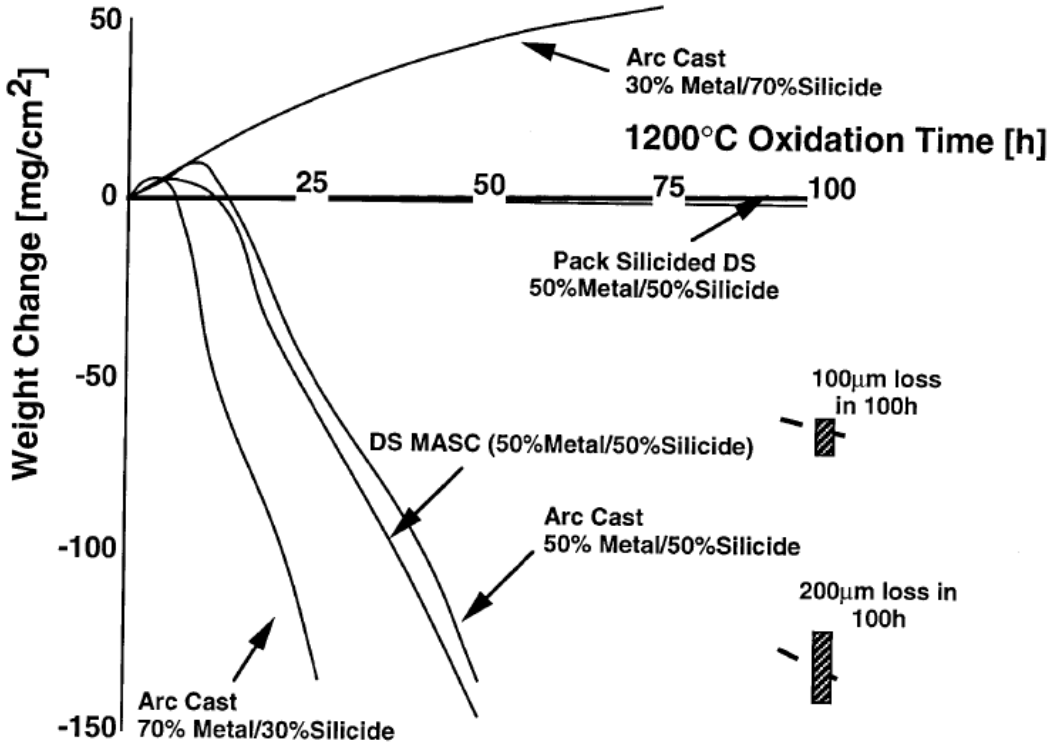

Figure 53. Oxidation behaviour of directionally solidified (DS) MASC (50% metal/ 50% silicide) compared with other similar silicide-based composites with volume fractions of the silicide phase in the range 30 - 70% (Bewlay et al., 1996).

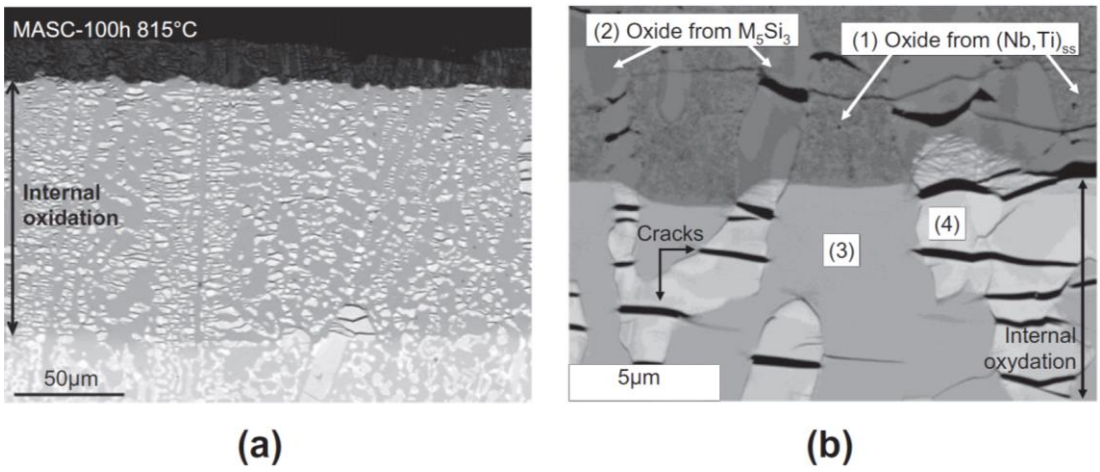

Figure 54. BSE-SEM microsections of the MASC alloy microstructure after oxidation at 815°C for 100h. (a) Overview of surface oxide and internal diffusion zone. (b) High magnification imaging of the oxide scale and internally oxidised microstructure. Point (3) is the Nb_{ss} and (4) is the Nb_5Si_3 silicide exhibiting cracking (Mathieu et al., 2012).

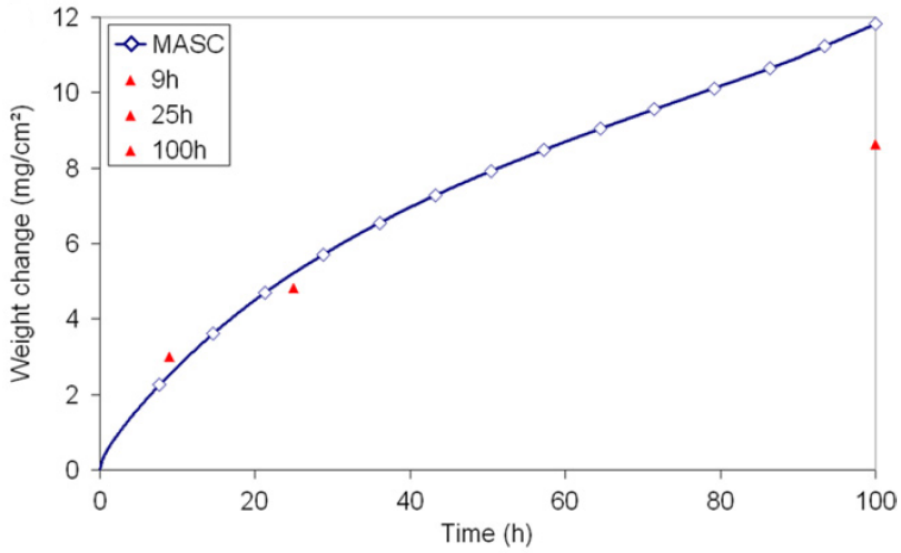

Figure 55. Thermogravimetric isothermal oxidation kinetics of the MASC alloy at 815°C for 100h (Mathieu et al., 2012).

As is typical for Nb-silicide based alloys, the addition of Ti is considered essential to enhance the toughness and oxidation resistance of the Nb_{ss}. As discussed, Nb and Ti are miscible in a bcc $(Nb,Ti)_{ss}$, thereby Ti can preferentially react with penetrating O as TiO_2 formation is slightly more thermodynamically stable than Nb_2O_5 (refer to Figure 56 and Figure 57). However, this does not usually sustain exclusive TiO_2 growth as Nb will still compete with Ti to absorb O and oxidise to form Nb_2O_5 that will grow inward. TiO_2 is not particularly protective anyway but offers better protection than Nb_2O_5. Even more Nb_2O_5 can form after Ti depletion from the solid solution. The formation of these oxides from the $(Nb,Ti)_{ss}$ is known to dominate the oxidation behaviour of the solid solution (Chan, 2004a).

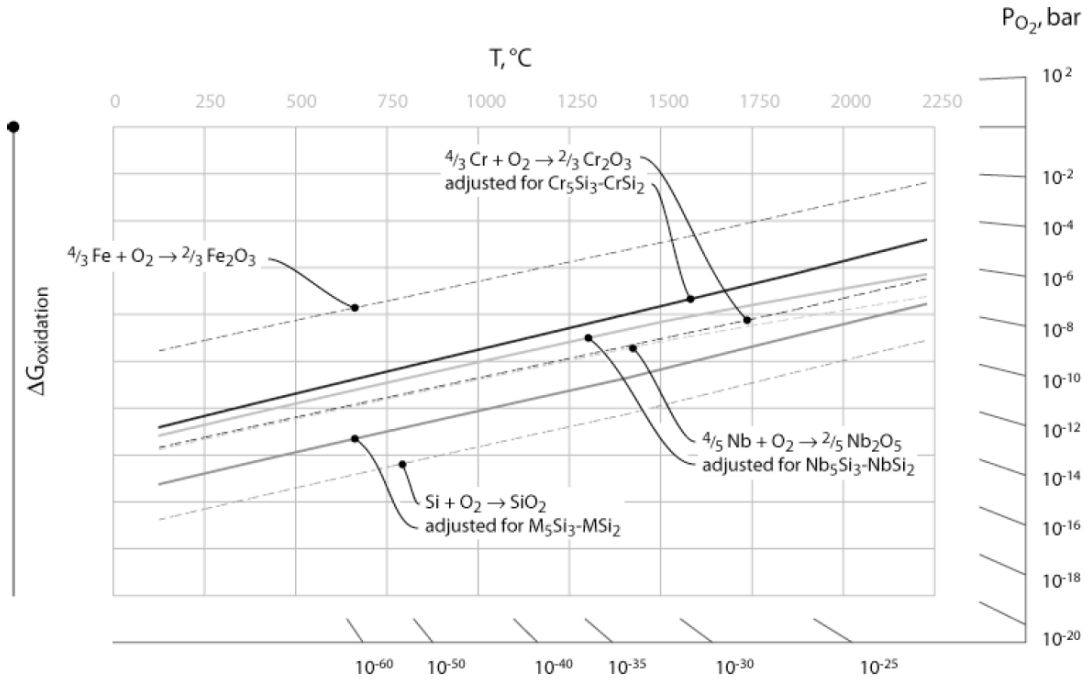

Figure 56. Constructed Ellingham diagram for the oxidation of Cr, Nb, Si and Fe (Novak and Levi, 2008).

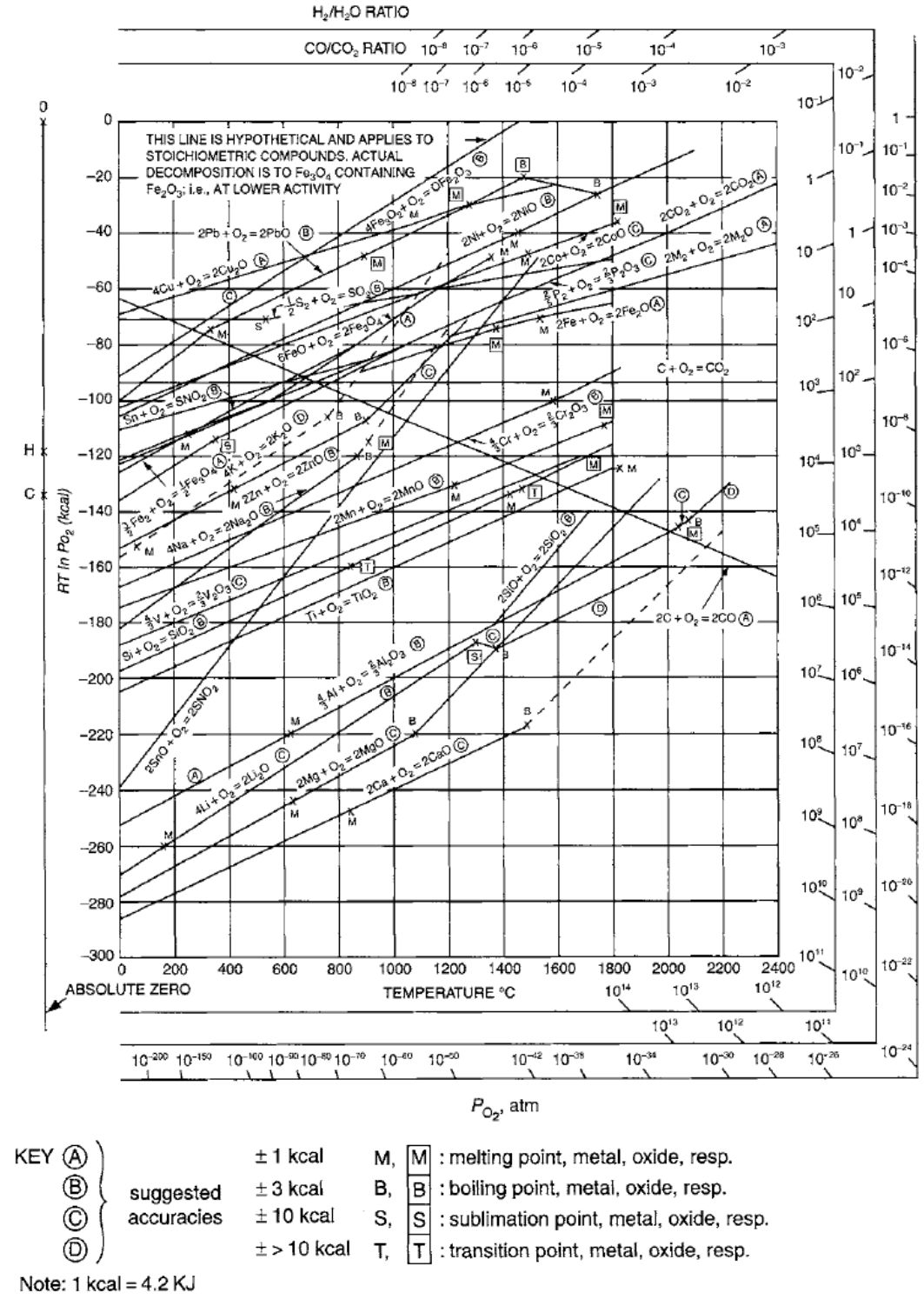

Figure 57. Ellingham diagram of free energy of formation of oxides as a function of temperature (Bose, 2007a).

Considering the Nb_2O_5 – TiO_2 binary system shown in Figure 47, the binary Nb and Ti oxide constituents will tend to react and form several intermediate oxides namely $Nb_{24}TiO_{62}$, $Nb_{14}TiO_{37}$, $Nb_{10}Ti_2O_{29}$, and Nb_2TiO_7 (see Table 18 for a detailed summary and note that the $Nb_2Ti_2O_{19}$ also exists in the Nb_2O_5 – TiO_2 system but is not stable below 1420°C).

The $Nb_{10}Ti_2O_{29}$ and Nb_2TiO_7 are commonly identified by XRD in the oxide scales of Nb-silicide based alloys above 1000°C for isothermal or cyclic conditions ranging from 10 to 500h of exposure time. They have also been detected at 800°C. However, formation at such a lower temperature is not as prevalent (Chan, 2004a; Geng et al., 2006b; Zelenitsas and Tsakiropoulos, 2006b; Ventura and Varma, 2009; Natividad et al., 2010; Mathieu et al., 2012, 2014).

Table 18. Crystal structure data of commonly detected niobate oxides formed on Nb-silicide alloys.

Oxide	Pearson symbol	Space group	Lattice parameters (Å)				Prep. notes	Ref.
			a	b	c	β°		
(Orth) $Nb_{10}Ti_2O_{29}$	oS164	Amma	28.50	3.805	20.51	90	Rutile TiO_2 + Nb_2O_5	(Wadsley, 1961a)
(Mono) $Nb_{10}Ti_2O_{29}$	mS82	A12/m1	15.57	3.814	20.054	113.68	Rutile TiO_2 + Nb_2O_5	(Wadsley, 1961a)
(Mono) Nb_2TiO_7	ms60	C12/m1	20.351	3.801	11.882	120.19	$BaCO_3$ + Nb_2O_5, + Rutile TiO_2	(Gasperin, 1984)
(Mono) Nb_2TiO_7	ms60	A12/m1	11.93	3.81	20.044	120.17	Rutile TiO_2 + Nb_2O_5	(Wadsley, 1961b)
(Tet) $NbTiO_4$	tP6	$P4_2/mnm$	4.712	4.712	2.996	90	Ti_2O_3 + 64wt.% Nb_2O_5	(Keller, 1962)
(Tet) $NbTiO_4$	tP6	$P4_2/mnm$	4.743	4.743	2.9944	90	Ti_2O_3 + Nb_2O_5 (Nb:Ti=1:1)	(Petersen and Müller-Buschbaum, 1992)
(Tet) $NbCrO_4$	tP6	$P4_2/mnm$	4.6484	4.6484	3.0113	90	Cr_2O_3 + Nb_2O_5 (Nb:Cr=1:1)	(Petersen and Müller-Buschbaum, 1992)
(Tet) $NbCrO_4$	tP6	$P4_2/mnm$	4.645	4.645	3.012	90	Cr_2O_3 + Nb_2O_5	(Khazai et al., 1981)
$CrTiNbO_6$	tP6	$P4_2/mnm$	4.60	4.60	2.98	90	High purity oxides	(Blasse, 1967)

The $Nb_{10}Ti_2O_{29}$ and Nb_2TiO_7 were reported to form in sequence on Nb-Ti alloys, firstly the reaction $5Nb_2O_5 + 2TiO_2 \rightarrow Nb_{10}Ti_2O_{29}$ occurs as an intermediate step, after which $Nb_{10}Ti_2O_{29} + 3TiO_2 \rightarrow 5Nb_2TiO_7$ occurs resulting in Nb_2TiO_7 in equilibrium with TiO_2 (Felten, 1969; Mathieu et al., 2012). The oxide notation Nb_2O_5:TiO_2 of ratios 5:2 and 1:1 have also been used to denote $Nb_{10}Ti_2O_{29}$ and Nb_2TiO_7 respectively (Chan, 2004b; Zelenitsas and Tsakiropoulos, 2006b; Vazquez and Varma, 2011)

The $TiNbO_4$ possessing a rutile TiO_2 prototype structure was also reported as an oxide product on Nb-silicide based alloys, identified by XRD (Geng et al., 2006b). It was not, however, included in the Nb_2O_5 - TiO_2 phase diagram (Figure 47). Comprehensive literature discussing $TiNbO_4$ is rather elusive. Its production under inert conditions requires the reaction of TiO_2 and/or Ti_2O_3 with Nb_2O_5 (Keller, 1962; Petersen and Müller-Buschbaum, 1992).

The oxide formation on Nb-silicide alloys is further complicated for alloys possessing significant content of Cr in addition to Ti. High alloying with Cr is another approach used to reduce the severity of O saturation into the alloy by counterbalancing the Nb_{ss} volume fraction with $NbCr_2$. This approach was shown effective for either increasing silicide fraction (Figure 53) and/or the $NbCr_2$ Laves phase fraction, as shown by Figure 58 where the Nb-18Si-18Ti-20Cr-7Hf-2Al (at.%) alloy had a significant improvement in oxidation performance in comparision to the MASC alloy (Bewlay and Jackson, 2000). The Nb-18Si-18Ti-20Cr-7Hf-2Al (at.%) alloy microstructure volume fraction consisted of ~ 25% Nb_{ss}, 33% $NbCr_2$ and 42% Nb_5Si_3. Unfortunately, Bewlay and Jackson (2000) did not clarify the silicide crystal structure in this alloy and the oxide scale products, nor did they present any oxidised microstructures or compositional phase analysis.

Fortunately, other works do outline the improvements in higher Cr content alloys (Chan, 2004a, 2004b), a key feature being that not only does a high alloying with Cr counterbalance the Nb_{ss} phase fraction with $NbCr_2$, but it offers Cr to be oxidised which results in Cr-niobate formation via the reaction $Cr_2O_3 + Nb_2O_5 \rightarrow 2CrNbO_4$ (Khazai et al., 1981). Nb-silicide alloys forming $CrNbO_4$ scales tend to display better oxidation performance than those containing none or little Cr that would grow Ti-niobate scales or very little $CrNbO_4$ (Chan, 2004a, 2004b; Chen and Guo, 2013; Dasary-Sierra and Varma, 2014; Su et al., 2014b; Thomas and Varma, 2015b, 2015a, 2013; Varma et al., 2010; Voglewede et al., 2012). By comparing weight gains of $CrNbO_4$ and Ti-niobate forming alloys of such different works, such conclusion may, however, be premature.

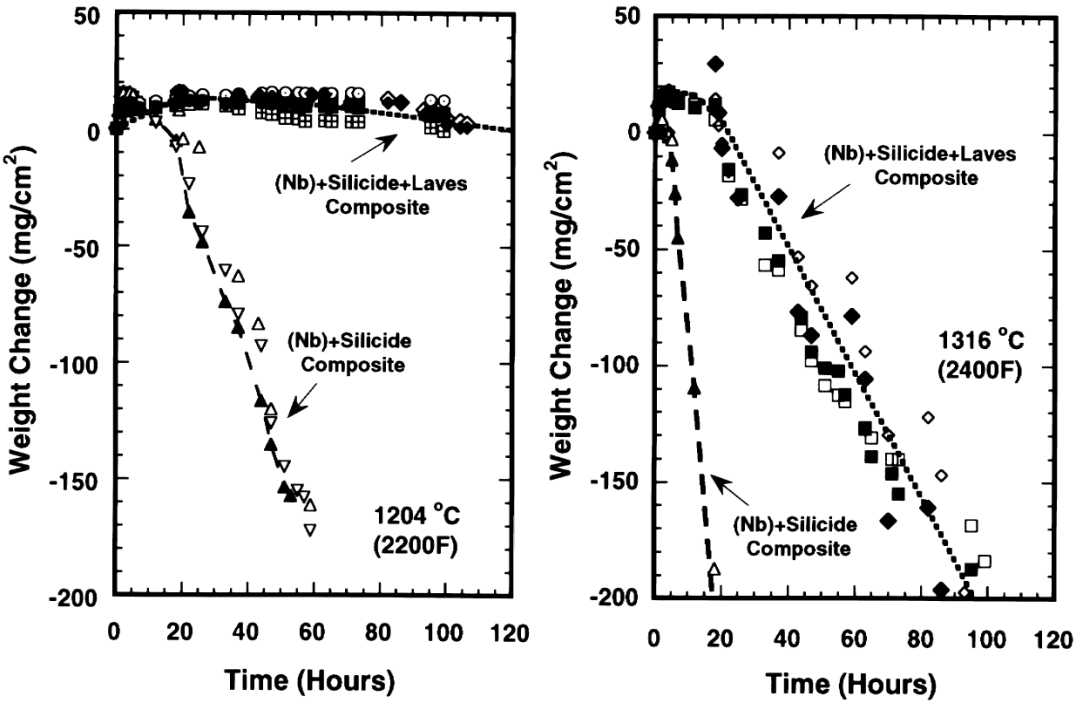

Figure 58. Comparison of 1204°C (left) and 1316°C (right) oxidation resistance of a Nb-18Ti-7Hf-20Cr-2Al-18Si (at.%) alloy to the MASC alloy (Bewlay and Jackson, 2000).

For example, microstructures and weight gain kinetics of $CrNbO_4$ formers investigated by the work of Voglewede et al., (2012) are presented in Figure 59 and Figure 60, with oxidised microstructures shown in Figure 61. Example Ti-niobate forming alloy data from the work of Geng et al., (2006b) and Yao et al., (2009) are presented in Figure 62 and Figure 63 respectively. At 1200°C after 24h (86400s) of isothermal oxidation the weight gain of the Ti-niobate formers were close to that of the $CrNbO_4$ formers. Only the $CrNbO_4$ forming Nb-20Cr-42Si alloy performed better, which (alike the Nb-20Cr-30Si alloy) had no Nb_{ss} in the microstructure (see Figure 59) while the Ti-niobate formers possessed appreciable Nb_{ss} volume fractions from 35 to 55%. The protectiveness of the $CrNbO_4$ forming alloys studied by Voglewede et al., (2012) seem very peculiar at 1000 and 1100°C (Figure 60), at these temperatures the weight gain and metal loss were significantly worse than at 1200°C.

These $CrNbO_4$ vs $TiNbO_4$ examples are not a like-for-like comparison of alloys because the Ti-niobate forming alloys did have some Cr content and other minor alloying additions of Mo, Al, and Hf. Chan (2004a) investigated the cyclic oxidation of various alloys (see Table 19) that contained minor alloying elements such as Al, Ge, Fe, Sn, Hf and concluded that the greater formation of $CrNbO_4$ relative to Ti-niobate resulted in better oxidation resistance. See Figure 64 for oxidative weight change data and Figure 65 for the correlation of metal recession to $CrNbO_4$ formation and Nb_{ss} volume fraction. The $CrNbO_4$ quantity is based upon the relative XRD peak intensity of $CrNbO_4/Nb_2O_5$. It is noteworthy that the better performing alloys also had lower Nb_{ss} volume fractions.

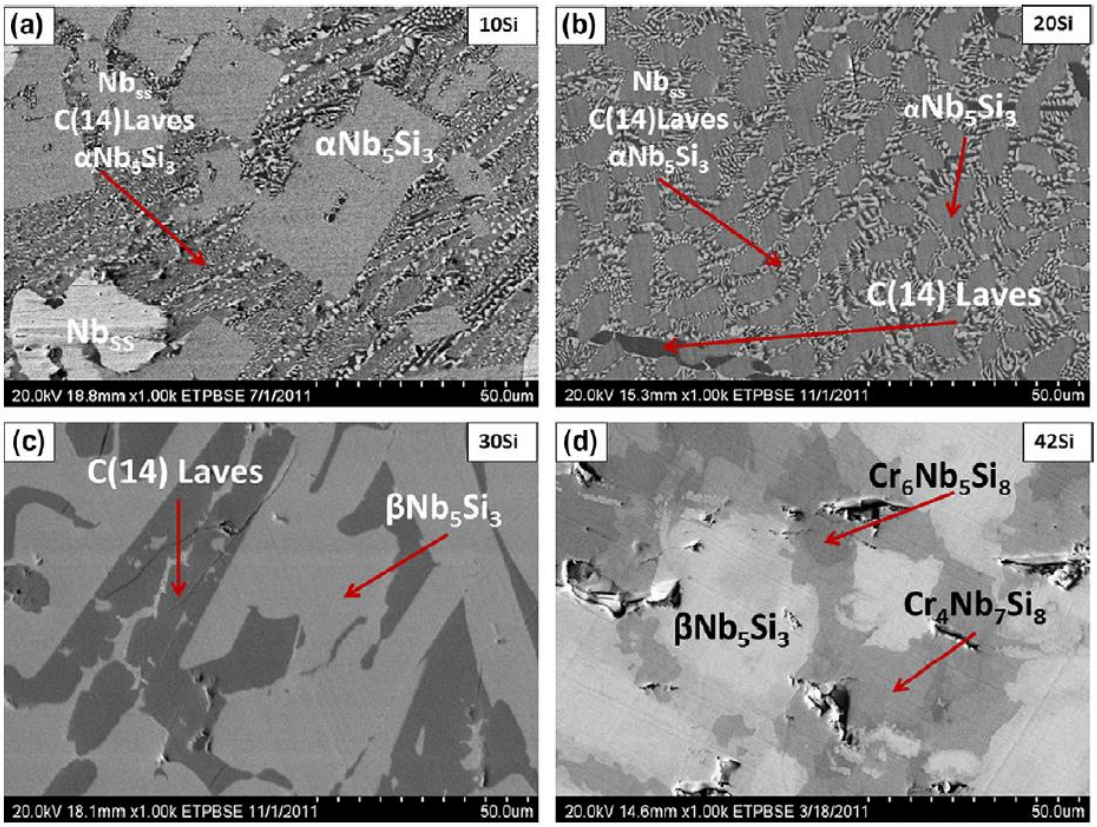

Figure 59. As-cast microstructures of (at.%) Nb-20Cr-XSi alloys where X=10, 20, 30, and 42 (Voglewede et al., 2012).

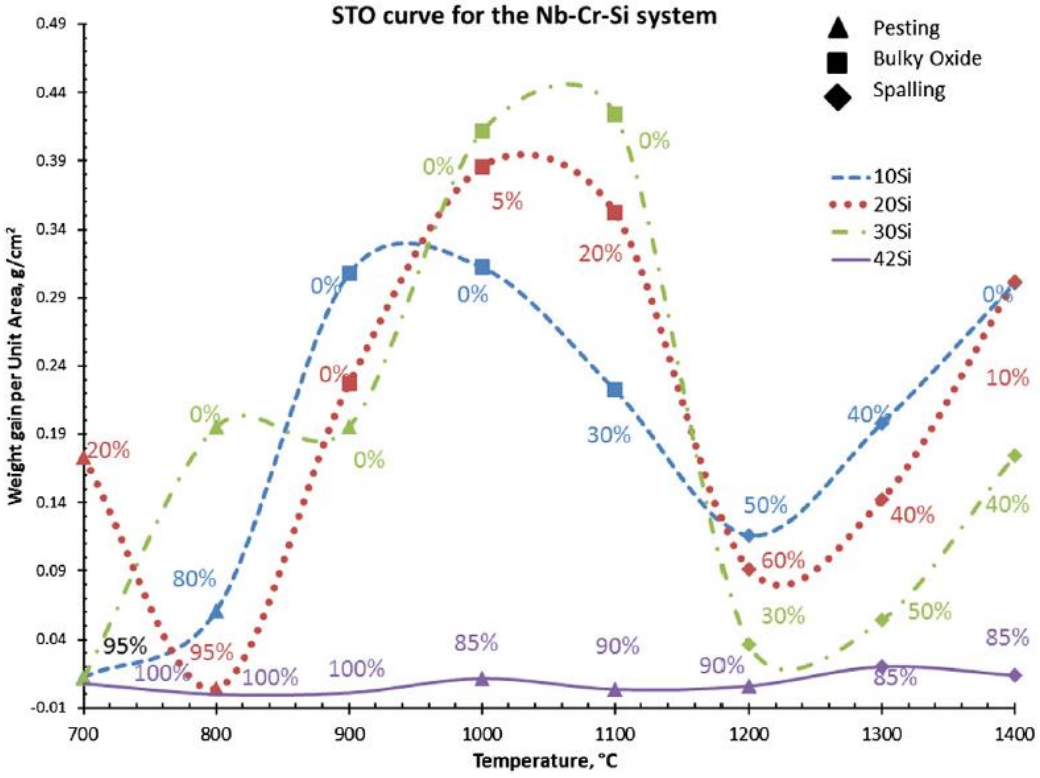

Figure 60. Plot of isothermal short term oxidation (STO) weight gains for (at.%) Nb-20Cr-XSi alloys at various temperatures where X= 10, 20, 30, and 42. STO tests are one 24h isothermal run. % values indicate remaining metal after each test (Voglewede et al., 2012).

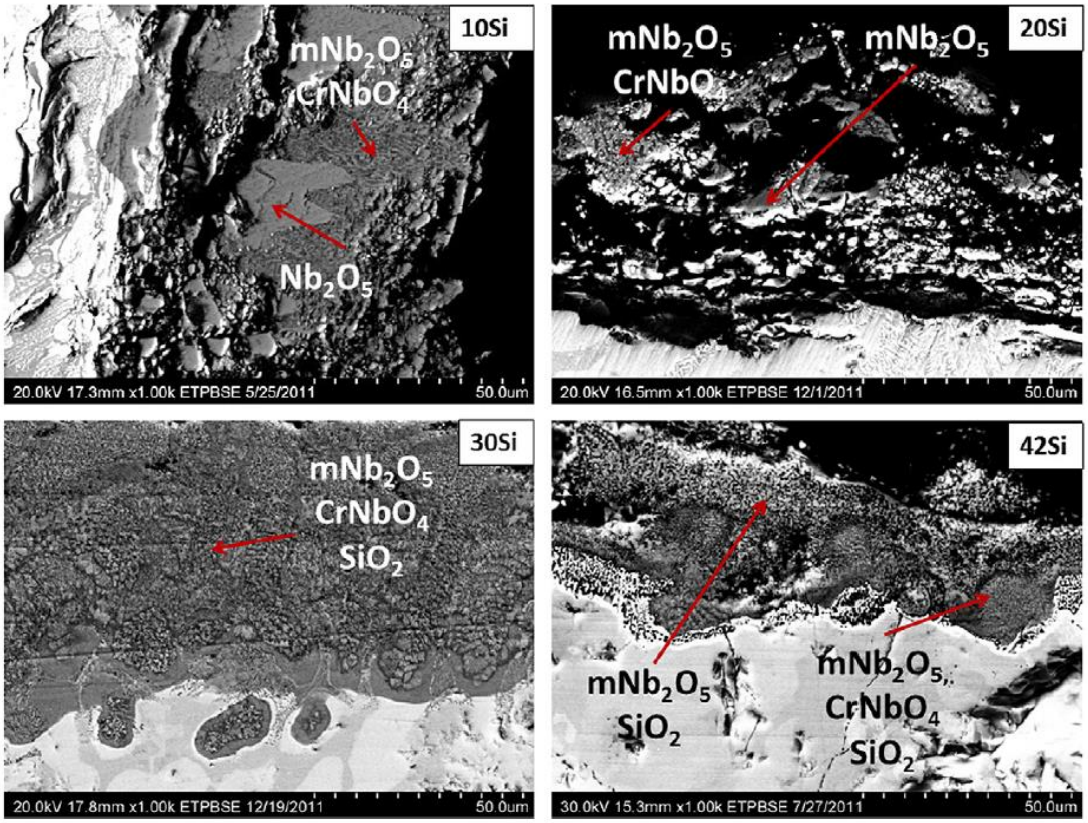

Figure 61. Examples of oxide scale formation on (at.%) Nb-20Cr-XSi alloys where X=10, 20, 30, and 42. Isothermal oxidation was performed at 1200°C for 24h. $CrNbO_4$ formation has occurred in each case (Voglewede et al., 2012).

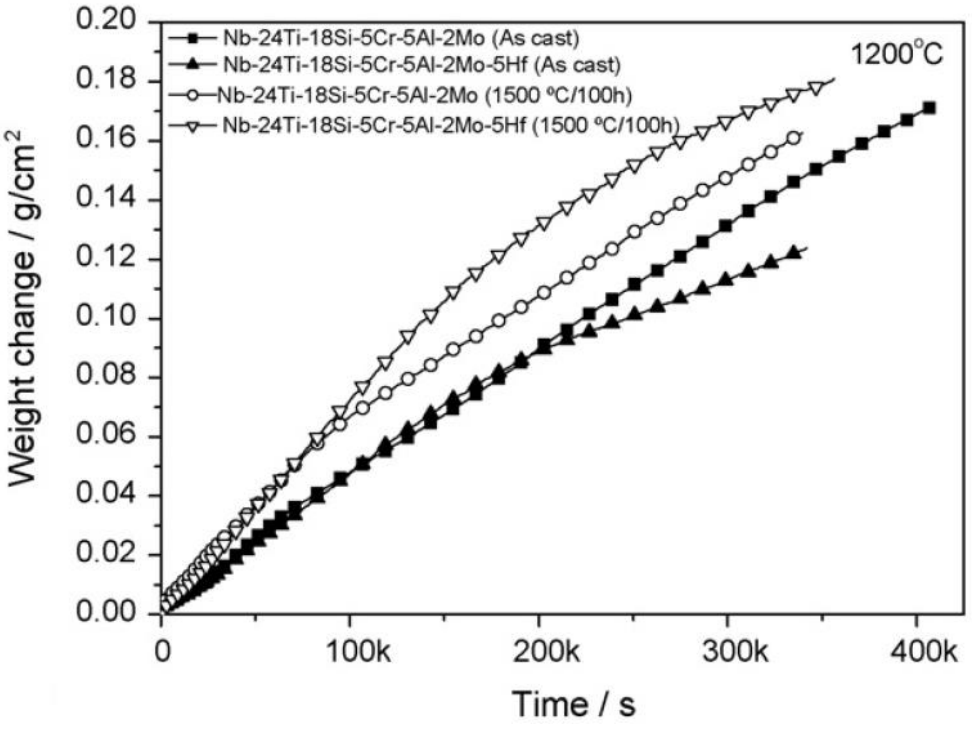

Figure 62. Thermogravimetric weight gain plot of various Ti-niobate forming Nb-silicide alloys with low Cr content (Geng et al., 2006b).

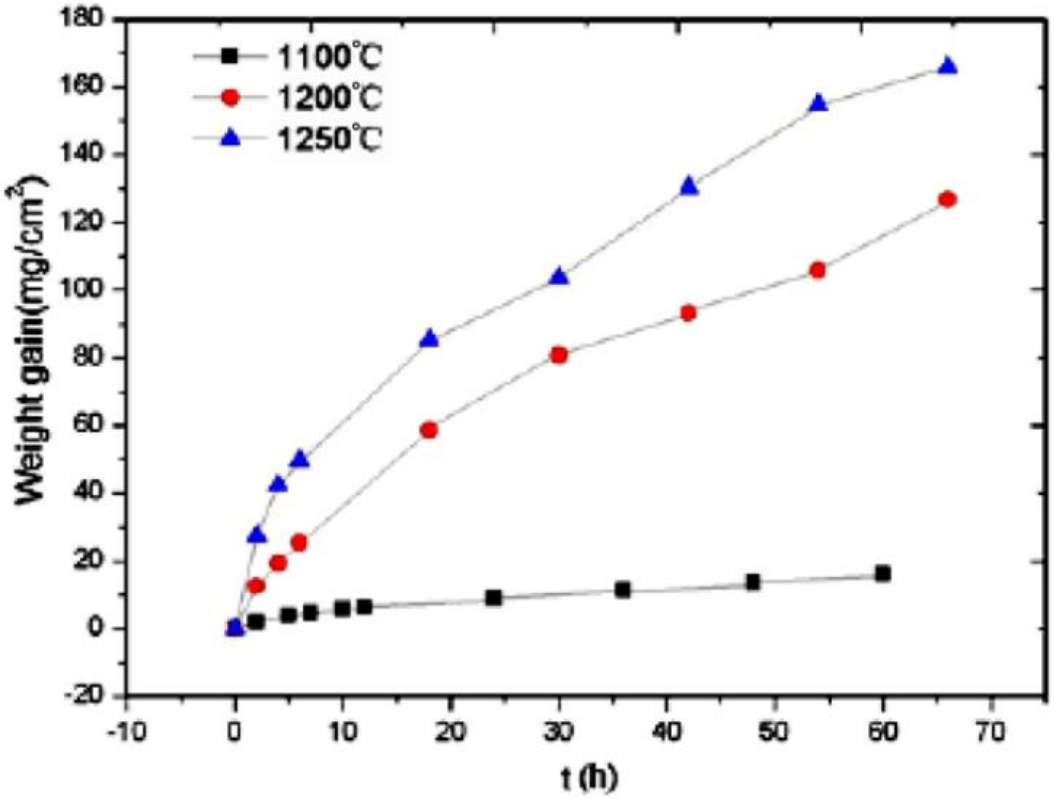

Figure 63. Isothermal oxidation plot for alloy Nb-16Si-24Ti-6Cr-6Al-2Hf (at.%) for various temepratures. Sample weights were noted at various times and oxidation resumed. Refer to Figure 67 for microstructural depiction (Yao et al., 2009).

Table 19. Chemical compositions of Nb-silicide alloys investigated by Chan (2004).

	Compositions (At. Pct)					
Alloy	Nb	Ti	Hf	Cr	Si	Ge
Nbx	62.7	26.6	4.2	2.5	1.0	3.0
M1	46.3	22.2	4.4	12.3	9.7	5.1
M2	35.8	22.5	4.0	15.6	17.3	4.8
AX	41.3	22.4	3.9	12.5	14.8	5.1
UES-AX	41.2	23.0	4.7	11.2	15.2	4.7
CNG-1B*	48.7	21.5	2.0	6.7	9.0	4.7

*Also contained 3.5 pct Fe, 2.6 pct Al, and 1.3 pct Sn.

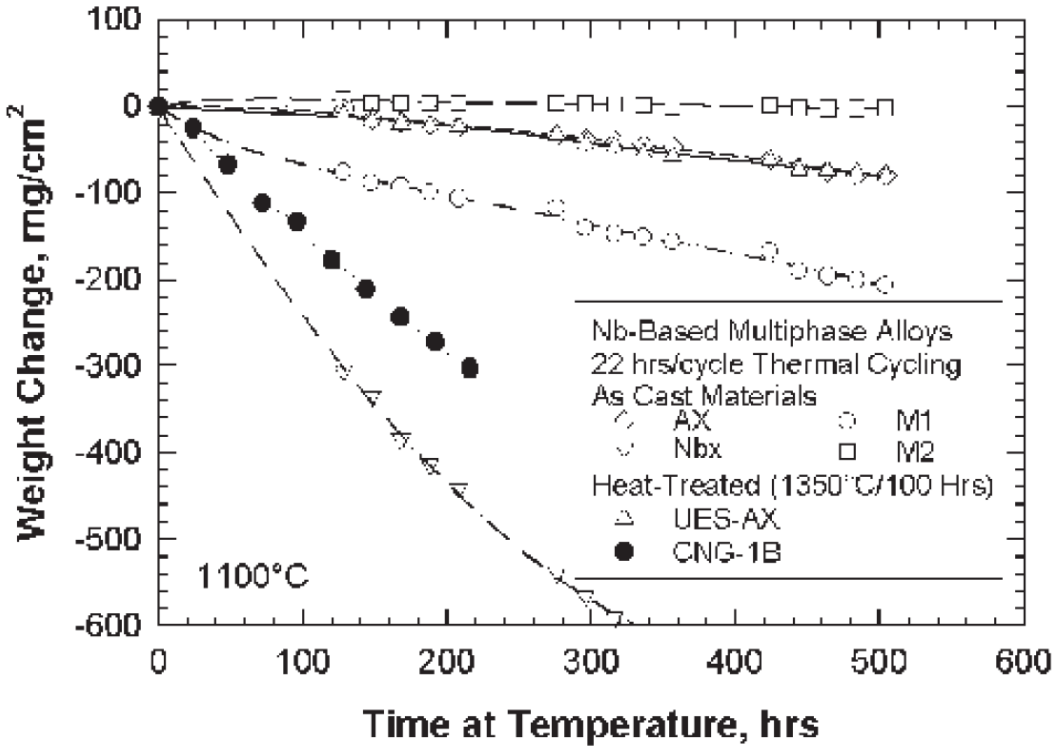

Figure 64. Weight change data of various alloys investigated by Chan (2004). Oxidation was cyclic of 22h intervals with 2h of furnace cooling. Refer to Table 19 for alloy compositions.

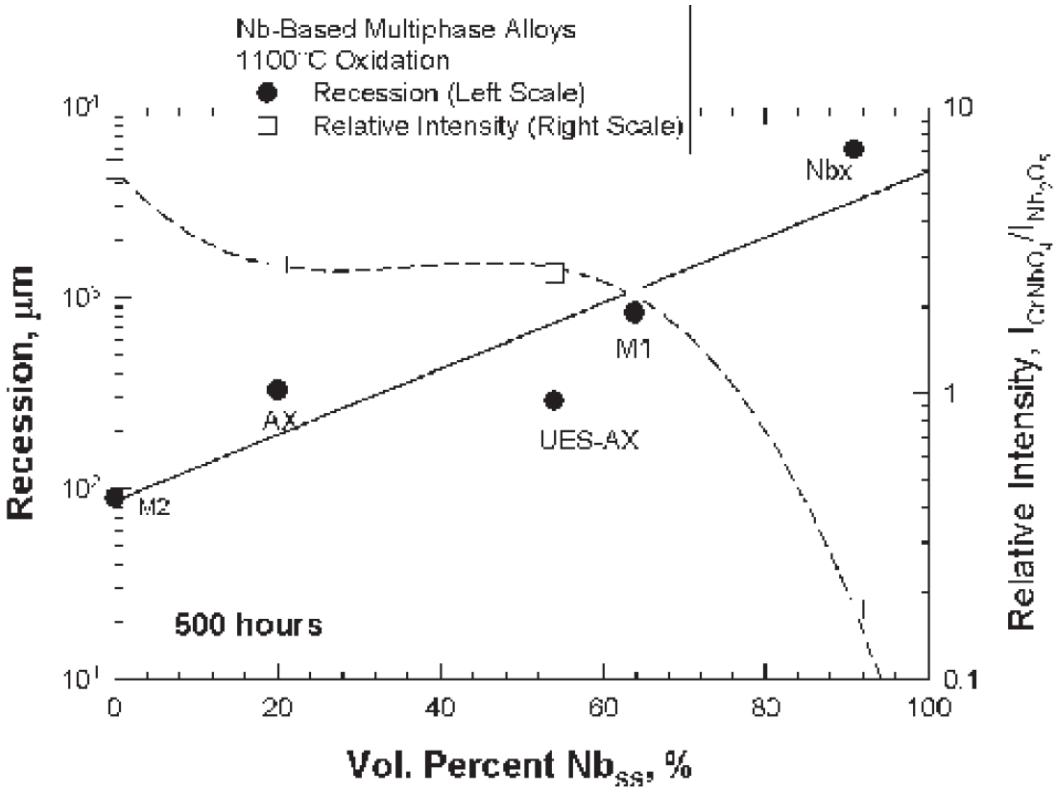

Figure 65. Metal recession (left scale) and relative $CrNbO_4/Nb_2O_5$ XRD intensity (right scale) against volume fraction % of Nb_{ss} for alloys investigated by Chan (2004). Note the low metal recession rate of alloys with low Nb_{ss} fraction and high relative $CrNbO_4/Nb_2O_5$ intensity.

Although these comparisons are not like-for-like, various deductions can still be made. $CrNbO_4$ formation may not necessarily be more protective than Ti-niobates and, hence, the reported oxidation improvement may be attributed to a microstructure with low Nb_{ss} volume fraction. As suggested by the comparision, the lack of solid solution does not necessarily provide better oxidation behaviour than microstructures possessing Nb_{ss} and may be attributed to the effects of other alloying additions.

The disordered rutile tetragonal TiO_2 structure, which both $CrNbO_4$ and $TiNbO_4$ possess (Table 18) rather than the orthorhombic/monoclinic of the $Nb_{10}Ti_2O_{29}$ and Nb_2TiO_7, may actually be more relevant to oxidation resistance than specifically $CrNbO_4$. To encourage $CrNbO_4$ formation, alloys with Cr content of at least 10 at.% is required, which will have a side effect of reducing the Nb_{ss} volume fraction, which generally improves oxidation resistance. This may be misconstrewed as benefit from $CrNbO_4$ alone. As $CrNbO_4$ and $TiNbO_4$ have the same structure they predictably can form mixed niobates, in particular $(Cr,Ti)NbO_4$ or $CrTiNbO_6$ (Blasse, 1967; Mani et al., 2010). These oxides show a wide range in solubilities and have various stable slightly modified stoichiometries, making identification by XRD especially difficult, additionally their reflections are very similar to TiO_2.

It is important to be aware that Ti-niobate formation is not exclusive, for example see Figure 66 and Figure 67. Ti-niobate formation is also accompanied with Nb_2O_5 and TiO_2 from the $(Nb,Ti)_{ss}$ and SiO_2 from the oxidised silicide and internal oxide formation.

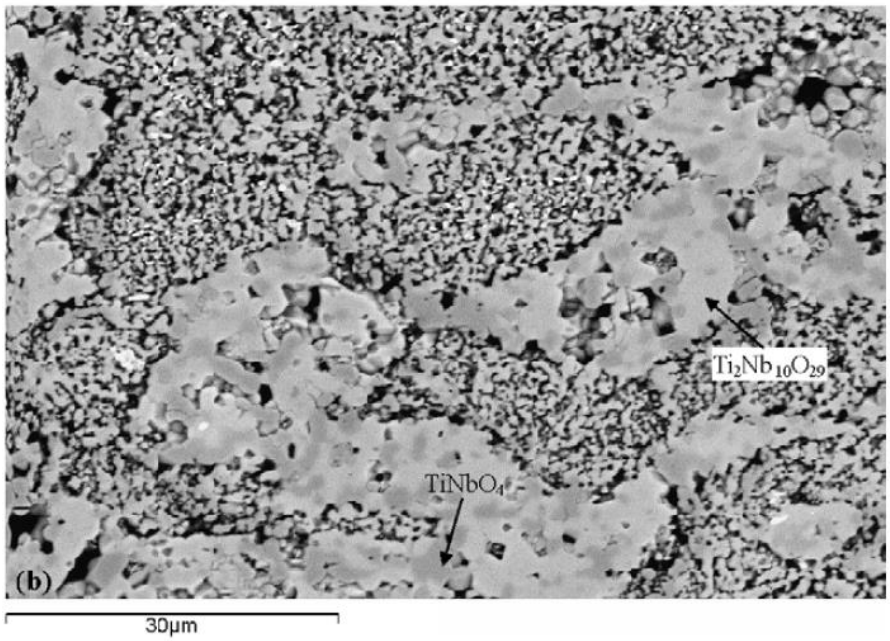

Figure 66. Example of $Ti_2Nb_{10}O_{29}$ and $TiNbO_4$ formed upon alloy JG4-HT of composition Nb-18Si-24Ti-5Al-5Cr-2Mo-5Hf (at.%) after oxidation at 1200°C (Geng et al., 2006b).

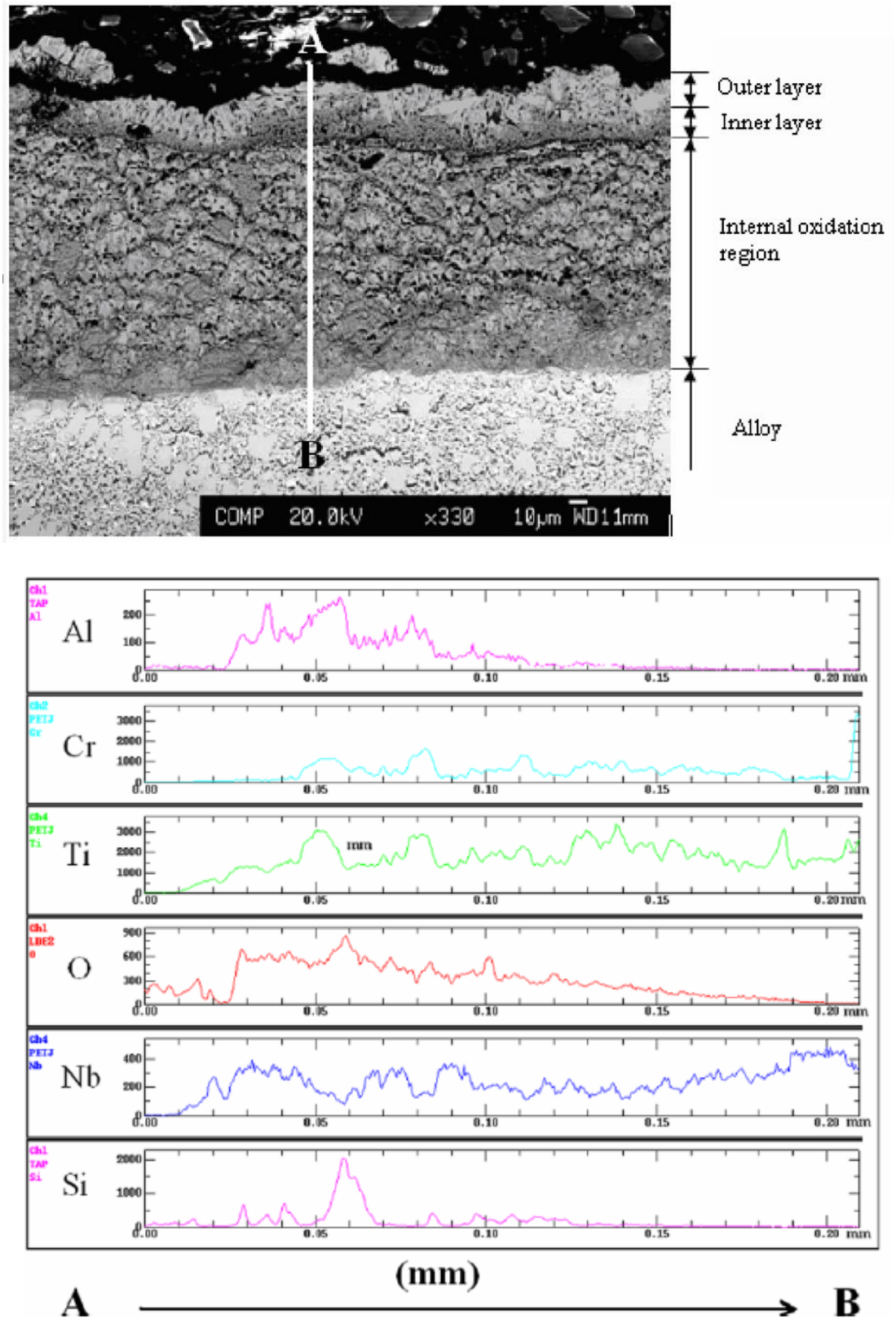

Figure 67. Oxidised cross section example and element concentration profile of an Nb-16Si-24Ti-6Cr-6Al-2Hf (at.%) alloy after oxidation at 1250°C for 70h. The outer oxide layer is identified by TEM to consist of $Nb_{10}Ti_2O_{29}$, Nb_2TiO_7, Nb_2O_5 and TiO_2 . The initial alloy microstructure after heat treatment was two phase Nb_{ss} + αNb_5Si_3 (Yao et al., 2009).

The intermetallic alloy phenomena of pest degradation at intermediate temperatures (700 – 1000°C) should also be addressed. Pesting is dependent on the preferential internal oxidation and hardening of an intermetallic alloy via microstructural features, particularly grain boundaries. This results in the catastrophic disintergration of the alloy into powder (Westbrook and Wood, 1964). Disintergration of this nature does not require much oxide formation to occur and alloys merely need to be cycled through the critical temperature range or held isothermally for pesting to commence. Pesting is a basic first test that requires passing by any Nb-silicide based alloy. Geng et al., (2007) found the addition of 5 at.% Sn to a Nb-24Ti-18Si-5Al-5Cr-2Mo-5Hf (at.%) alloy eliminated pesting and was attributed to a change in the nature of the Nb_{ss}. The elimination of pest behaviour with 1.5 at.% Sn addition to various alloys was also reported by Bewlay et al., (2003). How Sn benefits the Nb-silicide based alloy oxidation behaviour is an interesting and potentially fruitful area of research for oxidation performance. However, for the present moment it is not the topic of this PhD thesis. The synergy of Ti, Cr and Al additions to prevent pesting by reducing O diffusivity through the $(Nb,Ti)_{ss}$ was deduced by Zelenitsas and Tsakiropoulos (2006b) in their investigation of Nb-silicide based alloys oxidised at 800°C. Such a method of pest prevention is within the scope of this PhD thesis.

The internal oxidation of Nb-silicide based alloys was briefly mentioned earlier and presented in Figure 54 where the MASC alloy had been oxidised at 800°C up to 100h. The microstructure displayed some thermally grown oxide and internal oxidation, yet minimal oxide precipitates formed. At 1100°C, however, the internal oxidation of the MASC alloy was more severe, as shown in Figure 68 where the solid solution has visible dissolution of O to a greater depth and was riddled with internal precipitates of TiO_2 and HfO_2. Silicide grains caught within the diffusion zone will suffer oxidative attack (Figure 69), especially those closest to the alloy edge. The attack of the silicide phase will inevitably allow Si to react with penetrating O, resulting in SiO_2 formation that is not exclusive given the preliminary mixture of Ti/Cr-niobate and/or TiO_2 oxide growth. SiO_2 grains tend to reside mixed amongst the growing Ti/Cr-niobate in the oxide scale (Su et al., 2014b).

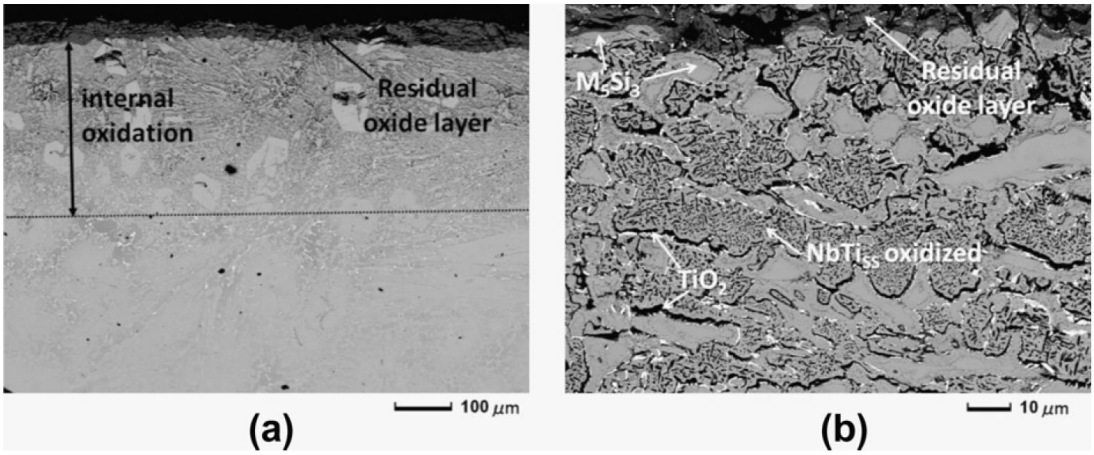

Figure 68. BSE-SEM microsections of the MASC alloy microstructure after oxidation at 1100°C for 100h. (a) Overview of the residual surface oxide layer and internal oxidised microstructure. (b) High magnification image of the internally oxidised microstructure (Mathieu et al., 2012).

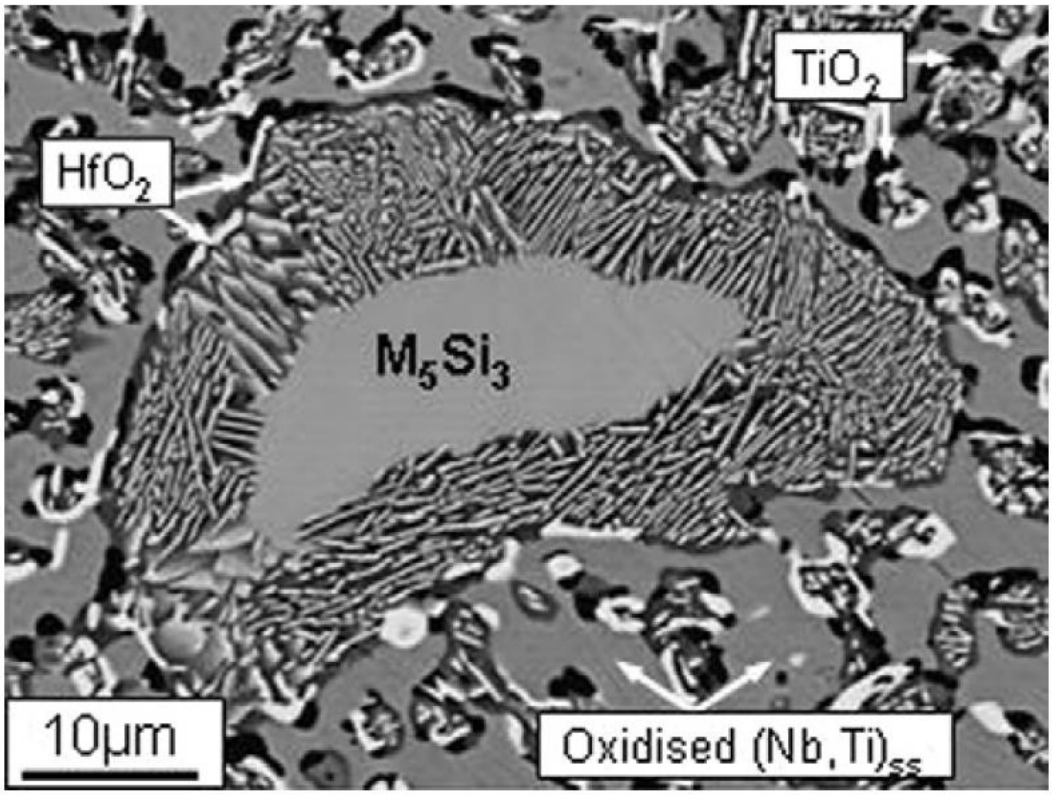

Figure 69. Oxidative attack of the M_5Si_3 silicide grain located in the internal oxidation zone of a MASC alloy subjected to 100h isothermal oxidation at 1100°C (Mathieu et al., 2012).

3 Experimental Procedure

3.1 Selection of Alloy Compositions

The nominal composition of alloys GB1 and GB2 selected for investigation are given in Table 20.

Table 20. Nominal alloy compositions (at.%).

Alloy	Nb	Si	Ti	Cr	Al	Ge	Hf
GB1	29.5	17	22	20	2.5	-	9
GB2	35.5	17.5	20	18	-	5	4

The alloys were chosen on the following basis:

- A significantly high content of Cr was needed for both alloys in order to investigate the influence of high $NbCr_2$ Laves phase fraction on Nb-silicide based alloy oxidation performance. The Cr content need not be too excessive to make the alloys Cr based or to dimish their melting point.
- To investigate the synergistic effect of Cr and Hf, with the latter acting as an O getter. The strong affinity of Hf for O was hypothosised to prevent early O penetration into the Nb_{ss} matrix, which is widely reported and accepted as the oxidation mechanism of Nb-silicide based alloys.
- To investigate the influence of Ge addition on oxide scale formation. Mueller et al., (1992) found for Ge doped $MoSi_2$ coatings on Nb alloy substrates had formed a SiO_2 + GeO_2 glassy oxide during high temperature oxidation up to 1370°C. This glassy oxide enabled the self healing of cracks in the oxide scale and subsequently enhanced the overall oxidation resistance. As the mixed oxides scales formed on Nb-silicide based alloys are prone to spallation the benefit of self healing cracks would be highly beneficial and is worth investigation.
- The Ti concentration was chosen below 25 at.% to try and avoid hexagonal γNb_5Si_3 silicide formation as it is detrimental to creep performance yet Ti is ideally retained above 20 at.% to sufficiently enhance the oxidation resistance and ductility of the Nb_{ss}.
- The Si concentration was selected near to or at the eutectic composition in the Nb-Si binary as within 16 – 20 at.% Nb-silicide based alloys exhibit the best creep properties. The intention was to have no Nb_3Si as this is an undesirable phase due to inferior mechanical properties and less phase stability during prolonged high temperature testing than Nb_5Si_3. The combination of near eutectic Si and high Cr is aimed to have the effect of destabilising Nb_3Si and stabilising $NbCr_2$ and Nb_5Si_3.

- Due to the high alloying of GB1 and GB2 the Nb balance was relatively low compared to the majority of Nb-silicide based alloys reported throughout literature which usually contain > 40 at.%. This was intended to produce a microstructure with low Nb_{ss} phase fraction to potentially improve high temperature oxidation.

3.2 Alloy Prepartion

High purity elements Nb, Si, Ti, Cr, Al, Ge, Hf with purity no less than 99.98 wt.% were used as the starting materials for arc melting into ingots. The arc melting process utilised the Edmond Buehler arc melter shown in Figure 70 with water cooled Cu crucible depicted in Figure 71. As part of the casting process prior to metling, the arc melting chamber was evacuated by rotary and diffusion pumps to a vacuum of $<10^{-3}$ Pa, at which point the chamber was back filled with Ar to an overpressure of ~ 50 kPa prior to melting. In addition to the elements for casting, Ti getter was included in the chamber and was initially melted to absorb any O that may have remained in the chamber. Each alloy ingot was turned in the chamber and remelted 4 times to ensure homogensation of chemical composition. The ingot of alloy GB1 is shown in Figure 72.

A 600g ingot of alloy GB2 was manufactured by plasma arc melting, courtesy of the University of Birmingham. The process was essentially the same as electric arc melting other than raw elements were initially compacted using a hydraulic press.

Figure 70. Edmond Buehler arc melter used for casting the GB1 and GB2 ingots. Courtesy of the Department of the Materials Science & Metallurgy of the University of Cambridge.

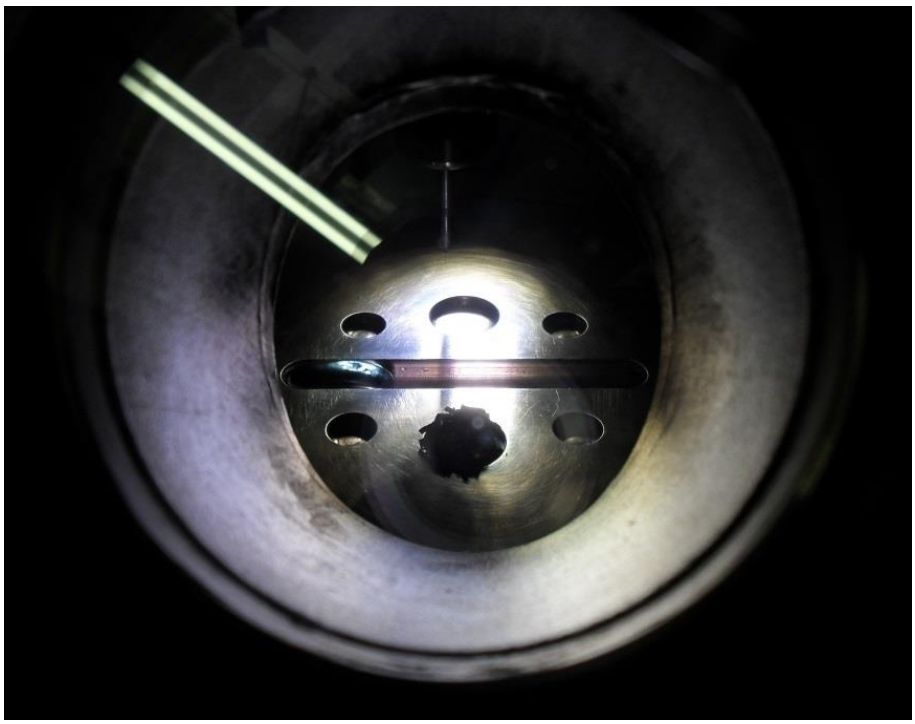

Figure 71. View into the arc melter chamber via the inspection window. The troughs of the various ingot shapes for raw element placement are visible on the Cu crucible. The Ti getter was placed in the central trough section and initially melted to absorb any remnant O in the chamber before alloy making.

Figure 72. Example ingot of alloy GB1-AC produced using the Edmond Buehler arc melter.

3.3 Sample Preparation

From the AC ingots, two 2mm thick slices (per ingot) were extracted from the centre, one used for inspection of the AC condition and the other for heat treatment (HT). The latter was performed in a tube furnace and required wrapping the ingot in Ta foil and heating at 1300°C for 100h in an Ar atmosphere with neighbouring Ti getter residing on a alumina crucible. The HT of 1300°C was decided based on differential thermal analysis (DTA) results shown in Figure 73 and Figure 74 so as not to risk the occurrence of melting.

The ingots were cut using a Buhler Isomet 5000 precision saw with diamond tipped blade. Slices were used for metallographic preparation to inspect the respective AC/HT conditions by microscopy techniques. The metallographic preparation of specimens consisted of mounting in Buehler KonductoMount Bakelite and grinding using SiC paper progressively from p120, p240, p400, p800, p1200, p4000 and penultimately polished with 1 μm diamond suspension and finally polished with collodical silica (aka Silco) of ~ 0.25 μm size.

Oxidised specimens were mounted in Buehler thermoplastic epoxy resin as such medium offers slow curing and imposes lower external stress than Bakelite to prevent potential damage to the oxide scale during mount solidification. For effective study using electron microscopy techniques, all samples were silver dagged (Agar Scientific) to ensure adequate conductivity. For electron microprobe analysis (EPMA) samples required an additional ~ 20 nm carbon coating to ensure conductivity over the sample surface and, in particular, over any oxide scales. To measure such coating, an accompanying polished brass sample was placed in the carbon sputter coater to be simultaneously coated. A ~20nm thick carbon coating would be achieved upon the polished brass surface becoming an indigo red colour (Kerrick et al., 1973).

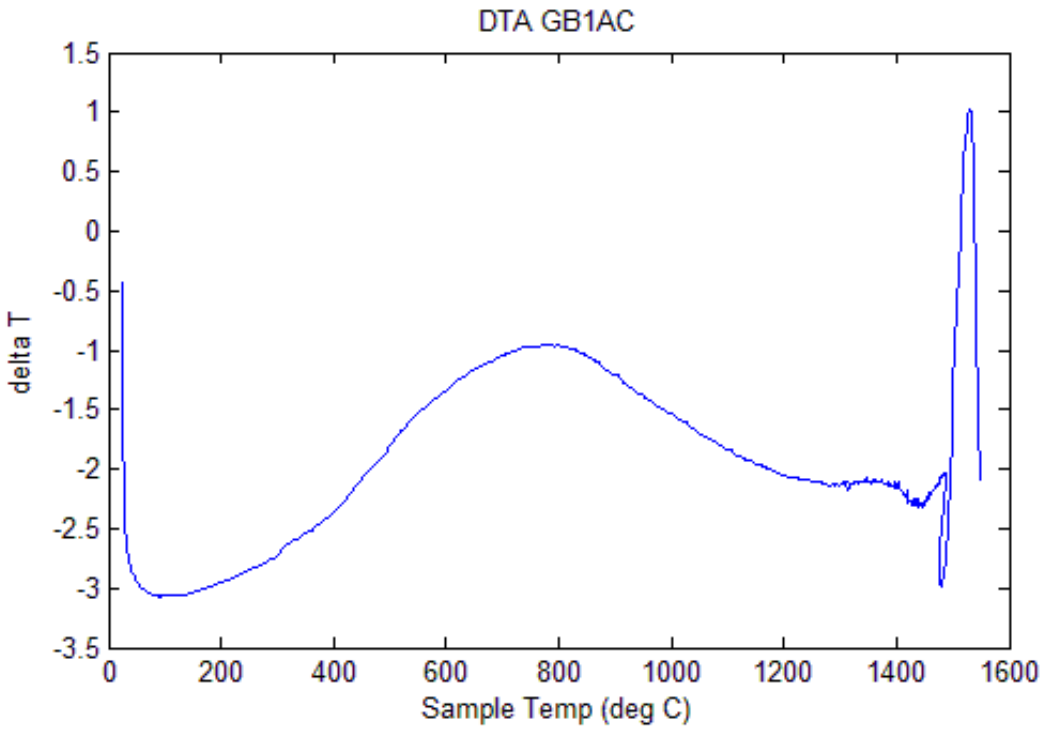

Figure 73. DTA plot for alloy GB1-AC.

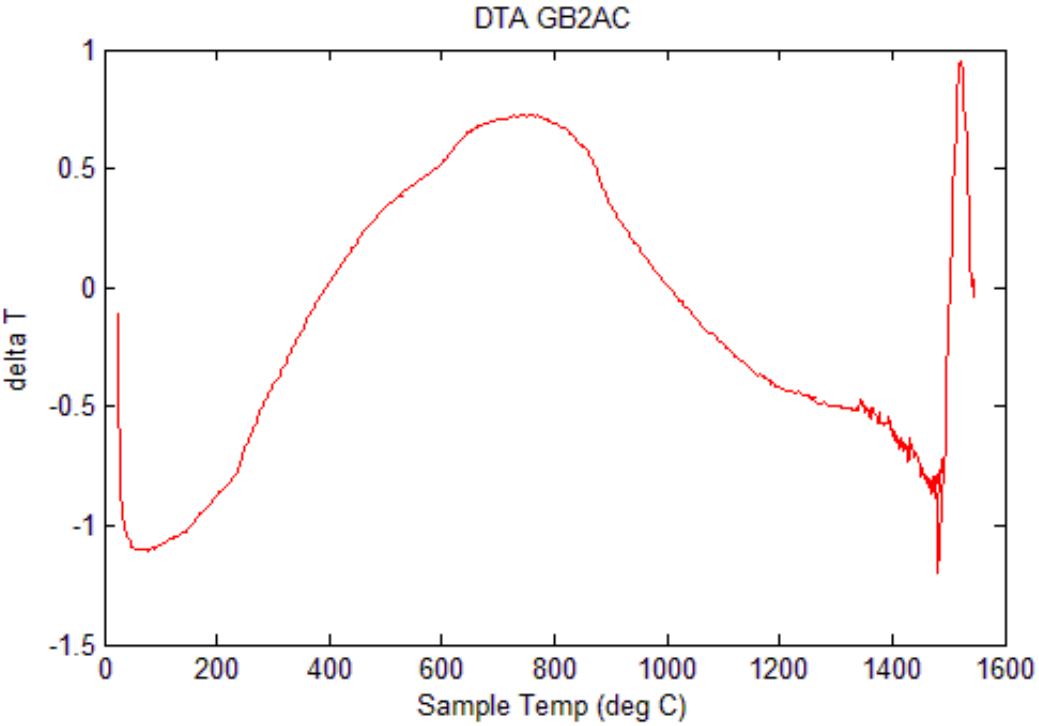

Figure 74. DTA plot for alloy GB2-AC.

3.4 Electron Microscopy Techniques

The microstructures were characterised using different electron microscopy (EM) equipment and spectroscopic techniques. Scanning electron microscopes (SEM) equipped with energy dispersive spectrometers (EDS) or wavelength dispersive spectrometers (WDS, aka Electron Microprobe Analysis EPMA) were utilised for quantitative and/or qualitative analysis.

The Jeol JSM 6400 (15 or 20KV) and Phillips PSEM 500 (25KV) were used for quantitative EDS analysis with high purity (99.99 wt%) Nb, Si, Ti, Cr, Al, Ge, and Hf standards in conjunction with a Co calibration standard for effective ZAF matrix corrections to be computed. A Philips XL30 high resolution SEM fitted with a Bruker Quantax EDS detector was used for qualitative X-ray mapping (Courtesy of Rolls-Royce Plc) and a FEI InspectF high resolution SEM fitted with Octane SDD EDS detector was utilised for imaging and standardless quantative and qualitative EDS analysis.

Quantative WDS was used to analyse the O composition of samples after oxidation tests. Analysis was conducted using a Cameca SX 100 microprobe with WDS spectrometer. The Phi-Rho-Z matrix correction approach was used to quantitatively determine compositions. The standards used were pure Nb, TiO_2 rutile (for Ti), pure Ge, pure Cr, Al_2O_3 corundum (for Al), SiO_2 quartz (for Si), $HfSiO_4$ hafnon (for Hf), and $ZrSiO_4$ zircon (for O).

The microstructures from the top, centre and bottom regions of the ingots were studied. Large area analysis was performed only by EDS at a relatively low ~ 300x magnification and point analysis of individual phases was performed using both EDS and WDS for various specimens and, unless otherwise stated, at least five analyses were taken from phases/grains no smaller than 9 μm^2. Quantitative X-ray maps were recorded by WDS whilst qualitative maps by EDS.

Transmission Electron Microscopy (TEM) was performed using a FEI Tecnai 20 to investigate sub-micron sized microstructural features of oxidised specimens. Bright field (BF) images were obtained for various samples and were also analysed by qualitative EDS. To obtain sufficienctly thin TEM specimens, Focused Ion Beam (FIB) milling was performed using a Nova 600 Nanolab DualBeam FIB-SEM (training and SEM courtesy of Dr Geoff West at the University of Loughborough). Such technique utilises a Ga^+ ion gun, 5-axis stage, and probes to appropriately rotate samples and ablate matter in order to mill and obtain sufficiently thin TEM samples.

3.5 X-ray Diffraction

For phase analysis purposes, Powder X-ray diffraction (PXRD) was performed on AC, HT and the oxide scale product of various oxidised specimens. The powder method was used to eliminate any texture effects that may be present when analysing bulk specimens, thus optimising identification of phases against XRD databases. The oxide of some oxidised specimens was not volumous enough to provide a PXRD specimen, therefore Glancing Angle X-ray diffraction (GXRD) was utilised to analyse oxidised specimens at various X-ray penetration depths.

PXRD was conducted using a STOE STADI P diffractometer with Cu$K\alpha_1$ radiation (λ=1.54056 Å) with a linear position sensitive detector for lattice parameter collection and an image plate detector for phase identification. The radiation source was generated by an acceleration voltage of 40 kV and 35 mA with a step size of 0.1 °/s. GXRD was conducted using a Siemens D5000 X-ray Diffractometer with Cu$K\alpha_1$ (λ= 1.54056 Å) at various angles shown in the results section.

3.6 Thermogravimetric Analysis

Isothermal thermogravimetric analysis (TGA) was performed on the alloys GB1 and GB2 at 800, 1000, and 1200°C on ~ 27 mm^3 cube specimens for up to 100 h using a Netzch STA 449 Jupiter F4 Simultaneous TGA-DSC, or Perkin Elmer Pyris 1 TGA, or Setram SETSYS Evolution TGA. During oxidation the samples were held in alumina crucibles and mounted on the TGA balance for the Netzch TGA or suspended on hanging balance for the Pyris and Setram TGA. TGA furnance heating was initiated upon sealing the apparatus. Heat up and cool down was programmed at a rate of 3°C/min to negate any effects of thermal shock and prevent sudden contraction and spallation of surface oxide formed throughout the oxidation test. TGA data presented is purely the isothermal section.

4 Results: Solidification & Microstructure of Alloys

4.1 Alloy GB1

4.1.1 Summary

The main phases present in alloy GB1 in both the as-cast (AC) and after heat-treatment (HT) at 1300°C for 100h were the hexagonal γNb_5Si_3 silicide, hexagonal Cr rich C14 $NbCr_2$ Laves phase, and a body centred cubic (bcc) Ti and Cr rich Nb solid solution that may be denoted $(Nb,Ti,Cr)_{ss}$. Some PXRD and EDS data indicated the presence of a highly substituted $(Nb,Ti,Cr,Hf)_3Si$ only in the AC condition. Therefore, the eutectoid decomposition reaction $Nb_3Si \rightarrow Nb_{ss} + Nb_5Si_3$ was concluded to occur after HT. A fine grained interdendritic formation of 5-3 silicide in both the AC and HT conditions was present, such grains were richer in Ti than the large dendrites, particularly at the bottom of the ingot and after HT. They are suggested by composition to be the Ti_5Si_3 silicide rich in Nb and Hf and are likely from the eutectoid decomposition of Nb_3Si modified by high Ti and Hf additions. The $(Nb,Ti,Cr)_{ss}$ of the HT condition had a notably lower Cr content.

4.1.2 Cast and Heat Treated Microstructures

The PXRD diffraction patterns for the AC and HT conditions are presented in Figure 75 and are indexed for hexagonal γNb_5Si_3, hexagonal C14 $NbCr_2$, and bcc Nb_{ss} using the JCPDS database. X-ray peaks corresponding to tP32 Nb_3Si overlapped with peaks of other phases (Figure 75) and was rich in Ti, Cr, Hf. The Si content was consistent with Nb_3Si as assessed by Schlesinger et al., (1993) for the Nb-Si binary system (EDS data in Table 22). Nb_3Si was not indexed in the diffractogram of the HT condition as the pattern showed sharper peaks, higher peak intensities, and less noise, which was expected due to the homogenisation of the microstructure. As Nb_3Si could not be found in the HT condition by EDS it is rather decisively metastable.

According to JCPDS card 34-370 a pure Nb PXRD pattern will possess (110), (200), and (211), peaks reflections at 2Θ angles of 38.5, 55.6, and 69.7°. In both of the PXRD diffractograms the Nb_{ss} peak positions for these lattice planes had shifted to higher 2Θ angles; 39.0, 56.6, 70.9° for the AC and 39.0, 56.4, 70.8° for the HT condition. The cause of this shift was the contraction of the lattice parameter from Ti and Cr substituting for Nb in the body-centre-cubic (bcc) crystal structure. The lattice contraction of the solid solution was supported by

Nelson-Riley lattice parameter extrapolation, calculating a_{GB1AC}= 3.24 Å and a_{GB1HT}= 3.26 Å compared to a_{Nb}= 3.30 Å for pure Nb.

The microstructures of the alloy GB1 from the top, centre, and bottom of the ingot are presented in Figure 76 for the AC and Figure 77 for the HT. Large area EDS data taken using the Jeol JSM 6400 SEM are shown in Table 21 and phase EDS analysis using the same instrument are in Table 22. The typical GB1 microstructure displayed relatively large and faceted silicide grains existing in a variety of shapes and sizes with some cracking. Their faceted hexagonal shape, coupled with the bright BSE contrast, was indicative of hcp Hf-rich γNb_5Si_3, which was supported by the PXRD data (Figure 75). The γNb_5Si_3 remained after HT with negligible change in chemical composition. Surrounding the large silicides was interdendritic $(Nb,Ti,Cr)_{ss}$ and C14 $NbCr_2$ Laves phase with small silicide grains dispersed thoughout. Visually, the $(Nb,Ti,Cr)_{ss}$ and $NbCr_2$ showed similar phase contrast under BSE-SEM imaging making them difficult to distinguish, the presence of metastable Nb_3Si in these regions (Figure 76d) did not help matters either. Fortunately, WDS X-ray mapping helped to resolve these phases based on their Nb and Cr content (Figure 80).

After the HT, the redistribution of solutes moved the microstructure closer to equilibrium where the $(Nb,Ti,Cr)_{ss}$ and $NbCr_2$ contrast became much more distinct (Figure 77 b, d, f), likely owing to the decomposition of Nb_3Si, which was not found in the HT condition. The alloy GB1 showed cracks throughout but, noticeably in the HT microstructure, striation type cracks were present only in $(Nb,Ti,Cr)_{ss}$ grains. This is best seen in the upper left corner of Figure 77d. Again, WDS X-ray mapping helped to resolve phases in the HT condition (Figure 81).

Considering the large area EDS data of alloy GB1-AC (Table 21), there was significant macrosegregation of Si, Ti, and Hf between the bottom and the top of the ingot. In alloy GB1-AC the bottom ingot microstructure contained an architecture denoted the transition zone (T-zone, Figure 76e) and was categorised into three distinct regions (refer to Figure 78):

- **Ultra Fine Zone (UFZ)** where the microstructure was the finest.
- **Growth zone (GZ)** where there was some initial coarsening of the silicide compared with the UFZ.
- **Coarse zone (CZ)** microstructure where there was a faceted shape of large silicide grains. This was the predominant microstructure throughout alloy GB1-AC and remained after HT.

The UFZ microstructure was only formed directly at the bottom edge of the ingot where the highest cooling rates prevailed during arc melting and solidification. There was little compositional difference between the bottom CZ microstructure and the UFZ/GZ regions, and subsequently the T-zone itself (Table 21). Along the bottom ingot edge there were regions where the T-zone was not present and a CZ microstructure existed (Figure 78). After HT the chemical inhomogeneity of Ti and Hf between the CZ microstructure and T-zone was reduced but not that of Si (Table 21).

In the AC ingot the Nb_{ss} was rich in Si, with the average from the top, centre and bottom not exceeding the maximum Si content (~ 3.5 at.%), as indicated by the Nb-Si binary. However, the standard deviation was significant in all regions (Table 22). Arguably the AC condition Nb_{ss} in the bottom region microstructure was a Ti_{ss} based as opposed to Nb. Analysis of the AC condition interdendritic $(Nb,Ti,Cr)_{ss}/NbCr_2$ regions is also presented in Table 21. Note that data for the interdendritic $(Nb,Ti,Cr)_{ss}/NbCr_2$ is only from the CZ regions as the T-zone was fine grained and included the silicide phase.

The Bewlay ratio (Bewlay and Jackson, 2000) is a rule of thumb used to indicate γNb_5Si_3 formation. If the alloy and silicide composition ratio Nb:(Ti + Hf) < 1, γNb_5Si_3 presence is most likely due to a high ratio of Ti and Hf content against Nb. Of the γNb_5Si_3 analysed in GB1-AC, the ratio was found to be 0.97 top, 0.92 centre, and 0.78 bottom. In conjunction with PXRD, the γNb_5Si_3 silicide was identified in the AC condition due to stabilisation by their high Ti and Hf contents (Bewlay et al., 1999; Bewlay & Jackson 2000; Geng et al., 2007). In general the notation, $\gamma(Nb,Ti,Hf)_5Si_3$ is a more accurate description to denote the Ti and Hf rich content of the dominant 5-3 silicide. Generally, a significant Ti and/or Hf content should be assumed by the reader whenever γNb_5Si_3 silicide is discussed, at least in this thesis. However, the Bewlay ratio is even lower for the fine interdendritic 5-3 silicide grains at the centre (0.68) and bottom (0.52). The fine interdendritic silicide is equal in Ti and Nb in the centre, and much richer in Ti than Nb in the bottom, posing a strong suggestion for Ti_5Si_3 in at least the bottom. The PXRD was likely unable to detect the Ti_5Si_3 due to its small size, low phase fraction, and the inability to resolve detected peaks due to overlap of similar hexagonal structures.

After HT the $(Nb,Ti,Cr)_{ss}$ decreased in Si to a minimal ~ 1 at.%, Cr was reduced by ~4 at.% while Nb increased significantly and Ti increased mostly at the top and centre but only slightly so for the T-zone. The T-zone after HT had coarsend (Figure 79) and its $(Nb,Ti,Cr)_{ss}$ composition was much similar to the CZ microstructure of the top and centre. The large area analysis also indicated homogenisation throughout the microstructure after HT.

The high phase fraction (~ 40%) of C14 $NbCr_2$ Laves in the microstructure is attributed to the high Cr content of the alloy and Si stabilising Laves to lower temperatures (Geng et al., 2006a). The Si + Al content of the Laves phase decreased slightly after HT. However, the Cr + Al + Si content increased from ~ 57 at.% to ~ 60 at.%, which was due to enrichment in Cr. The Nb_3Si rich in Ti, Cr and Hf is rather elusive but visible in the Si X-ray map (Figure 80d) and supported by EDS (Table 22 and Figure 76d) where the γNb_5Si_3 borders the $(Nb,Ti,Cr)_{ss}/NbCr_2$ with Si content ranging from 11.94 (light blue) to 23.89 at.% (light green). The wide Si range of the Nb_3Si is attributed to its metastable state (Table 22 and Figure 80d). The high Nb, Ti and Cr content of the Nb_3Si would explain it residing adjacent to $(Nb,Ti,Cr)_{ss}$ and $NbCr_2$ grains. After HT there was no Nb_3Si found.

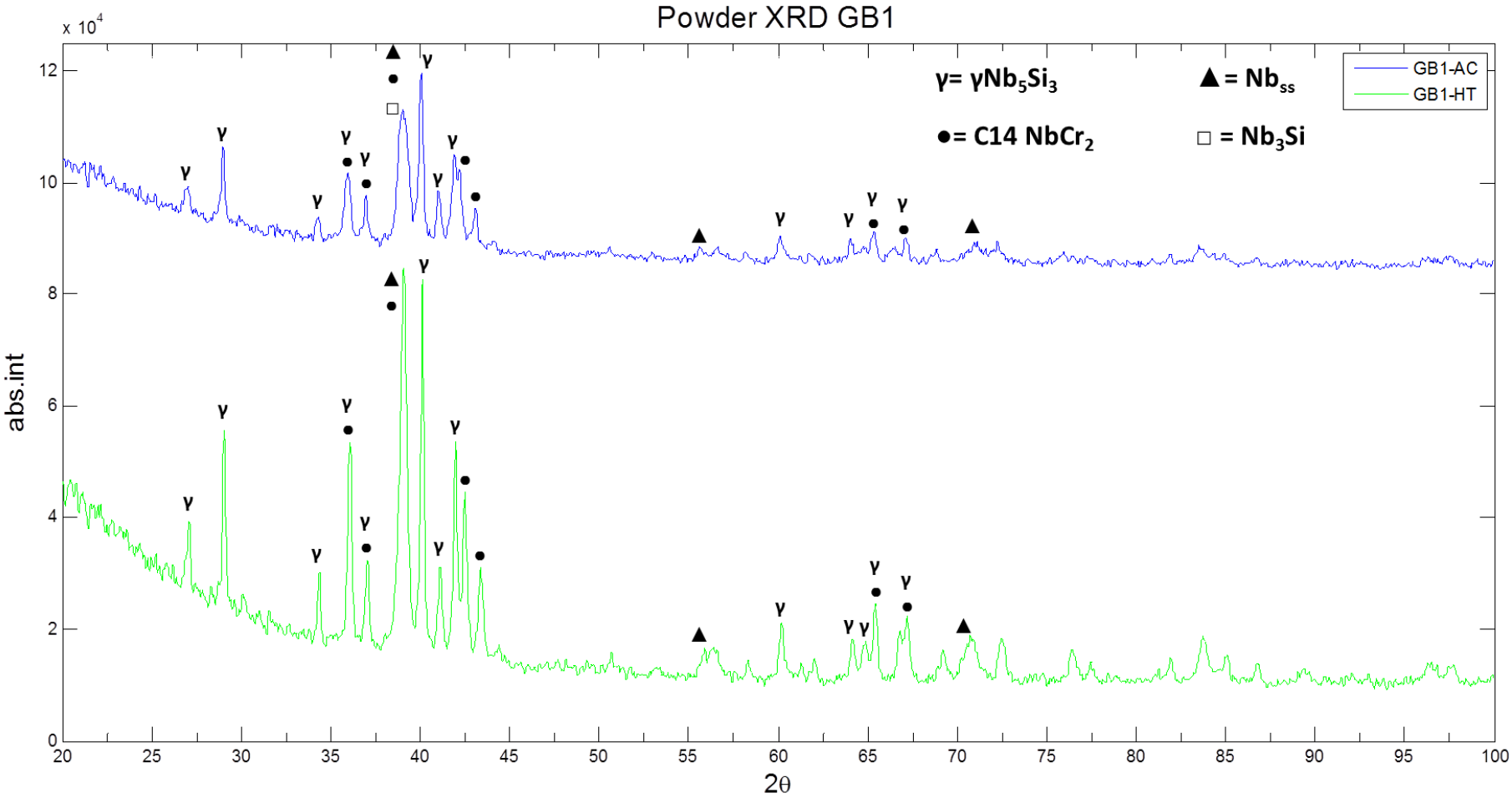

Figure 75. PXRD diffractogram of alloy GB1 samples in the AC and HT conditions.

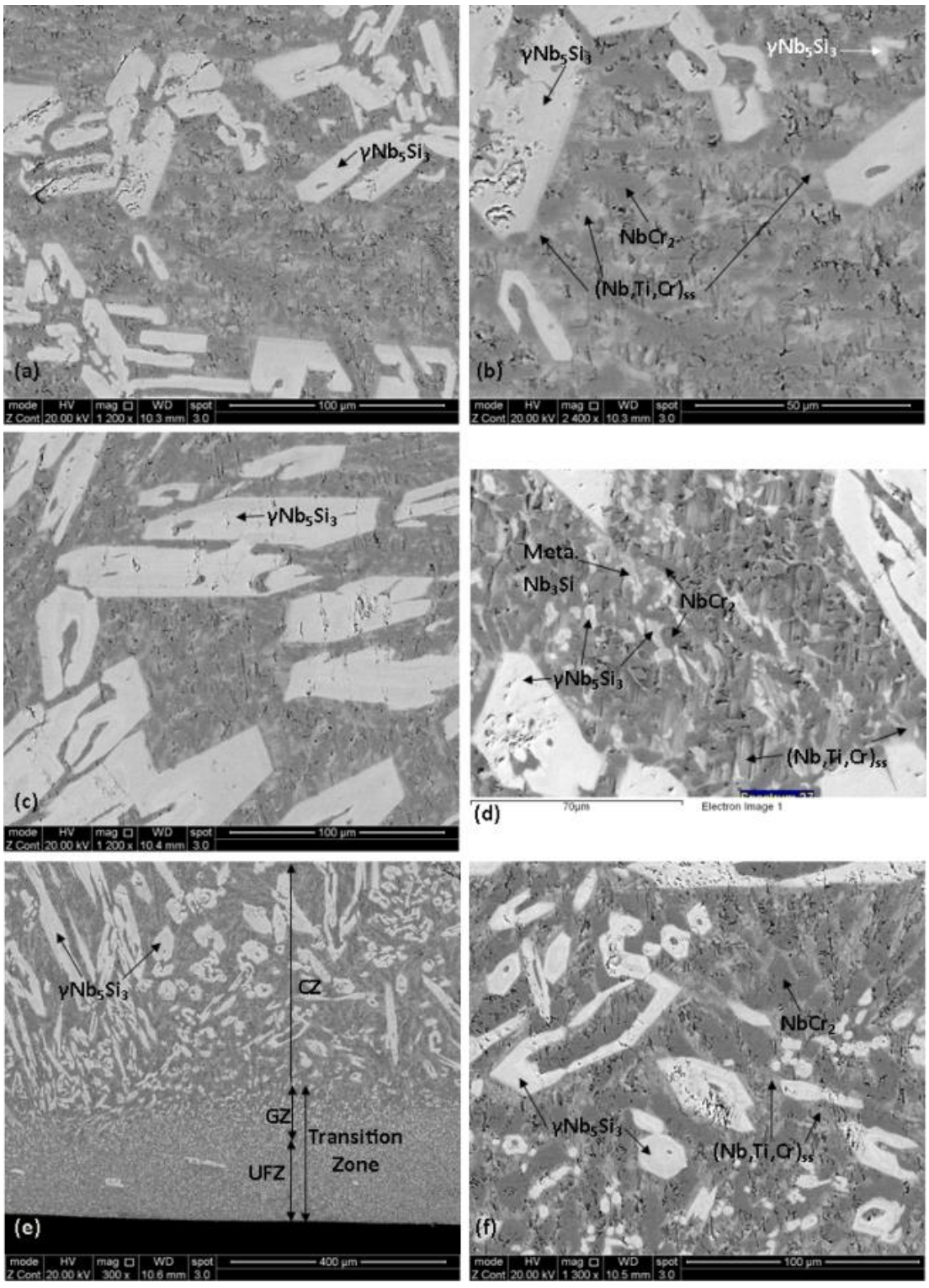

Figure 76. BSE microstructure images of alloy GB1-AC. The images show the microstructure from the top (a-b), centre (c-d), and bottom (e-f) ingot positions. Notations in (e); UFZ – Ultra Fine Zone, GZ – Growth Zone, CZ – Coarsening Zone.

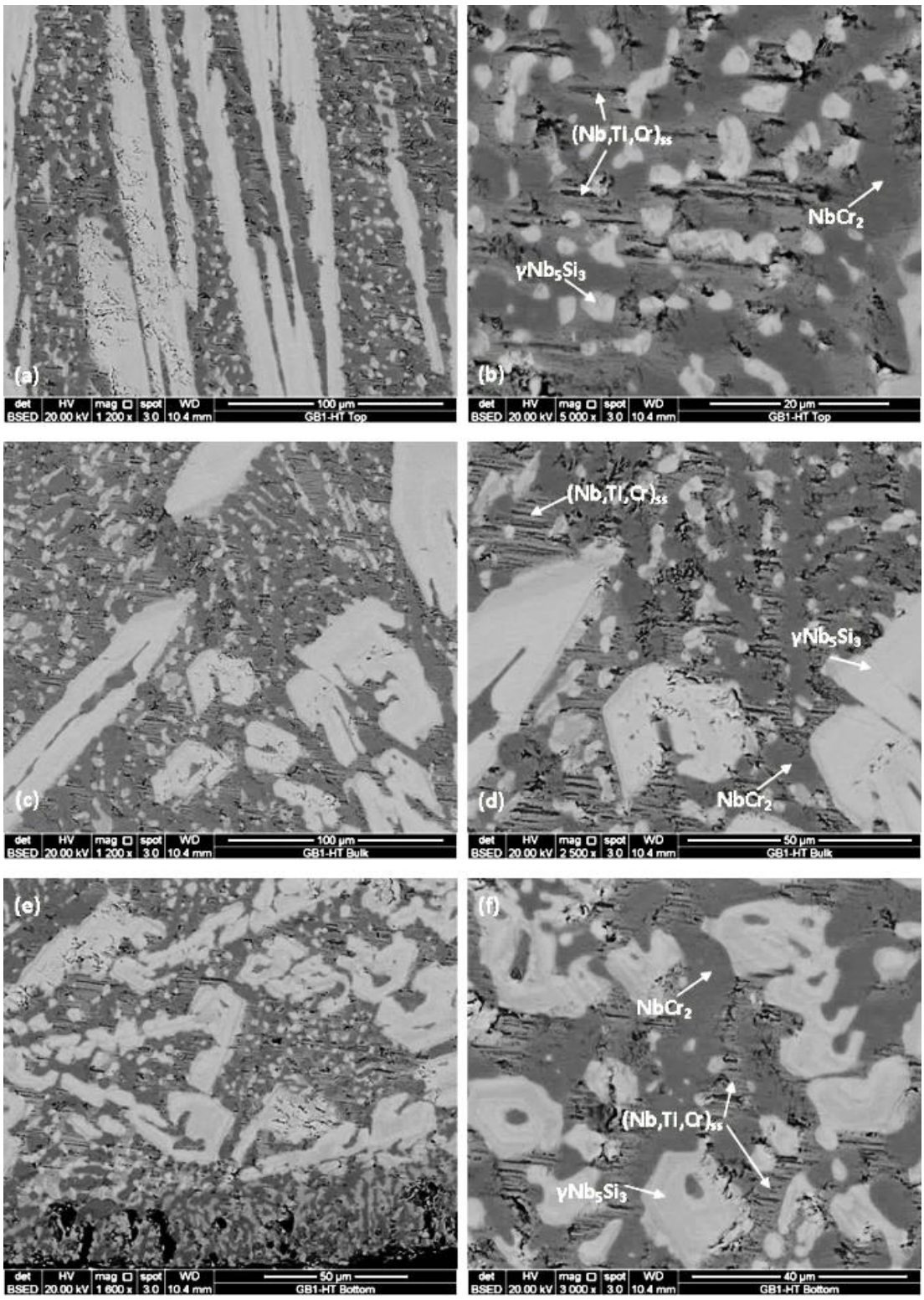

Figure 77. BSE microstructure images of alloy GB1-HT. Images show the microstructure from the top (a-b), centre (c-d) and bottom (e-f) ingot positions.

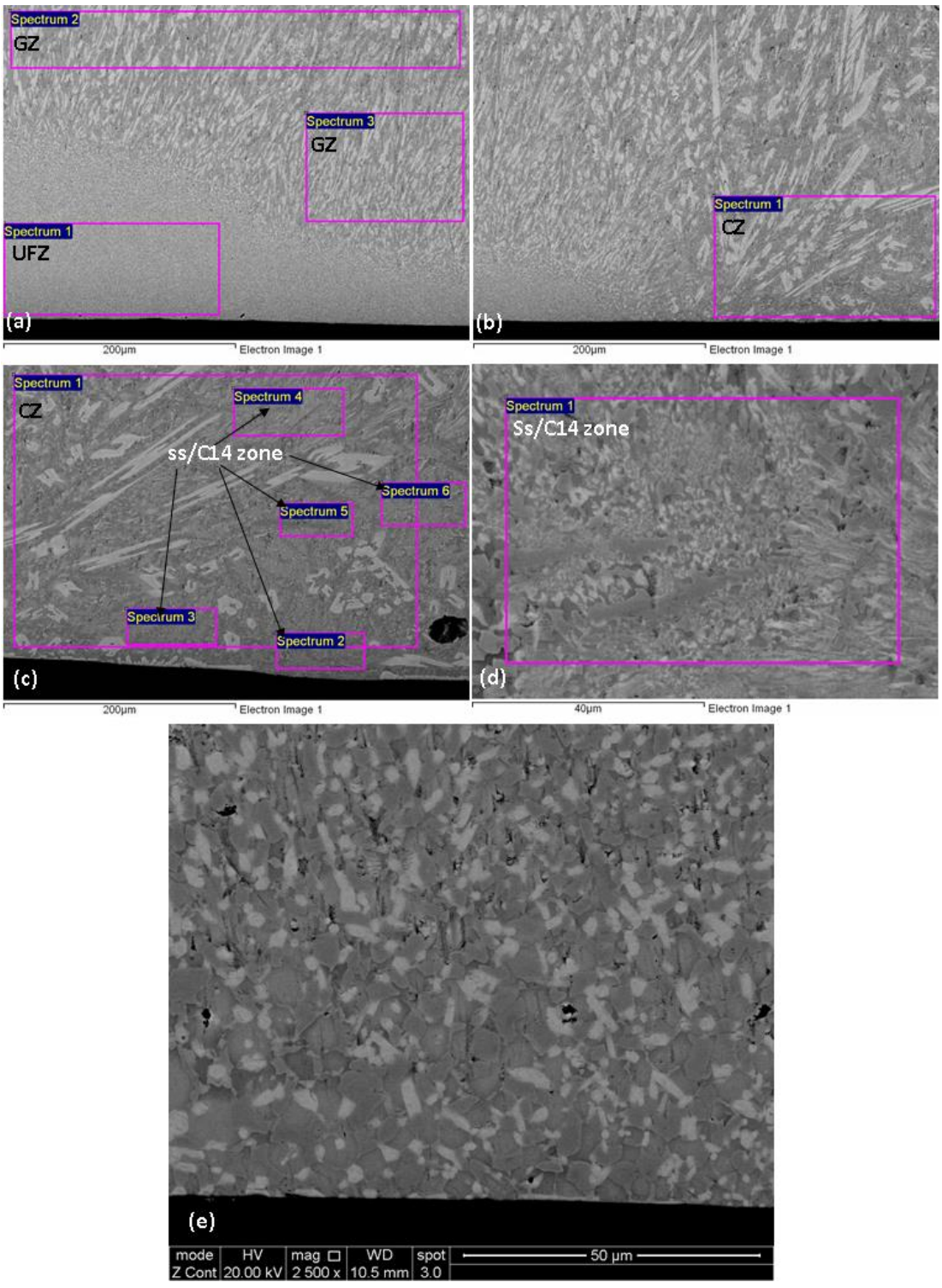

Figure 78. Bottom position microstructure of alloy GB1-AC showing the various regions analysed by EDS. (a) The ultra fine zone (UFZ) and growth zone (GZ) regions anlsysed, (b) The coarse zone was analysed, (c) The coarse zone and various $Nb_{ss}/NbCr_2$ zones were analysed, (d) The $Nb_{ss}/NbCr_2$ zone taken from the CZ microstructure. (e) Magnficiation of the T-Zone's UFZ at the bottom of the ingot, the γNb_5Si_3 is clearly identified as the brighter phase however the Nb_{ss} and $NbCr_2$ are difficult to distinguish by BSE contrast. It is important to notice example regions such as (c) showed no T-zone which would suggest at some bottom ingot areas the cooling rate was not high enough to induce the T-zone.

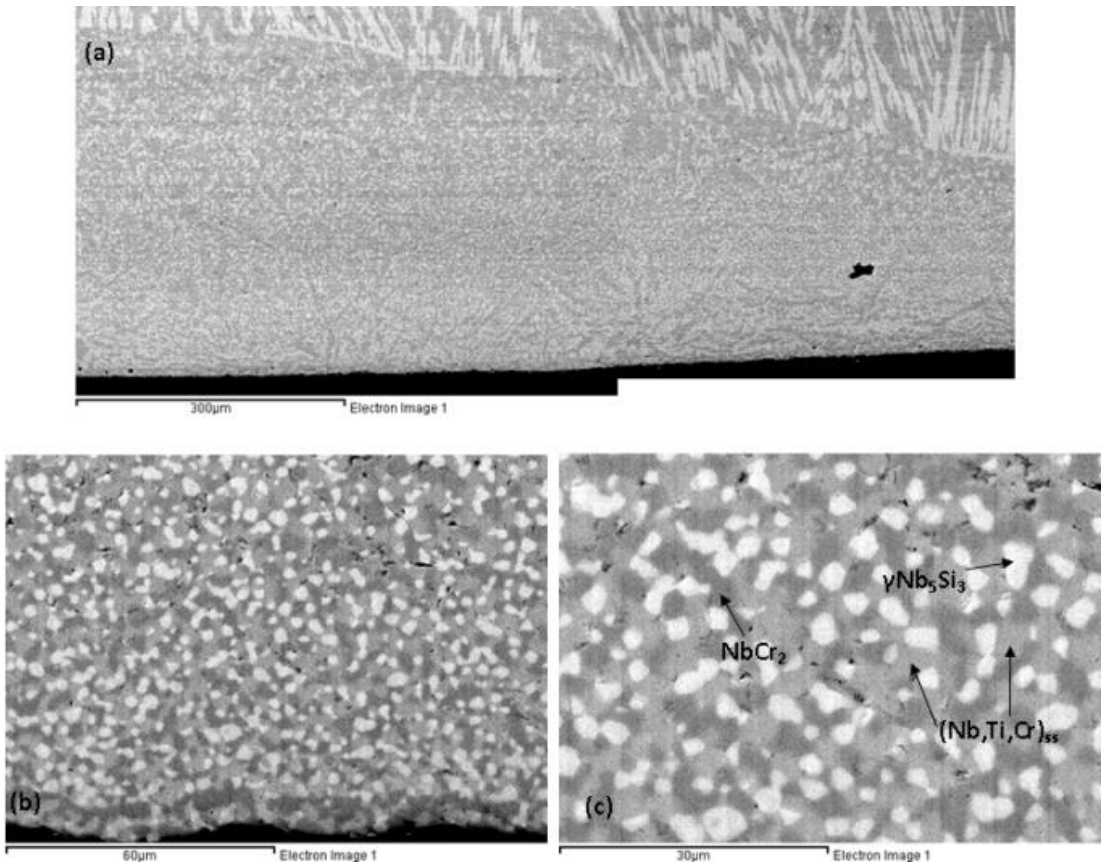

Figure 79. BSE images of the GB1-HT ingot microstrucure. (a) Low magnification over view of the transition zone, (b) heat treated UFZ, c) high magnification image of the UFZ.

Table 21. Large Area EDS data in at.% for alloy GB1-AC taken from the JEOL JEM 6400 SEM. Unless otherwise stated, data presented was taken from the coarse zone (CZ) microstructure.

	Position	Nb	Si	Ti	Cr	Al	Hf
	Nominal.	29.5	17	22	20	2.5	9
GB1-AC	Top	30.7 ± 0.4 31.6 - 30.4	19.5 ± 0.4 20.3 - 19.0	14.1 ± 0.4 14.6 - 13.5	21.9 ± 0.5 22.7 - 21.2	2.7 ± 0.2 3.0 - 2.5	11.2 ± 0.9 12.3 - 10.0
	Centre	30.1 ± 0.2 30.4 - 29.7	20.7 ± 1.4 21.9 - 18.2	18.9 ± 1.2 20.3 - 16.5	18.4 ± 1.2 20.7 - 16.7	2.3 ± 0.2 2.5 - 2.1	9.7 ± 0.5 10.6 - 9.1
	Bottom	29.5 ± 0.3 29.8 - 29.0	15.4 ± 0.7 16.6 - 14.7	24.5 ± 1.0 25.9 - 22.7	20.4 ± 1.0 21.8 - 18.7	2.7 ± 0.1 2.9 - 2.5	7.6 ± 0.5 8.4 - 7.1
	Bottom (GZ)	30.1 ± 0.5 31.4 - 29.4	15.3 ± 0.6 16.4 - 13.8	22.4 ± 0.6 23.5 - 21.7	21.8 ± 0.4 22.4 - 21.0	2.7 ± 0.1 2.9 - 2.5	7.8 ± 0.7 8.9 - 7.1
	Bottom (UFZ)	29.9 ± 0.2 30.2 - 29.5	14.4 ± 0.8 15.4 - 13.1	23.1 ± 1.2 25.1 - 21.5	22.0 ± 0.3 22.6 - 21.7	2.7 ± 0.2 2.9 - 2.5	7.8 ± 0.8 9.0 - 7.1
	Bottom (T-zone) [UFZ + GZ]	30.0 ± 0.4 31.4 - 29.4	14.9 ± 0.8 16.4 - 13.1	22.7 ± 1.0 25.1 - 21.5	21.9 ± 0.3 22.6 - 21.0	2.7 ± 0.2 2.9 - 2.5	7.8 ± 0.7 9.0 - 7.1
	Top (ss/C14)	31.3 ± 0.6 31.9 - 30.0	11.9 ± 0.5 12.8 - 11.2	15.2 ± 0.7 16.8 - 14.0	28.8 ± 1.4 31.9 - 26.0	3.0 ± 0.2 3.3 - 2.7	9.8 ± 0.3 10.3 - 9.2
	Centre (ss/C14)	30.5 ± 0.6 31.7 - 29.7	11.2 ± 0.8 12.0 - 10.0	21.1 ± 2.0 24.1 - 17.2	26.9 ± 1.6 31.0 - 25.2	2.9 ± 0.1 3.2 - 2.7	7.5 ± 0.4 8.4 - 6.9
	Bottom (ss/C14)	29.6 ± 0.8 30.7 - 28.3	12.4 ± 0.8 13.4 - 11.3	26.2 ± 1.0 27.0 - 24.3	22.4 ± 1.6 25.5 - 20.8	2.8 ± 0.2 3.0 - 2.5	6.6 ± 0.2 6.8 - 6.3

Table continued on next page…

		Nb			Si			Ti			Cr			Al			Hf		
GB1-HT	Top	30.4	±	0.5	18.7	±	1.6	20.3	±	0.4	19.2	±	1.5	2.7	±	0.2	8.7	±	0.4
		31.3	-	29.5	22.0	-	17.1	21.0	-	19.6	21.3	-	15.9	3.0	-	2.4	9.8	-	8.2
	Centre	30.3	±	0.5	18.5	±	1.3	20.4	±	0.4	19.4	±	1.0	2.7	±	0.2	8.7	±	0.4
		30.9	-	29.1	22.1	-	16.8	20.9	-	19.6	21.0	-	17.2	2.9	-	2.3	9.7	-	8.3
	Bottom	30.4	±	0.3	18.1	±	1.1	20.8	±	0.2	19.4	±	0.8	2.7	±	0.1	8.6	±	0.1
		30.7	-	30.2	19.0	-	17.0	20.9	-	20.6	20.3	-	18.7	2.7	-	2.6	8.8	-	8.5
	Bottom (T zone)	32.4	±	0.7	12.5	±	0.7	22.0	±	0.7	23.3	±	0.6	2.6	±	0.6	7.2	±	0.2
		33.8	-	31.0	13.4	-	10.6	23.2	-	20.9	24.5	-	22.3	3.5	-	1.8	7.5	-	6.6

Table 22. Phase EDS data in at.% for the alloy GB1 in the AC and HT conditions taken using the Jeol JSM 6400 SEM. Unless otherwise stated, data was taken from within the coarse zone (CZ) microstructure.

	Position	Phase	Nb	Si	Ti	Cr	Al	Hf
GB1-AC	Top	γNb_5Si_3	28.2 ± 0.6 29.2 - 27.2	38.2 ± 0.5 39.0 - 36.3	12.7 ± 0.9 15.7 - 11.6	2.6 ± 0.2 3.0 - 1.8	1.9 ± 0.3 2.7 - 1.3	16.5 ± 1.1 18.4 - 13.7
	Centre	γNb_5Si_3	27.5 ± 0.8 29.9 - 25.7	39.0 ± 0.7 39.8 - 35.5	16.8 ± 1.5 19.9 - 14.4	2.1 ± 0.2 2.6 - 1.7	1.4 ± 0.3 2.4 - 1.0	13.1 ± 0.8 14.8 - 11.4
	Bottom	γNb_5Si_3	25.4 ± 0.8 26.4 - 23.5	38.0 ± 0.5 38.8 - 37.4	22.4 ± 0.5 23.4 - 21.7	2.2 ± 0.3 2.5 - 1.5	1.9 ± 0.3 2.2 - 1.3	10.2 ± 0.5 11.2 - 9.7
	Centre (small interdendritic)	γNb_5Si_3	23.8 ± 2.4 29.6 - 20.5	35.6 ± 2.5 37.9 - 28.7	23.5 ± 1.1 25.8 - 22.2	3.1 ± 1.3 6.5 - 2.0	2.4 ± 0.2 2.9 - 2.0	11.6 ± 0.8 13.0 - 9.9
	Bottom (small interdendritic)	γNb_5Si_3	19.8 ± 1.5 21.8 - 18.6	36.7 ± 0.9 37.4 - 35.3	27.8 ± 0.6 28.3 - 27.0	2.8 ± 0.3 3.2 - 2.5	2.0 ± 0.1 2.1 - 1.8	11.1 ± 0.3 11.5 - 10.7
	Top	$NbCr_2$	23.3 ± 1.0 25.0 - 21.9	11.0 ± 0.9 12.0 - 9.1	9.6 ± 1.8 13.1 - 7.7	43.6 ± 1.5 45.3 - 40.5	2.3 ± 0.2 2.6 - 2.0	10.2 ± 0.7 11.1 - 9.2
	Centre	$NbCr_2$	22.9 ± 1.3 24.4 - 19.5	11.0 ± 0.7 12.2 - 8.9	11.6 ± 1.9 17.9 - 9.5	44.7 ± 1.4 45.6 - 39.3	1.9 ± 0.2 2.6 - 1.7	7.9 ± 0.6 9.3 - 7.2
	Bottom	$NbCr_2$	19.9 ± 1.7 22.1 - 17.2	10.3 ± 0.7 11.4 - 9.1	14.9 ± 1.5 17.0 - 12.9	45.8 ± 0.7 46.6 - 44.1	1.6 ± 0.1 1.7 - 1.4	7.5 ± 0.6 8.2 - 6.5
	Top	$(Nb,Ti,Cr)_{ss}$	53.3 ± 1.9 56.6 - 51.2	2.7 ± 0.9 4.5 - 2.0	21.7 ± 1.3 23.4 - 19.4	12.9 ± 0.5 13.5 - 12.4	4.5 ± 0.2 4.8 - 4.3	4.9 ± 0.3 5.5 - 4.7
	Centre	$(Nb,Ti,Cr)_{ss}$	47.3 ± 3.4 51.3 - 41.5	3.6 ± 2.1 7.9 - 1.9	27.6 ± 2.2 32.2 - 25.8	12.7 ± 0.6 13.6 - 11.3	4.3 ± 0.3 4.9 - 3.9	4.5 ± 0.6 5.7 - 4.0

GB1-AC	Bottom	$(Nb,Ti,Cr)_{ss}$	35.3	±	1.9	2.1	±	1.2	40.8	±	2.4	14.1	±	0.5	4.0	±	0.2	3.6	±	0.2
			37.3	-	32.5	4.3	-	1.4	44.6	-	38.0	14.9	-	13.7	4.2	-	3.8	3.9	-	3.4
	Top	M-Nb_3Si	37.9	±	3.4	17.2	±	3.7	19.2	±	1.7	12.2	±	3.8	3.7	±	0.4	9.8	±	1.1
			43.2	-	31.8	24.4	-	11.6	22.4	-	16.0	21.6	-	5.8	4.3	-	3.2	11.5	-	7.9
	Centre	M-Nb_3Si	34.4	±	5.1	20.1	±	6.8	23.7	±	2.8	10.1	±	5.9	3.3	±	0.5	8.4	±	1.4
			42.4	-	28.4	31.9	-	8.9	27.8	-	18.0	28.1	-	4.7	4.2	-	2.6	10.6	-	6.4
	Bottom	M-Nb_3Si	30.1	±	5.0	17.1	±	4.7	26.9	±	4.4	16.4	±	8.3	2.7	±	0.4	7.0	±	1.1
			36.6	-	24.5	21.5	-	11.1	31.8	-	22.0	28.1	-	8.4	3.2	-	2.2	8.5	-	5.3
	Position	**Phase**	**Nb**			**Si**			**Ti**			**Cr**			**Al**			**Hf**				
GB1-HT	Top	γNb_5Si_3	27.1	±	0.5	38.6	±	0.4	18.7	±	0.6	1.6	±	0.4	1.8	±	0.1	12.2	±	0.8
			27.8	-	26.4	39.0	-	37.9	20.1	-	18.1	2.2	-	1.1	1.9	-	1.8	13.4	-	11.0
	Centre	γNb_5Si_3	26.7	±	0.4	38.8	±	0.2	18.2	±	0.5	1.6	±	0.3	1.7	±	0.1	13.0	±	0.4
			27.2	-	26.0	39.2	-	38.5	19.0	-	17.6	2.1	-	1.2	1.9	-	1.5	13.5	-	12.5
	Bottom (T-zone)	γNb_5Si_3	19.9	±	0.9	38.5	±	1.0	25.6	±	0.4	1.5	±	0.2	1.7	±	0.2	12.9	±	0.2
			21.1	-	19.0	39.4	-	37.0	26.1	-	25.1	1.8	-	1.3	2.1	-	1.5	13.2	-	12.8
	Table continued on next page…																					

	Position	Phase	Nb			Si			Ti			Cr			Al			Hf		
GB1-HT	**Top**	**$NbCr_2$**	20.7	±	0.3	8.8	±	0.4	11.9	±	0.2	49.7	±	0.5	1.8	±	0.1	7.0	±	0.1
			21.0	-	20.2	9.5	-	8.3	12.4	-	11.7	50.4	-	49.1	1.9	-	1.6	7.2	-	6.8
	Centre	**$NbCr_2$**	20.1	±	0.1	8.7	±	0.3	12.3	±	0.1	49.7	±	0.2	1.9	±	0.1	7.3	±	0.1
			20.3	-	19.9	9.2	-	8.4	12.6	-	12.1	50.0	-	49.4	2.1	-	1.7	7.5	-	7.2
	Bottom (T-zone)	**$NbCr_2$**	20.0	±	0.2	8.5	±	0.4	12.6	±	0.2	51.3	±	0.3	0.8	±	0.2	6.8	±	0.1
			20.4	-	19.8	9.1	-	7.8	13.1	-	12.5	51.7	-	50.8	1.0	-	0.4	7.0	-	6.7
GB1-HT	**Top**	**$(Nb,Ti,Cr)_{ss}$**	51.9	±	0.4	0.6	±	0.2	31.3	±	0.3	8.5	±	0.3	5.0	±	0.2	2.7	±	0.1
			52.3	-	51.1	0.8	-	0.4	31.8	-	31.1	8.9	-	8.1	5.3	-	4.8	2.9	-	2.5
	Centre	**$(Nb,Ti,Cr)_{ss}$**	49.7	±	0.6	1.0	±	0.3	32.5	±	0.4	9.0	±	0.6	5.1	±	0.2	2.8	±	0.2
			50.4	-	48.9	1.7	-	0.6	33.0	-	31.6	10.5	-	8.5	5.4	-	4.8	3.2	-	2.5
	Bottom (T-zone)	**$(Nb,Ti,Cr)_{ss}$**	52.5	±	0.9	0.7	±	0.2	32.9	±	0.8	8.7	±	1.1	2.5	±	0.3	2.6	±	0.1
			54.1	-	51.1	1.0	-	0.3	34.1	-	31.5	10.9	-	7.8	2.9	-	2.0	2.8	-	2.5

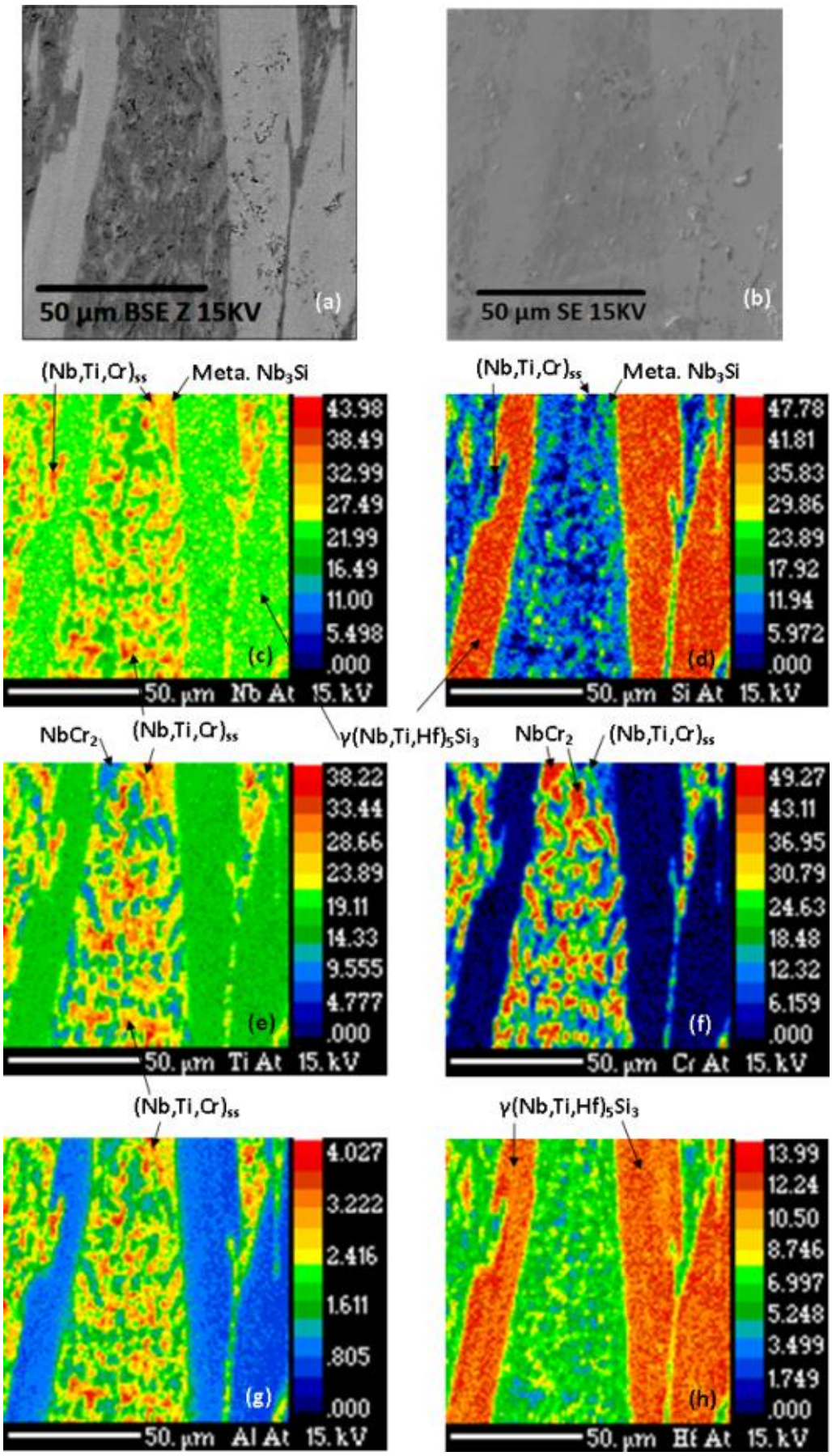

Figure 80. Semi-quantitive WDS X-ray maps of alloy GB1-AC. (a) BSE image of the mapped region, (b) SE image of the mapped region, (c-h) the Nb, Si, Ti, Cr, Al, Hf maps as labelled.

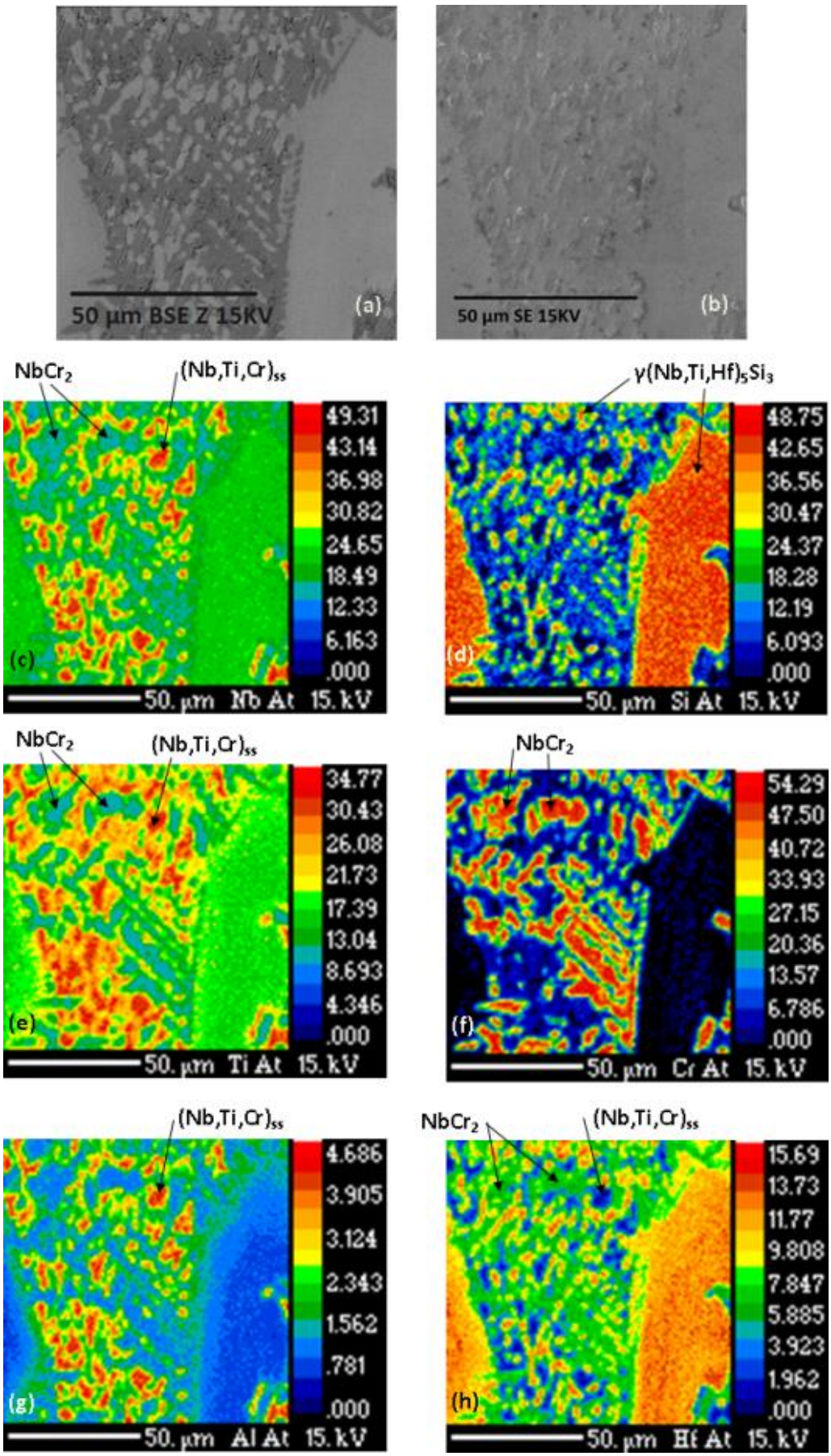

Figure 81. Semi-quantitive WDS X-ray maps of alloy GB1 in the heat-treated condition (a) BSE image of the mapped region, (b) SE image of the mapped region, (c-h) the Nb, Si, Ti, Cr, Al, Hf maps respectively.

4.1.3 Alloy GB1 Discussion

The solidification path of alloy GB1-AC to form the CZ microstructure is proposed to be:

$L \rightarrow L + (\gamma Nb_5Si_3)_{primary} \rightarrow L + (\gamma Nb_5Si_3)_{primary} + C14NbCr_2 \rightarrow$

$L + (\gamma Nb_5Si_3)_{primary} + C14NbCr_2 + (Nb_3Si)_{metastable} \rightarrow$

$(\gamma Nb_5Si_3)_{primary} + C14NbCr_2 + (Nb_3Si)_{metastable} + ((Nb,Ti,Cr)_{ss} + (\gamma Nb_5Si_3)_{secondary})_{eutectoid}$

After HT the equilibrium microstructure was found to be:

$(\gamma Nb_5Si_3)_{primary} + C14NbCr_2 + ((Nb,Ti,Cr)_{ss} + (\gamma Nb_5Si_3)_{secondary})_{eutectoid}$

Primary Nb_5Si_3 formation is clear based on the large faceted dendrites coarsened throughout the solidification process making alloy GB1-AC hypereutectic in the Nb-Si binary that is also evidenced by Si content of 19.5 and 20.7 at.% respectively at the top and centre ingot positions (the Nb-Si eutectic is 17.5 at.%).

The bottom GB1-AC ingot position displayed a fine microstructure region denoted the T-zone (Figure 76). However, the dominant CZ microstructure was still found at the bottom of the ingot (Figure 78c). The bottom T-zone and CZ regions possessed almost identical compositions (Table 21), different to the centre and top positions with lower Si of ~ 5 at.% and higher Ti of ~ 7 at.% while the Si difference to the Nb-Si eutectic composition was ~ 2 at.% lower. As the T-zone had similar composition to neighbouring CZ regions, it was most likely formed due to locally higher cooling rates in contact with the water-cooled Cu hearth preventing primary 5-3 silicide grain coarsening.

The presence of a hypereutectic CZ microstructure containing a Si content 2.1 at.% lower than the Nb-Si binary eutectic suggests 5-3 silicide stabilisation effects are in play or, alternatively, Nb_3Si destabilisation effects, and quite possibly the reduction of the Nb-Si eutectic composition due to alloying additions. Zelenitsas and Tsakiropoulos (2005) had shown Al and Cr have a strong destabilising effect on Nb_3Si, with the former being more potent, and suggested to reduce the Nb-Si eutectic composition, as found by their Nb-24Ti-18Si-5Al (KZ7) alloy. Chromium was discussed in section 1.7 for the Nb-Si-Cr system where it destabilises Nb_3Si and stabilises Nb_5Si_3. The data of the CZ and T-zone microstructures for GB1-AC would agree with the above points and although Al is considered more potent at destabilising Nb_3Si the very high Cr content is considered a more weighty factor in GB1-AC.

With alloy GB1-AC decidedly hypereutectic in the Nb-Si binary, it is unclear if the solidification process bypassed βNb_5Si_3 formation that immediately transformed into γNb_5Si_3 or if the latter nucleated originally. In either case, the formation of hP16 γNb_5Si_3 was the dominant 5-3 silicide formed as no βNb_5Si_3 was found in the final AC microstructure. The γNb_5Si_3 formation was due to the high Ti and Hf content of the alloy stabilising the hP16 structure, as discussed in section 1.4 for the Nb-Si-Ti and section 1.13 for the Nb-Si-Hf ternary systems. For alloys of the Nb-Si-Ti-Hf system or higher order, γNb_5Si_3 stabilised by Ti and Hf is well documented by numerous authors (Bewlay and Jackson, 2000; Bewlay et al., 2002b; Geng et al., 2007b; Yang et al., 2007; Grammenos and Tsakiropoulos, 2010; Zhang and Guo, 2015a).

The C14 $NbCr_2$ Laves formation occurred after γNb_5Si_3 due to a Cr rich melt at this stage of solidification and was aided by Si stabilisation (Goldschmidt and Brand, 1961a), its formation is consistent with literature (Zelenitsas and Tsakiropoulos, 2005). Nb_3Si was found in alloy GB1-AC evidenced by the EDS and PXRD data, the stabilisation is likely due to Ti extending the Nb_3Si phase field down to lower temperatures, hence Nb_3Si is not fully supressed by Cr, Al and Hf additions (Zelenitsas and Tsakiropoulos, 2005; Grammenos and Tsakiropoulos, 2010). The Nb_3Si is deemed metastable as it had decomposed during HT. Typically in the Nb-Si binary system the Nb_3Si may undergo eutectoid decomposition due to HT resulting in $Nb_{ss} + \alpha Nb_5Si_3$. Bewlay et al., (1998) and Zhao et al., (2001a) respectively found in the Nb-Ti-Si and Nb-Hf-Si systems the eutectoid decomposition of $(Nb,X)_3Si$ (where X = Ti or Hf) resulted in $(Nb,X)_{ss} + \alpha(Nb,X)_5Si_3$, supporting the affinity of Ti and Hf for the 5-3 silicide. Bewlay et al., (2004) and Grammenos & Tsakiropoulos (2010) later reported an alternate eutectoid decomposition reaction for their respective quaternary Nb-16Si-33Ti-12.5Hf and Nb-18Si-24Ti-5Hf (YG3) alloys that due to their significant Ti and Hf content the hP16 γNb_5Si_3 silicide was formed after Nb_3Si eutectoid decomposition instead of αNb_5Si_3.

The above is a consistent finding with what should be expected as Hf will form a stable 5-3 silicide but does not have a 3-1 silicide and will therefore destabilise the Nb_3Si, Cr does, however, possess a 3-1 silicide but is not isomorphous with Nb_3Si, therefore also destabilises it (Zhao et al., 2001a; Zelenitsas and Tsakiropoulos, 2005). Hence, the synergistic effect of Hf and Cr destabilising the Nb_3Si (with some destabilisation effect from the little Al content), and the significant Ti and Hf content stabilising hP16 γNb_5Si_3, resulted in the eutectoid decomposition reaction of $Nb_3Si \rightarrow (Nb,Ti,Cr)_{ss} + \gamma Nb_5Si_3$ to occur for alloy GB1-AC after HT. The reaction is evidenced by the lack of Nb_3Si in GB1-HT, increased prevalance of small interdendritic γNb_5Si_3 grains amongst the $(Nb,Ti,Cr)_{ss}/NbCr_2$, and clearer contrast between $(Nb,Ti,Cr)_{ss}$ and $NbCr_2$ (compare Figure 76 and Figure 77).

4.1.4 Alloy GB1 Conclusions

- The microstructure of alloy GB1-AC was comprised of primary hP16 γNb_5Si_3 dendrites surrounded by interdendritic $(Nb,Ti,Cr)_{ss}$ and C14 $NbCr_2$ Laves phase with some minor presence of Nb_3Si that was metastable and rich in Ti, Cr, and Hf.
- The microstructure of alloy GB1-HT was comprised of the same phases as the AC condition without the Nb_3Si. The instability of the Nb_3Si in GB1 was attributed to the synergy of Cr, Al and Hf.
- The synergy of Hf and Cr destabilised the Nb_3Si to decompose by eutectoid reaction during HT.
- The synergy of Ti and Hf stabilised the formation of the primary hexagonal hP16 γNb_5Si_3 in the AC and HT conditions.
- The Hf and Cr synergy prompted the eutectoid decomposition of Nb_3Si during HT to result in $(Nb,Ti,Cr)_{ss}$ and the γNb_5Si_3 silicide due to stabilisation by Ti and Hf.
- The high area fraction (~40%) of C14 $NbCr_2$ Laves phase was stabilised by the high Cr content of the alloy with Si stabilising the C14 structure to lower temperatures.

4.2 Alloy GB2

4.2.1 Summary

The phases present in alloy GB2 in the AC condition were the tetragonal tI32 βNb_5Si_3 silicide, hexagonal Cr-rich C14 $NbCr_2$ Laves phase, a bcc Ti and Cr rich Nb solid solution denoted $(Nb,Ti,Cr)_{ss}$, some presence of the tetragonal tI32 αNb_5Si_3 silicide, and the hexagonal hP16 γNb_5Si_3 silicide was identified at the bottom and centre of the ingot being more prevalent at the bottom. After HT of 1300°C for 100h, the microstructural architecture was essentially the same as the AC but the βNb_5Si_3 had transformed to isomorphous tI32 αNb_5Si_3, although the transformation was incomplete. The γNb_5Si_3 silicide had decomposed but was not entirely removed from the microstructure as it became incredibly scarce. On these basis an equilibrium microstructure was not fully achieved after the HT but was considered close to.

4.2.2 Cast and Heat Treated Microstructures

The PXRD diffractograms presented in Figure 82 confirmed the α and β Nb_5Si_3 silicide with a stronger presence of the latter, C14 $NbCr_2$ Laves phase, and a bcc $(Nb,Ti,Cr)_{ss}$ in the AC condition. The microstructures in the top, centre and bottom of the AC and HT conditions are shown in Figure 83 and Figure 84 respectively. The AC microstructure comprised of coarse primary βNb_5Si_3 dendrites with interdendritic Nb_{ss} and $NbCr_2$. The Nb_{ss} peak positions were slightly shifted to higher angles owing to Ti and Cr substituting with Nb and inducing lattice contraction. The Nb_{ss} lattice parameter was calculated to be a_{GB2AC}= 3.24 and a_{GB2HT}= 3.28 Å by Nelson-Riley extrapolation showing significant redistribution of the solutes after HT, this was confirmed by EDS data that is to be discussed.

The PXRD tenuously indexed the presence of the hexagonal γNb_5Si_3 silicide in the AC condition but was not indexed after the HT of 1300°C for 100h (Figure 82). Inspection of the microstructure by SEM found the characteristically bright white hexagonal γNb_5Si_3 silicide (under BSE-SEM contrast), residing at interdendritic $(Nb,Ti,Cr)_{ss}/NbCr_2$ regions in minor proportion at the bottom of the ingot, with little in the centre and virtually none at the top (Figure 83). Correspondingly to its stabilisation the γNb_5Si_3 possessed more than twice the Hf and ~5 at.% more Ti than the primary βNb_5Si_3 (Table 25), which is in spite of Hf and Ti macrosegregation had not occurred (Table 23 and Table 24). X-ray mapping of the AC and HT microstructures are presented in Figure 85 and Figure 86 respectively to aid the reader in visually identifying phases in corroboration with the EDS phase data.

Large area EDS analysis is presented in Table 23 and Table 24, taken using the PSEM 500 and Jeol JSM 6400 SEMs giving the average GB2-AC alloy composition (at.%) as 34.9Nb-19.2Si-

20.5Ti-17.3Cr-4.1Ge-4Hf and 37.3Nb-19.3Si-19.6Ti-17.5Cr-2.4Ge-4Hf respectively. There was only a small discrepancy between the instruments and note the bottom position was not evaluated with the Jeol instrument. The large area EDS analysis indicated macrosegregation of Si and Cr but such ranges are much reduced after HT, as analysed by both instruments indicating homogenisation of elements. Analysis from both SEMs averaged an Si (and Si + Ge) content higher than the eutectic composition in the Nb-Si binary system making the GB2-AC microstructure hypereutectic and hence the primary βNb_5Si_3 formation had occurred.

The Ge partitioned to the βNb_5Si_3 rather than the Nb_{ss} upon solidification. The βNb_5Si_3 structure was stabilised with appreciable Hf + Ti content (~20 at.% in Table 25) despite these elements being known to stablise γNb_5Si_3. After HT, PXRD (Figure 82) indicated the $\beta Nb_5Si_3 \rightarrow \alpha Nb_5Si_3$ isomorphous structure transformation had occurred and the 5-3 enriched in Ge proportional to reductions in Cr and Hf. The high ~28% area fraction of $NbCr_2$ Laves was again expected in the GB2 microstructure due to the high Cr content of the alloy and stabilisation to lower tempeartures by Si. After HT there was a slight reduction in Si, Hf, and a proportional increase in Cr and Ti of the $NbCr_2$ Laves phase. The $(Nb,Ti,Cr)_{ss}$ reduced in Ti, Cr, and Hf solutes after HT and enriched proportionally with Nb.

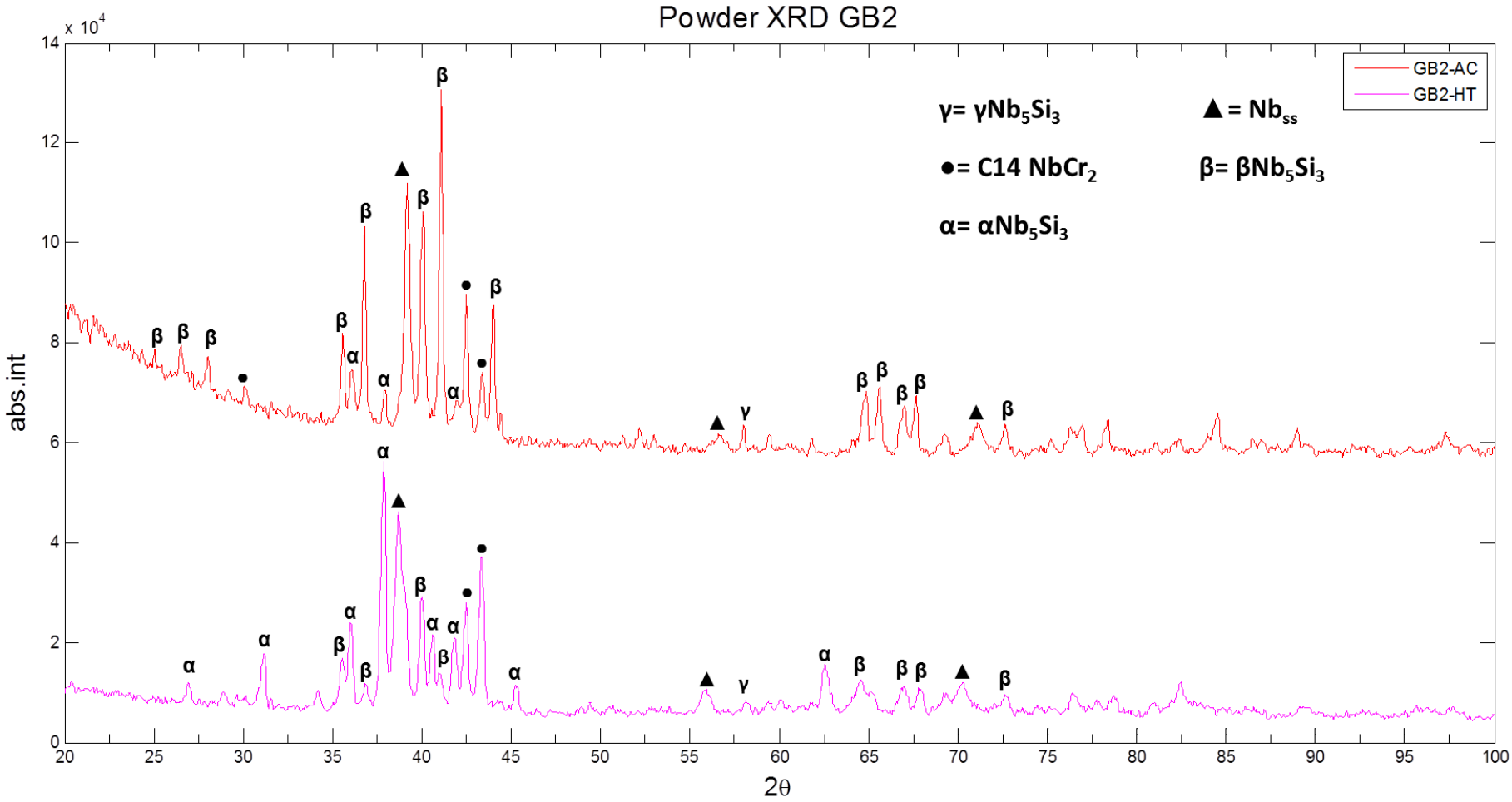

Figure 82. PXRD diffractograms of alloy GB2 in the AC and HT conditions.

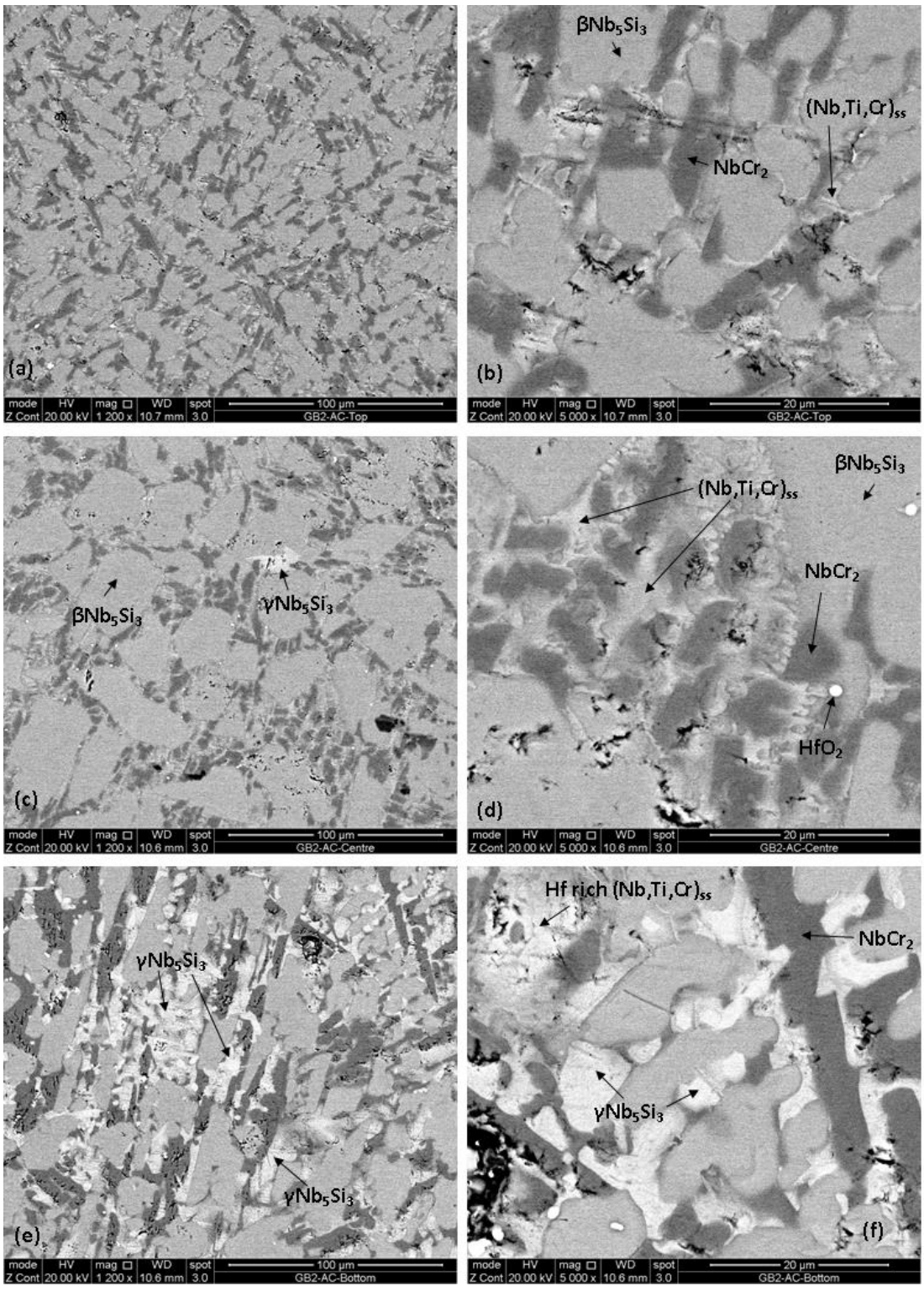

Figure 83. BSE-SEM images of the GB2-AC microstructure. (a-b) Top ingot microstructure, (c-d) Centre ingot microstructure, (e-f) Bottom ingot microstructure.

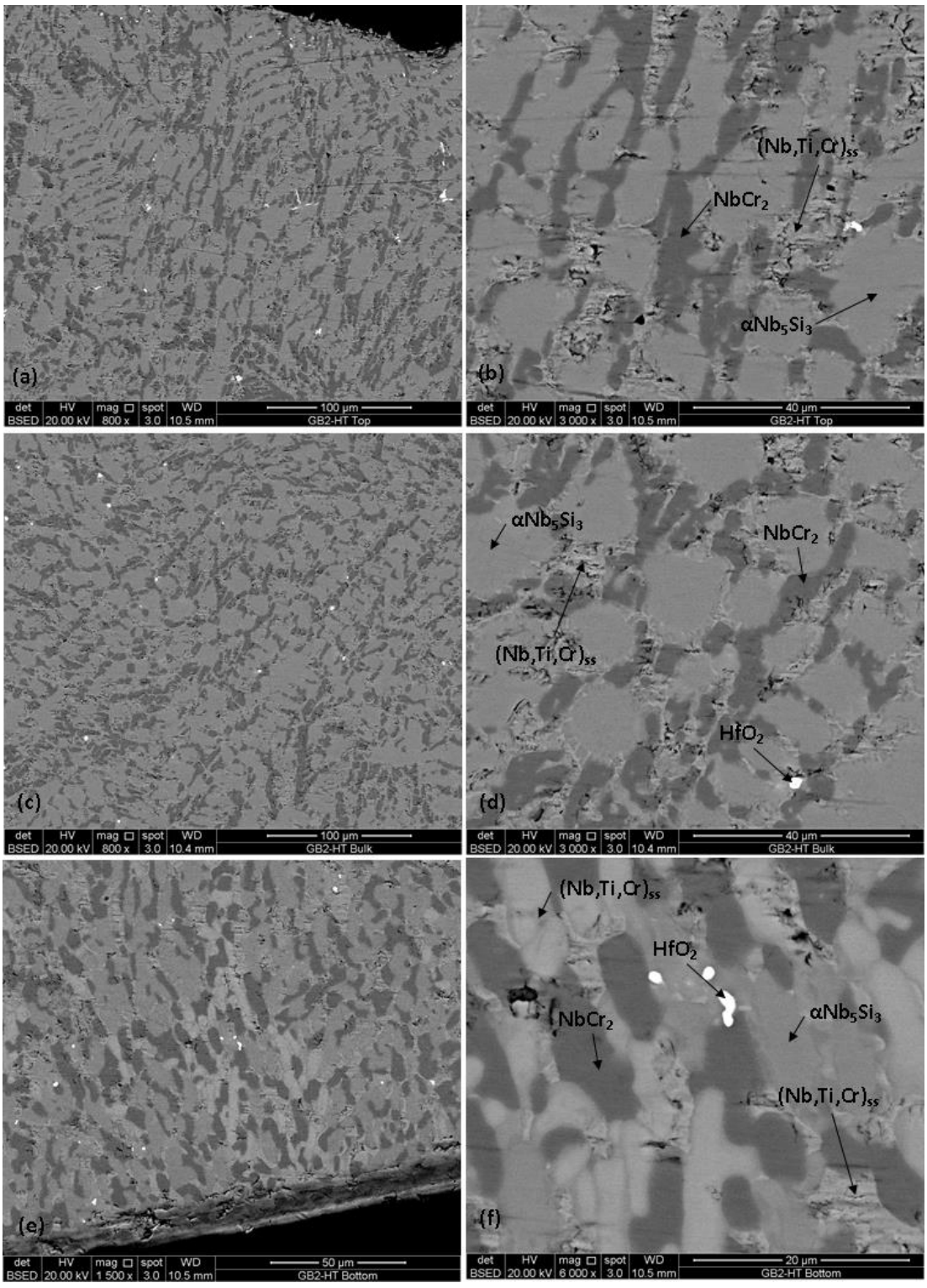

Figure 84. BSE-SEM images of GB2-HT microstructure. (a-b) Top ingot microstructure, (c-d) Centre ingot microstructure, (e-f) Bottom ingot microstructure.

Table 23. Large area EDS analysis of alloy GB2 in the AC and HT condition taken using the PSEM 500 SEM.

	Position	Nb	Si	Ti	Cr	Ge	Hf
	Nominal	**35.5**	**17.5**	**20**	**18**	**5**	**4**
GB2-AC	**Top**	**34.7** ± 0.2 35.0 - 34.4	**19.0** ± 0.3 19.4 - 18.4	**20.8** ± 0.2 21.1 - 20.3	**17.5** ± 0.3 17.9 - 16.9	**4.0** ± 0.1 4.3 - 3.7	**4.0** ± 0.1 4.2 - 3.8
	Centre	**35.4** ± 0.7 37.0 - 34.4	**20.0** ± 0.9 21.3 - 18.6	**20.2** ± 0.4 20.8 - 19.4	**16.4** ± 1.1 18.1 - 14.7	**4.1** ± 0.3 4.6 - 3.8	**4.0** ± 0.2 4.2 - 3.5
	Bottom	**34.7** ± 0.4 35.2 - 34.0	**18.6** ± 1.1 20.1 - 16.3	**20.4** ± 0.4 21.6 - 20.0	**18.1** ± 1.5 21.7 - 16.7	**4.1** ± 0.3 4.6 - 3.6	**4.1** ± 0.2 4.3 - 3.7
GB2-HT	**Top**	**33.4** ± 0.3 33.7 - 32.9	**19.7** ± 0.4 20.2 - 19.2	**21.1** ± 0.3 21.7 - 20.5	**17.4** ± 0.4 18.2 - 16.8	**4.1** ± 0.1 4.2 - 4.0	**4.2** ± 0.1 4.4 - 4.1
	Centre	**34.1** ± 0.4 34.8 - 33.5	**19.5** ± 0.7 20.9 - 18.6	**20.4** ± 0.2 20.7 - 20.1	**17.2** ± 0.8 18.3 - 15.5	**4.3** ± 0.2 4.7 - 4.1	**4.4** ± 0.1 4.6 - 4.1
	Bottom	**33.5** ± 0.4 34.2 - 33.0	**19.6** ± 1.1 22.3 - 18.6	**21.3** ± 0.5 21.8 - 20.4	**17.3** ± 1.3 18.2 - 14.1	**4.2** ± 0.3 4.8 - 3.7	**4.1** ± 0.1 4.4 - 4.0

Table 24. Large area EDS analysis of alloy GB2 in the AC and HT conditions taken using the Jeol JSM 6400 SEM.

	Position	Nb	Si	Ti	Cr	Ge	Hf
	Nominal	**35.5**	**17.5**	**20**	**18**	**5**	**4**
GB2-AC	**Top**	36.8 ± 0.8	18.4 ± 0.9	19.8 ± 0.6	18.2 ± 1.3	2.8 ± 2.2	4.0 ± 0.2
		37.9 - 35.9	20.0 - 17.5	20.4 - 19.0	19.7 - 16.9	5.2 - 0.9	4.3 - 3.8
	Centre	37.8 ± 1.0	20.1 ± 1.6	19.3 ± 0.9	16.8 ± 2.2	2.0 ± 1.8	4.0 ± 0.1
		39.9 - 36.6	23.7 - 18.4	20.3 - 17.4	19.4 - 11.5	5.7 - 0.6	4.3 - 3.8
GB2-HT	**Top**	36.6 ± 0.7	18.5 ± 0.5	18.5 ± 1.1	17.4 ± 0.3	5.2 ± 0.4	3.8 ± 0.3
		37.6 - 36.0	19.2 - 18.0	19.3 - 16.7	17.9 - 17.0	5.8 - 4.7	4.1 - 3.4
	Centre	36.3 ± 0.3	18.2 ± 0.6	19.0 ± 0.5	17.4 ± 1.0	5.2 ± 0.5	3.9 ± 0.3
		36.7 - 36.0	19.1 - 17.5	19.4 - 18.1	18.1 - 15.7	5.9 - 4.7	4.1 - 3.4
	Bottom	36.5 ± 0.9	17.4 ± 0.4	18.7 ± 0.8	18.3 ± 0.6	5.3 ± 0.2	3.8 ± 0.2
		38.3 - 35.8	18.1 - 16.9	19.6 - 17.4	18.9 - 17.4	5.6 - 5.0	4.1 - 3.4

Table 25. Phase EDS analysis of alloy GB2 in the AC and HT conditions taken using the Jeol JSM 6400 SEM.

	Pos.	Phase	Nb	Si	Ti	Cr	Ge	Hf
GB2-AC	Top	βNb_5Si_3	41.1 ± 1.3 43.3 - 39.5	30.0 ± 0.6 31.4 - 28.9	16.6 ± 0.9 19.6 - 15.6	3.5 ± 0.4 5.0 - 3.1	5.0 ± 2.8 7.4 - 1.0	3.7 ± 0.1 3.9 - 3.5
	Centre	βNb_5Si_3	42.1 ± 1.5 45.6 - 39.3	30.8 ± 0.6 32.5 - 28.9	16.6 ± 0.9 19.0 - 15.2	3.4 ± 0.3 4.0 - 2.8	3.5 ± 2.5 7.3 - 0.9	3.7 ± 0.2 4.2 - 3.3
	Bottom	βNb_5Si_3	39.6 ± 0.6 40.7 - 38.8	28.8 ± 1.1 31.1 - 25.6	16.7 ± 0.8 19.6 - 15.4	3.7 ± 0.4 4.2 - 2.4	7.4 ± 0.4 8.7 - 6.7	3.8 ± 0.2 4.2 - 3.4
	Centre	γNb_5Si_3	33.7 ± 0.7 34.6 - 33.2	32.0 ± 0.1 32.1 - 32.0	21.5 ± 0.4 21.8 - 21.0	2.8 ± 0.1 2.9 - 2.7	1.7 ± 0.1 1.8 - 1.6	8.3 ± 0.2 8.4 - 8.1
	Bottom	γNb_5Si_3	30.5 ± 1.6 32.4 - 25.7	28.4 ± 0.8 29.5 - 26.3	21.6 ± 1.6 25.9 - 19.5	2.5 ± 0.5 3.8 - 1.8	8.6 ± 0.5 9.5 - 7.9	8.4 ± 0.5 9.0 - 7.4
	Top	$NbCr_2$	26.6 ± 0.2 27.2 - 26.1	10.6 ± 0.3 11.1 - 9.9	9.8 ± 0.4 10.7 - 9.1	48.2 ± 0.7 49.0 - 47.0	0.8 ± 0.6 1.5 - 0.0	4.0 ± 0.3 4.4 - 3.5
	Centre	$NbCr_2$	26.3 ± 0.9 27.5 - 22.7	10.4 ± 0.7 13.1 - 9.6	10.5 ± 1.8 17.6 - 9.3	48.0 ± 2.0 49.3 - 41.0	0.7 ± 0.7 2.4 - 0.0	4.0 ± 0.6 6.6 - 3.3
	Bottom	$NbCr_2$	26.8 ± 0.6 28.3 - 24.8	10.1 ± 0.4 11.1 - 9.3	9.9 ± 0.8 13.7 - 9.1	48.2 ± 1.1 49.6 - 44.1	1.2 ± 0.3 1.7 - 0.0	3.8 ± 0.2 4.4 - 3.2

Table continued on next page…

GB2-AC	Top	$(Nb,Ti,Cr)_{ss}$	51.5 ± 3.6 54.8 - 40.1	2.0 ± 0.7 4.2 - 1.3	29.3 ± 2.5 37.6 - 27.0	13.8 ± 1.1 16.4 - 12.2	0.6 ± 0.5 1.6 - 0.0	2.8 ± 0.4 3.4 - 2.1
	Centre	$(Nb,Ti,Cr)_{ss}$	47.2 ± 3.1 50.8 - 41.8	3.3 ± 2.0 8.3 - 1.7	31.6 ± 2.2 34.5 - 27.4	14.4 ± 1.3 16.4 - 12.0	0.5 ± 0.5 1.8 - 0.1	3.2 ± 0.5 4.0 - 2.4
	Bottom	$(Nb,Ti,Cr)_{ss}$	54.2 ± 2.3 57.3 - 48.0	1.8 ± 1.3 5.6 - 0.0	26.9 ± 1.8 31.4 - 24.4	13.8 ± 0.9 15.2 - 11.6	1.2 ± 0.6 2.9 - 0.0	2.1 ± 0.4 3.3 - 1.3
	Pos.	**Phase**	**Nb**	**Si**	**Ti**	**Cr**	**Ge**	**Hf**
GB2-HT	Top	αNb_5Si_3	41.0 ± 0.4 41.7 - 40.4	29.8 ± 0.6 30.9 - 28.8	18.1 ± 1.9 20.3 - 15.4	1.4 ± 1.2 3.2 - 0.3	7.5 ± 0.4 8.4 - 7.0	2.3 ± 0.9 3.6 - 1.2
	Centre	αNb_5Si_3	40.8 ± 0.4 41.2 - 39.7	29.8 ± 0.4 30.7 - 29.0	15.7 ± 0.3 16.1 - 15.4	3.0 ± 0.8 5.3 - 2.2	7.2 ± 0.2 7.5 - 6.9	3.4 ± 0.2 3.8 - 3.2
	Bottom	αNb_5Si_3	40.7 ± 0.2 41.2 - 40.4	30.4 ± 0.5 31.1 - 29.5	17.8 ± 0.4 18.2 - 17.1	0.7 ± 0.6 2.3 - 0.4	7.3 ± 0.4 8.1 - 6.7	3.0 ± 0.3 3.3 - 2.4
	Top	$NbCr_2$	26.3 ± 0.8 27.6 - 25.2	8.0 ± 0.5 8.9 - 7.6	11.2 ± 1.6 14.2 - 9.8	51.5 ± 1.7 53.1 - 48.3	1.2 ± 0.1 1.4 - 1.0	1.8 ± 0.6 2.5 - 0.9
	Centre	$NbCr_2$	24.7 ± 0.2 25.2 - 24.4	8.4 ± 0.4 9.8 - 8.1	11.1 ± 0.4 12.4 - 10.7	51.6 ± 1.3 52.4 - 47.4	1.1 ± 0.5 2.7 - 0.7	3.1 ± 0.2 3.3 - 2.6
	Bottom	$NbCr_2$	25.9 ± 0.9 27.3 - 24.6	8.3 ± 1.4 12.1 - 7.4	11.5 ± 1.9 16.7 - 10.3	50.7 ± 4.2 53.7 - 39.3	1.2 ± 0.4 2.3 - 0.8	2.4 ± 0.6 3.0 - 1.5

Table continued on next page…

	Pos.	Phase	Nb	Si	Ti	Cr	Ge	Hf
GB2-HT	Top	$(Nb,Ti,Cr)_{ss}$	65.3 ± 2.1	0.6 ± 0.4	23.7 ± 2.1	9.3 ± 0.3	0.5 ± 0.1	0.5 ± 0.3
			70.3 - 62.8	1.5 - 0.3	26.2 - 18.9	10.0 - 8.9	0.7 - 0.4	1.1 - 0.2
	Centre	$(Nb,Ti,Cr)_{ss}$	64.4 ± 1.4	0.9 ± 1.0	23.9 ± 0.4	9.1 ± 0.8	0.5 ± 0.3	1.3 ± 0.3
			65.4 - 60.8	3.8 - 0.3	25.0 - 23.4	9.8 - 7.4	1.0 - 0.1	2.0 - 1.0
	Bottom	$(Nb,Ti,Cr)_{ss}$	66.0 ± 2.0	1.0 ± 0.5	22.0 ± 0.8	9.5 ± 2.4	0.6 ± 0.3	0.9 ± 0.2
			67.5 - 60.7	2.3 - 0.3	23.1 - 20.1	15.3 - 7.6	1.1 - 0.1	1.3 - 0.7

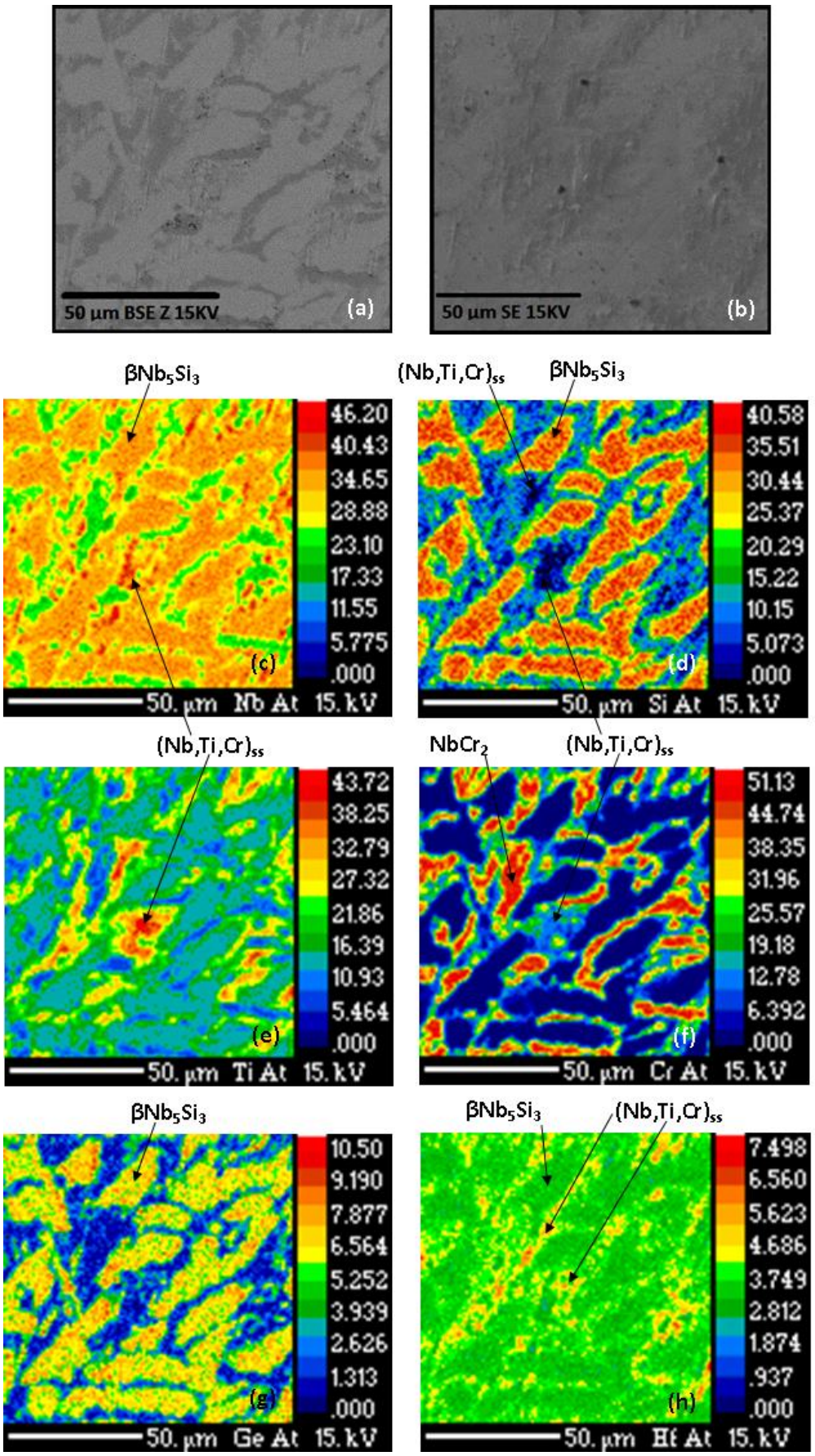

Figure 85. Semi-quantatitive WDS X-ray mapping of alloy GB2-AC. (a) BSE image of the mapped region, (b) SE image of the mapped region, (c-h) the Nb, Si, Ti, Cr, Ge, Hf maps respectively.

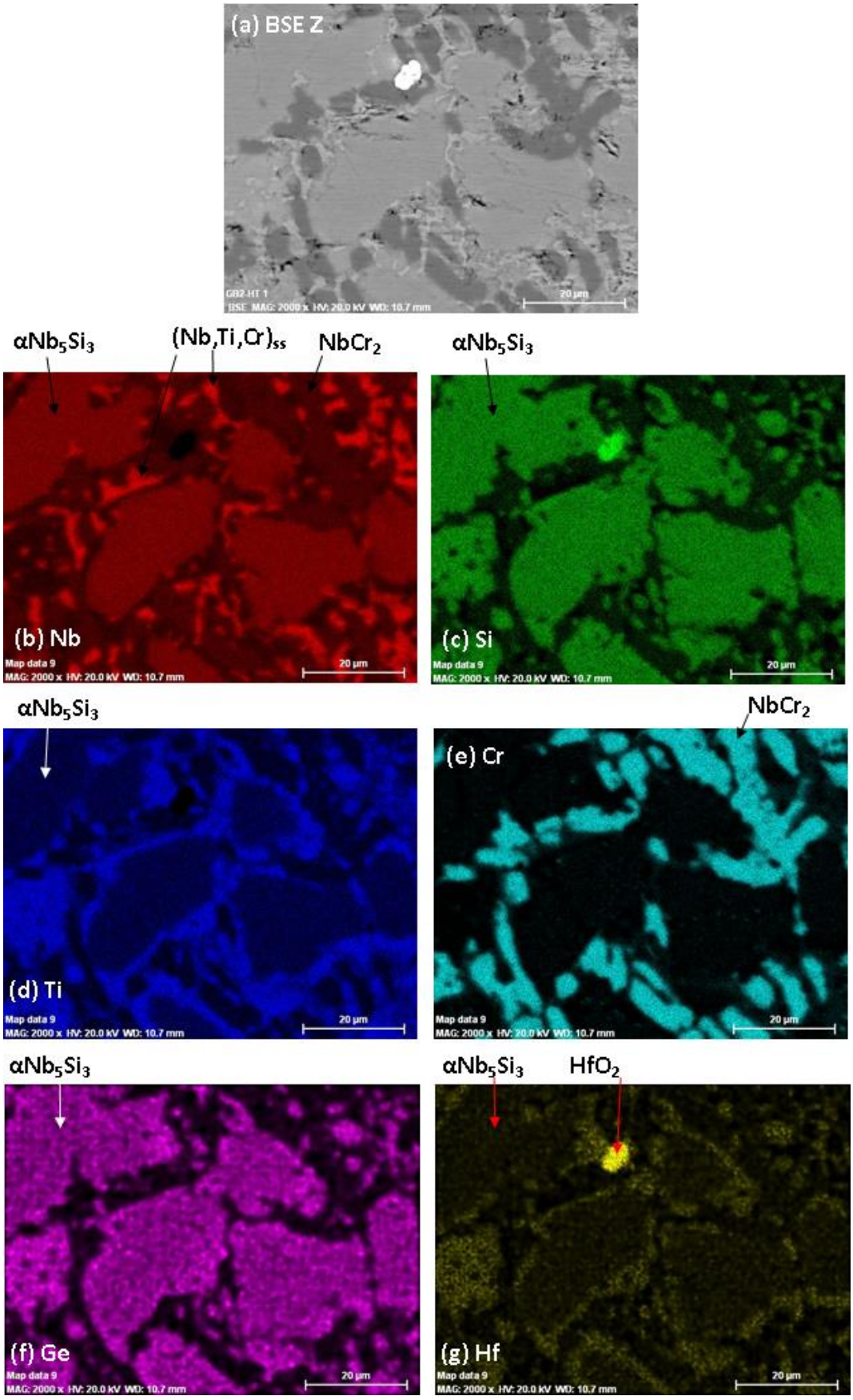

Figure 86. Qualitative EDS X-ray mapping of alloy GB2-HT. (a) BSE-SEM image of the mapped region, (b – g) X-ray maps of elements Nb, Si, Ti, Cr, Ge, and Hf respectively.

4.2.3 Alloy GB2 Discussion

The solidification path of alloy GB2-AC is proposed to be:

$L \rightarrow L + \beta Nb_5Si_3 \rightarrow L + \beta Nb_5Si_3 + C14NbCr_2 \rightarrow L + \beta Nb_5Si_3 + C14NbCr_2 + (Nb,Ti,Cr)_{ss} \rightarrow$

$\beta Nb_5Si_3 + C14NbCr_2 + (Nb,Ti,Cr)_{ss} + (\gamma Nb_5Si_3)_{metastable} + \alpha Nb_5Si_3$

After HT at 1300°C for 100h the microstructure was:

$(\beta Nb_5Si_3)_{untransformed} + C14\ NbCr_2 + (Nb,Ti,Cr)_{ss} + \alpha Nb_5Si_3$

Alloy GB2-AC was considered hypereutectic in the Nb-Si binary, as indicated by the coarse primary Nb_5Si_3 dendrites in the microstructure and the > 17.5 at.% Si content at all ingot positions (Table 23 and Table 24). The initial silicide formation was suggested to be the tI32 βNb_5Si_3 structure, with some αNb_5Si_3 formation due to the $\beta Nb_5Si_3 \rightarrow \alpha Nb_5Si_3$ isomorphous structure transformation during solidification, as opposed to αNb_5Si_3 forming simultaneously. The timing of which this transformation intiated during solidification is unclear, hence, the αNb_5Si_3 phase is added at the end of the solidification path for simplicity (see above).

Evidence to the isomorphous structure transformation was based upon the PXRD data (Figure 82), strongly indicating the βNb_5Si_3 dominance in the AC and αNb_5Si_3 in the HT conditions. Low intensity βNb_5Si_3 peaks in the HT condition indicated equilibrium was not fully achieved and some βNb_5Si_3 was untransformed. It is plausible that Cr and Ge additions partially stabilised the βNb_5Si_3 isomorph and hence the transformation after HT was sluggish (see section 1.7 and 1.16).

The lack of Nb_3Si in alloy GB2 was consistent with literature that Ge has a strong impact on its destabilisation, any such destabilisation would be enhanced by synergy with the high Cr and appreciable Hf content (Zelenitsas and Tsakiropoulos, 2005; Grammenos and Tsakiropoulos, 2010; Zifu and Tsakiropoulos, 2010; Li and Tsakiropoulos, 2011).

In the AC condition, X-ray mapping (Figure 85) showed the interdendritic enrichment of Ti and Hf, logically the γNb_5Si_3 was only present in these regions (Figure 83 e and f). This is clear evidence for the partitioning of Ti and Hf to the interdendritic regions (i.e. the melt) during solidification. Although Li & Tsakiropoulos, (2011) for their Nb-24Ti-18Si-5Ge (ZF3) alloy found that Ge additions enchanced the partitioning of Ti to the melt, there was however, no macrosegregation of Ti and Hf or Ge in alloy GB2-AC. Since γNb_5Si_3 was predominantly formed in the bottom of the ingot where cooling rates were the highest, cooling rates are suspected to

be the cause of Ti and Hf partitioning resulting in γNb_5Si_3 formation and not due to any influence of Ge on Ti partitioning.

The formation of primary βNb_5Si_3 would leave the melt particularly Cr rich and, consistently with literature, $NbCr_2$ Laves phase formation occurred with a C14 structure stabilised to lower temperatures by Si (Goldschmidt and Brand, 1961a; Zelenitsas and Tsakiropoulos, 2005).

After HT at 1300°C for 100h, the microstructural architecture was essentially the same. In addition to the $\beta Nb_5Si_3 \rightarrow \alpha Nb_5Si_3$ transformation mentioned above, the 5-3 enriched in Ge and reduced in Hf, the C14 $NbCr_2$ Laves phase had slightly reduced in Si and Hf but gained Ti, and the $(Nb,Ti,Cr)_{ss}$ that was significantly enriched with Nb and reduced in Ti, Cr and Hf. PXRD suggested some small presence of γNb_5Si_3 which was consistent with inspection under SEM but grains were incredibly scarce. αNb_5Si_3 was the stable silicide in GB2-HT although a further HT was deemed necessary to reach complete equilibrium.

Considering the GB2-HT X-ray map (Figure 86), there was an apparent micro-segregation of Ti to either the grain boundary of the 5-3 silicide that would now be the α isomorph, or to the interdendritic region of the microstructure, this is difficult to visually resolve with the micrographs available. Such Ti rich zones are distinctly separated to the Nb_{ss}. This may be evidence to the influence of Ge on the partitioning of Ti from the 5-3 silicide, or, it may be due to the $\beta \rightarrow \alpha$ transformation. Table 25 conveys only a small if any Ge increase of the 5-3 silicide after HT and virtually no change in Ti content, making Ge's influence on Ti partitioning inconclusive for alloy GB2.

4.2.4 Alloy GB2 Conclusions

- The microstructure of alloy GB2-AC consisted of primary tI32 βNb_5Si_3 dendrites, interdendritic C14 $NbCr_2$ Laves, $(Nb,Ti,Cr)_{ss}$, some tI32 αNb_5Si_3 due to βNb_5Si_3 structure transformation during solidification, and hP16 γNb_5Si_3 that had formed predominantly in the bottom of the ingot.
- Higher cooling rates at the bottom of the ingot were responsible for the partitioning of Ti and Hf to the melt resulting in formation of γNb_5Si_3 at interdendritic regions.
- The microstructure of alloy GB2-HT was the same as the AC condition, however, the $\beta Nb_5Si_3 \rightarrow \alpha Nb_5Si_3$ structure transformation had occurred. Some untransformed βNb_5Si_3 remained and γNb_5Si_3 became incredibly scarce and was considered metastable. Equilibrium was not quite achieved but considered close to.
- The high Cr and minor Hf content synergistically destabilised Nb_3Si, preventing its formation.

5 Oxidation Behaviour

5.1 Introduction

The oxidation behaviour of alloys GB1 and GB2 was studied in the AC and HT conditions at 800, 1000, and 1200°C for different times up to 100h, please refer to section 3.6 for the experimental procedure. The oxidation rate constants were determined using the rate equations; $\left(\frac{\Delta W}{A}\right) = k_l t$ for linear oxidation and $\left(\frac{\Delta W}{A}\right)^2 = k_p t$ for parabolic oxidation behaviours where ΔW = weight change (g), A= surface area (cm^2), k_l= linear rate constant, k_p= parabolic rate constant, and t = time (s).

Oxidation rate constants and accompanying data for alloys GB1 and GB2 are presented in Table 26. For comparison purposes, oxidation data of various Nb-silicide alloys and Ni-superalloy CMSX-4 from literature are presented in Table 27 and Table 28. The TGA behaviours of alloys GB1 and GB2 are plotted in Figure 87 with photographs of the post oxidised specimens presented in Figure 88, Figure 89, and Figure 90. A nonmenclature of 'Alloy-Condition-Temperature(in°C)-Hours(h)' is used to denote the various specimens. For example; 'GB1-AC-800C-100h' identifies alloy GB1 in the AC condition oxidised at 800°C for 100h. The abbreviation 'BIR' is used to denote alloy GB2 samples taken from the 600g ingot produced courtesy of the University of Birmingham's plasma arc metling facility. All other samples were produced by electric arc melting courtesy of the University of Cambridge.

In summary, the data indicates better oxidation behaviour of the alloys GB1 and GB2 compared with other Nb-silicide based alloys, but are far from the single crystal CMSX-4. Spallation was not always observed, particularly for alloy GB2, which is a significant improvement compared with other Nb-silicide based alloys. The following chapter sections, separated by temperature, will discuss the oxidation results in more detail.

Table 26. Oxidation rate constants and final weight gain for the alloys GB1 and GB2 oxidised at various temperatures and times. Unless otherwise stated the rate constants refer to an isothermal test lasting 100h. K_l units are g $cm^{-2}s^{-1}$ and K_p are in g^2 $cm^{-4}s^{-1}$.

Alloy	Area %			800°C			1000°C			1200°C	
	Nb_{ss}	Silicide	Laves	K_l	K_p	ΔW/A (mg/cm^2)	K_l	K_p	ΔW/A (mg/cm^2)	K_p	ΔW/A (mg/cm^2)
GB1-AC	20	40	40	$2x10^{-9}$	-	0.8	$2x10^{-8}$ (80h)	-	4.9	$3x10^{-10}$	10.7
GB1-HT	20	40	40	-	-	-	-	-	-	$2x10^{-10}$ (35h)	4.5
										$5x10^{-10}$	14.2
GB2-AC	25	50	25	-	$1x10^{-12}$	0.6	-	$3x10^{-10}$	9.9*	$4x10^{-10}$ (37h, Run 1)	6.6
										$1x10^{-10}$ (37-100h, Run 1)	8.9 (total)
										$5x10^{-10}$ (Run2)	13.9
GB2-HT	22	50	28	-	-	-	-	-	-	$1x10^{-10}$ (10h)	2.1
										$1x10^{-10}$ (50h)	4.3
										$1x10^{-10}$	6.2

*The cube test specimen used displayed after oxidation a corner where an irregularly volumous amount of oxide growth had occurred in comparison to the majority of the specimen. Such growth may be due to cracks in the original test specimen enabling.

Table 27. Oxidation rate constants of various Nb-silicide alloys reported in the literature. Unless otherwise stated the rate constants refer to an isothermal test lasting 100h. K_l units are g $cm^{-2}s^{-1}$ and K_p are in g^2 $cm^{-4}s^{-1}$.

Alloy and Tested Composition (at.%)	Area %			800°C			1200°C		
	Nb_{ss}	Silicide	Laves	K_l	K_p	Δw/A (mg/cm^2)	K_l	K_p	Δw/A (mg/cm^2)
KZ5-HT (Nb-24Ti-18Si-5Cr-5Al) (Zelenitsas and Tsakiropoulos, 2005)	48-55	45-52	0	-	-	~35	-	-	-
KZ7-HT (Nb-24Ti-18Si-5Cr) (Zelenitsas and Tsakiropoulos, 2005)	48-55	45-52	0	-	-	~23	-	-	-
JG3-AC (Nb-24Ti-18Si-5Cr-5Al-2Mo) (Geng and Tsakiropoulos, 2007)	35.9	64.1	0	-	$2.5x10^{-11}$	~4	$4.4x10^{-7}$	-	~150
JG3-HT (Nb-24Ti-18Si-5Cr-5Al-2Mo) (Geng and Tsakiropoulos, 2007)	47.2	52.8	0	$8x10^{-8}$	-	~28	$6.7x10^{-7}$ (0-24h)	-	~160
JG4-AC (Nb-23.4Ti-19.5Si-4.3Cr-4.5Al-1.8Mo-5.2Hf) (Geng and Tsakiropoulos, 2007)	39.1	59.9	~1	-	$4.7x10^{-11}$	~4.8	$4.4x10^{-7}$ (0-56h), $2.4x10^{-7}$ (>56h)	-	~120
JG4-HT (Nb-24.2Ti-18.2Si-4.6Cr-4.8Al-1.7Mo-5.1Hf) (Geng and Tsakiropoulos, 2007)	55.4	44.6	0	$1x10^{-7}$	-	~37.5	$6.7x10^{-7}$ (0-24h)	$1.1x10^{-7}$ (>24h)	~180

Table 28. Oxidation rate constants for various Nb-silicide alloys and Ni-based superalloy CMSX-4 reported from literature. Unless otherwise stated the rate constants refer to an isothermal test lasting 100h. K_l units are g $cm^{-2}s^{-1}$ and K_p are in g^2 $cm^{-4}s^{-1}$.

Alloy and Tested Composition (at%)	Area %			800°C		1200°C		
	Nb_{ss}	Silicide	Laves	K_p	Δw/A (mg/cm^2)	K_l	K_p	Δw/A (mg/cm^2)
JG6-AC (Nb-25Ti-18Si-5Cr-5Al-2Mo-5Hf-5Sn) (Geng et al., 2007a)	~47.5*	~47.5*	~5*	$1x10^{-11}$	~1.9	$2.9x10^{-7}$ (>9h)	$1.4x10^{-9}$ (0-9h)	~90
JG6-HT (Nb-25Ti-18Si-5Cr-5Al-2Mo-5Hf-5Sn) (Geng et al., 2007a)	~60*	~35*	~5*	$7.2x10^{-12}$	~1.4	$5.2x10^{-7}$ (0-41h)	$6x10^{-8}$ (>41h)	~140
ZF6-AC (Nb-24Ti-18Si-5Cr-5Al-5Ge) (PhD Thesis Zifu Li)	17	-	-	$2.3x10^{-12}$	0.91	$9.7x10^{-8}$ (>20h)	$2.3x10^{-9}$ (<20h)	39.9
ZF6-AC (Nb-24Ti-18Si-5Cr-5Al-5Ge-5Hf) (PhD Thesis Zifu Li)	-	-	-	$8.4x10^{-13}$	0.55	$1x10^{-7}$ (>20h)	$1.8x10^{-9}$ (<20h)	41.4
DS MASC (Nb-24.7Ti-8.2Hf-2Cr-1.9Al-16Si) (Bewlay et al., 1996)	50	50	0	-	-	-	-	-150 (50h test)
CMSX-4 (Ni-10Co-6Cr-5.6Al-1Ti-6Ta-0.6Mo-6W-3Re-0.1Hf wt.%) (Göbel et al., 1993)	n/a			$6.1x10^{-15}$ (1000h)	~0.175	-	-	-2 (1000h)

*Area % were assessed using ImageJ from images in the authors publication as no values were reported by the respective author.

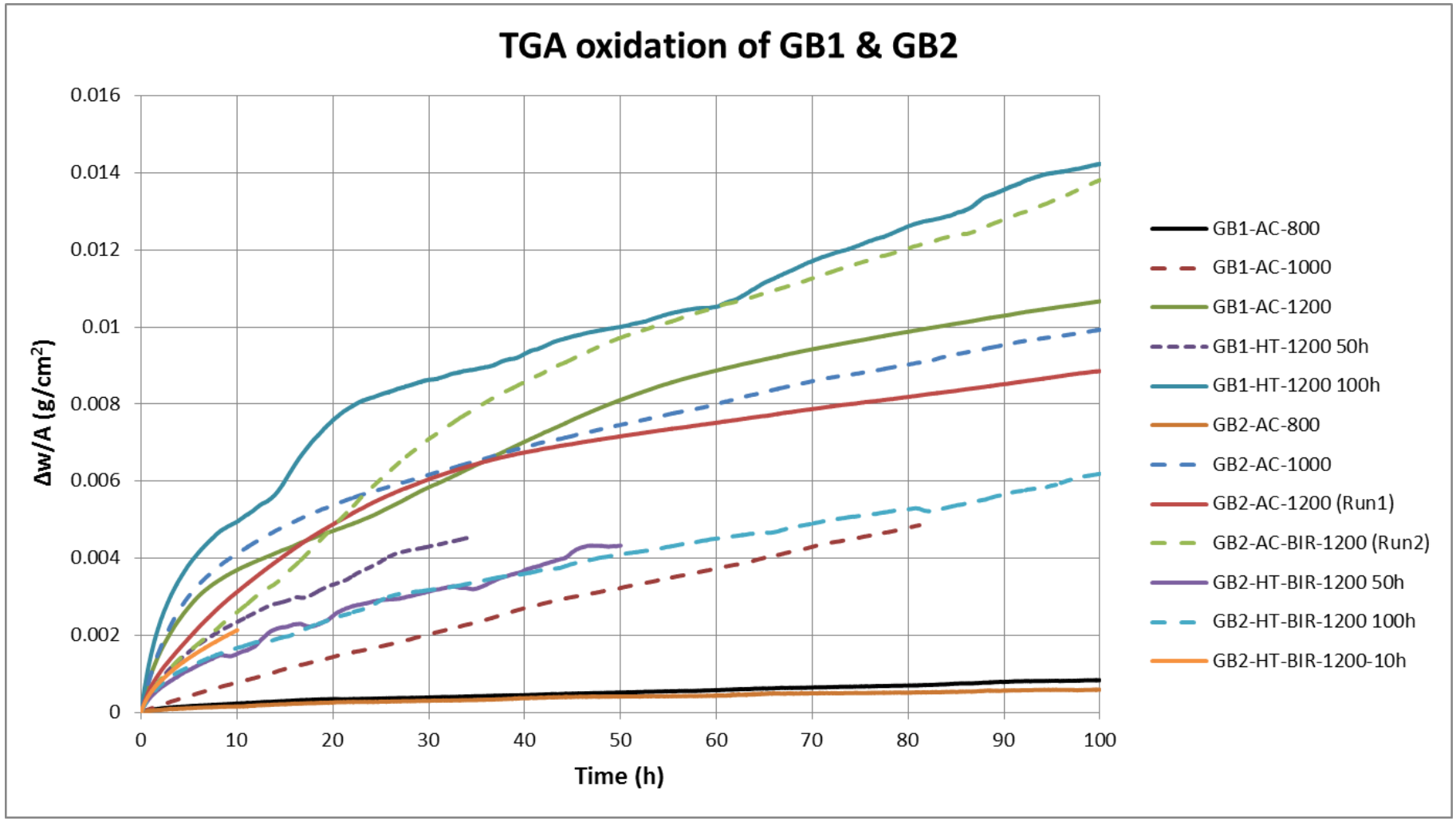

Figure 87. Isothermal thermogravimetric (TGA) weight gain summary of all GB1 and GB2 test specimens oxidised at various temperatures and times.

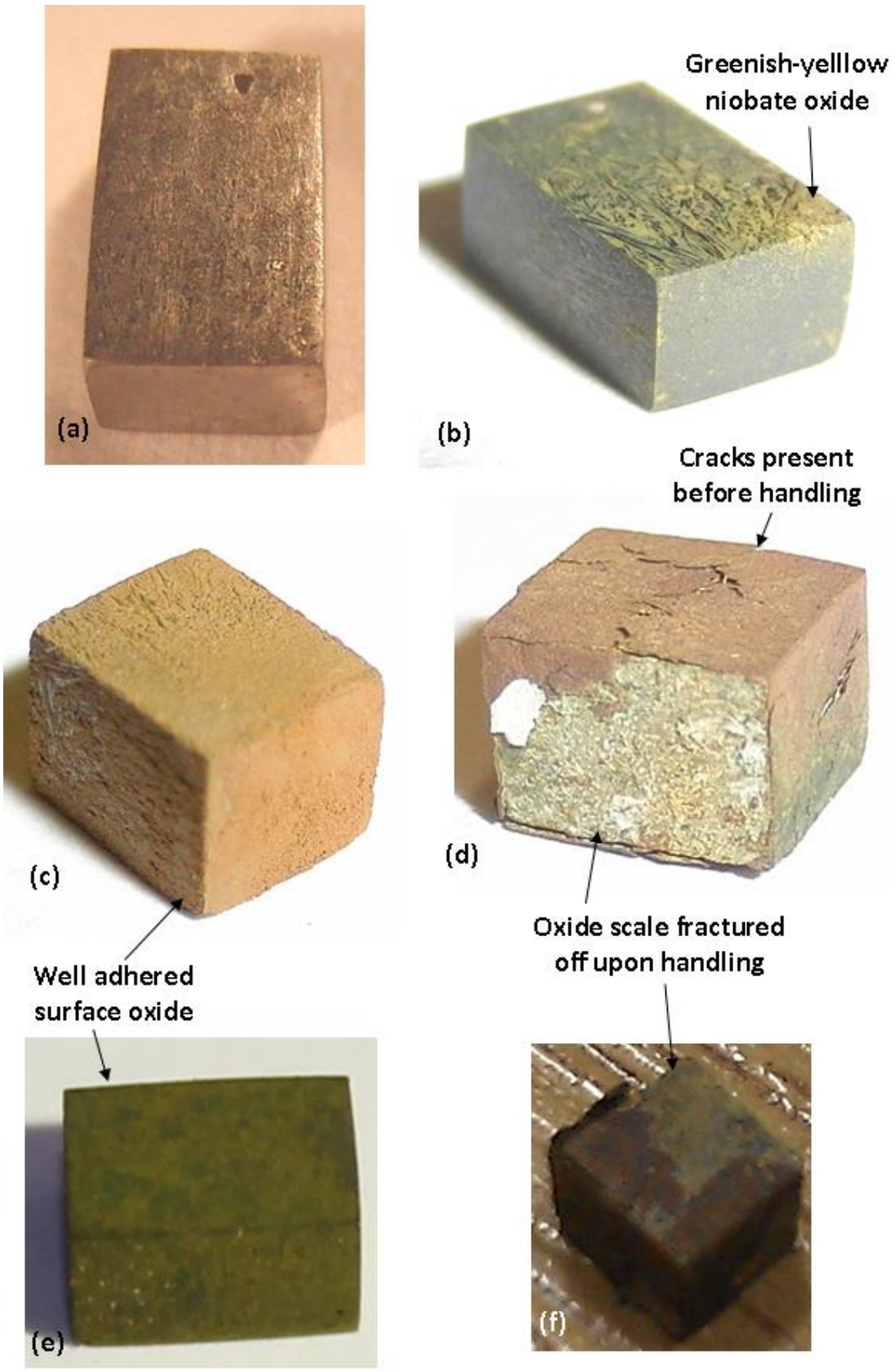

Figure 88. Oxidised alloy GB1 specimens. (a) Appearance of an unoxidised TGA specimen ground to 800p SiC paper. (b) GB1-AC-800-100h. (c) GB1-AC-1000-80h. (d) GB1-AC-1200-100h. (e) GB1-HT-1200-50h. (f) GB1-HT-1200-100h.

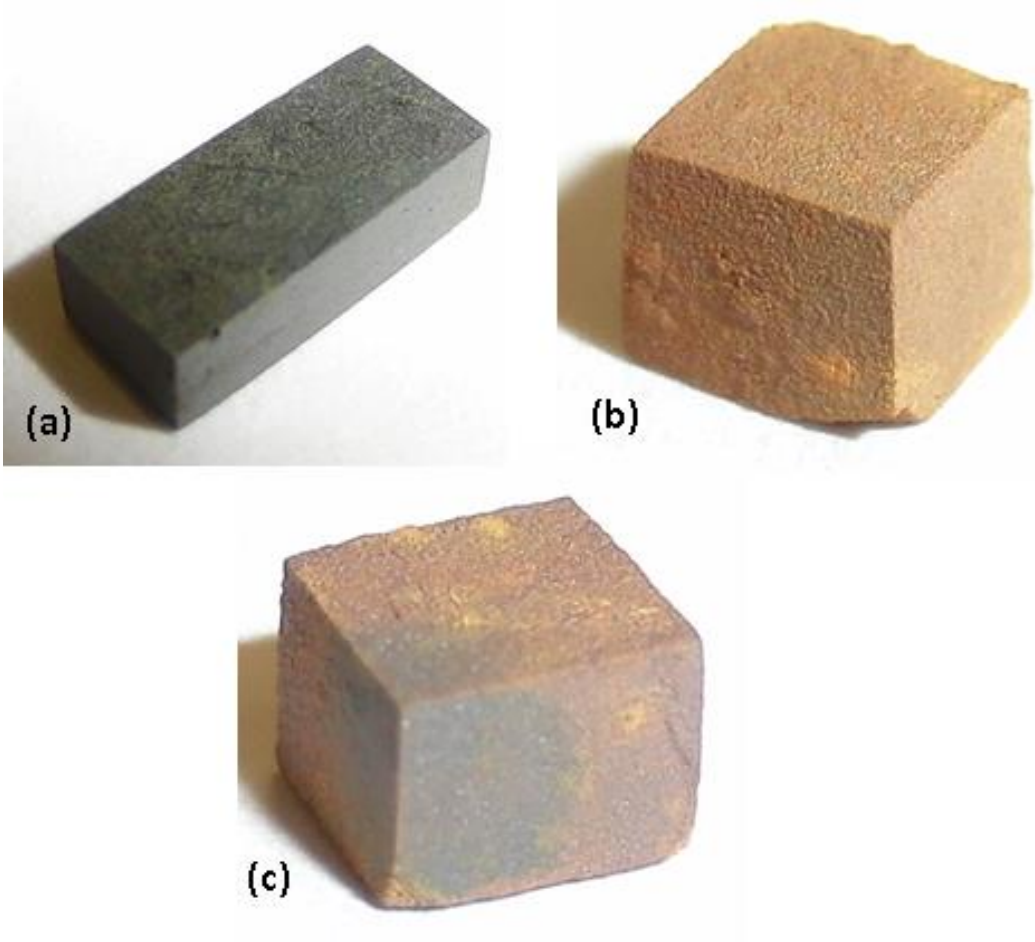

Figure 89. Alloy GB2-AC oxidised speciemens. (a) GB2-AC-800-100h, (b) GB2-AC-1000-100h, (c) GB2-AC-1200-100h.

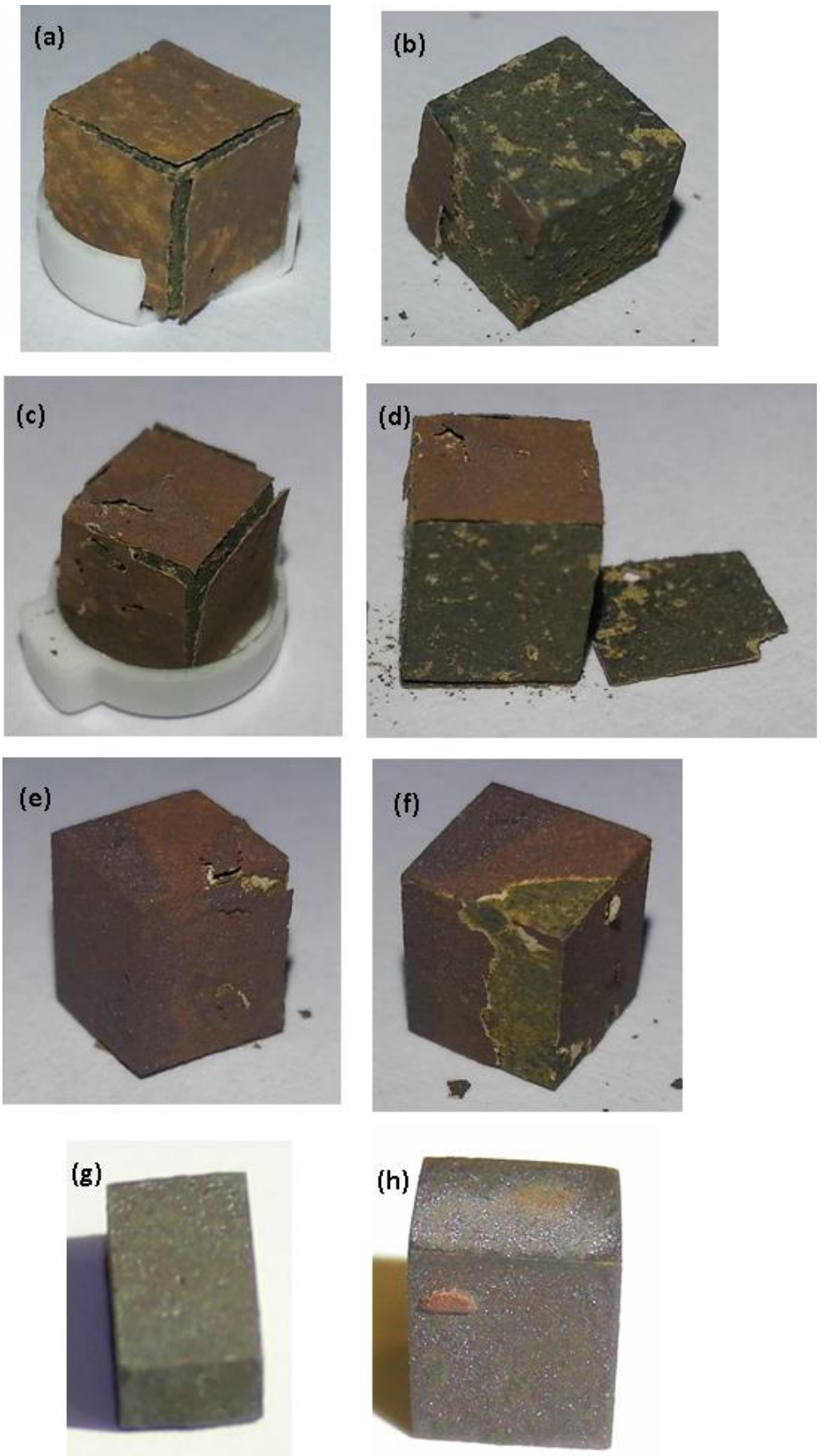

Figure 90. Alloy GB2-HT oxidised specimens after oxidation at 1200°C for various times. (a) 5h specimen with oxide attached, (b) 5h specimen after oxide fracture, (c) 10h specimen with oxide attached, (d) 10h specimen after oxide fracture, (e) 25h specimen with oxide attached, (f) 25h specimen after oxide fracture, (g) 50h specimen with well adhered oxide, (h) 100h specimen with well adhered oxide.

5.2 Isothermal Oxidation at 800°C

5.2.1 Alloy GB1-AC

The TGA data is best illustrated in Figure 91 where it is compared with the behaviour of specimen GB2-AC-800-100h. The GB1-AC oxidation behaviour was considered linear with a rate constant K_l = 2x10^{-9} g cm^{-2} s^{-1} (Table 26). The final 15h of the test displays a subtle parabolic behaviour but complete passivation was not achieved. Compared with Nb-silicide based alloys reported in the literature, the rate constant and overall weight gain of GB1-AC was lower (see Table 27 and Table 28). The surface of the oxidised specimen (Figure 88b) displayed a greenish-yellow scale formation indicative of a Ti/Cr-niobate type oxide that formed on the interdendritic $(Nb,Ti,Cr)_{ss}/NbCr_2$ regions, as shown in Figure 92. Due to the thin formation of the surface oxide, it was not possible to perform WDS phase analysis on its microsection.

The GXRD diffractograms in Figure 93 identify the presence of mixed T/Cr-niobates and TiO_2, all of which possess tetragonal crystal structures. Evidence for the formation of exclusively Nb type oxides such as NbO, NbO_2 or Nb_2O_5 was not found. Nb_2O_5 grown on pure Nb is reported by Kofstad (1988) to form as whisker-like oxides, clearly not the case on alloy GB1, as illustrated (Figure 92). Tetragonal oxides of various stoichiometrys could be indexed, namely TiO_2, $Ti_2Nb_{10}O_{20}$, $TiNbO_4$, $CrNbO_4$, $(Ti/Cr)NbO_4$, and $TiNb_2O_7$. Each of these oxides has a wide range in stoichiometry making it difficult to unambiguously identify the precise surface oxide stoichiometry formed. SiO_2 was not found despite the high Si content of the alloy. This was not a surprising result due to the incredibly slow growth kinetics of SiO_2 at temperatures below 1000°C. For example, pure Si is reported to form < 1 µm thick SiO_2 in dry O at 800°C under 1 atm pressure (Deal and Grove, 1965; Birks et al., 2006; Bose, 2007b).

Cross section images of the oxidised microstructure are shown in Figure 94. They display cracking parallel to the surface and signs of oxidative attack of the $(Nb,Ti,Cr)_{ss}$ in which there was formation of sub-micron size precipitates. These precipitates could not be analysed by WDS due to their small size and are assumed to be oxides or nitrides at this stage of analysis as such are reported by various publications to form within Nb-silicide based alloys after HT or oxidation testing (Menon et al., 2004; Zelenitsas and Tsakiropoulos, 2006b; Geng et al., 2006b; Mathieu et al., 2012).

The main phases in the alloy were analysed and the data is presented in Table 29. Contamination by O was recorded in all phases. It is worth noting the oxidation process is an inadvertent heat-treatment in itself, albiet at a lower temperature. A HT at 800°C would induce solute redistribution at a much slower rate than the 1300°C HT actually performed in the previous chapter. The Si concentration of the γNb_5Si_3 decreased after oxidation when compared with the average GB1-AC/HT alloy composition. The $NbCr_2$ analysed closer to the substrate surface had a reduction in Si and Cr, and recorded the highest O content (see Table 22, Table 29, and Table 30). No reliable $(Nb,Ti,Cr)_{ss}$ data was obtained, peculiarly high Si and Cr contents were found in such analysis [not shown] and were deemed due to analysis error owing to the neighbouring of $(Nb,Ti,Cr)_{ss}$ grains with $NbCr_2$ that is rich in both Si and Cr. Note in the GB1-AC condition it was difficult to distinguish $(Nb,Ti,Cr)_{ss}$ by SEM contrast.

Elemental WDS X-ray maps of the oxidised microstructure are presented in Figure 95 where there were no clear signs of elemental depletion or formation of a single oxide. The O map shows penetration near the surface, particularly at $(Nb,Ti,Cr)_{ss}$ regions. Such O ingress is best seen by comparing the O map with the low Cr regions (light blue) of the Cr map (regions of $(Nb,Ti,Cr)_{ss}$ are indicated in the Cr map). Additionally, the Nb and Ti maps support correlation of the $(Nb,Ti,Cr)_{ss}$ with O ingress into the microstructure.

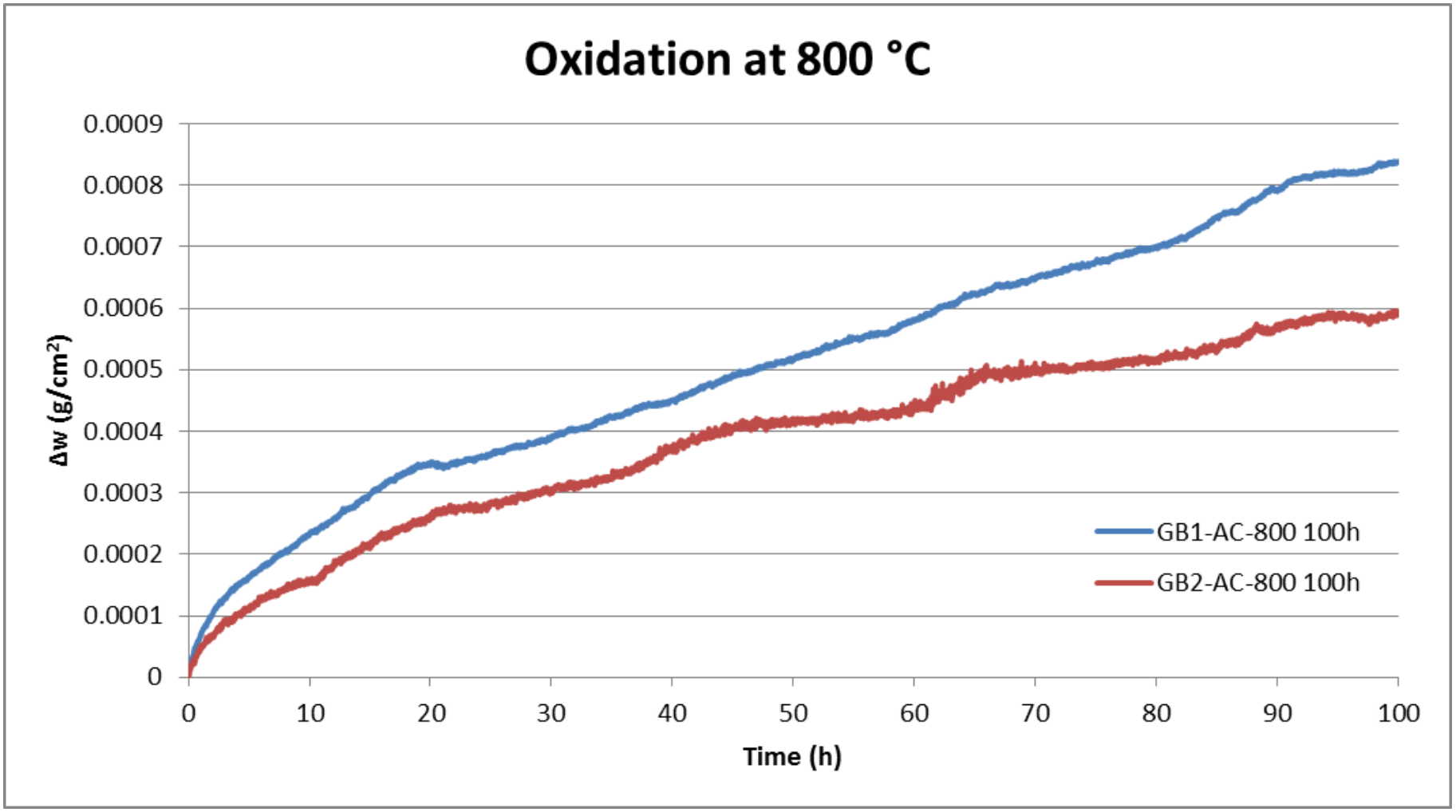

Figure 91. Isothermal TGA data for the 800°C oxidation tests.

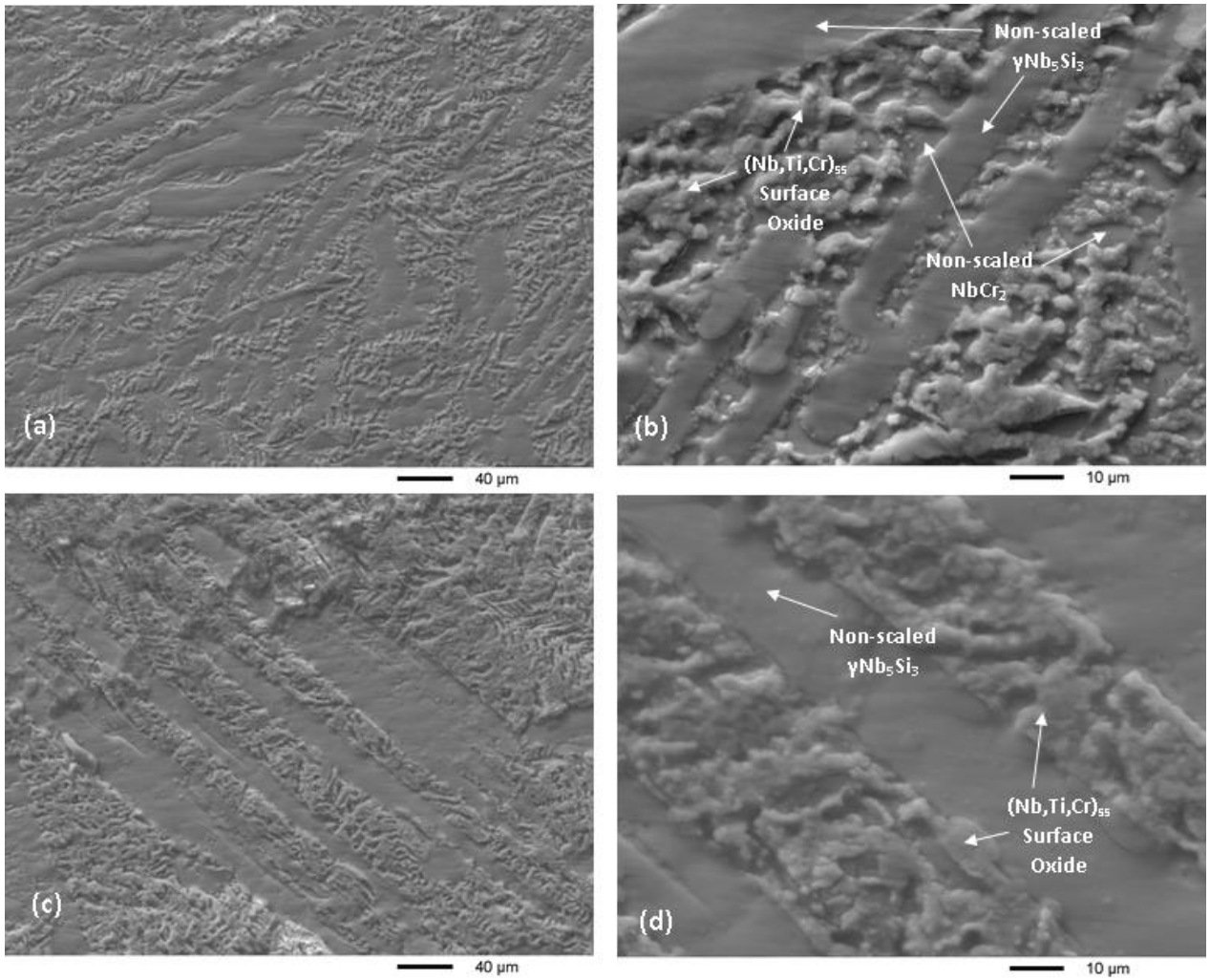

Figure 92. Surface oxide scales formed on GB1-AC-800-100h.

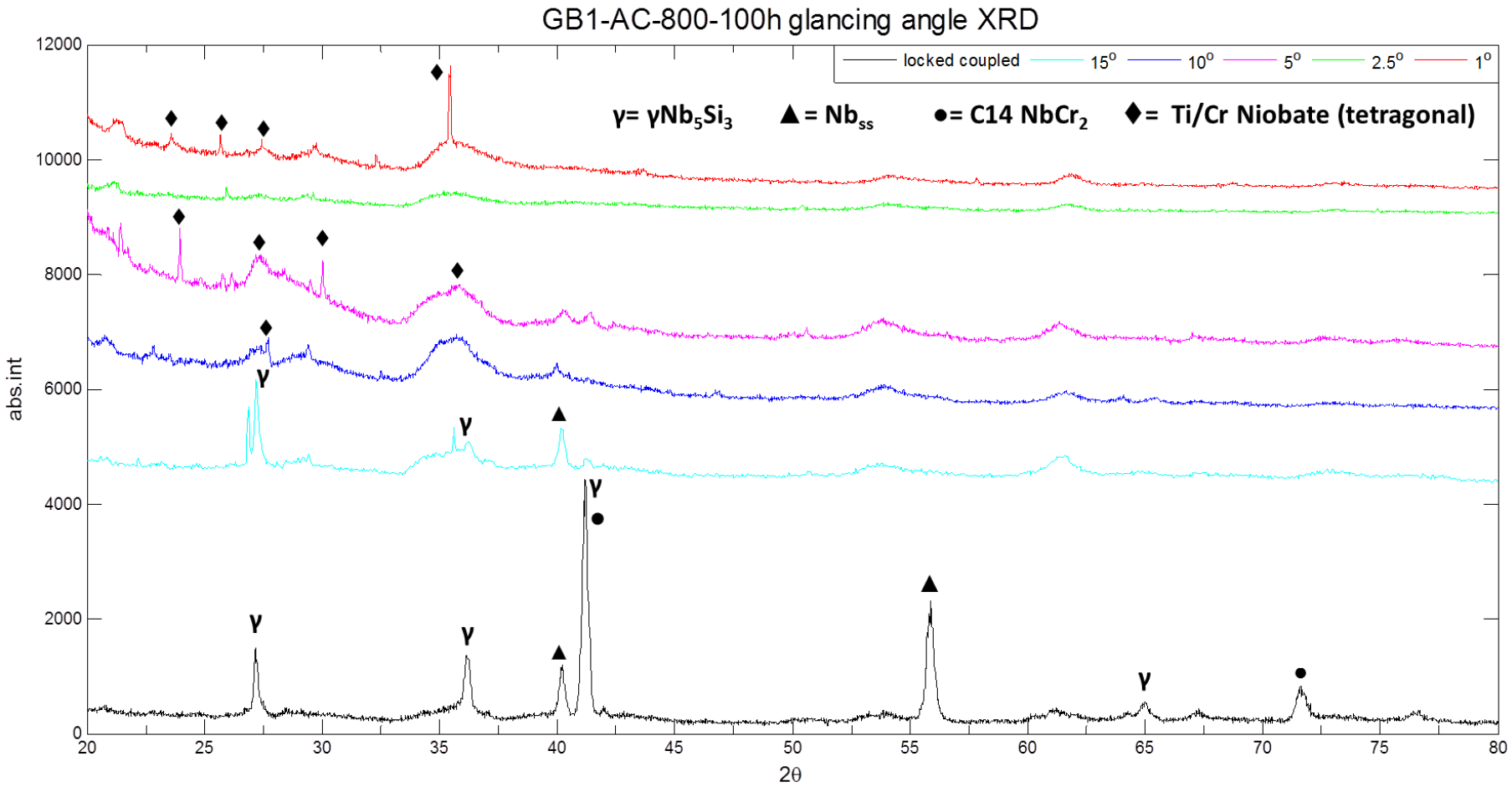

Figure 93. Specimen GB1-AC-800-100h GXRD diffractograms for different glancing angles.

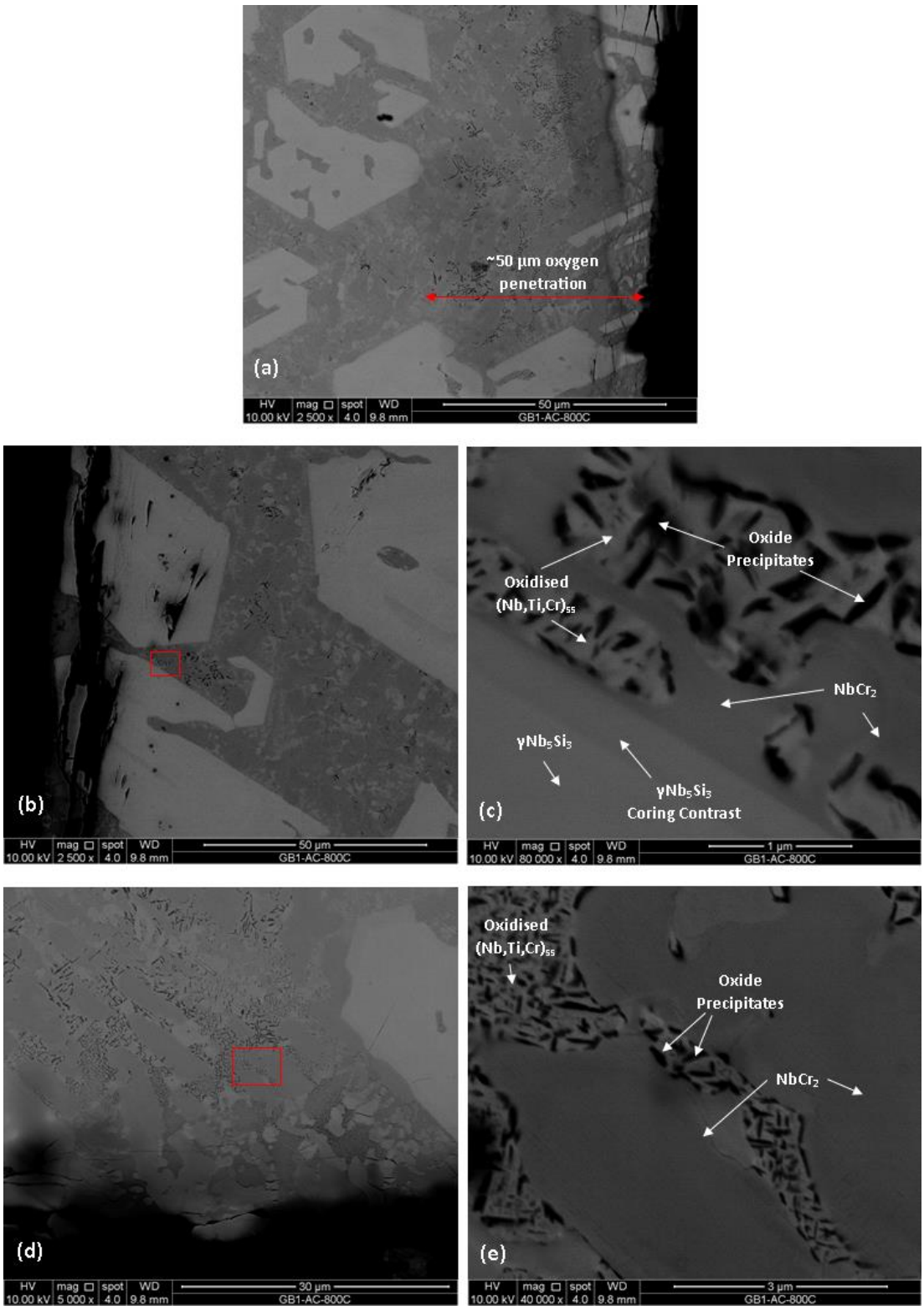

Figure 94. BSE-SEM images of alloy GB1-AC-800-100h. (a) Approximate O penetration depth, (b) cracks and faults are parallel to the alloy surface, (c) Magnification of red box area in image (b) displaying oxide precipitation within the $(Nb,Ti,Cr)_{ss}$ adjacent to the $NbCr_2$ and γNb_5Si_3, which is exhibiting coring contrast. (d) Cracks at sample edge and darkend contrast of $(Nb,Ti,Cr)_{ss}$, (e) Magnification of the red box area in image (d) displaying oxide precipitation in $(Nb,Ti,Cr)_{ss}$.

Table 29. Phase WDS data in at.% for GB1-AC-800-100h.

Phase	Depth (µm)	Nb	Si	Ti	Cr	Al	Hf	O
γNb_5Si_3	25 - 75	26.3 ± 0.7 26.8 - 25.1	34.5 ± 2.3 38.6 - 32.9	18.5 ± 1.0 19.4 - 16.7	2.1 ± 0.0 2.1 - 2.0	1.1 ± 0.1 1.2 - 1.1	13.1 ± 0.5 13.4 - 12.2	4.4 ± 0.5 4.9 - 3.8
	100 - 300	26.4 ± 0.5 27.0 - 25.6	35.8 ± 1.4 37.5 - 33.1	18.0 ± 1.0 19.6 - 16.8	2.1 ± 0.1 2.3 - 1.9	1.1 ± 0.1 1.3 - 0.9	12.9 ± 0.8 14.6 - 11.6	3.7 ± 0.9 4.9 - 2.0
$NbCr_2$	5	22.6	5.6	13.1	36.6	1.8	5.2	14.9
	10	20.7	7.9	12.3	42.6	1.6	6.4	8.6
	25	22.9	9.1	11.3	46.7	1.6	6.4	2.0
	100	26.9	5.7	16.3	39.9	1.9	6.2	3.2
	150	19.2	6.8	15.2	46.8	1.5	8.5	2.0
	350	21.8	7.2	12.5	47.6	1.6	7.1	2.2

Table 30. Comparision of GB1-AC-800-100h WDS phase data shown in Table 29 to the average phase data of GB1-AC EDS data shown in Table 22.

Phase	Depth (µm)	Difference of GB1-AC-800-100h to Jeol GB1-AC data						
		Nb	Si	Ti	Cr	Al	Hf	O
Nb_5Si_3	≤ 75	-0.8	-3.9	+1.2	-0.2	-0.6	-0.2	+4.4
	100 - 300	-0.7	-2.6	+0.7	-0.2	-0.6	-0.3	+3.7
$NbCr_2$	5	+0.6	-5.1	+1.1	-8.1	-0.1	-3.3	+14.9
	10	-1.4	-2.9	+0.3	-2.1	-0.4	-2.1	+8.6
	25	+0.9	-1.7	-0.7	+2.0	-0.3	-2.2	+2.0
	100	+4.9	-5.1	+4.3	-4.8	-0.1	-2.4	+3.2
	150	-2.9	-4.0	+3.2	+2.1	-0.4	-0.0	+2.0
	350	-0.2	-3.5	+0.5	+2.9	-0.4	-1.4	+2.2

Table 31. Comparision of GB1-AC-800-100h WDS phase data shown in Table 29 to the average phase data of GB1-HT EDS data shown in Table 22.

Phase	Depth (µm)	Difference of GB1-AC-800-100h to Jeol GB1-HT data						
		Nb	Si	Ti	Cr	Al	Hf	O
Nb_5Si_3	≤ 75	+1.7	-4.1	-2.3	+0.5	-0.6	+0.4	+4.4
	100 - 300	+1.8	-2.8	-2.8	+0.5	-0.6	+0.2	+3.7
$NbCr_2$	5	+2.4	-3.0	+0.9	-13.6	+0.3	-1.8	+14.9
	10	+0.4	-0.8	+0.0	-7.6	+0.1	-0.6	+8.6
	25	+2.7	+0.4	-0.9	-3.5	+0.1	-0.7	+2.0
	100	+6.6	-3.0	+4.0	-10.3	+0.4	-0.9	+3.2
	150	-1.1	-1.9	+3.0	-3.4	+0.0	+1.5	+2.0
	350	+1.6	-1.4	+0.3	-2.6	+0.1	+0.1	+2.2

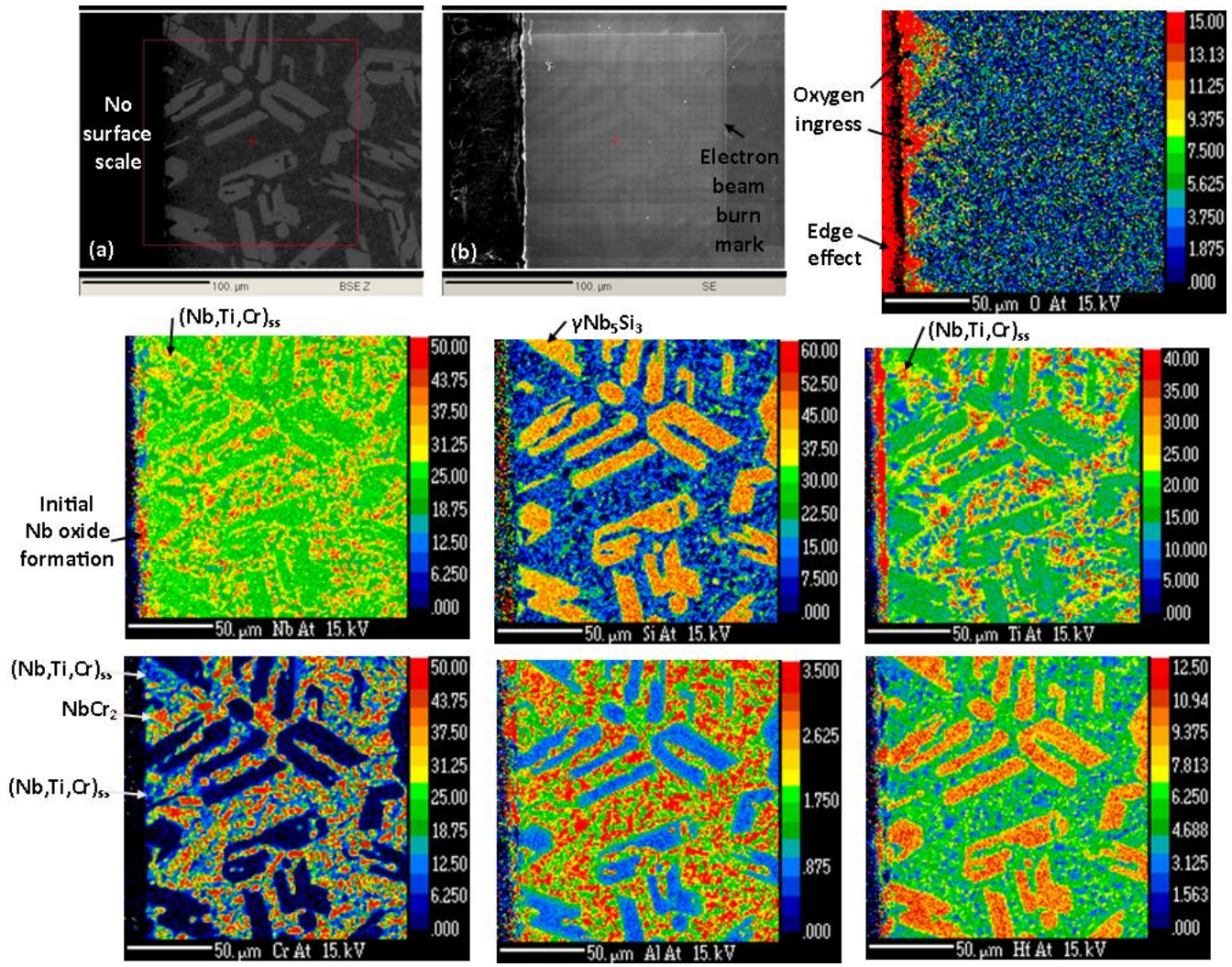

Figure 95. WDS X-Ray maps of specimen GB1-AC-800-100h.

5.2.2 Alloy GB2-AC

The TGA behaviour of GB2-AC is best illustrated in Figure 91. Alloy GB2-AC exhibited better oxidation kinetics and lower overall weight gain than GB1-AC, the behaviour is considered parabolic with rate constant of $1x10^{-12}$ g^2 cm^{-4} s^{-2} as summarised in Table 26. However, the behaviour should be more aptly described as being *para-linear* due to the breakaway oxidation and re-growth in the TGA profile and complete passivation not being achieved. The oxidised surface (Figure 89a) displayed a greenish-yellow oxide formation but to a much lesser extent than that found on GB1-AC, again occurring at the interdendritic $(Nb,Ti,Cr)_{ss}/NbCr_2$ regions and suspected of orginating from the $(Nb,Ti,Cr)_{ss}$, as shown in Figure 96. As was the case for GB1-AC, no whisker-like oxides were found on GB2-AC.

Similarly to GB1-AC, the GB2-AC GXRD diffractogram (Figure 97) suggested the presence of Ti and Cr mixed niobates. SiO_2 is not indexed, as was mentioned for GB1-AC, due to its slow growth kinetics below 1000°C. Figure 98 shows a cross section of the oxidised specimen, again displaying cracks parallel to the surface and oxidative attack of the $(Nb,Ti,Cr)_{ss}$. The formation of sub-micron size precipitates to a depth of ~ 100 µm occurred similar to GB1-AC-800-100h.

The microstructure phases were analysed by WDS and are presented in Table 32. Differences to the GB2-AC and HT condition data are shown in Table 33 and Table 34. All phases were contaminated by O. The $NbCr_2$ Laves phase had a lower average O content and standard deviation than the equivalent GB1-AC oxidation test. Although, phases were not measured as close to the specimen surface. The reduction in O could be attributed to the absence of Al and the lower Hf content in the $NbCr_2$ of alloy GB2-AC as these elements have a strong O affinity and are considered “reactive” elements. The $(Nb,Ti,Cr)_{ss}$ recorded an appreciable average O content of 5.1 at.% even at a depth between 150 – 400 µm below the sample surface, with the highest O content analysed nearest to the sample surface (8.6 at.% at 30 µm depth). The presence of un-oxidised $(Nb,Ti,Cr)_{ss}$ surrounded by $NbCr_2$ and βNb_5Si_3 (Figure 98c and e) suggest the latter two intermetallics were shielding the solid solution from O contamination.

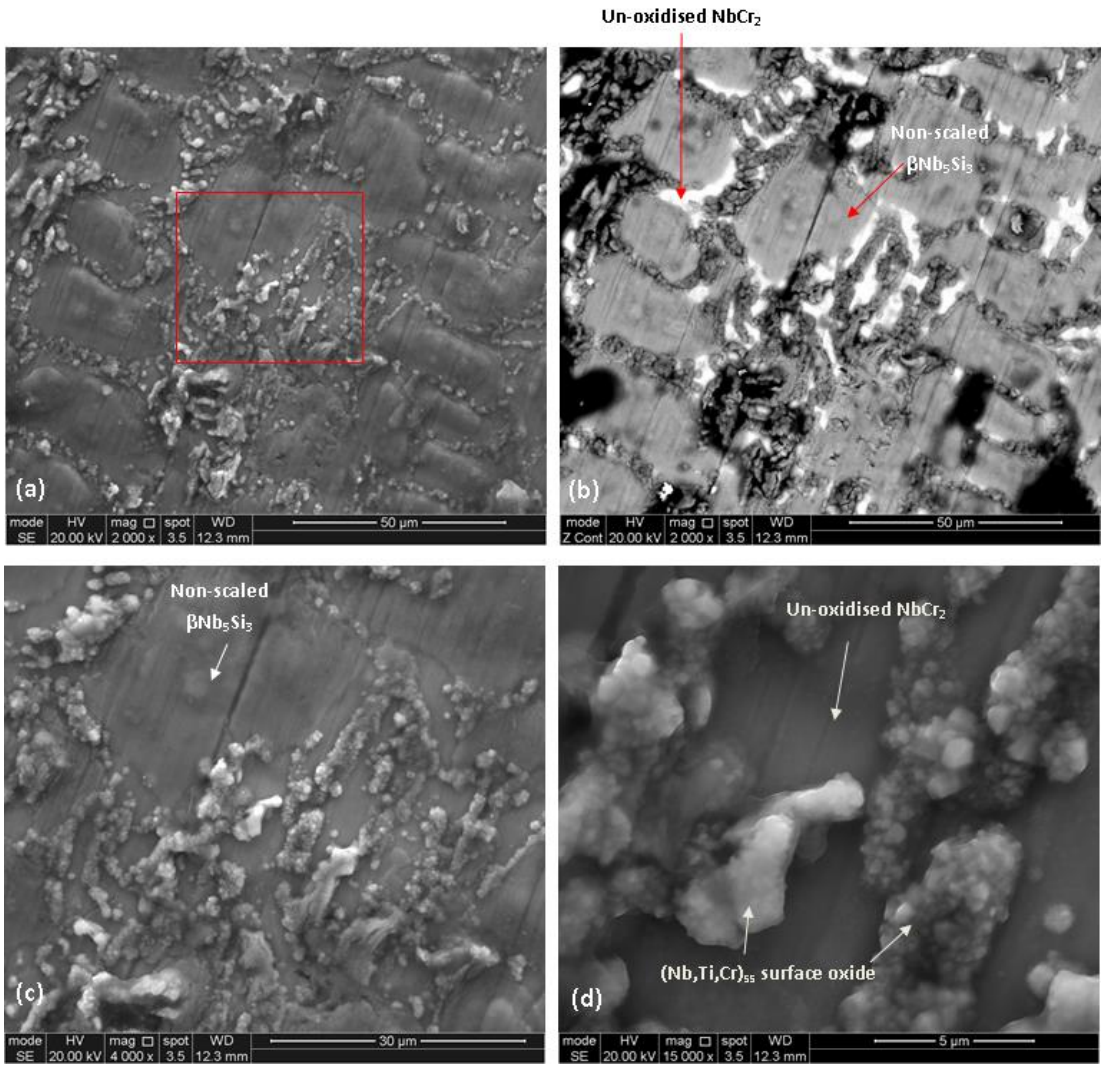

Figure 96. Images of surface oxide formed on GB2-AC-800-100h. (a) SE-SEM image overview of the surface oxide formed. (b) BSE-SEM image of (a) indicating un-oxidised and unscaled $NbCr_2$ and βNb_5Si_3. (c) Magnification of the red box region in (a). (d) High magnification SE-SEM image of surface oxides.

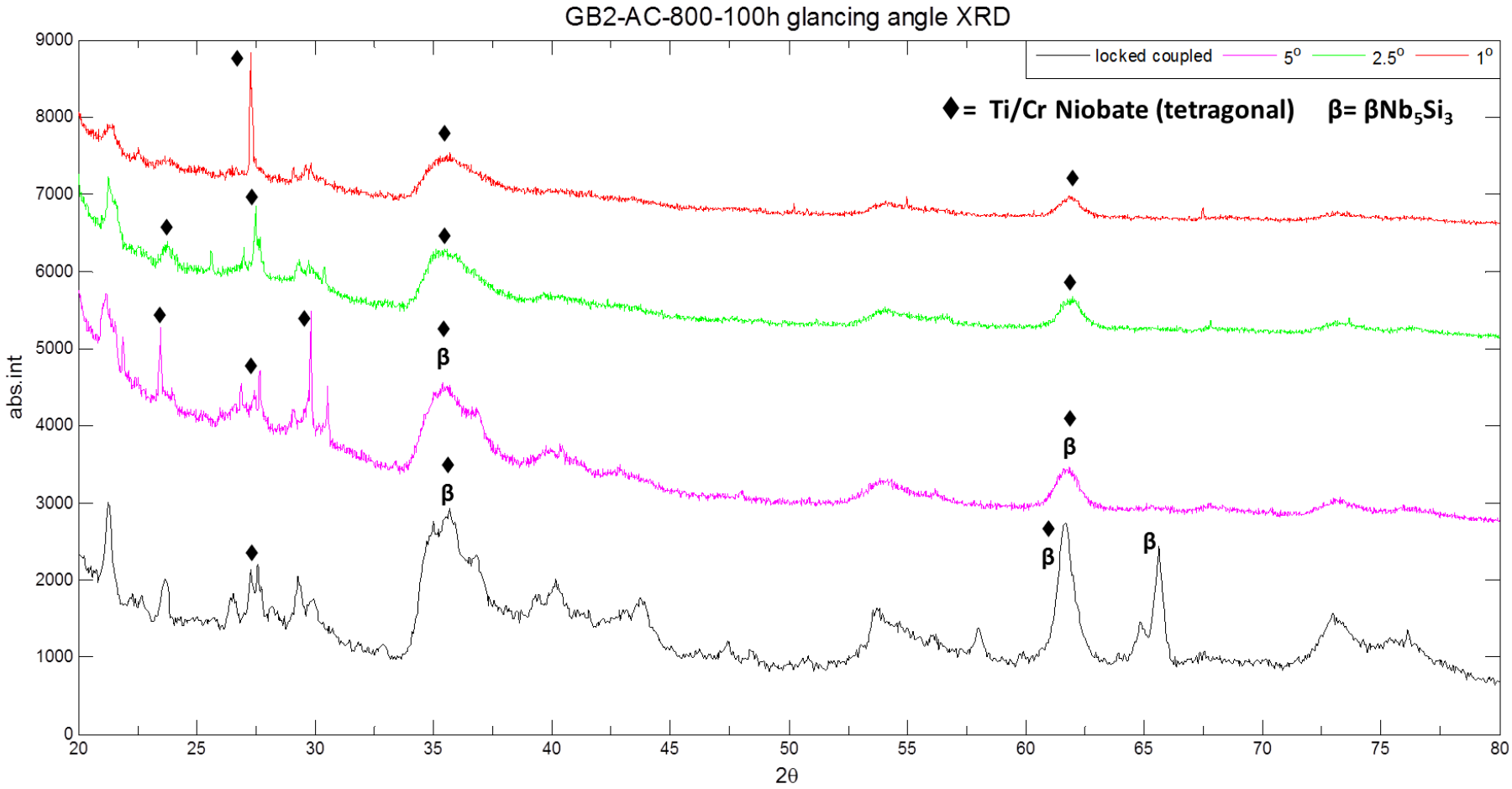

Figure 97. GXRD diffractograms of specimen GB2-AC-800-100h at different glancing angles.

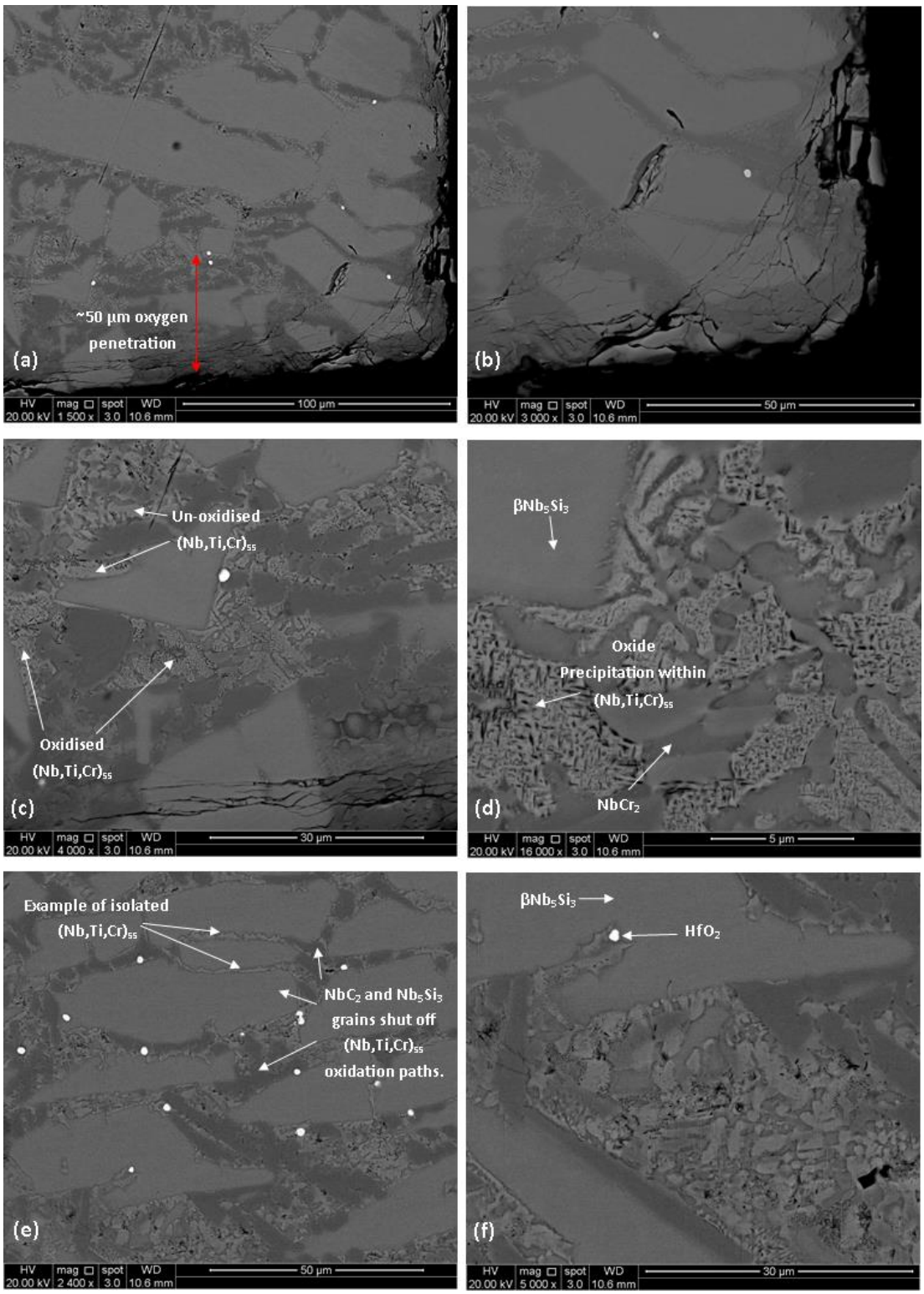

Figure 98. BSE-SEM images of alloy GB2-AC-800-100h illustrating; (a) Oxygen penetration throughout the solid solution, (b) cracking of sample corner, (c) oxidised and un-oxidised $(Nb,Ti,Cr)_{ss}$, (d) oxide precipitation within the $(Nb,Ti,Cr)_{ss}$, (e) isolated un-oxidised $(Nb,Ti,Cr)_{ss}$ grains, (f) locally oxidised $(Nb,Ti,Cr)_{ss}$.

Table 32. Phase WDS data in at.% for GB2-AC-800-100h.

Phase	Depth (µm)	Nb	Si	Ti	Cr	Ge	Hf	O
βNb_5Si_3	75 - 400	37.9 ± 0.3 38.6 - 37.7	29.1 ± 0.7 30.1 - 28.1	16.0 ± 0.3 16.4 - 15.3	3.6 ± 0.1 3.8 - 3.4	7.1 ± 0.2 7.5 - 6.9	3.1 ± 0.1 3.2 - 2.9	3.1 ± 0.3 3.7 - 2.8
$NbCr_2$	15 - 75	25.8 ± 1.9 29.1 - 23.8	9.0 ± 2.0 10.7 - 5.2	12.2 ± 3.9 19.6 - 8.7	44.8 ± 4.5 48.1 - 37.0	1.4 ± 0.2 1.7 - 1.3	3.5 ± 0.3 3.9 - 3.2	3.4 ± 0.9 4.8 - 2.5
	150 - 400	25.0 ± 0.4 25.3 - 24.2	11.0 ± 0.7 11.6 - 9.5	8.8 ± 0.8 10.1 - 8.1	48.3 ± 0.5 49.0 - 47.6	1.3 ± 0.1 1.5 - 1.2	3.2 ± 0.1 3.4 - 3.1	2.3 ± 0.3 2.6 - 1.7
$(Nb,Ti,Cr)_{ss}$	30	43.8	1.2	32.6	10.3	1.3	2.2	8.6
	75	42.4	1.2	33.4	12.4	1.1	2.3	7.2
	75	49.8	1.6	29.0	12.0	1.2	2.1	4.3
	150 - 400	47.3 ± 2.3 48.9 - 43.8	1.3 ± 0.8 2.2 - 0.2	29.4 ± 3.5 32.6 - 24.4	13.8 ± 5.3 21.3 - 8.6	1.1 ± 0.1 1.2 - 1.0	2.1 ± 0.2 2.4 - 1.9	5.1 ± 0.5 5.6 - 4.7

Table 33. Comparision of GB2-AC-800-100h EPMA phase data shown in Table 32 to the positional average of GB2-AC EDS data shown in Table 25.

Difference of GB2-AC-800-100h to GB2-AC Jeol Data								
Phase	**Depth (µm)**	**Nb**	**Si**	**Ti**	**Cr**	**Ge**	**Hf**	**O**
βNb_5Si_3	75 - 400	-3.0	-0.7	-0.6	+0.1	+1.8	-0.7	+3.1
$NbCr_2$	15 - 75	-0.8	-1.4	+2.1	-3.4	+0.5	-0.4	+3.4
	150 - 400	-1.6	+0.7	-1.3	+0.2	+0.4	-0.7	+2.3
$(Nb,Ti,Cr)_{ss}$	30	-7.2	-1.2	+3.3	-3.7	+0.6	-0.5	+8.6
	75	-8.5	-1.2	+4.1	-1.6	+0.3	-0.4	+7.2
	75	-1.2	-0.8	-0.3	-2.0	+0.5	-0.6	+4.3
	Average (30-75)	-5.7	-1.1	+2.4	-2.4	+0.5	-0.5	+6.7
	150 - 400	-3.7	-1.1	+0.1	-0.2	+0.3	-0.6	+5.1

Table 34. Comparison of GB2-AC-800-100h EPMA phase data shown in Table 32 to the positional average of GB2-HT EDS data shown in Table 25.

Difference of GB2-AC-800-100h to GB2-HT Jeol data								
Phase	**Depth (µm)**	**Nb**	**Si**	**Ti**	**Cr**	**Ge**	**Hf**	**O**
Beta	75 - 400	-2.9	-0.9	-1.2	+1.9	-0.2	+0.2	+3.1
Laves	15 - 75	+0.1	+0.8	+0.9	-6.5	+0.3	+1.1	+3.4
	150 - 400	-0.6	+2.8	-2.5	-2.9	+0.2	+0.8	+2.3
(Nb,Ti,Cr)ss	30	-21.5	+0.4	+9.4	+1.0	+0.8	+1.3	+8.6
	75	-22.8	+0.3	+10.2	+3.1	+0.6	+1.4	+7.2
	75	-15.5	+0.7	+5.8	+2.7	+0.7	+1.2	+4.3
	Average (30 – 75)	-19.9	+0.5	+8.5	+2.3	+0.7	+1.3	+6.7
	150 - 400	-18.0	+0.4	+6.2	+4.5	+0.5	+1.2	+5.1

5.3 Oxidation at 1000°C

5.3.1 Alloy GB1-AC

The TGA data is best illustrated in Figure 99 displaying the 1000°C oxidation behaviours of both alloy GB1-AC and GB2-AC. The oxidation behaviour of GB1-AC was linear with $K_l = 2x10^{-8}$ $gcm^{-2}s^{-1}$ and weight gain of 4.8 mg/cm^2 (Table 26). The TGA test was intended to be 100h but only ran 80h due to power cut. The surface of the oxidised specimen (Figure 88c) appeared almost completely covered by a well adhered yellowish scale formation. The most servere attack and growth of oxide had occurred over the $(Nb,Ti,Cr)_{ss}/NbCr_2$ regions (Figure 100) but there were parts of silicide grains un-covered by oxide. Removal of the oxide with a chisel was attempted but deemed not possible without risking the fracture of the specimen. GXRD suggested mixed Ti/Cr niobates, TiO_2, SiO_2 and $HfSiO_4$ (Figure 101). No whisker-like oxides were found.

The cross section of the oxidised specimen (Figure 102) displayed a greater prevalence of oxide precipitation throughout the interdendrtic $(Nb,Ti,Cr)_{ss}$ than seen at 800°C. The depth of significant O penetration was ~ 100 µm. The black precipitates were large enough to appear in the Ti map as red contrasts, rich in Ti > 45 at.% (Figure 103). X-ray mapping also shows the O rich oxide scale, O penetration into the microstructure and a subtle depletion of Ti and Cr near the metal surface. Single metal oxide formation had not occurred, the X-ray maps show element overlap of Nb with Ti and Cr, and Si with Hf in the oxide scale. Discontinuous Si and Hf rich regions of the oxide scale are visibly connected to substrate silicide grains, this would be expected since the silicide is Si and Hf rich.

The $(Nb,Ti,Cr)_{ss}$ was not successfully analysed, thus no WDS data is presented for this phase. However, phase data for the γNb_5Si_3 and $NbCr_2$ is shown in Table 35 with differences to AC and HT data shown in Table 36 and Table 37. γNb_5Si_3 and $NbCr_2$ were contaminated by O to a higher concentration than at 800°C, especially for analysis near the substrate surface. There is insufficient phase analysis to clearly formulate a behaviour of elements from phases.

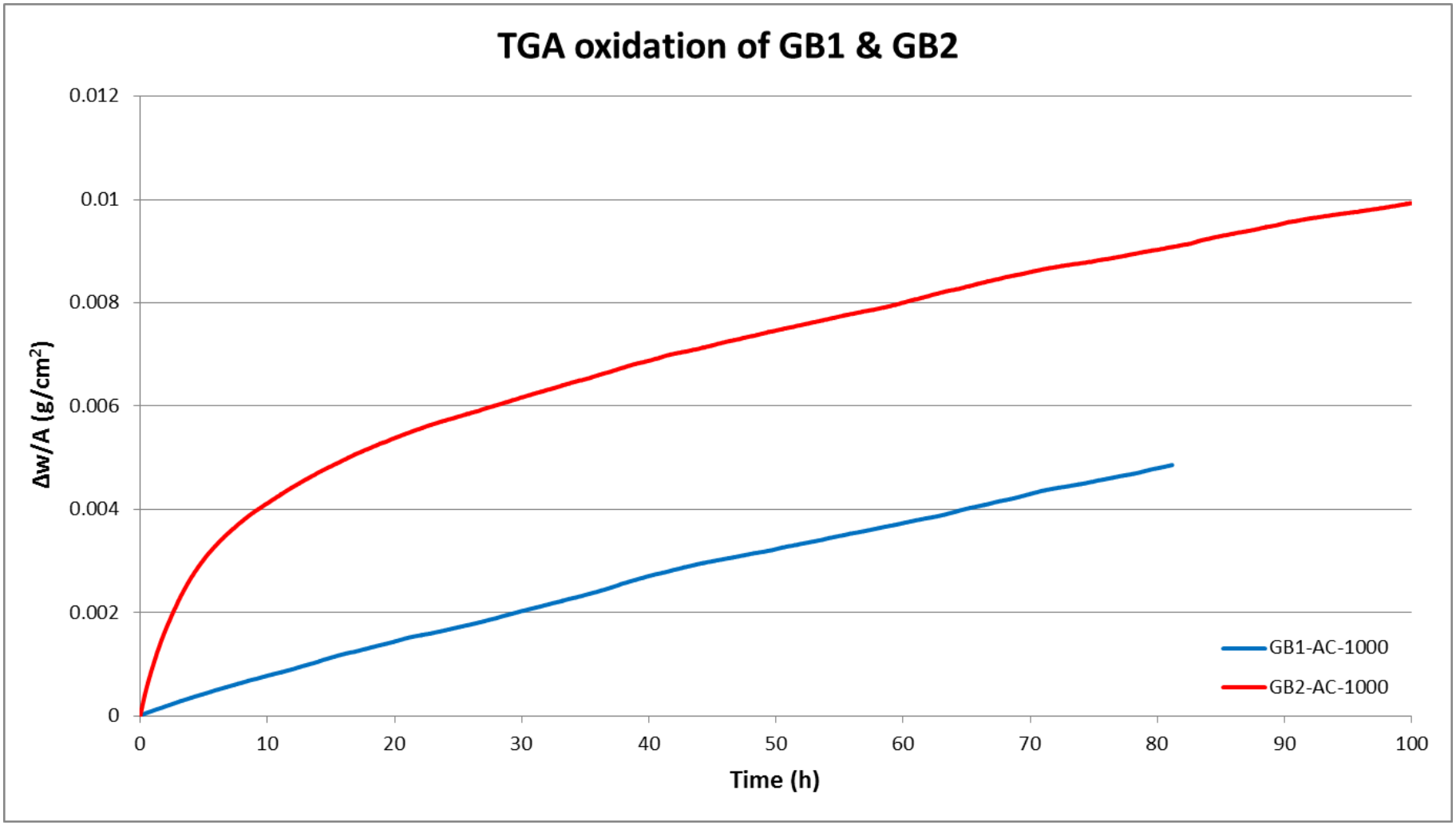

Figure 99. Isothermal TGA data for the 1000°C oxidation tests.

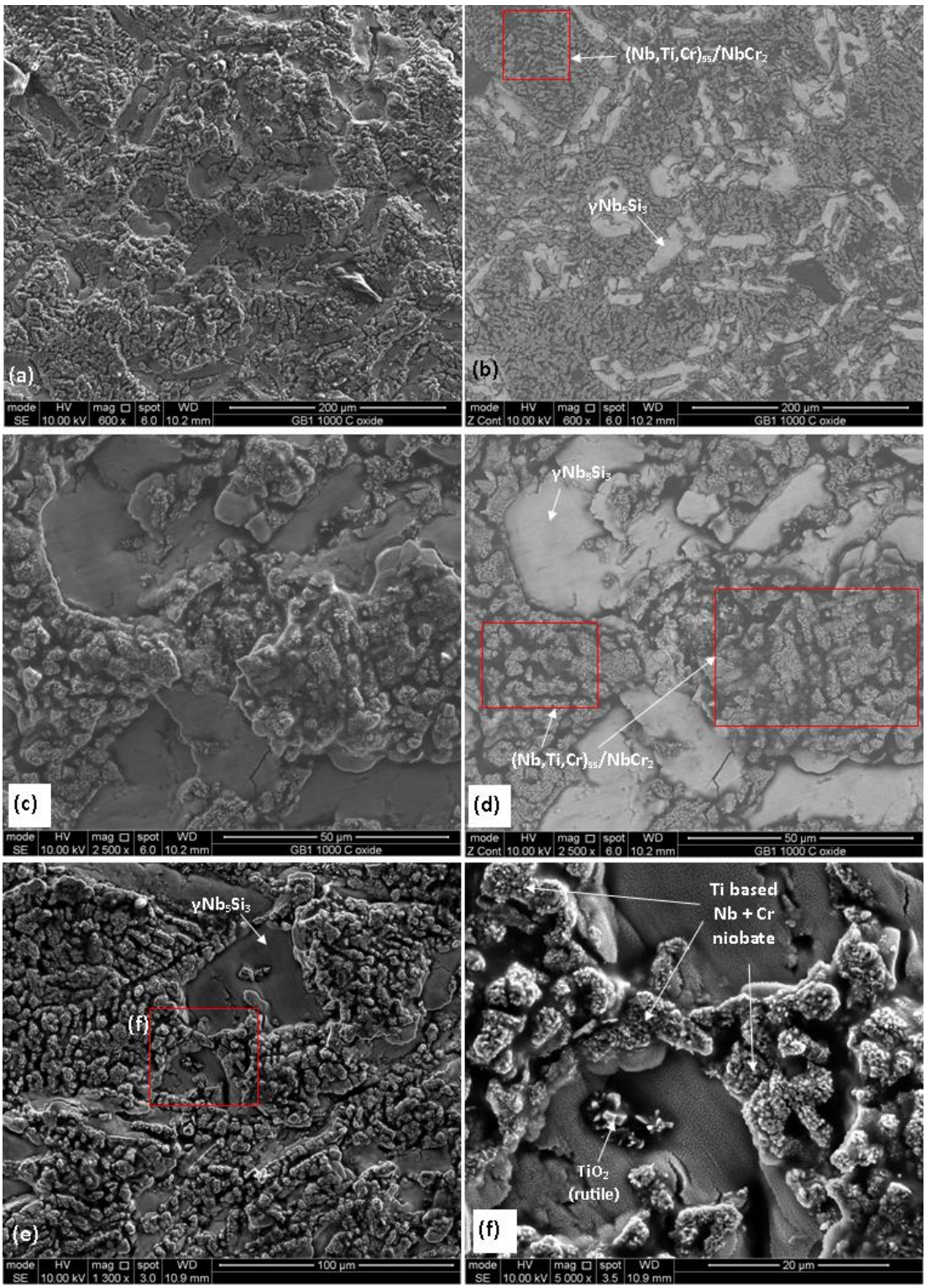

Figure 100. SEM images of the surface oxide formed on GB1-AC-1000-80h. (a) Low magnification SE-SEM image overview. (b) BSE-SEM image of (a) indicating silicide grains and $(Nb,Ti,Cr)_{ss}/NbCr_2$ regions. (c) SE-SEM image of oxide formed on $(Nb,Ti,Cr)_{ss}/NbCr_2$ regions as indicated in (d) a BSE-SEM image of image (c), note that the silcide is void of oxide scale. (e) SE-SEM surface oxide overview indicating the location of image (f), which shows surface oxides identified to be Ti based niobates and TiO_2 by qualitiative EDS analysis.

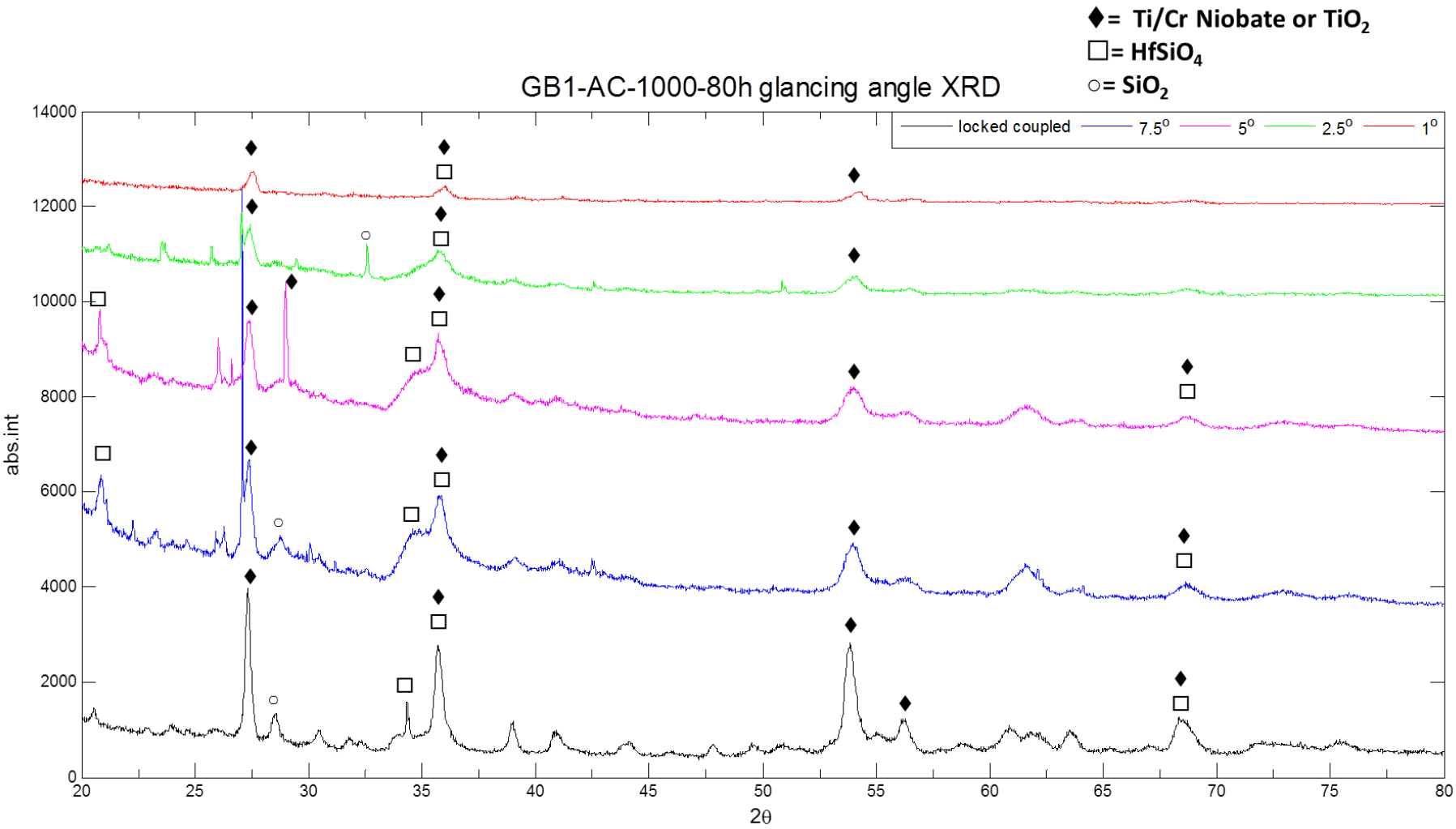

Figure 101. GXRD diffractograms of GB1-AC-1000-80h at different glancing angles.

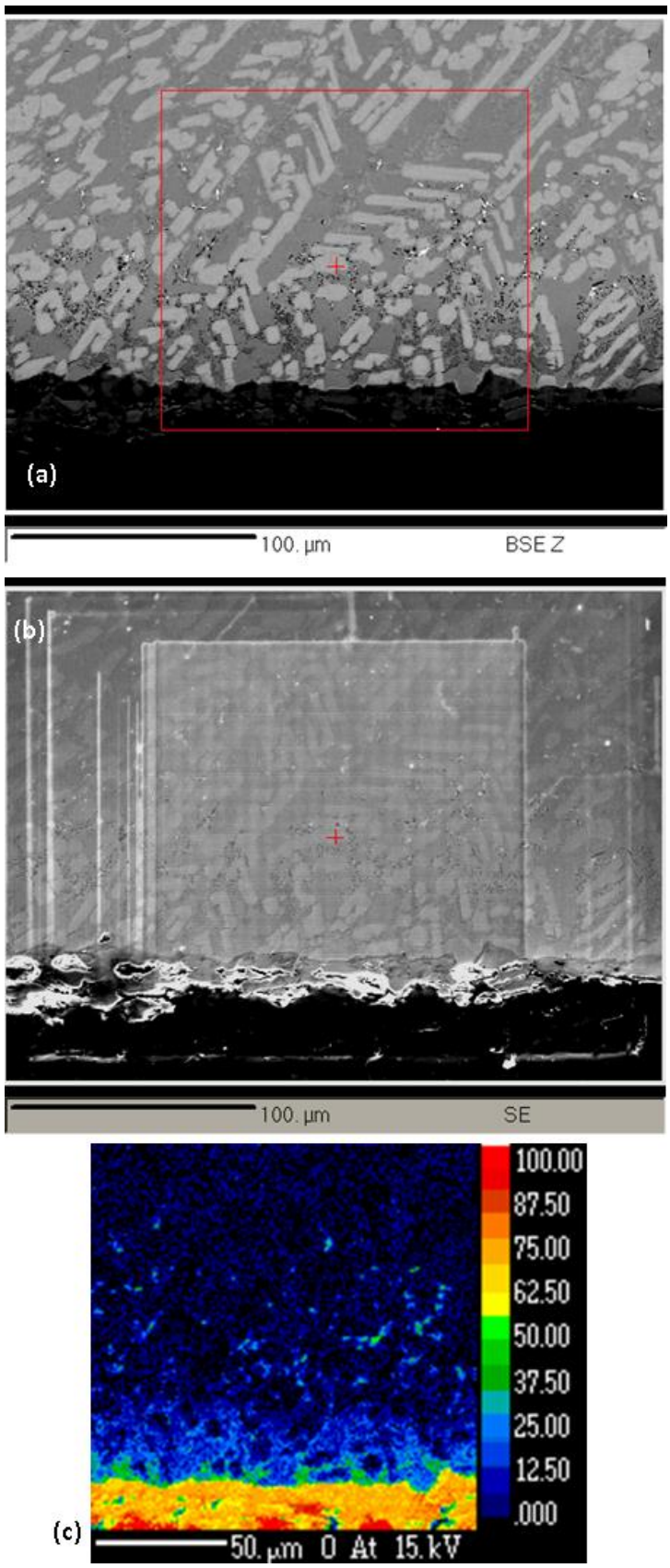

Figure 102. (a) BSE and (b) SE images of the WDS X-ray mapped region of the GB1-AC-1000-80h microstructure. The red box in (a) indicates the specific region mapped and can be seen as an electron burn mark in (b). (c) The O map. Refer to Figure 103 for the Nb, Si, Ti, Cr, Al, and Hf maps.

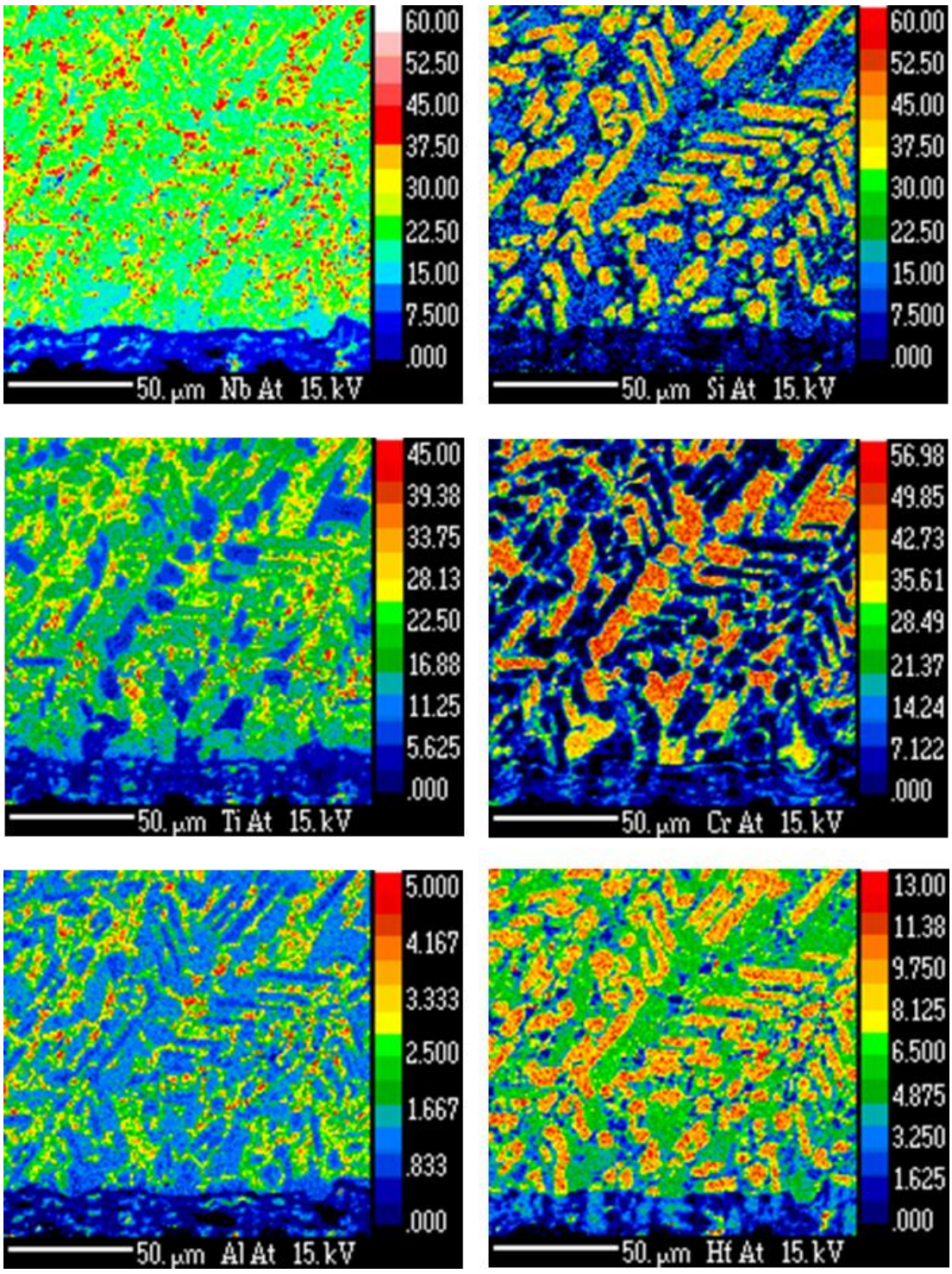

Figure 103. The Nb, Si, Ti, Cr, Al and Hf WDS X-ray maps for GB1-AC-1000-80h. Refer to Figure 100 for BSE and SE images of the mapped location and the O map.

Table 35. Phase WDS data for GB1-AC-1000-80h.

Phase	Depth (µm)	Nb	Si	Ti	Cr	Al	Hf	O
γNb_5Si_3	20	25.7	31.7	18.0	2.0	1.1	11.9	9.4
	20	26.4	30.5	19.2	2.0	1.2	13.0	7.7
	50 - 125	27.4 ± 0.6 27.9 - 26.6	33.2 ± 0.7 34.1 - 32.1	19.5 ± 0.3 20.1 - 18.9	2.4 ± 0.2 2.6 - 2.1	1.3 ± 0.1 1.5 - 1.2	12.1 ± 0.3 12.8 - 11.7	4.1 ± 0.4 4.6 - 3.3
$NbCr_2$	edge	22.8	9.7	9.6	48.0	1.4	7.1	1.3
	edge	21.5	7.7	9.0	44.3	1.4	6.5	9.6
	edge	19.2	7.5	7.9	39.6	1.3	5.9	18.7
	105	23.0	6.5	13.1	46.6	1.5	6.5	2.8
	145	22.5	9.5	9.9	48.0	1.4	6.8	1.8

Table 36. Comparison of GB1-AC-1000-80h EPMA phase data shown in Table 35 to the average GB1-AC EDS data shown in Table 22.

GB1-AC-1000-80h phase	Depth (µm)	Difference to GB1-AC Jeol data						
		Nb	Si	Ti	Cr	Al	Hf	O
γNb_5Si_3	20	-1.3	-6.7	+0.7	-0.3	-0.6	-1.3	+9.4
	20	-0.6	-7.9	+1.9	-0.3	-0.5	-0.2	+7.7
	50 - 125	+0.4	-5.2	+2.2	+0.1	-0.4	-1.2	+4.1
		+0.9	-4.3	+2.8	+0.3	-0.2	-0.5	+4.6
$NbCr_2$	edge	+0.8	-1.0	-2.4	+3.3	-0.5	-1.4	+1.3
	edge	-0.5	-3.1	-3.0	-0.4	-0.5	-2.0	+9.6
	edge	-2.8	-3.3	-4.1	-5.1	-0.7	-2.7	+18.7
	105	+1.0	-4.3	+1.0	+1.9	-0.4	-2.0	+2.8
	145	+0.5	-1.3	-2.1	+3.3	-0.5	-1.7	+1.8

Table 37. Comparison of GB1-AC-1000-80h EPMA phase data shown in Table 35 to the average GB1-HT EDS data shown in Table 22.

GB1-AC-1000-80h phase	Depth (µm)	Difference to GB1-HT Jeol data						
		Nb	Si	Ti	Cr	Al	Hf	O
γNb_5Si_3	20	+1.1	-6.9	-2.8	+0.5	-0.6	-0.8	+9.4
	20	+1.8	-8.1	-1.7	+0.4	-0.5	+0.3	+7.7
	50 - 125	+2.9	-5.5	-1.3	+0.8	-0.4	-0.6	+4.1
		+3.4	-4.5	-0.8	+1.0	-0.2	+0.1	+4.6
$NbCr_2$	edge	+2.5	+1.1	-2.7	-2.2	-0.1	+0.1	+1.3
	edge	+1.2	-1.0	-3.2	-6.0	-0.1	-0.5	+9.6
	edge	-1.0	-1.2	-4.4	-10.7	-0.2	-1.2	+18.7
	105	+2.8	-2.2	+0.8	-3.6	+0.0	-0.5	+2.8
	145	+2.3	+0.8	-2.4	-2.2	-0.1	-0.2	+1.8

5.3.2 Alloy GB2-AC

The TGA data shown in Figure 99 indicates that GB2-AC performed worse than GB1-AC, although with a parabolic rate constant $K_p = 3x10^{-10}$ g^2 cm^{-4} s^{-2} and weight gain of 9 mg/cm^2 after 80h (for comparison to GB1-AC) and 9.9 mg/cm^2 after 100h. The oxidised specimen (Figure 89b) showed a dense covering of the substrate surface (greater than that found on GB1-AC) by a well adhered yellowish oxide. All phases were covered by oxide (Figure 104). Using a chisel to remove the oxide scale was attempted but aborted as after failed attempts there was risk of fracturing the specimen.

A corner of the GB2-AC specimen exhibited signs of more severe oxidation as it showed visibly greater oxide growth compared with the other surfaces/edges of the specimen (Figure 105). With this in mind, the higher weight gain is possibly an over representation, making the comparison to GB1-AC arguably unfair. The cause of the excessive oxide growth is presumed due to unforeseen cracks of the TGA specimen. The GB2-AC kinetic behaviour is again more aptly described as para-linear as passivation was achieved. The linear portion of the TGA data is parallel to that of alloy GB1-AC indicating similar oxide growth reactions are taking place. GXRD confirmed mixed Ti/Cr niobates and, also detected, SiO_2 and $HfSiO_4$ (Figure 107). No whisker-like oxides indicative of Nb_2O_5 were found.

The oxidised microstructure displayed a greater prevalence of internal black and white precipitates throughout the microstructure, with the former originating from the solid solution and the latter at grains boundaires (Figure 106). Such internal precipitates were too small to be reliably analysed. At this stage of analysis based upon GXRD analysis and past literature, the black precipitates are suggested to be Ti-based oxides or nitrides and the white precipitates to be HfO_2.

X-ray maps (Figure 108 and Figure 109) showed a strong presence of Nb and Ti with some Cr presence throughout the oxide scale. There was particular overlap of Nb and Ti, these elements appeared subtly depleted from the internal microstructure immediately under the substrate edge (Figure 109). The oxide scale had intermittent patches of Si richness, and was especially rich in Ge at the substrate edge. This was likely due to the Ge rich βNb_5Si_3 suffering oxidation and providing Si and Ge for reaction. O diffusion into the microstructure was evident (Figure 108c). Analysis of the substrate phases and oxide scale are shown in Table 38, corroborating all phases were contaminated by O. Two contrasts within the oxide scale are analysed (Figure 105c and d) and are denoted Niobate 1 and 2. Niobate 1 comprised the majority of the oxide scale and presented a highly mixed composition rich in Nb and Ti with

some Cr. Niobate 2 was seldom present with a composition dominated by Nb (24.9 – 22.3 at.%) and with Ti ≤ 5.4 at.%.

The solute concentration of βNb_5Si_3 was only minorly changed from the AC and HT conditions (Table 38 and Table 39). The change in the $(Nb,Ti,Cr)_{ss}$ is unclear as limited phase data was obtained. Some analysis found grains that contained zero Si that also had the highest O content and higher Nb than the AC condition, while the Si containing grains had less Nb than the AC. There is insufficient analysis to deduce the solute behaviour of the solid solution due to oxidation.

The WDS line scan (Figure 110) records a base level of ~ 5 at.% O up to a depth of ~ 160 µm from the substrate/oxide interface. Spikes in O appear to occur upon transition of the scan path from typically low O containing βNb_5Si_3 to the interdendritic $(Nb,Ti,Cr)_{ss}/NbCr_2$ (Figure 110). The outer 10 µm of the oxide scale suggest Nb dominance with some Ti and Si although the Ti and Si do not clearly overlap in the X-ray maps.

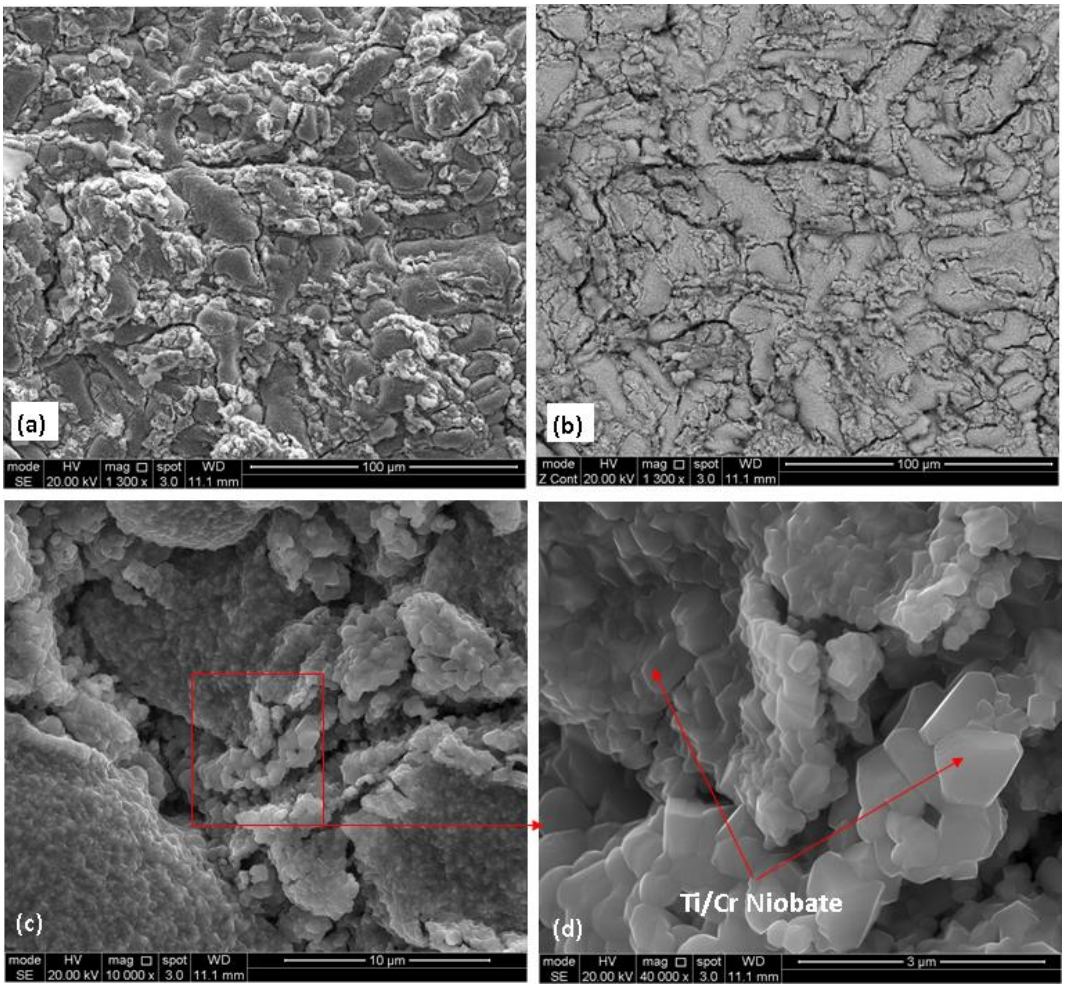

Figure 104. Surface oxide SEM image of GB2-AC-1000-100h. (a) Low magnification SE SEM image, (b) Low magnification BSE SEM image, (c) High magnification SE image, (d) High magnification SE image indicating the Ti/Cr niobate oxides.

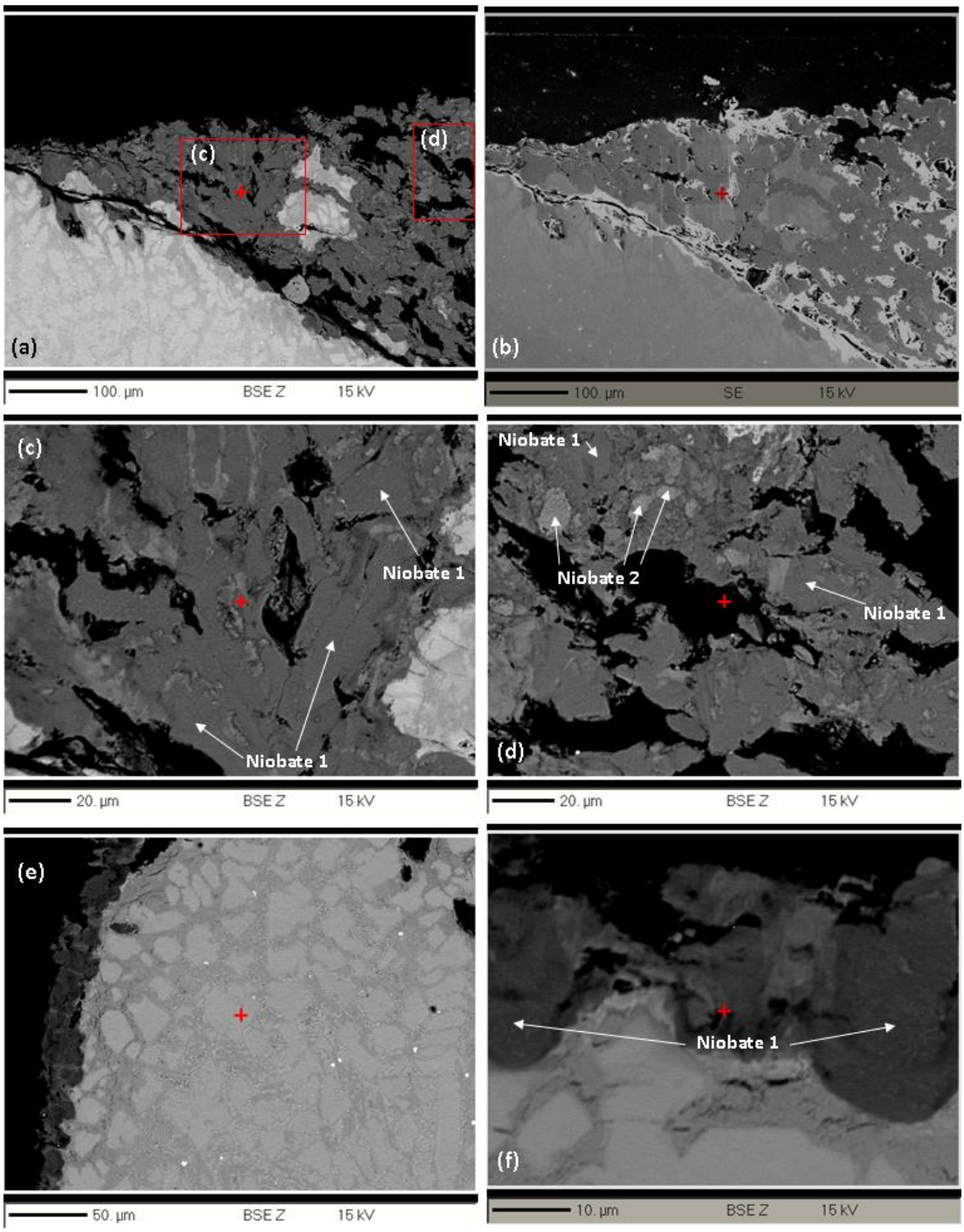

Figure 105. BSE-SEM images of the GB2-AC-1000-100h microstructure. (a) Imaging of the severe oxidation at the sample corner, (b) SE image of (a), (c) and (d) indicate oxides appearing of a different contrast under BSE-SEM, (e) imaging away from the severely oxidised sample corner, (f) regular oxide formation on sample.

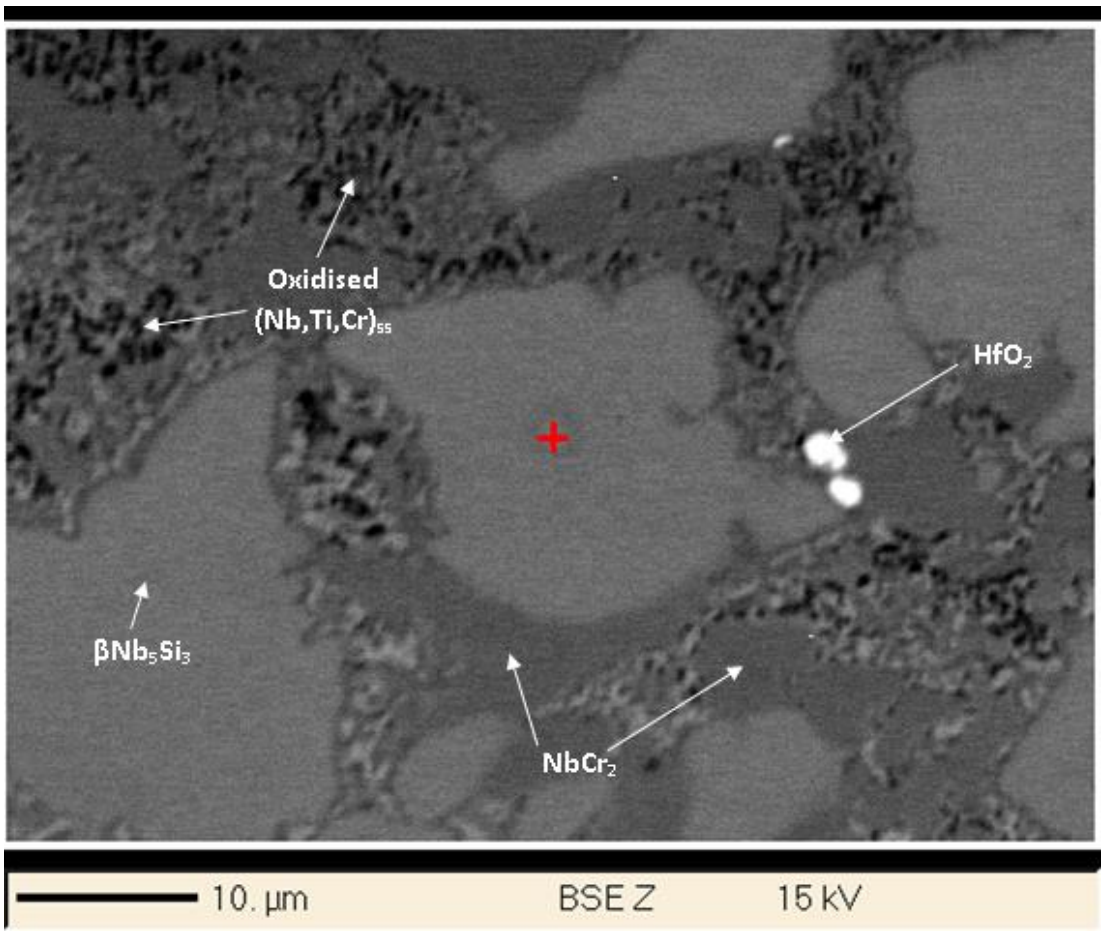

Figure 106. BSE-SEM image of oxidised GB2-AC-1000-100h substrate microstructure.

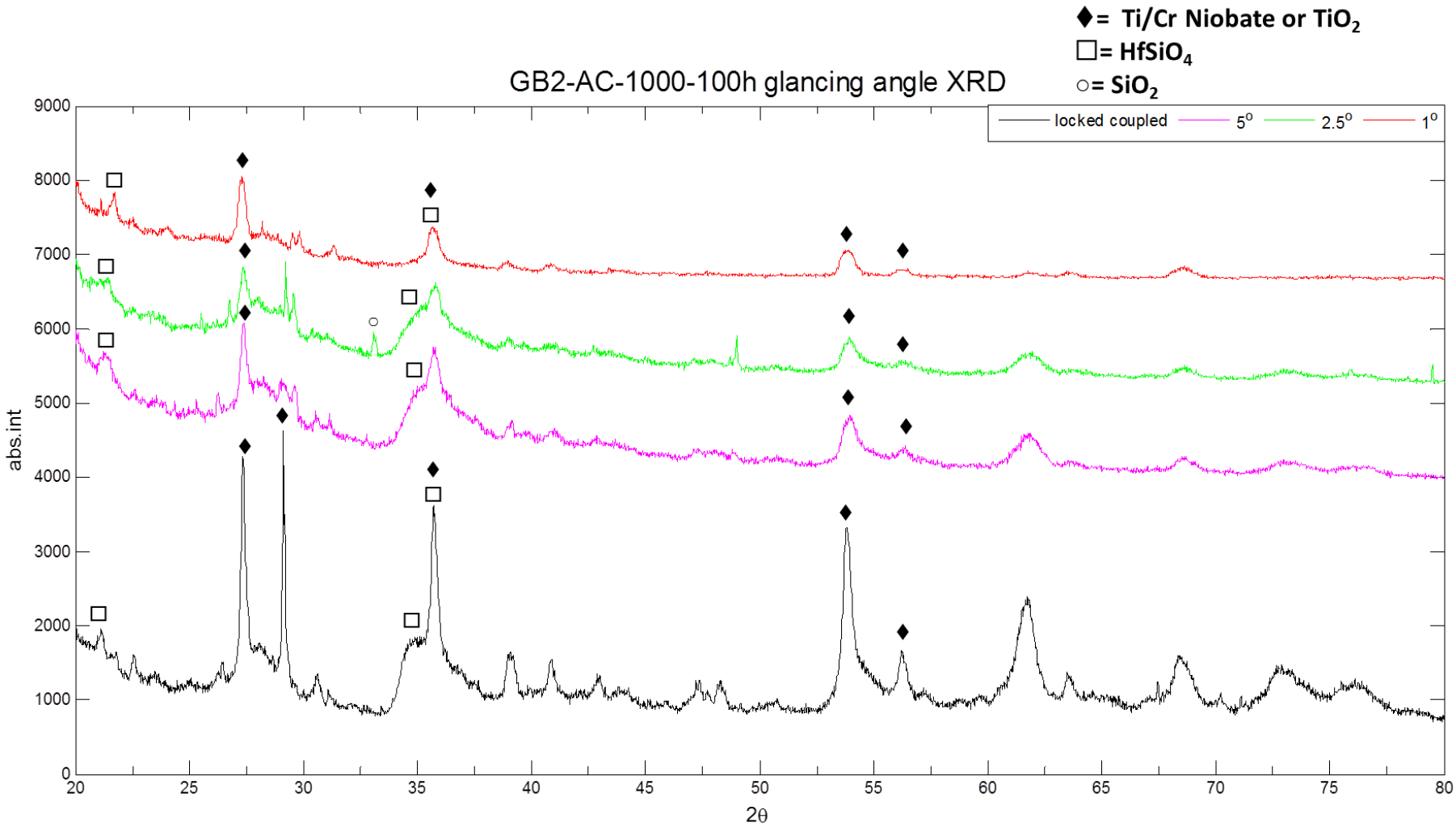

Figure 107. GXRD patterns for GB2-AC-1000-100h taken at different glancing angles.

Table 38. Phase WDS data of GB2-AC-1000-100h.

Phase	Depth (µm)	Nb	Si	Ti	Cr	Ge	Hf	O
βNb_5Si_3	5 - 150	39.3 ± 1.2	29.1 ± 1.9	14.7 ± 1.0	3.1 ± 0.1	7.0 ± 0.3	3.3 ± 0.6	3.5 ± 1.0
		42.4 - 37.0	32.4 - 25.1	17.2 - 13.4	3.4 - 2.9	7.6 - 6.4	5.0 - 2.4	7.0 - 2.2
$NbCr_2$	25-150	25.1 ± 1.3	8.4 ± 1.3	10.3 ± 1.7	47.0 ± 2.3	1.6 ± 0.3	4.0 ± 0.8	3.8 ± 4.2
		27.7 - 21.5	10.7 - 5.2	13.2 - 6.4	49.8 - 38.7	2.2 - 1.1	5.8 - 2.9	22.1 - 1.6
$(Nb,Ti,Cr)_{ss}$	50 - 100	43.0 ± 8.9	3.8 ± 2.5	26.9 ± 2.4	15.3 ± 5.0	2.7 ± 1.3	2.7 ± 1.2	5.5 ± 1.1
		50.8 - 30.5	7.4 - 1.5	29.9 - 23.8	22.3 - 10.9	4.6 - 1.2	4.4 - 1.7	6.7 - 4.0
$(Nb,Ti,Cr)_{ss}$ (Si= 0)	< 50	55.3	0.0	24.7	6.9	1.3	1.4	10.5
		63.8	0.0	18.1	4.4	0.9	6.4	6.4
Niobate 1	n/a	14.1 ± 1.1	7.3 ± 1.1	6.1 ± 1.4	2.2 ± 1.8	0.8 ± 0.4	1.2 ± 0.3	68.4 ± 1.0
		16.0 - 11.9	8.4 - 4.4	9.3 - 3.2	6.3 - 0.8	1.5 - 0.4	2.2 - 0.9	69.7 - 66.7
Niobate 2*	n/a	23.8 ± 1.4	0.3 ± 0.4	3.5 ± 1.7	0.9 ± 0.5	1.0 ± 1.0	1.1 ± 0.6	69.4 ± 0.8
		24.9 - 22.3	0.8 - 0.0	5.4 - 2.5	1.5 - 0.4	2.1 - 0.4	1.8 - 0.7	69.9 - 68.4
*3 analysis points.								

Table 39. Comparison of GB2-AC-1000-100h EPMA phase data shown in Table 38 to the average GB2-AC EDS data shown in Table 25.

GB2-AC-1000-100h phase	Depth (µm)	Element difference to GB2-AC Jeol data						
		Nb	Si	Ti	Cr	Ge	Hf	O
βNb_5Si_3	5 - 150	-1.6	-0.8	-1.9	-0.4	+1.7	-0.4	+3.5
$NbCr_2$	25 - 150	-1.5	-2.0	+0.2	-1.1	+0.7	+0.1	+3.8
$(Nb,Ti,Cr)_{ss}$	50 - 100	-8.0	+1.4	-2.4	+1.3	+1.9	+0.0	+5.5
$(Nb,Ti,Cr)_{ss}$ (Si= 0) analysis 1	< 50	+4.3	-2.4	-4.6	-7.1	+0.5	-1.3	+10.5
$(Nb,Ti,Cr)_{ss}$ (Si= 0) analysis 2	< 50	+12.8	-2.4	-11.2	-9.6	+0.1	+3.7	+6.4

Table 40. Comparison of GB2-AC-1000-100h EPMA phase data shown in Table 38 to the average GB2-HT EDS data shown in Table 25.

GB2-AC-1000-100h phase	Depth (µm)	Element difference to GB2-HT Jeol data						
		Nb	Si	Ti	Cr	Ge	Hf	O
βNb_5Si_3	5 - 150	-1.5	-0.9	-2.5	+1.4	-0.3	+0.4	+3.5
$NbCr_2$	25 - 150	-0.5	+0.2	-1.0	-4.3	+0.4	+1.6	+3.8
$(Nb,Ti,Cr)_{ss}$	50 - 100	-22.2	+3.0	+3.7	+6.0	+2.2	+1.8	+5.5
$(Nb,Ti,Cr)_{ss}$ (Si= 0) analysis 1	< 50	-9.9	-0.8	+1.5	-2.4	+0.8	+0.5	+10.5
$(Nb,Ti,Cr)_{ss}$ (Si= 0) analysis 2	< 50	-1.4	-0.8	-5.1	-4.9	+0.4	+5.5	+6.4

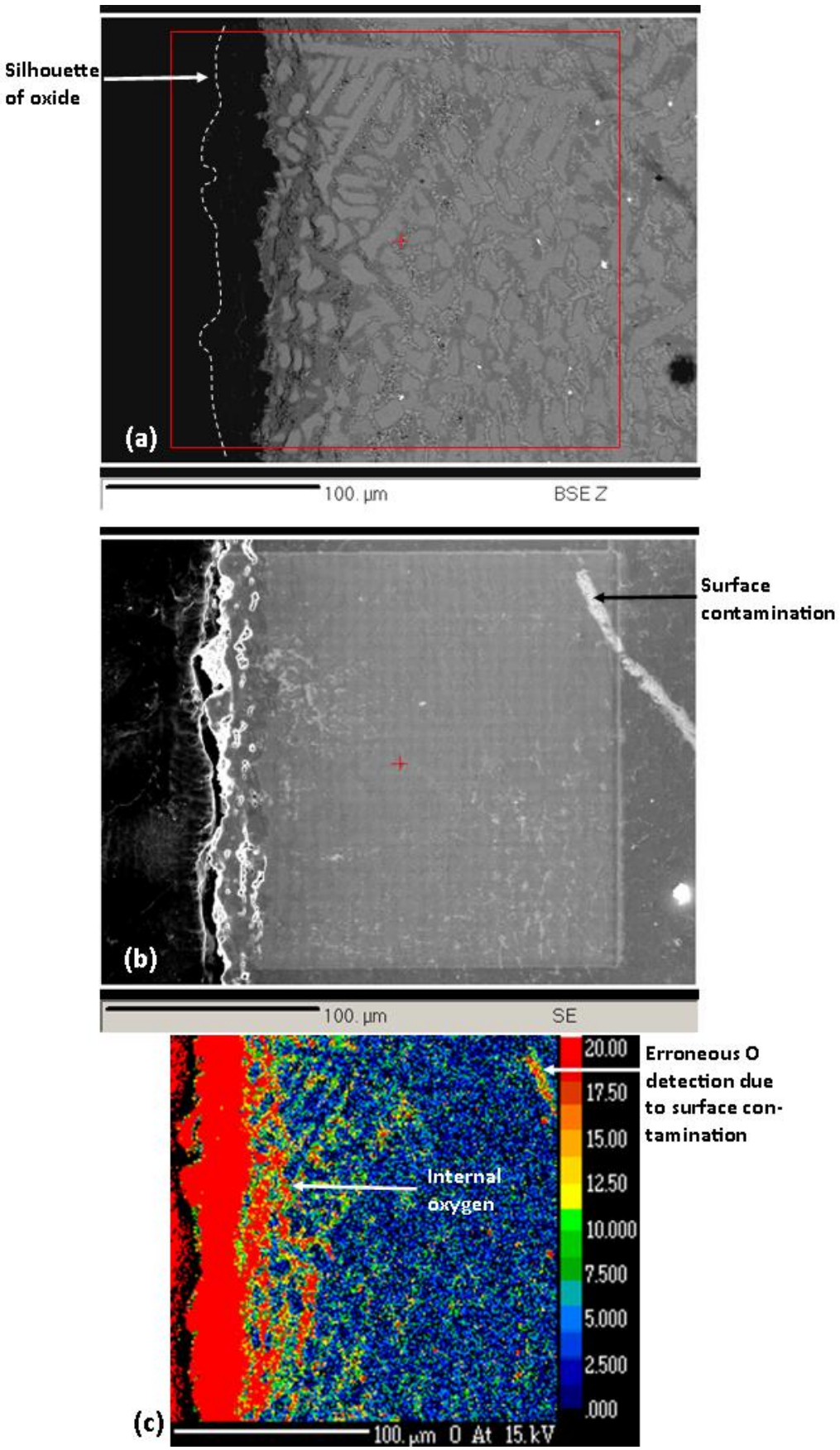

Figure 108. (a) BSE and (b) SE images of the WDS X-ray mapped region of the GB2-AC-1000-100h microstructure. The red box in (a) indicates the specific region mapped and can be seen as an electron burn mark in (b). (c) The O map. Refer to Figure 109 for the Nb, Si, Ti, Cr, Ge, and Hf maps.

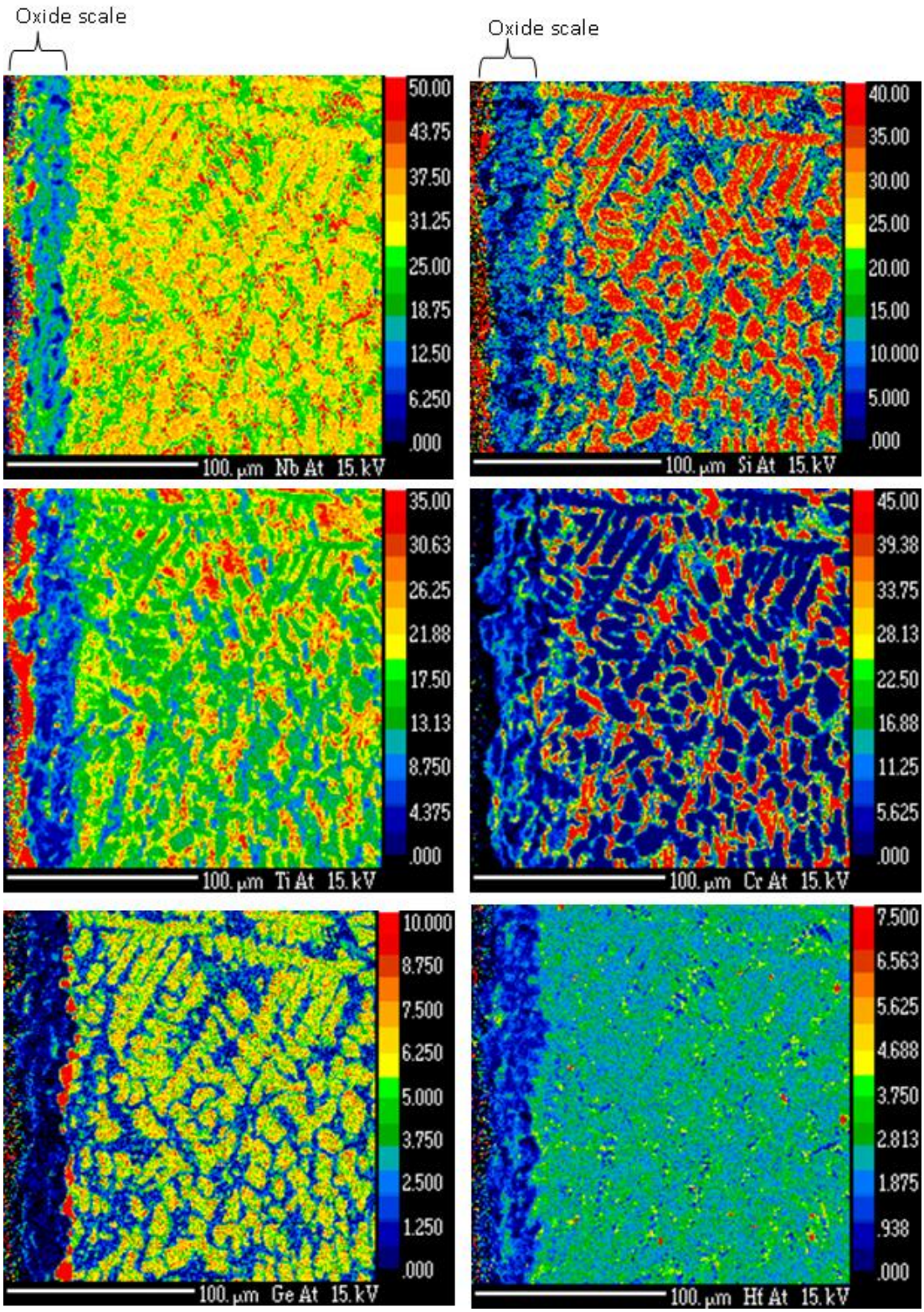

Figure 109. The Nb, Si, Ti, Cr, Ge and Hf WDS X-ray maps for GB2-AC-1000-100h. Refer to Figure 108 for BSE and SE images of the mapped location and the O map.

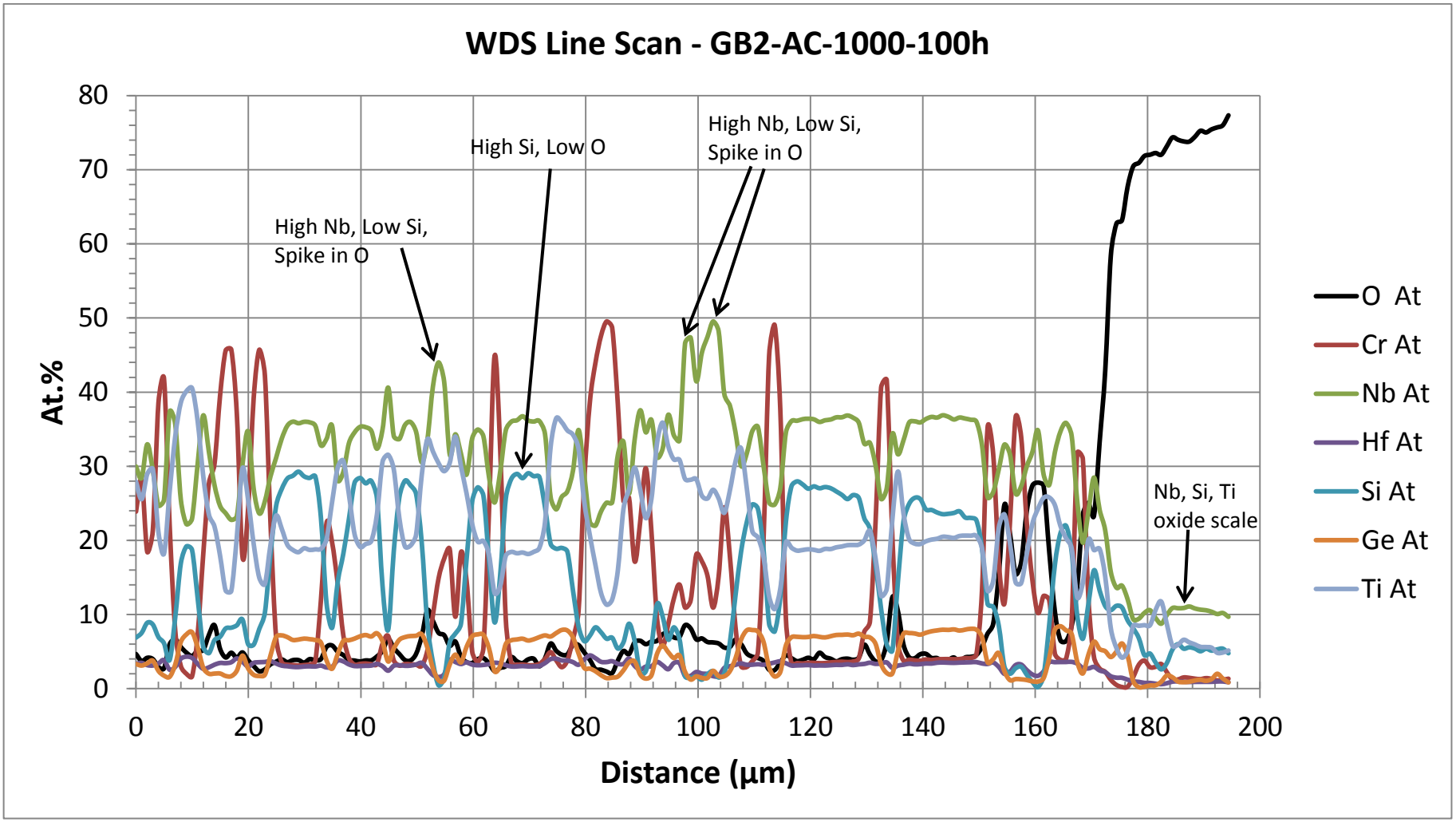

Figure 110. The WDS Line scan of GB2-AC-1000-100h. Refer to Figure 111 for BSE and SE SEM images of the scan path.

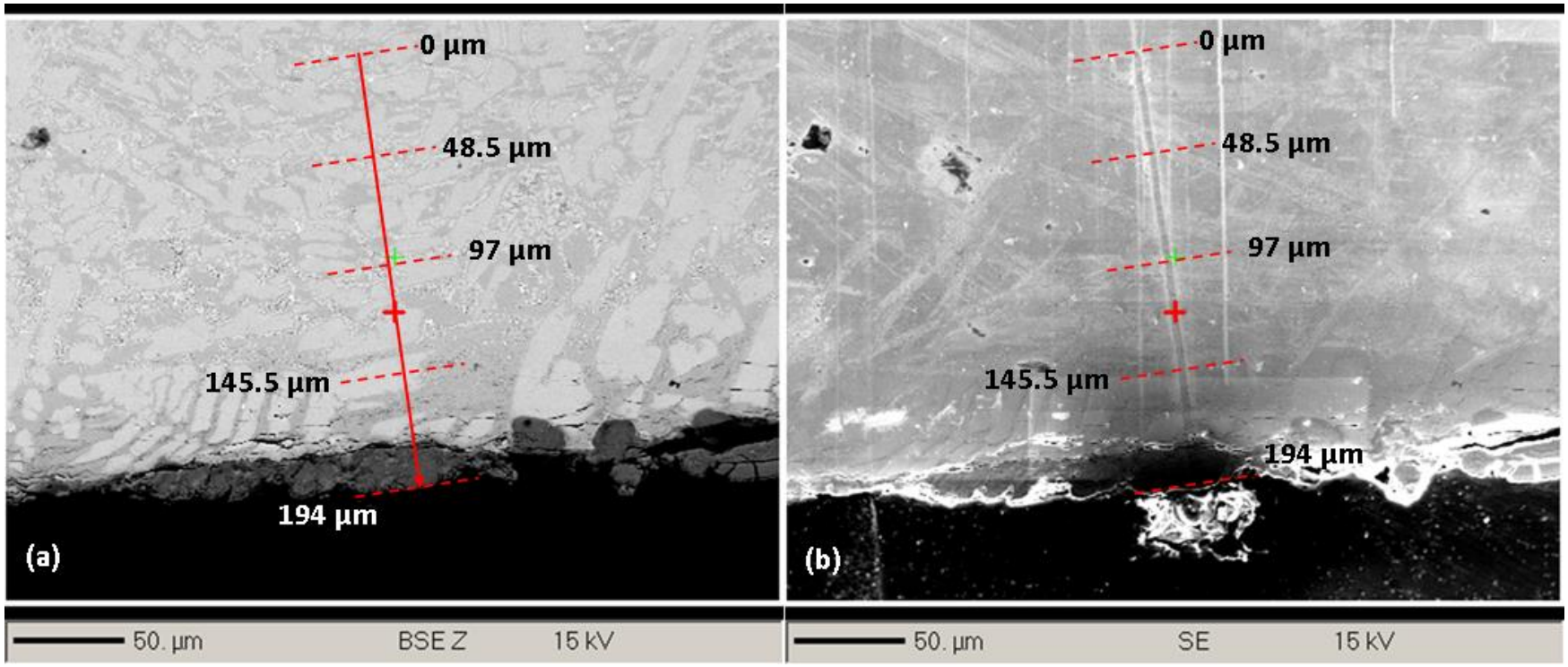

Figure 111. (a) BSE and (b) SE SEM images indicating the WDS line scan path of the data in Figure 110 for GB2-AC-1000-100h.

5.4 Oxidation at 1200°C

5.4.1 Introduction

The alloys GB1 and GB2 were oxidised at 1200°C in the AC and HT conditions for various times. The isothermal TGA data of all the 1200°C oxidation tests are shown in Figure 112. The oxidation rate constants most closely match parabolic growth behaviour. However, as previously mentioned, the behaviours should be more aptly described as para-linear due to complete passivation not being achieved. For both alloys in all conditions the parabolic rate constants were of the magnifitude 10^{-10} g^2 cm^{-4} s^{-1} (Table 26).

Photographs of the 1200°C oxidised specimens are shown in Figure 88, Figure 89, and Figure 90. The oxide scale had spalled from the 100h GB1 AC/HT specimens and the 5, 10, and 25h GB2-HT specimens. The oxide scale was powdered for PXRD analysis. For specimens that suffered no spallation a chisel was required to remove the oxide. The adherence of the scale on the 50 and 100h GB2 AC/HT specimens was surprising as a significant amount of force was required to break it off. The PXRD diffractograms were indexed against the PDF-4+ ICDD databse as shown in Figure 113. Essentially, the same oxides had formed on both GB1 and GB2. However, their oxide scales were of a different layering structure. Such oxidation results will be discussed in more detail in the following sub sections.

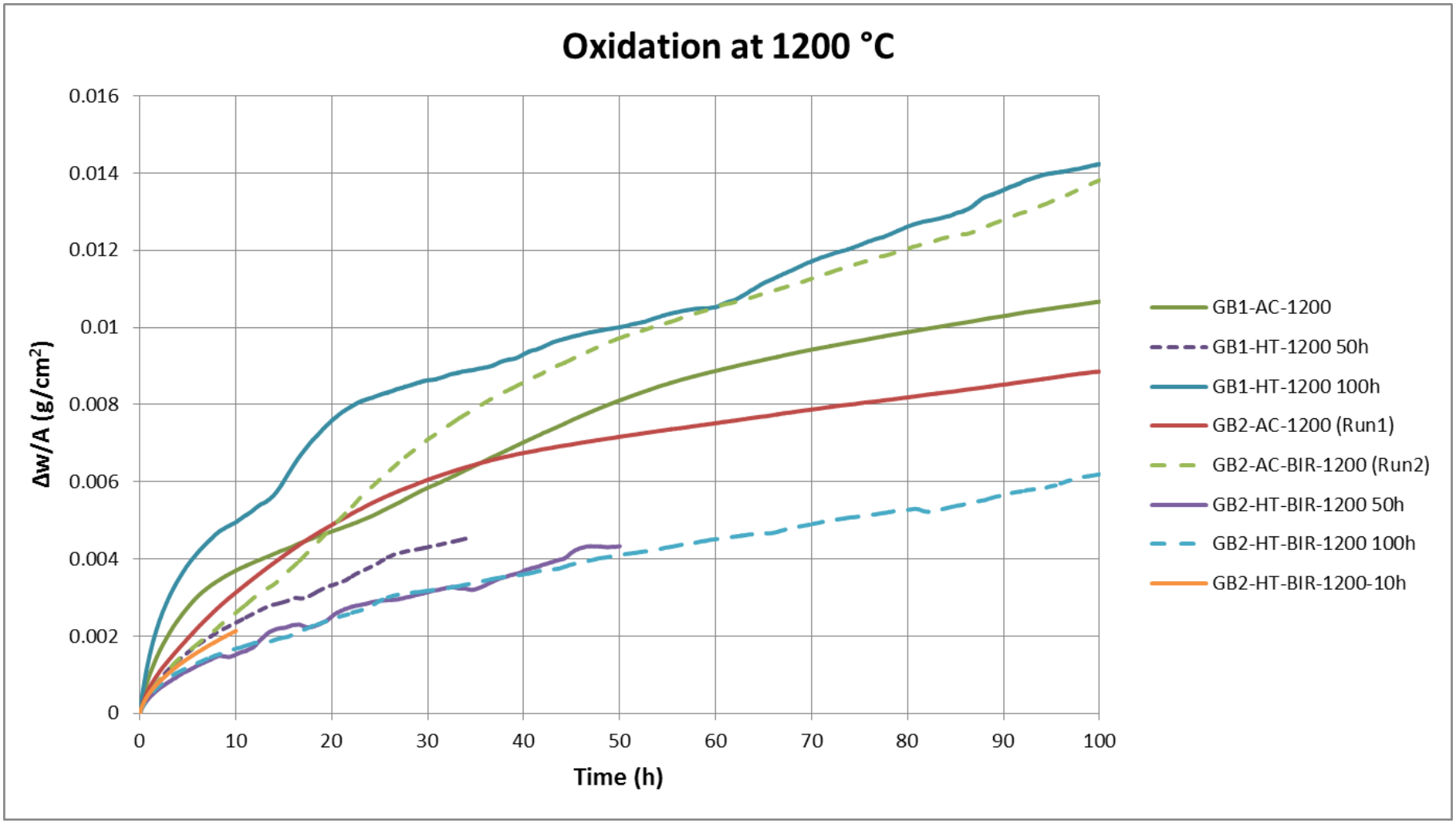

Figure 112. Isothermal TGA data of the GB1 and GB2 alloys oxidised at 1200°C.

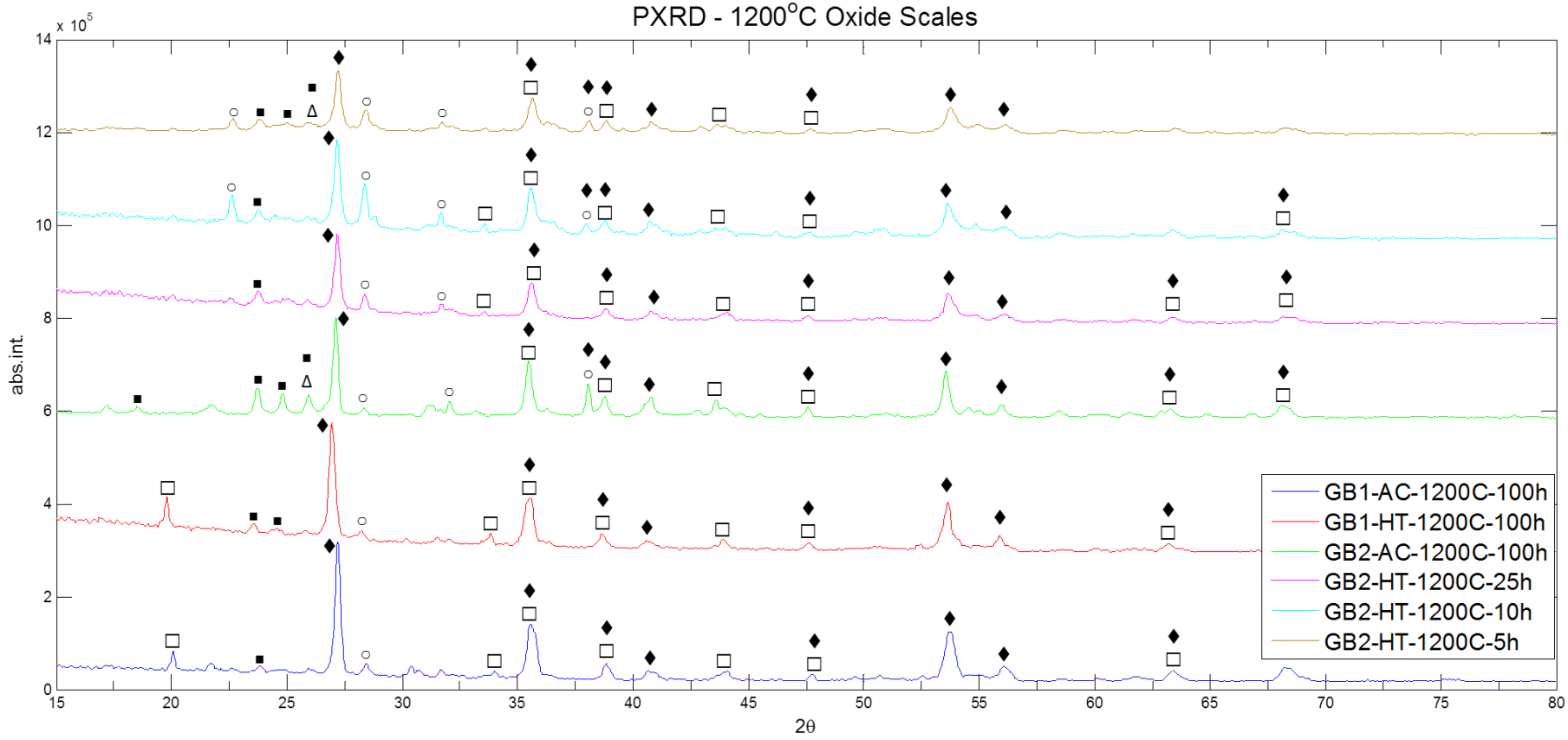

Figure 113. PXRD diffractograms of the oxide scale products from alloys GB1 and GB2 after oxidation at 1200°C for different times of various conditions. The symbols denote; ♦ $CrTiNbO_4$, $TiNbO_4$, $CrNbO_4$, TiO_2, $Ti_xCr_yNb_zO_2$ (tetragonal). ■ $CrNb_{11}O_{29}$ (monoclinic). □ $HfSiO_4$ (tetragonal). Δ GeO_2 (hexagonal). ○ SiO_2 (hexagonal).

5.4.2 Alloy GB1: Kinetics & Internal Microstructure

The GB1 AC/HT specimens after 100h oxidation (Figure 88 d and f) were completely covered by oxide scale that had various cracks and exposed the base metal. Upon handling the specimen the oxide scale fractured off. Refering to Table 26, the 100h test of the HT condition specimen had a slightly higher overall weight gain than the AC (14.2 vs 10.7 mg/cm^2) but the rate constants were of the same magnitude (5x10^{-10} vs 3x10^{-10} g^2 cm^{-4} s^{-1}). Only ~35h of TGA data was recorded for the 50h test due to software error, despite this the isothermal programme did complete. The 50h oxidised GB1-HT specimen had a visually different and better adhered oxide scale showing no signs of cracking nor did it fracture upon handling (Figure 88e). After the ~35h a weight gain of 4.5 mg/cm^2 was recorded, this is roughly a third of the 100h sample approximating the weight gain/h to be ~ 0.14 mg/cm^2.

WDS analysis of phases are presented in Table 41 for the 100h AC condition and Table 42 for the 100h HT condition. Phase analysis was separated into that taken within or outside the black precipitate diffusion zone (BPDZ) and the depth of analysis below the substrate edge is given in ranges. All phases showed contamination by O. Figure 114 and Figure 115 illustrate the respective microstructures and the clear appearance of internal oxidative attack of the alloys. The WDS analysis suggest the white and black precipitates to be HfO_2 and a Ti-based phase respectively. The HfO_2 identification is consistent with literature, however, the black Ti-based precipitates are not.

As was mentioned, the formation of black Ti oxide/nitride precipitates have been reported in literature but the average O concentration of the black Ti-based precipitates in GB1-AC (Table 41) does not correspond to TiO_2 or TiO. EDS using the high resolution FEI InspectF FEG SEM was also used to supplement analysis and depiction of these internal precipitates. The HfO_2 identification was corroborated (Figure 116). However, a distinct N peak in addition to O was found for spectra of the Ti-based precipitate, variation in peaks counts was commonplace for different grains analysed (Figure 117 and Figure 118). The detection of N in addition to O was not pursued by WDS analysis as it was deemed beyond the capability of the equipment and any attempts would have required copious amounts of calibration time, which was not available.

The detection of N by EDS here is not entirely reliable though due to the close energies and wavelengths of the TiLα, NKα and OKα X-rays (TiLα = 0.452keV and λTiLα= 27.4Å, NKα= 0.392keV and λNKα= 31.6Å, OKα= 0.523KeV and λOKα= 23.6Å) and given the EDS detector had a resolution of 0.121 keV that would be incapable to resolve the TiLα and NKα energies that posing significant problem for N detection by EDS due to overlap. Furthermore, X-rays from

OKα will overlap with TiLα as well, and since the sample was carbon coated C should be included in the analysis, as was done in Figure 118a. If the overlap with TiLα is ignored for arguments sake, the reduction in N when C is included in analysis is significant. With these considerations in mind, the black precipitates analysed in GB1-AC should not be prematurely identified as either Ti-oxides or TiN and may much more likely be O/N-rich Ti_{ss}.

According to the Ti-O binary phase diagram, as discussed in section 2.2, at 1200°C the single phase βTi_{ss} has O solubility up to ~ 4 at.%. Above this the two phase βTi_{ss} + αTi_{ss} region resides up until ~10 at.% O, beyond which content only the hcp αTi_{ss} is stabilised with O solubility up to 33 at.% (Figure 45). Nitrogen on the other hand, according to the Ti-N binary phase diagram (Figure 119) at 1200°C, is soluble in βTi_{ss} up to ~3 at.%. Above this the two phase βTi_{ss} + αTi_{ss} region resides up to ~ 6 at.% and beyond this only the hcp αTi_{ss} is stabilised with N solubility up to ~ 23 at.% where the two phase αTi_{ss} + TiN region begins. Only at a high N content of ~ 29 at.% does the single phase TiN field begin (see Figure 119). Thus, the competing dissolution of O and N into the $(Nb,Ti,Cr)_{ss}$ and precipitation of hcp αTi is a very plausible occurrence (Figure 3) and is stabilised by O and N at 1200°C. With limitations of analysis kept in mind, the N and O composition are not definitively significant enough to be oxides or nitrides. Therefore, the black precipitates are identified as a O/N-rich Ti_{ss}, most likely the hcp αTi_{ss}.

The oxidative attack of the substrate microstructure is clear in Figure 114f and Figure 115f, appearing more prevalent throughout the $NbCr_2$, as opposed to the $(Nb,Ti,Cr)_{ss}$. The reason for this may be attributed to the low $(Nb,Ti,Cr)_{ss}$ area fraction and the $NbCr_2$ having formed a physical barrier around the O susceptible $(Nb,Ti,Cr)_{ss}$. The lack of a interconnecting $(Nb,Ti,Cr)_{ss}$ network, which typically acts as a direct oxidation path through the Nb-silicide microstructure may explain the lower oxidation kinetics of the alloy GB1 when compared with Nb-silicide based alloys reported in the literature (Table 26, Table 27, and Table 28). In certain areas, such as in Figure 121, the microstructure appears heavily oxidised but un-oxidised $(Nb,Ti,Cr)_{ss}$ grains are present.

The AC and HT microstructures after 100h of oxidation displayed two oxide precipitation depths, the first and most severe was the immediate substrate microstructure below the oxide scale that contained both the HfO_2 and O/N-rich Ti_{ss} up to ~ 100 µm. The second was beyond 100 µm where only HfO_2 precipitates were present up to a depth of ~ 400 µm into the bulk of the sample. For both the 100h oxidised AC and HT specimens, HfO_2 and O/N-rich Ti_{ss} were seen to originate at $(Nb,Ti,Cr)_{ss}$ and $NbCr_2$ grain boundaries. The SEM image of the 50h oxidised HT microstructure in Figure 120 shows only O/N-rich Ti_{ss} formation at $(Nb,Ti,Cr)_{ss}/NbCr_2$ grain boundaries.

It is important not to make a direct comparison of the GB1-AC phase data with the 100h oxidised AC phase data as reductions in solute of phases should also be attributed to the pseudo HT effect of the 1200°C oxidation conditions and, hence, the 100h oxidised GB1-HT condition should be a more appropriate reference point for comparison. Comparing the data of GB1-HT (Table 22) with GB1-HT-1200-100h results in the data presented in Table 43. Analysis is separated into those taken within or outside the BPDZ. The chemical changes would suggest HfO_2 was formed using Hf from $(Nb,Ti,Cr)_{ss}$ while the O/N-rich Ti_{ss} was formed using Ti from both $(Nb,Ti,Cr)_{ss}$ and some from $NbCr_2$. The changes of Ti and Cr from the $(Nb,Ti,Cr)_{ss}$ and $NbCr_2$ grains analysed within the BPDZ is close to the stoichiometric composition of $(Ti/Cr)NbO_4$ where for stoichiometry (Ti/Cr)= 16.67 at.% (Table 43). This diffusion of Ti and Cr from these phases may be to the alloy surface as part of oxide scale formation.

In the 100h oxidation tests at 800°C, HfO_2 did not form within the $(Nb,Ti,Cr)_{ss}$, only micron sized black precipitates were observed. These precipitates are assumed to be the same O/N-rich Ti_{ss} phase and, therefore, the affinity of O to form O/N-rich Ti_{ss} is greater than that to form HfO_2. The lack of HfO_2 formation at 800°C and after 50h oxidation at 1200°C suggests Hf is not as effective as Ti at gettering O and preventing its ingress throughout the alloy GB1 microstructure. The higher concentration of Ti than Hf in the alloy has likely a strong influence on this.

Figure 122 shows oxidative attack of a γNb_5Si_3 grain from the 100h oxidised AC specimen resulting in HfO_2 precipitation at the silicide grain boundary and the formation of an oxidative phase boundary. Only γNb_5Si_3 grains within the BPDZ showed signs of oxidative attack and HfO_2 precipitation. Internal precipitation can be seen at high magnification within the silicide. Based on the bright white contrast of the micron sized precipitates it is reasonable to assume they were HfO_2, however, this was not confirmed by analysis.

Table 41. WDS phase analysis in at.% for GB1-AC-1200-100h. Depth of analysis from the substrate surface is indicated. Note the distinction between analysis taken inside or outside of the BPDZ.

Phase	In/Out BPDZ	Depth (µm)	Nb	Si	Ti	Cr	Al	Hf	O
γNb_5Si_3	In	30 - 60	23.4 ± 0.5 23.8 - 22.6	44.7 ± 1.8 46.3 - 41.7	13.7 ± 0.5 14.3 - 13.0	2.0 ± 0.1 2.1 - 1.9	1.0 ± 0.1 1.1 - 0.9	9.7 ± 0.2 10.0 - 9.4	5.5 ± 2.9 10.5 - 3.0
	Out	75 - 200	24.0 ± 0.3 24.4 - 23.6	45.7 ± 1.2 47.4 - 44.1	13.0 ± 1.1 15.9 - 11.8	2.0 ± 0.1 2.1 - 1.9	1.1 ± 0.1 1.2 - 0.9	10.1 ± 0.6 11.1 - 9.3	4.1 ± 0.6 5.0 - 3.1
$NbCr_2$	In	50 - 75	25.7 ± 2.1 27.6 - 22.7	6.4 ± 1.2 8.2 - 5.1	8.6 ± 1.8 10.5 - 5.7	50.7 ± 1.6 52.6 - 48.7	3.0 ± 0.3 3.3 - 2.6	3.3 ± 1.8 5.3 - 1.2	2.2 ± 0.3 2.6 - 1.9
	Out	80 - 110	21.4 ± 0.9 23.6 - 20.6	9.0 ± 0.9 10.3 - 7.6	6.1 ± 1.0 7.2 - 4.4	53.6 ± 0.9 54.7 - 51.6	1.9 ± 0.3 2.4 - 1.5	5.6 ± 0.4 6.1 - 4.9	2.4 ± 0.3 3.1 - 2.0
$(Nb,Ti,Cr)_{ss}$	In[a]	40 - 100	54.8 ± 6.4 63.6 - 49.5	0.0 ± 0.0 0.0 - 0.0	24.2 ± 7.5 31.2 - 15.1	8.0 ± 0.0 8.0 - 7.9	6.5 ± 1.7 8.7 - 5.1	0.1 ± 0.1 0.2 - 0.0	6.4 ± 0.3 6.8 - 6.0
	Out	110 - 700	47.5 ± 1.6 50.5 - 46.1	0.0 ± 0.0 0.1 - 0.0	33.1 ± 0.7 33.9 - 32.1	7.8 ± 0.5 8.6 - 7.1	4.7 ± 0.2 5.0 - 4.4	1.4 ± 0.6 2.0 - 0.4	5.6 ± 1.4 6.7 - 3.4
O/N-rich Ti_{ss}	In	25 - 75	2.3 ± 0.9 3.6 - 1.4	0.2 ± 0.3 0.7 - 0.0	78.3 ± 5.6 84.3 - 67.4	1.0 ± 1.2 3.6 - 0.2	0.4 ± 0.4 1.4 - 0.1	0.9 ± 0.7 2.1 - 0.3	16.9 ± 5.9 28.2 - 9.3
HfO_2	-	-	0.1 ± 0.1 0.4 - 0.0	0.8 ± 0.6 1.6 - 0.0	0.2 ± 0.1 0.6 - 0.1	0.5 ± 0.2 0.9 - 0.3	0.0 ± 0.1 0.2 - 0.0	33.8 ± 1.3 35.9 - 32.5	64.5 ± 1.4 66.6 - 62.4

[a]: 4 analysis points.

Table 42. WDS phase analysis in at.% for GB1-HT-1200-100h. Depth of analysis from the substrate surface is indicated. Note the distinction between analysis taken inside or outside of the BPDZ.

Phase	In/Out BPDZ	Depth (μm)	Nb	Si	Ti	Cr	Al	Hf	O
γNb_5Si_3	In	0 - 75	25.0 ± 1.5	33.2 ± 2.1	16.8 ± 0.9	1.9 ± 0.5	1.1 ± 0.1	11.4 ± 0.4	10.6 ± 4.3
			27.0 - 22.6	36.2 - 30.4	18.0 - 15.7	3.0 - 1.3	1.4 - 1.0	12.0 - 10.7	17.7 - 6.8
	Out	80 - 275	26.1 ± 0.4	36.5 ± 0.8	18.1 ± 0.5	1.7 ± 0.3	1.2 ± 0.1	12.3 ± 0.5	4.0 ± 0.4
			27.0 - 25.4	38.3 - 35.3	18.8 - 17.5	2.2 - 1.2	1.4 - 1.0	13.4 - 11.8	4.6 - 3.4
$NbCr_2$	In[a]	15 - 40	20.7 ± 1.6	8.5 ± 1.7	7.9 ± 3.0	34.0 ± 1.9	2.1 ± 0.7	6.4 ± 0.5	20.4 ± 0.7
			22.3 - 18.6	10.7 - 6.6	11.1 - 4.2	35.8 - 31.5	3.1 - 1.4	6.8 - 5.7	21.1 - 19.5
	Out	75 - bulk	21.1 ± 2.7	9.1 ± 3.0	11.4 ± 2.2	47.8 ± 4.8	1.7 ± 0.5	6.4 ± 0.9	2.6 ± 0.4
			28.3 - 19.3	14.5 - 6.0	13.4 - 5.2	52.5 - 38.4	3.1 - 1.3	6.9 - 3.7	3.1 - 1.9
$(Nb,Ti,Cr)_{ss}$	In[b]	20 - 75	56.2 ± 9.9	4.9 ± 5.4	7.7 ± 7.4	22.1 ± 15.8	3.7 ± 3.0	0.3 ± 0.1	5.0 ± 1.3
			63.7 - 44.9	11.0 - 0.7	15.4 - 0.5	39.1 - 7.9	5.6 - 0.3	0.4 - 0.2	6.4 - 3.8
	Out	90 - bulk	46.7 ± 5.7	1.3 ± 1.6	29.1 ± 4.4	10.8 ± 8.1	4.5 ± 0.9	1.7 ± 1.3	5.9 ± 1.0
			52.0 - 32.2	5.4 - -0.1	32.3 - 19.2	32.5 - 7.5	5.5 - 2.5	4.5 - 0.4	7.2 - 3.8
HfO_2[b]	-	-	0.1 ± 0.1	1.3 ± 0.3	0.4 ± 0.4	0.4 ± 0.2	0.0 ± 0.0	34.2 ± 0.5	63.6 ± 0.4
			0.2 - 0.0	1.6 - 0.9	0.9 - 0.2	0.6 - 0.2	0.0 - 0.0	34.7 - 33.6	63.9 - 63.2

[a]: 4 analysis points. [b]: 3 analysis points.

Table 43. Compositional change in at.% of average GB1-HT Jeol EDS data against GB1-HT-1200-100h. Positive table values signify increase after oxidation, Negative table values signify decrease after oxidation.

Phase	In/Out BPDZ	Depth (um)	Element difference to GB1-HT Jeol data						
			Nb	Si	Ti	Cr	Al	Hf	O
γNb_5Si_3	In	0 - 75	+0.4	-5.5	-4.0	+0.3	-0.6	-1.3	+10.6
	Out	80 - 275	+1.5	-2.1	-2.7	+0.2	-0.5	-0.4	+4.0
$NbCr_2$	In	15 - 40	+0.4	-0.2	-4.4	-16.2	+0.6	-0.6	+20.4
	Out	75 - bulk	+0.8	+0.4	-0.9	-2.4	+0.2	-0.7	+2.6
$(Nb,Ti,Cr)_{ss}$	In	20 - 75	+4.8	+4.2	-24.5	+13.4	-0.5	-2.4	+5.0
	Out	90 - bulk	-4.7	+0.5	-3.1	+2.1	+0.3	-1.0	+5.9

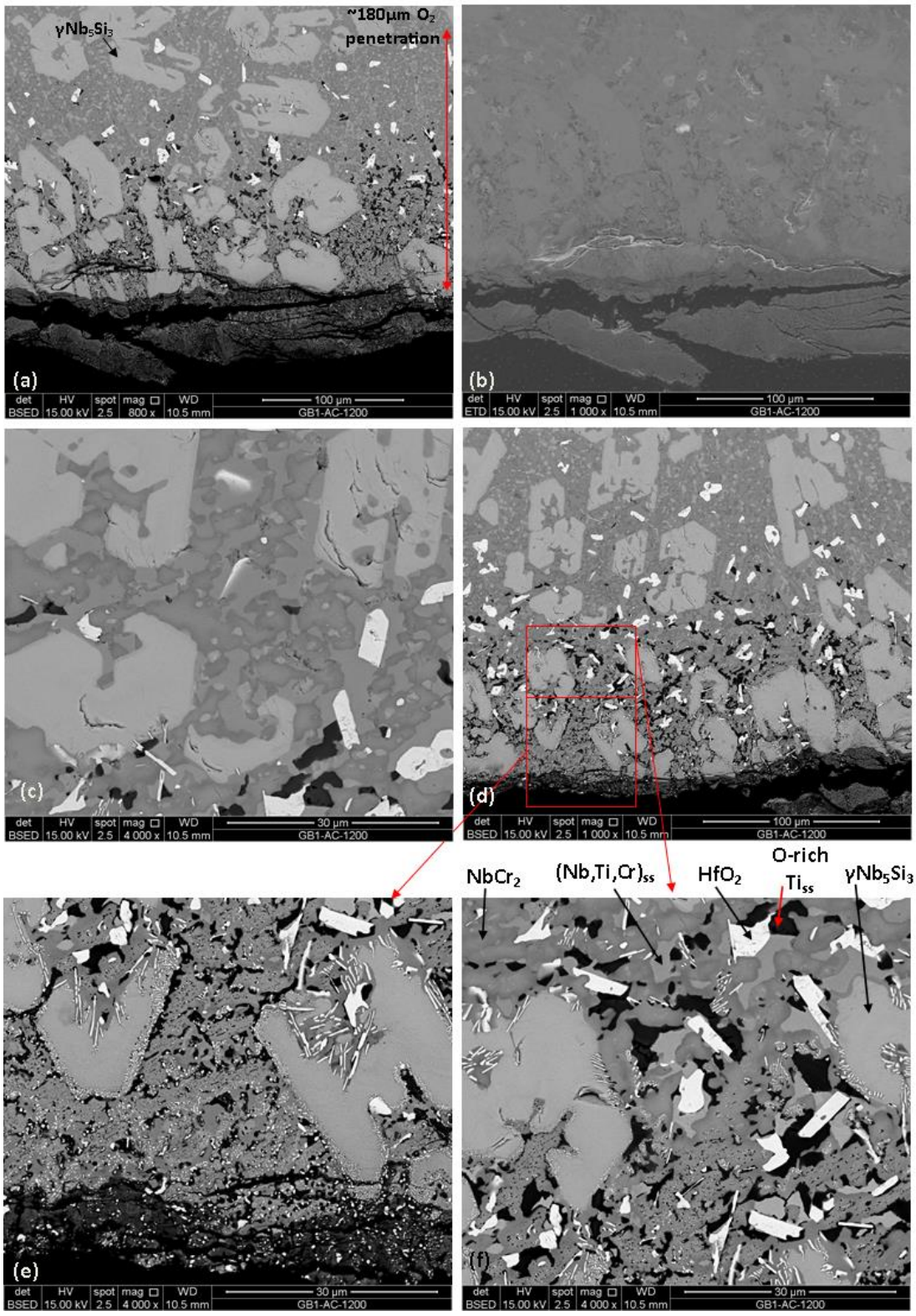

Figure 114. SEM images of the GB1-AC-1200-100h specimen. (a) Low magnification BSE image, (b) low magnification SE image, (c) BSE image of oxide precipitation within $(Nb,Ti,Cr)_{ss}/NbCr_2$ regions, (d) low magnification BSE image outlining; (e) BSE image displaying oxidation of silicide phase and (f) BSE image with identification of oxidised phases.

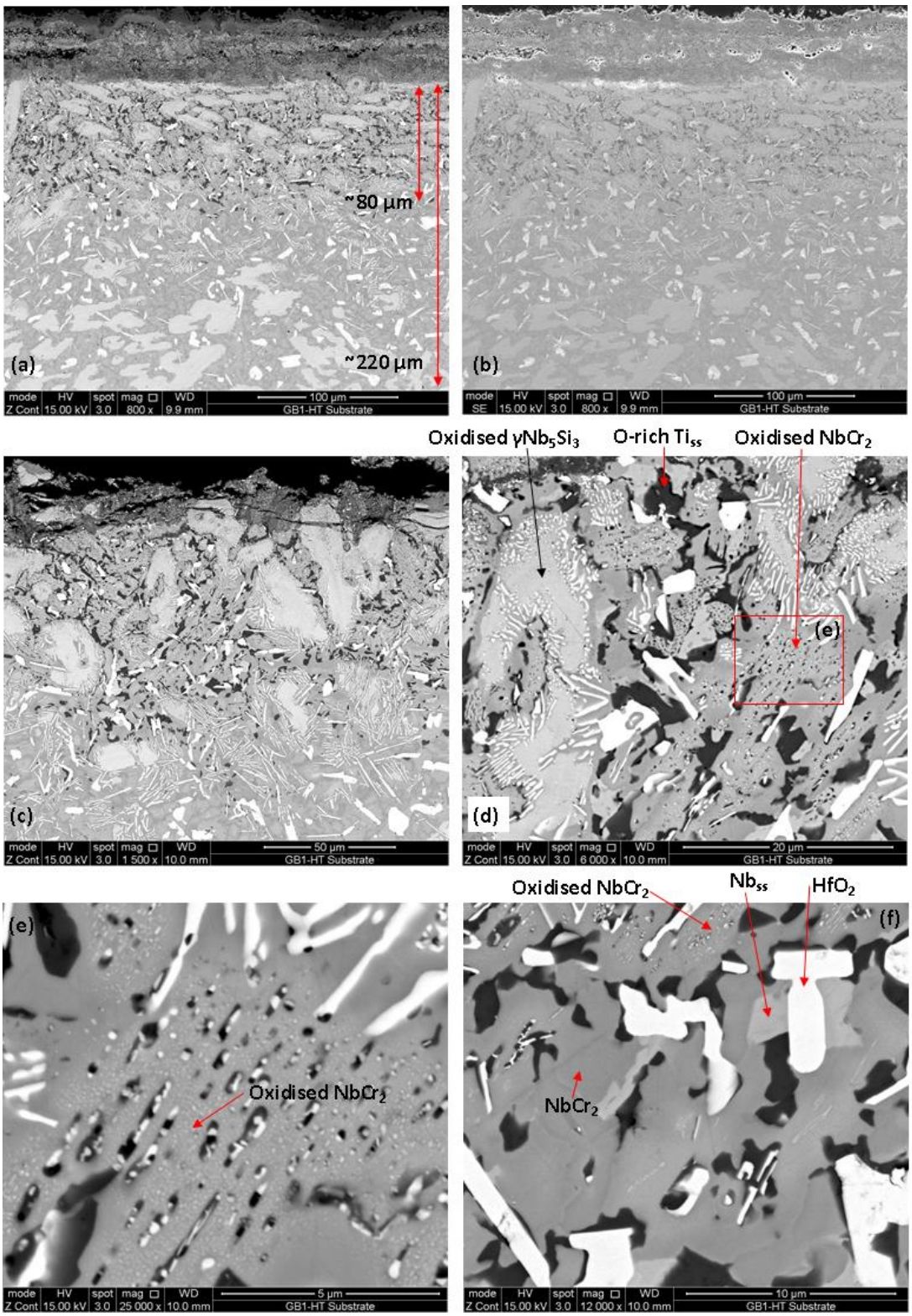

Figure 115. BSE imaging of GB1-HT-1200-100h. (a) Low magnification BSE image. (b) Low magnification SE image. (c) BSE image of oxide precipitation at $(Nb,Ti,Cr)_{ss}/NbCr_2$ regions. (d) Higher magnification BSE image of area in (c) showing silicide oxidation. (e) BSE image displaying oxidised $NbCr_2$. (f) High magnification BSE image of oxide precipitation amongst the $(Nb,Ti,Cr)_{ss}/NbCr_2$ regions with identification of phases.

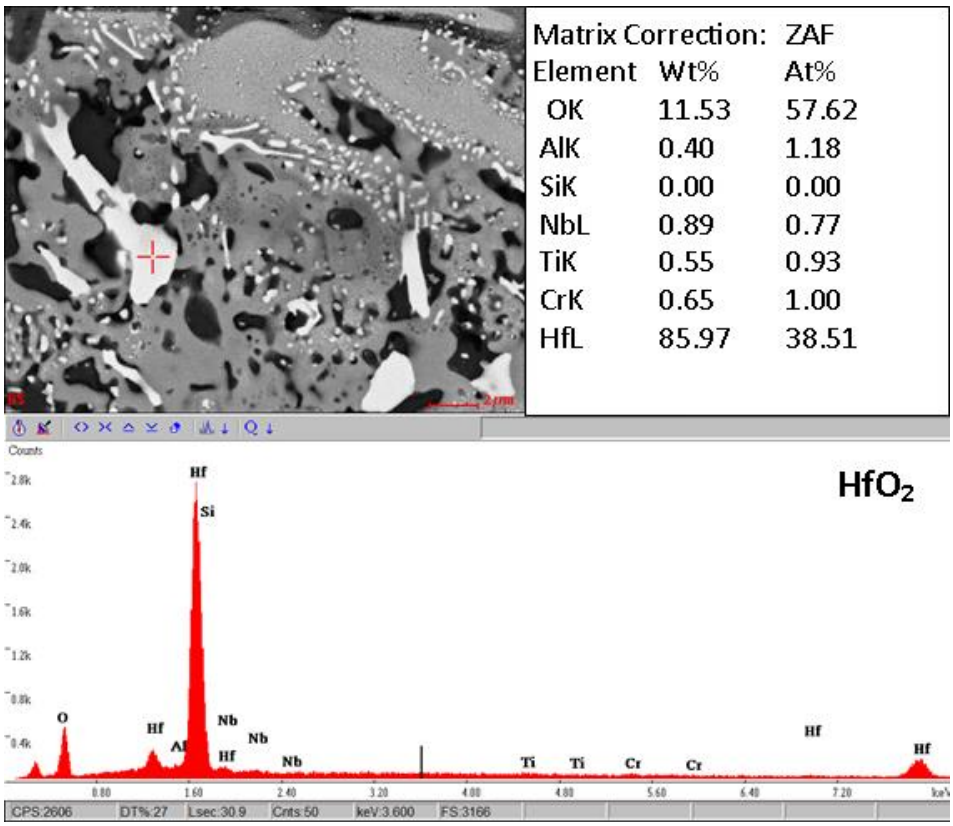

Figure 116. Standardless EDS using the FEI InspectF high resolution SEM. HfO_2 is identified.

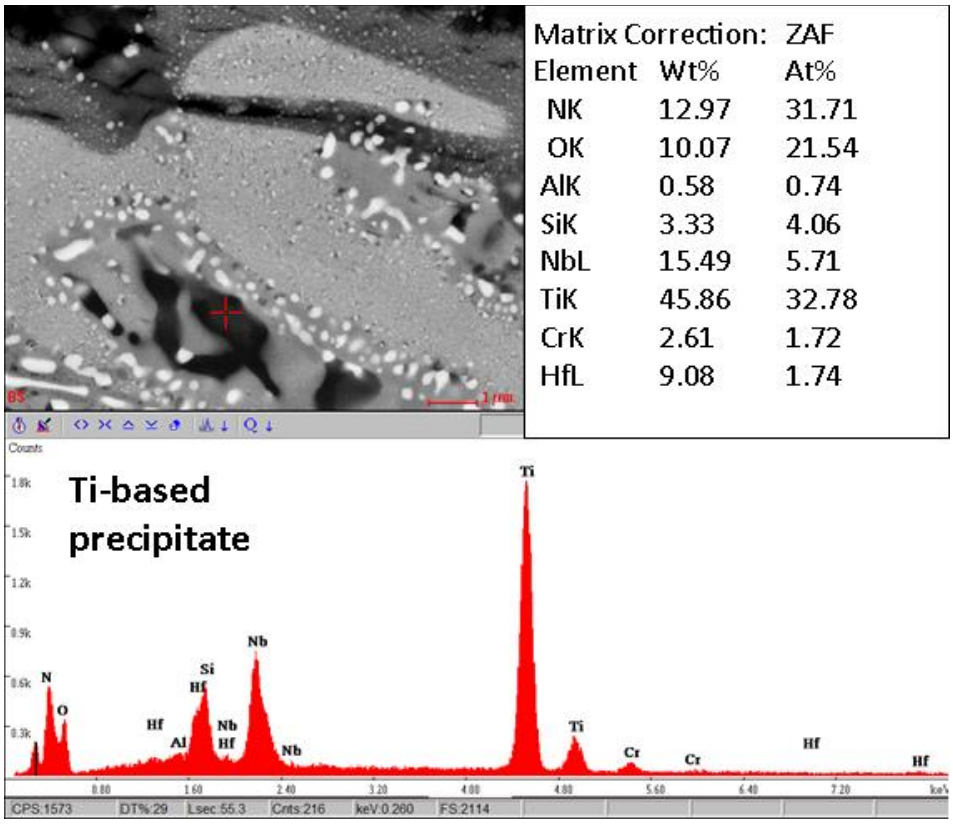

Figure 117. Standardless EDS using the FEI InspectF high resolution SEM. Ti-based precipitate is identified.

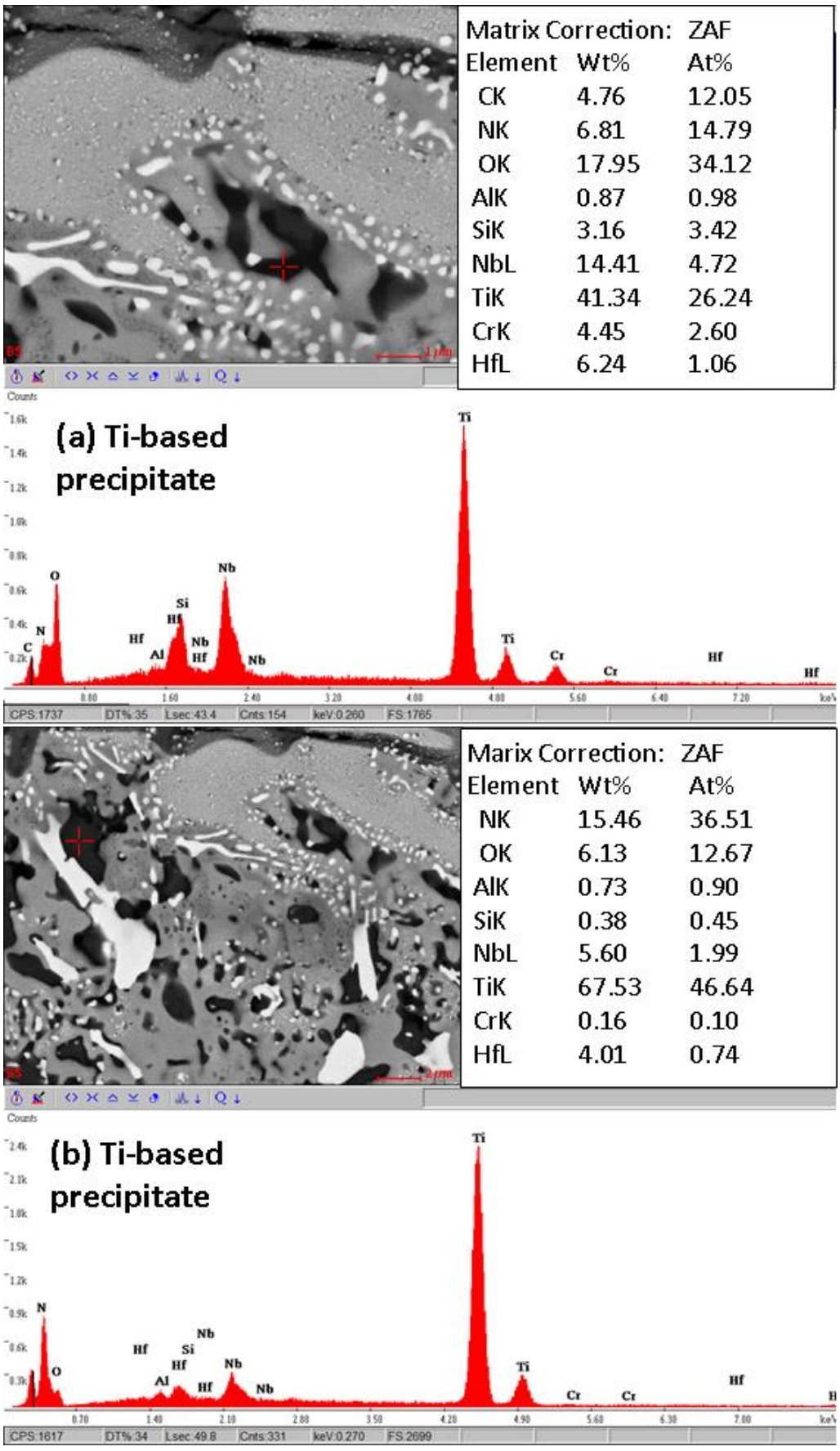

Figure 118. Standardless EDS using the FEI InspectF high resolution SEM. O/N-rich Ti based precipitate are identified in (a) and (b). There are distinct peaks for O and N detected, with C included in analysis in (a).

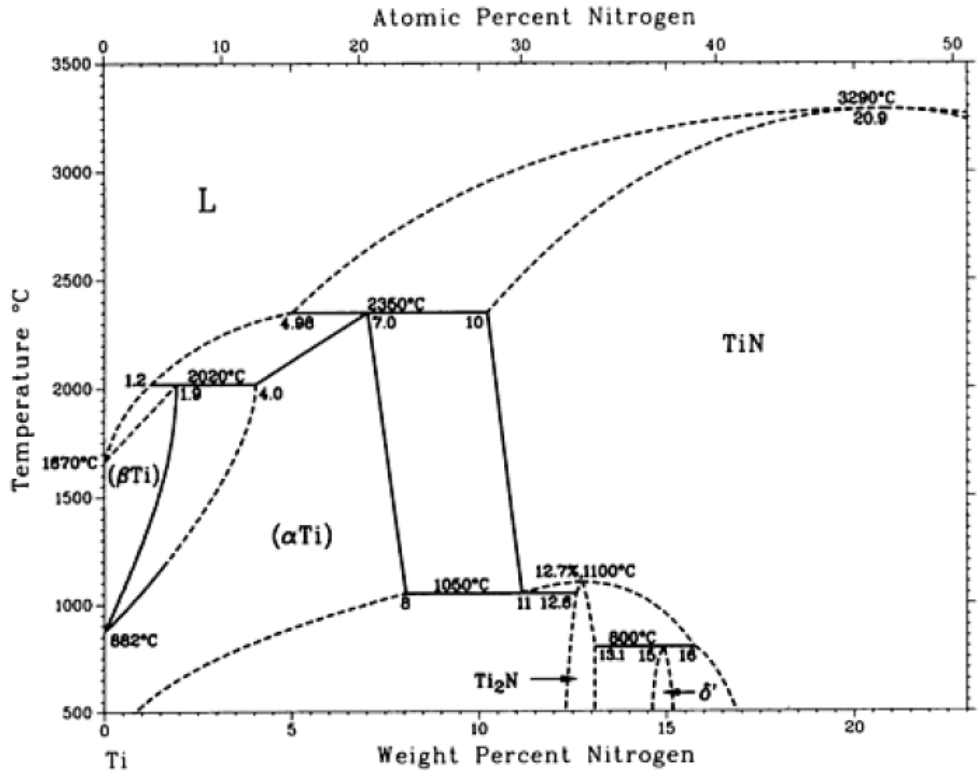

Figure 119. The Ti-N binary phase diagram (Wriedt and Murray, 1987).

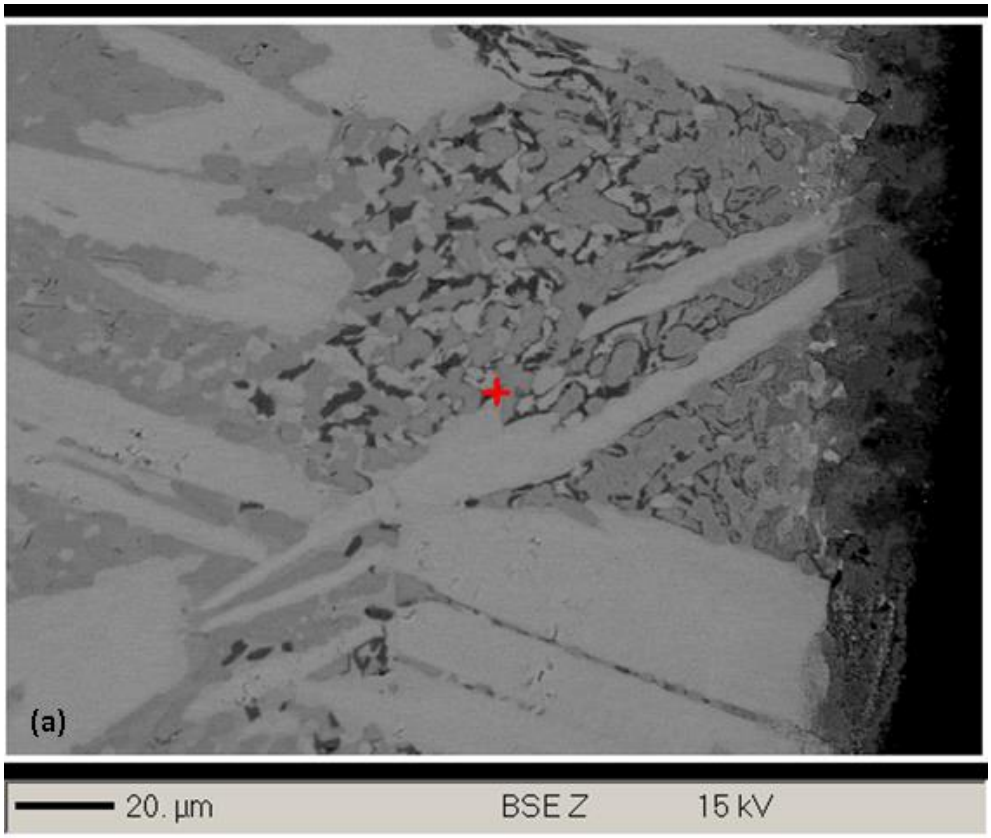

Figure 120. BSE image of GB1-HT oxidised at 1200°C for 50h.

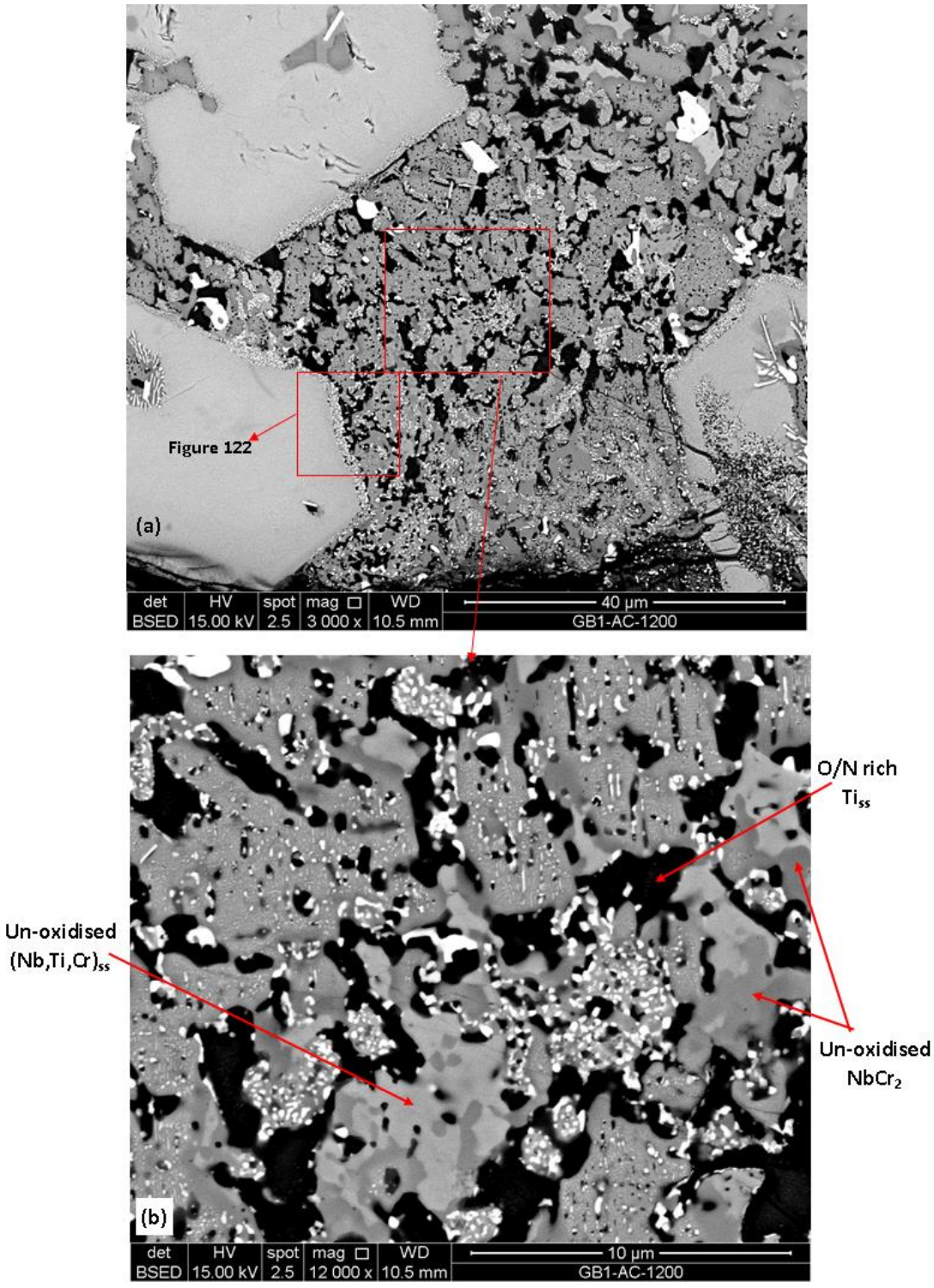

Figure 121. BSE images of the GB1-AC-1200-100h specimen. (a) Imaging of the immediate sub-scale microstructure, (b) High magnification BSE image showing the oxide precipitate formation within $(Nb,Ti,Cr)_{ss}$ and $NbCr_2$.

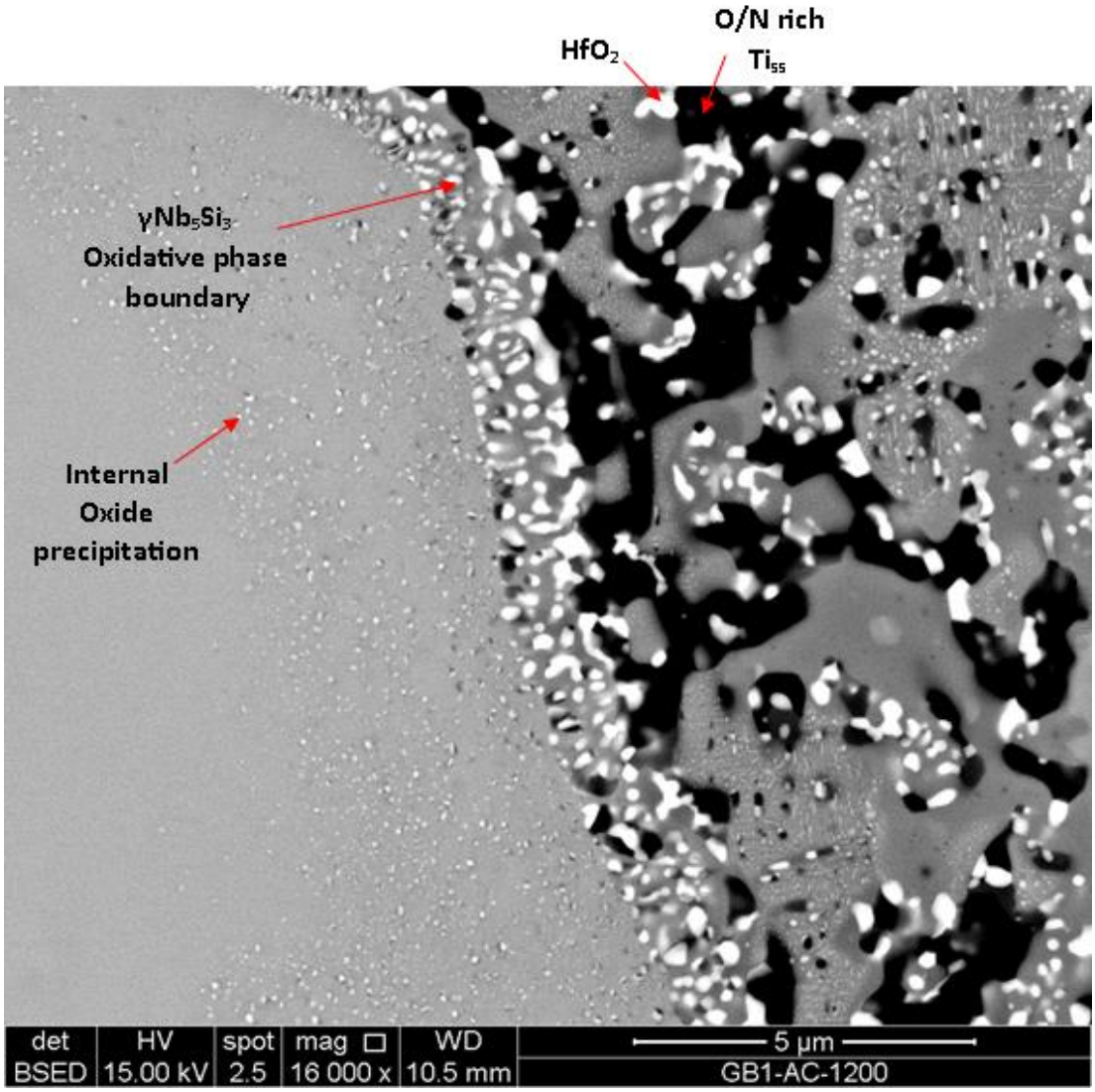

Figure 122. BSE-SEM image of the oxidative attack and oxide precipitation at a γNb_5Si_3 grain boundary resulting in the formation of an oxidative phase boundary and internal oxide precipitation within the γNb_5Si_3 grain.

5.4.3 Alloy GB1: Oxide Scale

The PXRD analysis of the oxide scale yielded almost identical diffractograms for both the AC and HT 100h oxidised specimens (Figure 113). The strongest peaks corresponded to mixed Nb-Ti/Cr oxides; (Ti,Cr)NbO_4, $TiNbO_4$, $CrNbO_4$, TiO_2, $Ti_xCr_yNb_zO_2$, and $HfSiO_4$ (hafnon) all of which posses tetragonal rutile-like crystal structures. The mixed Nb-Ti-Cr oxides are particularly difficult to decisively index due to their virtually identical peak positions.

On both the AC and HT 100h oxidised GB1 specimens at 1200°C a relatively thick oxide scale had formed that showed preference of reaction based on the element layering and depletion of Ti and Cr from the substrate microstructure. This is apparent in Figure 124 for the AC condition and in Figure 125 and Figure 126 for the HT condition. The outer oxide layer was identified as a Ti-based oxide of TiO_2 stoichiometry based on WDS (Table 44) and EDS analysis (Figure 127a) with some Nb content (Figure 123 and Figure 126) giving the possibility of Ti-niobate formation, however, Nb content is low. Based on the significantly stronger Ti detection, the outer oxide layer is decidedly TiO_2. Annotated overview of the oxide scales are shown in Figure 128 and Figure 129. WDS X-ray mapping of the 50h specimen strongly showed a Ti-rich outer layer consistent with findings after 100h of exposure (Figure 130).

Immediately underneath the TiO_2 was a thin semi-continuous Cr-niobate layer, likely of $CrNbO_4$ stoichiometry presenting a particularly dark contrast under BSE imaging and recording low Ti content (see Cr X-ray maps of Figure 124, Figure 125 and Figure 126). Beneath the thin Cr-niobate layer were relatively large Ti/Cr-niobate grains (Table 44 and Figure 128) mixed amongst a fine oxide region denoted Nb-Si-Ti-Hf-O mixed oxide (Table 44) that high resolution SEM images reveal to be multi-grained of sub-micron size (see Figure 129f). As analysis of individual oxide grains in the Nb-Si-Ti-Hf-O mixed oxide region were beyond the capability of the Cameca SX 100 microprobe, the WDS anlaysis of these regions reported in Table 44 should be treated with caution. It does, however, offer an indication to the elements present. In these regions (Figure 129f) it is reasonable to assume the brighter white phase was a Hf-based oxide, possibly HfO_2, while the grey phase that has similar contrast to the large Ti/Cr-niobate grain is a niobate. As SiO_2 was indexed for low intensity peaks of the diffractogram it may arguably have formed in these Nb-Si-Ti-Hf-O mixed oxide regions as they contained the highest Si content.

The Hf based oxide in the oxide scale may actually be $HfSiO_4$ (hafnon), accounting for the Si and Hf content recorded in Table 44. Hafnon does not form in nature but can be formed by reacting HfO_2 + SiO_2 at high temperatures (1400 - 1500°C) for approximately 18 h (Salt and Hornung, 1967). This temperature range is beyond that studied here, however Ti was reported by Hoppe et al., (2013) to catalyse $HfSiO_4$ formation, thereby reducing the formation temperature to 900°C (note that the authors used a hold time of 192 h in their experiments). Glassy Ti-silicate $TiSiO_4$ is a required prerequisite compound formed by Ti + SiO_2 → $TiSiO_4$ finally followed by the reaction HfO_2 + $TiSiO_4$ → $HfSiO_4$ + TiO_2. The Nb-Si-Ti-Hf-O mixed oxide region is thus tentatively identified as a mixture of Niobate + SiO_2 + HfO_2 + $HfSiO_4$.

The oxidation of Ti and Hf rich γNb_5Si_3 would release Nb, Si, Ti, and Hf into the oxide scale, making such elements available to react as described above to form $HfSiO_4$. Hence, discrete SiO_2 would be present. The TiO_2 formed in this way may further react with Nb and Cr resulting in niobate within these fine mixed regions. Note in the X-ray map of the 50h HT sample (Figure 131) much less oxidation of the silicide grains had occurred and consistently Nb-Si-Ti-Hf-O mixed oxide regions were less prevalent than in the 100h specimens. This reiterates the lower reactivity of the silicide and the requirement of its oxidation to release Nb, Si, Ti and Hf into the oxide scale. In summary, the oxide layering formed on both GB1-AC/HT after oxidation at 1200°C for 100h from outer to inner layer are:

TiO_2 || Cr-niobate || $(Ti,Cr)\text{-}Niobate_{coarse}$ + $(Niobate + HfO_2 + SiO_2 + HfSiO_4)_{fine}$

Table 44. WDS phase analysis of the oxide scale formed on GB1-HT-1200-100h.

Phase	Position	Nb	Si	Ti	Cr	Al	Hf	O
TiO_2	Outer layer	4.3 ± 1.2 6.2 - 3.1	1.1 ± 1.1 2.5 - 0.0	23.2 ± 2.1 25.1 - 19.8	3.9 ± 1.0 5.7 - 3.0	0.4 ± 0.1 0.6 - 0.3	0.5 ± 0.3 0.8 - 0.1	66.7 ± 0.5 67.4 - 66.0
Ti/Cr-niobate	Mid layer	10.4 ± 1.7 13.0 - 8.6	0.3 ± 0.6 1.5 - 0.0	10.4 ± 2.4 13.8 - 6.5	10.3 ± 1.6 12.6 - 7.5	0.2 ± 0.3 0.8 - 0.0	1.5 ± 0.4 2.2 - 1.1	66.8 ± 0.6 67.8 - 66.0
Nb-Si-Ti-Hf-O mixed oxide	Mid layer	10.1 ± 3.4 17.2 - 3.6	8.8 ± 3.0 13.1 - 2.8	6.0 ± 2.9 13.7 - 2.0	1.4 ± 1.6 6.9 - 0.0	0.4 ± 0.4 1.3 - 0.0	4.2 ± 1.5 7.5 - 0.7	69.1 ± 1.2 71.5 - 65.9

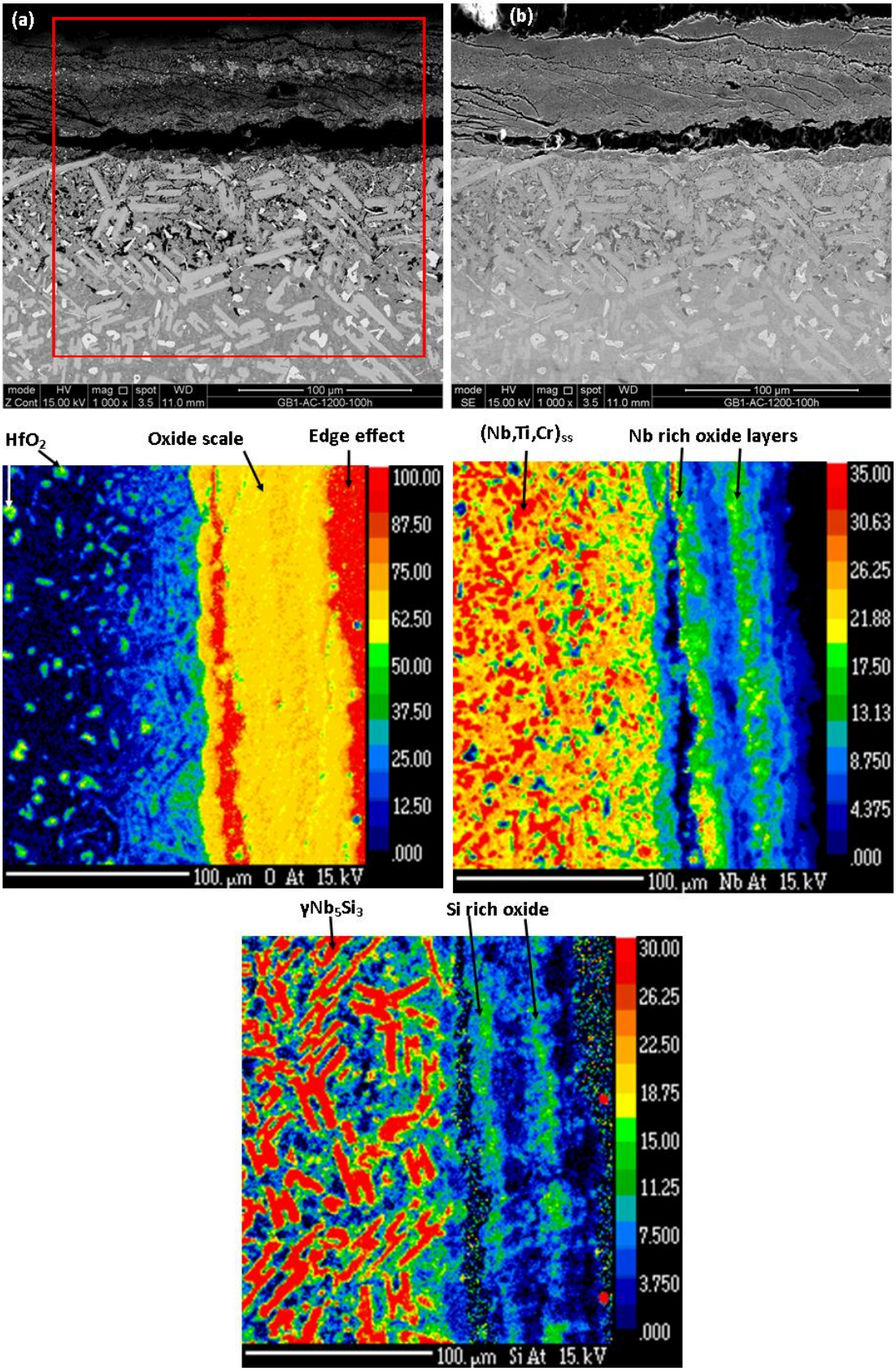

Figure 123. SEM images and WDS X-ray maps of the GB1-AC-1200-100h specimen. (a) BSE-SEM image where the mapped region corresponds to the red box. (b) SE-SEM image of (a). The O, Nb and Si X-ray maps are labelled respectively, see Figure 124 for the Ti, Cr, Al and Hf maps.

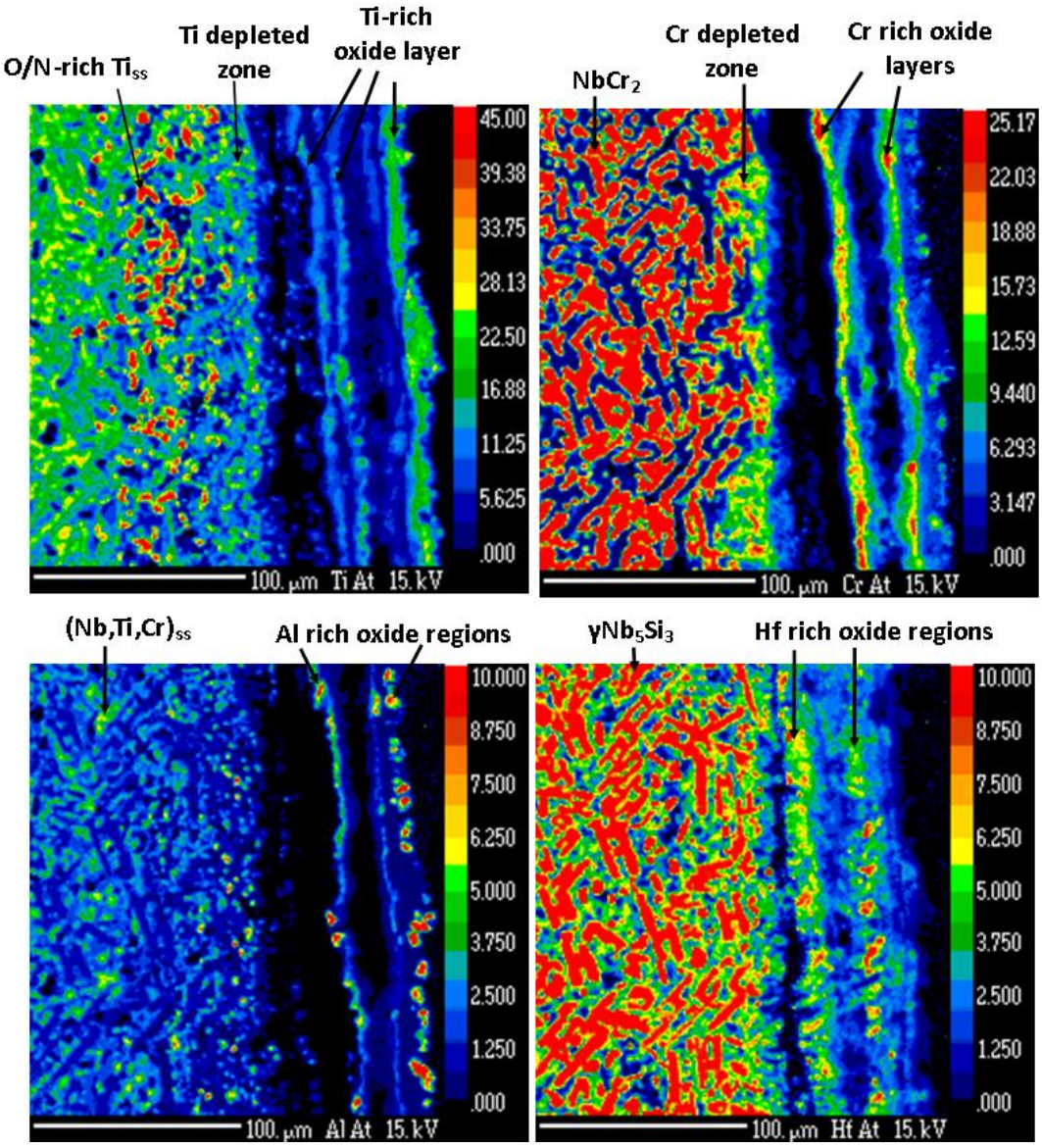

Figure 124. The Ti, Cr, Al and Hf WDS X-ray maps of the GB1-AC-1200-100h specimen for the region depicted in Figure 123.

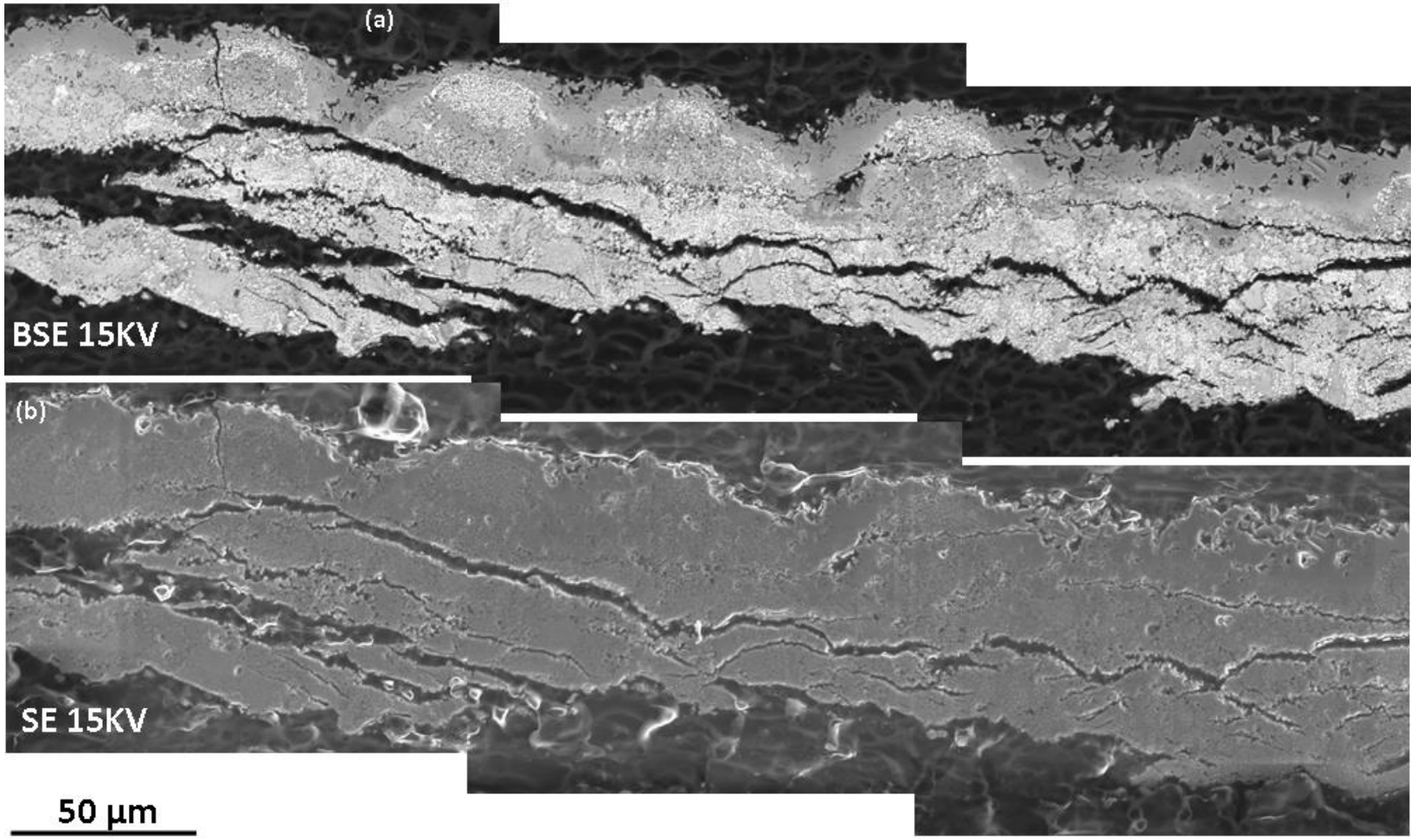

Figure 125. SEM images of the WDS X-ray mapped region of the GB1-HT-1200-100h oxide scale. (a) BSE image, (b) SE image. In the images the top edge of the scale is the outer oxide edge. For element maps see Figure 126.

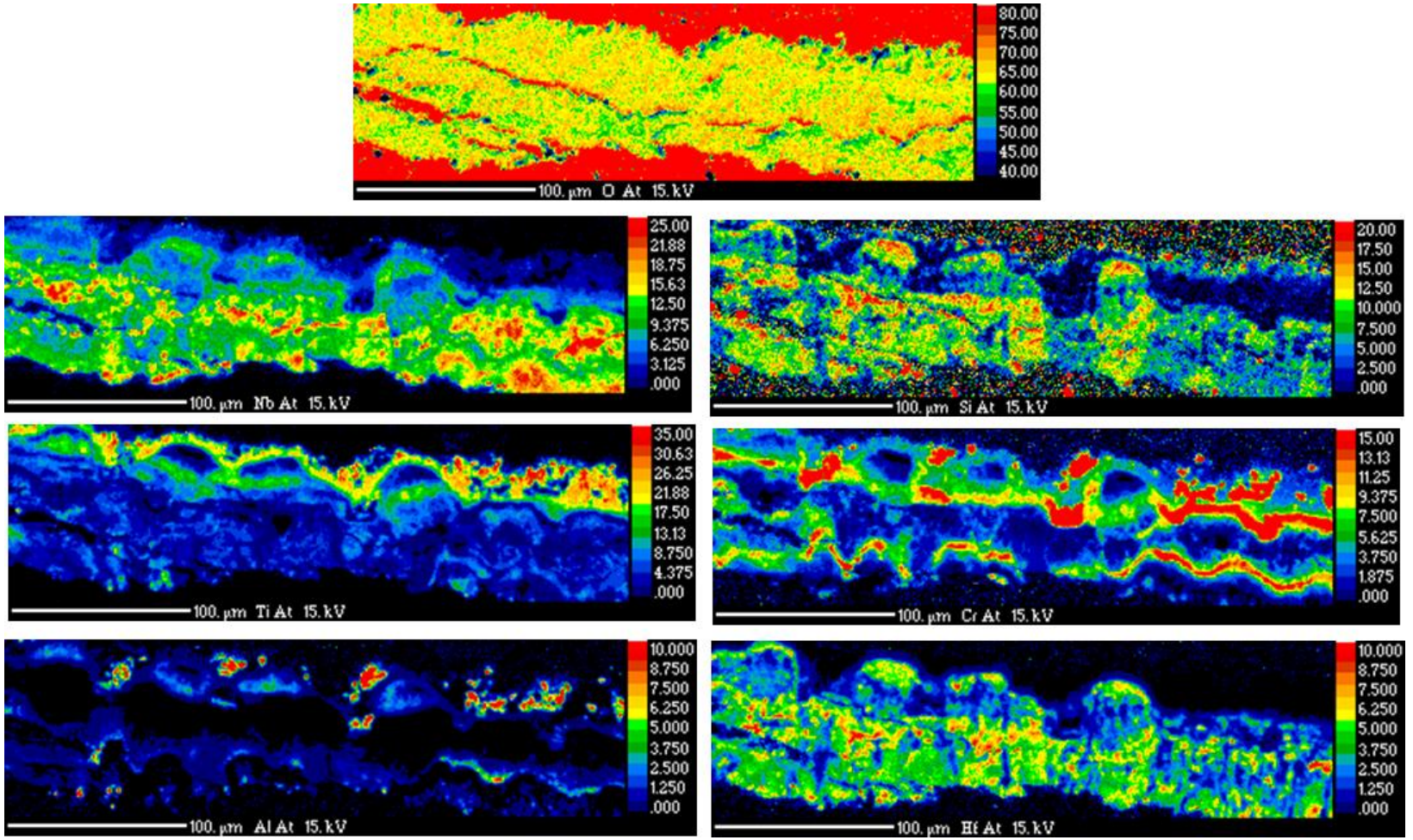

Figure 126. The O, Nb, Si, Ti, Cr, Al and Hf WDS element X-ray maps for the GB1-HT-1200-100h oxide scale. In the images the top edge of the scale is the outer oxide edge. For SEM images of the region analysed see Figure 125.

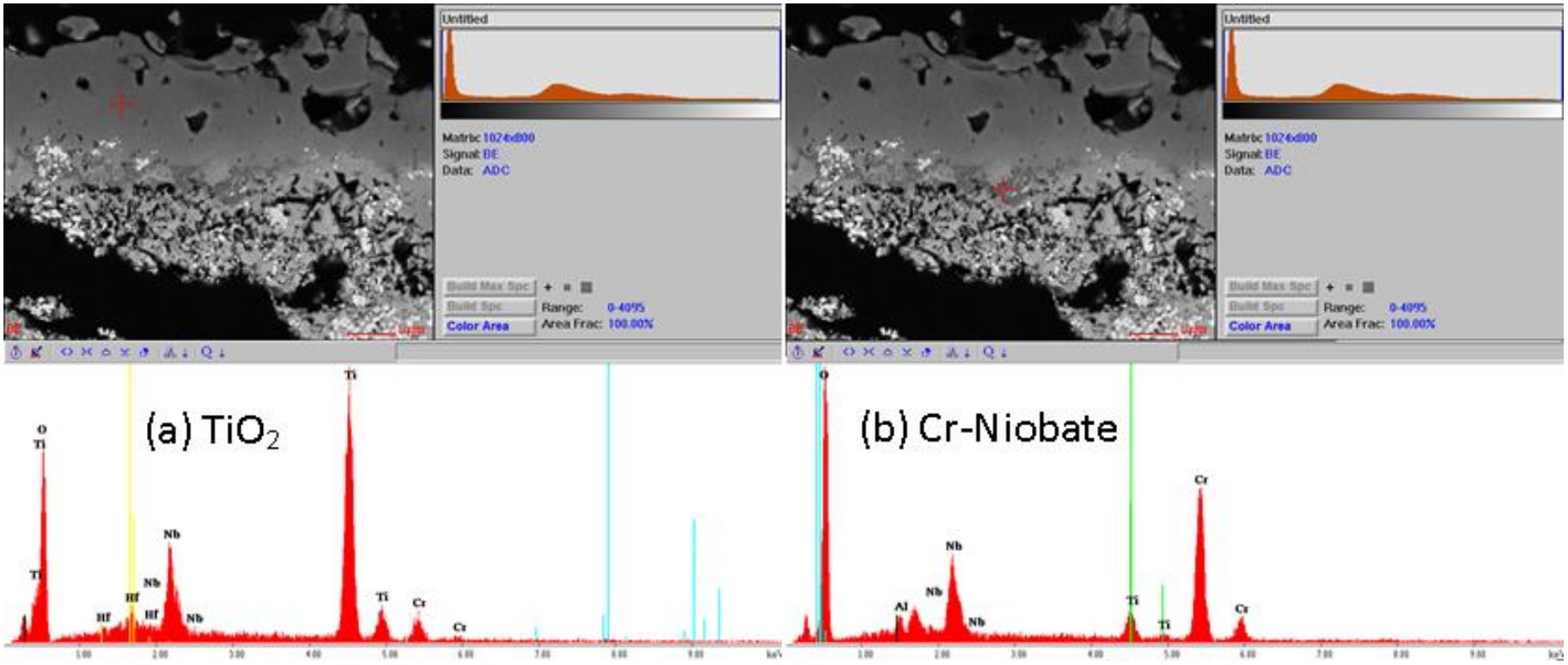

Figure 127. Qualitative EDS spectra of the oxide scale formed on the GB1-HT-1200-100h specimen, analysed using the FEI InspectF FEG SEM. (a) Outer TiO_2 layer with some Nb content and (b) a thin Cr-niobate underlying layer was identified.

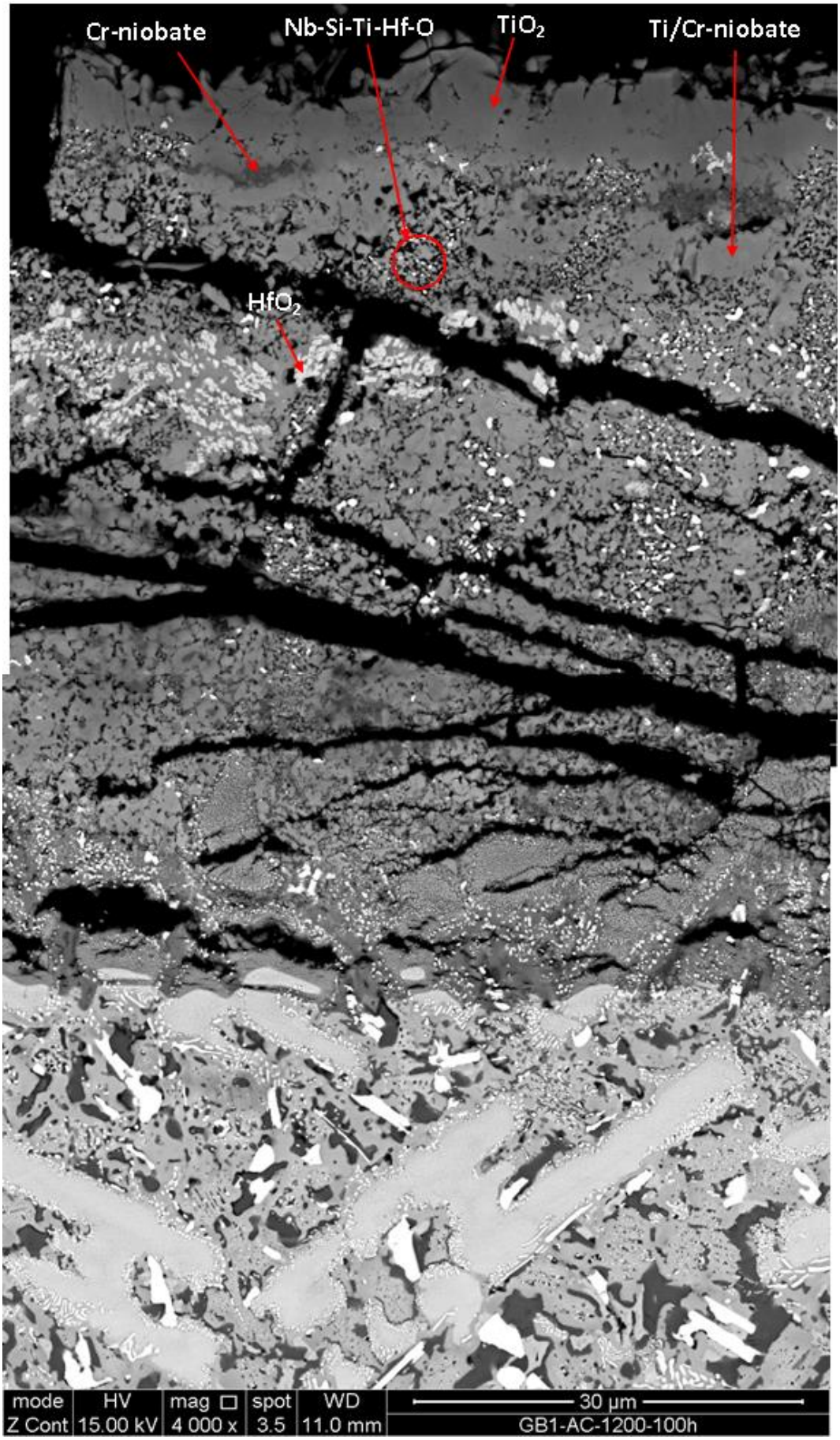

Figure 128. BSE image of the oxide scale formed on the GB1-AC-1200-100h specimen.

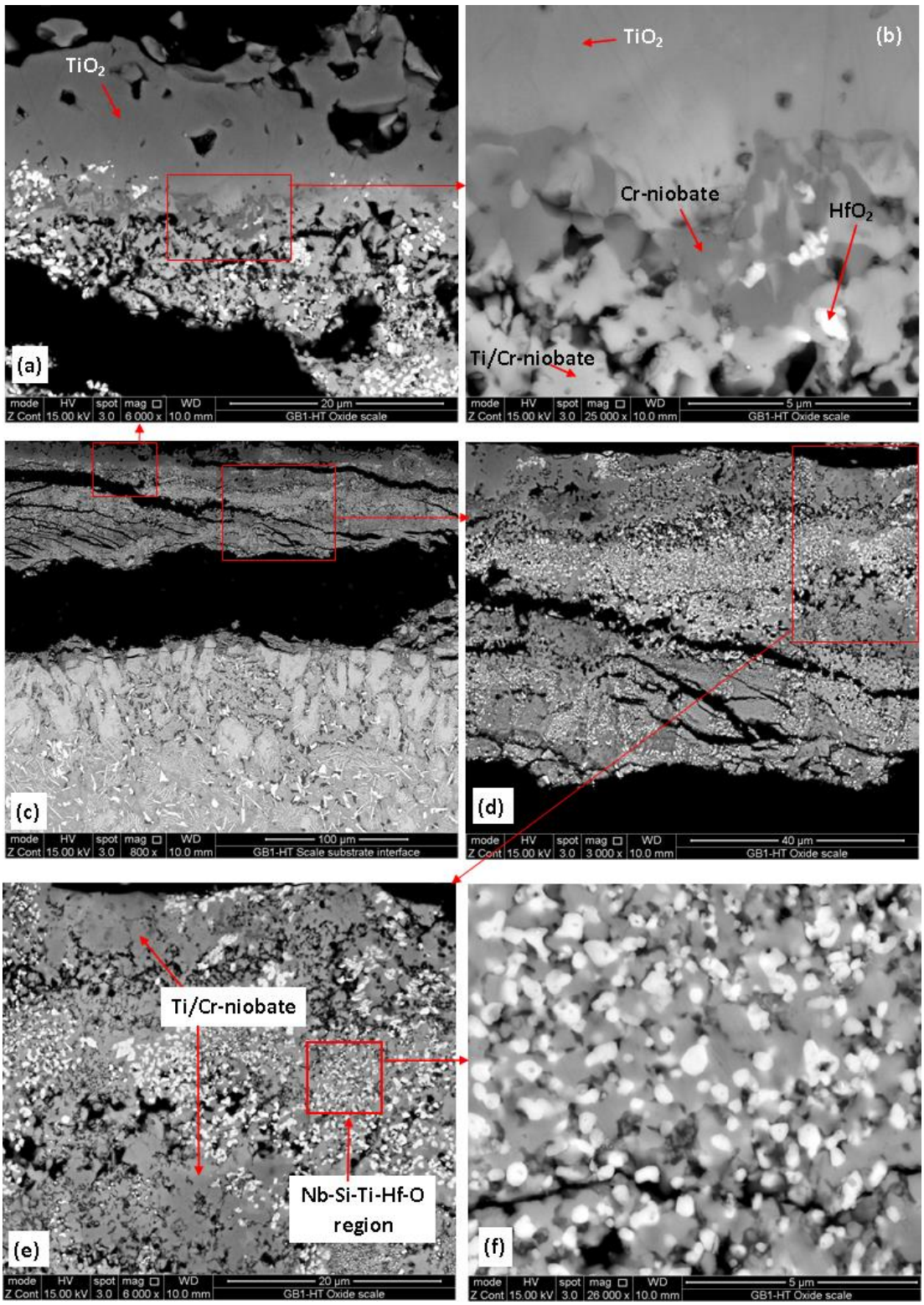

Figure 129. BSE images of the oxide scale formed on the GB1-HT-1200-100h specimen. (a) Depiction of the dense TiO_2 outer oxide layer. (b) Close up of the thin Cr-niobate layer underneath the TiO_2, showing a darker contrast. (c) Low magnification overview of the specimen denoting the locations of image (a) and (d). (d) Depiction of (e) a mid-layer region which is comprised of larger Ti/Cr-niobate grains and the Nb-Si-Ti-Hf-O mixed oxide. (f) Magnification of the Nb-Si-Ti-Hf-O mixed oxide showing multiple contrasts suggested to be a mixture niobate, SiO_2, HfO_2 and/or $HfSiO_4$.

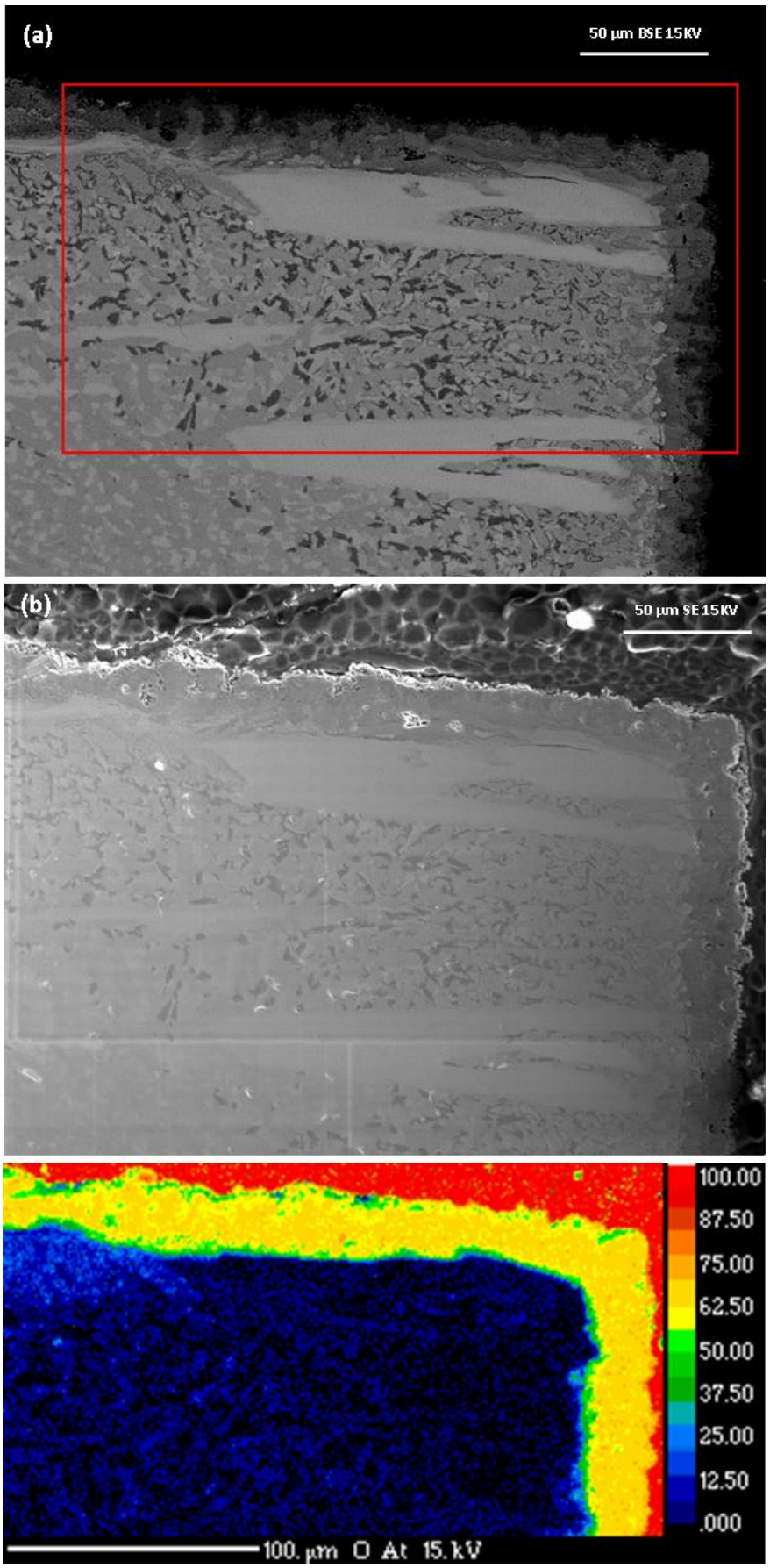

Figure 130. WDS X-ray mapping of the GB1-HT-1200-50h specimen. (a) BSE-SEM image, the red box indicates the mapped area, and (b) SE image. The O map is labelled and shown here, for the Nb, Si, Ti, Cr, Al, and Hf maps see Figure 131.

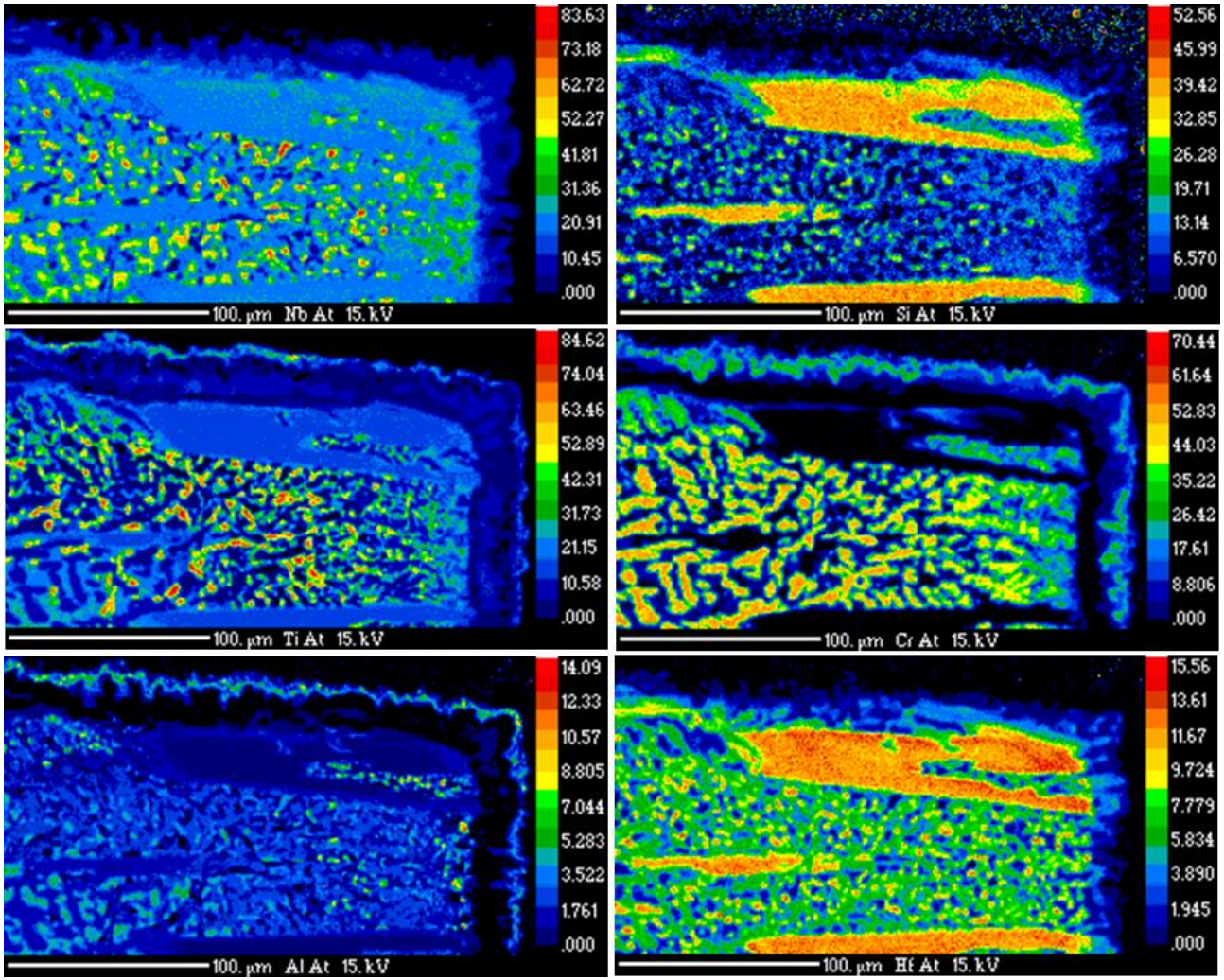

Figure 131. WDS X-ray maps for the GB1-HT-1200-50h specimen. See Figure 130 for SEM images of the mapped region.

5.4.4 Alloy GB2: Kinetics & Internal Microstructure

The TGA test runs were performed for alloy GB2 at 1200°C for 100h, two for the AC condition and one for the HT condition. The oxidation behaviour for all specimens was parabolic, or as previously mentioned should more adptly be described as para-linear, alike alloy GB1, since no complete passivation was achieved. For the AC tests, Run1 showed a noticeable drop in K_p from $4x10^{-10}$ in the first 37h to $1x10^{-10}$ g^2 cm^{-4} s^{-1} for the remaining 63h of the test. Run2 had a K_p= $5x10^{-10}$ g^2 cm^{-4} s^{-1} for the entire test duration and, hence, had an overall higher weight gain of 13.9 mg/cm^2 compared with that of 8.9 mg/cm^2 by Run1. The 100h HT specimen had a K_p of $1x10^{-10}$ g^2 cm^{-4} s^{-1} with a maximum weight gain of 6.2 mg/cm^2. The repeat runs convey minor fluctuation in K_p and overall weight gain but the important fact is that the overall power of the K_p values were the same. Refer to Figure 112 for the TGA plot and Table 26 for summary of GB2 rate constants. Table 27 and Table 28 present rate constants reported for various Nb-silicide based alloys and Ni-based superalloy CMSX-4 for comparison.

Alloy GB2 showed internal oxidation with the formation of white and black precipitates, like alloy GB1, that were again identified as HfO_2 and O/N-rich Ti_{ss} respectively (Figure 132 and Table 45). Quantitative WDS data is only presented for the O/N-rich Ti_{ss} analysed from the GB2-AC-1200-100h condition (Table 45) and reports an O content of 8.8 and 12.6 at.%, which is much lower than the 16.9 at.% found in GB1-AC-1200-100h. This low content of O is further evidence that the precipitate cannot be TiO or TiO_2, and due to the arguable detection of N by standardless EDS (see Figure 132 and as was discussed in section 5.4.2), the O/N-rich Ti_{ss} identification was also applied to the internal black precipitates of alloy GB2 after oxidation at 1200°C for 100h. Figure 133 and Figure 134 present an overview of the oxidised AC and HT specimen microstructures. Compared with the alloy GB1, GB2 appeared to suffer less internal oxidation, although the depth of HfO_2 and O/N-rich Ti_{ss} formation was virtually the same. The HfO_2 formation in GB2 was deeper than the O/N-rich Ti_{ss} with a maximum depth of ~300µm in all oxidised GB2 samples, which is significantly less than the ~400µm depth found in alloy GB1.

Table 47 compares the GB2-HT and GB2-HT-1200-100h phase data for grains analysed within or outside the BPDZ, as was done for alloy GB1. The comparison of these data would suggest $NbCr_2$ is acting as a Ti source for oxide scale and/or O/N-rich Ti_{ss} precipitate formation, while the significant reduction of Nb from the $(Nb,Ti,Cr)_{ss}$ suggests the diffusion and use of Nb at the substrate surface for oxide scale formation. As was the case for alloy GB1 (Table 43), it is logical to assume that Ti had also diffused from $(Nb,Ti,Cr)_{ss}$ in the BPDZ from alloy GB2.

The GB2-AC/HT microstructures, like GB1, possessed a disconnected $(Nb,Ti,Cr)_{ss}$ where the $NbCr_2$ may be acting as an internal diffusion barrier, isolating $(Nb,Ti,Cr)_{ss}$ grains, preventing O

access (Figure 133d,f). Inevitably, the $(Nb,Ti,Cr)_{ss}$ was oxidised (Figure 134f) but notably surrounded by $NbCr_2$, which showed appreciable signs of oxidation. The oxidative attack after 100h did affect the βNb_5Si_3 silicide, as had occurred for the γNb_5Si_3 of GB1, specifically for grains caught in the BPDZ (Figure 135). The βNb_5Si_3 suffered less grain boundary HfO_2 formation than γNb_5Si_3, likely due to lower Hf content.

The GB2-HT-1200-50h microstructure (Figure 136) displays an oxide scale that fluctuates in thickness, peaking at ~55µm. The BPDZ formation depth is only slightly shallower at ~75µm than the ~90-100µm for the 100h specimens. The 50h specimen's BPDZ was visibly less severe (Figure 136e,d). Oxidative attack of βNb_5Si_3 in the 50h oxidised speicmen was only found for grains at the substrate-scale interface despite many grains residing in the shallower BPDZ. Figure 136(f) shows an example silicide grain displaying the aforementioned HfO_2 and O/N-rich Ti_{ss} formation but also reveals sub-grain boundary formation within the grain and additional phase formations emenating at grain boundaries that at this stage of analysis are unidentified. TEM was used to investigate these microstructural features, the results of which are discussed later in section 5.5.

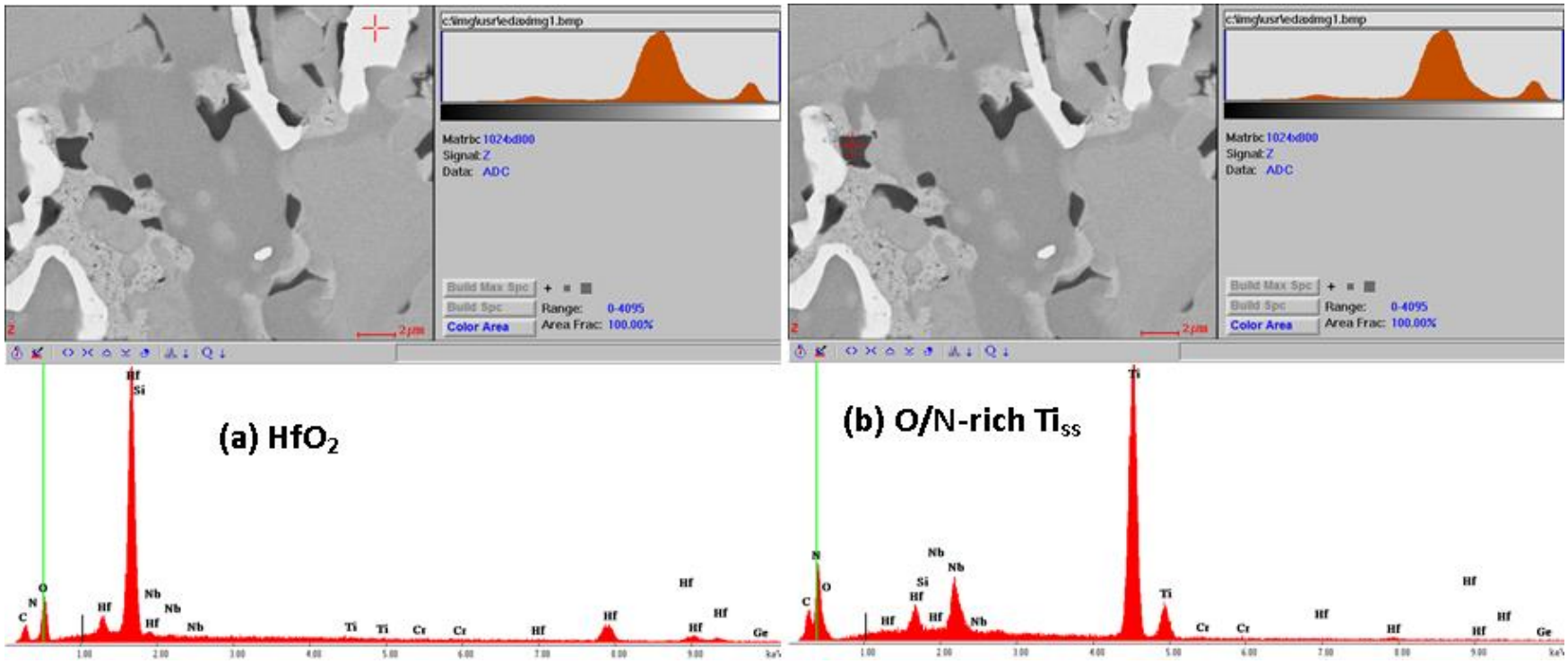

Figure 132. Standardless EDS using the FEI InspectF high resolution SEM. (a) HfO_2 and (b) O/N-rich Ti_{ss} are identified.

Table 45. WDS phase analysis in at.% for GB2-AC-1200-100h. Depth of analysis from the substrate surface is indicated. Note the distinction between analysis taken inside or outside of the BPDZ.

Phase	In/Out BPDZ	Depth (µm)	Nb	Si	Ti	Cr	Ge	Hf	O
βNb_5Si_3	In	15-50	37.2 ± 1.0	34.6 ± 1.5	10.7 ± 0.4	2.9 ± 0.1	6.8 ± 0.2	2.7 ± 0.1	5.0 ± 2.8
			38.3 - 35.0	36.1 - 32.2	11.4 - 10.1	3.0 - 2.7	7.0 - 6.4	2.8 - 2.5	10.8 - 2.5
	Out	80-150+	39.1 ± 0.6	27.9 ± 4.4	15.1 ± 2.0	2.9 ± 0.5	7.2 ± 0.3	3.8 ± 1.0	4.1 ± 1.3
			40.1 - 38.4	34.9 - 23.9	16.6 - 11.4	3.7 - 2.2	7.8 - 6.9	4.5 - 2.4	5.4 - 2.3
$NbCr_2$	In[a]	60-75	25.7 ± 0.3	7.0 ± 0.5	6.1 ± 0.2	55.0 ± 1.2	1.7 ± 0.4	2.5 ± 0.3	2.0 ± 0.8
			25.9 - 25.4	7.4 - 6.4	6.2 - 5.9	56.3 - 54.0	2.1 - 1.4	2.8 - 2.3	2.6 - 1.1
	Out	100-200	24.2 ± 0.8	5.8 ± 2.9	10.0 ± 1.7	54.1 ± 3.6	1.3 ± 0.6	2.7 ± 0.6	2.0 ± 0.6
			25.9 - 23.2	12.5 - 2.6	12.4 - 8.0	58.3 - 44.4	2.8 - 0.8	4.1 - 2.1	3.3 - 1.2
$(Nb,Ti,Cr)_{ss}$	Out	100-125	64.0 ± 0.8	0.0 ± 0.0	22.5 ± 0.7	7.8 ± 0.4	0.8 ± 0.1	0.4 ± 0.2	5.1 ± 1.0
			64.6 - 62.5	0.0 - 0.0	23.5 - 21.9	8.2 - 7.2	1.0 - 0.7	0.7 - 0.3	6.3 - 4.0
O/N-rich Ti_{ss}	In	n/a	9.8	0.0	78.7	0.6	0.2	1.8	8.8
			4.4	0.0	81.1	0.4	0.2	1.3	12.6

[a]: 3 analysis

Table 46. WDS phase analysis in at.% for GB2-HT-1200-100h. Depth of analysis from the substrate surface is indicated. Note the distinction between analysis taken inside or outside of the BPDZ.

Phase	In/Out BPDZ	Depth (µm)	Nb	Si	Ti	Cr	Ge	Hf	O
βNb_5Si_3	In	5 - 60	37.6 ± 1.2	32.1 ± 1.7	14.6 ± 0.5	2.8 ± 0.7	6.7 ± 0.2	2.6 ± 0.7	3.6 ± 1.3
			39.2 - 36.1	34.4 - 28.9	15.7 - 13.6	3.9 - 1.4	7.2 - 6.2	3.3 - 1.8	6.5 - 2.1
	Out	100 - 250	36.4 ± 5.1	31.8 ± 1.6	17.1 ± 4.9	2.5 ± 1.1	7.0 ± 0.8	2.7 ± 0.9	2.6 ± 0.3
			39.0 - 26.0	33.8 - 30.1	27.0 - 14.2	4.1 - 1.1	8.6 - 6.4	4.0 - 1.9	2.8 - 1.9
$NbCr_2$	In	40 - 90	28.7 ± 0.4	10.4 ± 2.7	4.0 ± 1.5	49.8 ± 3.4	2.3 ± 0.7	2.5 ± 0.7	2.3 ± 0.7
			29.1 - 28.0	13.3 - 6.3	6.4 - 2.2	55.9 - 46.8	3.1 - 1.1	3.2 - 1.5	3.5 - 1.4
	Out[a]	250+	23.2 ± 0.2	8.3 ± 0.2	11.2 ± 0.2	51.4 ± 0.9	1.1 ± 0.1	3.1 ± 0.1	1.8 ± 0.5
			23.5 - 23.0	8.6 - 8.1	11.4 - 10.9	52.3 - 50.1	1.2 - 0.9	3.2 - 3.0	2.3 - 1.3
$(Nb,Ti,Cr)_{ss}$	Out	250+	58.5	1.9	22.0	10.9	1.0	1.2	4.6
			54.3	4.7	23.4	8.2	2.5	2.4	4.5

[a]: 4 analysis.

Table 47. Compositional change in at.% of average GB2-HT Jeol EDS data against GB2-HT-1200-100h. Positive table values signify increase after oxidation, Negative table values signify decrease after oxidation.

Phase	In/Out BPDZ	Depth (µm)	Element difference to GB2-HT Jeol data						
			Nb	Si	Ti	Cr	Ge	Hf	O
βNb_5Si_3	In	5 - 60	-3.1	+2.2	-2.7	+1.2	-0.7	-0.4	+3.6
	Out	100 - 250	-4.3	+1.8	-0.2	+0.8	-0.3	-0.3	+2.6
$NbCr_2$	In	40-90	+3.1	+2.1	-7.3	-1.4	+1.2	+0.1	+2.3
	Out	250+	-2.5	+0.1	-0.1	+0.1	-0.1	+0.7	+1.8
$(Nb,Ti,Cr)_{ss}$	Out	250+	-6.7	+1.0	-1.2	+1.5	+0.4	+0.3	+4.6
		250+	-11.0	+3.9	+0.2	-1.1	+2.0	+1.5	+4.5

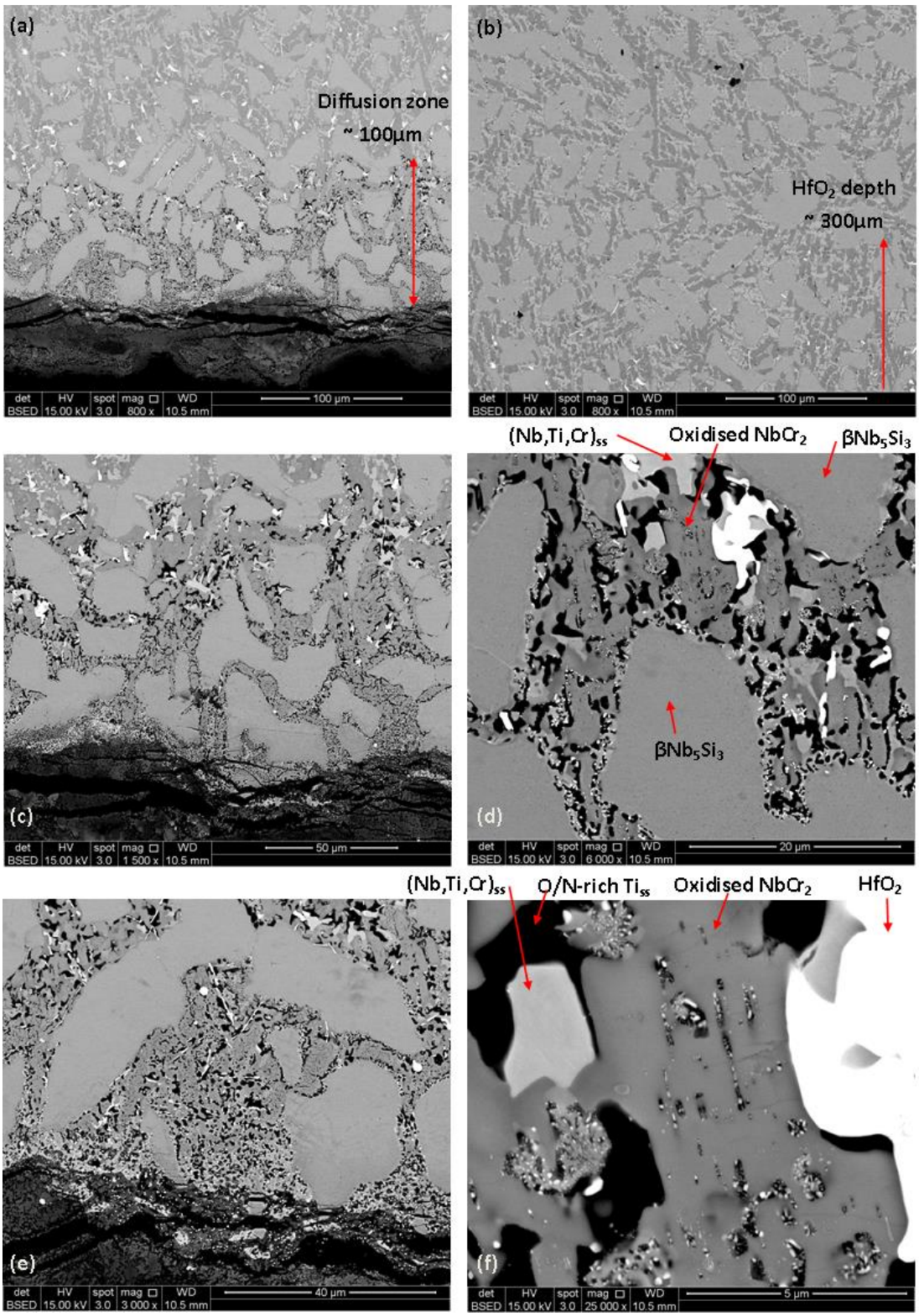

Figure 133. BSE images of the GB2-AC-1200-100h specimen microstructure. (a) Overview, (b) bulk microstructure overview continued from (a). (c-f) High magnification imaging of the internal oxidation products.

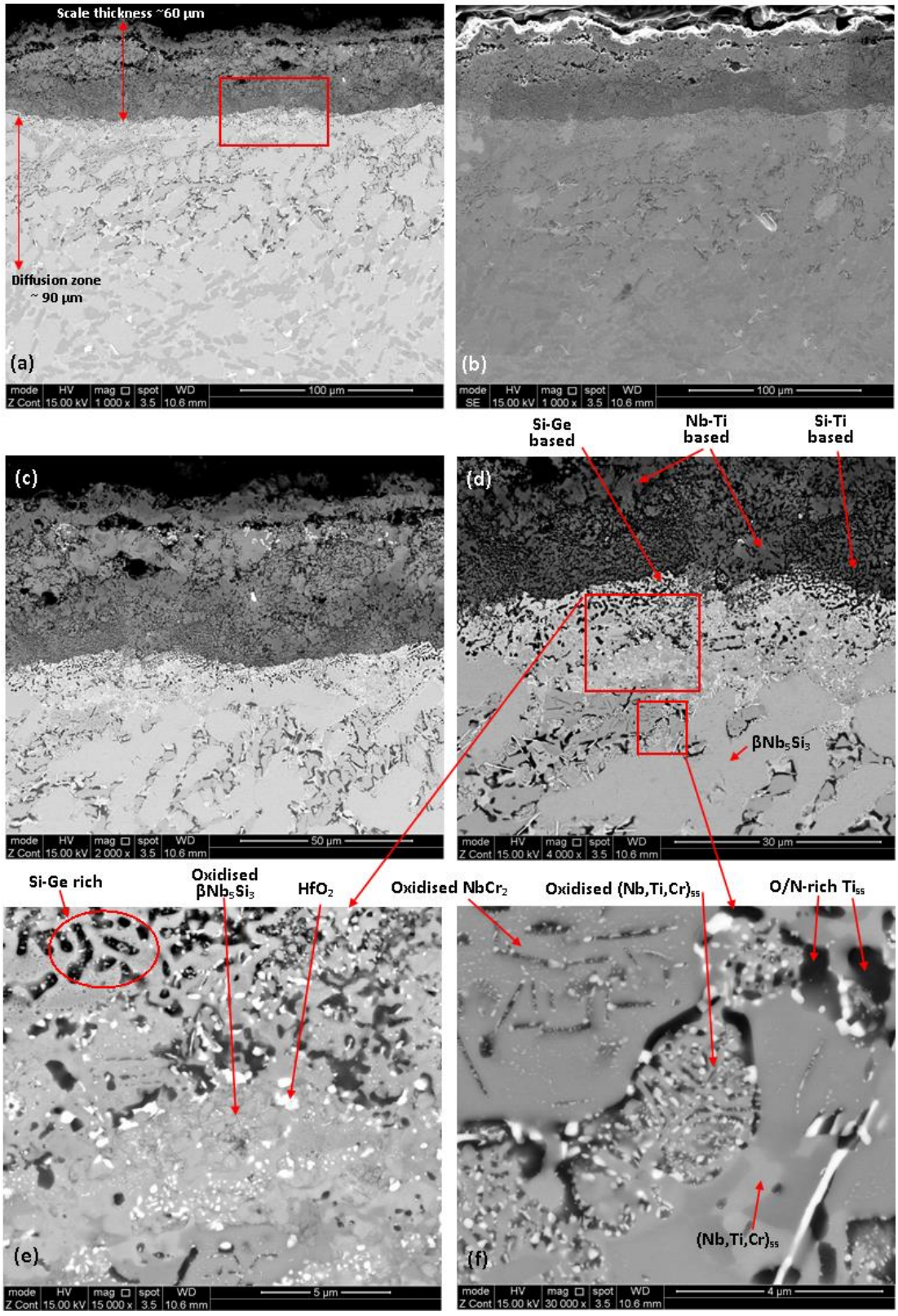

Figure 134. SEM images of the GB2-HT-1200-100h specimen microstructure. (a) BSE overview, (b) SE image of (a), (c) BSE image of the oxide scale, (d) annotated BSE image of the substrate edge and oxide scale, (e) BSE image of the oxidised substrate edge microstructure, (f) BSE image identifying oxidised $NbCr_2$, $(Nb,Ti,Cr)_{ss}$, and O/N-rich Ti_{ss}.

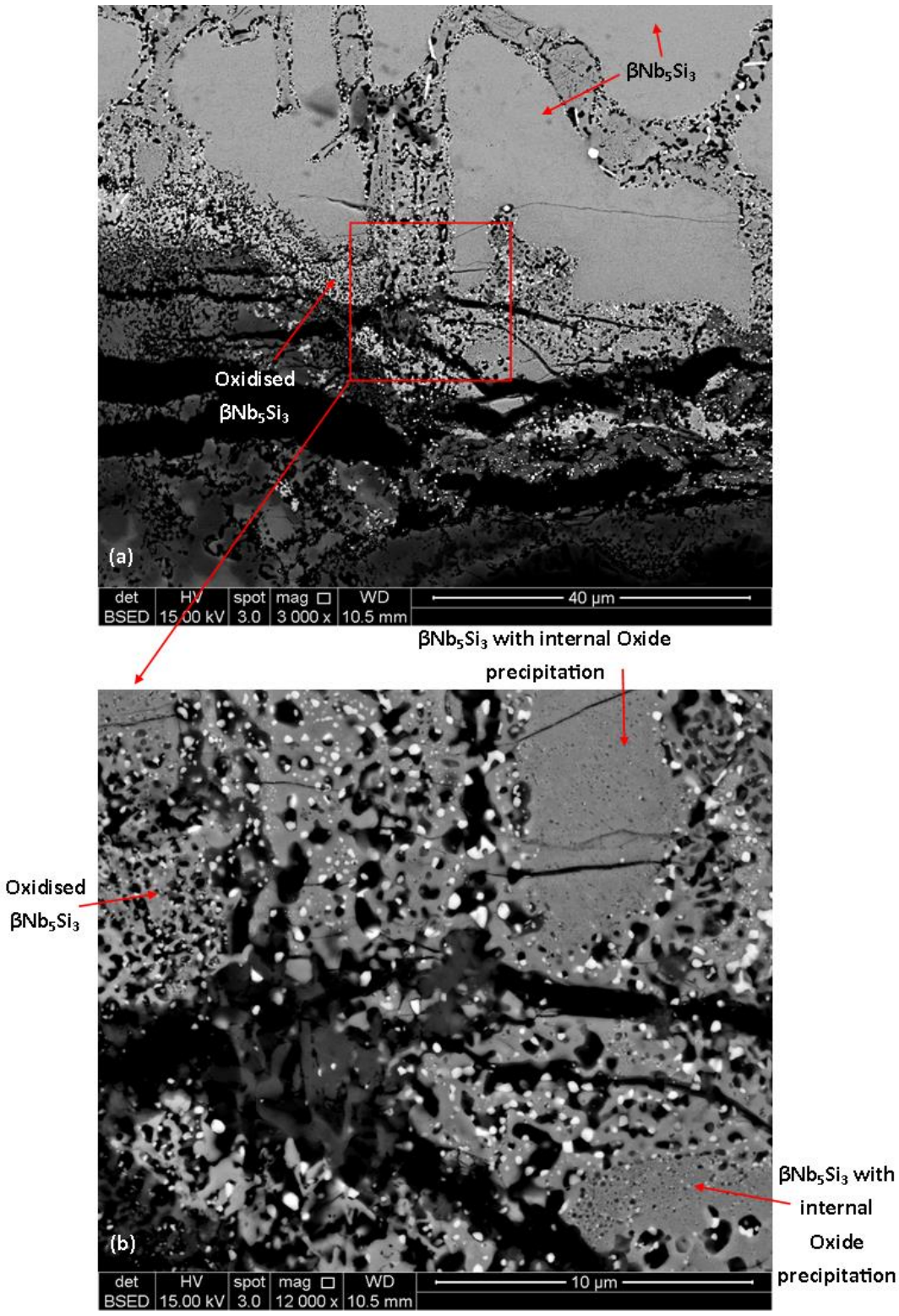

Figure 135. BSE images of a substrate-scale region showing the attack of a βNb_5Si_3 grain in the GB2-AC-1200-100h specimen. (a) Low magnification image of oxidative attack. (b) High magnification image illustrating the oxidation and consumption of the βNb_5Si_3 grains into the oxide scale. Internal precipitation is also apparent within the βNb_5Si_3 grain.

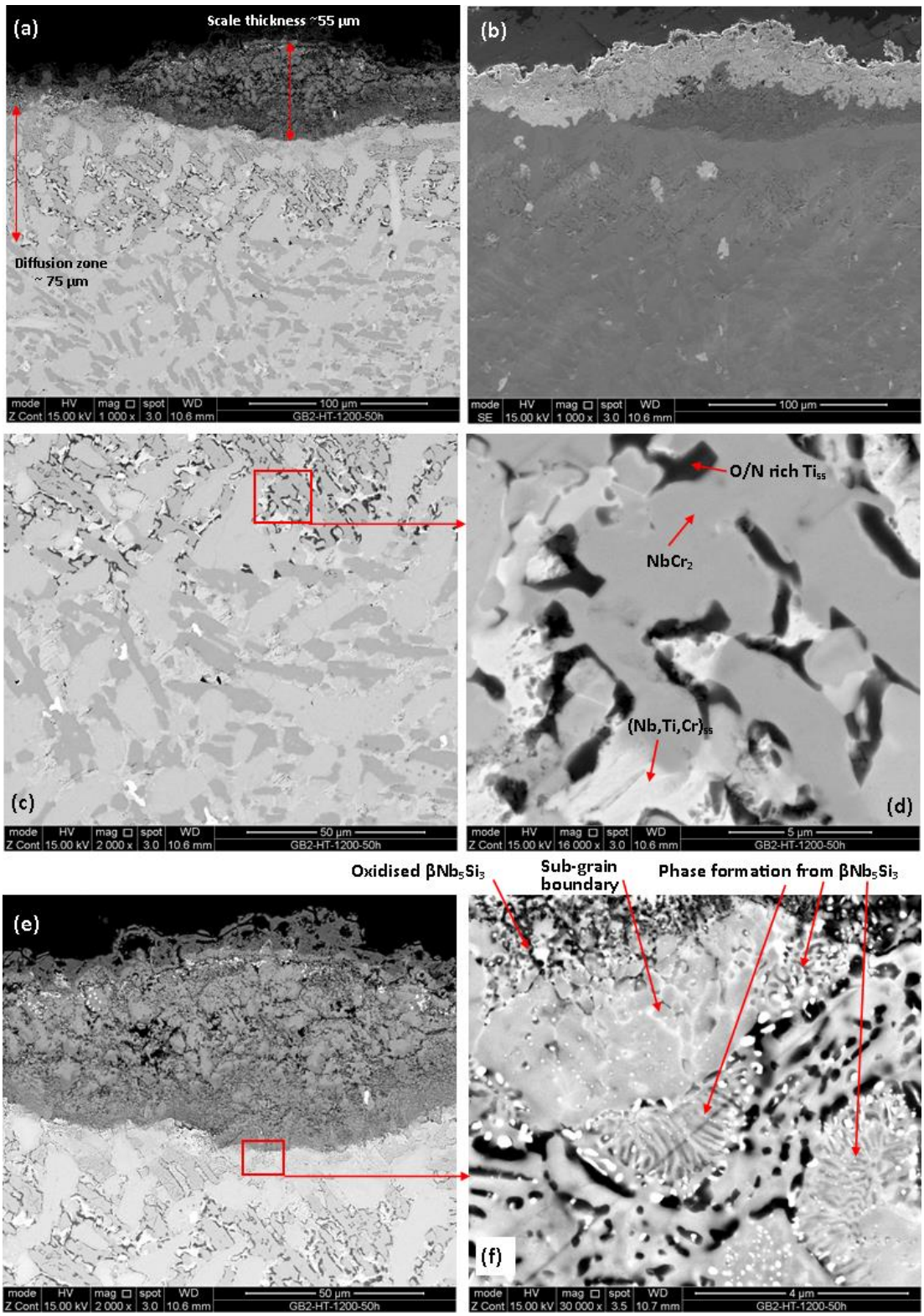

Figure 136. SEM images of the GB2-HT-1200-50h specimen. (a) BSE image overview of oxide scale and BPDZ depth, (b) SE image of (a). (c) BSE image overview of the internal microstructure, (d) magnified BSE image of the red boxed region from (c). (e) and (f) show the oxidative attack of a βNb_5Si_3 grain at the substrate-scale interface.

5.4.5 Alloy GB2: Oxide Scale

The PXRD patterns of the GB2 oxide scales at 1200°C presented very similar peaks to those of alloy GB1 (Figure 113). The major peaks were again identified as mixed Nb-Ti-Cr oxides; $CrTiNbO_4$, $TiNbO_4$, $CrNbO_4$, TiO_2, and $Ti_xCr_yNb_zO_2$, all of which possess a tetragonal crystal structure. As mentioned earlier, the mixed Nb-Ti-Cr oxides were difficult to decisively index due to their almost identical peak positions. Alloy GB2 also showed peaks for SiO_2, $HfSiO_4$, GeO_2, and $CrNb_{11}O_{29}$ but are susceptible to being overlapped and dwarfed by the stronger Nb-Ti-Cr niobate peaks.

The oxide scale formed on the AC and HT specimens at 1200°C are very similar, with subtle differences. The outer oxide layer was identified as a Cr/Ti-niobate on both the AC and HT specimens with notably much less Cr content in the AC specimen than the HT (see X-ray maps Figure 137, Figure 138, Figure 140, Figure 141, Figure 142 and WDS line scans Figure 143, Figure 144, Figure 145). WDS phase analysis was obtained for the HT specimen after 100h and 50h of oxidation (Table 48 and Table 49) and would corroborate the Cr-richness of the maps and line scans leading to an identity of the oxide as a Cr/Ti-niobate possibly $(Cr,Ti)NbO_4$ as there was still some Ti content detected.

Underneath the outer Cr/Ti-niobate layer, the mid-layer region formed a fine grained Nb-Si-Hf-O mixed oxide (Table 49), as was similarly found for alloy GB1 (section 5.4.3 and Table 44). By following the same argument as before, the Nb-Si-Hf-O mixed oxide is tentatively identified to be a fine mixture of niobate + SiO_2 + HfO_2 + $HfSiO_4$. Coarser niobate grains were found amongst the Nb-Si-Hf-O mixed oxide (see Figure 146, Figure 147, Table 49). A thin Cr-rich oxide layer with some Ti content was also found in the mid-layer (see Cr X-ray maps and WDS line scans), identified to be a (Cr/Ti)-niobate and again, possibly, $(Cr,Ti)NbO_4$. Although all the examples here show it, the (Cr/Ti)-niobate mid-layer was not always present in the oxide scale. Figure 148 provides an annotated overview of the oxide scale.

At the substrate-scale interface, a Nb-Si-Ge-O mixed oxide was detected, being particularly rich in Ge and Si (see Table 48, Table 49 and the Ge X-ray maps of Figure 138, Figure 139, Figure 140, and Figure 142). Upon closer inspection (Figure 149 and Figure 150), it was clear these Nb-Si-Ge-O mixed oxide regions ementated from the βNb_5Si_3, which is logical as it was rich in these elements and retained virtually all the Ge of the alloy. At this stage of analysis, it was inconclusive to identify the causes of sub-grain boundary and internal precipitate formation within the silicide.

As there was some uncertainty to the mid-layer oxide and substrate-scale interface, TEM was utilised to further investigate and is discussed in thesis section 5.5. At this stage of analysis, the oxide scale layering of alloy GB2 AC/HT after 50h+ of oxidation from outer to inner layer was identified as:

(Cr,Ti)-Niobate || $Niobate_{coarse}$ + $(Niobate + SiO_2 + HfO_2 + HfSiO_4)_{fine}$ || (Cr,Ti)-Niobate ||

$Niobate_{coarse}$ + $(Niobate + SiO_2 + HfO_2 + HfSiO_4)_{fine}$ || Nb-Si-Ge-$O_{substrate\text{-}oxide}$

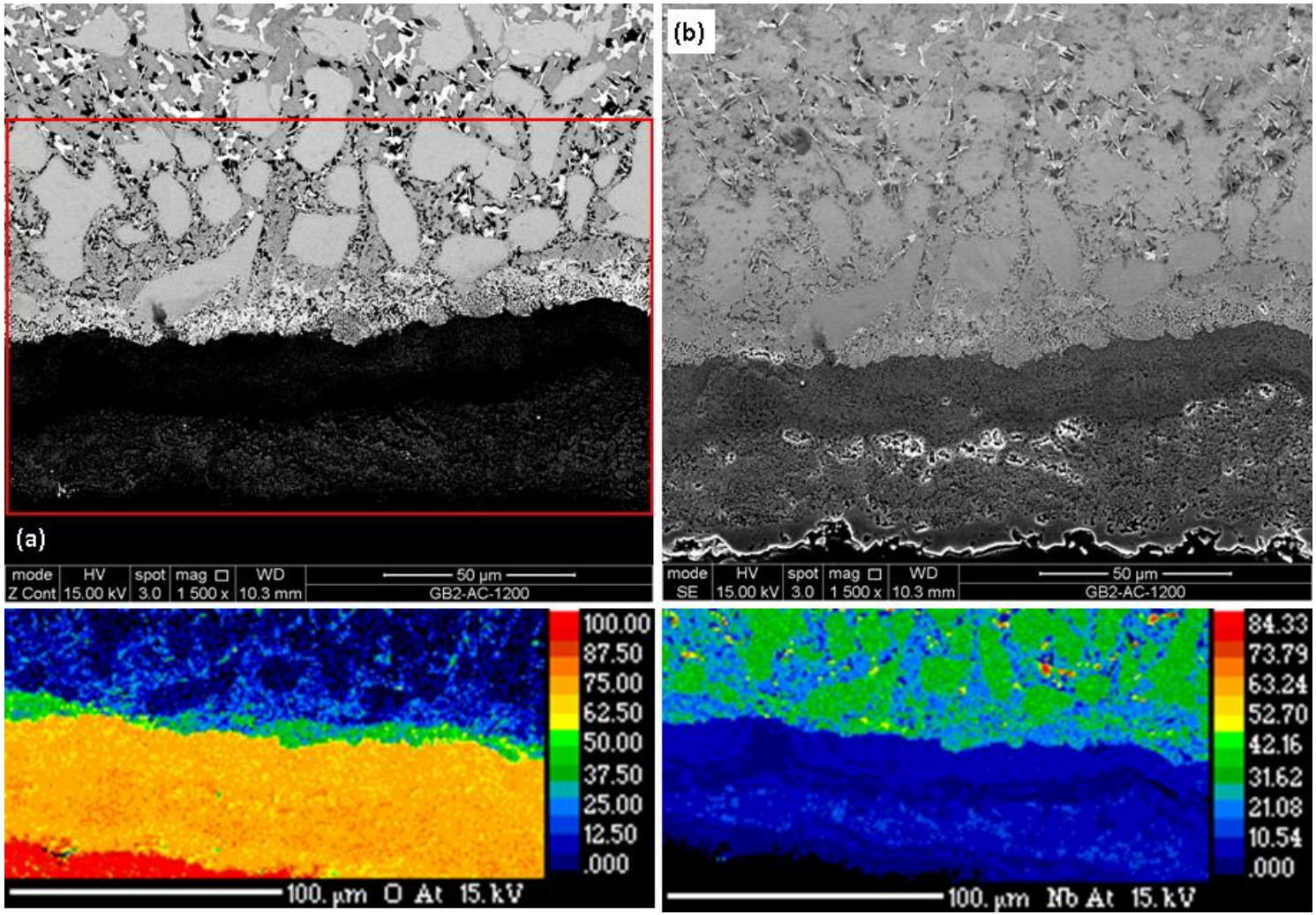

Figure 137. WDS X-ray mapped region of GB2-AC-1200-100h. (a) BSE-SEM image, the red box indicates the mapped area, (b) SE-SEM image of mapped area. The O and Nb are labelled respectively. See Figure 138 for the Si, Ti, Cr, Ge, and Hf maps.

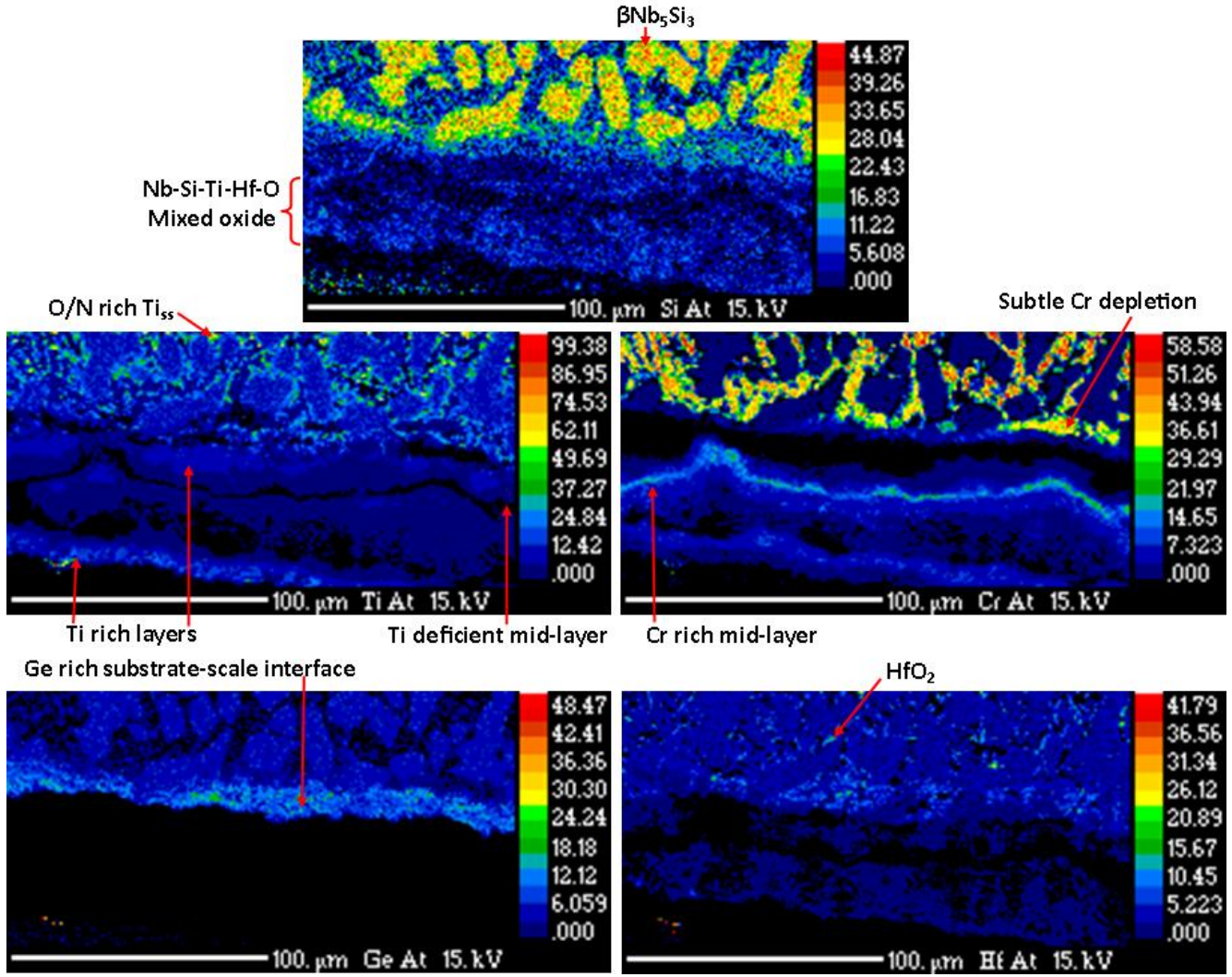

Figure 138. The Si, Ti, Cr, Ge, and Hf WDS X-ray maps for specimen GB2-AC-1200-100h for the area depicted in Figure 137. See such figure for the O and Nb maps.

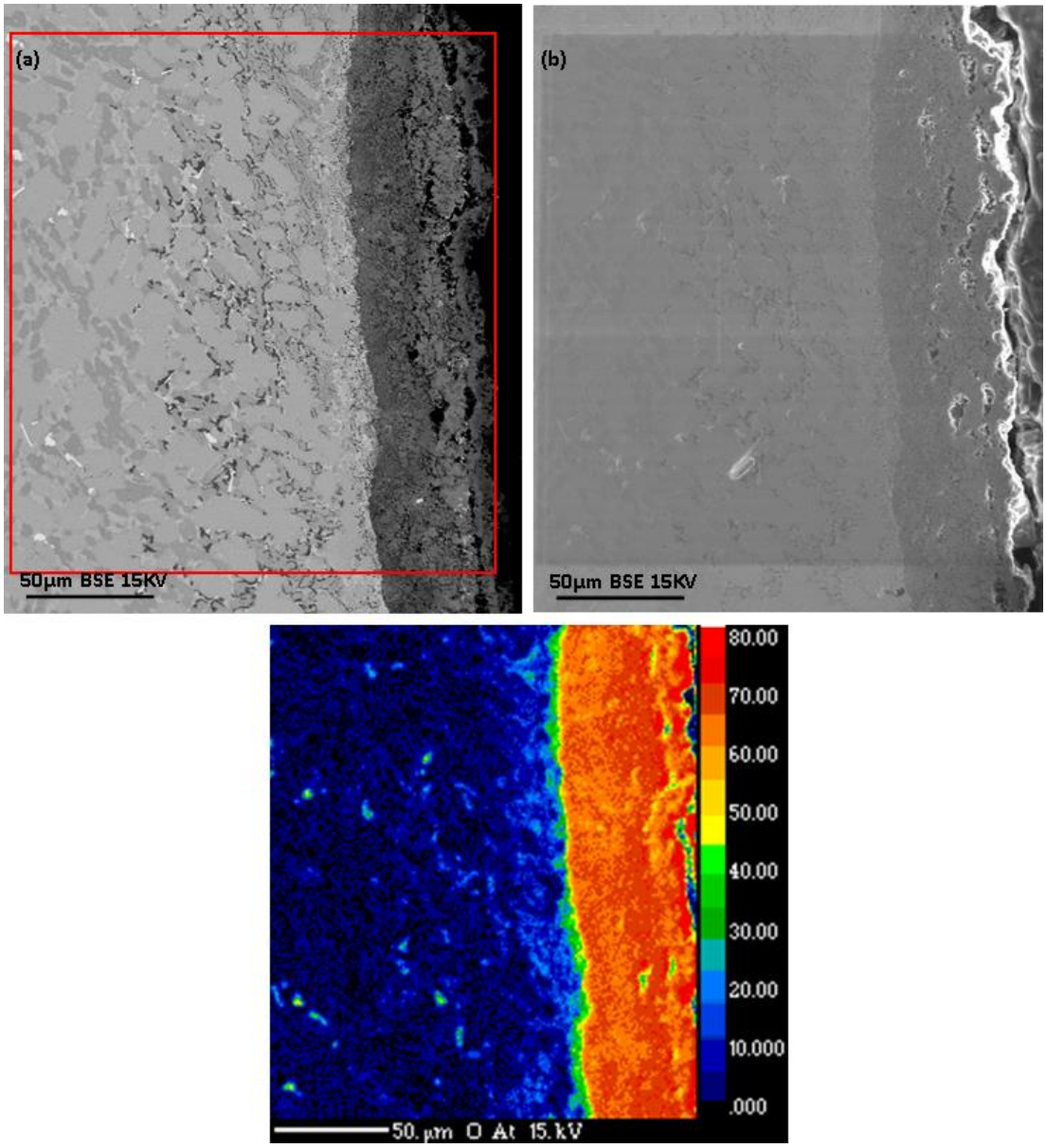

Figure 139. WDS X-ray mapped region of the GB2-HT-1200-100h specimen. (a) BSE-SEM image, the red box indicates the mapped area, (b) SE-SEM image of (a). The O map is labelled. See Figure 140 for the Nb, Si, Ti, Cr, Ge and Hf maps.

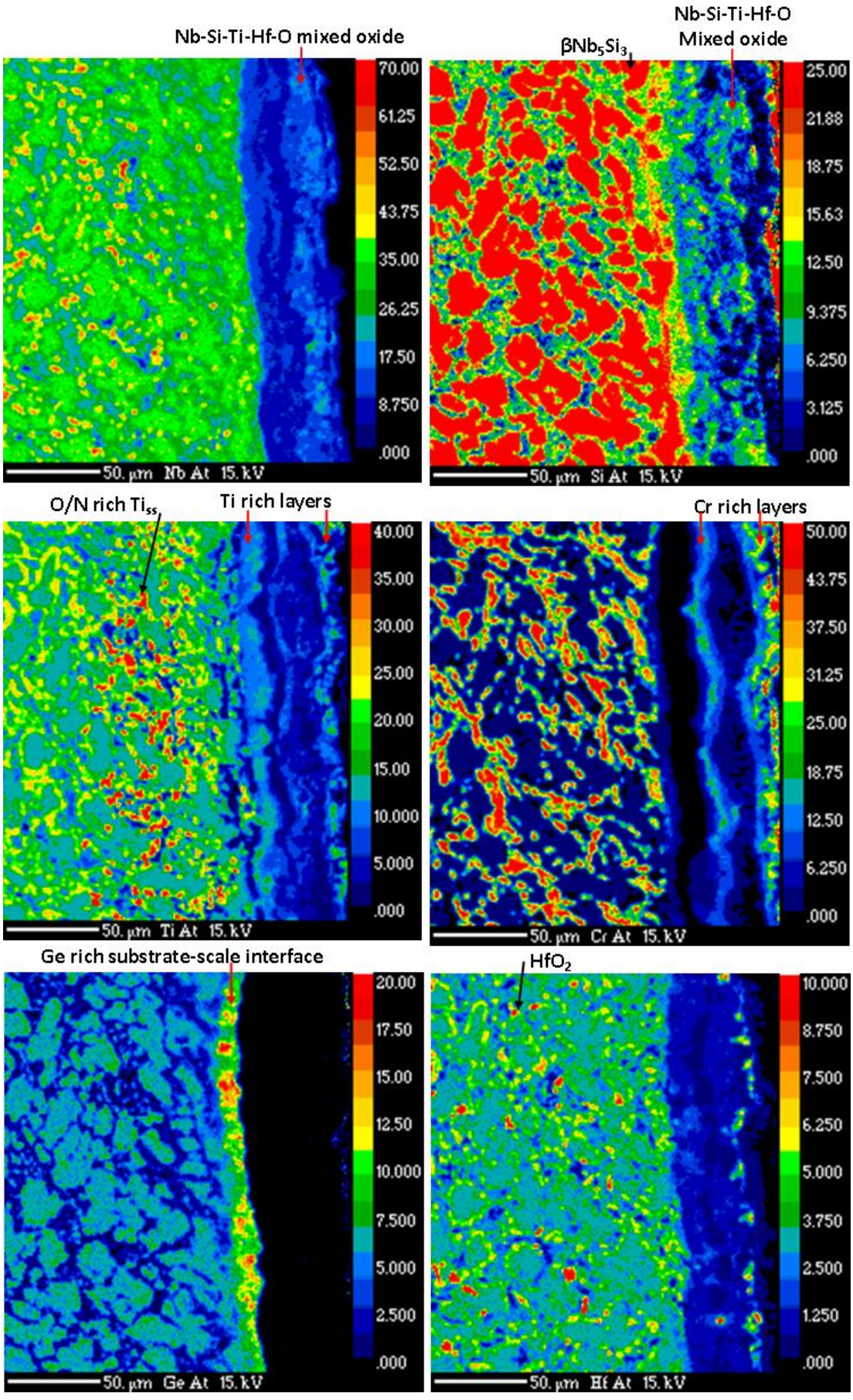

Figure 140. The Si, Ti, Cr, Ge, and Hf WDS X-ray maps of specimen GB2-HT-1200-100h for the area depicted in Figure 139. See such figure for the O and Nb maps.

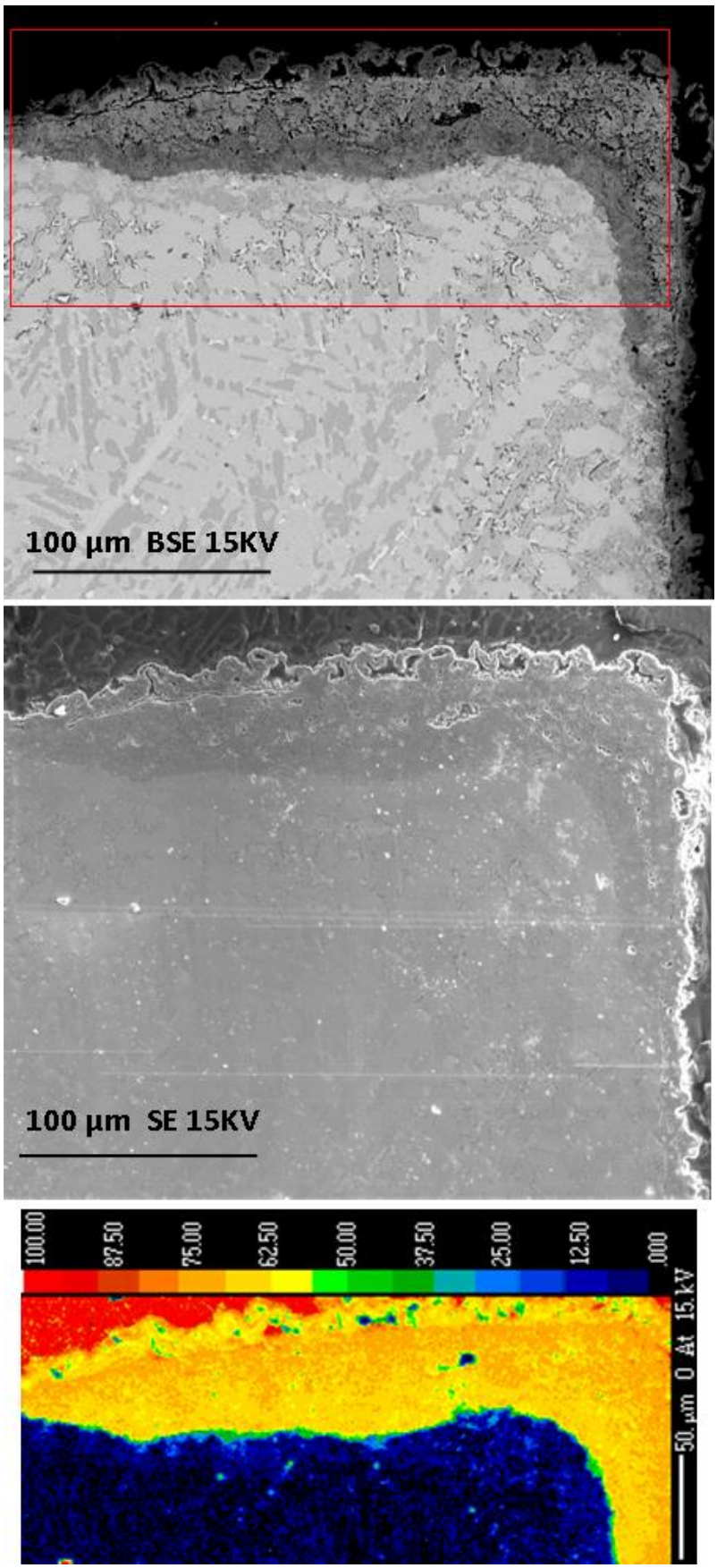

Figure 141. WDS X-ray map region of the GB2-HT-1200-50h specimen. (a) BSE-SEM image, the red box indicates the mapped area, (b) SE-SEM image of (a). The O X-ray maps is labelled. See Figure 142 for the Nb, Si, Ti, Cr, Ge and Hf maps.

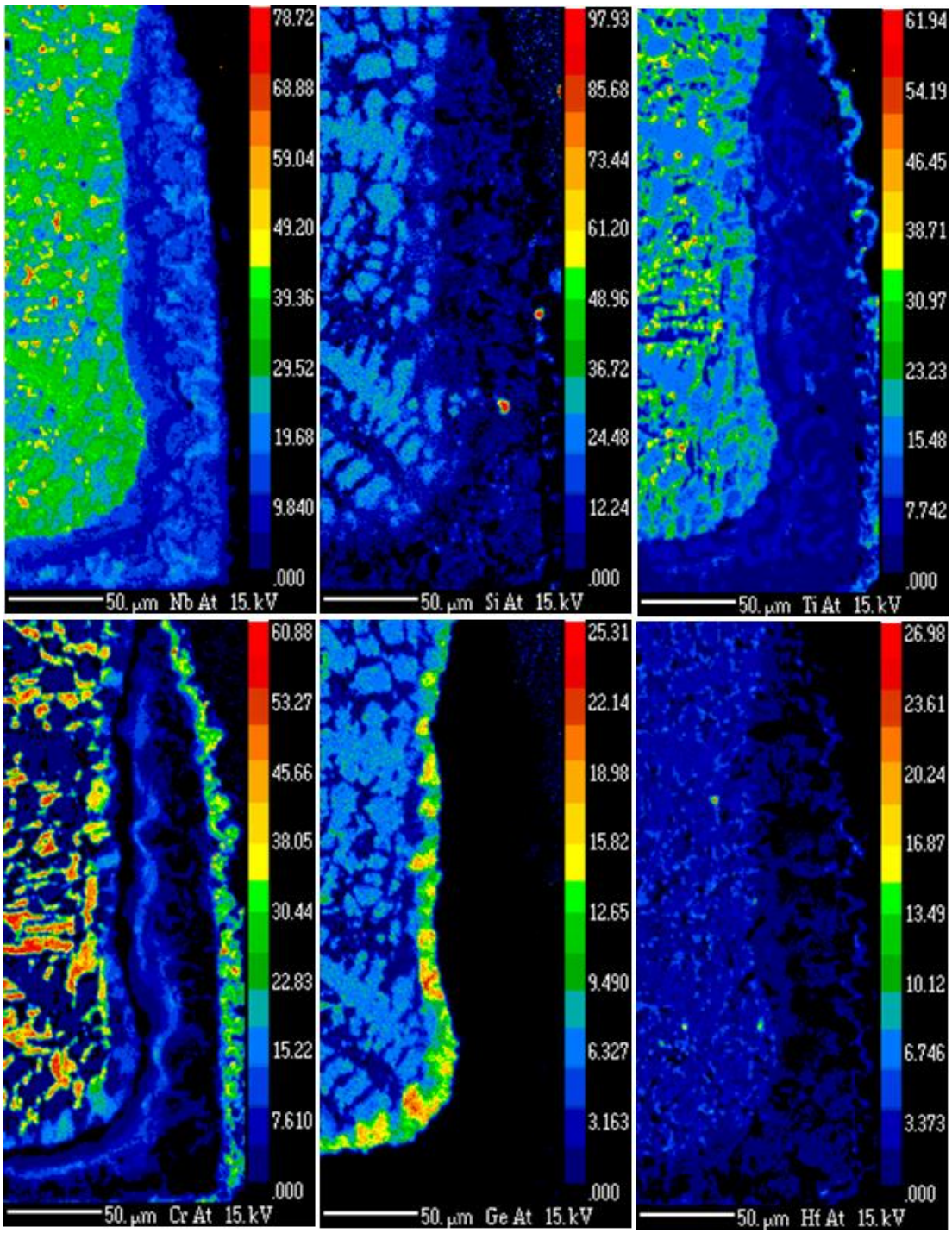

Figure 142. WDS X-ray maps of the GB2-HT-1200-50h specimen. (a) BSE-SEM image of the mapped area, (b) SE-SEM image of (a). The Nb, Si, Ti, Cr, Ge, Hf, and O maps are labelled respectively.

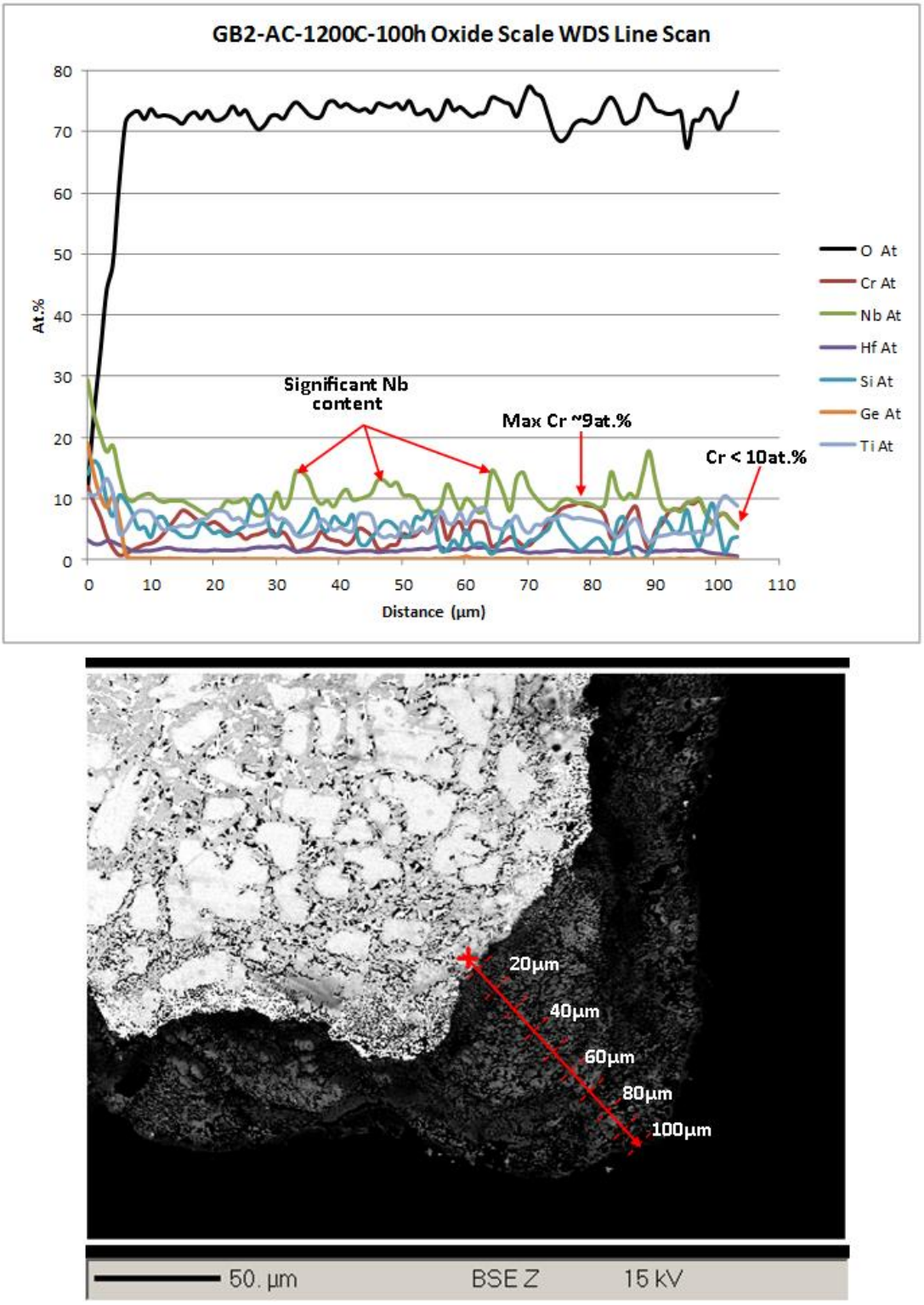

Figure 143. WDS line scan of the GB2-AC-1200-100h specimen oxide scale.

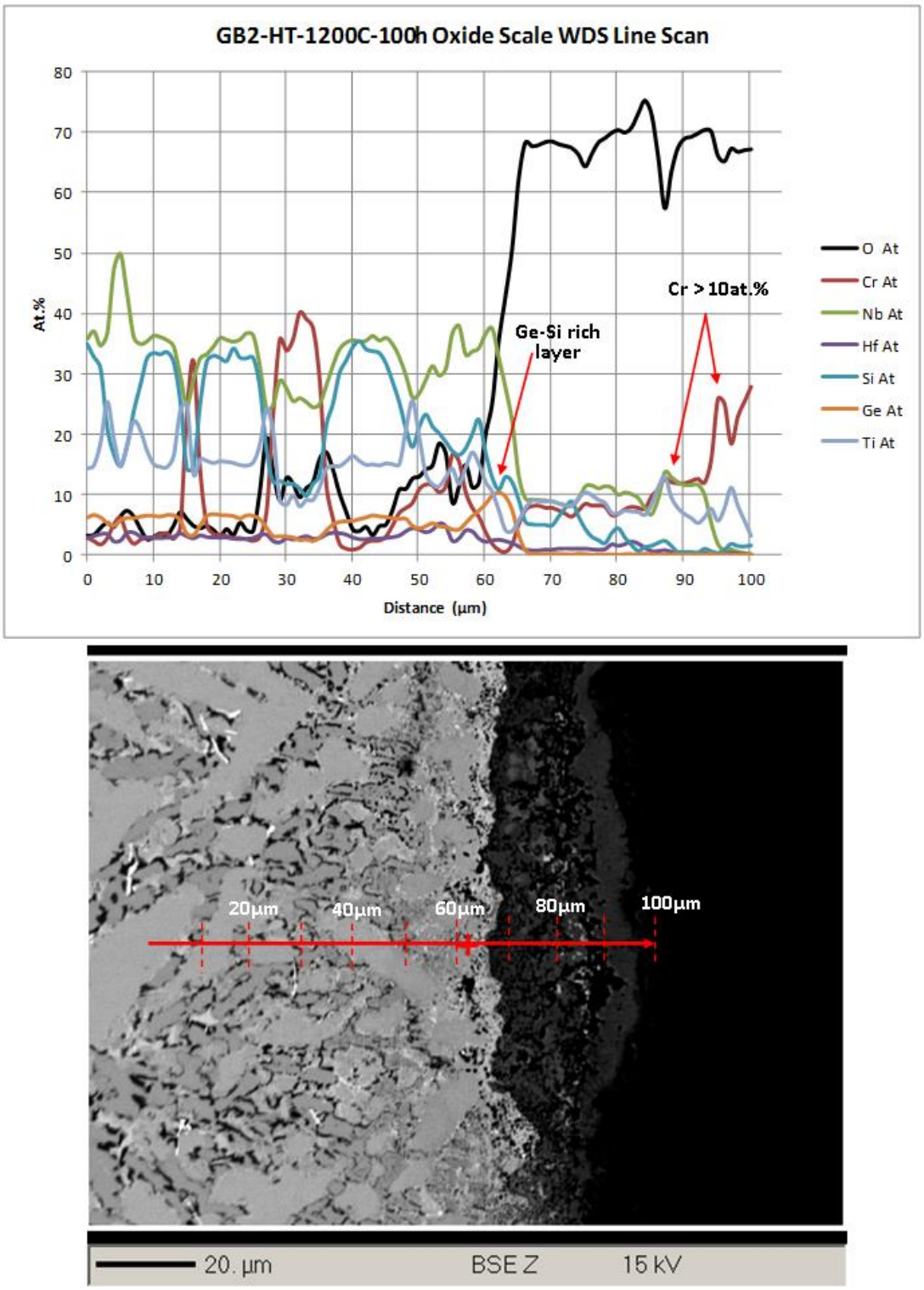

Figure 144. WDS line scan of of the GB2-HT-1200-100h specimens oxide scale.

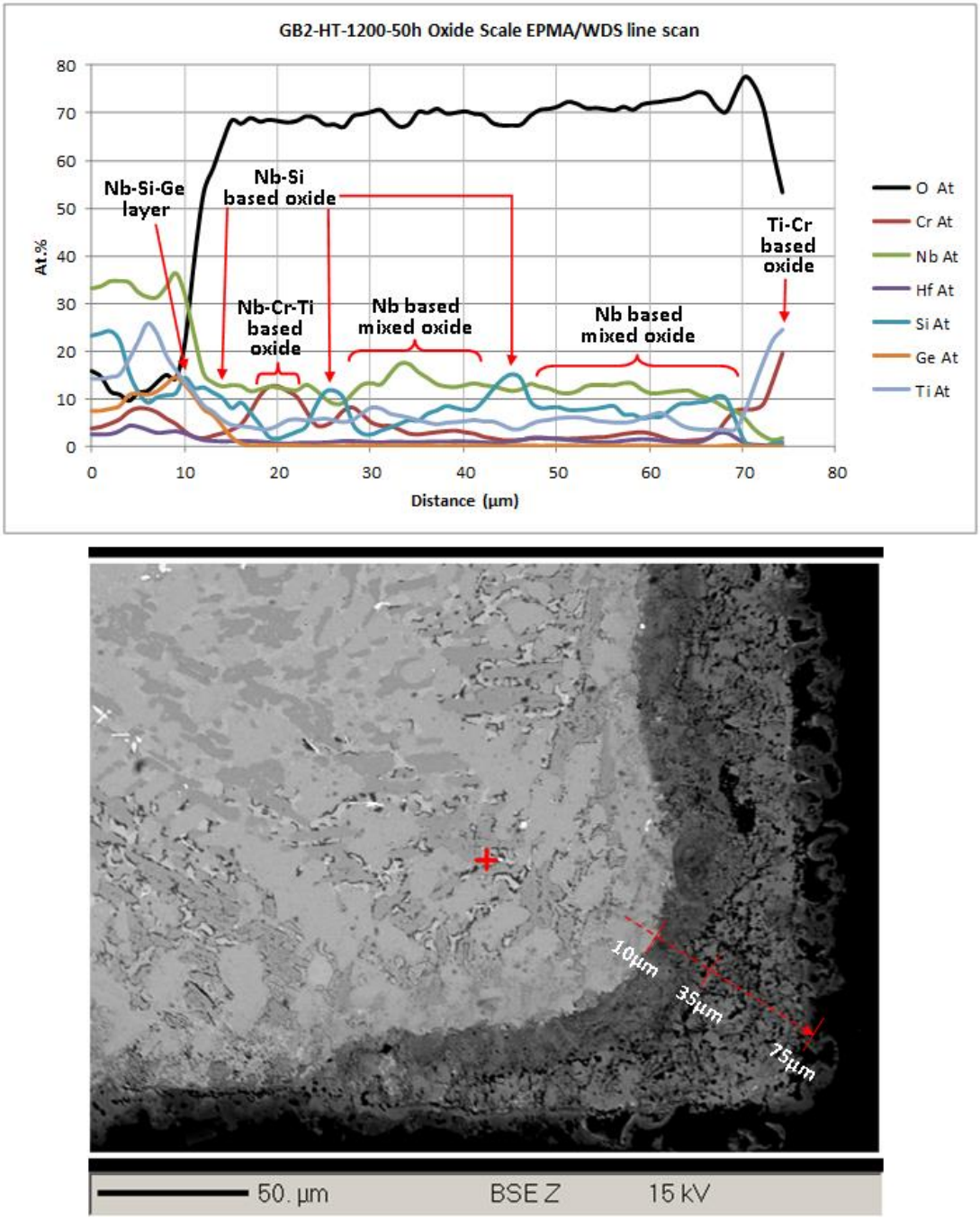

Figure 145. WDS line scan of the GB2-HT-1200-50h oxide scale.

Table 48. WDS phase analysis of the oxide scale formed on GB2-HT-1200-100h.

Oxide	Position	Nb	Si	Ti	Cr	Ge	Hf	O
Cr/Ti-Niobate	Outer layer	13.5	0.8	6.1	13.6	0.1	0.9	65.0
		2.6	1.8	11.0	17.4	0.0	0.3	66.9
		13.6	0.3	7.9	13.4	0.1	0.4	64.1
Nb-Si-Ti-Hf-O Mixed oxide	Part of Mid layer	12.9 ± 2.0	9.2 ± 3.3	9.0 ± 4.1	1.2 ± 0.6	0.5 ± 0.9	1.9 ± 1.2	65.2 ± 1.4
		15.1 - 9.7	12.8 - 4.5	14.0 - 4.4	2.2 - 0.6	2.2 - 0.1	4.2 - 0.9	66.3 - 62.5
Nb-Si-Ge-O	Substrate scale	17.1 ± 1.9	16.9 ± 1.7	1.8 ± 0.8	0.3 ± 0.1	5.7 ± 1.2	2.6 ± 1.2	55.6 ± 3.1
		19.4 - 15.0	19.1 - 14.6	3.3 - 0.6	0.5 - 0.1	7.6 - 4.3	4.4 - 1.5	59.5 - 51.6

Table 49. WDS phase analysis of the oxide scale formed on GB2-HT-1200-50h.

Oxide	Position	Nb	Si	Ti	Cr	Ge	Hf	O
Cr/Ti-Niobate	Outer layer	2.1 ± 2.0	1.4 ± 2.3	9.7 ± 5.5	19.4 ± 5.6	0.1 ± 0.0	1.6 ± 1.5	65.6 ± 1.7
		4.6 - 0.4	5.0 - 0.0	18.6 - 5.2	25.9 - 12.0	0.1 - 0.0	3.7 - 0.1	68.3 - 63.8
Niobate	Part of Mid layer	17.6 ± 5.5	2.8 ± 2.9	7.6 ± 3.0	7.3 ± 5.8	0.1 ± 0.0	1.0 ± 0.2	63.6 ± 1.4
		25.3 - 10.4	7.9 - 0.5	11.3 - 4.1	16.1 - 1.6	0.1 - 0.0	1.3 - 0.7	64.9 - 61.6
Nb-Si-Ti-Hf-O Mixed oxide	Part of Mid layer	14.7 ± 1.0	12.1 ± 0.6	4.6 ± 1.0	2.7 ± 2.0	0.1 ± 0.1	1.5 ± 0.1	64.3 ± 1.8
		15.4 - 13.6	12.5 - 11.4	5.5 - 3.5	5.0 - 1.4	0.2 - 0.0	1.6 - 1.4	65.9 - 62.3
Nb-Si-Ge-O	Substrate scale	23.5	14.3	0.8	0.4	12.7	2.1	46.3
		22.5	17.2	4.6	0.2	6.4	4.8	44.1

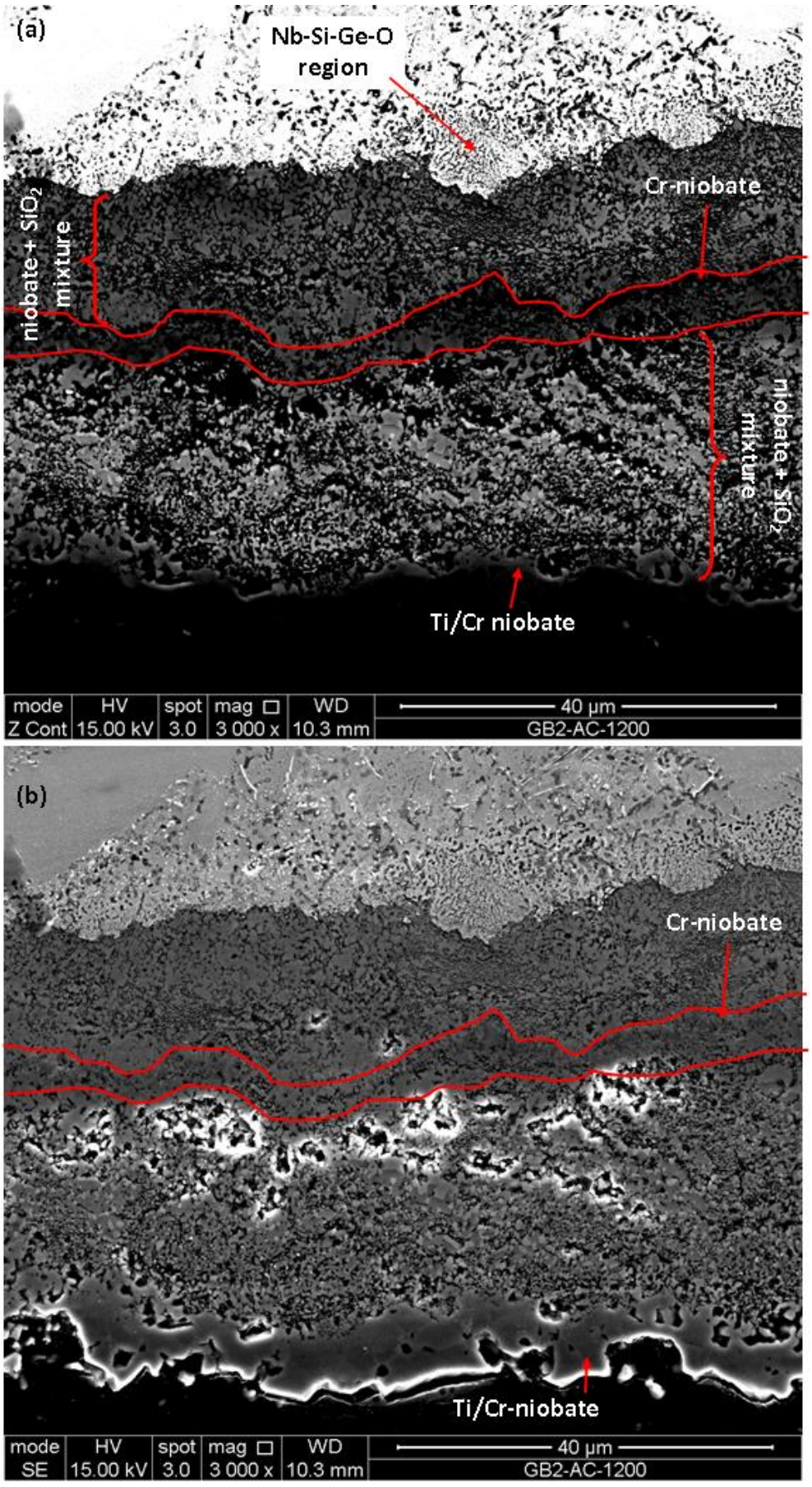

Figure 146. SEM images of the oxide scale formed on the GB2-AC-1200-100h specimen. (a) BSE image, (b) SE image.

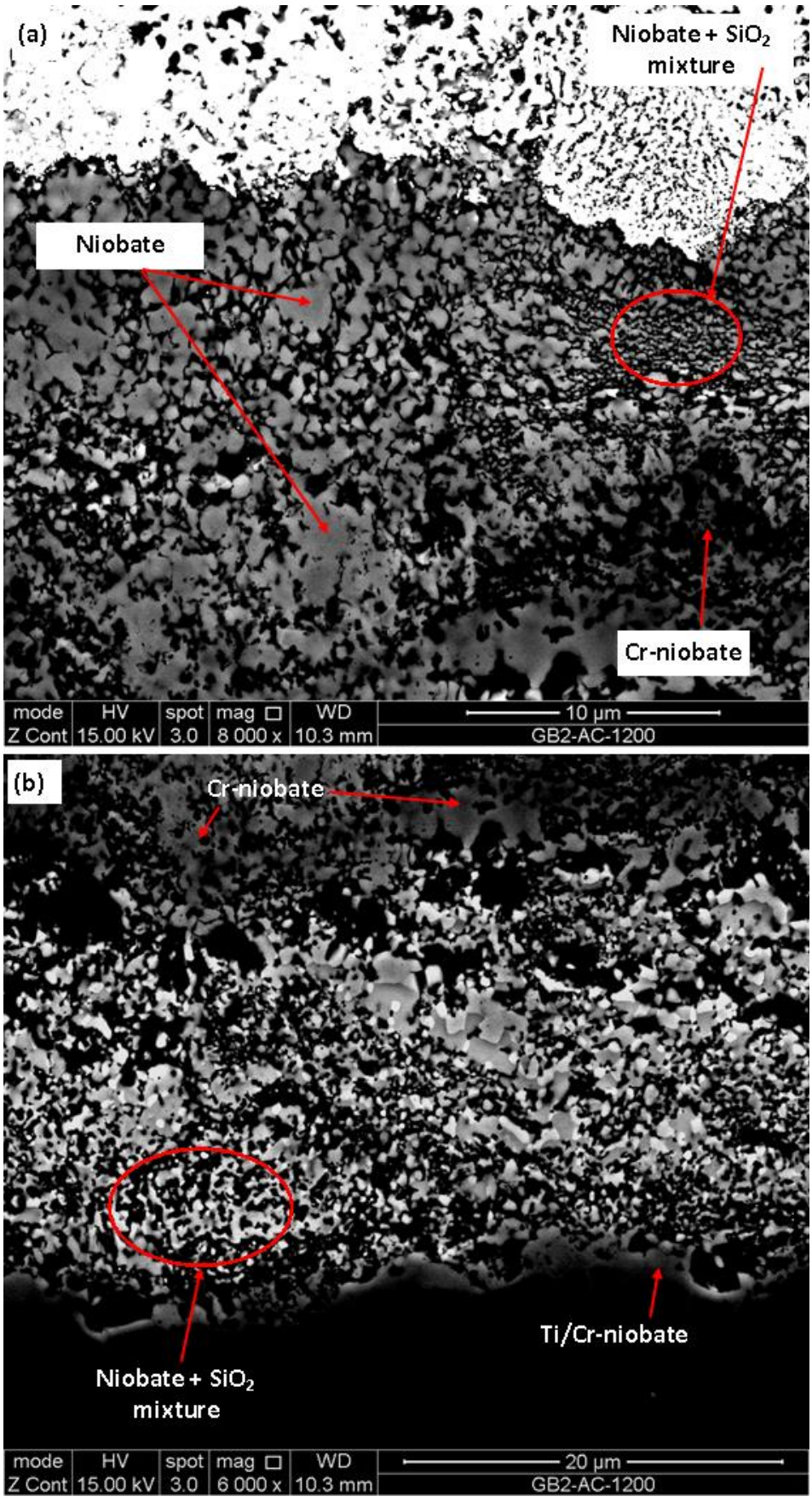

Figure 147. BSE images of the oxide scale formed on GB2-AC-1200-100h specimen. (a) The substrate-scale interface, oxide scale of Ti-niobate + SiO_2 mixture and Cr-niobate is depicted. (b) The Cr-niobate and Ti-niobate + SiO_2 mid-layer region is depicted as is the Ti/Cr-niobate outer oxide layer.

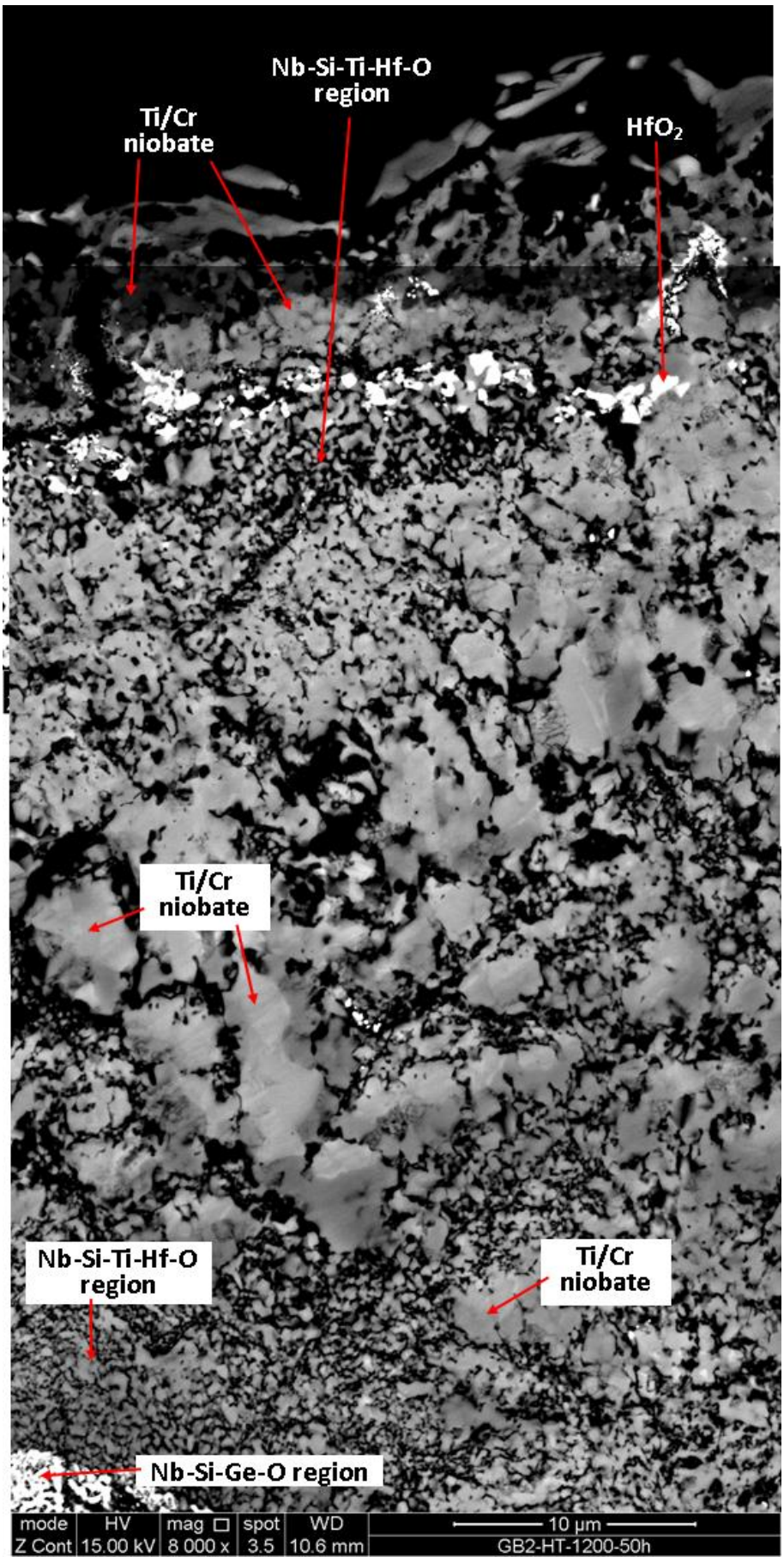

Figure 148. BSE image overview of the oxide scale formed on the GB2-HT-1200-50h specimen.

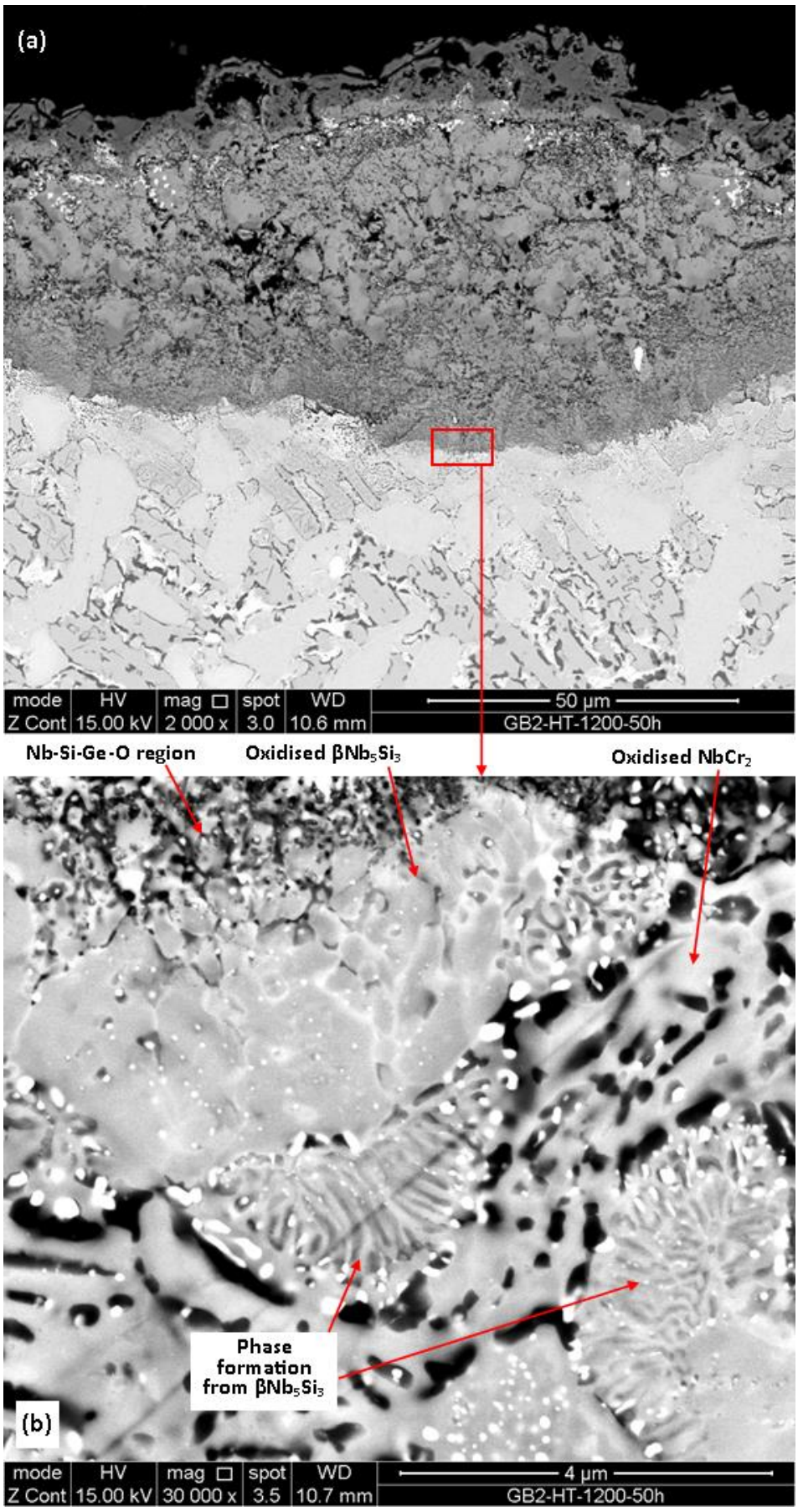

Figure 149. BSE images of the substrate-scale interface from the GB2-HT-1200-50h specimen. (a) Indicates the location of region (b). (b) High magnification image showing oxidative attack and internal precipitation of the βNb_5Si_3 grain resulting in the formation of sub-grain boundaries and multiple phase formations.

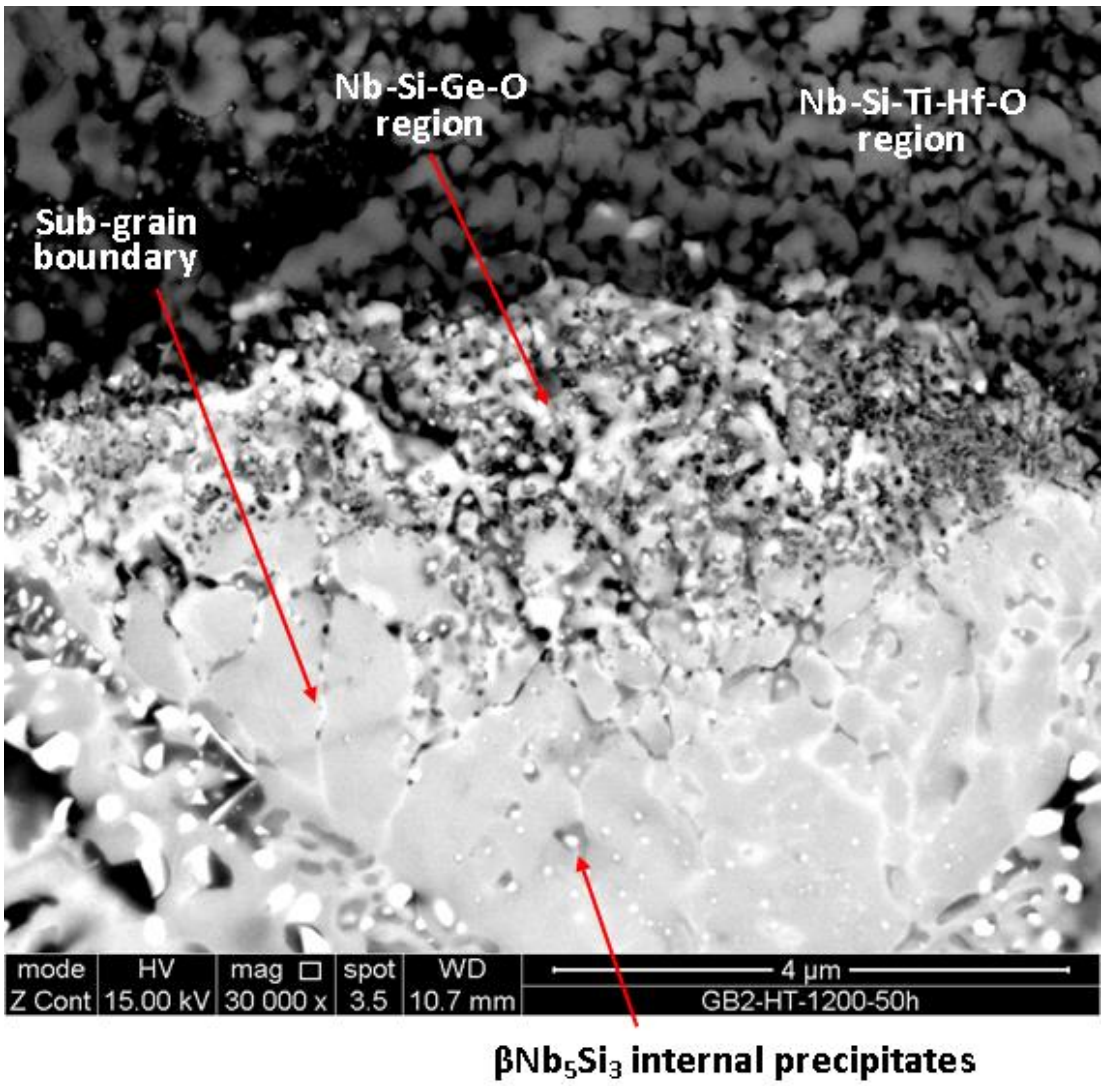

Figure 150. BSE image of an oxidised βNb_5Si_3 grain at the substrate-scale interface of the GB2-HT-1200-50h specimen.

5.5 TEM study of the Substrate-Scale Interface of GB2-HT-1200-100h

Unique to GB2 was the formation of a Nb-Si-Ge-O layer at the substrate edge originating from oxidised βNb_5Si_3 silicide. βNb_5Si_3 oxidative attack was visible in Figure 149 and Figure 150 for the 50h HT specimen. The Nb-Si-Ge-O region imaged under BSE-SEM presented various sub-micron sized precipitates beyond the capability of SEM techniques to analyse. Therefore, TEM was employed.

TEM_sample_1 is shown in Figure 151a and was extracted perpendicular to the substrate edge of the GB2-HT-1200-100h specimen. It is labelled with three sections of interest; (1) an oxidised βNb_5Si_3 grain, (2) the Nb-Si-Ge-O region emanating from the oxidised silicide, and (3) some remnants of the inner oxide scale layer (Figure 151b). The bright field (BF) TEM microstructure is depicted in Figure 152 and identifies the βNb_5Si_3 silicide, which presents an array of diffraction contrast due to nanometre sized internal precipitation. The internal precipitates were analysed. Large bright white precipitiates provide a strong Ti detection by EDS, with a very low O peak (Figure 153c) suggesting the precipitate to be the O/N-rich Ti_{ss}. Inspection at high magnification of precipitate pathways (Figure 153e), as previously seen in Figure 150, revealed locally Si and Ti depleted zones within the silicide that were adjacent small bright white precipitates found to be Si-based with appreciable O content (Figure 154b) that are likely to be SiO_2 precipitates. A small black phase within the white SiO_2 precipitate was Hf, Ti and Nb rich (Figure 154c) and may be $(Hf,Ti,Nb)_{ss}$ given the mixed detection of such elements. It may possibly be HfO_2, however the O content of the silicide was generally low (< 6.5 at.% Table 46) and there is little change in the Si and O peaks from the surrounding SiO_2 suggesting the $(Hf,Ti,Nb)_{ss}$ black precipitate is contributing such Hf, Ti, and Nb peaks.

Phases emanating from the silicide at the immediate substrate edge are illustrated in Figure 155 and were the $(Nb,Hf)_5Ge_3$ and SiO_2 that provided dark black and bright white BF diffraction contrasts respectively. In the SiO_2 provided exclusive detection of Si and O (Figure 155c) as opposed to the small precipitates found within the bulk of the βNb_5Si_3 silicide (Figure 154b). The intermediately dark phase region (Figure 155e) is deemed to be a combined detection of $(Nb,Hf)_5Ge_3$ and SiO_2 by inferring upon the diffraction contrast and the individual $(Nb,Hf)_5Ge_3$ and SiO_2 spectra. The FIB sample may be comprised of alternating layers of these phases, hence the combined detection of elements in Figure 155e. The formation of the SiO_2 and $(Nb,Hf)_5Ge_3$ is clearly due to the oxidation process, the penetrating O is likely leeching and reacting with Si from the silicide to form SiO_2 resulting in the silicide to be Ge rich enough to

stabilise $(Nb,Hf)_5Ge_3$ formation. Although Hf is more reactive with O than Si, the much larger content of Si in βNb_5Si_3 must be a factor.

Globular appearing phases presented varying contrasts (Figure 156). The spectra Figure 156(b) and (d) were lacking Ge and identified to be a combination of SiO_2 and $(Ti,Hf,Nb)_{ss}$ similar to Figure 154c. The spectrum Figure 156(c) may likely be from a mixture of all three SiO_2, $(Nb,Hf)_5Ge_3$ and $(Ti,Hf,Nb)_{ss}$ due to the strong Ti, Ge and Si peaks. The independent formation of $(Ti,Nb,Hf)_{ss}$ emanating from oxidised βNb_5Si_3 is strongly supported by Figure 157(c) and (d).

Table 50. WDS phase analysis summary of the Nb-Si-Ge-O layer formed at the substrate-scale interface of the GB2 specimens after 100 and 50h of oxidation at 1200°C.

Specimen	Nb	Si	Ti	Cr	Ge	Hf	O
100h AC	35.4 ± 4.2	11.8 ± 4.6	4.3 ± 3.9	2.7 ± 2.0	9.3 ± 3.5	5.9 ± 3.0	30.6 ± 7.1
	41.9 - 28.1	16.6 - 2.3	13.3 - 0.8	6.6 - 0.4	16.0 - 5.8	10.8 - 2.0	45.4 - 22.3
100h HT	17.1 ± 1.9	16.9 ± 1.7	1.8 ± 0.8	0.3 ± 0.1	5.7 ± 1.2	2.6 ± 1.2	55.6 ± 3.1
	19.4 - 15.0	19.1 - 14.6	3.3 - 0.6	0.5 - 0.1	7.6 - 4.3	4.4 - 1.5	59.5 - 51.6
50h HT	22.5	17.2	4.6	0.2	6.4	4.8	44.1
	23.5	14.3	0.8	0.4	12.7	2.1	46.3

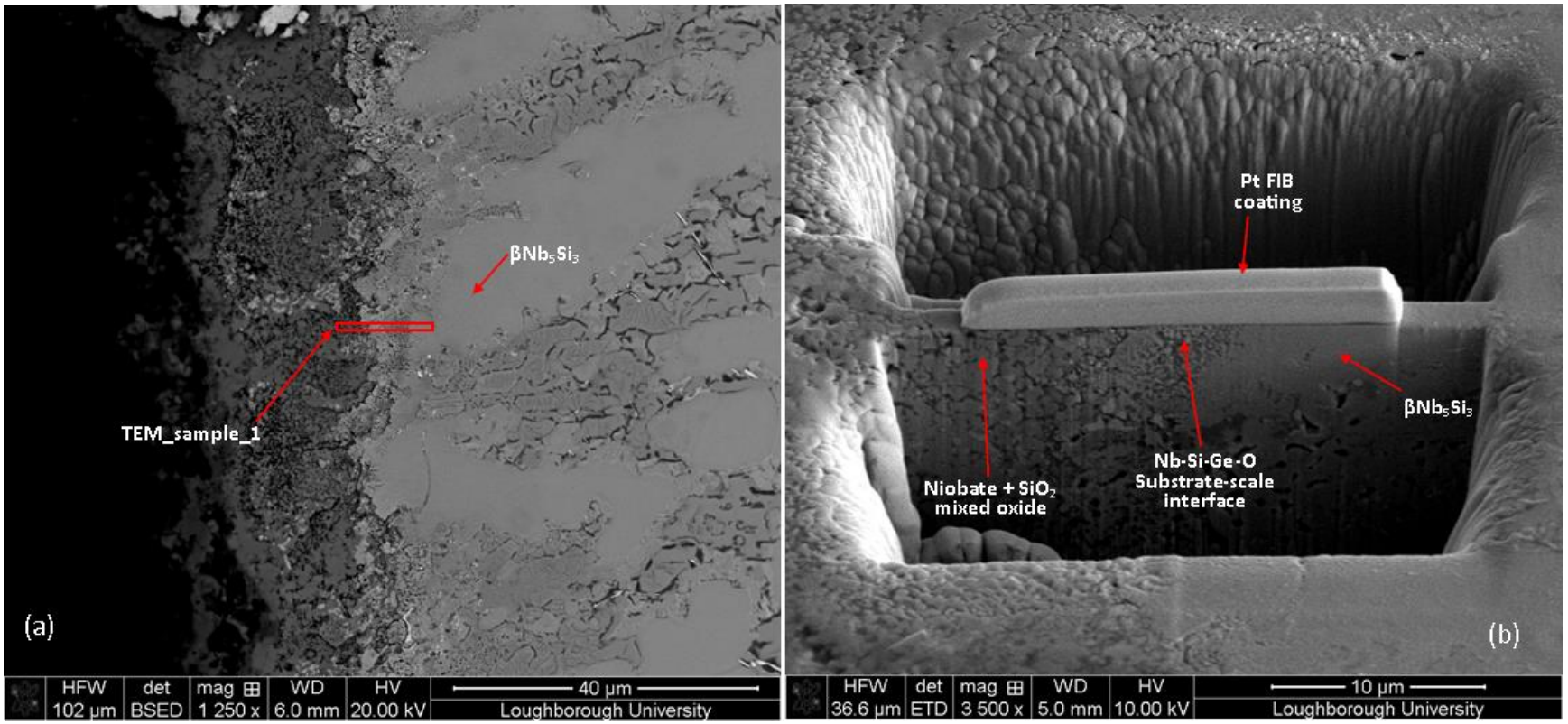

Figure 151. BSE-SEM imaging of TEM_Sample_1 taken from the substrate-scale edge of the GB2-HT-1200-100h specimen. (a) Location of the FIB specimen. (b) Image taken between ion beam milling and extraction of the FIB specimen, the Pt coating denotes the precise sample location extracted.

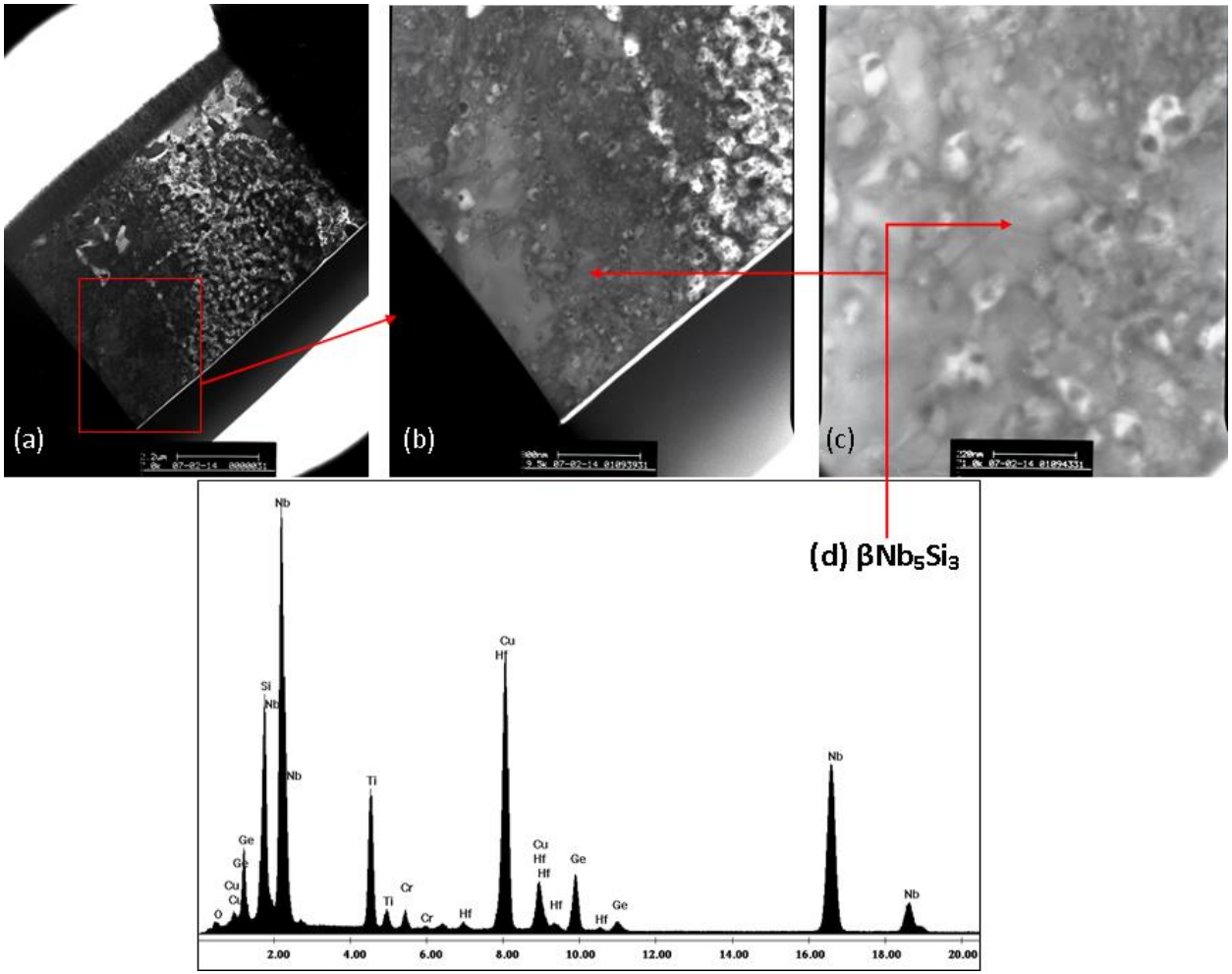

Figure 152. BF-TEM images and EDS spectrum of TEM_Sample_1 taken from the substrate-scale edge of the GB2-HT-1200-100h specimen. (a) Low magnification overview of the sample with the region of interest denoted with a red box, (b) and (c) show the location where analysis was performed. (d) Example EDS spectrum identifying the phase as βNb_5Si_3.

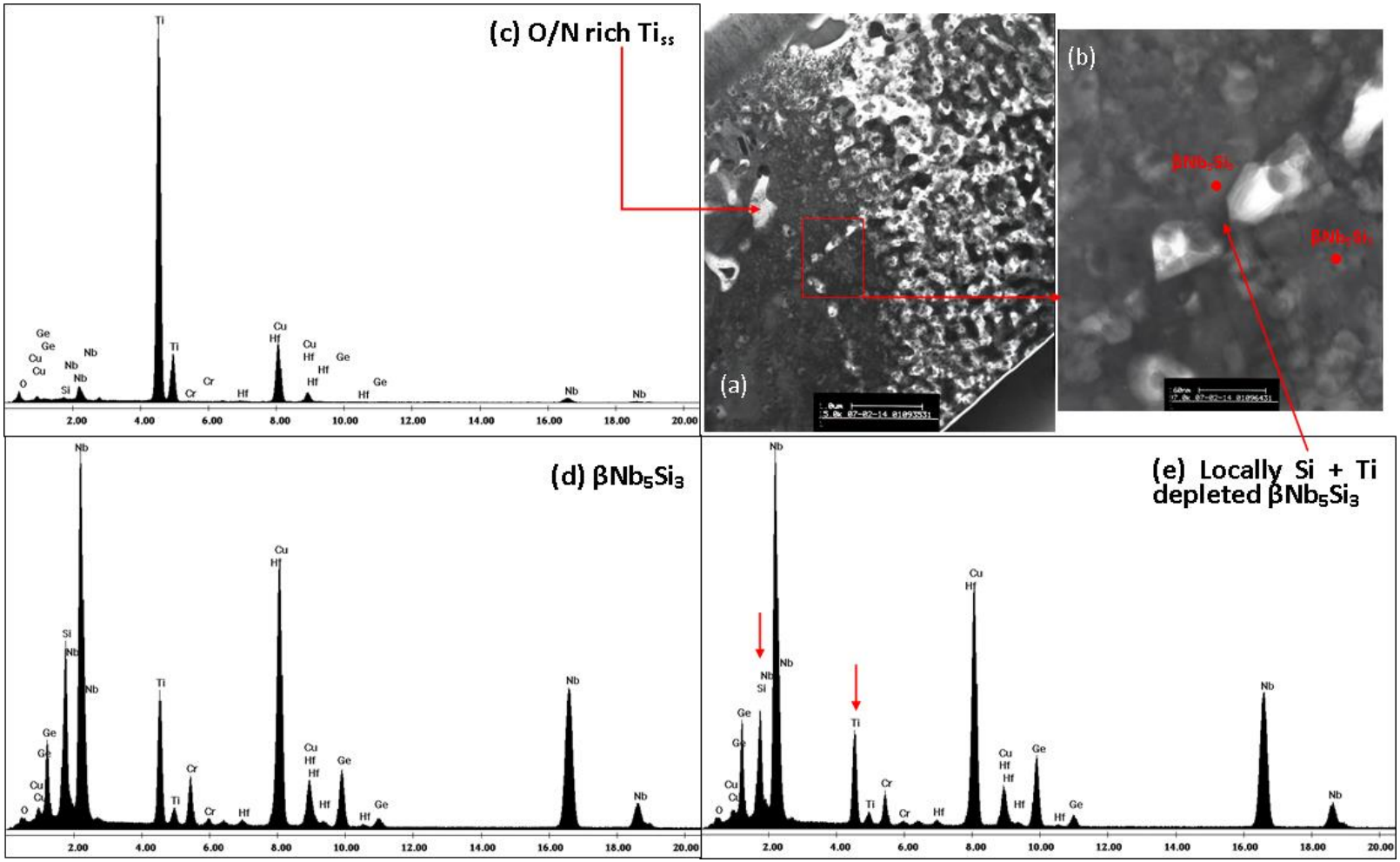

Figure 153. BF-TEM images and EDS spectra of TEM_Sample_1 taken from the substrate-scale edge of the GB2-HT-1200-100h specimen. (a) Overview image where the precipitate region within the βNb_5Si_3 is labelled by the red box, (b) depiction of internal precipiates at high magnification, (c) larger white precipitate identified as O/N-rich Ti_{ss}, (d) spectrum confirming βNb_5Si_3 phase, (e) locally Si and Ti depleted region adjacent to the white SiO_2 precipitates (see Figure 154).

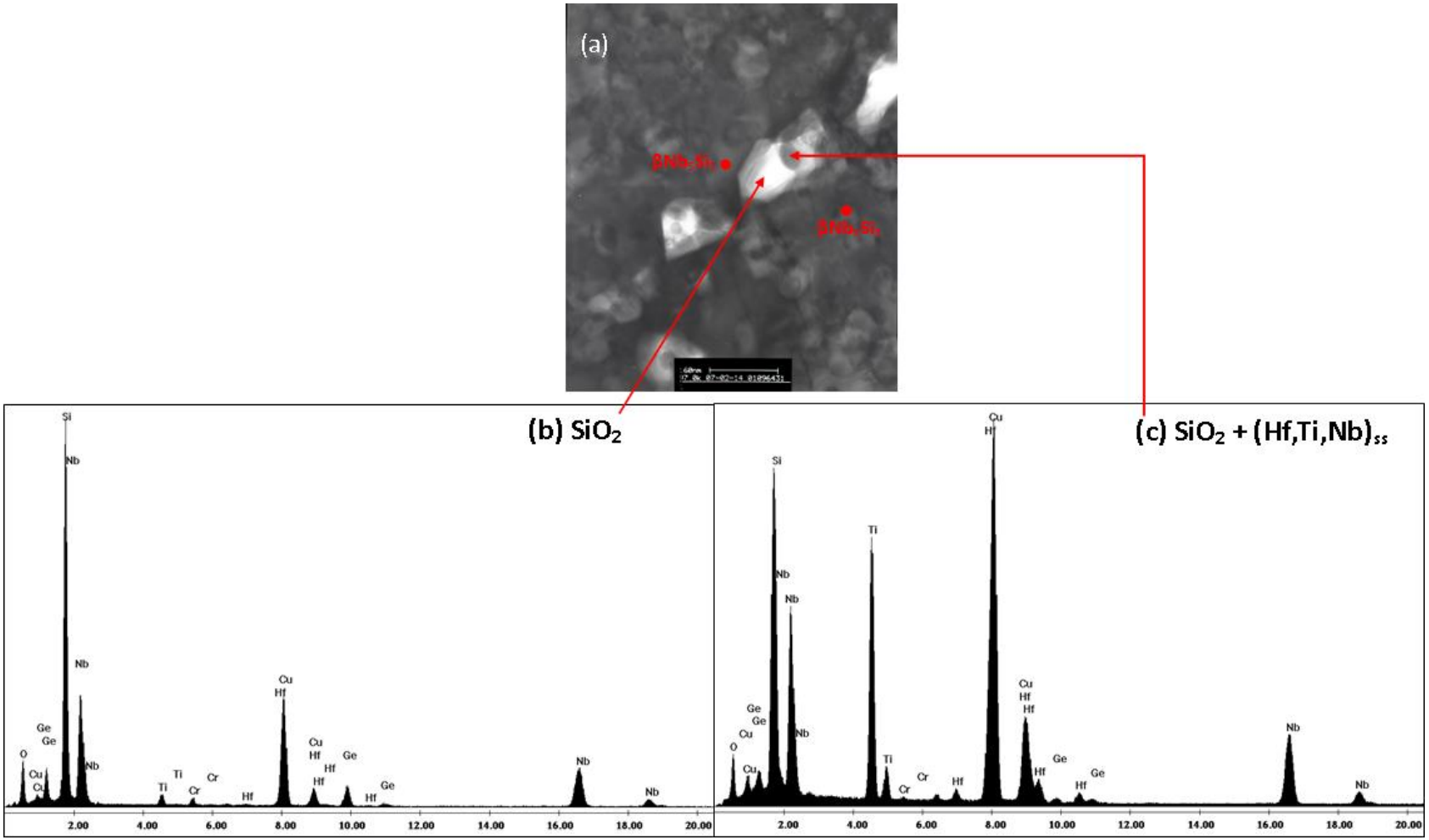

Figure 154. BF-TEM images and EDS spectra of TEM_Sample_1 taken from the substrate-scale edge of the GB2-HT-1200-100h specimen. (a) Image of internal precipiates formed within a βNb_5Si_3 silicide, (b) SiO_2 precipitate, (c) SiO_2 and $(Hf,Ti,Nb)_{ss}$.

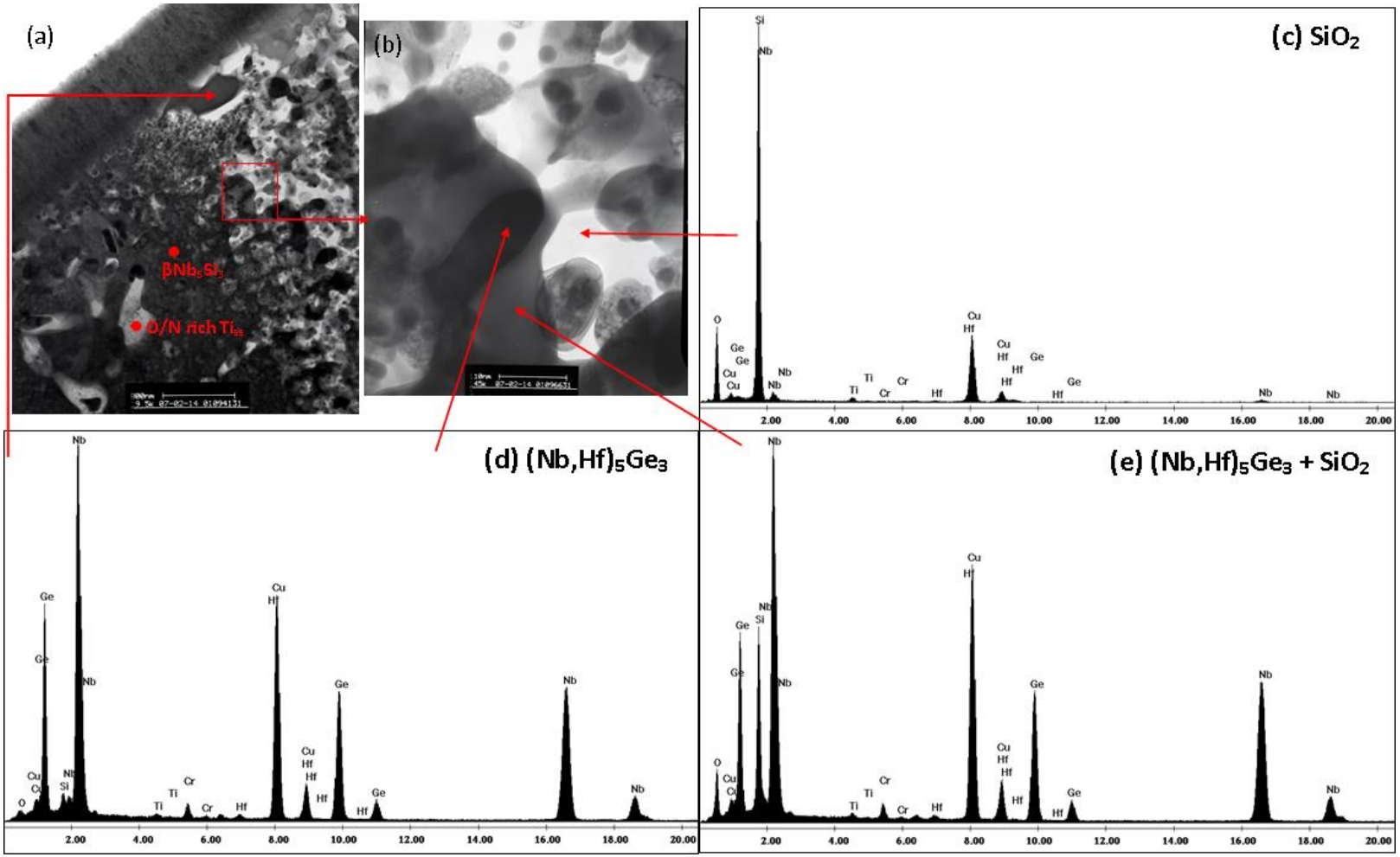

Figure 155. BF-TEM images and EDS spectra of TEM_Sample_1 taken from the substrate-scale edge of the GB2-HT-1200-100h specimen. (a) Overview image, (b) high magnification image of phases emmenating from the oxidised βNb_5Si_3 silicide. (c) Spectrum of the white phase region indicating SiO_2. (d) Spectrum of the dark phase indicating $(Nb,Hf)_5Ge_3$. (e) spectrum of grey phase region identified as a mixed detection of $(Nb,Hf)_5Ge_3$ and SiO_2.

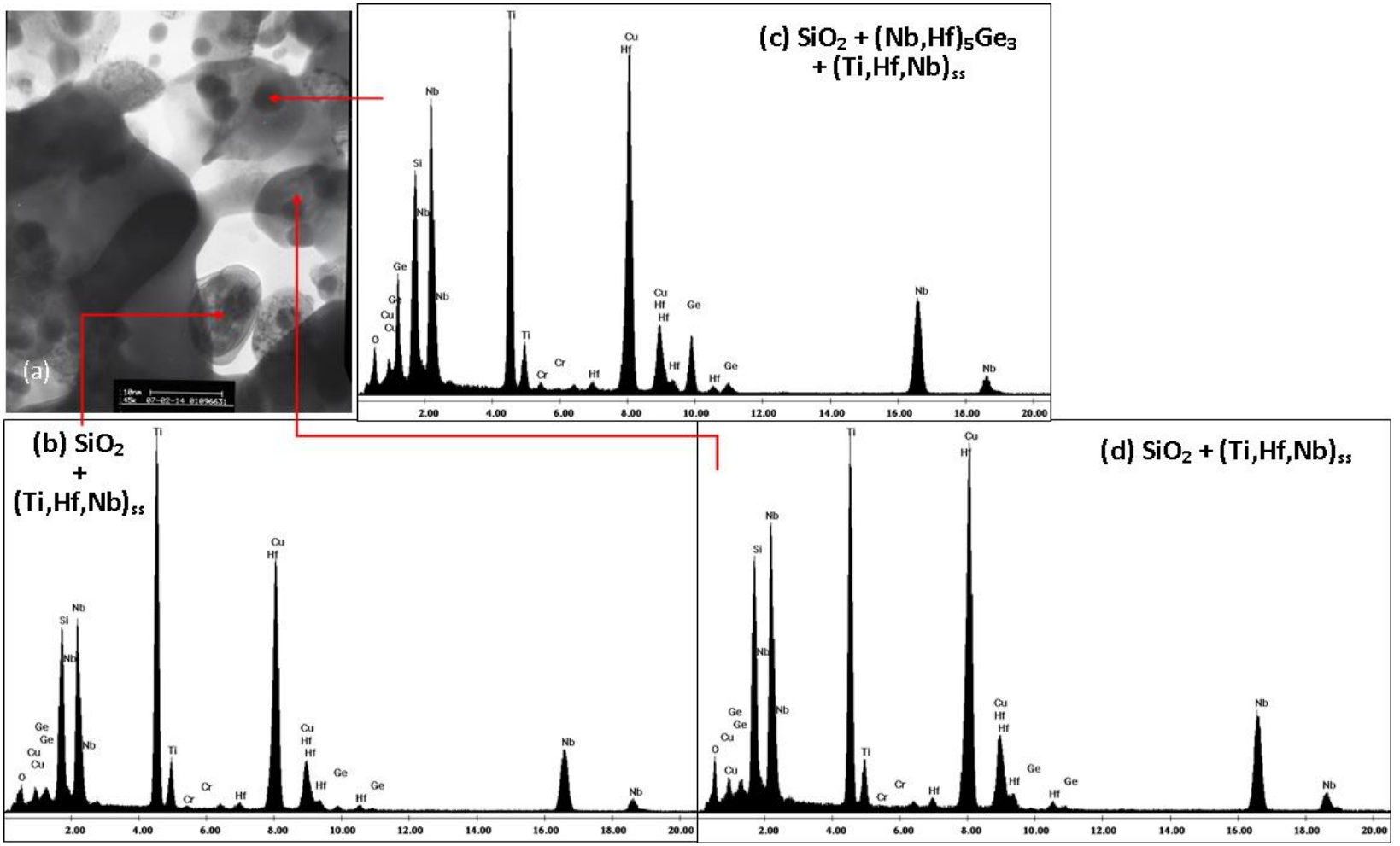

Figure 156. BF-TEM images and EDS spectra of TEM_Sample_1 taken from the substrate-scale edge of the GB2-HT-1200-100h specimen. (a) Image indicating analysis locations, (b) SiO_2 and $(Ti,Hf,Nb)_{ss}$, (c) SiO_2, $(Nb,Hf)_5Ge_3$ and $(Ti,Hf,Nb)_{ss}$, (d) SiO_2 and $(Ti,Hf,Nb)_{ss}$.

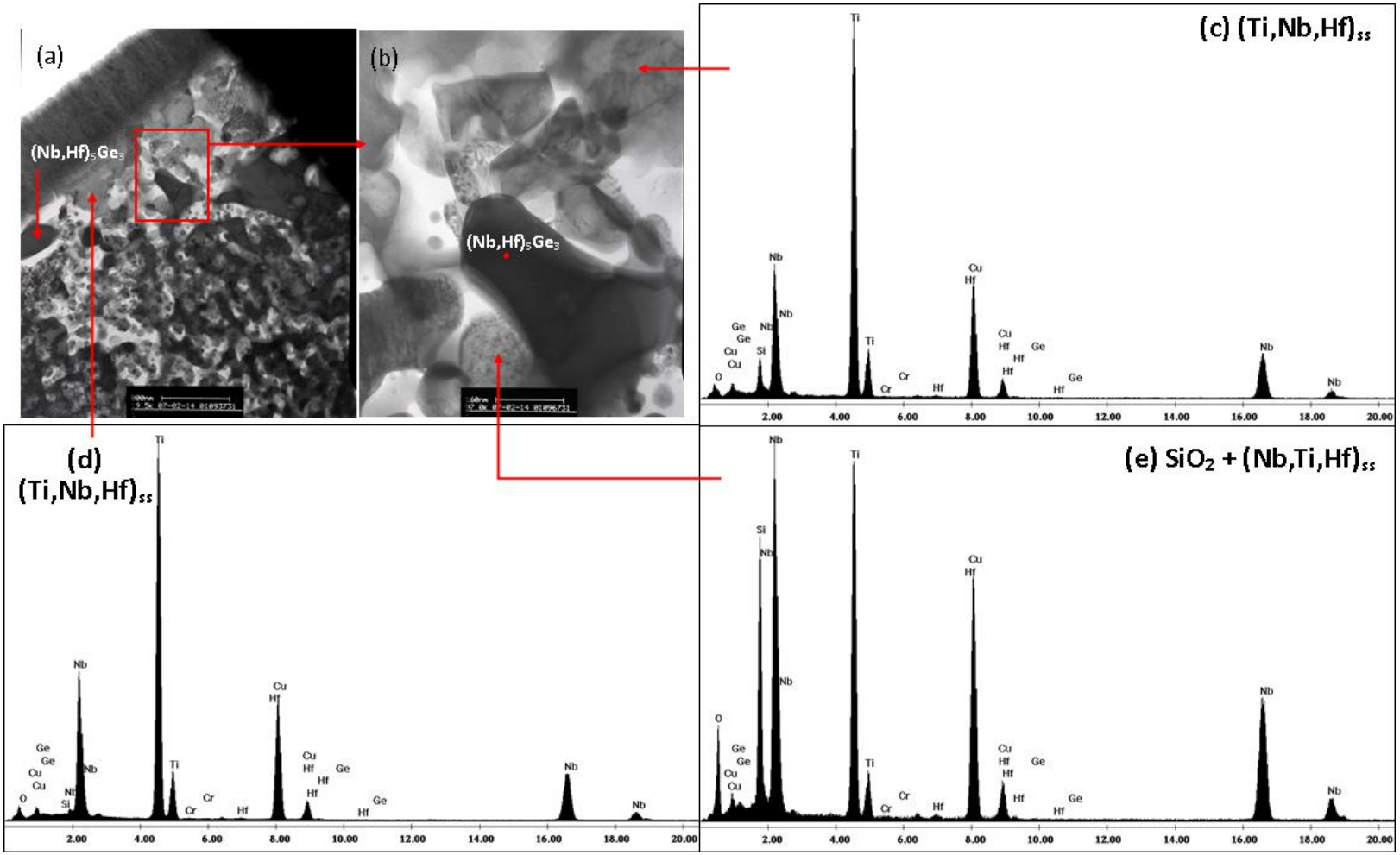

Figure 157. BF-TEM images and EDS spectra of TEM_Sample_1 taken from the substrate-scale edge of the GB2-HT-1200-100h specimen. (a) and (b) indiciate where analysis was performed. (c) and (d) are identified as $(Ti,Nb,Hf)_{ss}$ and (e) SiO_2 and $(Nb,Ti,Hf)_{ss}$.

5.6 Shorter Oxidation Testing (≤ 25 h)

5.6.1 Kinetics & Internal Microstructure

With the purpose of investigating the early stages of isothermal oxidation at 1200°C, shorter TGA tests were performed on the alloy GB2-HT of 25, 10, and 5h durations. Due to equipment error only the TGA data for the 10h specimen was saved and was shown in Figure 112. The parabolic rate constant was $1x10^{-10}$ g^2 cm^{-4} s^{-1} (Table 26), which is the same as specimens oxidised at 1200°C for 50 and 100h. Figure 158, Figure 159, Figure 160 show SEM images of the 25, 10 and 5h oxidised specimens respectively, of which the latter two show delamination of the oxide scale from the substrate occurred. Such delamination was also displayed by optical photographs in Figure 90.

Internal oxidation and precipitation were expectedly less for the shorter oxidation tests. The 25h specimen showed an irregularly deep diffusion zone in comparison to the 50 and 100h tests, this may be attributed to a local region of interconnecting $(Nb,Ti,Cr)_{ss}$ within the microstructure (Figure 158a). The internal precipitates were of micron size similar to the 10 and 5h tests. After only 5h of oxidation, not only did the $(Nb,Ti,Cr)_{ss}$ and $NbCr_2$ suffer oxidative attack, but so did the βNb_5Si_3 silicide grains within the diffusion zone, resulting in the formation of an oxidative phase boundary and discrete internal precipitates within the bulk of the grain (Figure 161).

SEM-EDS X-ray maps (Figure 162) identified the substrate phases and indicated high Ti content of the black precipitates that formed a semi-continuous border around the silicide and solid solution. The white precipitates were too small for the maps to resolve. However, qualitative TEM-EDS analysis of TEM_Sample_2 (Figure 163) suggested them to be HfO_2 (Figure 164b). TEM-EDS suggest the black precipitates (under BSE-SEM contrast) to be O/N-rich Ti_{ss} (Figure 164d), appearing bright white under BF-TEM contrast. This identity is preferred as opposed to TiO or TiO_2 due to the high solid solubility of O and nitrogen in Ti, the low O peak intensity found here, and the previously discussed overlap issue of NKα with TiLα X-rays.

TEM-EDS after 5h of oxidation also revealed two forms of silicide oxidative attack; (1) internal precipitate formation (Figure 165b) and (2) HfO_2 and O/N-rich Ti_{ss} formation at the silicide grain boundary creating an oxidative phase boundary (Figure 165c). The internal precipitates were rich in Cr (Figure 166), there identity was unclear.

WDS data of the substrate phases for the 25 and 10h conditions were again divided into those taken within or outside the BPDZ and is presented in Table 50 and Table 51. Comparison with the non-oxidised GB2-HT EDS data is presented in Table 53 and Table 54. All substrate phases recorded a significant content of O. The range in O varied widely in some cases but in general grains analysed outside the BPDZ reported less O.

Comparison with non-oxidised GB2-HT EDS data showed for $(Nb,Ti,Cr)_{ss}$ within the BPDZ a depletion of Nb, Ti, and Cr (Table 54), for the $NbCr_2$ in the BPDZ there was most significantly a reduction in Ti but negligible change in Cr (Table 53). This suggests at the early stages of oxidation there was a greater affinity for diffusion of elements from the $(Nb,Ti,Cr)_{ss}$ as opposed to the $NbCr_2$ Laves. These compositional changes were difficult to decisively quantify due to the limited volume of data. However, greater element mobility within the $(Nb,Ti,Cr)_{ss}$ would suggest weaker binding energies and greater reactivity of elements in comparison with the $NbCr_2$ Laves. Similar composition changes of phases were found for the longer term oxidation data of both alloys (Table 43 and Table 47).

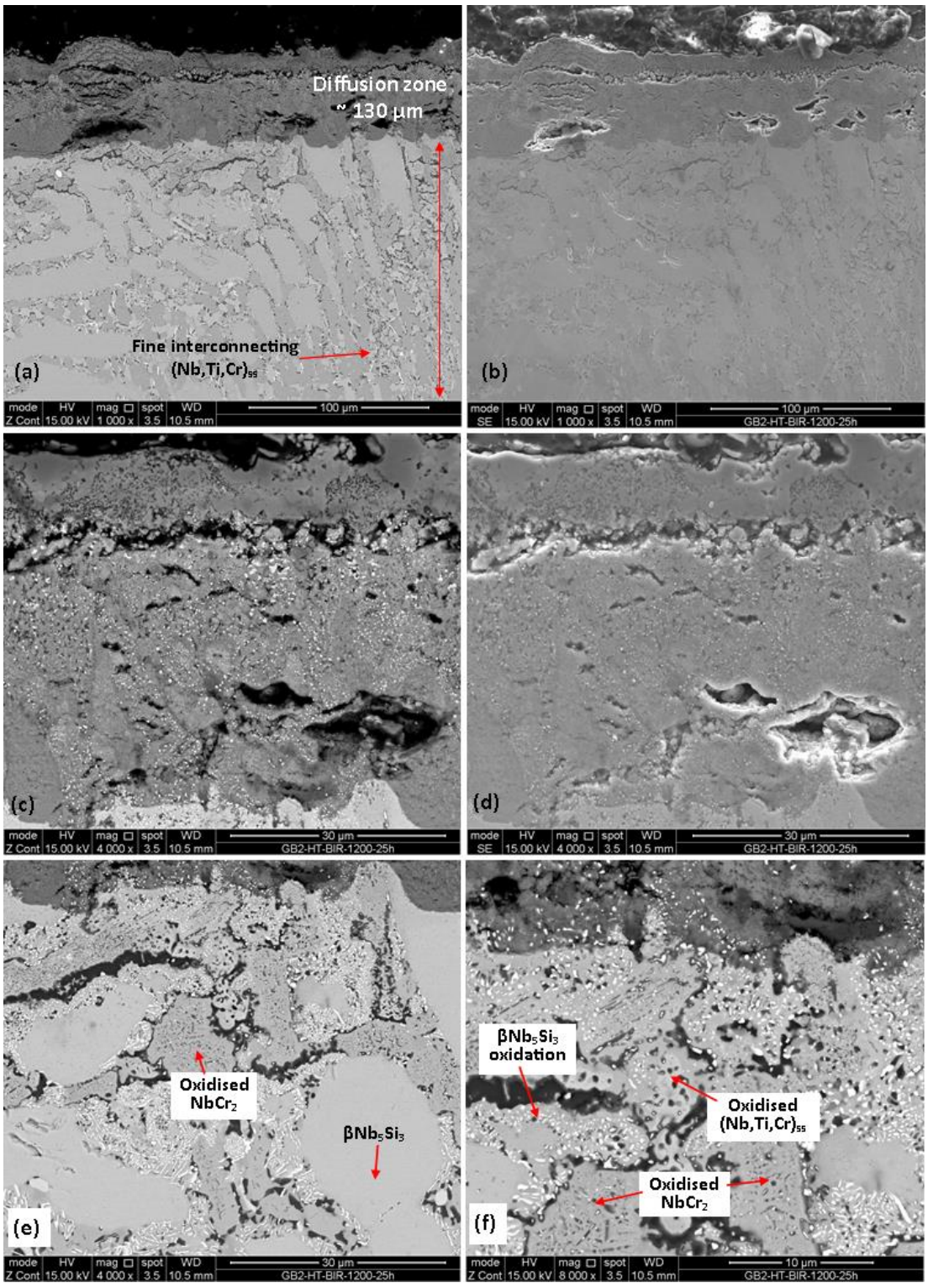

Figure 158. SEM images of specimen GB2-HT-1200-25h. (a) BSE low magnification overview displaying an adhered oxide scale. (b) SE image of (a). (c) BSE high magnification of the oxide scale. (d) SE image of (c). (e) BSE images of the internally oxidised microstructure. (f) high magnification of interdendritic internal oxidation.

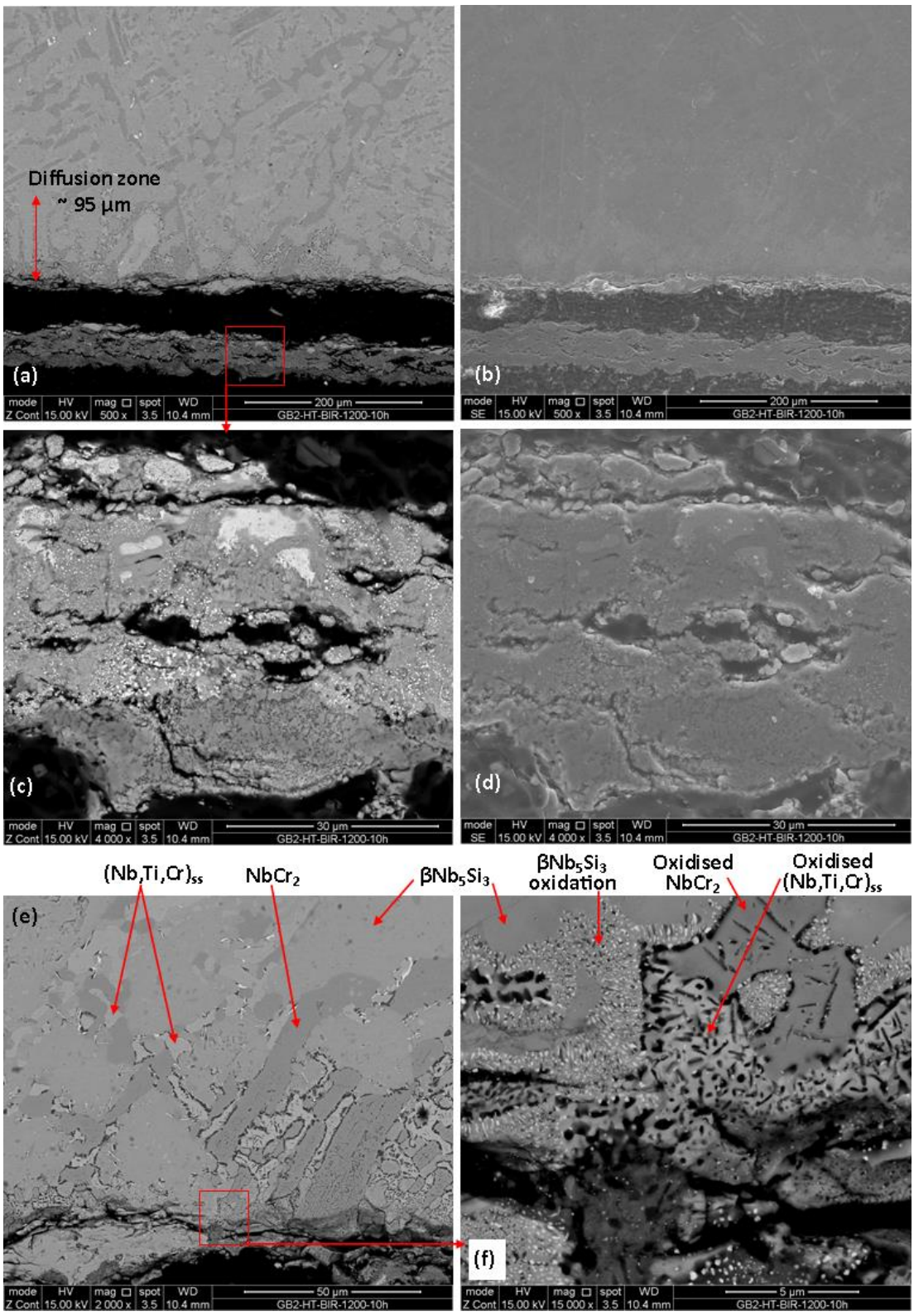

Figure 159. SEM images of specimen GB2-HT-1200-10h. (a) BSE low magnification overview displaying a delaminated oxide scale. (b) SE image of (a). (c) BSE high magnification of the oxide scale. (d) SE image of (c). (e) BSE image of the internally oxidised microstructure. (f) high magnification BSE image of the interdendritic internal oxidation.

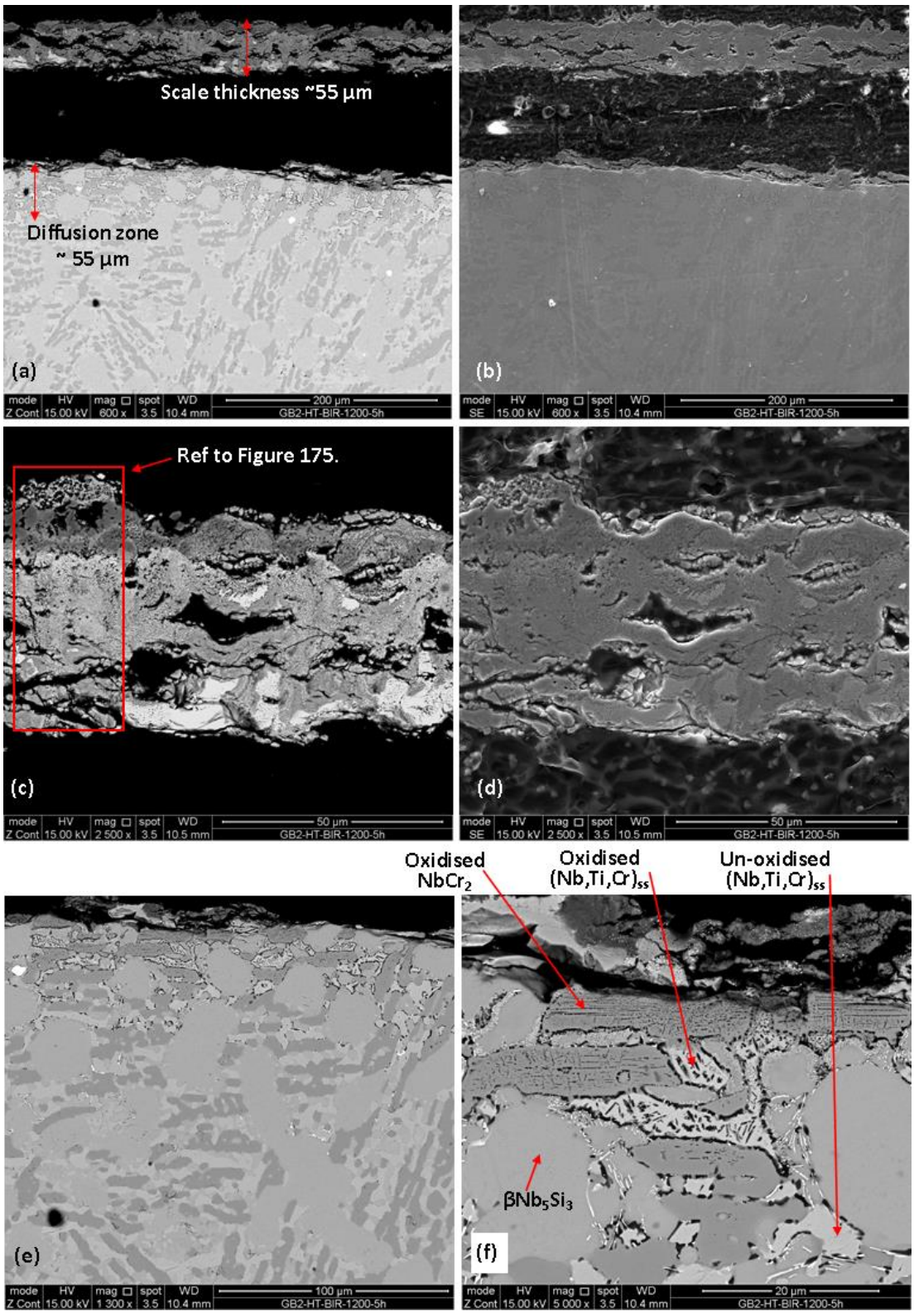

Figure 160. SEM images of specimen GB2-HT-1200-5h. (a) BSE low magnification overview displaying a delaminated oxide scale. (b) SE image of (a). (c) BSE high magnification of the oxide scale. (d) SE image of (c). (e) BSE image of the internally oxidised microstructure showing a shallow BPDZ. (f) high magnification image of the interdendritic internal oxidation at the substrate edge.

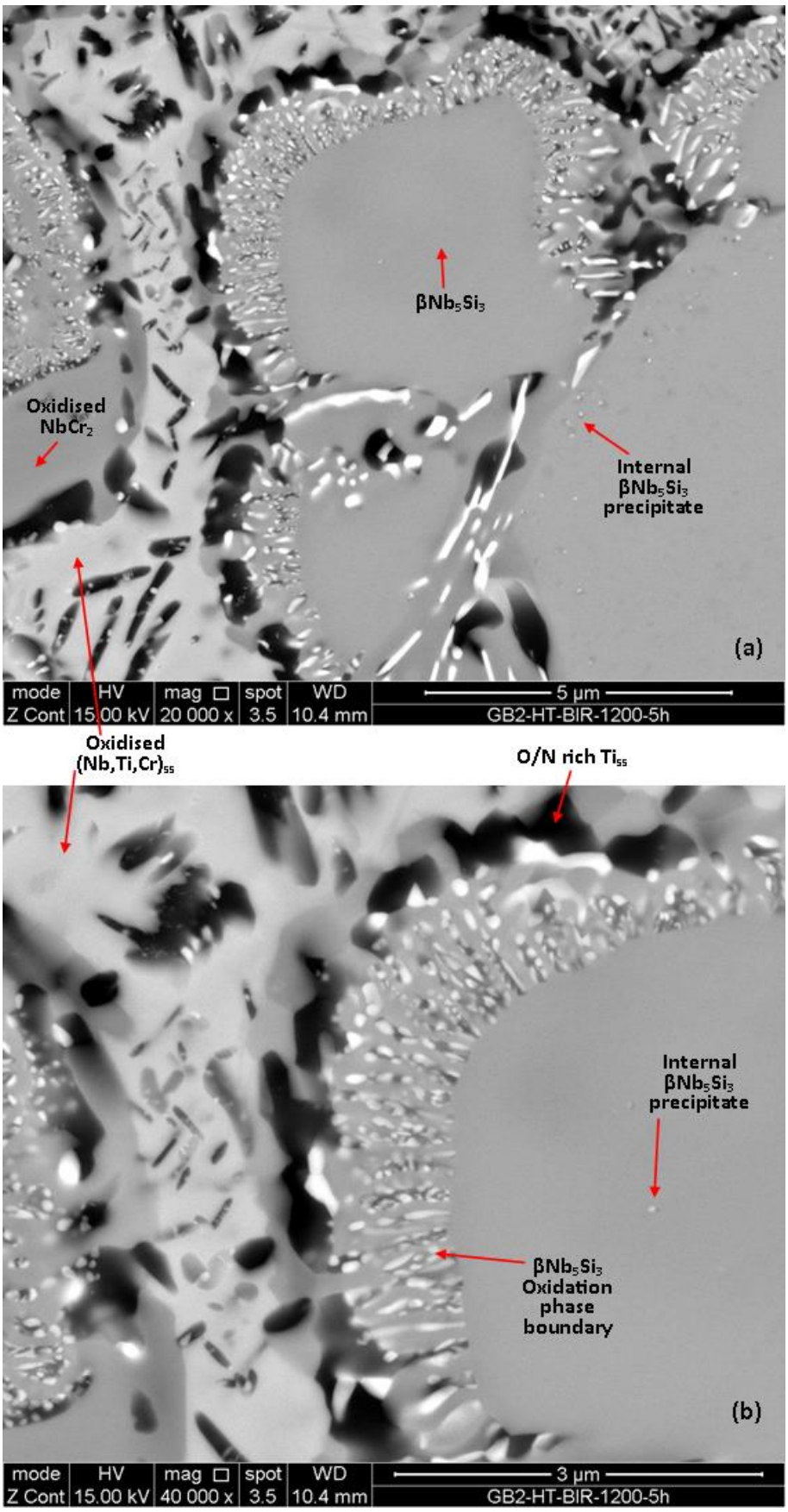

Figure 161. BSE images of specimen GB2-HT-1200-5h displaying the oxidative attack of an βNb_5Si_3 silicide grain. An oxidative phase boundary of precipitates had formed around the silicide. HfO_2 and O/N Ti_{ss} precipitates are visible within the $(Nb,Ti,Cr)_{ss}$ and $NbCr_2$. For a lower magnification overview of these figures please refer to Figure 160f.

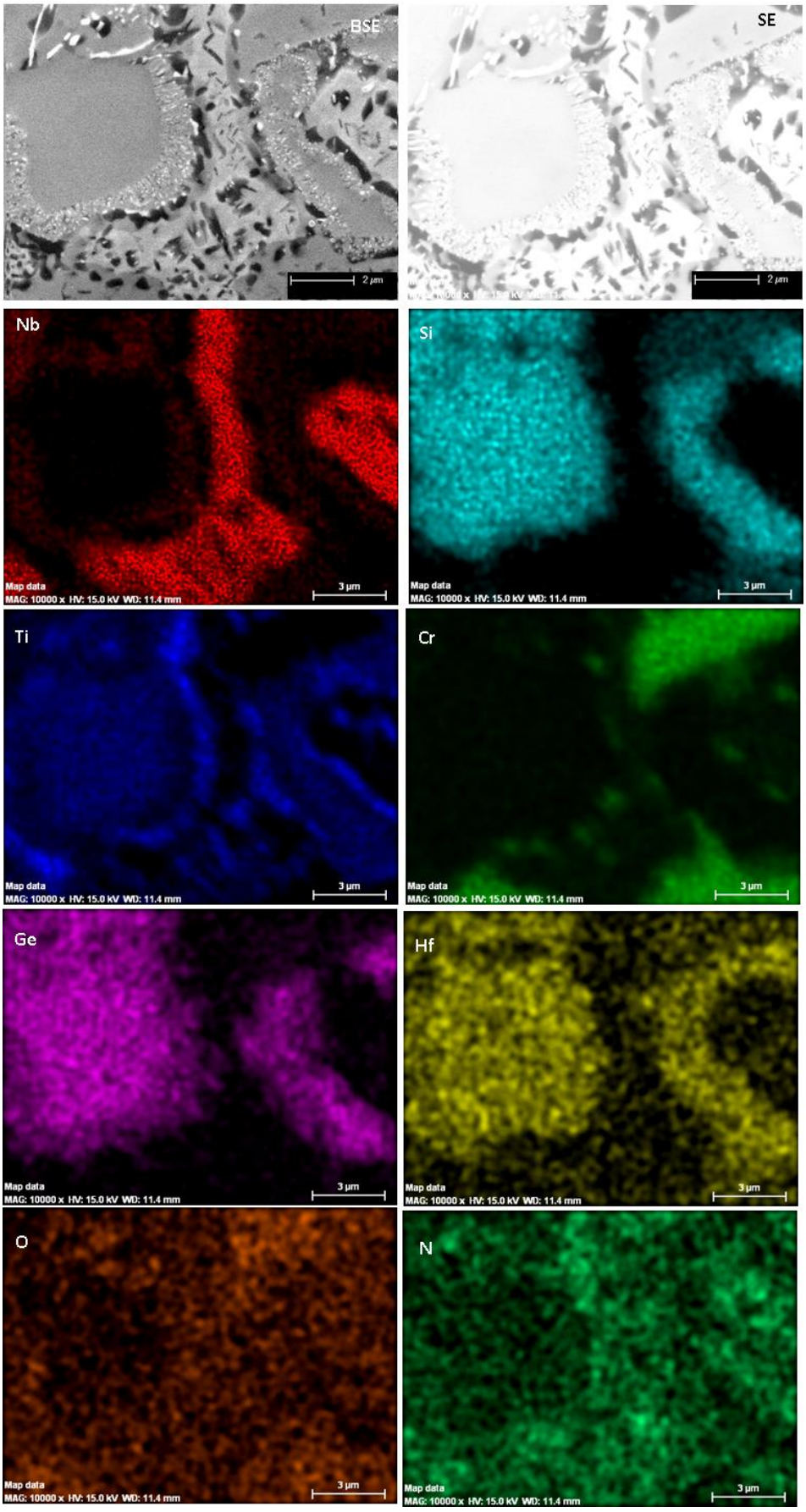

Figure 162. EDS X-ray maps of specimen GB2-HT-1200-5h of the region depicted in Figure 161a, note that image is inverted in this figure.

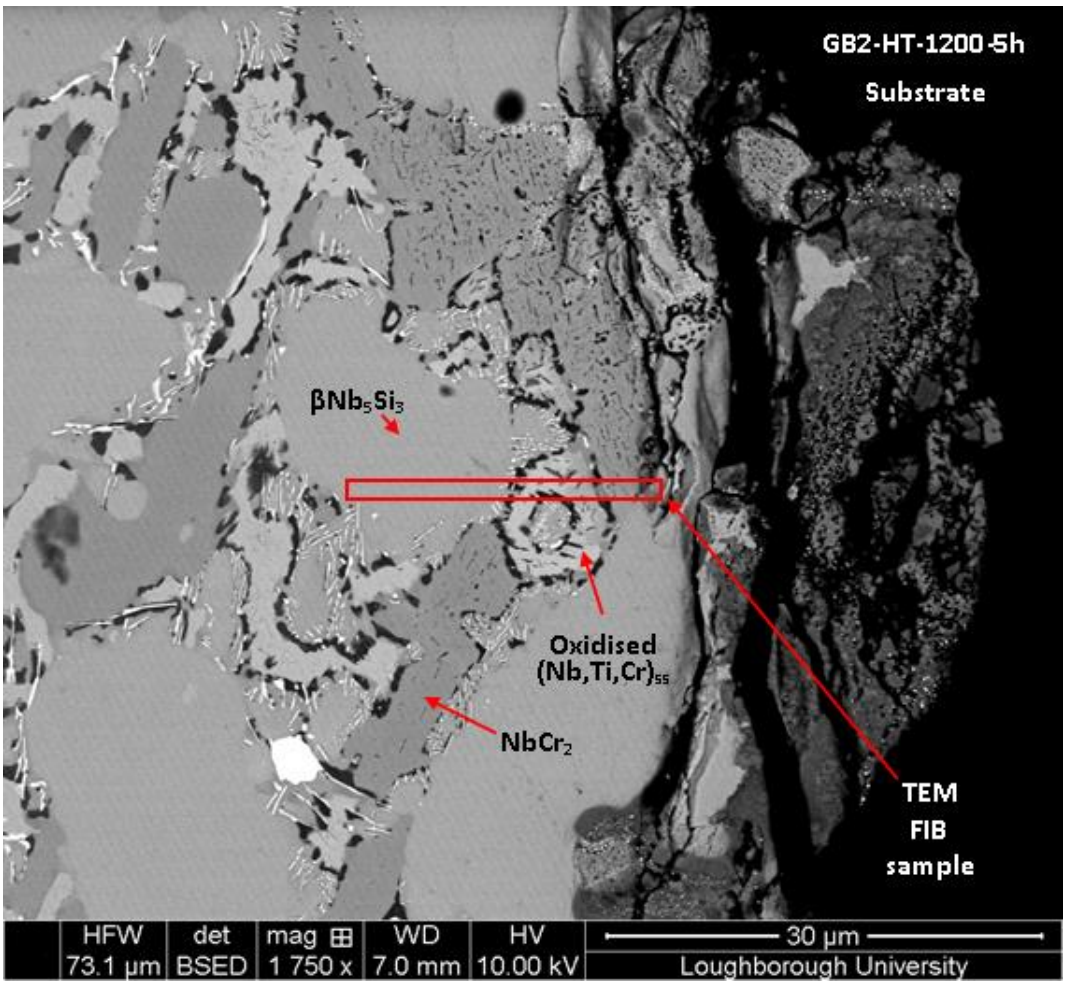

Figure 163. BSE-SEM image locating TEM_Sample_2 extracted from the substrate edge of specimen GB2-HT-1200-5h.

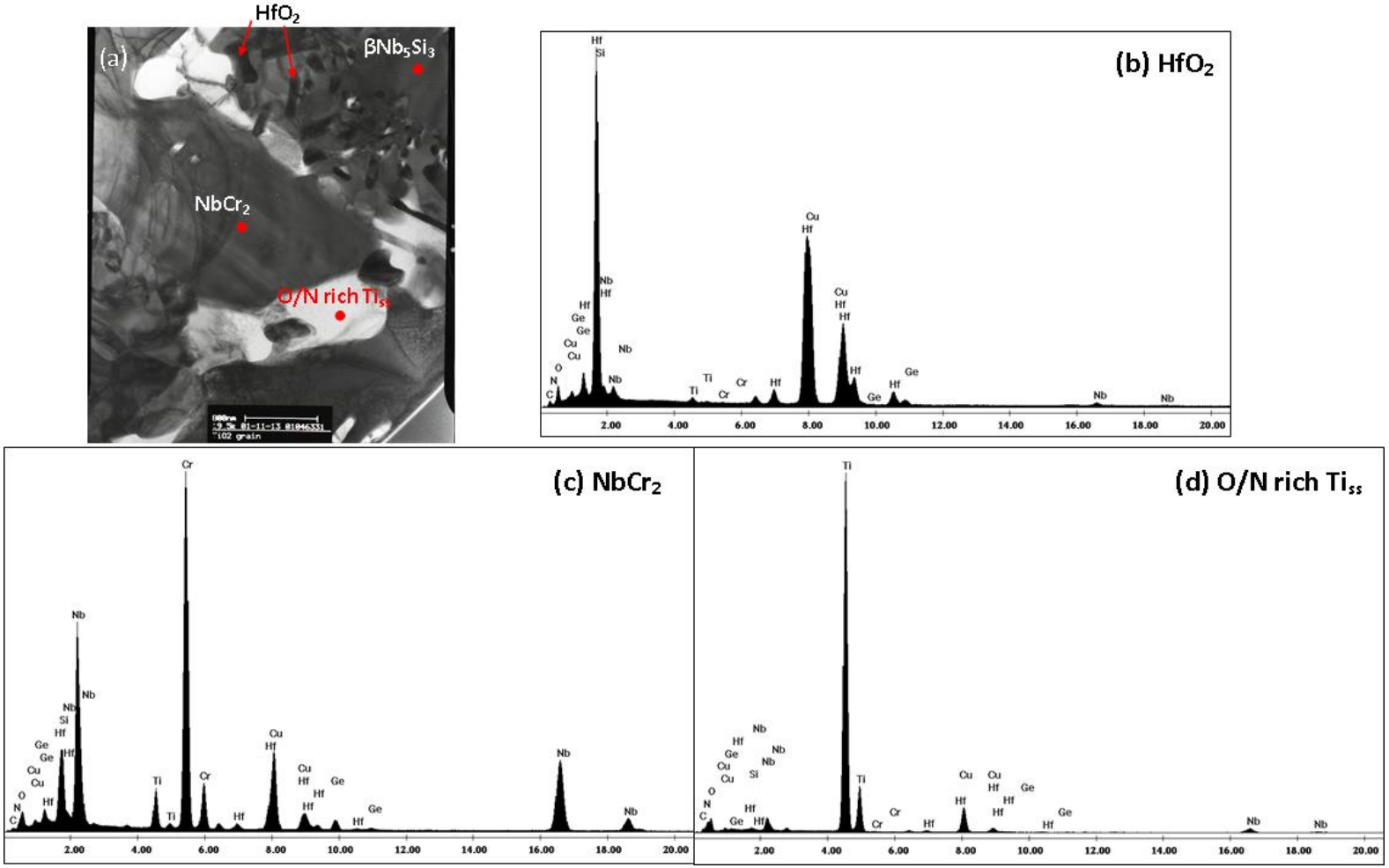

Figure 164. BF-TEM image and qualitive EDS spectra of TEM_Sample_2 extracted from the substrate microstructure of the GB2-HT-1200-5h specimen. (a) BF-TEM overview image, and the spectra of (b) HfO_2, (c) $NbCr_2$ and (d) O/N-rich Ti_{ss}.

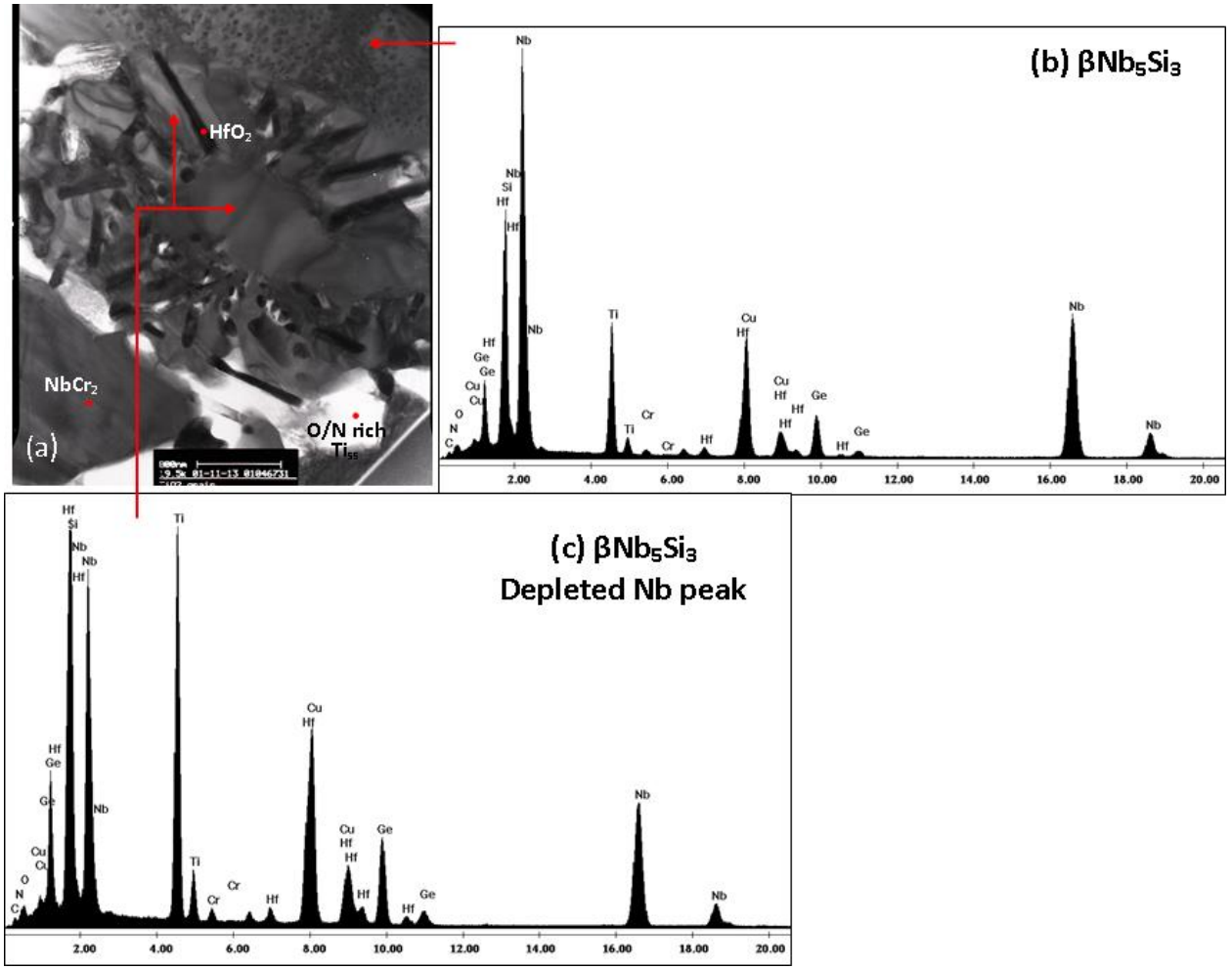

Figure 165. BF-TEM image and EDS spectra of TEM_Sample_2 extracted from the substrate microstructure of the GB2-HT-1200-5h specimen. (a) BF-TEM overview image, (b) a spectrum from the βNb_5Si_3 grain with internal precipitation, (c) a spectrum from a βNb_5Si_3 grain displaying grain boundary precipitation of HfO_2 and O/N-rich Ti_{ss}.

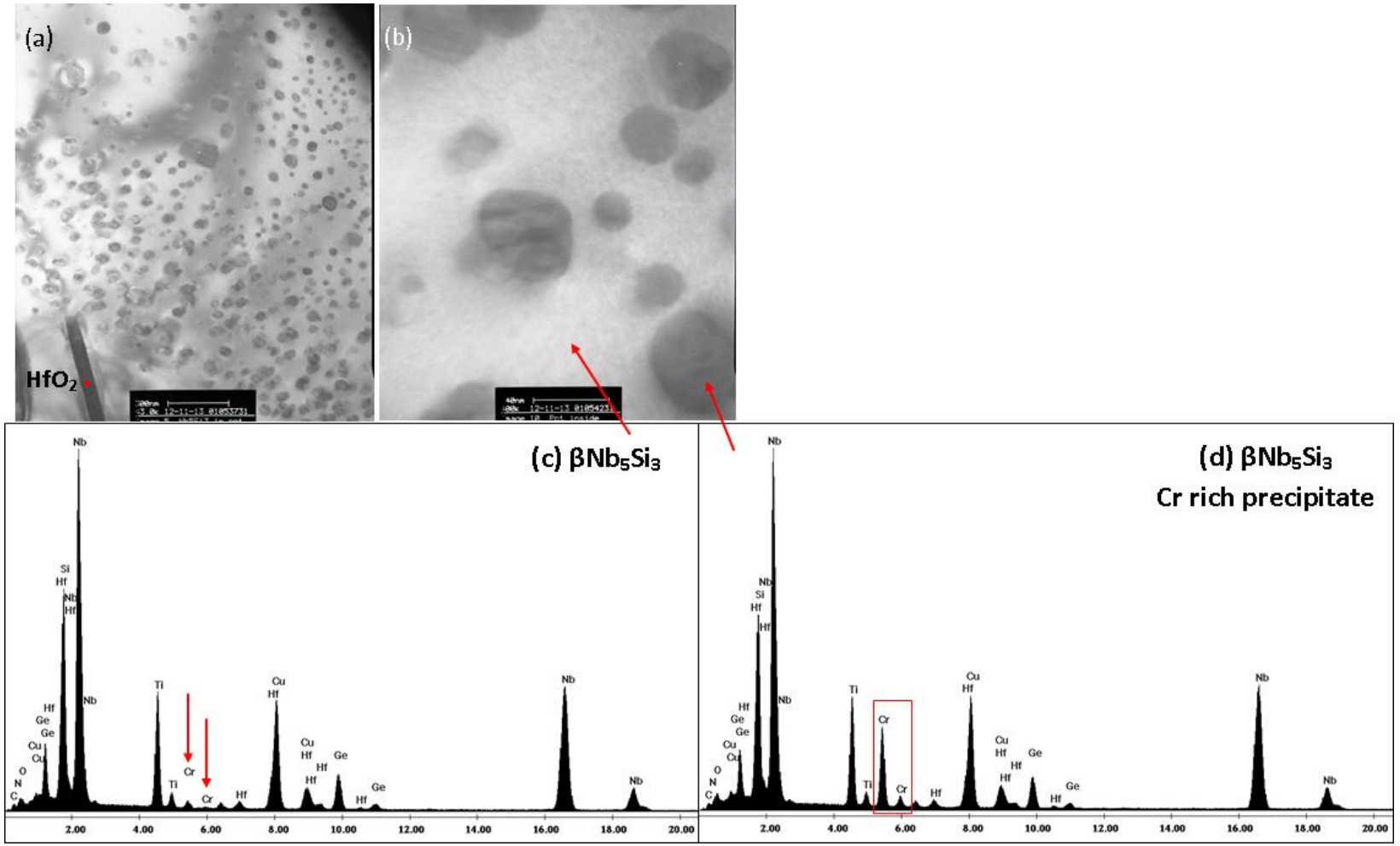

Figure 166. BF-TEM image and EDS spectra of TEM_Sample_2 extracted from the substrate microstructure of the GB2-HT-1200-5h specimen. (a) BF-TEM overview image, (b) BF-TEM image of precipitates formed within the βNb_5Si_3, (c) βNb_5Si_3 spectrum and (d) a spectrum of a Cr rich precipitate from within the βNb_5Si_3.

Table 51. WDS phase data from the GB2-HT-1200-25h specimen.

Phase	In/Out BPDZ	Depth (µm)	Nb	Si	Ti	Cr	Ge	Hf	O
βNb_5Si_3	In	25 - 100	39.4 ± 1.1 40.4 - 37.1	28.1 ± 1.0 29.1 - 25.9	15.1 ± 0.3 15.4 - 14.6	3.1 ± 0.8 4.1 - 1.7	7.0 ± 0.2 7.2 - 6.6	3.1 ± 0.1 3.3 - 2.9	4.3 ± 2.5 9.7 - 2.6
	Out	100 - bulk	39.9 ± 0.3 40.3 - 39.5	29.4 ± 0.7 30.1 - 28.2	14.5 ± 0.5 15.3 - 14.1	3.1 ± 0.4 3.7 - 2.7	6.9 ± 0.1 7.0 - 6.7	3.0 ± 0.1 3.1 - 3.0	3.2 ± 0.3 3.6 - 2.9
$NbCr_2$	In[a]	60 - 90	25.2 ± 0.8 26.1 - 24.4	7.9 ± 2.4 11.4 - 6.5	8.8 ± 2.7 12.8 - 7.1	50.4 ± 6.4 55.2 - 41.0	2.1 ± 1.2 3.9 - 1.5	2.7 ± 0.5 3.5 - 2.5	2.9 ± 1.0 4.4 - 2.2
	Out	100 - bulk	24.1 ± 0.4 24.7 - 23.8	6.5 ± 0.7 7.5 - 5.7	9.9 ± 1.0 11.5 - 8.9	54.0 ± 1.8 55.1 - 50.8	1.0 ± 0.4 1.6 - 0.7	2.5 ± 0.2 2.9 - 2.4	2.0 ± 0.2 2.4 - 1.7
$(Nb,Ti,Cr)_{ss}$	Out	100 - bulk	5.0 ± 0.7 6.1 - 4.3	65.3 ± 3.5 71.5 - 63.1	0.1 ± 0.7 0.9 - 0.0	20.1 ± 2.9 21.7 - 15.0	8.0 ± 0.4 8.4 - 7.3	1.0 ± 0.1 1.1 - 0.9	0.6 ± 0.4 1.0 - 0.0

[a]: 4 analysis points.

Table 52. WDS phase data from the GB2-HT-1200-10h specimen.

Phase	In/Out BPDZ	Depth (μm)	Nb	Si	Ti	Cr	Ge	Hf	O
βNb_5Si_3	In	5 - 75	40.2 ± 0.6	28.9 ± 1.2	14.9 ± 0.7	2.9 ± 0.7	7.1 ± 0.5	3.1 ± 0.1	2.9 ± 0.6
			40.9 - 39.2	31.0 - 26.6	16.1 - 14.1	4.0 - 2.0	8.2 - 6.5	3.2 - 3.0	4.1 - 2.3
	Out	100 - bulk	38.5 ± 4.6	28.9 ± 1.4	15.9 ± 4.0	3.0 ± 0.9	7.3 ± 0.7	3.4 ± 1.0	3.0 ± 0.6
			40.8 - 23.5	30.4 - 25.2	29.2 - 14.4	4.8 - 1.4	9.4 - 6.4	6.8 - 3.0	4.4 - 2.2
$NbCr_2$	In	0 - 60	24.8 ± 0.7	7.7 ± 1.4	9.1 ± 2.4	51.9 ± 3.7	1.5 ± 0.4	2.7 ± 0.3	2.2 ± 0.7
			25.9 - 24.0	9.4 - 5.8	12.3 - 5.9	56.1 - 47.7	2.1 - 0.9	3.1 - 2.5	3.5 - 1.4
	Out[a]	bulk	24.0 ± 0.2	6.2 ± 1.3	10.5 ± 1.3	53.3 ± 3.8	1.2 ± 0.7	2.7 ± 0.3	2.1 ± 0.2
			24.2 - 23.9	7.7 - 5.1	12.0 - 9.6	55.6 - 48.9	2.0 - 0.8	3.0 - 2.5	2.2 - 1.9
$(Nb,Ti,Cr)_{ss}$	In	20	55.6	0.6	16.0	6.8	0.9	0.4	19.6
		40	59.8	3.5	18.8	6.9	2.3	1.2	7.4
	Out	70 - bulk	62.3 ± 4.4	1.0 ± 2.1	21.2 ± 1.2	8.2 ± 1.0	1.2 ± 0.9	0.9 ± 0.7	5.3 ± 0.8
			65.3 - 54.5	4.7 - 0.0	23.2 - 20.2	8.9 - 6.5	2.8 - 0.5	2.0 - 0.2	6.2 - 4.5

[a]: 3 analysis points.

Table 53. Compositional change of substrate phases in at% by comparing average GB2-HT EDS data (Table 25) with GB2-HT-1200-25h WDS data (Table 51).

Phase	In/Out BPDZ	Depth (µm)	Nb	Si	Ti	Cr	Ge	Hf	O
βNb_5Si_3	In	25 - 100	-1.3	-1.9	-2.2	+1.4	-0.4	+0.2	+4.3
	Out	100 - bulk	-0.8	-0.6	-2.8	+1.4	-0.5	+0.1	+3.2
$NbCr_2$	In	60 - 90	-0.4	-0.4	-2.4	-0.9	+1.0	+0.3	+2.9
	Out	100 - bulk	-1.5	-1.7	-1.4	+2.7	-0.2	+0.1	+2.0
$(Nb,Ti,Cr)_{ss}$	Out	100 - bulk	+0.1	-0.8	-3.1	-1.3	+0.5	-0.3	+5.0

Table 54. Compositional change of substrate phases in at% by comparing average GB2-HT EDS data (Table 25) with GB2-HT-1200-10h WDS data (Table 52).

Phase	In/Out BPDZ	Depth (µm)	Nb	Si	Ti	Cr	Ge	Hf	O
βNb_5Si_3	In	5 - 75	-0.5	-1.1	-2.4	+1.2	-0.3	+0.2	+2.9
	Out	100 - bulk	-2.2	-1.1	-1.4	+1.4	-0.1	+0.4	+3.0
$NbCr_2$	In	0 - 60	-0.8	-0.6	-2.2	+0.7	+0.4	+0.3	+2.2
	Out	bulk	-1.6	-2.0	-0.8	+2.0	+0.1	+0.3	+2.1
$(Nb,Ti,Cr)_{ss}$	In	20	-9.6	-0.2	-7.2	-2.5	+0.4	-0.5	+19.6
		40	-5.4	+2.7	-4.4	-2.4	+1.8	+0.3	+7.4
	Out	70 - bulk	-3.0	+0.2	-2.0	-1.1	+0.6	0.0	+5.3

5.6.2 Oxide Scale

After only 5h of oxidation at 1200°C the oxide scale displayed some elemental layering, as indicated by the X-ray mapping (Figure 167 and Figure 168). Inspection of TEM_Sample_3 extracted from the outer oxide edge (Figure 169) confirmed the fine grained oxide layer consisted of (Ti,Cr)-based and Nb-based niobates (Figure 170) surrounded by a SiO_2 matrix (Figure 171) while the coarse niobate layer underneath was a combination of Ti/Cr and Nb niobates (Figure 172). Inspection of another coarse oxide region (TEM_Sample_4 in Figure 173) was confirmed by TEM-EDS to consist of large Ti-based oxides and a small layer of Cr-rich niobate (Figure 174). Below the niobate layers the oxide scale was a broad mixture of niobate + SiO_2 + HfO_2, similar to what was identified after 50 and 100h of oxidation (Figure 175, Figure 176 and Figure 177). A Ge rich phase within the oxide scale was detected (Figure 177f) that showed a weak O peak count making it unlikely to be GeO_2, this phase was not found in FIB TEM samples and is unfortunately left inconclusive.

The substrate edge of the 5h and 10h specimens showed little oxidation of the βNb_5Si_3 and was devoid of a Nb-Si-Ge-O layer at the substrate edge. The 25h specimen, however, possessed an adhered oxide scale as opposed to the 10 and 5h specimens and presented βNb_5Si_3 grains consumed by oxidative attack. Although X-ray maps of the 25h specimen was not performed, it is speculated the more severe oxidation of the βNb_5Si_3 silicide induced the formation of the Nb-Si-Ge-O layer at the substrate edge and was responsible for the enhance oxide scale adhesion of alloy GB2 than GB1.

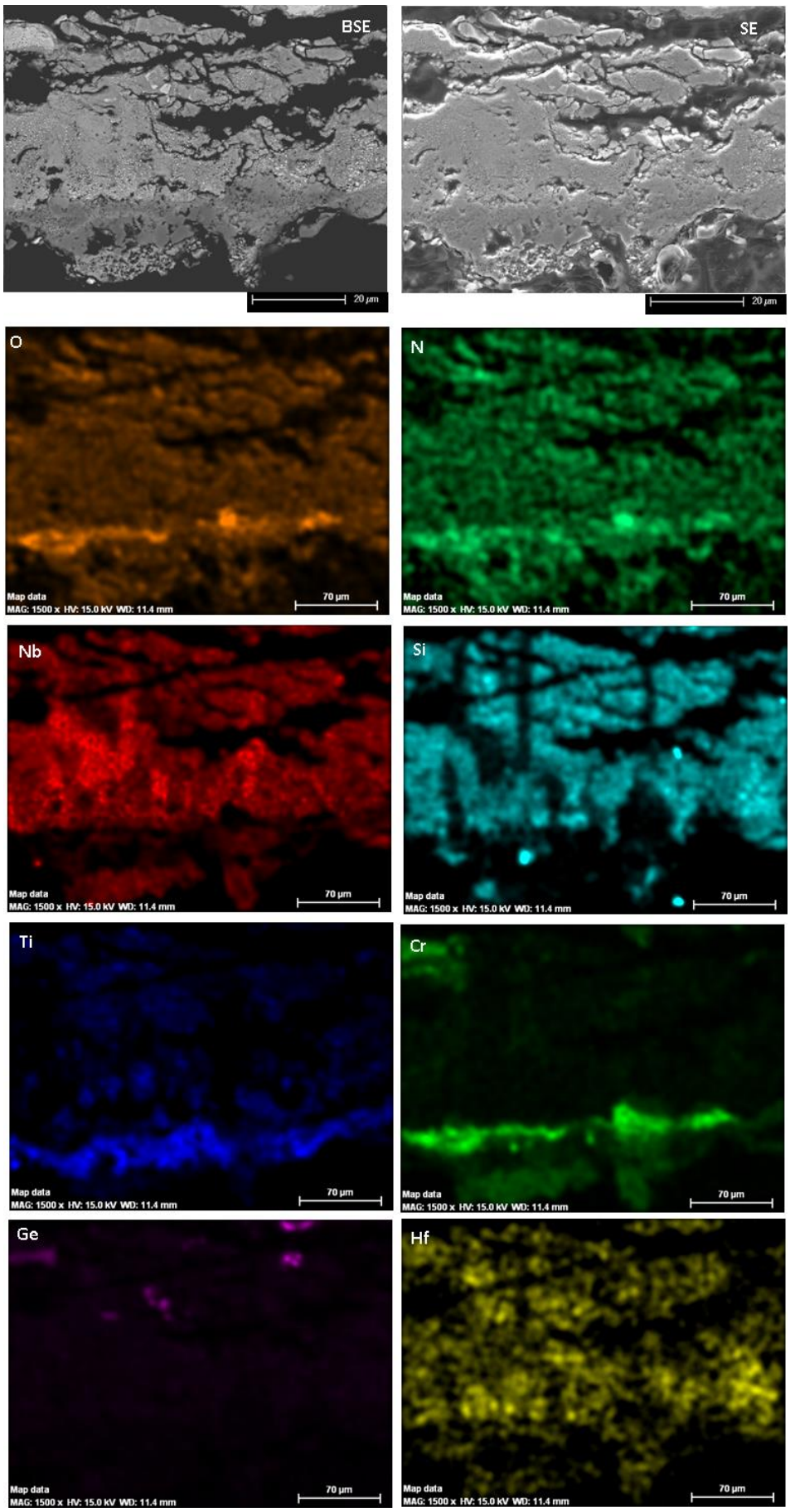

Figure 167. EDS X-ray maps of the oxide scale formed on the GB2-HT-1200-5h specimen. The botton edge of the image is the exposed outer surface of the oxide scale.

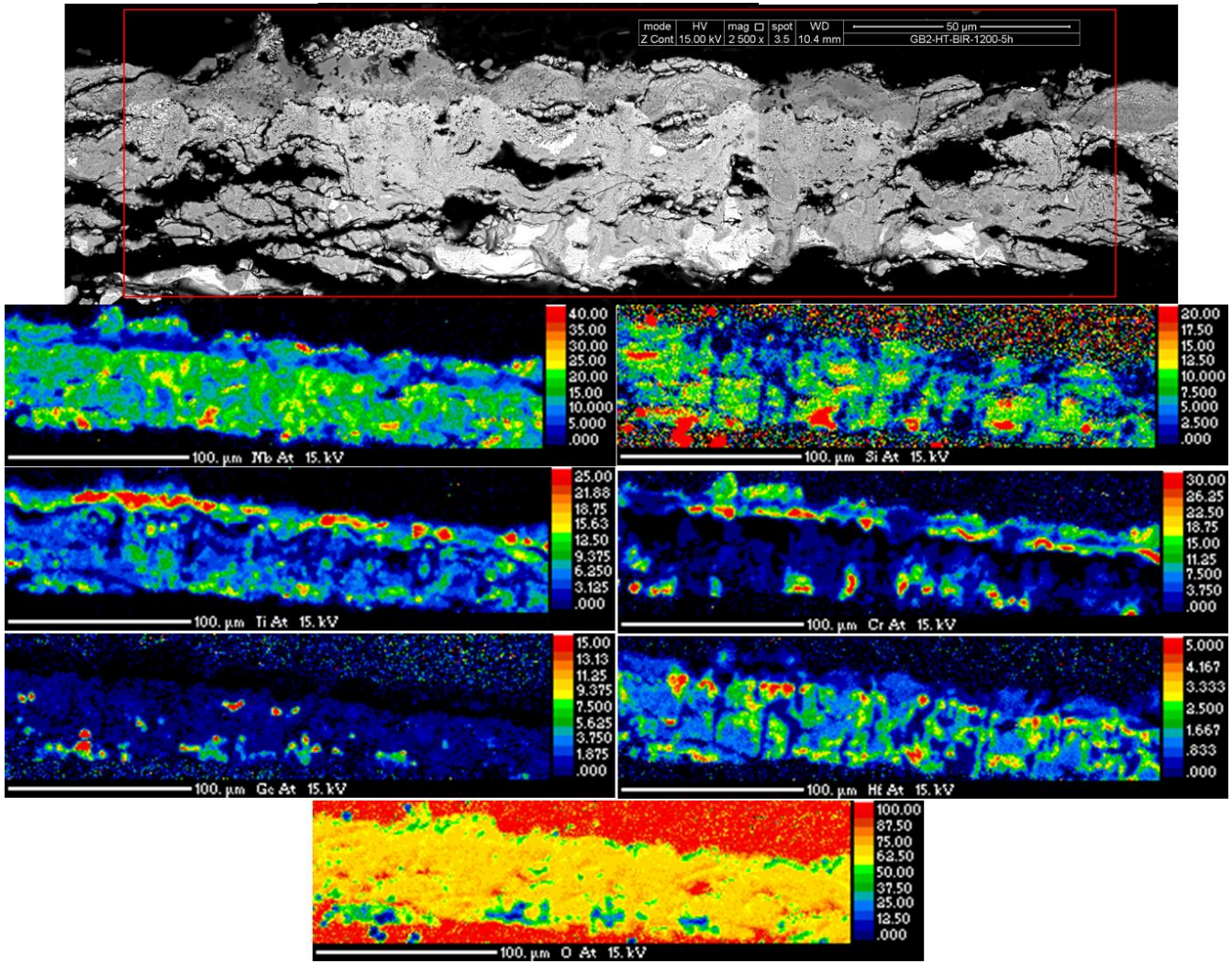

Figure 168. WDS X-ray maps of the oxide scale formed on the GB2-HT-1200-5h specimen. The outer oxide edge is at the top of the respective maps.

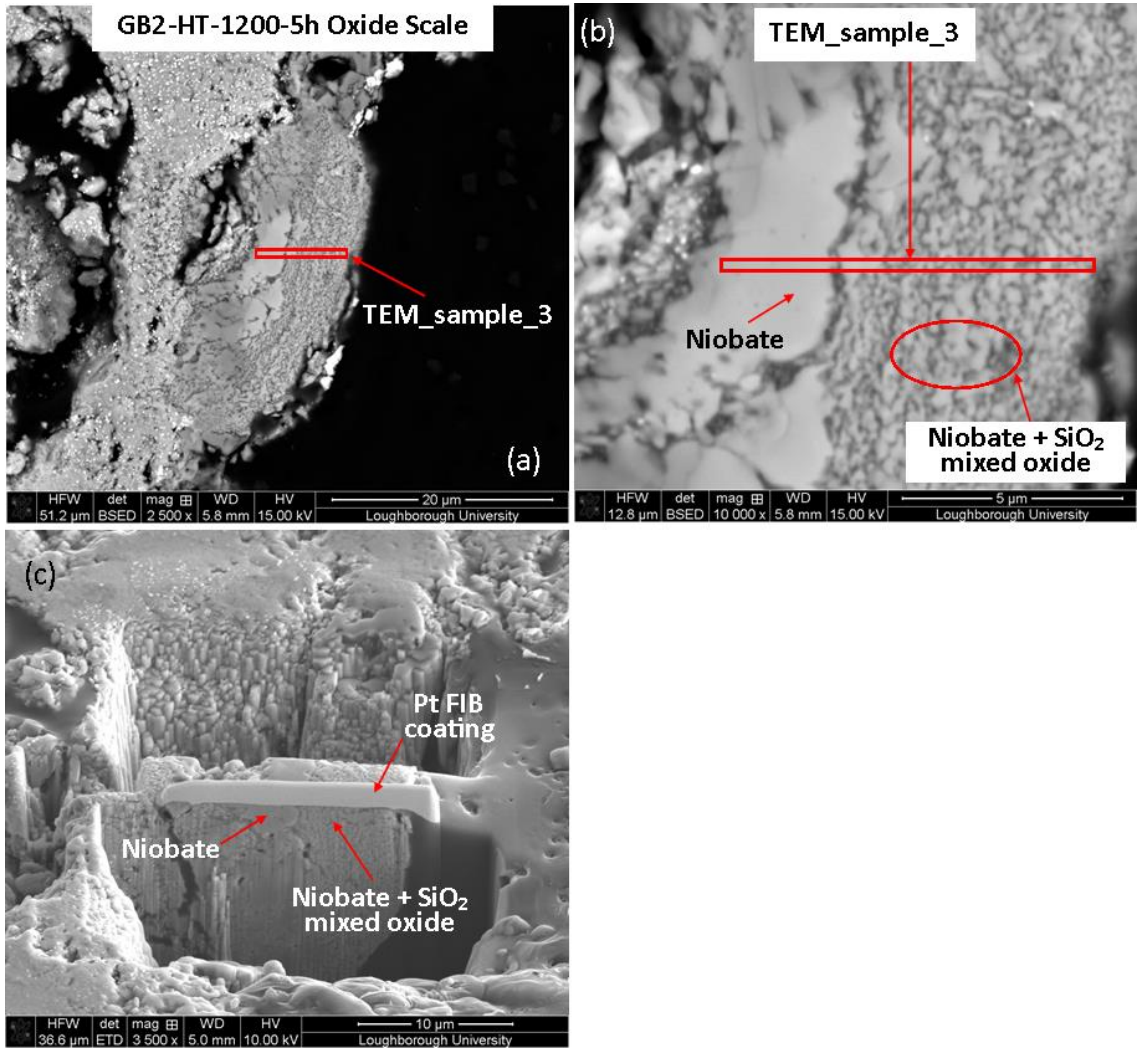

Figure 169. BSE-SEM image locating TEM_Sample_3 extracted from the oxide scale of the GB2-HT-1200-5h specimen.

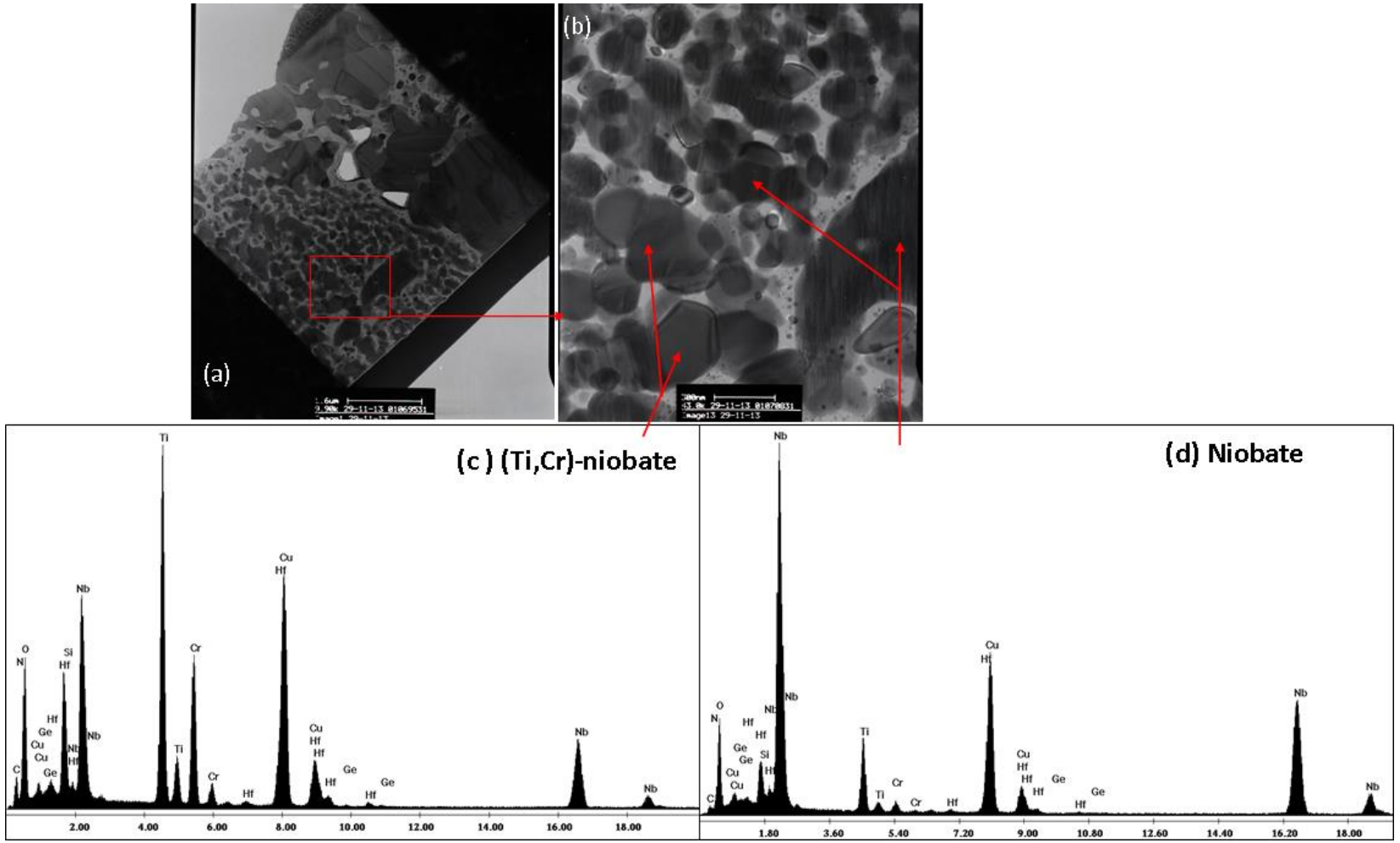

Figure 170. BF-TEM image and qualitive EDS spectra of TEM_Sample_3 extracted from the oxide scale of the GB2-HT-1200-5h specimen. (a) BF-TEM image, (b) region where EDS spectra (c) of a Ti-niobate grain and (d) of a niobate grain were taken.

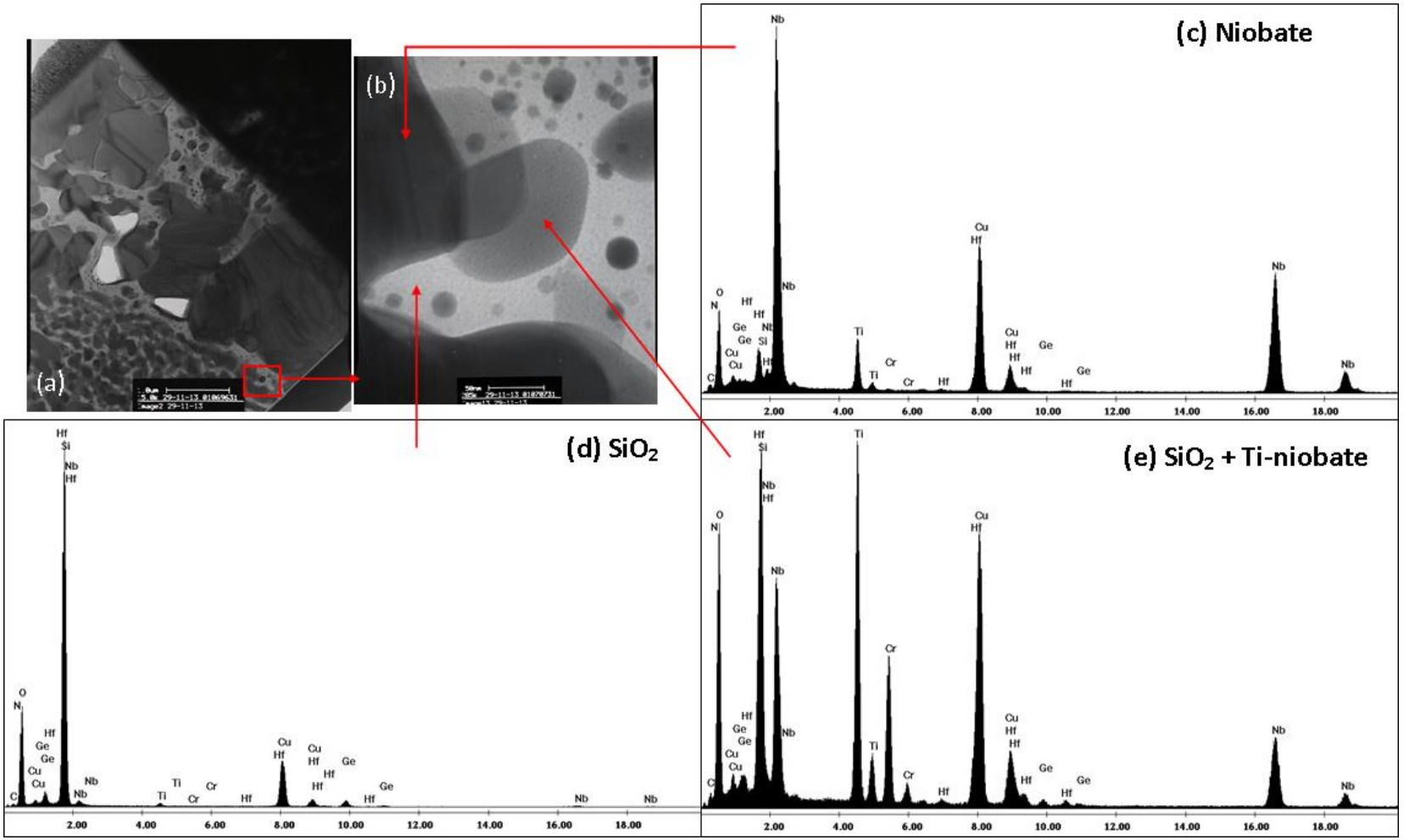

Figure 171. BF-TEM image and qualitive EDS spectra of TEM_Sample_3 extracted from the oxide scale of the GB2-HT-1200-5h specimen. (a) BF-TEM image, (b) region where EDS spectra (c) of a niobate grain , (d) of SiO_2 and (e) a combined detection of SiO_2 and Ti-niobate.

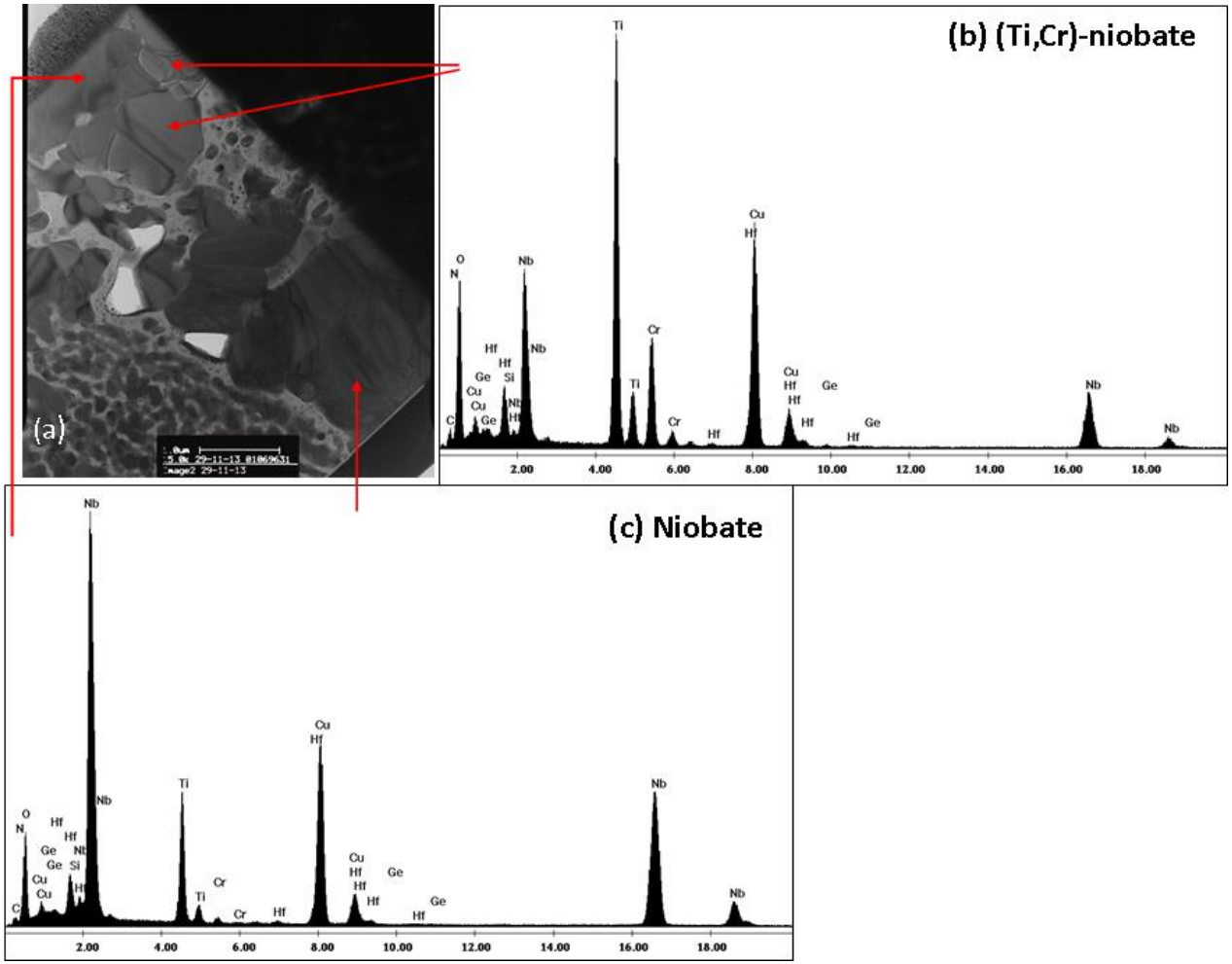

Figure 172. BF-TEM image and qualitive EDS spectra of TEM_Sample_3 extracted from the oxide scale of the GB2-HT-1200-5h specimen. (a) BF-TEM image where EDS spectra (b) of larger (Ti,Cr)-niobate grains and (c) larger niobate grains were taken.

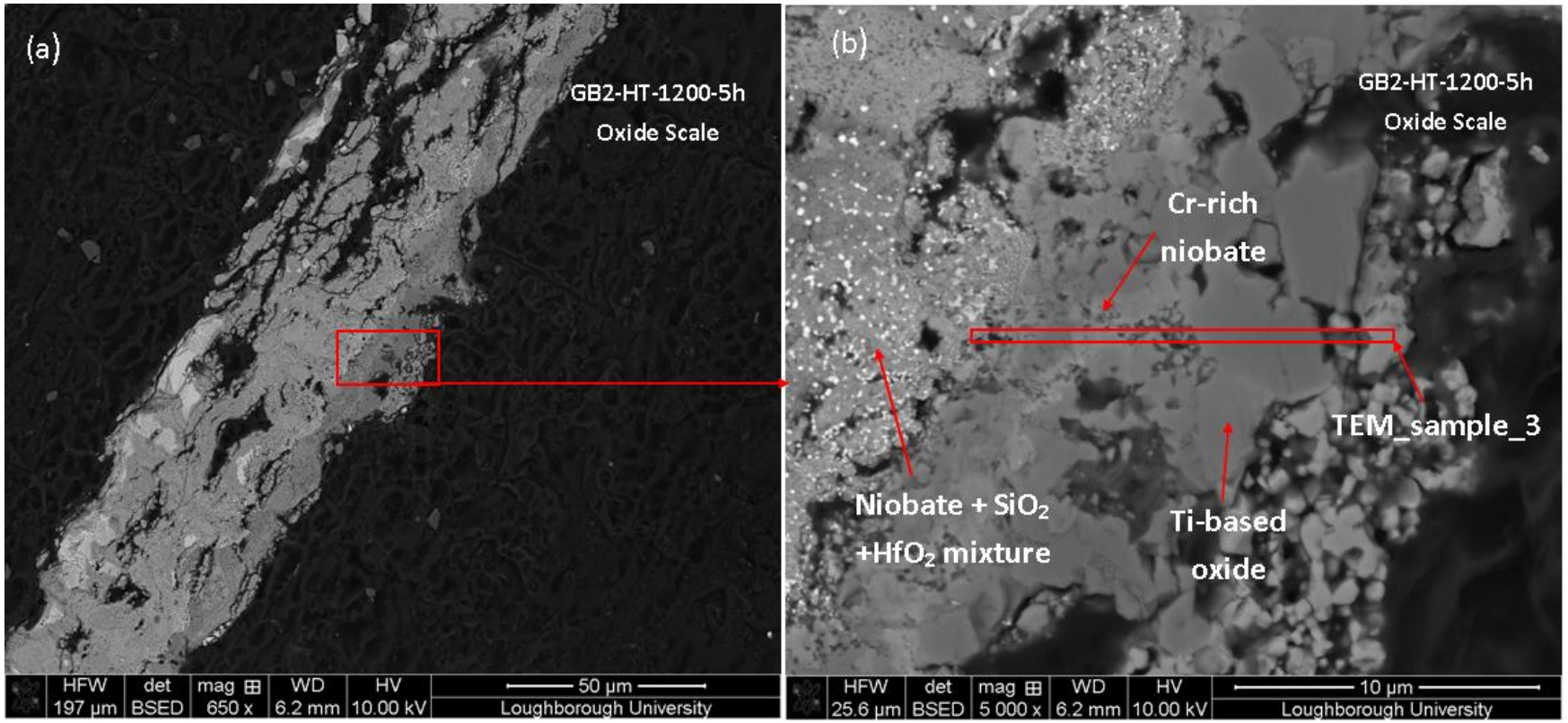

Figure 173. BSE-SEM image locating TEM_Sample_4 extracted from the outer oxide scale of the GB2-HT-1200-5h specimen. Note the oxide scale had delaminated from the substrate alloy.

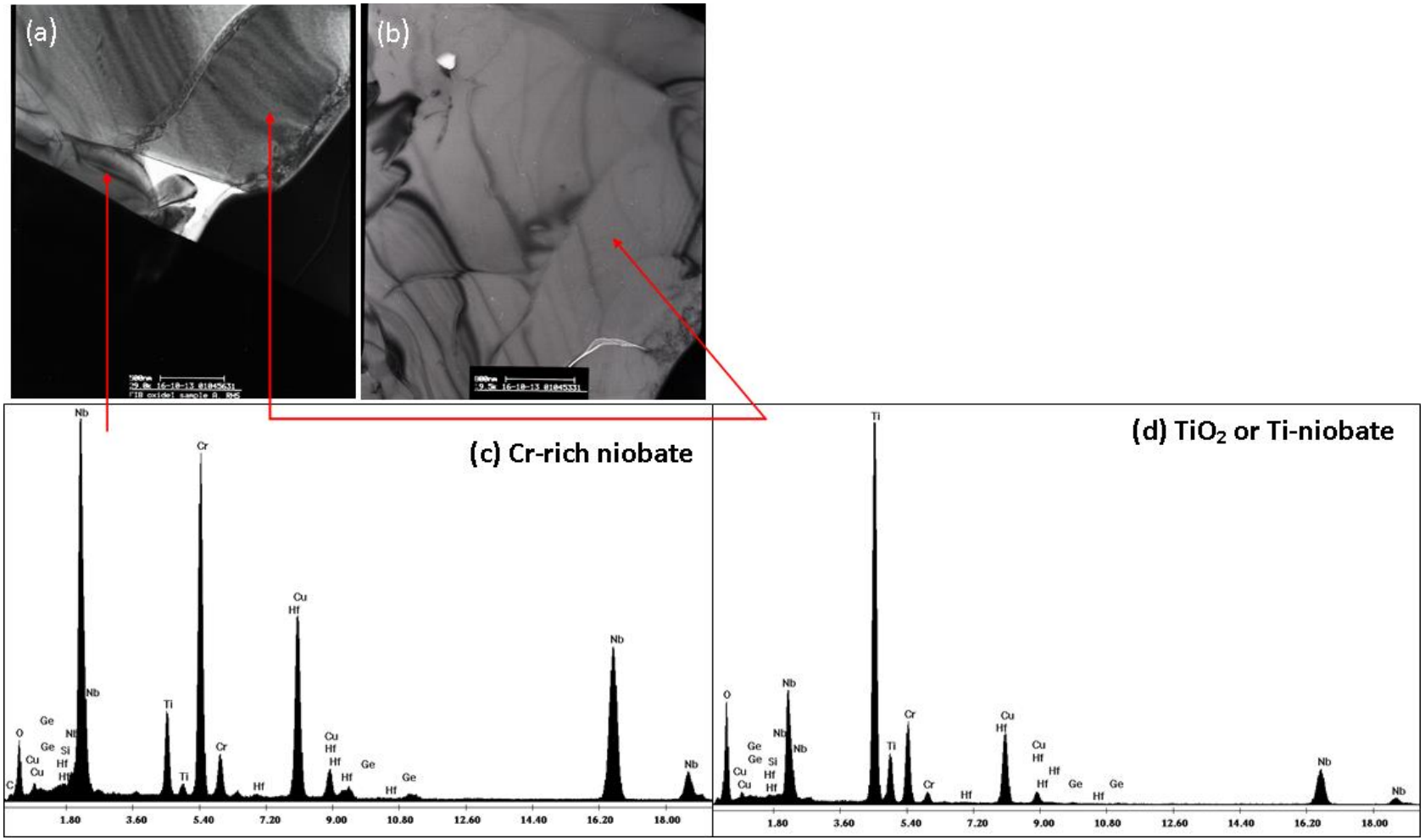

Figure 174. BF-TEM image and qualitive EDS spectra of TEM_Sample_4 extracted from the oxide scale of the GB2-HT-1200-5h specimen. (a) and (b) are BF-TEM images where EDS spectra (c) of a Cr-rich niobate and (d) of a Ti based oxide possibly TiO_2 or Ti-niobate were taken.

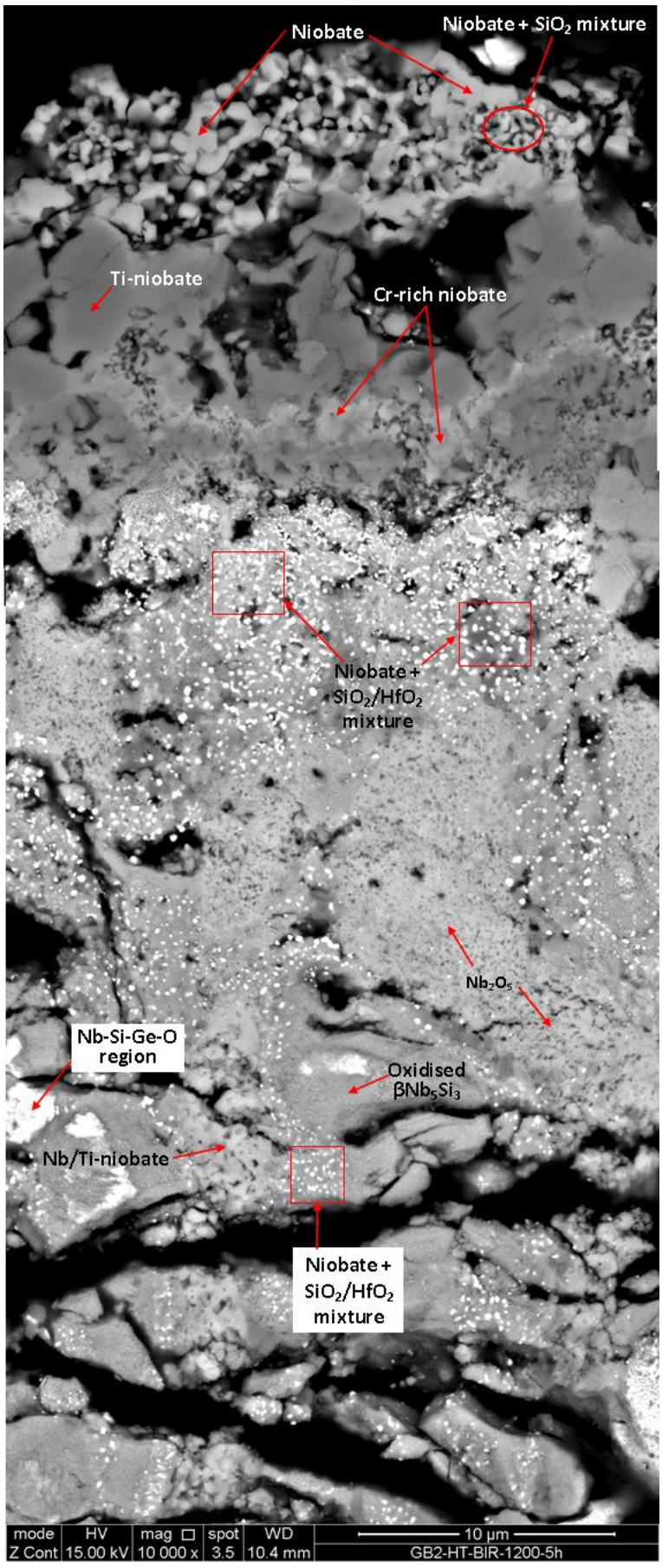

Figure 175. High magnification BSE-SEM images providing an overview of the oxide scale formed on the GB2-HT-1200- 5h specimen. The top edge of the image depicts the outer oxide layers.

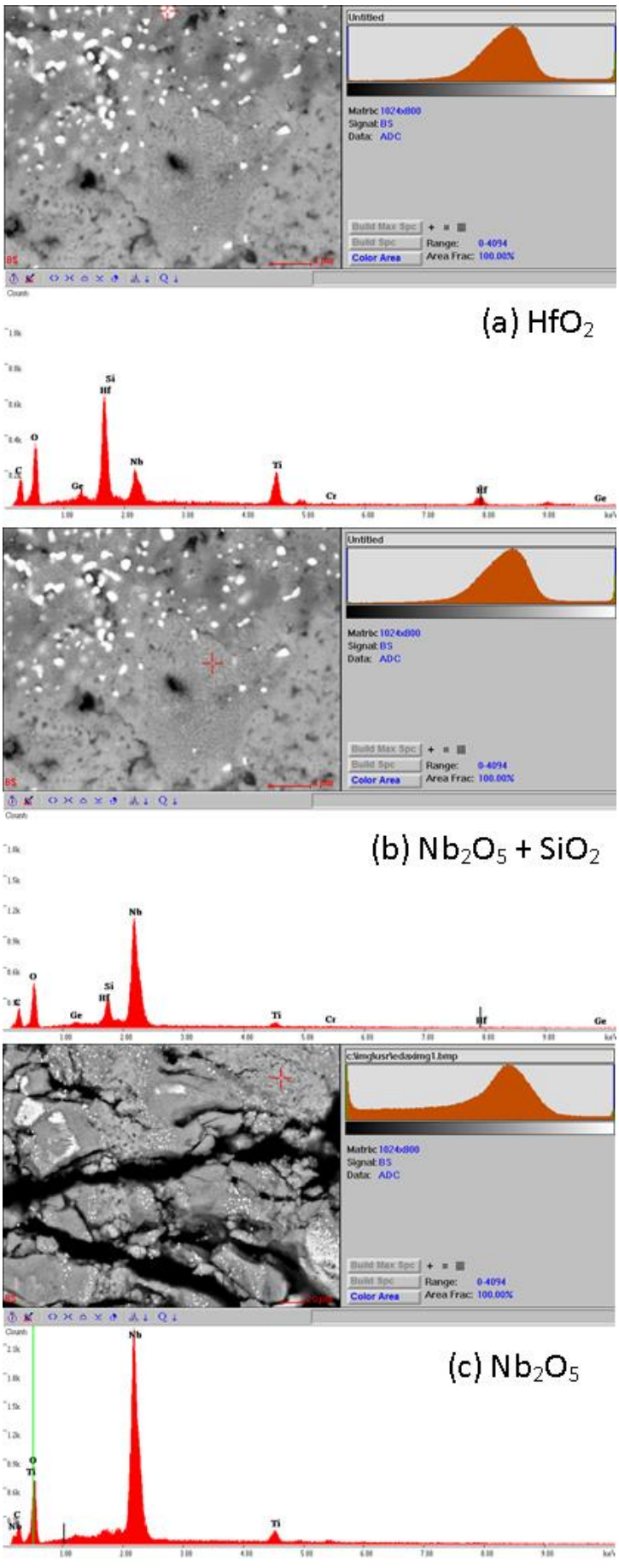

Figure 176. Standardless EDS using the FEI InspectF high resolution SEM of the oxide scale formed on the GB2-HT-1200-5h specimen. Spectra of the (a) HfO_2, (b) $Nb_2O_5 + SiO_2$, (c) Nb_2O_5.

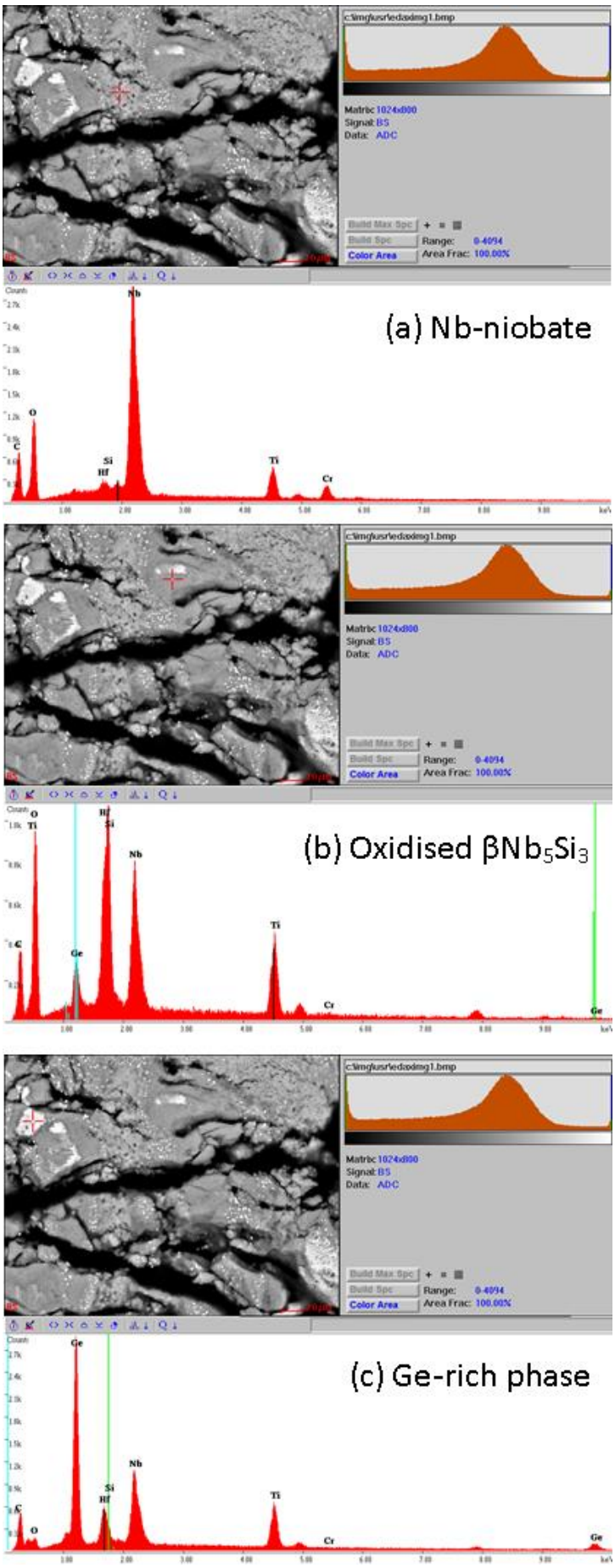

Figure 177. Standardless EDS using the FEI InspectF high resolution SEM of the oxide scale formed on the GB2-HT-1200-5h specimen. Spectra of the (a) Nb-niobate, (b) oxidised βNb_5Si_3, (c) Ge-rich phase.

5.7 Discussion

5.7.1 Kinetics & Internal Oxidation

The slow oxide growth kinetics, low O penetration, and good specimen integrity after oxidation at 800 and 1000°C indicated that no pest oxidation had occurred for alloys GB1 and GB2. For alloy GB2 oxidised at 1200°C, there was insufficient evidence to clarify if the slightly better overall weight gains (Figure 112) of the HT condition was due to the $\beta Nb_5Si_3 \rightarrow \alpha Nb_5Si_3$ transformation that had altered the dominant silicide of the microstructure. For all the 1200°C oxidised specimens, despite some test-to-test variation in overall weight gain, the parabolic rate constants were the same magnitude of 10^{-10} $g^2cm^{-4}s^{-1}$, and similar oxide scale thickness' formed. Futhermore, the internal oxidation of the GB2-AC/HT specimens were remarkably similar, hence, for the time being β and α Nb_5Si_3 are considered to have the same influence on oxidation performance.

The microstructures of both alloys were different to those reported in literature that do or do not pest. The lack of pesting and overall good oxidation behaviour relative to other Nb-silicide alloys at the three temperatures studied in this work was attributed to the low volume fraction of the Nb_{ss} and the high volume fraction of the $NbCr_2$ Laves phase. Additionally, the location of the Laves phase in the microstructure was considered significant as the high phase fraction resulted in a disconnected $(Nb,Ti,Cr)_{ss}$ throughout both of the GB1 and GB2 microstructures. This microstrucral architecture allowed the $NbCr_2$ Laves phase to act as a diffusion barrier for the $(Nb,Ti,Cr)_{ss}$, preventing direct access of inwardly diffusing O and forcing it to diffuse more slowly through the $NbCr_2$. This would suggest grain boundary diffusion was the mode of interstitial transport to the $(Nb,Ti,Cr)_{ss}$ before the $NbCr_2$ Laves phase became saturated in O.

The benefits of having a low Nb_{ss} phase fraction and a high Laves phase fraction is proposed based on the comparison of alloys GB1 and GB2 with other alloys that possess a large phase fraction of Nb_{ss} and only little to zero Laves phase fraction in their microstructures. For example, in the work of Geng and Tsakiropoulos, (2007) the alloys JG1-AC (Nb-18Si-5Al-5Cr-5Mo), JG2-AC (Nb-24Ti-18Si-5Al-5Cr-5Mo), JG3-HT (Nb-24Ti-18Si-5Al-5Cr-2Mo), and JG4-HT (Nb-24Ti-18Si-5Al-5Cr-2Mo-5Hf) degraded by pesting completely (JG1) or partially (JG2, JG3, JG4) and had poorer oxidation behaviour than GB1 and GB2, which suffered less internal attack and oxide growth (see Table 26, Table 27, and Table 28). Other than the lower Cr and higher Nb content of the JG alloys, the only other compositional difference to GB1 and GB2 was a small Mo addition, making this a reasonable comparison of alloys with or without high Laves phase fraction.

Comparison of the GB1-AC and GB2-AC specimens oxidised at 800 and 1000°C showed there was little difference between the oxide products formed, with the latter alloy performing slightly better in weight gain, rate constant, and forming less surface oxide at 800°C. At 1000°C, alloy GB1-AC showed lower overall weight gain than alloy GB2-AC but linear kinetics. The higher weight gain of GB2-AC may be attributed to the irregularly volumous oxide growth at a corner of the specimen due to an unforeseen crack in the sample (as was discussed in section 5.3.2). At 1000°C, Nb_5Si_3 grains appeared engulfed and part of the thin oxide scale that was predominatly Ti-niobate or TiO_2. $NbCr_2$ grains could not be identified in the oxide scale but were most likely oxidised after attacking O consumed $(Nb,Ti,Cr)_{ss}$ and grew a voluminous enough scale. It is clear that Nb-silicide based alloys suffer internal attack via the solid solution, the findings of this thesis indicate the $NbCr_2$ and Nb_5Si_3 have a much lower reactivity than $(Nb,Ti,Cr)_{ss}$ to O. At the lower temperatures of 800 and 1000°C diffusion via grain boundaries is suggested to be the mode of diffusion for O to reach and react with $(Nb,Ti,Cr)_{ss}$ as the $NbCr_2$ showed little oxidation at these temperatures yet precipitation occurred from the $(Nb,Ti,Cr)_{ss}$.

At 800°C circular precipitates of HfO_2 had formed at silicide/interdendritic boundaries only in GB2-AC despite alloy GB1-AC possessing twice as much Hf. At 1000°C both alloys formed slightly more HfO_2 with a significant presence formed after oxidation at 1200°C. At 1200°C, formation of HfO_2 occurred for both alloys predominately at $(Nb,Ti,Cr)_{ss}/NbCr_2$ grain boundaries or within the $(Nb,Ti,Cr)_{ss}$, but only micron size precipitates formed in the $NbCr_2$, reiterating its lower reactivity and suseptibility to oxidation. Alloys GB1-AC/HT precipitated more HfO_2 than GB2-AC/HT, which is consistent with the higher Hf content of alloy GB1. Alloy GB1-HT was, however worse than GB1-AC and formed HfO_2 to a greater depth (Figure 115), the cause of which is unclear as the $NbCr_2$ and $(Nb,Ti,Cr)_{ss}$ in the HT condition showed less Hf content than in the AC (Table 22). Oxidation of the Hf-rich γNb_5Si_3 silicide in such specimens resulted in HfO_2 formation at grain boundaries. However, this only occurred for grains caught in the BPDZ (compare Figure 114c and e). As HfO_2 was not found in the GB1-HT-1200-50h specimem yet O/N-rich Ti_{ss} was particularly present at $(Nb,Ti,Cr)_{ss}/NbCr_2$ grain boundaires, this suggests a stronger affinity for O dissolution and stabilisation of Ti_{ss} from the $(Nb,Ti,Cr)_{ss}$ than the formation of HfO_2. The preference of Ti_{ss} precipitation from the $(Nb,Ti,Cr)_{ss}$ is supported by WDS data highlighting Ti depletion of the $(Nb,Ti,Cr)_{ss}$ (Table 43).

At 1200°C, alloy GB2-AC/HT had similar amounts of HfO_2 formation that was noticeably less than in alloy GB1, which was logical as there was approximately half the Hf content in GB2 than in GB1. The HfO_2 formed deeper than Ti_{ss}, at $(Nb,Ti,Cr)_{ss}/NbCr_2$ grain boundaries, within the $(Nb,Ti,Cr)_{ss}$, and at Nb_5Si_3 grain boundaries for silicide grains engulfed in the BPDZ. Similar

to GB1, any HfO_2 or Ti_{ss} precipitation in $NbCr_2$ was micron sized and restrained to the BPDZ (Figure 133 and Figure 134). The higher 1200°C oxidation temperature was a factor for enhancing Hf reactivity from the $(Nb,Ti,Cr)_{ss}$ as HfO_2 was not seen in this phase for the 1000°C specimens. The lesser precipitation from the $NbCr_2$ reiterates its better oxidation resistance and capability to act as a diffusion barrier for $(Nb,Ti,Cr)_{ss}$. Generally WDS phase analysis records the $NbCr_2$ Laves phase to contain ≤ half the O of the $(Nb,Ti,Cr)_{ss}$ (Table 32, Table 38, Table 45, Table 46).

In addition to HfO_2, micron sized precipitates appearing black under BSE-SEM had formed at all three test temperatures for both alloys and were identified as O/N-rich Ti_{ss}, as discussed in section 5.4.2. This identification is in conflict to findings by numerous authors of whom conflict with each other for their Nb-silicide based alloys that all possess significant Ti content (15 - 25 at.%). The black precipitates (under BSE-SEM contrast) have previously been identified as either internal TiO_2 (or Ti-oxides) for samples oxidised in air at eleveated temperatures (Geng et al., 2006b; Jun et al., 2009; Knittel et al., 2014a; Su et al., 2014a; Zhang and Guo, 2015b) or TiN found in alloys after HT (Geng et al., 2006b, 2006c; Guo and Guo, 2011; Zelenitsas and Tsakiropoulos, 2005, 2006a). Hence, to the awareness of the author of this thesis, TiO_2 and TiN internal precipitates have not been reported together for a single alloy microstructure after oxidation or HT.

Firstly, reviewing the lesser formed and reported TiN found in heat treated alloys. The HT apparatus and environment utilises flowing Ar gas to remove any air atmosphere in the HT furnace in addition to a pure Ti getter or sponge adjacent to the sample of interest. Any O or N from air not displaced by argon in the furnace should be preferentially reacted by the getter/sponge and not the alloy under HT that is most likely less reactive than pure Ti. There are two trains of thought to the exclusive detection of TiN in the HT alloys. When considering stabilies of comparably basic oxides and nitrides; TiO and TiN, their enthalpies of formation; $-\Delta H_{t^o}$TiO= -123.92 ± 0.28 (kcal/mol) $-\Delta H_{t^o}$TiN= -80.47 ±0.27 (kcal/mol), the TiO oxide is more stable (Humphrey, 1951a, 1951b) and that Ti shows a stronger reactivity and rate of corrosion product growth with O than N (Gulbransen and Andrew, 1949). This would lead to the speculation that in the HT furnace, O from the air was preferentially absorbed and saturated the getter/sponge, leaving a higher than normal N content in the furnace that was capable of dissolving into the alloy being heat treated.

Another explanation for the exclusive TiN detection after HT is that the TiN analysis had error. This could either stem from detection difficulties and/or insufficient calibration due to the well known WDS overlap of $Ti_{L\alpha}$ and $N_{K\alpha}$ X-rays energy peaks and their close wavelengths ($Ti_{L\alpha}$ =

0.4522 keV & 27.417 Å, $N_{K\alpha}$= 0.3924 keV & 31.596 Å) causing deconvolution problems. The various literature (metioned above) that detected TiN after HT do not provide description of their calibration process to how the close element X-rays were resolved. Another source of WDS error may be due to the omission of O from the detection. As O has not been analysed for it cannot be completely excluded and should not be since the attacking atmosphere contains it, and especially since Ti has a stronger affinity for O than N. This omission of detection may also apply in vice-versa for N detection in the internal Ti oxide precipitates found after oxidation tests.

An omission of N detection for oxidised specimens was not only performed in this thesis but also by the authors mentioned above (Geng et al., 2006b; Jun et al., 2009; Knittel et al., 2014a; Su et al., 2014a; Zhang and Guo, 2015b). Geng et al., (2007a) did, however, identify by WDS the internal black precipitates that formed in their Nb-24Ti-18Si-5Al-5Cr-2Mo-5Hf-5Sn (JG6) alloy after oxidation at 1200°C for 96h to be TiN, although in a older publication by the same authors for Nb-24Ti-18Si-5Cr-5Al-2Mo (JG3) and Nb-24Ti-1Si-5Al-5Cr-2Mo-5Hf (JG4) alloys that were oxidised at 1200°C after HT, the internal black precipitates were identified as TiO_x (Geng et al., 2006b). Clearly, there is some conflict and conjecture amongst the literature to the identity of the internal black precipitate formed and whether the formation is exclusively oxide or nitride. At least this thesis, and the authors mentioned, can agree the precipitate is Ti based.

The omission of N in the analysis of GB1 and GB2 is admittedly an oversight. However, calibration of the CAMECA SX-100 microprobe to deconvolute analysis with confidence between $Ti_{L\alpha}$ and $N_{K\alpha}$ X-rays in addition to detecting O from micron size precipitates would have been a great struggle. Limited equipment availability would not help the calibration difficulty either. This problem was likely the same for the authors mentioned. The TEM-EDS spectra obtained only conveyed low N peak intensities with an EDS detector capable of ~ 0.1 KV resolution that cannot definitively resolve $Ti_{L\alpha}$ and $N_{K\alpha}$ or $O_{K\alpha}$ X-ray peaks.

Unfortunately, the results of this thesis do not resolve the Ti based precipitates identity, they infact add more conjecture since a Ti oxide could not be identified by the data and a O/N-rich Ti_{ss} has been concluded. The precipitation of interstitial rich Ti_{ss} from a $(Nb,Ti,Cr)_{ss}$ is logical given the known dissolution of O and N into Nb-silicide based alloys and preferred reactivity of Ti. The factors governing whether the initial Ti_{ss} precipitates result in oxide or nitride formation, and then the successive oxide formation and growth are still to be understood. Competitive TiO_2 and TiN formation may be an overlooked factor in the oxidation of Nb-silicide based alloys. A key finding of Geng et al., (2007a) was TiN formation in JG6 during oxidation

reduced O penetration into the base alloy. Alloy JG6 had better oxidation performance than JG3 that internally formed TiO_x instead. These findings are in partial agreement with Chaze and Coddet (1986) who compared the oxidation of Ti in air and pure O between 500 – 700°C. They found the formation of TiN decreased the O diffusion rate in Ti_{ss} and reduced the growth rate of TiO_2.

The influence of N during the oxidation of Nb-silicide based alloys should not be overlooked. The clarification of the Ti-based precipitates composition, whether it exclusively contains O or N, its structure, and how it forms, may lead to a better understanding of the mechanism of internal oxidative attack of the Nb_{ss} and the formation and growth of oxide scales on Nb-silicide based alloys.

5.7.2 Oxide Scale

At 800°C the oxide scale products on alloys GB1 and GB2 are minimal, forming mixed Ti/Cr-niobates and TiO_2 on the specimen surface. Oxide formation was not epitaxial and would initially occur at interdendritic regions of the alloy surface, specifically surface $(Nb,Ti,Cr)_{ss}$ grains were absoption sites of O. This also indicates the relatively low reactivity of the silicide and $NbCr_2$ with O. At 1000°C complete oxide scale coverage of both alloys occurred forming a denser mixed Ti-niobate and TiO_2 scale around the specimens. Preferential element layering/segregation in the oxide scale is evidenced by X-ray mapping and SiO_2 was weakly indexed in the PXRD diffractogram and may be present in minor proportion. However, due to its slow growth kinetics on pure Si at 1000°C it was not expected to form at this temperature. The majority of oxide scale experiments were performed on samples oxidised at 1200°C and will make the bulk of the oxide scale discussion from herein.

At 1200°C the oxide scale formed on both alloys GB1 and GB2, regardless of alloy condition, comprised of different oxide layers, indicating preferential oxidation of elements. From outer to inner layer the oxide scale on GB1 was comprised of:

TiO_2 || Cr-niobate || (Ti,Cr)-$Niobate_{coarse}$ + $(Niobate + HfO_2 + SiO_2 + HfSiO_4)_{fine}$

and for GB2:

(Cr,Ti)-Niobate || $Niobate_{coarse}$ + $(Niobate + SiO_2 + HfO_2 + HfSiO_4)_{fine}$ || (Cr,Ti)-Niobate ||

$Niobate_{coarse}$ + $(Niobate + SiO_2 + HfO_2 + HfSiO_4)_{fine}$ || || SiO_2 + $(Nb,Hf)_5Ge_{3substrate-oxide}$

Despite the similar oxidation kinetics and variation in multi-sample testing (Figure 112), alloy GB2 was deemed to have performed better than GB1 at 1200°C due to lower overall weight gain, less visible internal oxidation and the formation of a slightly thinner oxide scale by approximately 20µm. This is especially the case for GB2-HT. The SiO_2 + $(Nb,Hf)_5Ge_3$ layer at the GB2 substrate edge is deemed the key oxidation product responsible for improving oxide scale adhesion and preventing excessive O penetration into the microstructure.

5.7.3 Proposed Oxidation Mechanism of the alloys GB1 and GB2 at 1200°C

1. O absorption occurs at $(Nb,Ti,Cr)_{ss}$ grains on the sample surface, leading to an initially high rate of weight gain. Progressive dissolution and saturation of $(Nb,Ti,Cr)_{ss}$ with O leads to internal precipitation of Ti_{ss} and HfO_2 (refer to Figure 178).
2. After neighbouring $(Nb,Ti,Cr)_{ss}$ grains are saturated with O some internal precipitation occurs in $NbCr_2$. The outward diffusion of Nb, Ti and Cr from the $(Nb,Ti,Cr)_{ss}$ and $NbCr_2$, coupled with the locally high O concentration at the alloy surface, results in initial oxide scale growth from these phases. Internally penetrating O must diffuse through $NbCr_2$ before further attacking $(Nb,Ti,Cr)_{ss}$ grains. Grain boundary precipitation of the silicide phase occurs with no oxide scale formed as it is relatively much less reactive to oxidation (refer to Figure 179).
3. Oxide scale growth from $(Nb,Ti,Cr)_{ss}$ and $NbCr_2$ eventually coalesces into an epitaxial layer. The depth of internal O diffusion through the interdendritic matrix eventually engulfs the sub-surface silicide grains making the O concentration at their boundaries significant enough for their oxidation resulting in an oxidative phase boundary of Ti_{ss} and HfO_2. At this stage of the oxidation process, some differences between alloy GB1 and GB2 arise:
    - For GB1, the build up of stresses from the O saturated $(Nb,Ti,Cr)_{ss}$ and $NbCr_2$ leads to cracking of the hexagonal γNb_5Si_3 (refer to Figure 180).
    - For GB2, none or minimal cracking of the tetragonal βNb_5Si_3 silicide occurs (refer to Figure 181).
4. Inward growth of the oxide scale occurs, fully oxidising the microstructure phases building a volumous oxide scale.
    - For GB1, the γNb_5Si_3 oxidises to form SiO_2, HfO_2 and $HfSiO_4$ within the oxide scale. Progressive build up of stresses leads to crack propogation (refer to Figure 182).
    - For GB2, the βNb_5Si_3 oxidises to form SiO_2, HfO_2 and $HfSiO_4$ within the oxide scale. The βNb_5Si_3 forms sub-grain boundaries of SiO_2 and local $(Hf,Ti,Nb)_{ss}$ precipitates whilst being resilient to cracking (refer to Figure 183).

5. Growth of the oxide scale progresses for both alloys.
    - For GB1, depending upon the propogation of cracks, the oxide scale may spall (refer to Figure 184). The oxidation process repeats/resumes.
    - For GB2, the βNb_5Si_3 further oxidises to form a SiO_2 + $(Nb,Hf)_5Ge_3$ layer at the substrate edge (refer to Figure 185). Further oxidation leads to the complete coverage of the substrate edge with the SiO_2 + $(Nb,Hf)_5Ge_3$ layer that is considered responsible for the improved oxide scale adherence on alloy GB2 (refer to Figure 186).

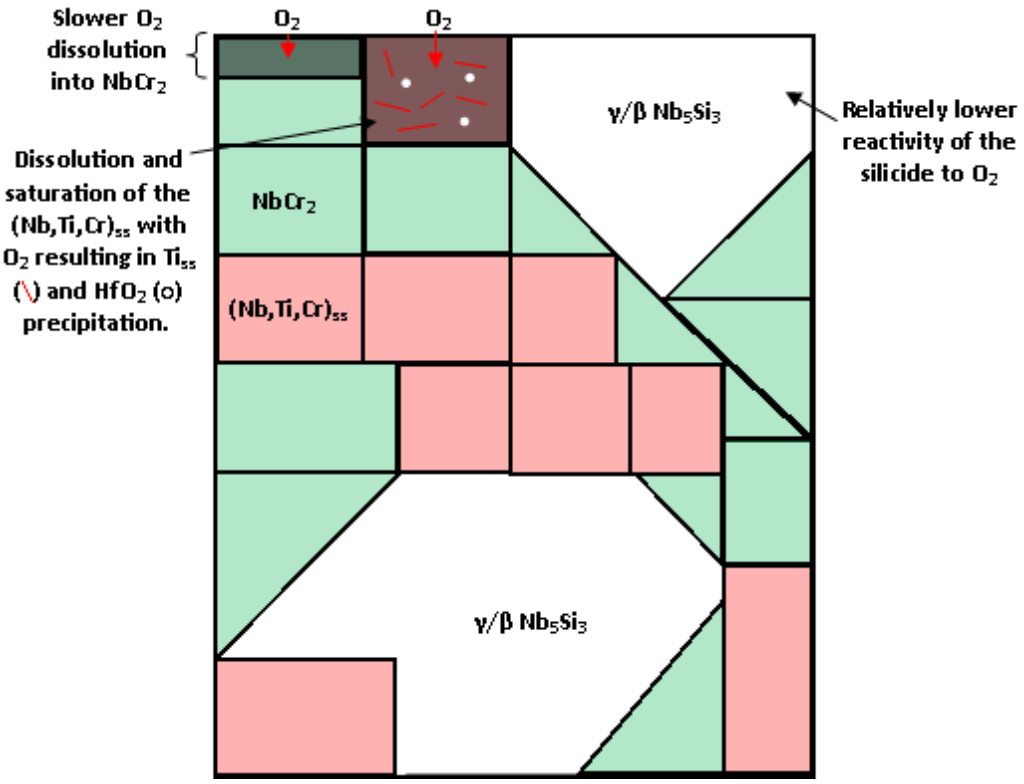

Figure 178. Schematic diagram of GB1/GB2 early stage oxidation depicting initial O dissolution and precipitation within the $(Nb,Ti,Cr)_{ss}$.

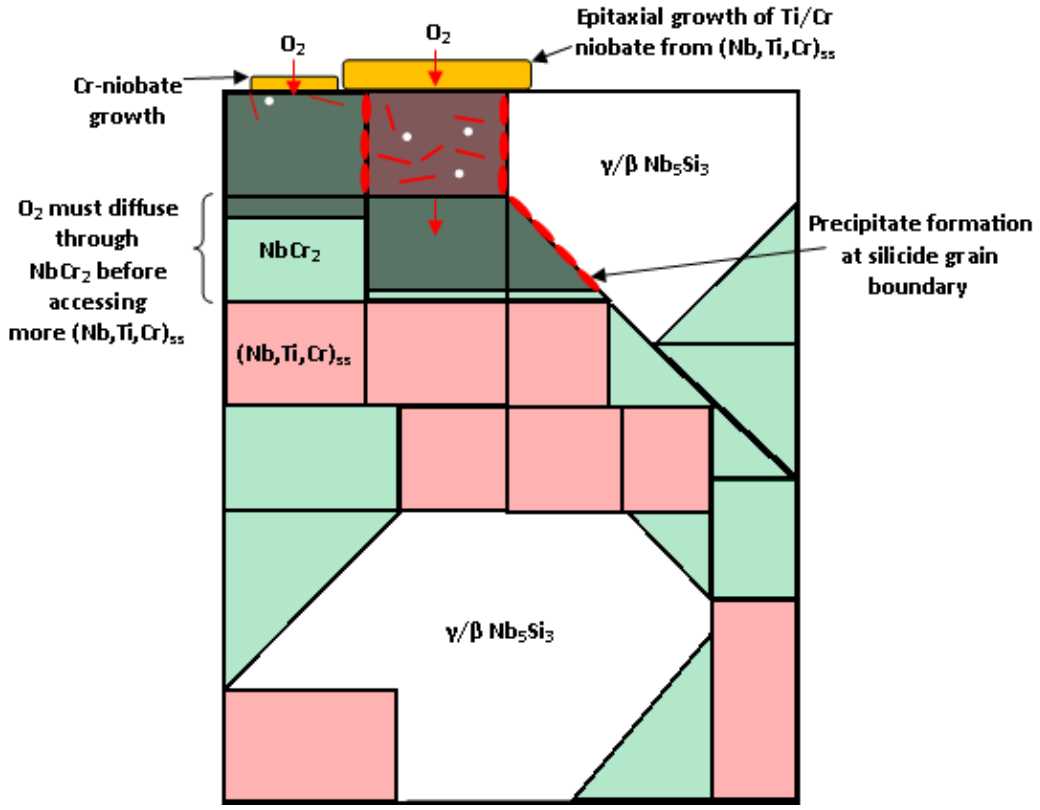

Figure 179. Schematic diagram of GB1/GB2 oxidation depicting initial oxide scale growth and internal precipitation at silicide grain boundaries.

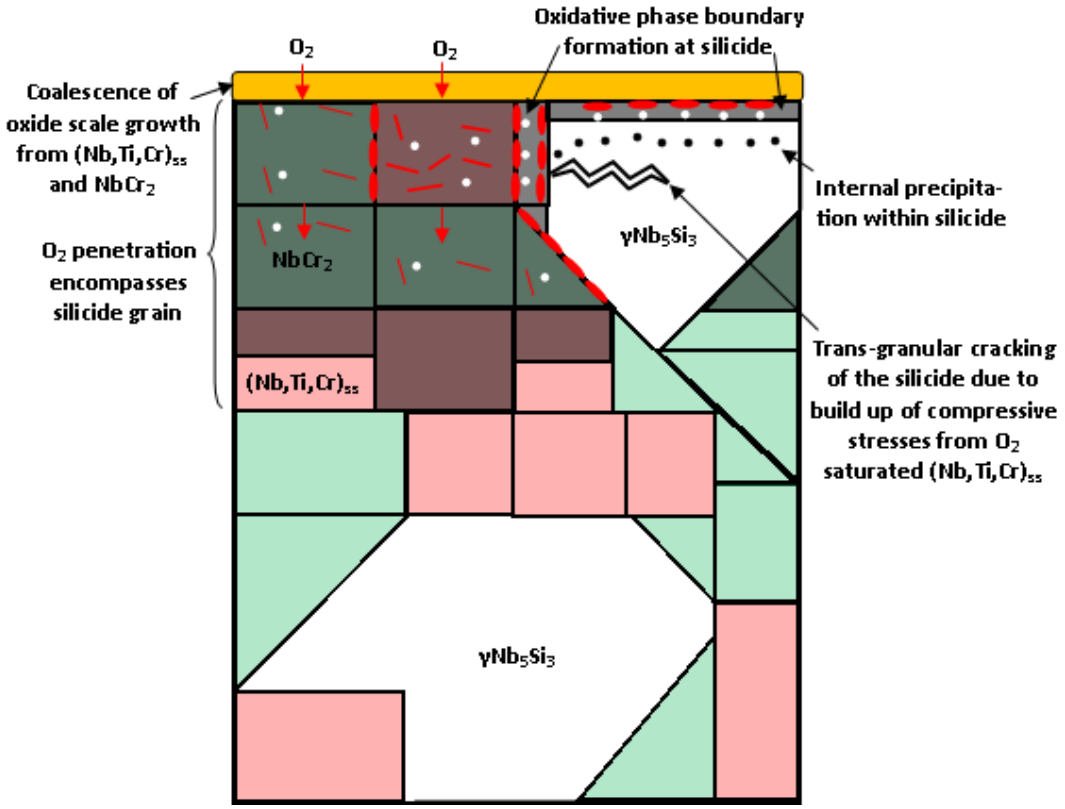

Figure 180. Schematic diagram of GB1 mid-stage oxidation depicting oxide scale growth, oxidative phase boundary formation and cracking of the hexagonal γNb_5Si_3 silicide.

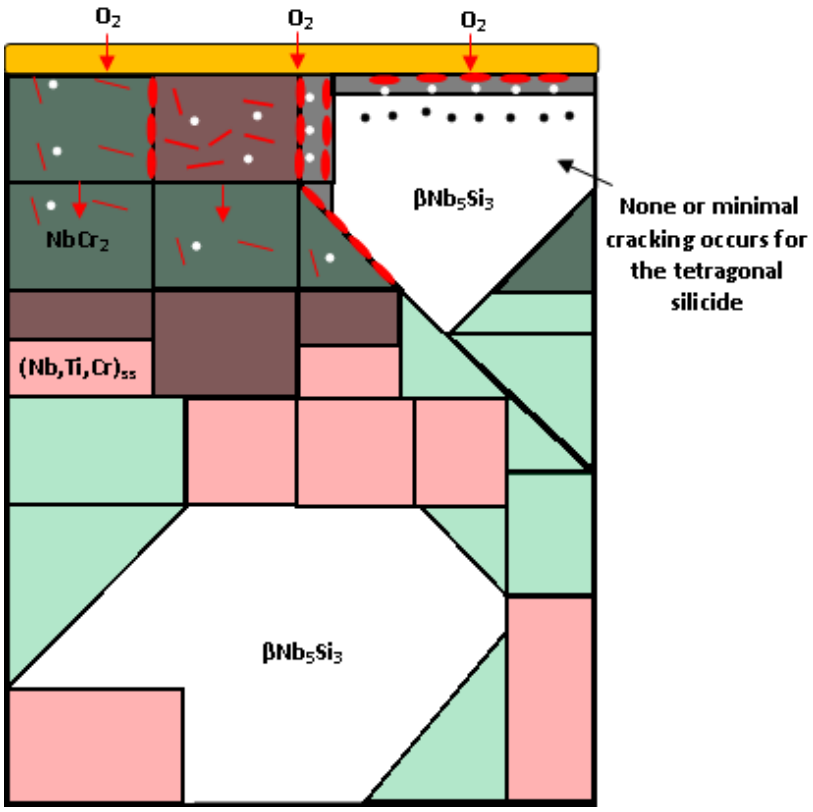

Figure 181. Schematic diagram of GB2 mid-stage oxidation depicting oxide scale growth, oxidative phase boundary formation and a lack of cracking of the tetragonal βNb_5Si_3.

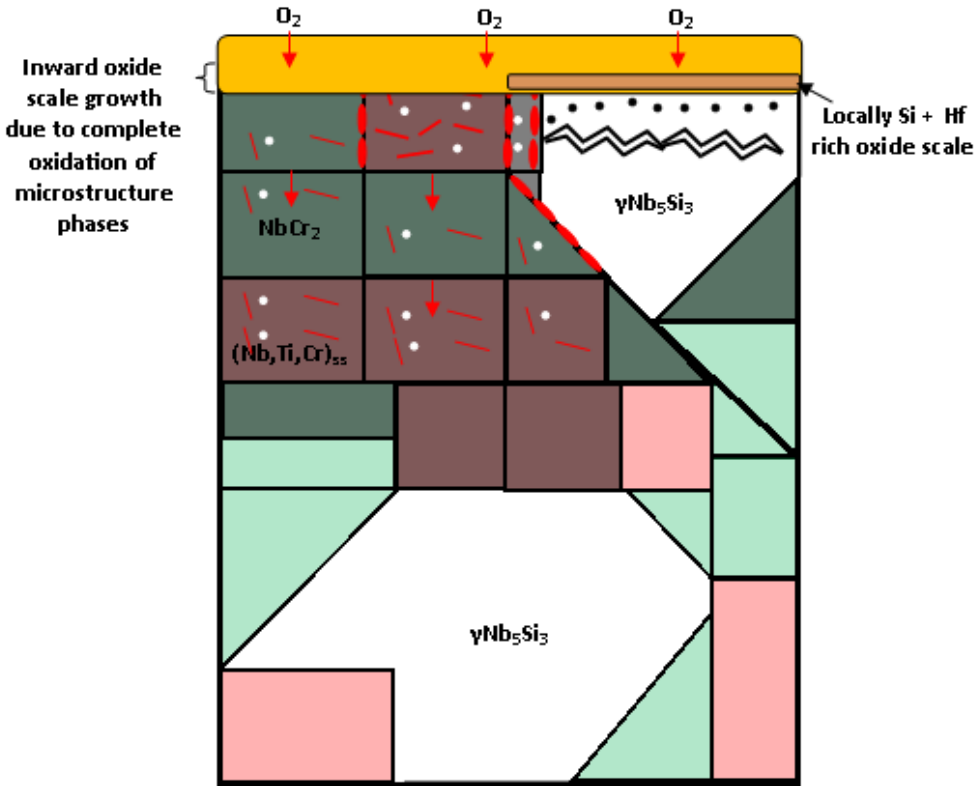

Figure 182. Schematic diagram of GB1 later stage oxidation depicting oxide scale growth and the initial stages of sub-surface γNb_5Si_3 oxidation, dispersing Si and Hf into the oxide scale resulting in SiO_2, HfO_2 and $HfSiO_4$ formation. Cracking propagates.

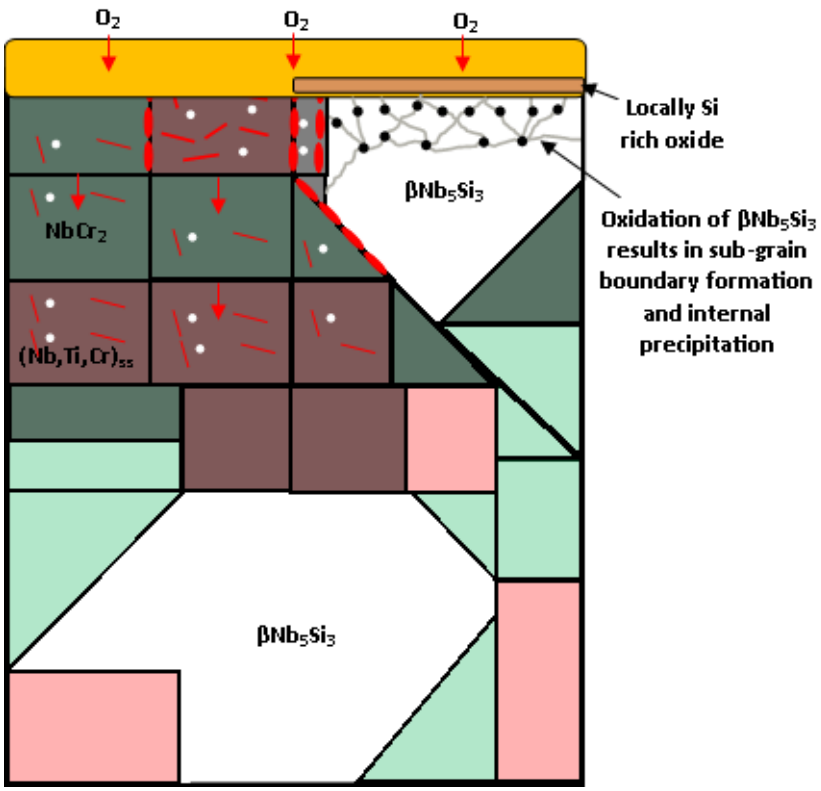

Figure 183. Schematic diagram of GB2 later stage oxidation depicting oxide scale growth and the initial stages of sub-surface βNb_5Si_3 oxidation resulting in SiO_2, HfO_2 and $HfSiO_4$ formation.

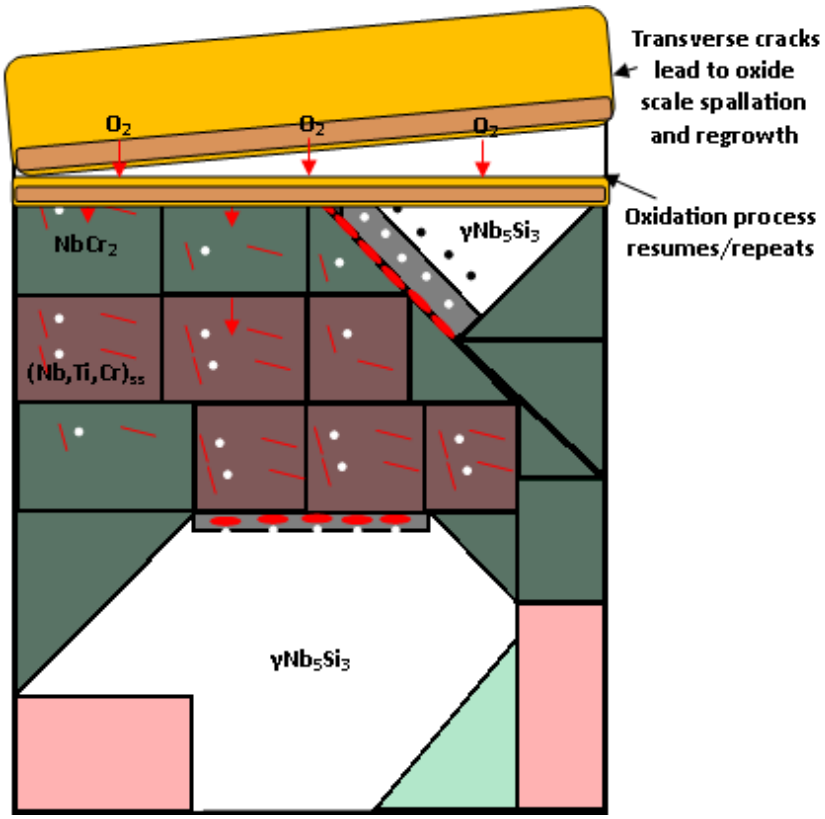

Figure 184. Schematic diagram of GB1 displaying spallation of the oxide scale due to propogation of transverse cracking. Oxidation would resume with an initial spike in growth kinetics as seen by the breakaway behaviour in the TGA plot.

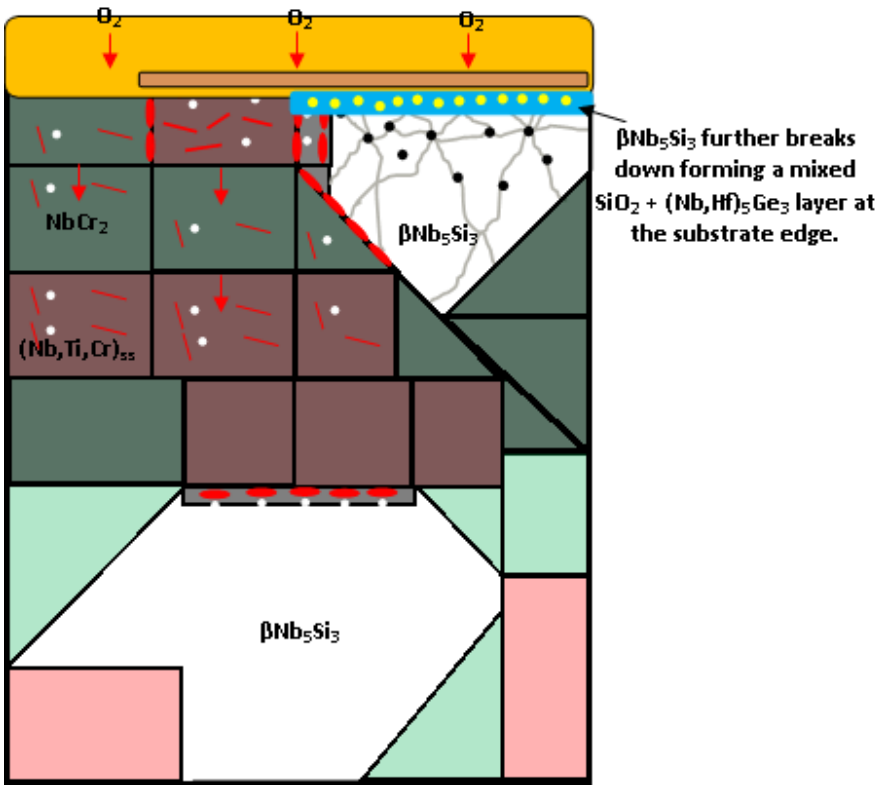

Figure 185. Schematic diagram of GB2 displaying later stage oxidation resulting in the formation of SiO_2 + $(Nb,Hf)_5Ge_3$ from the oxidised βNb_5Si_3 silicide.

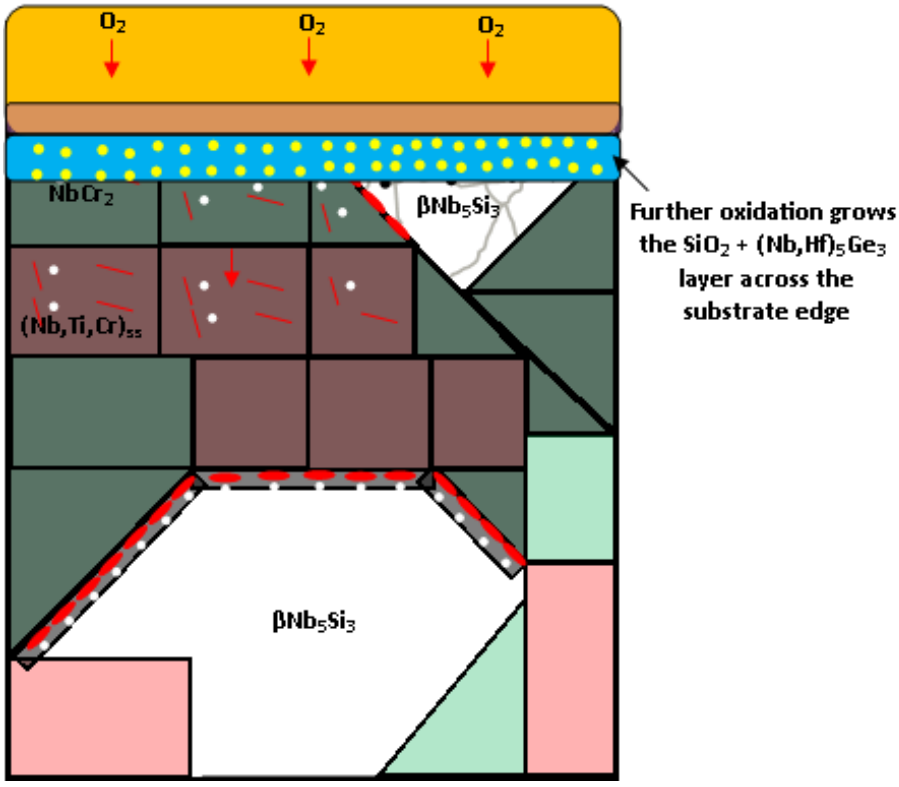

Figure 186. Schematic diagram of end stage GB2 oxidation and complete oxide scale growth for testing up to 100h at 1200°C. Further oxidation of βNb_5Si_3 the silicide forms a complete layer of SiO_2 + $(Nb,Hf)_5Ge_3$ at the substrate edge that is considered to reduce O diffusion into the substrate and enhance oxide scale adherence by preventing cracking.

5.8 Conclusions: Oxidation Behaviour

- Oxidative attack of the Nb-silicide based alloys GB1 and GB2 studied in this work, occurred due to inward O penetration and dissolution into the O soluble bcc Nb_{ss}.
- The Nb-silicide microstructures with a relatively low phase fraction of Nb_{ss} and high phase fraction of $NbCr_2$ Laves phase had significantly improved oxidation performance compared with alloys without such microstructures. The alloys GB1 and GB2:
    - Did not show pest behaviour at 800 or 1000°C for up to 100h oxidation.
    - Had microstructure architectures consisting of a disconnected Nb_{ss}. This benefitted oxidation by the $NbCr_2$ acting as an internal diffusion barrier, preventing direct access of O to the Nb_{ss} and by arresting local Nb_{ss} oxidation.
- Solubility in and reactivity of the Nb_5Si_3 silicide and $NbCr_2$ Laves phase with O was significantly less than the Nb_{ss}.
- The diffusion path of O to attack the Nb_{ss} was predominantly intergranular.
- The ability for Hf to 'getter' internally diffusing O to form HfO_2 was diminished at temperatures below 1200°C.
- Hf was more reactive to form HfO_2 from the Nb_{ss} than the Nb_5Si_3 and $NbCr_2$, particularly at 1200°C.
- The affinity for O dissolution into the Nb_{ss} and stabilisation of Ti_{ss} precipitation was greater than the reactivity of Hf from the Nb_{ss} to form HfO_2. N was also suspected of stabilising Ti_{ss} but could not be proved in this works.
- Initially during oxidation, Ti and Cr diffused from the $(Nb,Ti,Cr)_{ss}$ to the metal surface for formation of an oxide scale. Simultaneously, the local internal depletion of Ti and Cr of the microstructure resulted in internal precipitation of Ti_{ss}. With cumulative O dissolution and saturation of the microstructure, inward oxide growth was a result. Hence, a layered oxide scale structure existed.
- The better oxide scale adherence of GB2 compared with GB1 was attributed to the SiO_2 + $(Nb,Hf)_5Ge_3$ layer formed at the substrate edge. Its formation requires the oxidative breakdown of Ge rich Nb_5Si_3.
- The oxidation of Hf rich γNb_5Si_3 resulted in precipitation and sub-grain boundary formation. The build up of internal stresses due to precipitation resulted in cracking and the spallation of the oxide scale.
- The formation of a disconnected Nb_{ss} microstructure due to significant enough $NbCr_2$ Laves phase formation was critical for Cr addition to benefit oxidation performance.

6 Conclusions

6.1 Alloy Microstructures

- Hf and Ti additions synergistically stabilised and partition to hexagonal hP16 γNb_5Si_3.
- Synergy of Hf and Cr additions destabilise Nb_3Si formation.
- With sufficient Hf and Ti alloy addition, the eutectoid decomposition of Nb_3Si results in Nb_{ss} and the hP16 γNb_5Si_3 silicide as opposed to tI32 αNb_5Si_3.
- A high area fraction of C14 $NbCr_2$ Laves phase can be stabilised by high Cr addition and is aided by Si stabilising the C14 structure to lower temperatures.
- Ge addition partially stabilise and partition to tI32 βNb_5Si_3.
- The high Cr and Ti content of alloys GB1 and GB2 resulted in microstructures with a disconnected $(Nb,Ti,Cr)_{ss}$ where grains were surrounded by $NbCr_2$ Laves phase and Nb_5Si_3 silicide.
- The solubilities of Al/Ge, Cr, and Si in the C14 $NbCr_2$ Laves phase of both alloys was essentially the same.

6.2 Oxidation Behaviour

- At 800°C:
    - The isothermal oxidation behaviour of alloys GB1-AC and GB2-AC was linear and parabolic, respectively, with the latter alloy gaining slightly less weight.
    - Both alloys did not pest.
    - The change of Al by Ge between alloys GB1 and GB2 did not make any noticeable diference to the oxide scales.
    - The oxide scales were identified as mixtures of Ti/Cr-niobate and TiO_2.
    - There was O contamination of the sub-surface microstructure in both alloys.
    - HfO_2 was not observed in alloy GB1 despite the alloy possessing approximately twice as much Hf than alloy GB2, which did form a small proportion of HfO_2 within interdendritic $Nb_{ss}/NbCr_2$ region. This may be due to the partitioning effect Ge had on Ti and Hf in GB2, making Hf more available for reaction.

- At 1000°C:
    - The isothermal oxidation behaviour of GB1-AC and GB2-AC was linear and parabolic respectively.
    - A yellowish well adhered oxide scale formed over both alloys. For GB1 the scale was locally thicker over the Nb_{ss} while for GB2 the scale was more evenly distributed.
    - In both alloys the oxide scales consisted of the same mixture of Ti/Cr-niobate and TiO_2 as in the 800°C tests.
    - Internal contamination of the alloy microstructures was most prevalent throughout the Nb_{ss}.
- At 1200°C:
    - The isothermal oxidation of the AC and HT alloys was para-linear to parabolic.
    - The GB1 samples with the highest and lowest weight gains were the HT condition with 14.2mg/cm^2 and AC condition with 10.7 mg/cm^2.
    - The GB2 samples with the highest and lowest weight gains were the AC condition (Run2) with 13.9 mg/cm^2 and HT condition with 6.2 mg/cm^2.
    - Both alloys displayed multi-layered oxide scales after 50-100h of oxidation that were virtually the same to their AC and HT conditions.
    - The alloy GB1 oxide scale layers from outer to inner was:
        - TiO_2 || Cr-niobate || (Ti,Cr)-$Niobate_{coarse}$ + (Niobate + HfO_2 + SiO_2 + $HfSiO_4)_{fine}$
    - The alloy GB2 oxide scale layers from outer to inner was:
        - (Cr,Ti)-Niobate || $Niobate_{coarse}$ + (Niobate + SiO_2 + HfO_2 + $HfSiO_4)_{fine}$ || (Cr,Ti)-Niobate ||$Niobate_{coarse}$ + (Niobate + SiO_2 + HfO_2 + $HfSiO_4)_{fine}$ || (SiO_2 + $(Nb,Hf)_5Ge_3)_{substrate\text{-}oxide}$
    - For alloy GB2 at the SiO_2 + $(Nb,Hf)_5Ge_3$ layer, there was insufficient evidence to conclude GeO_2 had formed.
    - The internal contamination of both alloys was worse than in the 1000°C tests.
    - Internal contamination with O (and likely N) resulted in the formation of HfO_2 and O/N-rich Ti_{ss} in both alloys.
    - Alloy GB2 showed less severe internal oxidation than alloy GB1.
    - No internal Ti oxide or nitride phases were decisively identified, but are deemed highly possible.
    - The 5-3 silicides of both alloys were attacked and degraded by oxidation. Only grains that were engulfed in the internal diffusion zone were noticeably attacked by O.

- The internal attack of the γNb_5Si_3 in GB1 resulted in more HfO_2 formation than the $\beta/\alpha Nb_5Si_3$ of GB2.
- Oxidative attack of Nb_5Si_3 in alloy GB2 was a prerequisite to the SiO_2 + $(Nb,Hf)_5Ge_3$ layer formation at the substrate-scale interface. This layer was deemed responsible for the better oxide scale adhesion and less internal attack of the alloy in comparison with GB1, which did not form this layer.
- The prevention of oxide scale spallation is a significant improvement compared with other Nb-silicide based alloys.
- The disconnected Nb_{ss} microstructures of both alloys where $NbCr_2$ and Nb_5Si_3 isolated Nb_{ss} grains was deemed responsible for the relatively better oxidation performance in comparison with alloys from literature that did have interconnecting Nb_{ss} microstructures.
- The reactivity of phases to oxidation are ranked, from most to least as; Nb_{ss}, $NbCr_2$, γNb_5Si_3 and $\beta/\alpha Nb_5Si_3$.
- The β and α Nb_5Si_3 isomorphs were considered to have the same reactivity and influence on oxidation performance.
- Grain boundary diffusion was suggested to be the mode of O ingress into the alloys to initiate oxidation of the Nb_{ss}, due to the apparent lower reactivity of O with the other phases.
- The synergy of Cr + Hf + Ge was more effective than Cr + Hf + Al for oxidation performance.

7 Considerations for Future Work & Outlook of Nb-Silicide based alloy Research & Development

It is with much pride of this thesis that the author has obtained a mini victory by unearthing the particular benefit of Nb-silicide based alloys possessing high $NbCr_2$ Laves phase fraction and Ge rich βNb_5Si_3 on their high temperature oxidation behaviour. This victory, however, is short lived, considering the mountain to climb in progressing Nb-silicide based alloy oxidation performance close to that of, let alone equal to, uncoated Ni-based superalloys at the same operating temperatures, let alone higher, despite Nb-silicides generally possessing higher melting points (1400 – 1700°C). The competition is best portrayed by comparing alloy GB2, the better performing alloy of this thesis and notably better than most Nb-silicide based alloys throughout the literature, to Ni-based superalloy CMSX-4 of wt.% Ni-10Co-6Cr-5.6Al-1Ti-6Ta-0.6Mo-6W-3Re-0.1Hf. Göbel et al., (1993) reported under isothermal air oxidation conditions at 1200°C for 1000h, the AC condition single crystal alloy CMSX-4 suffered only -2 mg/cm^2 weight change with Kp = 3.9 x 10^{-14} $g^2cm^{-4}s^{-1}$ while this thesis results show GB2-HT after 100h of oxidation at 1200°C had a weight change of +6.9 mg/cm^2 with Kp = 1 x 10^{-10} $g^2cm^{-4}s^{-1}$. A sports analogy may be suitable here, if CMSX-4 plays Premier Leauge Football, alloy GB2-HT is a non-league team.

All, however, is not lost. CMSX-4 contains ten different elements as it is from a highly researched and developed alloy system, used as single crystal alloys. Single crystal superalloys are known to have better oxidation performance than equivalent polycrystalline or directionally solidified versions due to the removal of diffusion susceptible grain boundaries (Bose, 2007b). There is definite scope for the further development of directionally solidified Nb-silicide based alloys to reduce grain boundaries, and to investigate higher order alloying, particularly with more exotic elements such as B, Sn, Y, Re, Rh, La, and Ce. One reason for using such elements is simply because they are used in and found to benefit Ni-based superalloys (Reed, 2006; Bose, 2007a). On a more scientific basis for example, Sn has been found beneficial for oxidation behaviour by eliminating pesting and improving overall oxidation kinetics with 5 at.% addition (Geng et al., 2007a; Geng and Tsakiropoulos, 2007) while B and Ge modified $MoSi_2$ and $TiSi_2$ coatings deposited on pure Ti and Ti-Al-Nb alloys by halide activated pack cementation (HAPC) are found to have superior oxidation behaviour at 1000°C than the non-modified coating, aluminised coatings, and Si, B, Al CVD coatings (Cockeram and Rapp, 1995; Cockeram, 1995; Cockeram and Rapp, 1996). Mueller et al., (1992) investigated

$(Mo,W)(Si,Ge)_2$ silicide coatings, also deposited by HAPC, but on pure Nb samples and found (in tests up to 1370°C) enhancement to oxidation behaviour versus non-modified coatings, and the avoidance of pesting. Concisely, the benefit by both authors' work was attributed to boro or germania silicate "glassy" films healing cracks and pores in the oxide scale. Not quite the same benefit as was found with Ge in alloy GB2. However, the formation of the SiO_2 +Nb_5Ge_3 layer was deemed responsible for improved oxide sale adhesion and potentially acting as a diffusion barrier.

This opens multiple doors for future investigation and development of Nb-silicide based alloys such as through more complex/exotic alloying and the improvement by environmental coatings. Specifically, the investigation of high $NbCr_2$ Laves phase fraction Nb-silicide based alloys with Ge, Sn and/or B additions would be a recommended next step from this PhD thesis.

On a slightly different perspective, it was mentioned in section 5.7.1 that the influence of N and not only O needs more investigation and consideration for its influence on Nb-silicide based alloy oxidation, specifically for investigating the precipitation of oxide/nitride/Ti_{ss} phases from the Nb_{ss}. Understanding the atomistic reactions of Nb_{ss} with and without substitutional elements will likely benefit the reasearch and make strides to improvement. Benefits of understanding atomistic oxidation reactions should also apply to the $NbCr_2$ and Nb_5Si_3 phases and to oxide products such as the SiO_2 + Nb_5Ge_3 substrate layer formed in alloy GB2.

The use of EDS and WDS SEM techniques are more often than not being pushed to their limits when analysing oxidised microstructures and are not capable to decisively resolve the composition of micron and sub-micron size phases hence, TEM techniques should be more employed to acquire Selected Area Diffraction (SAD) patterns and/or Electron Energy Loss Spectroscopy (EELS-TEM) data as this would lead to decisive identification of O and/or N oxidation products. There would be challenge in producing thin enough samples for effective analysis thus FIB-SEM techniques would be a recommended preparation method.

As concluding remarks, this thesis was focused upon oxidation while mechanical properties and manufacturing techniques have not been mentioned, they too need refining and improvement to satisfy standards posed by Ni-based superalloys. This would compound the so called mountain to climb for Nb-silicide based alloys to become feasible gas turbine materials. However, as the alloys are relatively less researched, less understood, and simpler when compared to their rival, there is still a wide scope for their development.

References

Alyamovskii, S.I., Gel'd, P.V., Matveenko, I.I., 1962. Concentration Regions of Niobium Silicide Stability at 1250°C. Zhurnal Neorganichesko Khimii Vol: 7.

Andersson, S., Collén, B., Kuylenstierna, U., Magnéli, A., Magnéli, A., Pestmalis, H., Åsbrink, S., 1957. Phase Analysis Studies on the Titanium-Oxygen System. Acta Chemica Scandinavica 11, 1641–1652. doi:10.3891/acta.chem.scand.11-1641

Babich, T.G., Zagorodnyuk, A.., Khodos, M.Y., Zhirnova, A.P., 1988. The Nb2O5-TiO2 System. Russian Journal of Inorganic Chemistry 33, 560–563.

Balachandran, U., Eror, N.G., 1982. Raman spectrum of the high temperature form of Nb2O5. J Mater Sci Lett 1, 374–376. doi:10.1007/BF00724842

Balsone, S.J., Bewlay, B.P., Jackson, M.R., Subramanian, P.R., Zhao, J.-C., Chatterjee, A., Heffernan, T.M., 2001. Materials Beyond Superalloys: Exploiting High-Temperature Composites.

Bewlay, B. p., Sitzman, S. d., Brewer, L. n., Jackson, M. r., 2004. Analyses of Eutectoid Phase Transformations in Nb–Silicide In Situ Composites. Microscopy and Microanalysis 10, 470–480. doi:10.1017/S1431927604040760

Bewlay, B.P., Briant, C.L., Davis, A.W., Jackson, M.R., 2001. The effect of silicide volume fraction on the creep behaviour of Nb-silicide based in-situ composites. Materials Research Society Symposium Proceedings 646, N2.7.1-N2.7.6.

Bewlay, B.P., Briant, C.L., Sylven, E.T., Jackson, M.R., 2003. The Effects of Substitutional Additions on Creep Behavior of Tetragonal and Hexagonal Nb-Silicides, in: Materials Research Society Symposium - Proceedings. pp. 321–326.

Bewlay, B.P., Briant, C.L., Sylven, E.T., Jackson, M.R., 2002a. The Effects of Substitutional Additions on Creep Behavior of Tetragonal and Hexagonal Nb-Silicides. MRS Online Proceedings Library 753, null-null. doi:10.1557/PROC-753-BB5.24

Bewlay, B.P., Jackson, M.R., 2000. 3.22 - High-temperature In Situ Composites: Processing and Properties, in: Editors-in-Chief: Anthony Kelly, Carl Zweben (Eds.), Comprehensive Composite Materials. Pergamon, Oxford, pp. 579–615.

Bewlay, B.P., Jackson, M.R., 2000. High-temperature In Situ Composites: Processing and Properties, in: Comprehensive Composite Materials. Pergamon, Oxford, pp. 579–615.

Bewlay, B.P., Jackson, M.R., Bishop, R.R., 1998. The Nb-Ti-Si ternary phase diagram: Determination of solid-state phase equilibria in Nb- and Ti-rich alloys. Journal of Phase Equilibria 19, 577–586. doi:10.1361/105497198770341789

Bewlay, B.P., Jackson, M.R., Briant, C.L., 1999. Creep Mechanisms in High Temperature In-situ Composites (No. FQ8671–96005872306/AS). GE Corporate Research & Development, Schenectady, NY 12301.

Bewlay, B.P., Jackson, M.R., Gigliotti, M.F.X., 2002b. Niobium Silicide High Temperature In Situ Composites, in: Intermetallic Compounds: Principles and Practice. John Wiley & Sons, Ltd, Chichester, UK, pp. 541–560.

Bewlay, B.P., Jackson, M.R., Lipsitt, H.A., 1997. The Nb-Ti-Si ternary phase diagram: Evaluation of liquid- solid phase equilibria in Nb-and Ti-rich alloys. Journal of Phase Equilibria 18, 264–278. doi:10.1007/BF02647850

Bewlay, B.P., Jackson, M.R., Lipsitt, H.A., 1996. The balance of mechanical and environmental properties of a multielement niobium-niobium silicide-basedIn Situ composite. Metallurgical and Materials Transactions A 27, 3801–3808. doi:10.1007/BF02595629
Bewlay, B.P., Jackson, M.R., Reeder, W.J., Lipsitt, H.A., 1994. Microstructures and Properties of Ds in-Situ Composites of Nb-Ti-Si Alloys. MRS Online Proceedings Library 364. doi:10.1557/PROC-364-943
Bewlay, B.P., Sutliff, J.A., Bishop, R.R., 1999. Evidence for the existence of Hf5Si3. Journal of Phase Equilibria 20, 109–112. doi:10.1007/s11669-999-0008-y
Bewlay, B.P., Yang, Y., Casey, R.L., Jackson, M.R., Chang, Y.A., 2009. Experimental study of the liquid–solid phase equilibria at the metal-rich region of the Nb–Cr–Si system. Intermetallics 17, 120–127. doi:10.1016/j.intermet.2008.10.005
Bewlay, Jackson, Subramanian, Zhao, 2003. A review of very-high-temperature Nb-silicide-based composites. Metallurgical and Materials Transactions A 34, 2043–2052. doi:10.1007/s11661-003-0269-8
Birks, N., Meier, G.H., Pettit, F.S., 2006. Introduction to the High Temperature Oxidation of Metals. Cambridge University Press.
Blasse, G., 1967. Crystal structure and fluorescence of compositions ATiNbO6, ATiTaO6 and ATiSbO6. Materials Research Bulletin 2, 497–502. doi:10.1016/0025-5408(67)90024-4
Bose, S., 2007a. High temperature coatings. Butterworth-Heinemann.
Bose, S., 2007b. Oxidation, in: High Temperature Coatings. Butterworth-Heinemann, Burlington, pp. 29–52.
Brady, M.P., Liu, C.T., Zhu, J.H., Tortorelli, P.F., Walker, L.R., 2005. Effects of Fe additions on the mechanical properties and oxidation behavior of Cr2Ta Laves phase reinforced Cr. Scripta Materialia 52, 815–819. doi:10.1016/j.scriptamat.2005.01.016
Brady, M.P., Zhu, J.H., Liu, C.T., Tortorelli, P.F., Walker, L.R., 2000. Oxidation resistance and mechanical properties of Laves phase reinforced Cr in-situ composites. Intermetallics 8, 1111–1118. doi:10.1016/S0966-9795(00)00046-7
Brauer, G., 1941. Die Oxyde des Niobs. Zeitschrift für anorganische und allgemeine Chemie 248, 1–31. doi:10.1002/zaac.19412480101
Brauer, G., Müller, H., Kühner, G., 1962. Oxide der Tieftemperaturoxydation von Niob und Tantal. Journal of the Less Common Metals 4, 533–546. doi:10.1016/0022-5088(62)90042-5
Brukl, C.E., 1968. Ternary Phase Equilibria in Transition Metal-B-C-Si Systems. Part I. Binary Systems, Vol. 13. The Zr-Si and Hf-Si Systems. (Technical Report No. AFML-TR-65-2). Air Force Materials Laboratory, WPAFB, OH.
Bryant, R.., 1962. The solubility of oxygen in transition metal alloys. Journal of the Less Common Metals 4, 62–68. doi:10.1016/0022-5088(62)90060-7
Cancarevic, M., Zinkevich, M., Aldinger, F., 2007. Thermodynamic description of the Ti–O system using the associate model for the liquid phase. Calphad 31, 330–342. doi:10.1016/j.calphad.2007.01.009
Chan, 2004a. Cyclic-Oxidation Resistance of Niobium-Base in situ Composites: Modeling and Experimentation. Oxidation of Metals 61, 165–194. doi:10.1023/B:OXID.0000025330.65837.d1
Chan, 2004b. Cyclic oxidation response of multiphase niobium-based alloys. Metallurgical and Materials Transactions A 35, 589–597. doi:10.1007/s11661-004-0370-7

Chan, K.S., 2005. Alloying effects on the fracture toughness of Nb-based silicides and Laves phases. Materials Science and Engineering: A 409, 257–269. doi:10.1016/j.msea.2005.06.077
Chan, K.S., 2002. Alloying effects on fracture mechanisms in Nb-based intermetallic in-situ composites. Materials Science and Engineering A 329–331, 513–522. doi:10.1016/S0921-5093(01)01502-7
Chan, K.S., Davidson, D.L., 2003. Improving the fracture toughness of constituent phases and Nb-based in-situ composites by a computational alloy design approach. Metallurgical and Materials Transactions A 34, 1833–1849. doi:10.1007/s11661-003-0149-2
Chaze, A.M., Coddet, C., 1986. The role of nitrogen in the oxidation behaviour of titanium and some binary alloys. Journal of the Less Common Metals 124, 73–84. doi:10.1016/0022-5088(86)90478-9
Cheetham, A.K., Rao, C.N.R., 1976. A neutron diffraction study of niobium dioxide. Acta Crystallographica Section B 32, 1579–1580. doi:10.1107/S0567740876005876
Chen, L.-Q., Guo, X.-P., 2013. Effect of Cr content on microstructure and oxidation resistance of Nb-Ti-Si-Cr based ultrahigh-temperature alloy. Cailiao Rechuli Xuebao/Transactions of Materials and Heat Treatment 34, 30–36.
Chen, Y., Shang, J.-X., Zhang, Y., 2007. Bonding characteristics and site occupancies of alloying elements in different Nb5 Si3 phases from first principles. Physical Review B 76, 184204. doi:10.1103/PhysRevB.76.184204
Cockeram, B., Rapp, R.A., 1996. Isothermal and cyclic oxidation resistance of boron-modified and germanium-doped silicide coatings for titanium alloys. Oxidation of Metals 45, 427–468. doi:10.1007/BF01046846
Cockeram, B.V., 1995. Growth and oxidation resistance of boron-modified and germanium-doped silicide diffusion coatings formed by the halide-activated pack cementation method. Surface and Coatings Technology 76–77, 20–27. doi:10.1016/0257-8972(95)02492-1
Cockeram, B.V., Rapp, R.A., 1995. Oxidation-resistant boron- and germanium-doped silicide coatings for refractory metals at high temperature. Materials Science and Engineering A 192–193, 980–986. doi:10.1016/0921-5093(95)03342-4
Dasary-Sierra, R.M., Varma, S.K., 2014. Short-Term Oxidation Response of Nb–15Re–15Si–20Cr–15Ti Alloy. Metallography, Microstructure, and Analysis 3, 224–232. doi:10.1007/s13632-014-0139-3
Davidson, D.L., Chan, K.S., 1999. The fatigue and fracture resistance of a Nb-Cr-Ti-Al alloy. Metall and Mat Trans A 30, 2007–2018. doi:10.1007/s11661-999-0011-2
Davidson, D.L., Chan, K.S., Anton, D.L., 1996. The effects on fracture toughness of ductile-phase composition and morphology in Nb-Cr-Ti and Nb-Si in situ composites. MMTA 27, 3007–3018. doi:10.1007/BF02663850
Deal, A., Heward, W., Ellis, D., Cournoyer, J., Dovidenko, K., Bewlay, B., 2007. Phase Identification in Nb-Cr-Si Alloys. Microscopy and Microanalysis 13, 90–91. doi:10.1017/S1431927607079275
Deal, B.E., Grove, A.S., 1965. General Relationship for the Thermal Oxidation of Silicon. Journal of Applied Physics 36, 3770–3778. doi:10.1063/1.1713945
Delheusy, M., 2008. X-ray investigation of Nb/O interfaces.
Donachie, M.J., 2002. Superalloys: A Technical Guide. ASM International.
Dosch, H., Schwerin, A. v., Peisl, J., 1986. Point-defect-induced nucleation of the ω phase. Phys. Rev. B 34, 1654–1661. doi:10.1103/PhysRevB.34.1654

Du, Y., Schuster, J.C., 2002. Experimental investigation and thermodynamic description of the Cr-Si-Ti system. Scandinavian Journal of Metallurgy 31, 25–33. doi:10.1034/j.1600-0692.2002.310105.x
Dyson, P., 1957. The unit cell and space group of the compound TiNb2O7. Acta Crystallographica 10, 140–140. doi:10.1107/S0365110X57000420
Elliot, R.P., 1960. Columbium-Oxygen system. Transactions of American Society for Metals 52, 990–1014.
Elliott, R.P., 1960. Columbium-Oxygen System. Transactions of American Society for Metals 52.
Erickson, G.L., 1996. The Development and Application of CMSX-10, in: Superalloys 1996: Proceedings of the 8th International Symposium on Superalloys. pp. 35–44.
Farrell, H.H., Isaacs, H.S., Strongin, M., 1973. The interaction of oxygen and nitrogen with the niobium (100) surface: II. Reaction kinetics. Surface Science 38, 31–52. doi:10.1016/0039-6028(73)90272-0
Felten, E.J., 1969. The interaction of the alloy niobium-25Titanium with air, oxygen and nitrogen I. The unusual oxidation behavior of Nb-25Ti at 1000 ° C. Journal of the Less Common Metals 17, 185–197. doi:10.1016/0022-5088(69)90052-6
Franke, P., Neuschütz, D., 2006. Nb-O, in: Franke, P., Neuschütz, D. (Eds.), Binary Systems. Part 4: Binary Systems from Mn-Mo to Y-Zr, Landolt-Börnstein - Group IV Physical Chemistry. Springer Berlin Heidelberg, pp. 1–2.
Gasperin, M., 1984. Affinement de la structure de TiNb2O7 et répartition des cations. Journal of Solid State Chemistry 53, 144–147. doi:10.1016/0022-4596(84)90238-X
Gatehouse, B.M., Wadsley, A.D., 1964. The crystal structure of the high temperature form of niobium pentoxide. Acta Crystallographica 17, 1545–1554. doi:10.1107/S0365110X6400384X
Geddes, B., Leon, H., Huang, X., 2010. Superalloys: Alloying and Performance. ASM International.
Geng, Shao, G., Tsakiropoulos, P., 2006a. Study of three-phase equilibrium in the Nb-rich corner of Nb–Si–Cr system. Intermetallics 14, 832–837. doi:10.1016/j.intermet.2005.12.004
Geng, T., Li, C., Du, Z., Guo, C., Zhao, X., Xu, H., 2011. Thermodynamic assessment of the Nb–Ge system. Journal of Alloys and Compounds 509, 3080–3088. doi:10.1016/j.jallcom.2010.12.005
Geng, Tsakiropoulos, P., 2007. A study of the microstructures and oxidation of Nb-Si-Cr-Al-Mo in situ composites alloyed with Ti, Hf and Sn. Intermetallics 15, 382–395. doi:10.1016/j.intermet.2006.08.016
Geng, Tsakiropoulos, P., Shao, G., 2007a. A thermo-gravimetric and microstructural study of the oxidation of Nbss/Nb5Si3-based in situ composites with Sn addition. Intermetallics 15, 270–281. doi:10.1016/j.intermet.2006.06.003
Geng, Tsakiropoulos, P., Shao, G., 2007b. A study of the effects of Hf and Sn additions on the microstructure of Nbss/Nb5Si3 based in situ composites. Intermetallics 15, 69–76. doi:10.1016/j.intermet.2006.03.001
Geng, Tsakiropoulos, P., Shao, G., 2006b. Oxidation of Nb-Si-Cr-Al in situ composites with Mo, Ti and Hf additions. Materials Science and Engineering: A 441, 26–38. doi:10.1016/j.msea.2006.08.093
Geng, Tsakiropoulos, P., Shao, G., 2006c. The effects of Ti and Mo additions on the microstructure of Nb-silicide based in situ composites. Intermetallics 14, 227–235. doi:10.1016/j.intermet.2005.04.021

Göbel, M., Rahmel, A., Schütze, M., 1993. The isothermal-oxidation behavior of several nickel-base single-crystal superalloys with and without coatings. Oxidation of Metals 39, 231–261. doi:10.1007/BF00665614
Gokhale, A.B., Abbaschian, G.J., 1989. The Hf-Si (hafnium-silicon) system. Bulletin of Alloy Phase Diagrams 10, 390–393. doi:10.1007/BF02877595
Gokhale, A.B., Abbaschian, G.J., 1987. The Cr−Si (Chromium-Silicon) system. Journal of Phase Equilibria 8, 474–484. doi:10.1007/BF02893156
Goldschmidt, H.J., Brand, J.A., 1961a. The constitution of the chromium-niobium-silicon system. Journal of the Less Common Metals 3, 34–43. doi:10.1016/0022-5088(61)90041-8
Goldschmidt, H.J., Brand, J.A., 1961b. The constitution of the chromium-niobium-molybdenum system. Journal of the Less Common Metals 3, 44–61. doi:10.1016/0022-5088(61)90042-X
Grammenos, I., Tsakiropoulos, P., 2010. Study of the role of Al, Cr and Ti additions in the microstructure of Nb-18Si-5Hf base alloys. Intermetallics 18, 242–253. doi:10.1016/j.intermet.2009.07.020
Gulbransen, E.A., Andrew, K.F., 1949. Reactions of Zirconium, Titanium, Columbium, and Tantalum with the Gases, Oxygen, Nitrogen, and Hydrogen at Elevated Temperatures. J. Electrochem. Soc. 96, 364–376. doi:10.1149/1.2776800
Guo, B., Guo, X., 2011. Effect of high temperature treatments on microstructure of Nb-Ti-Cr-Si based ultrahigh temperature alloy. Transactions of Nonferrous Metals Society of China 21, 1710–1716. doi:10.1016/S1003-6326(11)60919-9
Halbritter, J., 1987. On the oxidation and on the superconductivity of niobium. Appl. Phys. A 43, 1–28. doi:10.1007/BF00615201
Heilmaier, M., Krüger, M., Saage, H., Rösler, J., Mukherji, D., Glatzel, U., Völkl, R., Hüttner, R., Eggeler, G., Somsen, C., Depka, T., Christ, H.-J., Gorr, B., Burk, S., 2009. Metallic materials for structural applications beyond nickel-based superalloys. JOM 61, 61–67. doi:10.1007/s11837-009-0106-7
Holtzberg, F., Reisman, A., Berry, M., Berkenblit, M., 1957. Chemistry of the Group VB Pentoxides. VI. The Polymorphism of Nb2O5. Journal of the American Chemical Society 79, 2039–2043. doi:10.1021/ja01566a004
Hoppe, E.E., Cisneros-Morales, M.C., Aita, C.R., 2013. Ti-catalyzed HfSiO4 formation in HfTiO4 films on SiO2 studied by Z-contrast scanning electron microscopy. APL Materials 1, 022108. doi:10.1063/1.4818171
Humphrey, G.L., 1951a. The Heats of Formation of TiO, Ti2O3, Ti3O5 and TiO2 from Combustion Calorimetry1. J. Am. Chem. Soc. 73, 1587–1590. doi:10.1021/ja01148a051
Humphrey, G.L., 1951b. The Heats of Combustion and Formation of Titanium Nitride (TiN) and Titanium Carbide (TiC). J. Am. Chem. Soc. 73, 2261–2263. doi:10.1021/ja01149a100
Jiang, N., Spence, J.C.H., 2004. Electron energy-loss spectroscopy of the O K edge of NbO2,MoO2, and WO2. Physical Review B 70, 245117. doi:10.1103/PhysRevB.70.245117
Joshi, A., Strongin, M., 1974. Surface segregation of oxygen in Nb-O and Ta-O alloys. Scripta Metallurgica 8, 413–424. doi:10.1016/0036-9748(74)90147-1
Jun, W., Xiping, G., Jinming, G., 2009. Effects of B on the Microstructure and Oxidation Resistance of Nb-Ti-Si-based Ultrahigh-temperature Alloy. Chinese Journal of Aeronautics 22, 544–550. doi:10.1016/S1000-9361(08)60139-9

Kato, K., Tamura, S., 1975. Die Kristallstruktur von T-Nb2O5. Acta Crystallographica Section B 31, 673–677. doi:10.1107/S0567740875003603
Keller, C., 1962. Über ternäre Oxide des Niobs und Tantals vom Typ ABO4. Zeitschrift für anorganische und allgemeine Chemie 318, 89–106. doi:10.1002/zaac.19623180108
Kerrick, D.M., Eminhizer, L.B., Villaume, J.F., 1973. The Role of Carbon Film Thickness in Electron Microprobe Analysis. American Mineralogist 58, 920–925.
Khazai, B., Kershaw, R., Dwight, K., Wold, A., 1981. Preparation and properties of the system Fe1−xCrxNbO4. Journal of Solid State Chemistry 39, 395–400. doi:10.1016/0022-4596(81)90275-9
Kloska, M., Haase, E.L., 1984. On the existence of the hexagonal Nb3Ge2 phase. Journal of the Less Common Metals 99, 241–248. doi:10.1016/0022-5088(84)90221-2
Knittel, S., Mathieu, S., Portebois, L., Vilasi, M., 2014a. Effect of tin addition on Nb–Si-based in situ composites. Part II: Oxidation behaviour. Intermetallics 47, 43–52. doi:10.1016/j.intermet.2013.12.010
Knittel, S., Mathieu, S., Vilasi, M., 2014b. Effect of tin addition on Nb–Si-based in situ composites. Part I: Structural modifications. Intermetallics 47, 36–42. doi:10.1016/j.intermet.2013.12.008
Kobyakov, V.P., Ponomarev, V.I., 2002. Specific features of oxygen dissolution in refractory metals in gas-phase deposition. Crystallogr. Rep. 47, 106–110. doi:10.1134/1.1447036
Kofstad, P., 1988. High temperature corrosion. Elsevier Applied Science.
Kofstad, P., 1966. High-temperature oxidation of metals. Wiley.
Kofstad, P., Anderson, P.B., Krudtaa, O.J., 1961. Oxidation of titanium in the temperature range 800–1200°C. Journal of the Less Common Metals 3, 89–97. doi:10.1016/0022-5088(61)90001-7
Kubaschewski, O., Hopkins, B.E., 1960. Oxidation mechanisms of niobium, tantalum, molybdenum and tungsten. Journal of the Less Common Metals 2, 172–180. doi:10.1016/0022-5088(60)90012-6
Lapitskii, A.V., Simanov, Y.P., Yarembash, E.I., 1952. On Some Properties of Niobium Pentoxide. Zh. Fiz. Khim 16, 56–59.
Laves, F., Witte, H., 1935. Die Kristallstruktur des MgNi2 und seine Beziehungen zu den Typen des MgCu2 und MgZn2. Metallwirtschaft 14, 645–649.
Li, Z., Tsakiropoulos, P., 2013. The microstructures of Nb–18Si–5Ge–5Al and Nb–24Ti–18Si–5Ge–5Al in situ composites. Journal of Alloys and Compounds 550, 553–560. doi:10.1016/j.jallcom.2012.10.170
Li, Z., Tsakiropoulos, P., 2011. Study of the effect of Ti and Ge in the microstructure of Nb–24Ti–18Si–5Ge in situ composite. Intermetallics 19, 1291–1297. doi:10.1016/j.intermet.2011.04.010
Lindau, I., Spicer, W.E., 1974. Oxidation of Nb as studied by the uv-photoemission technique. Journal of Applied Physics 45, 3720–3725. doi:doi:10.1063/1.1663849
Lysenko, L.A., Markiv, V.Y., Tsybukh, O.V., Gladyshevskii, E.I., 1971. Cr-Si-Ti System. Inorganic Materials 7, 157–159.
Majumdar, S., Sharma, I.G., 2011. Oxidation behavior of MoSi2 and Mo(Si, Al)2 coated Mo-0.5Ti-0.1Zr-0.02C alloy. Intermetallics 19, 541–545. doi:10.1016/j.intermet.2010.12.002

Majumdar, S., Sharma, I.G., Suri, A.K., 2008. Development of oxidation resistant coatings on Mo-30W alloy. International Journal of Refractory Metals and Hard Materials 26, 549–554. doi:10.1016/j.ijrmhm.2008.01.005
Mani, R., Achary, S.N., Chakraborty, K.R., Deshpande, S.K., Joy, J.E., Nag, A., Gopalakrishnan, J., Tyagi, A.K., 2010. Dielectric properties of some MM′O4 and MTiM′O6 (M=Cr, Fe, Ga; M′=Nb, Ta, Sb) rutile-type oxides. Journal of Solid State Chemistry 183, 1380–1387. doi:10.1016/j.jssc.2010.04.022
Mathieu, S., Knittel, S., Berthod, P., Mathieu, S., Vilasi, M., 2012. On the oxidation mechanism of niobium-base in situ composites. Corrosion Science. doi:10.1016/j.corsci.2012.03.037
Mathieu, S., Knittel, S., François, M., Portebois, L., Mathieu, S., Vilasi, M., 2014. Towards the improvement of the oxidation resistance of Nb-silicides in situ composites: A solid state diffusion approach. Corrosion Science 79, 119–127. doi:10.1016/j.corsci.2013.10.033
Mendiratta, M.., Dimiduk, D.., 1991. Phase relations and transformation kinetics in the high Nb region of the Nb-Si system. Scripta Metallurgica et Materialia 25, 237–242. doi:10.1016/0956-716X(91)90387-G
Mendiratta, M.G., Lewandowski, J.J., Dimiduk, D.M., 1991. Strength and ductile-phase toughening in the two-phase Nb/Nb5Si3 alloys. MTA 22, 1573–1583. doi:10.1007/BF02667370
Menon, E.S.K., Parthasarathy, T.A., Mendiratta, M.G., 2004. Microstructural Effects and Kinetics of High Temperature Oxidation in Nb-Si Base Alloys, in: Senkov, O.N., Miracle, D.B., Firstov, S.A. (Eds.), Metallic Materials with High Structural Efficiency, NATO Science Series II: Mathematics, Physics and Chemistry. Springer Netherlands, pp. 315–326.
Mueller, A., Wang, G., Rapp, R.A., Courtright, E.L., 1992a. Deposition and Cyclic Oxidation Behavior of a Protective (Mo,W)(Si,Ge)[sub 2] Coating on Nb-Base Alloys. J. Electrochem. Soc. 139, 1266–1275. doi:10.1149/1.2069395
Mueller, A., Wang, G., Rapp, R.A., Courtright, E.L., Kircher, T.A., 1992b. Oxidation behavior of tungsten and germanium-alloyed molybdenum disilicide coatings. Materials Science and Engineering: A 155, 199–207. doi:10.1016/0921-5093(92)90326-V
Murray, J.L., 1987a. The Niobium-Titanium System, in: ASM Handbook Alloy Phase Diagrams. ASM International, Materials Park, Ohio.
Murray, J.L., 1987b. The Silicon-Titanium System, in: ASM Handbook Alloy Phase Diagrams. ASM International, Materials Park, Ohio.
Murray, J.L., Wriedt, H.A., 1987. The O–Ti (Oxygen-Titanium) system. Journal of Phase Equilibria 8, 148–165. doi:10.1007/BF02873201
Natividad, S., Acosta, A., Amato, K., Ventura, J., Protillo, B., Varma, S.K., 2010. Heat Treatment and Oxidation Characteristics of Nb-20Mo-15Si-5B-20(Cr,Ti) Alloys from 700 to 1400°C. Materials Science Forum 638–642, 2351–2356. doi:10.4028/www.scientific.net/MSF.638-642.2351
Nevitt, M.V., Beck, P.A., 1963. Electronic Structure and Alloy Chemistry of the Transition Elements. Wiley-Interscience, New York.
Niebuhr, J., 1966. Die niederen Oxide des Niobs. Journal of the Less Common Metals 11, 191–203. doi:10.1016/0022-5088(66)90005-1
Nikishina, E.E., Lebedeva, E.N., Drobot, D.V., 2012. Niobium- and tantalum-containing oxide materials: Synthesis, properties, and application. Inorg Mater 48, 1243–1260. doi:10.1134/S002016851213002X

Norman, N., 1962. Metallic oxide phases of niobium and tantalum I. X-ray investigations. Journal of the Less Common Metals 4, 52–61. doi:10.1016/0022-5088(62)90059-0
Norman, N., Kofstad, P., Krudtaa, O.J., 1962. Metallic oxide phases of niobium and tantalum II. Metallographic studies. Journal of the Less Common Metals 4, 124–137. doi:10.1016/0022-5088(62)90011-5
Novak, M.D., Levi, C.G., 2008. Oxidation and volatilization of silicide coatings for refractory niobium alloys, in: ASME International Mechanical Engineering Congress and Exposition, Proceedings. pp. 261–267.
Nowak, I., Ziolek, M., 1999. Niobium Compounds: Preparation, Characterization, and Application in Heterogeneous Catalysis. Chemical Reviews 99, 3603–3624. doi:10.1021/cr9800208
Okamoto, H., 2012. Ge-Nb (Germanium-Niobium). Journal of Phase Equilibria and Diffusion 33, 250–251. doi:10.1007/s11669-012-0023-2
Okamoto, H., 2011. O-Ti (Oxygen-Titanium). Journal of Phase Equilibria, 32, 473–474. doi:10.1007/s11669-011-9935-5
Okamoto, H., 2007. O-Si (Oxygen-Silicon). Journal of Phase Equilibria, 28, 309–310. doi:10.1007/s11669-007-9062-5
Okamoto, H., 2005. Nb-Si (niobium-silicon). Journal of Phase Equilibria, 26, 649–649. doi:10.1007/s11669-005-0022-7
Okamoto, H., 2002. Cr-Ti (chromium-titanium). Journal of Phase Equilibria, 23, 382–383. doi:10.1361/105497102770331659
Okamoto, H., 2001. Cr-Si (Chromium-Silicon). Journal of Phase Equilibria, 22, 593–593. doi:10.1361/105497101770332866
Okamoto, H., 1997a. Cr-Si (Chromium-Silicon). Journal of Phase Equilibria, 18, 222–222. doi:10.1007/BF02665714
Okamoto, H., 1997b. Cr-O (chromium-oxygen). Journal of Phase Equilibria, 18, 402–402. doi:10.1007/s11669-997-0072-0
Okamoto, H., 1991. The Hf-Nb (Hafnium-Niobium) system. Journal of Phase Equilibria, 12, 211–214. doi:10.1007/BF02645719
Okamoto, H., 1990. Nb-O Phase Diagram, in: ASM Binary Alloy Phase Diagrams. Materials Park, Ohio, 2006.
Olesinski, R.W., Abbaschian, G.J., 1984. The Ge−Si (Germanium-Silicon) system. Bulletin of Alloy Phase Diagrams 5, 180–183. doi:10.1007/BF02868957
Pan, V.M., Kulik, O.G., Popov, A.G., 1982. Influence of alloying with Germanium and Copper on the conditions of formation of the superconducting compound Nb3Si. Russian Metallurgy 167–171.
Pan, V.M., Latysheva, V.I., Shishkin, E.A., 1995. Phase Diagram of the Nb-Ge System. Physics and Metallurgy of Superconductors.
Pan, V.M., Latysheva, V.I., Shishkin, E.A., 1970. Phase Diagram of the Nb—Ge System, in: Savitskii, E.M., Baron, V.V. (Eds.), Physics and Metallurgy of Superconductors / Metallovedenie, Fiziko-Khimiya I Metallozipika Sverkhprovodnikov / Металловедение Физико-Химип и Металлофизика Сверхпроводников. Springer US, pp. 179–182. doi:10.1007/978-1-4684-8220-1_31
Papadimitriou, I., Utton, C., Tsakiropoulos, P., 2015. On the Nb-Ge Binary System. Metallurgical and Materials Transactions A 46, 5526–5536. doi:10.1007/s11661-015-3149-0
Pearson, W.B., 1968. Laves structures, MgCu2, MgZn2, MgNi2. Acta Crystallographica Section B Structural Crystallography and Crystal Chemistry 24, 7–9. doi:10.1107/S0567740868001627

Perepezko, J.H., 2015. Surface Engineering of Mo-Base Alloys for Elevated-Temperature Environmental Resistance. Annual Review of Materials Research 45, 519–542. doi:10.1146/annurev-matsci-070214-020959
Perepezko, J.H., 2009. The Hotter the Engine, the Better. Science 326, 1068–1069. doi:10.1126/science.1179327
Perepezko, J.H., Pint, B.A., Forrest, D.R., 2014. Structural intermetallics: Alloy design, processing, and applications. Advanced Materials and Processes 172, 22–26.
Perkins, Meier, 1990a. The oxidation behavior and protection of niobium. JOM 42, 17–21.
Perkins, Meier, 1990b. The oxidation behavior and protection of niobium. JOM 42, 17–21. doi:10.1007/BF03221046
Petersen, A., Müller-Buschbaum, H., 1992. Ein Beitrag über Oxide vom Typ AMO4 (A = Ti3+, Cr3+; M = Nb5+, Ta5+). Z. anorg. allg. Chem. 609, 51–54. doi:10.1002/zaac.19926090309
Petrovic, J.J., 1995. Mechanical behavior of MoSi2 and MoSi2 composites. Materials Science and Engineering A 192–193, 31–37. doi:10.1016/0921-5093(94)03246-7
Pialoux, A., Joyeux, M.., Cizeron, G., 1982. Étude du comportement du niobium sous vide par diffraction des rayons X à haute température. Journal of the Less Common Metals 87, 1–19. doi:10.1016/0022-5088(82)90036-4
Pint, B.A., DiStefano, J.R., Wright, I.G., 2006. Oxidation resistance: One barrier to moving beyond Ni-base superalloys. Materials Science and Engineering: A 415, 255–263. doi:10.1016/j.msea.2005.09.091
Pollock, T.M., Dibbern, J., Tsunekane, M., Zhu, J., Suzuki, A., 2010. New Co-based γ-γ′ high-temperature alloys. JOM 62, 58–63. doi:10.1007/s11837-010-0013-y
Powers, R.W., Doyle, M.V., 1959. Diffusion of Interstitial Solutes in the Group V Transition Metals. Journal of Applied Physics 30, 514–524. doi:10.1063/1.1702398
Reed, R.C., 2006. The superalloys: fundamentals and applications. Cambridge University Press.
Reich, C. m., Kaiser, A., Irvine, J. t. s., 2001. Niobia Based Rutile Materials as SOFC Anodes. Fuel Cells 1, 249–255. doi:10.1002/1615-6854(200112)1:3/4<249::AID-FUCE249>3.0.CO;2-A
Reisman, A., Holtzberg, F., 1959. Further Comments on the Polymorphism of Nb2O5. The High Temperature Metastable Phaseε. Journal of the American Chemical Society 81, 3182–3184. doi:10.1021/ja01522a003
Richter, K.W., Flandorfer, H., Franzen, H.F., 2001. On the stability of hexagonal Ge7Nb10. Journal of Alloys and Compounds 320, 87–92. doi:10.1016/S0925-8388(00)01499-7
Salt, D.J., Hornung, G., 1967. Synthesis and X-Ray Study of Hafnium Silicate. Journal of the American Ceramic Society 50, 549–550. doi:10.1111/j.1151-2916.1967.tb14993.x
Samsonov, G.V., 1973. The Oxide handbook. IFI/Plenum.
Sato, J., Omori, T., Oikawa, K., Ohnuma, I., Kainuma, R., Ishida, K., 2006. Cobalt-Base High-Temperature Alloys. Science 312, 90–91. doi:10.1126/science.1121738
Schachner, H., Cerwenka, E., Nowotny, H., 1954. Neue Silizide vom M5Si3-Typ mitD 88-Struktur. Monatshefte für Chemie 85, 245–254. doi:10.1007/BF00900443

Schäfer, H., Gruehn, R., Schulte, F., 1966a. The Modifications of Niobium Pentoxide. Angewandte Chemie International Edition in English 5, 40–52. doi:10.1002/anie.196600401
Schäfer, H., Gruehn, R., Schulte, F., 1966b. Die Modifikationen des Niobpentoxids. Angewandte Chemie 78, 28–41. doi:10.1002/ange.19660780104
Schlesinger, M.E., Okamoto, H., Gokhale, A.B., Abbaschian, R., 1993. The Nb-Si (Niobium-Silicon) system. JPE 14, 502–509. doi:10.1007/BF02671971
Schulz, W.W., Wentzcovitch, R.M., 1993. Electronic band structure and bonding in Nb3O3. The American Physical Society 48, 16986–16991.
Seybolt, A., 1954. Solid Solubility of O2 in Nb. Journal of Metals 774.
Shah, D.M., 1992. MoSi2 and other silicides as high temperature structural materials, in: Superalloys 1992: Proceedings of the Seventh International Symposium on Superalloys. pp. 409–422.
Shao, G., 2005. Thermodynamic modelling of the Cr–Nb–Si system. Intermetallics 13, 69–78. doi:10.1016/j.intermet.2004.06.003
Smith, J.F., 1981. The Si–V (Silicon-Vanadium) system. Bulletin of Alloy Phase Diagrams 2, 42–48. doi:10.1007/BF02873702
Spyridelis, J., Delavignette, P., Amelinckx, S., 1967. On the Superstructures of Ta2O5 and Nb2O5. physica status solidi (b) 19, 683–704. doi:10.1002/pssb.19670190220
Steinmetz, J., Roques, B., 1977. Une famille de siliciures ternaires isotypes de V6Si5: (T, T′)6Si5 OÙ T = V, Cr, Mn ET T′ = Ti, Nb, Ta. Journal of the Less Common Metals 52, 247–258. doi:10.1016/0022-5088(77)90006-6
Stringer, J., Rosenfield, A.R., 1963. Interstitial Solid Solutions In Body-Centred Cube Metals. Nature 199, 337–339. doi:10.1038/199337a0
Su, L., Jia, L., Weng, J., Hong, Z., Zhou, C., Zhang, H., 2014a. Improvement in the oxidation resistance of Nb–Ti–Si–Cr–Al–Hf alloys containing alloyed Ge and B. Corrosion Science 88, 460–465. doi:10.1016/j.corsci.2014.08.006
Su, L., Jia, L., Weng, J., Hong, Z., Zhou, C., Zhang, H., 2014b. Improvement in the oxidation resistance of Nb–Ti–Si–Cr–Al–Hf alloys containing alloyed Ge and B. Corrosion Science 88, 460–465. doi:10.1016/j.corsci.2014.08.006
Subramanian, P.R., Mendiratta, M.G., Dimiduk, D.M., 1994. Microstructure and Mechanical Behaviour of Nb-Ti Base Beta + Silicide Alloys. Materials Research Society Symposium Proceedings 322, 491–502.
Suzuki, A., DeNolf, G.C., Pollock, T.M., 2007. Flow stress anomalies in γ/γ′ two-phase Co–Al–W-base alloys. Scripta Materialia 56, 385–388. doi:10.1016/j.scriptamat.2006.10.039
Suzuki, A., Pollock, T.M., 2008. High-temperature strength and deformation of γ/γ′ two-phase Co–Al–W-base alloys. Acta Materialia 56, 1288–1297. doi:10.1016/j.actamat.2007.11.014
Takasugi, T., Yoshida, M., Hanada, S., 1996. Deformability improvement in C15 NbCr2 intermetallics by addition of ternary elements. Acta Materialia 44, 669–674. doi:10.1016/1359-6454(95)00174-3
Taylor, A., Doyle, N.J., 1967. The solid-solubility of oxygen in Nb and Nb-rich Nb-Hf, Nb-Mo and Nb-W alloys: Part I: the Nb-O system. Journal of the Less Common Metals 13, 313–330. doi:10.1016/0022-5088(67)90140-3
Terao, N., 1965. Structure des Oxydes de Niobium: Transformation de Structure du Nb_2O_5-γ en Nb_2O_5-α et la Formation du NbO_2. Japanese Journal of Applied Physics 4, 8–15. doi:10.1143/JJAP.4.8
Terao, N., 1963. Structures des Oxydes de Niobium. Japanese Journal of Applied Physics 2, 156–174. doi:10.1143/JJAP.2.156

Thoma, D.J., Perepezko, J.H., 1992. An experimental evaluation of the phase relationships and solubilities in the Nb---Cr system. Materials Science and Engineering: A 156, 97–108. doi:10.1016/0921-5093(92)90420-6
Thomas, K.S., Varma, S.K., 2015a. Oxidation response of three Nb–Cr–Mo–Si–B alloys in air. Corrosion Science 99, 145–153. doi:10.1016/j.corsci.2015.06.026
Thomas, K.S., Varma, S.K., 2015b. Effects of Mo/Si Ratio Inversion on the Oxidation of Nb-Cr-Mo-Si-B Alloys. JOM 67, 2646–2652. doi:10.1007/s11837-015-1615-1
Thomas, K.S., Varma, S.K., 2013. A Comparison of Static and Cyclic Long-Term Oxidation of Two Nb-Cr-Mo-Si-B Alloys. Metall and Mat Trans A 45, 1124–1135. doi:10.1007/s11661-013-1797-5
Titus, M.S., Suzuki, A., Pollock, T.M., 2012. Creep and directional coarsening in single crystals of new γ–γ′ cobalt-base alloys. Scripta Materialia 66, 574–577. doi:10.1016/j.scriptamat.2012.01.008
Toker, N.Y., Darken, L.S., Muan, A., 1991. Equilibrium phase relations and thermodynamics of the Cr-0 system in the temperature range of 1500 °C to 1825 °C. Metallurgical Transactions B 22, 225–232. doi:10.1007/BF02652487
Varma, S.K., Parga, C., Amato, K., Hernandez, J., 2010. Microstructures and high temperature oxidation resistance of alloys from Nb–Cr–Si system. Journal of Materials Science 45, 3931–3937. doi:10.1007/s10853-010-4458-8
Vasudévan, A.K., Petrovic, J.J., 1992. A comparative overview of molybdenum disilicide composites. Materials Science and Engineering A 155, 1–17.
Vazquez, A., Varma, S.K., 2011. High-temperature oxidation behavior of Nb–Si–Cr alloys with Hf additions. Journal of Alloys and Compounds 509, 7027–7033. doi:10.1016/j.jallcom.2011.02.174
Venkatraman, M., Neumann, J.P., 1986. The Cr−Nb (Chromium-Niobium) system. Bulletin of Alloy Phase Diagrams 7, 462–466. doi:10.1007/BF02867811
Ventura, J., Varma, S., 2009. The oxidation resistance of Nb-20Mo-15Si-5B-20Cr up to 1,300°C. JOM Journal of the Minerals, Metals and Materials Society 61, 72–75. doi:10.1007/s11837-009-0108-5
Villars, P., Calvert, L.D., 1991. Pearsons Handbook of Crystallographic Data for Intermetallic Phases, 2nd edition. ed. ASM International, Ohio.
Voglewede, B., Rangel, V.R., Varma, S.K., 2012. The effects of uncommon silicides on the oxidation behavior of alloys from the Nb–Cr–Si system. Corrosion Science 61, 123–133. doi:10.1016/j.corsci.2012.04.029
Wadsley, A.D., 1961a. Mixed oxides of titanium and niobium. II. The crystal structures of the dimorphic forms Ti2Nb10O29. Acta Crystallographica 14, 664–670. doi:10.1107/S0365110X6100200X
Wadsley, A.D., 1961b. Mixed oxides of titanium and niobium. I. Acta Cryst, Acta Crystallogr 14, 660–664. doi:10.1107/S0365110X61001996
Waldner, P., Eriksson, G., 1999. Thermodynamic modelling of the system titanium-oxygen. Calphad 23, 189–218. doi:10.1016/S0364-5916(99)00025-5
Wallwork, G.R., Jenkins, A.E., 1959. Oxidation of Titanium, Zirconium, and Hafnium. Journal of The Electrochemical Society 106, 10–14. doi:10.1149/1.2427248
Westbrook, J.H., Wood, D.L., 1964. "PEST" degradation in beryllides, silicides, aluminides, and related compounds. Journal of Nuclear Materials 12, 208–215. doi:10.1016/0022-3115(64)90142-4
Wriedt, H.A., Murray, J.L., 1987. The N-Ti (Nitrogen-Titanium) system. Bulletin of Alloy Phase Diagrams 8, 378–388. doi:10.1007/BF02869274

Wrledt, H.A., 1990. The O-Si (Oxygen-Silicon) system. Bulletin of Alloy Phase Diagrams 11, 43–61. doi:10.1007/BF02841583
Yan, H.-Y., Vorontsov, V.A., Coakley, J., Jones, N.G., Stone, H.J., Dye, D., 2012. Quaternary Alloying Effects and the Prospects for a New Generation of Co-Base Superalloys, in: Huron, E.S., Reed, R.C., Hardy, rk C., Mills, M.J., Montero, R.E., Portella, P.D., Telesman, J. (Eds.), Superalloys 2012. John Wiley & Sons, Inc., pp. 705–714. doi:10.1002/9781118516430.ch78
Yang, Y., Bewlay, B., Chang, Y., 2007. Liquid-Solid Phase Equilibria in Metal-Rich Nb-Ti-Hf-Si Alloys. Journal of Phase Equilibria and Diffusion 28, 107–114. doi:10.1007/s11669-006-9000-y
Yang, Y., Chang, Y.., Zhao, J.-C., Bewlay, B.., 2003. Thermodynamic modeling of the Nb–Hf–Si ternary system. Intermetallics 11, 407–415. doi:10.1016/S0966-9795(03)00021-9
Yao, D., Cai, R., Zhou, C., Sha, J., Jiang, H., 2009. Experimental study and modeling of high temperature oxidation of Nb-base in situ composites. Corrosion Science 51, 364–370. doi:16/j.corsci.2008.11.004
Zelenitsas, K., Tsakiropoulos, P., 2006a. Study of the role of Ta and Cr additions in the microstructure of Nb-Ti-Si-Al in situ composites. Intermetallics 14, 639–659. doi:10.1016/j.intermet.2005.10.005
Zelenitsas, K., Tsakiropoulos, P., 2006b. Effect of Al, Cr and Ta additions on the oxidation behaviour of Nb-Ti-Si in situ composites at 800 °C. Materials Science and Engineering: A 416, 269–280. doi:10.1016/j.msea.2005.10.017
Zelenitsas, K., Tsakiropoulos, P., 2005. Study of the role of Al and Cr additions in the microstructure of Nb-Ti-Si in situ composites. Intermetallics 13, 1079–1095. doi:10.1016/j.intermet.2005.02.002
Zhang, S., Guo, X., 2015a. Effects of Cr and Hf additions on the microstructure and properties of Nb silicide based ultrahigh temperature alloys. Materials Science and Engineering: A 638, 121–131. doi:10.1016/j.msea.2015.04.003
Zhang, S., Guo, X., 2015b. Effects of Cr and Hf additions on the microstructure and properties of Nb silicide based ultrahigh temperature alloys. Materials Science and Engineering: A 638, 121–131. doi:10.1016/j.msea.2015.04.003
Zhao, J.-C., Bewlay, B.P., Jackson, M.R., 2001a. Determination of Nb–Hf–Si phase equilibria. Intermetallics 9, 681–689. doi:10.1016/S0966-9795(01)00057-7
Zhao, J.-C., Bewlay, B.P., Jackson, M.R., Chen, Q., 2000. Hf-Si binary phase diagram determination and thermodynamic modeling. Journal of Phase Equilibria, 21, 40–45. doi:10.1361/105497100770340408
Zhao, J.-C., Bewlay, B.P., Jackson, M.R., Peluso, L.A., 2001b. Alloying and phase stability in niobium silicide in-situ composites, in: Proceedings of the International Symposium on Structural Intermetallics. pp. 483–491.
Zhao, J.-C., Jackson, M.R., Peluso, L.A., 2003. Determination of the Nb–Cr–Si phase diagram using diffusion multiples. Acta Materialia 51, 6395–6405. doi:10.1016/j.actamat.2003.08.007
Zhao, J.-C., Jackson, M.R., Peluso, L.A., 2004a. Mapping of the Nb–Ti–Si phase diagram using diffusion multiples. Materials Science and Engineering: A 372, 21–27. doi:10.1016/j.msea.2003.08.008
Zhao, J.-C., Jackson, M.R., Peluso, L.A., 2004b. Mapping of the Nb-Cr-Ti phase diagram using diffusion multiples. Zeitschrift fuer Metallkunde/Materials Research and Advanced Techniques 95, 142–146.
Zifu, L., Tsakiropoulos, P., 2010. Study of the effects of Ge addition on the microstructure of Nb–18Si in situ composites. Intermetallics 18, 1072–1078. doi:10.1016/j.intermet.2010.02.012

This page is intentionally left blank.